10th edition

Copernicus Publications
Integrity by design. Driven by community.

STATE OF THE PLANET



COPERNICUS

OCEAN STATE REPORT

10th edition of the Copernicus Ocean State Report | 2026

PROGRAMME OF THE EUROPEAN UNION

Copernicus
Europe's eyes on Earth

Copernicus Marine Service

Implemented by
MERCATOR OCEAN INTERNATIONAL

About the Copernicus Ocean State Report

As part of the Copernicus Marine Service, the annual Copernicus Ocean State Report (OSR) launched in 2015 is the key tool of its ocean reporting framework. The OSR reports on the state, variability, and ongoing changes in the marine environment of the global ocean and the European regional seas over the past decades up to close to real time. Using observation-based (remote sensing, in situ) and ocean reanalysis data, the OSR provides a comprehensive 4-dimensional (latitude, longitude, depth, and time) analysis of the Blue, Green, and White Ocean. The OSR is intended to act as a reference, providing a unique ocean monitoring dashboard for the scientific community and for policy makers and others with decision making responsibilities.

Copernicus Marine Service

PROGRAMME OF THE EUROPEAN UNION

Copernicus Europe's eyes on Earth

Implemented by MERCATOR OCEAN INTERNATIONAL

STATE OF THE PLANET

About State of the Planet

State of the Planet (SP) is a journal dedicated to the publication of scientific synthesis reports and assessments on all subjects of the Earth and environmental sciences. In a rapidly changing world, expert-based assessments of academic findings curated for a wider audience to support decision making, science communication, education, and funder mandates are becoming more and more widespread. Such reports are extensive science community efforts offering timely, state-of-the-art insight into a specific field of the Earth sciences. State of the Planet is open to any reporting and assessment initiative by (inter-) governmental agencies, environmental services, learned societies or associations of researchers that aim to publish on a regular basis.

Copernicus Publications
Integrity by design. Driven by community.

publications@copernicus.org
http://publications.copernicus.org

This document was produced with funding by the European Union. Views and opinions expressed are however those of the author(s) only and the European Commission cannot be held responsible for any use which may be made of the information contained therein.

Cover photo: "Where the Oceans Collide", by Ali Osman Acar

von Schuckmann, K., Grégoire, M., Brasseur, P., Garric, G., Karstensen, J., Lionello, P., Marcos, M., Poulain, P.-M., and Staneva, J. (Eds.): 10th edition of the Copernicus Ocean State Report (OSR10), Copernicus Publications, State Planet, 7-osr10, https://doi.org/10.5194/sp-7-osr10, 2026.

State Planet, 7-osr10, 2, 2026
https://doi.org/10.5194/sp-7-osr10-2-2026
© Author(s) 2026. This work is distributed under
the Creative Commons Attribution 4.0 License.

Ocean changes and the impacts in the Polar Regions

Karina von Schuckmann[1], Flora Gues[2,1], Mahé Butel[1], Gilles Garric[1], Alvaro de Pascual[3], Axel Alonso Valle[3], Aurélien Liné[1], and Lorena Moreira Mendez[3]

[1]Mercator Ocean international, Toulouse, France
[2]CELAD, Toulouse, France
[3]Nologin Oceanic Weather Systems, Madrid, Spain

Correspondence: Karina von Schuckmann (karina.von.schuckmann@mercator-ocean.fr)

Published: 30 September 2026

Abstract. Covering about 20 % of the global ocean, the polar ocean areas are among the most sensitive regions of the Earth climate system, where today climate change is reshaping processes that influence global circulation, sea level, and climate far beyond the poles. Here, we develop an ocean narrative that integrates physical, ecological, and societal indicators, to illustrate polar ocean change. Across the region defined by the Arctic Monitoring and Assessment Programme (AMAP), which is a key scientific framework supporting environmental assessments of the Arctic Council, combined sea surface and sea-ice surface temperature has increased at an average rate of 1 °C per decade over 1982–2024, equivalent to approximately 4.2 °C of warming over the observational period. Strongest warming rates exceeding 1 °C per decade observed in the Large Marine Ecosystems (LMEs) Kara Sea, East Siberian and Laptev Sea, Barent Sea, Beauford Sea, Chukchi Sea, and Arctic Ocean. All Arctic polar LMEs with seasonal sea-ice cover have experienced sea-ice decline over the 1982–2024. LMEs, an ecologically defined framework that supports coordinated management of fisheries, biodiversity, habitat conservation, and other shared marine resources, show the strongest sea-ice cover losses in the Hudson Bay, Barents Sea, East Greenland Shelf, Chukchi Sea and Kara Sea. Also, areas of substantial sea-ice retreat consistently coincide with rapid coastal erosion in the Arctic, as sea-ice loss increases the exposure of Arctic coastlines to waves action, thereby further exacerbating coastal erosion and increasing risks to infrastructure and coastal communities. In the Southern Ocean, the spatial overlap between long-term sea-ice retreat and major penguin colonies illustrates a fundamental conservation challenge: the habitat supporting Southern Ocean biodiversity is itself changing. Effective biodiversity protection therefore requires both reducing local pressures through conservation and addressing the climate drivers of sea-ice loss through global mitigation. Together, these examples demonstrate that polar ocean change is not a collection of isolated environmental trends, but an interconnected transformation of physical systems, ecosystems, and societies, requiring integrated observations and coordinated climate, biodiversity, and ocean governance responses.

1 Introduction

The polar ocean areas occupy about 20 % of the global ocean surface, and they have a disproportionate influence on the trajectory of the Earth system (IPCC, 2019): they absorb and store large amounts of anthropogenic heat and carbon; they sustain the global overturning circulation that redistributes heat and carbon across the planet and shapes regional and global climate patterns; and they host some of the most rapidly changing components of the climate system, where strong feedbacks and potential tipping elements are concentrated. Consequently, changes in the polar ocean areas extend far beyond the high latitudes, influencing climate, sea level, and weather worldwide (IPCC, 2019), deeply affect Arctic communities and ecosystems (Baudry et al., 2026; Bronen, 2015; Bronen and Chapin, 2013; Deb and Bailey, 2023; Naik et al., 2026), and are crucial for local to global sustainability (Li et al., 2025). The growing recognition of the critical role of polar regions in the Earth system is reflected in the United Nations General Assembly's declaration of 2025–

Table 1. Products used and their documentation.

Product ref. No.	Product ID and type	Data access	Documentation
1	SEAICE_ARC_PHY_CLIMATE_L4_MY_011_016 Satellite observations (reprocessed)	E.U. Copernicus Marine Service Information (2021)	QUID: Karagali et al. (2025a) PUM: Karagali et al. (2025b)
2	Global Large Marine Ecosystems Expert-delineated ecological boundary	IW-LEARN (2020)	Sherman (2005)
3	Arctic AMAP assessment area Expert-delineated administrative-biogeographic boundary	Steenhuisen and Wilson (2013)	AMAP (1998)
4	SEAICE_GLO_SEAICE_L4_REP_OBSERVATIONS_011_009 Satellite observations	E.U. Copernicus Marine Service Information (2026)	QUID: Eastwood and Wettre (2026) PUM: Sørensen et al. (2026)
5	SST_GLO_SST_L4_REP_OBSERVATIONS_010_011 Satellite observations (reprocessed)	E.U. Copernicus Marine Service Information (2025)	QUID: Worsfold et al. (2026) PUM: Worsfold et al. (2022)
6	Arctic Coastal Dynamics (ACD) coastal geomorphology Expert-derived clasification (survey and remote sensing)	Lantuit et al. (2020)	Lantuit et al. (2012)
7	Permafrost extent for the Northern Hemisphere Physical model (satellite-forced)	Westermann et al. (2025)	Obu et al. (2019)
8	Building footprints Satellite and crowdsourced fusion	Manos and Witharana (2025)	Manos et al. (2025)
9	Indigenous Peoples of the Arctic Community-consulted, participatory-edited boundaries	Fiske (2021)	Berkman et al. (2022)
10	Distribution of Adelie penguin Expert-derived species range map	IUCN (2020a)	IUCN (2020a)
11	Distribution of Emperor penguin Expert-derived species range map	IUCN (2020b)	IUCN (2020b)
12	Distribution of Adéline and Emperor penguins Multi-source biogeographic database (in-situ + remote sensing)	Che-Castaldo et al. (2023a)	Che-Castaldo et al. (2023b)
13	Maritime Boundaries Geodatabase: High Seas Expert-delineated boundary	Flanders Marine Institute (VLIZ), Belgium (2024)	Claus et al. (2014)
14	Statistical areas, subareas and divisions Expert-delineated boundary	Commission for the Conservation of Antarctic Marine Living Resources (2026)	CCAMLR (2017), CCAMLR Secretariat (2026)

2034 as the "Decade of Action for Cryospheric Sciences", highlighting the increasing importance of coordinated scientific efforts and policy responses to understand and address cryospheric changes (Luo and Alverson, 2025).

The scale of the buffering role through polar ocean areas is remarkable: the Southern Ocean alone is responsible for about 70 ± 30 % of the anthropogenic heat absorbed by the world ocean each year, and about half of the uptake of anthropogenic carbon (e.g., Cheng et al., 2022; Frölicher et al., 2015; Gruber et al., 2009; Khatiwala et al., 2013; SOCHIC et al., 2023). However, this buffering capacity is coupled to a rapidly changing cryosphere: warming polar ocean waters contribute to ice-shelf thinning and glacier discharge, enhancing continental ice loss and sea-level rise (Rignot et al., 2019, 2026; Slater et al., 2021). Also, ocean warming and more frequent Arctic marine heatwaves are transforming marine food webs, species distributions, fisheries, and biodiversity, with consequences for Indigenous communities and Arctic economies, necessitating targeted conservation and adaptive strategies (He et al., 2024).

Both polar ocean areas host some of the most rapidly changing components of the climate system. The Arctic has warmed nearly six times faster than the global mean since 1980, with 2025 bringing the warmest autumn on record, and summer sea-ice extent declining at more than 10 % per decade since satellite records began (Englyst et al., 2026; WMO, 2026; Zhou et al., 2024). In addition, the Arctic ocean is experiencing a transformation from the northward

influx of warmer, saltier Atlantic water (so-called Atlantification), which is reshaping the Arctic Ocean itself (Årthun et al., 2025; Polyakov et al., 2025; Wang et al., 2024). In the Antarctic, a regime shift in 2016 has driven sea-ice extent far below its natural range of variability (Mercator Ocean international, 2026), and, in some respects, is more abrupt, nonlinear, and potentially irreversible than Arctic sea-ice loss (Abram et al., 2025; Hobbs et al., 2024; Purich and Doddridge, 2023). A decline in sea-ice formation linked to the observed regime shift has been suggested as a primary cause for an observed 30 % slowdown in bottom water production in the Weddell Sea since 1992 (Kusahara and Tatebe, 2025; Spira et al., 2026; Wu et al., 2025; Zhang et al., 2022; Zhou et al., 2023), known as a key process driving the Antarctic Overturning Circulation (Abram et al., 2025). Antarctic and Southern Ocean ecosystems are experiencing regime shifts as environmental change transforms habitats and pushes species beyond physiological limits (Griffiths et al., 2024). Arctic marine ecosystems are undergoing comparable transformations, as sea-ice loss and the Atlantification restructure habitats, disrupt historical pelagic-benthic coupling, and push species toward or beyond their thermal limits (Stern, 2025).

The polar ocean areas also host major climate feedbacks that can amplify or modulate future Earth system change. The sea-ice albedo feedback is one of the most prominent examples: the loss of reflective sea ice increases solar absorption by the ocean, amplifying regional and global warming (Goessling et al., 2025; Riihelä et al., 2021; Zhou et al., 2024). Another feedback includes ice-sheet melt that freshens surrounding ocean surface waters, affecting stratification, suppressing deep-water formation, and increasing basal melting of ice shelves (Lambert et al., 2025; Silvano et al., 2025; Zhang et al., 2025). Another important process includes the atmosphere-ocean coupling and cloud feedback. Declining sea-ice cover favours the formation of low-level liquid clouds over newly exposed open water. These clouds trap outgoing surface radiation that would otherwise escape to space, warming the surface and slowing sea-ice regrowth, thereby reinforcing sea-ice loss (Arouf et al., 2024). Together, these feedbacks illustrate how polar ocean changes can modify the response of the Earth system to ongoing warming, with consequences extending well beyond the high latitudes.

The Arctic and Southern Ocean areas are critical arenas for international governance, science diplomacy, and multilateral cooperation, where environmental protection, resource management, scientific collaboration, and geopolitical interests converge to shape the stewardship of globally significant marine commons (Berkman, 2025; Gaffey et al., 2024; Jayaram, 2022; Szkarłat et al., 2025). Unlike most ocean basins, large parts of the Arctic Ocean and especially the Southern Ocean cannot be managed by a single nation. Their governance relies on a mosaic of international agreements, including the United Nations Convention on the Law of the Sea (United Nations, 1982a), the Antarctic Treaty (https://www.ats.aq/index_e.html, last access: 14 July 2026), including the Commission for the Conservation of Antarctic Marine Living Resources (CCAMLR, https://www.ccamlr.org/en/organisation/home-page, last access: 14 July 2026), and the Arctic Council (https://arctic-council.org/, last access: 14 July 2026). As climate change reshapes these regions, governance increasingly requires multi-functional arrangements through international coordination across jurisdictions, sectors, and scientific disciplines, and genuine participation of nations, including Indigenous communities (Gaffey et al., 2024; IPCC, 2019, 2023; Young, 2016). This includes the need to track progress based on available science, enhancing data sharing practices, and securing long-term financing to sustain research (Gaffey et al., 2024).

Climate change is creating new governance challenges, challenging regional cooperation with a problem that is global by nature (Argüello and Rafaly, 2023; Nanni et al., 2024; Stokke, 2021; Wood-Donnelly, 2023; Young, 2016). In the Arctic for example, rapid sea-ice decline is opening new shipping routes, expanding access to fisheries, hydrocarbons, minerals, and tourism, while simultaneously increasing environmental risks (Crate and Nuttall, 2024). Notably, the Arctic Shipping recorded a 40 % increase from 2013 to 2025, with this growth coinciding with diminishing sea-ice (PAME, 2026). These changes are transforming the Arctic from a relatively isolated region into a globally connected governance space, where conservation, economic development, Indigenous and Local Peoples rights, maritime law, and geopolitical interests must be balanced (Crate and Nuttall, 2024; IPCC, 2019). In the Antarctic Ocean, rapid environmental change, particularly sea-ice decline and ecosystem shifts, is increasing accessibility to the region, and enabling expanded shipping, fisheries, and tourism, while simultaneously increasing environmental risks and governance challenges (Chavez-Molina et al., 2023; Constable, 2022, 2025; IPCC, 2019). Across both poles, these dynamics reflect a fragmented, multilevel governance landscape, where polar governance capacity has strengthened in recent years, but not rapidly or robustly enough to keep pace with the cascading risks and new external interests reshaping both regions (IPCC, 2019).

Together, these interconnected functions position the polar ocean areas as critical components of the Earth system, where physical changes translate into consequences for climate, ecosystems and societies worldwide. As Arctic and Antarctic change increases and governance challenges become increasingly interconnected, sustained ocean observations, indicators, and assessments are essential to understand emerging risks, track system responses, and support effective ocean governance. Here, we provide 3 themes for the polar ocean narrative, with focus on the ocean areas relevant for the polar regions, and their wider implications for the Earth system, ecosystems, and societies. The first theme sets the focus on Arctic Ocean change through the lens of sea-ice decline and surface warming, across different regions relevant for regional to international ocean governance. The sec-

ond explores how Arctic Ocean change translates into societal exposure, including coastal erosion, permafrost change, and communities. The third focuses on the Southern Ocean, where changes in sea ice, marine ecosystems, and biodiversity are closely linked to questions of conservation, climate change mitigation, and international governance.

2 Method

Ocean change is increasingly monitored and reported on through a growing range of physical, biological, and chemical ocean indicators, including ocean warming, sea-level rise, deoxygenation, and acidification. At the same time, socioeconomic datasets provide detailed information on, for example, human vulnerability, economic dependence, protection efforts, or governance capacity. However, these two domains are often analysed separately, making it difficult to understand how changes in the ocean translate into societal impacts and opportunities. The concept of ocean narratives addresses this gap, as they establish scientific linkages between ocean and socioeconomic indicators within a specific thematic context. By combining these datasets and scientific knowledge, the approach helps identify where ocean changes may be having the most impact on human well-being, economic development, and environmental sustainability.

Ocean narratives are a new concept to connect ocean data and indicators to human relevance. The concept has been introduced by an international and multidisciplinary team of scientists (Von Schuckmann et al., 2026), and implemented for the first time in the 9th Copernicus Ocean State Report (von Schuckmann et al., 2025a, b). Ocean narratives create a systematic bridge between ocean science, societal outcomes, and evidence-based knowledge transfer. They are based on the combination of ocean indicators such as ocean warming, sea level rise, ocean acidification, or sea ice change, together with socioeconomic data relevant to specific themes or regions. A key innovation of the framework is its integration of data-driven exploration with evidence-based interpretation. Spatial and temporal patterns of ocean change revealed by indicators can highlight potential socioeconomic relationships and emerging areas of concern, while peer-reviewed scientific literature is used to validate and explain these connections. Therefore, the narrative development follows a strict evidence-based approach: links between ocean change and socioeconomic data are only integrated in the ocean narrative when peer-reviewed literature shows scientifically quantified relationships. This ensures that narratives are both scientifically robust and accessible to decision-makers.

The approach offers several benefits. First, ocean narratives translate complex ocean science into societally relevant insights, as it provides a transparent framework for connecting environmental and socioeconomic information (see Table 1). Second, the approach helps to raise awareness on regions, sectors, and communities, that may be particularly exposed or resilient to ocean change. Third, ocean narratives can support policy development, as they link ocean conditions to tangible societal outcomes. And fourth, they enable communication of ocean knowledge and change through compelling, evidence-based stories, that resonate with diverse audiences. In other words, ocean narratives can serve as a bridge between observation and action, helping synthesize large, and often disconnected, datasets into coherent knowledge that can inform sustainable ocean governance, and into informed decision-making. By improving the accessibility and relevance of scientific information, ocean narratives can contribute to making data and science more actionable.

The narrative presented here focusses on the polar ocean areas, i.e. the Arctic and Antarctic ocean. This approach highlights critical questions: How are Arctic and Southern Ocean conditions changing in different regions relevant for regional to international ocean governance? How are these physical changes translating into consequences for ecosystems, biodiversity, and societies, including coastal communities in polar regions? How can observations and indicators support the understanding, conservation, and governance of rapidly changing polar ocean environments, including Areas Beyond National Jurisdictions (ABNJs) and shared global commons? By connecting physical ocean change with ecological responses and societal dimensions, ocean narratives aim to provide an integrated understanding of how polar ocean transformations unfold to help policymakers, practitioners, and scientists to move towards a more comprehensive view of the links between ocean change, ecosystem resilience and governance challenges. All data used for the narrative are documented in Product Table 1, together with information on data access and related references.

3 The Ocean Narrative

3.1 Sea ice extent and surface warming in the Arctic

Sea ice plays a major role in the Arctic Ocean due to its large cooling influence from its high reflectivity (IPCC, 2019). Sea ice supports all four ecosystem service categories (Steiner et al., 2021): supporting services, through habitat and nurseries for species such as Arctic cod and Antarctic krill; provisioning services, through harvesting and medicinal and genetic resources; cultural services, through Indigenous and local knowledge, identity, tourism, and research; and regulating services, through light regulation, biogenic aerosol production, halogen oxidation, and greenhouse gas exchange. Sea ice is not only ecologically, but socially and culturally foundational for Indigenous and Local Peoples. Millions of people live in close contact with the cryosphere in the Arctic, and sea ice underpins traditional subsistence practices, while also carrying deep cultural, spiritual, and identity-related significance (IPCC, 2019)(Steiner et al., 2021).

Arctic sea ice has dramatically retreated and thinned in recent decades, both of which are expected to continue under climate change (IPCC, 2021). These ongoing changes in the polar regions have strong impacts on sea-ice ecosystems and associated ecosystem services (Steiner et al., 2021). Decreasing sea ice reduces the surface albedo, resulting in more surface solar absorption, which amplifies surface warming and drives additional ice melt, known as the sea-ice albedo feedback (e.g., Zhang et al., 2025). Loss of Arctic sea ice is reducing habitat for key species and directly affecting the livelihoods of Indigenous communities and cultures (IPCC, 2019), while permafrost thaw, sea-level rise, and reduced sea-ice protection have already damaged or destroyed numerous cultural heritage sites across Arctic regions (IPCC, 2023). These changes are increasingly threatening Arctic livelihoods, culture, identity, health, and food security, with risks amplified for those most reliant on the environment for subsistence (IPCC, 2023). Traditional knowledge from I nupiaq and Yupik hunters in northern Alaska further documents how changing sea-ice patterns are altering the behaviour and accessibility of marine mammals, that remain a key subsistence food source, directly affecting hunting practices developed over generations (Huntington et al., 2016).

Large Marine Ecosystems (LMEs) are ecologically rather than politically defined ocean regions. They are relatively large regions of coastal water (200 000 km^2 or greater) thus defined by ecological criteria, such as bathymetry or productivity (Sherman, 2014). LMEs cut across national boundaries and provide a scientific basis for transboundary, ecosystem-based management that links ocean knowledge directly to action on, for example, fisheries, pollution, habitat restoration, and biodiversity conservation (Sherman, 2014). Arctic LMEs were identified as an Arctic marine strategic plan following its decision to adopt ecosystem-based management, and were endorsed by the Arctic Council Ministers in 2006 (PAME, 2013). The map of Arctic LMEs was revised in 2013 to better respect ecological features and integrate all zones which are included in the Arctic Council work. In total, 18 LMEs have been identified in the Arctic (PAME, 2013). We address here 13 out of the 18 LMEs as defined by the Arctic Council, as the remaining 5 are currently only partly or not covered by the regional product for surface temperature (Fig. 1). Except for Iceland Shelf and Norwegian shelf, where seasonal sea ice is generally absent, polar LMEs with seasonal sea-ice cover have experienced sea-ice decline over the period 1982–2024, reaching in some areas up to −16 % per decade relative to the climatology 1993–2010 (Fig. 1b). LMEs most affected by sea ice loss include the Hudson Bay (−16 % per decade), Barent Sea (−12 % per decade), East Greenland Shelf (−8 % per decade), Chukchi Sea and the Kara Sea (−7 % per decade) (Fig. 1b). Sea ice loss of −4 % per decade is reported for the AMAP area over the period 1982–2024.

The sea-ice albedo feedback is central to the Arctic amplification, where near-surface air temperature change over the Arctic are enhanced relative to lower latitude (Previdi et al., 2021), and well established in ocean sea surface and sea ice surface temperature (SST, Fig. 1). SST provides crucial insight into the mechanisms underlying extreme weather and climate events in the Arctic, as well as broader oceanic and atmospheric teleconnections linking the Arctic to lower latitudes (Carvalho and Wang, 2020). Arctic Ocean SST is strongly influenced by sea ice and related melt water, brine rejection, continental runoff, and upward heat fluxes from the deeper warm ocean (Stroh et al., 2015). Warmer SSTs directly shape marine ecosystems, influencing the timing and development of primary production cycles, the availability of habitat, and the occurrence of harmful algal blooms, with cascading effects on fisheries, food security, and the communities that depend on them (IPCC, 2019). Rising Arctic SST, together with associated sea-ice loss and habitat change, is contributing to significant northward shifts in the distribution of commercially and culturally important fish species, with direct consequences for fisheries management and the Indigenous and local communities who rely on these resources (Mueter et al., 2021). Sea surface and sea ice surface temperature is increasing in all Arctic LMEs included in this study (LME Hudson Bay excluded due to data product limitations, see Fig. 1), and has increased on average in the AMAP region at a rate of 1 °C per decade over the period 1982–2024, which accumulates to 4.2 °C on average since 1982 (Fig. 1). These values are consistent with the study of Englyst et al. (2026). LMEs most affected by strong increase in SST include the Kara Sea (1.68 °C per decade), East Siberian Sea and Laptev Sea (1.28 °C per decade), Barent Sea (1.23 °C per decade), Beaufort Sea (1.19 °C per decade), Chukchi Sea and Arctic Ocean (1.18 °C per decade) (Fig. 1b).

3.2 Arctic ocean change and human exposure

Sea ice loss also has consequences beyond the open ocean itself, extending to compound impacts on Arctic coasts through its role in coastal erosion. Rapid coastal erosion in the Arctic consistently coincides with substantial sea-ice retreat over the past four decades (Fig. 2). As sea ice retreats, it expands the fetch over which wind can generate waves and prolongs the open-water season, increasing the mechanical exposure of Arctic coastlines to wave action (Nielsen et al., 2022). This process compounds with permafrost thaw, which causes soil decohesion and slumping as the frozen ground that structurally binds coastal sediment disappears, and this compound effect drives coastal retreat rates, that have already increased by a factor of two or more across the Arctic in recent decades (Nielsen et al., 2022). Recent research shows that these hazards interact more severely in combination than previously understood. Particularly, accounting for the compound effects of permafrost thaw subsidence, sea-level rise, and erosion together projects 6 to 8 times more land loss along Alaska's Arctic Coastal Plain by 2100 than erosion alone would suggest, potentially damaging 40 %–65 % of infrastructure in present-day coastal villages (Creel et al.,

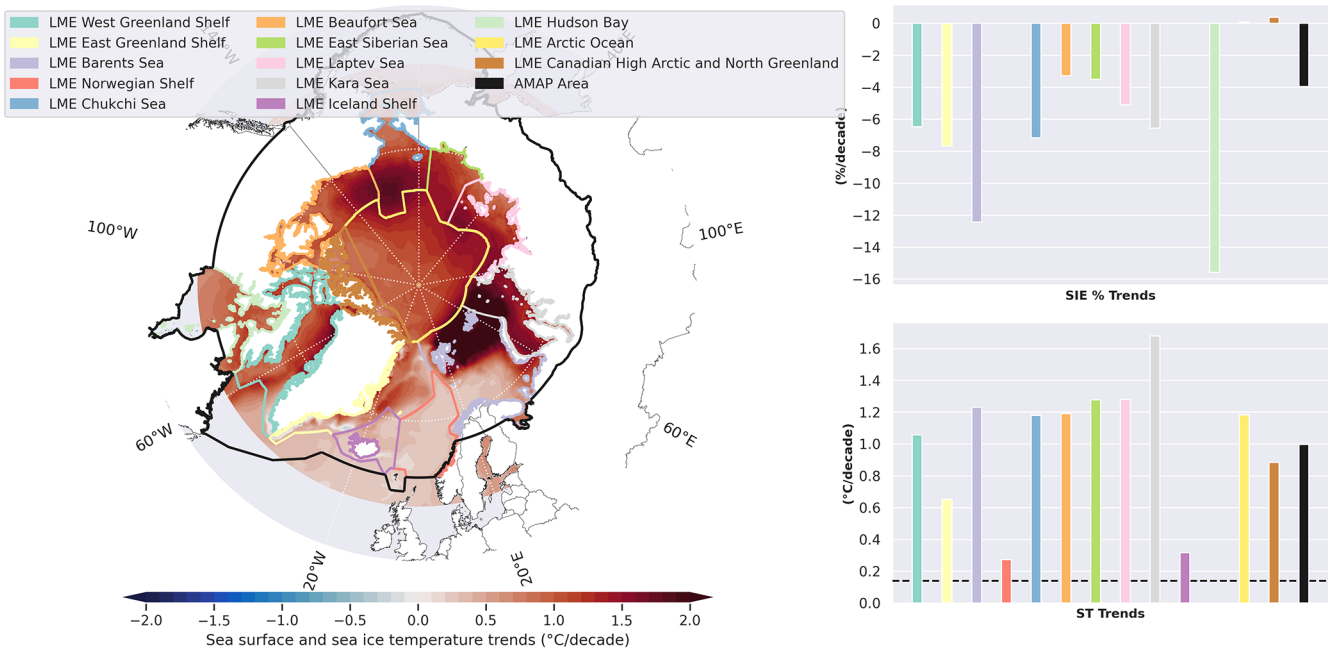


Figure 1. Physical state of the Arctic. **(a)** Map of the trend in combined sea and ice surface temperature anomalies for the Arctic Ocean over 1982–2024 (blue-red shading, based on product ref. no. 1), showing clearly how most of the region has heated up over more than four decades. The boundaries of the Large Marine Ecosystems (LMEs) in the Arctic are displayed on top (colored lines, based on product ref. no. 2), to allow an estimation and intercomparison of the differential warming in each zone. The work area of the Arctic Monitoring and Assessment Programme (AMAP) is also shown, enclosed by a solid black line (based on product ref. no. 3). **(b)** Trend per decade of the percentage of sea ice extent loss compared to the climatology (1993–2010) in each Polar LME and the AMAP area from 1982 to 2024 (based on product ref. no. 4). **(c)** Sea surface and sea ice surface temperature anomalies trends in Polar LMEs and the AMAP area over period 1982–2024, expressed as the average increase in temperature observed in each region per decade (based on product ref. no. 1). As reference, the value of the corresponding sea surface temperature anomalies trend at global scale (computed using product ref. no. 5) is indicated by the black dashed line. LMEs are ecologically rather than politically defined ocean regions. They are relatively large regions of coastal water (200 000 km^2 or greater) thus defined by ecological criteria, such as bathymetry or productivity (Sherman, 2014).

2024). Across the wider Arctic, 60 % of detected coastal infrastructure already sits in low-lying areas vulnerable to this compounding erosion and sea-level rise, underscoring the scale of the challenge facing coastal communities (Tanguy et al., 2024).

For many Arctic Indigenous and Local Peoples, sea ice is far more than a physical component of the environment, as it provides access to hunting grounds, supports food security, enables travel, and underpins cultural identity and knowledge systems (IPCC, 2019). The combined effects of declining sea ice, rising temperatures, increasing numbers of above-freezing days, and thawing permafrost are reducing the predictability and safety of travel, altering wildlife distributions and harvesting opportunities, and increasing risks to coastal settlements and traditional livelihoods (Grimmer et al., 2025; Hovelsrud et al., 2011; Huntington et al., 2022).

The annual number of days when Arctic surface waters exceed the seawater freezing point threshold (−1.8 °C) provides an integrated measure of changes in the seasonal sea-ice regime, as small shifts around this threshold can influence the timing and duration of sea-ice formation and persistence, with consequences for ocean–atmosphere exchanges, marine ecosystems, and human activities (Stroeve and Notz, 2018; Perovich et al., 2020; IPCC, 2019). All ocean areas adjacent to the Arctic coast show increasing trends in the annual number of days when conditions are above the seawater freezing point threshold (−1.8 °C), reflecting longer periods of warmer surface waters and reduced seasonal ice presence (Fig. 2). Trends range from approximately half a day per year to more than 3 d per year over the past four decades, with the strongest increases observed in the Barents Sea, Kara Sea, and Greenland Sea (Fig. 2). Over four decades, these trends result in an additional ∼ 20 to more than 120 d locally, with above-freezing conditions, compared with the beginning of the record in 1982, indicating a tremendous lengthening of the period during which Arctic waters remain exposed to warmer, ice-unfavourable conditions.

The impacts of Arctic change manifest differently across Indigenous and Local Peoples communities. For example, for Inuit Peoples across Canada, Alaska, and Greenland, declining and increasingly unpredictable sea ice is disrupting access to marine mammal hunting grounds and tradi-

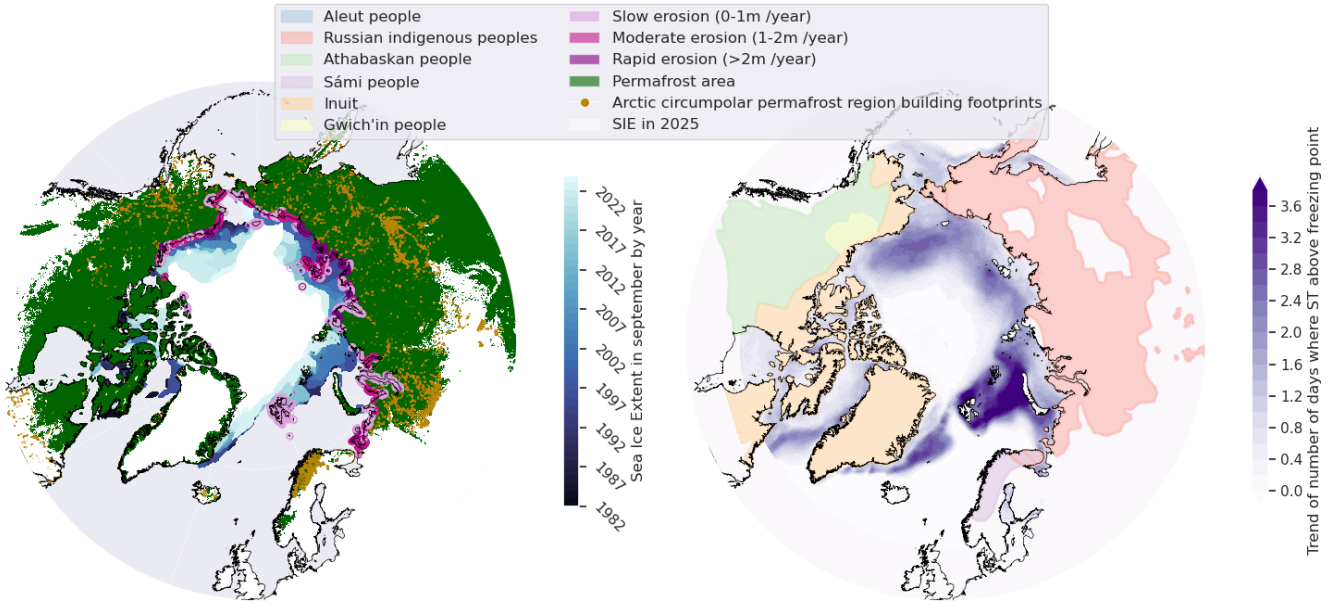


Figure 2. Arctic ocean change and human exposure. **(a)** Map of sea ice retreat and erosion in the Arctic and surrounding regions. The gradual reduction of the sea ice extent in the Arctic Ocean over the last decades is shown through the variation observed in the month of September from 1982 to 2025 (blue-white shaded area, based on product ref. no. 4). The prolonged presence of open waters along the bordering coastline is usually accompanied by an increase in local erosion rates (Lantuit et al., 2012) (pink-purple dots, based on product ref. no. 6). Inland, the sustained warming of the circumpolar region is inducing also a thawing of the permafrost (green area shows its total extent in 2023, based on product ref. no. 7), which, besides its effect on ecosystems, can cause severe damage to buildings erected on frozen ground due to foundation movement (Hjort et al., 2022): the zones that could be potentially affected by this are indicated on the map through their building footprints (brown dots, based on product ref. no. 8). The second map **(b)** indicates the trend of the number of days per year where the surface temperature is above the freezing point (−1.8 °C), computed from 1982 to 2024 (purple-shaded area; white area indicates that the temperatures are always below or above the freezing point; based on product ref. no. 1); it also shows the regions where the different Indigenous and Local Peoples of the Arctic live (coloured areas, based on product ref. no. 9).

tional travel routes, with direct consequences for food security, safety, and cultural practices (Ford et al., 2019; IPCC, 2019; Laidler and Ikummaq, 2008). Another example includes Yup'ik and I nupiat communities in Alaska that face similar challenges, as thinner and less predictable sea ice increasingly affects access to marine subsistence resources, and alters established patterns of travel and harvesting (Huntington et al., 2016; Meeker and Kettle, 2017).

As these environmental transitions evolve, Indigenous and Local communities face increasing challenges in maintaining traditional practices and livelihoods, highlighting the importance of integrating Indigenous and Local Peoples' knowledge systems with sustained environmental observations to inform adaptation and strengthen Arctic governance (Beaulieu et al., 2023; Bishop et al., 2026; Eerkes-Medrano and Huntington, 2021; Malik and Ford, 2025; Monakhova et al., 2026). Indigenous and Local Peoples knowledge is inseparable from culture: observing is stewardship, livelihood, and science all at once (Carroll, 2024; Carroll et al., 2020; Ladd et al., 2025).

3.3 Southern Ocean ecosystems, sea ice, and governance

Multilateral governance regimes, like the Antarctic Treaty System, play a central role in addressing complex, transboundary environmental problems, and their success depends heavily on effective exchange of knowledge between scientists and policymakers (Gardiner et al., 2025). The Antarctic treaty was signed in 1959, and entering into force in 1961, it set aside the region south of 60° S for peace, science, and international cooperation (The Antarctic Treaty, 1959). The Antarctic environmental conservation and protection is assured by the 1980 Convention on the Conservation of Antarctic Marine Living Resources (CCAMLR, entered into force in 1982; CCAMLR, 1980), and the 1991 Protocol on Environmental Protection to the Antarctic Treaty (the Madrid Protocol, entered into force in 1998). The Environmental Protocol of the Antarctic Treaty requires that the protection of the Antarctic environment and its ecosystems be a fundamental consideration in the planning and conduct of all activities in the Antarctic Treaty area, and, for example, bans mining and mineral exploitation except for scientific research (Antarctic Treaty Environmental Protocol, 1991).

CCAMLR governs an area of around 10 % of the world's ocean surface, and mandates conservation, but allows rational use, where fishing is permitted but under a strict, precautionary, ecosystem-based approach (Nocito and Brooks, 2023). Decision-making within CCAMLR, whose membership comprises 26 states and the European Union, operates by consensus. Decisions are codified as Conservation Measures, which are legally binding on all CCAMLR Member States. This science-based, precautionary approach directly influenced the design of the 2023 Agreement on the Conservation and Sustainable Use of Marine Biological Diversity of Areas Beyond National Jurisdiction (BBNJ Agreement) governing biodiversity in the high seas (Nocito and Brooks, 2023).

Today, the Southern Ocean is also a region of overlapping governance, where the Antarctic Treaty System and the newly established BBNJ framework may both have relevance for the conservation of marine biodiversity in areas beyond national jurisdiction (see Fig. 3). Since about 2016, negotiations on further Southern Ocean MPA proposals (e.g., East Antarctica, Weddell Sea, Antarctic Peninsula) have repeatedly failed to reach the consensus CCAMLR requires, leaving Southern Ocean MPA expansion effectively stalled for close to a decade (Nocito and Brooks, 2023). Against this backdrop, the 2023 adoption and 2026 entry into force of the BBNJ Agreement offers new momentum that CCAMLR can draw on to advance Southern Ocean protection (Haward, 2021; Nocito and Brooks, 2023). The Southern Ocean occupies an ambiguous position in both major global environmental conventions: it is formally excluded from Convention on Biological Diversity (CBD) assessments of progress toward its Strategic Plan for Biodiversity (Chown et al., 2017), and has no dedicated provisions within the UNFCCC process, leaving CCAMLR and the Antarctic Treaty System as the primary vehicles through which Southern Ocean conservation and climate-related action are pursued in practice (Chown et al., 2017; Constable, 2022; Lowther et al., 2022).

However, the Southern Ocean makes the case, more clearly than perhaps anywhere else, that climate and biodiversity action are two sides of the same problem. This interdependence becomes particularly evident where climate change directly alters the habitat that conservation policies seek to protect. Sea-ice-dependent species, such as the Emperor and Adélie penguin (Fig. 3), require both: (i) MPAs, advanced through the Antarctic Treaty System, and the emerging BBNJ framework, to reduce direct anthropogenic pressures, and (ii) the sea ice itself maintained, which requires deep emissions reductions under the Paris Agreement to limit long-term climate-driven sea-ice loss. These tracks are not alternatives but a single, intertwined agenda, and the Southern Ocean is where this relationship is particularly visible. For example, Emperor penguins, which breed exclusively on stable, shore-attached sea ice known as "fast ice", are especially vulnerable: record-low Antarctic sea ice in 2022 coincided with the first-ever recorded large-scale breeding failure, with four of five monitored colonies experiencing total breeding failure after early ice break-up, and modelling suggests over 90 % of emperor penguin colonies could become quasi-extinct by 2100 if current sea-ice loss rates persist (Fretwell et al., 2023; Fretwell and Trathan, 2021; Jenouvrier et al., 2021). The August-to-December window is especially relevant because it spans the most vulnerable phase of the breeding cycle of emperor penguins (Fig. 3): chicks hatch in July–August and only become waterproofed and ready to fledge by mid-December to early January. Since chicks cannot survive in open water before fledging, sea-ice persistence during this period is a critical determinant of breeding success. Changes in sea ice do not solely affect emperor penguins, but also other species such as Adélie penguins, whose access to the ocean and to prey is determined by the sea ice around their colonies (Quilestino-Olario, 2026). Although satellite-derived regional sea-ice extent does not directly measure fast-ice stability, it provides an important indicator of the surrounding sea-ice conditions that influence fast-ice persistence and colony viability (Aoki, 2017; Fretwell, 2024).

The spatial overlap between areas of sea ice retreat over the past 4 decades coincide with major pinguin colonies areas, particularly around the Antarctic Peninsula (Fig. 3), which illustrates how physical changes in the cryosphere are already translating into biological responses, providing one of the clearest examples of climate-driven ecosystem change anywhere on Earth. Emperor penguins provide one of the clearest biological examples of the consequences of sea-ice decline, but they are not an isolated case. Antarctic sea ice structures the entire Southern Ocean ecosystem, regulating primary production, krill recruitment, predator distributions, and the seasonal availability of habitat. Changes in sea-ice extent and duration therefore propagate across multiple trophic levels, from phytoplankton and Antarctic krill to fish, seals, whales, and seabirds, reshaping ecosystem functioning at the scale of the Southern Ocean. When climate alters the habitat itself, conservation and climate policy become inseparable. This dependence fundamentally changes the conservation challenge. Marine Protected Areas can reduce anthropogenic pressures from fishing, disturbance, and habitat degradation, but they cannot preserve sea-ice habitat itself. Conversely, climate mitigation alone cannot address local ecological pressures. Conserving Southern Ocean biodiversity therefore requires climate and biodiversity policies to operate together, making the Southern Ocean one of the clearest demonstrations that climate mitigation and biodiversity conservation cannot be pursued independently.

4 Conclusion

The three themes of the polar ocean narrative presented here illustrate that polar ocean change is not expressed through isolated environmental trends, but through interconnected transformations affecting physical systems, ecosystems and

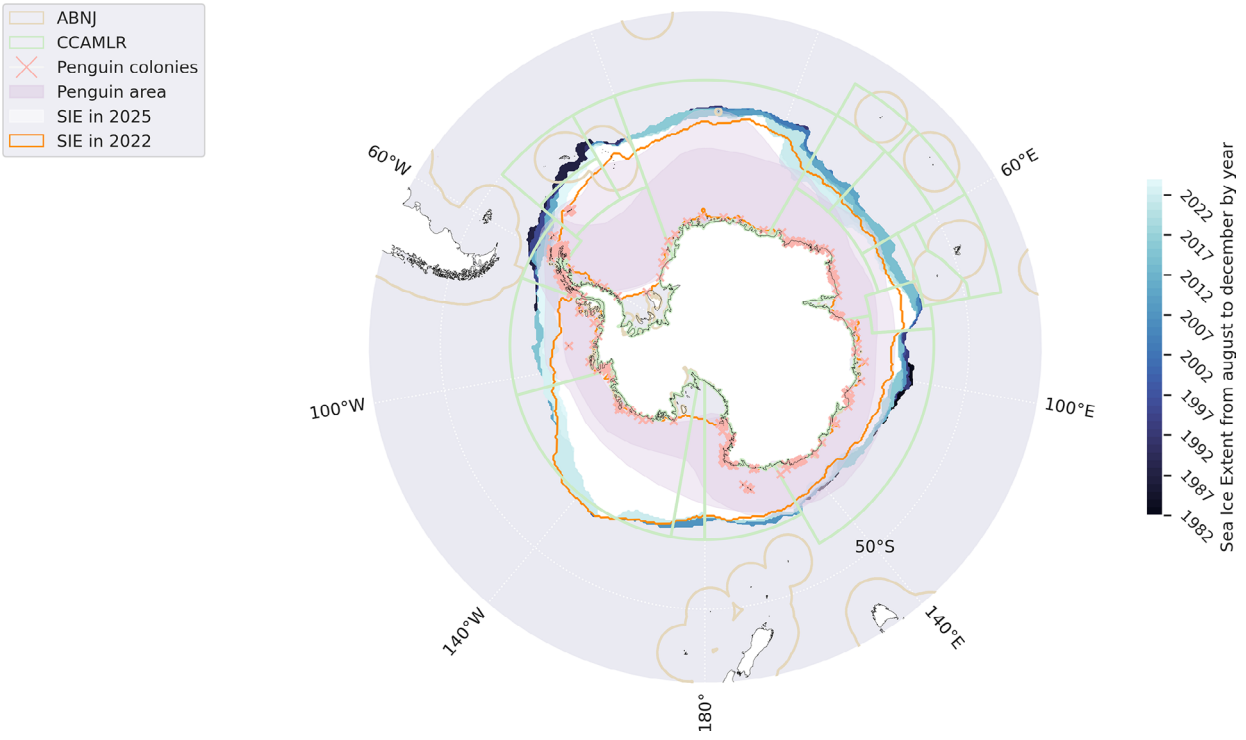


Figure 3. Map of Antarctica and the Southern Ocean combining data on Antarctic animal species, sea ice and governance. Around the continent, the habitat range (purple area, based on product ref. nos. 10 and 11) and known colonies from 1982 to 2022 (red crosses, based on product ref. no. 12) of Adelie and Emperor penguins (Pygoscelis adeliae, Aptenodytes forsteri) are shown, two bird species whose conservation status is monitored by the IUCN Red List. The observed extent variations of the circumpolar sea ice on which they live are also displayed as annual averages from August to December between 1982 and 2025 (blue-white shading, based on product ref. no. 4), with the particular value for year 2022 highlighted (orange contour line over the shaded area). In relation to conservation agreements over the Antarctic seas, the Areas Beyond National Jurisdiction (ABNJ) defined under the 1982 United Nations Convention on the Law of the Sea (United Nations, 1982b, 2023) are delimited on the map by brown lines (based on product ref. no. 13), and the areas and subareas defined by the Commission for the Conservation of Antarctic Marine Living Resources (CCAMLR, 2017) are delineated in green (based on product ref. no. 14).

societies. In the Arctic, declining sea ice and rising ocean and sea ice temperatures reveal a rapidly changing marine environment with consequences for ecosystem dynamics and ocean governance. These physical changes propagate beyond the open ocean, interacting with permafrost thaw and coastal processes to increase risks for infrastructure, ecosystems, and communities whose livelihoods and cultures depend on sea ice. In the Southern Ocean, the spatial relationship between sea-ice retreat and penguin colonies highlights a central conservation challenge: protecting biodiversity requires addressing both local pressures and the climate drivers reshaping the habitat itself. Together, these examples demonstrate why polar ocean observations must be translated into integrated knowledge to support effective adaptation, conservation and governance. The main insights from these narratives are captured in the following key messages:

Except for Iceland Shelf and Norwegian shelf, where seasonal sea ice is generally absent, polar LMEs with seasonal sea-ice cover have experienced sea-ice decline over the period 1982–2024, with the strongest losses observed in the Hudson Bay, Barent Sea, East Greenland Shelf, Chukchi Sea and the Kara Sea. Large Marine Ecosystems (LMEs) are ecologically defined ocean regions that provide a scientific framework for ecosystem-based management across national boundaries. By integrating oceanographic and ecological processes, they support coordinated management of fisheries, biodiversity, habitat conservation and other shared marine resources. Tracking sea-ice change at the LME scale therefore provides information directly relevant for transboundary ocean governance and the sustainable management of Arctic marine ecosystems.

Across the AMAP region, combined sea surface and sea-ice surface temperature has increased at an average rate of 1 °C per decade over 1982–2024, equivalent to approximately 4.2 °C of warming over the observational period, with the strongest warming rates (above 1 °C per decade) observed in the LMEs Kara Sea, East Siberian Sea and Laptev Sea, Barent Sea, Beaufort Sea, Chukchi Sea and Arctic Ocean. Sea surface temperature is a fundamental indicator of Arctic amplification and provides an integrated measure

of changes in the coupled ocean–sea ice–atmosphere system. Also, increasing ocean temperatures are transforming Arctic marine ecosystems, driving shifts in species distributions and ecosystem productivity, with implications for fisheries, food security and Indigenous and Local Peoples livelihoods.

Rapid coastal erosion in the Arctic consistently coincides with substantial sea-ice retreat over the past four decades. Sea-ice loss increases the exposure of Arctic coastlines to wave action by extending the open-water season and enlarging the fetch over which waves can develop. Combined with thawing permafrost that weakens coastal sediments, these interacting processes have accelerated coastal retreat across many Arctic regions, with important consequences for infrastructure and coastal communities.

All ocean areas adjacent to the Arctic coast show increasing numbers of days above the seawater freezing point threshold (−1.8 °C), with trends ranging from approximately 0.5 to more than 3 additional days per year over the past four decades. These trends correspond to approximately 20 to more than 120 additional days with above-freezing conditions since 1982, indicating longer periods of warmer surface waters and reduced seasonal ice presence, particularly in the Barents Sea, Kara Sea and Greenland Sea. As sea ice becomes less predictable and persistent, Arctic ecosystems, marine species distributions, and communities that rely on sea ice for travel, harvesting and cultural practices are increasingly affected. Understanding these interconnected changes requires sustained observations and the integration of Indigenous and Local Peoples' knowledge to support adaptation and informed Arctic governance.

The spatial overlap between long-term sea-ice retreat and major penguin colonies illustrates a fundamental conservation challenge: the habitat that supports Southern Ocean biodiversity is itself changing. Protecting biodiversity therefore requires both reducing local pressures through conservation and addressing the climate drivers of sea-ice loss through global mitigation.

Code availability. All codes are available upon request.

Data availability. All data used are available, and their sources are listed in the product table.

Author contributions. KvS: conceptualization, designing, methodology, writing (original draft), investigation, supervision, and formal analysis. FG: writing (original draft), conceptualization, mehtodology and formal analysis. All authors: writing (review and editing).

Competing interests. At least one of the (co-)authors serves as topic editor for the report to which this paper belongs. The peer-review process was guided by an independent editor, and the authors also have no other competing interests to declare.

Disclaimer. The Copernicus Marine Service offering is regularly updated to ensure it remains at the forefront of user requirements. In this process, some products may undergo replacement or renaming, leading to the removal of certain product IDs from the catalogue. If readers have any questions or require assistance regarding these modifications, please feel free to reach out to the Copernicus Marine Service user support team for further guidance. They will be able to provide the necessary information to address concerns and find suitable alternatives.

Publisher's note: Copernicus Publications remains neutral with regard to jurisdictional claims made in the text, published maps, institutional affiliations, or any other geographical representation in this paper. The authors bear the ultimate responsibility for providing appropriate place names. Views expressed in the text are those of the authors and do not necessarily reflect the views of the publisher.

Financial support. This research was carried out as part of the Copernicus Marine Service implemented by MOi under a contributing agreement with the European Commission, and "Ocean observations and indicators for climate and assessments" (ObsSea4Clim) is funded by the European Union Horizon Europe Funding Programme for Research and Innovation under grant no. 101136548.

Review statement. This paper was edited by Marilaure Grégoire.

References

Abram, N. J., Purich, A., England, M. H., McCormack, F. S., Strugnell, J. M., Bergstrom, D. M., Vance, T. R., Stål, T., Wienecke, B., Heil, P., Doddridge, E. W., Sallée, J.-B., Williams, T. J., Reading, A. M., Mackintosh, A., Reese, R., Winkelmann, R., Klose, A. K., Boyd, P. W., Chown, S. L., and Robinson, S. A.: Emerging evidence of abrupt changes in the Antarctic environment, Nature, 644, 621–633, https://doi.org/10.1038/s41586-025-09349-5, 2025.

AMAP: AMAP Assessment Report: Arctic Pollution Issues, Chapter 2 – Definitions, ISBN 82-7655-061-4, 1998.

Antarctic Treaty Environmental Protocol: Protocol on Environmental Protection to the Antarctic Treaty, https://www.ats.aq/e/protocol.html (last access: 21 September 2026), 1991.

Aoki, S.: Breakup of land-fast sea ice in Lützow-Holm Bay, East Antarctica, and its teleconnection to tropical Pacific sea surface temperatures, Geophys. Res. Lett., 44, 3219–3227, https://doi.org/10.1002/2017GL072835, 2017.

Argüello, G. and Rafaly, V.: Science diplomacy and Asian states: Transforming the governance landscape in the Arctic, Polar Rec., 59, e41, https://doi.org/10.1017/S0032247423000281, 2023.

Arouf, A., Chepfer, H., Kay, J. E., L'Ecuyer, T. S., and Lac, J.: Surface Cloud Warming Increases as Late Fall Arctic Sea Ice

Cover Decreases, Geophys. Res. Lett., 51, e2023GL105805, https://doi.org/10.1029/2023GL105805, 2024.

Årthun, M., Brakstad, A., Dörr, J., Johnson, H. L., Mans, C., Semper, S., and Våge, K.: Atlantification drives recent strengthening of the Arctic overturning circulation, Sci. Adv., 11, eadu1794, https://doi.org/10.1126/sciadv.adu1794, 2025.

Baudry, J., Didier, D., Dumont, D., Jourdain-Bonneau, C., Noah, T., Hamilton, A., and Bertrand, E.: Arctic sea-ice decline amplifies extreme wave exposure for coastalInuit communities, Nature Portfolio, https://doi.org/10.21203/rs.3.rs-9011874/v1, in review, 2026.

Beaulieu, L., Arreak, A., Holwell, R., Dicker, S., Qamanirq, O., Moorman, L., Wilson, K., Segal, R., Crichton, S., and Bell, T.: Indigenous self-determination in cryospheric science: The Inuit-led Sikumik Qaujimajjuti ("tools to know how the ice is") program in Inuit Nunangat, Canada, Front. Earth Sci., 11, 1076774, https://doi.org/10.3389/feart.2023.1076774, 2023.

Berkman, P. A.: Science diplomacy and the 5th International Polar Year (IPY-5): planetary considerations across centuries, Camb. Prisms Coast. Futures, 3, e6, https://doi.org/10.1017/cft.2025.2, 2025.

Berkman, P. A., Young, O. R., Vylegzhanin, A. N., Balton, D. A., and Øvretveit, O. R.: Introduction: Building Common Interests with Informed Decisionmaking for Sustainability, in: Building Common Interests in the Arctic Ocean with Global Inclusion, edited by: Berkman, P. A., Vylegzhanin, A. N., Young, O. R., Balton, D. A., and Øvretveit, O. R., Springer International Publishing, Cham, 3–54, https://doi.org/10.1007/978-3-030-89312-5_1, 2022.

Bishop, B., Andersen, B., Oliver, E. C. J., Aporta, C., and Anthony, K.: Co-developing a conceptual model rooted in Inuit Knowledge of the landfast sea ice season near Makkovik, Nunatsiavut, Arctic Science, 12, 1–23, https://doi.org/10.1139/as-2025-0047, 2026.

Bronen, R.: Climate-induced community relocations: using integrated social-ecological assessments to foster adaptation and resilience, Ecol. Soc., 20, 36, https://doi.org/10.5751/ES-07801-200336, 2015.

Bronen, R. and Chapin, F. S.: Adaptive governance and institutional strategies for climate-induced community relocations in Alaska, P. Natl. Acad. Sci. USA, 110, 9320–9325, https://doi.org/10.1073/pnas.1210508110, 2013.

Carroll, S. R.: Indigenous peoples breathing data back, Youtube, https://www.youtube.com/watch?v=jPS_3mZXWXw (last access: 10 September 2026), 2024.

Carroll, S. R., Garba, I., Figueroa-Rodríguez, O. L., Holbrook, J., Lovett, R., Materechera, S., Parsons, M., Raseroka, K., Rodriguez-Lonebear, D., Rowe, R., Sara, R., Walker, J. D., Anderson, J., and Hudson, M.: The CARE Principles for Indigenous Data Governance, Data Science Journal, 19, 43, https://doi.org/10.5334/dsj-2020-043, 2020.

Carvalho, K. S. and Wang, S.: Sea surface temperature variability in the Arctic Ocean and its marginal seas in a changing climate: Patterns and mechanisms, Global Planet. Change, 193, 103265, https://doi.org/10.1016/j.gloplacha.2020.103265, 2020.

CCAMLR: The Convention for the Conservation of Antarctic Marine Living Resources (CAMLR Convention), https://www.ccamlr.org/en/organisation/camlr-convention-text (last access: 10 September 2026), 1980.

CCAMLR: Map of the CAMLR Convention Area, https://www.ccamlr.org/ru/node/72742 (last access: 10 September 2026), 2017.

Commission for the Conservation of Antarctic Marine Living Resources: CCAMLR Geospatial Operations, GitHub [code], https://github.com/ccamlr/geospatial_operations, last access: 15 July 2026.

CCAMLR Secretariat: Geographical data layer: CCAMLR Statistical Areas, Subareas and Divisions (ASD) (0.6.3), https://spatial.ccamlr.org/ (last access: 10 September 2026), 2026.

Chavez-Molina, V., Nocito, E. S., Carr, E., Cavanagh, R. D., Sylvester, Z., Becker, S. L., Dorman, D. D., Wallace, B., White, C., and Brooks, C. M.: Managing for climate resilient fisheries: Applications to the Southern Ocean, Ocean Coast. Manage., 239, 106580, https://doi.org/10.1016/j.ocecoaman.2023.106580, 2023.

Che-Castaldo, C., Humphries, G., Lynch, H., and Van de Putte, A.: Antarctic Penguin Biogeography Project: Database of abundance and distribution for the Adélie, chinstrap, gentoo, emperor, macaroni, and king penguin south of 60 S. Version 2.3. SCAR – AntOBIS [data set], https://doi.org/10.48361/ZFTXKR, 2023a.

Che-Castaldo, C., Humphries, G., and Lynch, H.: Antarctic Penguin Biogeography Project: Database of abundance and distribution for the Adelie, chinstrap, gentoo, emperor, macaroni and king penguin south of 60 S, Biodiversity Data Journal, 11, e101476, https://doi.org/10.3897/BDJ.11.e101476, 2023b.

Cheng, L., Von Schuckmann, K., Abraham, J. P., Trenberth, K. E., Mann, M. E., Zanna, L., England, M. H., Zika, J. D., Fasullo, J. T., Yu, Y., Pan, Y., Zhu, J., Newsom, E. R., Bronselaer, B., and Lin, X.: Past and future ocean warming, Nat. Rev. Earth Environ., 3, 776–794, https://doi.org/10.1038/s43017-022-00345-1, 2022.

Chown, S. L., Brooks, C. M., Terauds, A., Le Bohec, C., Van Klaveren-Impagliazzo, C., Whittington, J. D., Butchart, S. H. M., Coetzee, B. W. T., Collen, B., Convey, P., Gaston, K. J., Gilbert, N., Gill, M., Höft, R., Johnston, S., Kennicutt, M. C., Kriesell, H. J., Le Maho, Y., Lynch, H. J., Palomares, M., Puig-Marcó, R., Stoett, P., and McGeoch, M. A.: Antarctica and the strategic plan for biodiversity, PLoS Biol., 15, e2001656, https://doi.org/10.1371/journal.pbio.2001656, 2017.

Claus, S., De Hauwere, N., Vanhoorne, B., Deckers, P., Souza Dias, F., Hernandez, F., and Mees, J.: Marine Regions: Towards a Global Standard for Georeferenced Marine Names and Boundaries, Mar. Geod., 37, 99–125, https://doi.org/10.1080/01490419.2014.902881, 2014.

Constable, A. J.: Imperatives for integrated science and policy in managing greenhouse gas risks to the Southern Polar Region, Glob. Change Biol., 28, 4489–4492, https://doi.org/10.1111/gcb.16219, 2022.

Constable, A. J.: Ecosystem Resilience, Fisheries and Conservation in the Southern Ocean, in: Antarctica and the Earth System, Routledge, London, 186–229, https://doi.org/10.4324/9781003406471-9, 2025.

Crate, S. A. and Nuttall, M. (Eds.): Anthropology and climate change: from transformations to worldmaking, 3rd edn., Routledge, New York, NY, ISBN 9781032150932, 2024.

Creel, R., Guimond, J., Jones, B. M., Nielsen, D. M., Bristol, E., Tweedie, C. E., and Overduin, P. P.: Permafrost thaw subsidence, sea-level rise, and erosion are transforming Alaska's Arc-

tic coastal zone, P. Natl. Acad. Sci. USA, 121, e2409411121, https://doi.org/10.1073/pnas.2409411121, 2024.

Deb, J. C. and Bailey, S. A.: Arctic marine ecosystems face increasing climate stress, Environ. Rev., 31, 403–451, https://doi.org/10.1139/er-2022-0101, 2023.

Eastwood, S. and Wettre, C.: EU Copernicus Marine Service Quality Information Document for SEAICE_GLO_SEAICE_L4_NRT_OBSERVATIONS_011_001 SEAICE_GLO_SEAICE_L4_REP_OBSERVATIONS_011_009, Mercator Ocean International, https://documentation.marine.copernicus.eu/QUID/CMEMS-SEAICE-QUID-011-001-009.pdf (last access: 10 Spetember 2026), 2026.

Eerkes-Medrano, L. and Huntington, H. P.: Untold Stories: Indigenous Knowledge Beyond the Changing Arctic Cryosphere, Front. Clim., 3, 675805, https://doi.org/10.3389/fclim.2021.675805, 2021.

Englyst, P., Karagali, I., Olsen, I. L., Gacitúa, G., Hayward, A., Dasgupta, N., Scheller, J. H., and Høyer, J. L.: Global satellite-based sea and sea-ice surface temperatures since 1982, Sci. Data, 13, 1052, https://doi.org/10.1038/s41597-026-07363-4, 2026.

E.U. Copernicus Marine Service Information (CMEMS): Arctic Ocean – Sea and Ice Surface Temperature REPROCESSED, Marine Data Store (MDS) [data set], https://doi.org/10.48670/moi-00123, 2021.

E.U. Copernicus Marine Service Information (CMEMS): Global Ocean OSTIA Sea Surface Temperature and Sea Ice Reprocessed, Marine Data Store (MDS) [data set], https://doi.org/10.48670/moi-00168, 2025.

E.U. Copernicus Marine Service Information (CMEMS): Global Ocean Sea Ice Concentration Time Series REPROCESSED (EUMETSAT OSI-SAF), Marine Data Store (MDS) [data set], https://doi.org/10.48670/moi-00136, 2026.

Fiske, G.: Indigenous Peoples of the Arctic boundary polygons, 2021, Arctic Data Center [data set], https://doi.org/10.18739/A2Z31NQ2H, 2021.

Flanders Marine Institute (VLIZ), Belgium: Maritime Boundaries Geodatabase: High Seas, version 2, VLIZ [data set], https://doi.org/10.14284/696, 2024.

Ford, J. D., Clark, D., and Naylor, A.: Food insecurity in Nunavut: Are we going from bad to worse?, Canadian Medical Associations Journal, 191, E550–E551, https://doi.org/10.1503/cmaj.190497, 2019.

Fretwell, P. T.: A 6 year assessment of low sea-ice impacts on emperor penguins, Antarct. Sci., 36, 3–5, https://doi.org/10.1017/S0954102024000130, 2024.

Fretwell, P. T. and Trathan, P. N.: Discovery of new colonies by Sentinel2 reveals good and bad news for emperor penguins, Remote Sens. Ecol. Conserv., 7, 139–153, https://doi.org/10.1002/rse2.176, 2021.

Fretwell, P. T., Boutet, A., and Ratcliffe, N.: Record low 2022 Antarctic sea ice led to catastrophic breeding failure of emperor penguins, Commun. Earth Environ., 4, 273, https://doi.org/10.1038/s43247-023-00927-x, 2023.

Frölicher, T. L., Sarmiento, J. L., Paynter, D. J., Dunne, J. P., Krasting, J. P., and Winton, M.: Dominance of the Southern Ocean in Anthropogenic Carbon and Heat Uptake in CMIP5 Models, J. Climate, 28, 862–886, https://doi.org/10.1175/JCLI-D-14-00117.1, 2015.

Gaffey, C. B., Bax, N., Krauzig, N., and Tougeron, K.: A call to strengthen international collaboration to assess climate change effects in polar regions, PLOS Clim., 3, e0000495, https://doi.org/10.1371/journal.pclm.0000495, 2024.

Gardiner, N. B., Liggett, D., Gilbert, N., and Cvitanovic, C.: Practitioners' perspectives on the enablers and barriers to successful Antarctic science-policy knowledge exchange, Env. Pol. Gov., 35, 362–381, https://doi.org/10.1002/eet.2143, 2025.

Goessling, H. F., Rackow, T., and Jung, T.: Recent global temperature surge intensified by record-low planetary albedo, Science, 387, 68–73, https://doi.org/10.1126/science.adq7280, 2025.

Griffiths, H. J., Cummings, V. J., Van De Putte, A., Whittle, R. J., and Waller, C. L.: Antarctic benthic ecological change, Nat. Rev. Earth Environ., 5, 645–664, https://doi.org/10.1038/s43017-024-00583-5, 2024.

Grimmer, M., Baggenstos, D., Schmitt, J., Krauss, F., Shackleton, S., Severinghaus, J. P., and Fischer, H.: AMOC Modulates Ocean Heat Content During Deglaciations, Geophys. Res. Lett., 52, e2024GL114415, https://doi.org/10.1029/2024GL114415, 2025.

Gruber, N., Gloor, M., Mikaloff Fletcher, S. E., Doney, S. C., Dutkiewicz, S., Follows, M. J., Gerber, M., Jacobson, A. R., Joos, F., Lindsay, K., Menemenlis, D., Mouchet, A., Müller, S. A., Sarmiento, J. L., and Takahashi, T.: Oceanic sources, sinks, and transport of atmospheric CO_2, Global Biogeochem. Cy., 23, 2008GB003349, https://doi.org/10.1029/2008GB003349, 2009.

Haward, M.: Biodiversity in Areas Beyond National Jurisdiction (BBNJ): the Commission for the Conservation of Antarctic Marine Living Resources (CCAMLR) and the United Nations BBNJ agreement, The Polar Journal, 11, 303–316, https://doi.org/10.1080/2154896X.2021.1984658, 2021.

He, Y., Shu, Q., Wang, Q., Song, Z., Zhang, M., Wang, S., Zhang, L., Bi, H., Pan, R., and Qiao, F.: Arctic Amplification of marine heatwaves under global warming, Nat. Commun., 15, 8265, https://doi.org/10.1038/s41467-024-52760-1, 2024.

Hjort, J., Streletskiy, D., Doré, G., Wu, Q., Bjella, K., and Luoto, M.: Impacts of permafrost degradation on infrastructure, Nat. Rev. Earth Environ., 3, 24–38, https://doi.org/10.1038/s43017-021-00247-8, 2022.

Hobbs, W., Spence, P., Meyer, A., Schroeter, S., Fraser, A. D., Reid, P., Tian, T. R., Wang, Z., Liniger, G., Doddridge, E. W., and Boyd, P. W.: Observational Evidence for a Regime Shift in Summer Antarctic Sea Ice, J. Climate, 37, 2263–2275, https://doi.org/10.1175/JCLI-D-23-0479.1, 2024.

Hovelsrud, G. K., Poppel, B., Van Oort, B., and Reist, J. D.: Arctic Societies, Cultures, and Peoples in a Changing Cryosphere, AMBIO, 40, 100–110, https://doi.org/10.1007/s13280-011-0219-4, 2011.

Huntington, H. P., Quakenbush, L. T., and Nelson, M.: Effects of changing sea ice on marine mammals and subsistence hunters in northern Alaska from traditional knowledge interviews, Biol. Lett., 12, 20160198, https://doi.org/10.1098/rsbl.2016.0198, 2016.

Huntington, H. P., Zagorsky, A., Kaltenborn, B. P., Shin, H. C., Dawson, J., Lukin, M., Dahl, P. E., Guo, P., and Thomas, D. N.: Societal implications of a changing Arctic Ocean, Ambio, 51, 298–306, https://doi.org/10.1007/s13280-021-01601-2, 2022.

IPCC: The Ocean and Cryosphere in a Changing Climate: Special Report of the Intergovernmental Panel on Cli-

mate Change, 1st edn., Cambridge University Press, https://doi.org/10.1017/9781009157964, 2019.

IPCC: Climate Change 2021 – The Physical Science Basis: Working Group I Contribution to the Sixth Assessment Report of the Intergovernmental Panel on Climate Change, 1st edn., Cambridge University Press, https://doi.org/10.1017/9781009157896, 2021.

IPCC: Climate Change 2022 – Impacts, Adaptation and Vulnerability: Working Group II Contribution to the Sixth Assessment Report of the Intergovernmental Panel on Climate Change, 1st edn., Cambridge University Press, https://doi.org/10.1017/9781009325844, 2023.

IUCN: Pygoscelis adeliae (Adelie Penguin): BirdLife International: The IUCN Red List of Threatened Species 2020: e.T22697758A157660553, IUCN [data set], https://doi.org/10.2305/IUCN.UK.2020-3.RLTS.T22697758A157660553.en, 2020a.

IUCN: Aptenodytes forsteri (Emperor Penguin). The IUCN Red List of Threatened Species 2020: e.T22697752A157658053, The International Union for Conservation of Nature (IUCN) Red List of Threatened Species [data set], https://doi.org/10.2305/IUCN.UK.2020-3.RLTS.T22697752A157658053.en, 2020b.

IW-LEARN: Global Large Marine Ecosystems, International Waters Learning Exchange and Resource Network (IW-LEARN), GeoNode [data set], https://archive.iwlearn.net/lme.edc.uri.edu/lme.edc.uri.edu/lme.edc.uri.edu/index.php/digital-data.html (last access: 10 September 2026), 2020.

Jayaram, D.: Geopolitics, Environmental Change and Antarctic Governance: A Region in Need of a Transformative Approach to Science Diplomacy, in: Assessing the Antarctic Environment from a Climate Change Perspective, edited by: Khare, N., Springer International Publishing, Cham, 1–17, https://doi.org/10.1007/978-3-030-87078-2_1, 2022.

Jenouvrier, S., Che-Castaldo, J., Wolf, S., Holland, M., Labrousse, S., LaRue, M., Wienecke, B., Fretwell, P., Barbraud, C., Greenwald, N., Stroeve, J., and Trathan, P. N.: The call of the emperor penguin: Legal responses to species threatened by climate change, Glob. Change Biol., 27, 5008–5029, https://doi.org/10.1111/gcb.15806, 2021.

Karagali, I., Kolbe, W., Gacitúa, G., Englyst, P., and Høyer, J.: EU Copernicus Marine Service Quality Information Document for Arctic Sea & Sea-Ice Surface Temperature SEAICE_ARC_PHY_CLIMATE_L4_MY_011_016 SEAICE_ARC_PHY_CLIMATE_L3S_MY_011_021, https://documentation.marine.copernicus.eu/QUID/CMEMS-SEAICE-QUID-011-016-021.pdf (last access: 10 September 2026), 2025a.

Karagali, I., Englyst, P., Kolbe, W., and Høyer, J.: EU Copernicus Marine Service Product User Manual for Arctic Ocean Sea and Sea-Ice Surface Temperature Products SEAICE_ARC_PHY_CLIMATE_L4_MY_011_016 SEAICE_ARC_PHY_CLIMATE_L3S_MY_011_021, Mercator Ocean International, https://documentation.marine.copernicus.eu/PUM/CMEMS-SEAICE-PUM-011-016-021.pdf (last access: 10 September 2026), 2025b.

Khatiwala, S., Tanhua, T., Mikaloff Fletcher, S., Gerber, M., Doney, S. C., Graven, H. D., Gruber, N., McKinley, G. A., Murata, A., Ríos, A. F., and Sabine, C. L.: Global ocean storage of anthropogenic carbon, Biogeosciences, 10, 2169–2191, https://doi.org/10.5194/bg-10-2169-2013, 2013.

Kusahara, K. and Tatebe, H.: Causes of the Abrupt and Sustained 2016–2023 Antarctic Sea-Ice Decline: A Sea Ice–Ocean Model Perspective, Geophys. Res. Lett., 52, e2025GL115256, https://doi.org/10.1029/2025GL115256, 2025.

Ladd, H.-M., Padula, V. M., Bishop, A., and Robson, B.: NOAA Arctic Report Card 2025: Indigenous Sentinels Network, NOAA technical report OAR ARC; 25-13 (Arctic Report Card), NOAA, https://doi.org/10.25923/QRM7-BV68, 2025.

Laidler, G. J. and Ikummaq, T.: Human geographies of sea ice: freeze/thaw processes around Igloolik, Nunavut, Canada, Polar Rec., 44, 127–153, https://doi.org/10.1017/S0032247407007152, 2008.

Lambert, E., Le Bars, D., van der Linden, E., Jüling, A., and Drijfhout, S.: Quantifying the feedback between Antarctic meltwater release and subsurface Southern Ocean warming, Earth Syst. Dynam., 16, 1303–1323, https://doi.org/10.5194/esd-16-1303-2025, 2025.

Lantuit, H., Overduin, P. P., Couture, N., Wetterich, S., Aré, F., Atkinson, D., Brown, J., Cherkashov, G., Drozdov, D., Forbes, D. L., Graves-Gaylord, A., Grigoriev, M., Hubberten, H.-W., Jordan, J., Jorgenson, T., Ødegård, R. S., Ogorodov, S., Pollard, W. H., Rachold, V., Sedenko, S., Solomon, S., Steenhuisen, F., Streletskaya, I., and Vasiliev, A.: The Arctic Coastal Dynamics Database: A New Classification Scheme and Statistics on Arctic Permafrost Coastlines, Estuar. Coast., 35, 383–400, https://doi.org/10.1007/s12237-010-9362-6, 2012.

Lantuit, H., Overduin, P. P., Couture, N., Wetterich, S., Are, F., Atkinson, D., Brown, J., Cherkashov, G. A., Drozdov, D. S., Forbes, D. L., Graves-Gaylord, A., Grigoriev, M. N., Hubberten, H.-W., Jordan, J., Jorgenson, M. T., Ødegård, R. S., Ogorodov, S., Pollard, W. H., Rachold, V., Sedenko, S., Solomon, S., Steenhuisen, F., Streletskaya, I., and Vasiliev, A.: The ACD Classification of Arctic Coasts, PANGAEA [data set], https://doi.org/10.1594/PANGAEA.919573, 2020.

Li, X., Guo, H., Cheng, G., Song, X., Ran, Y., Feng, M., Che, T., Li, X., Wang, L., Duan, A., Shangguan, D., Chen, D., Jin, R., Deng, J., Su, J., and Cao, B.: Polar regions are critical in achieving global sustainable development goals, Nat. Commun., 16, 3879, https://doi.org/10.1038/s41467-025-59178-3, 2025.

Lowther, A., Von Quillfeldt, C., Assmy, P., De Steur, L., Descamps, S., Divine, D., Elvevold, S., Forwick, M., Fransson, A., Fraser, A., Gerland, S., Granskog, M., Hallanger, I., Hattermann, T., Itkin, M., Hop, H., Husum, K., Kovacs, K., Lydersen, C., Matsuoka, K., Miettinen, A., Moholdt, G., Moreau, S., Myhre, P. I., Orme, L., Pavlova, O., and Tandberg, A. H.: A review of the scientific knowledge of the seascape off Dronning Maud Land, Antarctica, Polar Biol., 45, 1313–1349, https://doi.org/10.1007/s00300-022-03059-8, 2022.

Luo, Y. and Alverson, K.: A Global Call to Action: The Decade of Action for Cryospheric Sciences and the First World Day for Glaciers, Adv. Atmos. Sci., 42, 2559–2565, https://doi.org/10.1007/s00376-025-5389-2, 2025.

Malik, I. H. and Ford, J. D.: Barriers and limits to adaptation in the Arctic, Curr. Opin. Env. Sust., 73, 101519, https://doi.org/10.1016/j.cosust.2025.101519, 2025.

Manos, E. and Witharana, C.: Arctic circumpolar permafrost region building footprints from < 1 meter resolution Maxar satellite im-

agery and OpenStreetMap Version 2 (2018–2023), Arctic Data Center [data set], https://doi.org/10.18739/A28K74Z87, 2025.

Manos, E., Witharana, C., and Liljedahl, A. K.: Permafrost thaw-related infrastructure damage costs in Alaska are projected to double under medium and high emission scenarios, Commun. Earth Environ., 6, 221, https://doi.org/10.1038/s43247-025-02191-7, 2025.

Meeker, D. and Kettle, N.: A synthesis of climate adaptation planning needs in Alaska Native Communities., Alaska Center for Climate Assessment and Policy, Fairbanks, AK, https://uaf-accap.org/wp-content/uploads/2019/08/Synthesis-CAP-Alaska-Native-Communities_2017.pdf (last access: 10 September 2026), 2017.

Mercator Ocean international: Mercator Ocean Sea Ice Bulletin, https://www.mercator-ocean.eu/bulletin/sea-ice-bulletin-highlights-2025/ (last access: 10 September 2026), 2026.

Monakhova, M., York, A., Peterson, M., McCracken Pringle, J. A., BurnSilver, S., and Degai, T.: Co-production of Arctic sea ice knowledge: A systematic review, Ambio, 55, 1198–1217, https://doi.org/10.1007/s13280-025-02303-9, 2026.

Mueter, F. J., Planque, B., Hunt, G. L., Alabia, I. D., Hirawake, T., Eisner, L., Dalpadado, P., Chierici, M., Drinkwater, K. F., Harada, N., Arneberg, P., and Saitoh, S.-I.: Possible future scenarios in the gateways to the Arctic for Subarctic and Arctic marine systems: II. prey resources, food webs, fish, and fisheries, ICES J. Mar. Sci., 78, 3017–3045, https://doi.org/10.1093/icesjms/fsab122, 2021.

Naik, N., Bot, K., Whiteman, G., Fleming, L. E., Morrissey, K., Bellerby, R. G. J., Dupont, S., Yumashev, D., Hancock, S., Rogers, B. M., Ebi, K. L., and Rocklöv, J.: A framework for assessing global health impacts of polar change: An urgent call for interdisciplinary research, Ambio, 55, 529–545, https://doi.org/10.1007/s13280-025-02255-0, 2026.

Nanni, U., DeRepentigny, P., Lundén, A., Popovaitė, V., Shen, Y., Basaran, I. K., Duarte Neubern, N., Mascorda-Cabre, L., Bennett, A., Vold Hansen, T., Holmes, F. A., Kavvatha, E., Meyer, A., Prakash, A., and Wołoszyn, A.: Redefining Arctic boundaries in a changing climate: interdisciplinary perspectives on governance strategies, Polar Geography, 47, 127–155, https://doi.org/10.1080/1088937X.2024.2359926, 2024.

Nielsen, D. M., Pieper, P., Barkhordarian, A., Overduin, P., Ilyina, T., Brovkin, V., Baehr, J., and Dobrynin, M.: Increase in Arctic coastal erosion and its sensitivity to warming in the twenty-first century, Nat. Clim. Chang., 12, 263–270, https://doi.org/10.1038/s41558-022-01281-0, 2022.

Nocito, E. S. and Brooks, C. M.: The influence of Antarctic governance on marine protected areas in the Biodiversity Beyond National Jurisdiction Agreement negotiations, npj Ocean Sustain., 2, 13, https://doi.org/10.1038/s44183-023-00019-5, 2023.

Obu, J., Westermann, S., Bartsch, A., Berdnikov, N., Christiansen, H. H., Dashtseren, A., Delaloye, R., Elberling, B., Etzelmüller, B., Kholodov, A., Khomutov, A., Kääb, A., Leibman, M. O., Lewkowicz, A. G., Panda, S. K., Romanovsky, V., Way, R. G., Westergaard-Nielsen, A., Wu, T., Yamkhin, J., and Zou, D.: Northern Hemisphere permafrost map based on TTOP modelling for 2000–2016 at 1 km2 scale, Earth-Sci. Rev., 193, 299–316, https://doi.org/10.1016/j.earscirev.2019.04.023, 2019.

PAME: Large Marine Ecosystems (LMEs) of the Arctic area. Revision of the Arctic LME map, https://pame.is/ourwork/ecosystem-approach-to-management-ea/large-marine-ecosystems/ (last access: 10 September 2026), 2013.

PAME: The increase in Arctic shipping 2013–2025, https://arctic-council.org/news/increase-in-arctic-shipping/ (last access: 10 September 2026), 2026.

Perovich, D., Meier, W., Tschudi, M., Hendricks, S., Petty, A. A., Divine, D., Farrell, S., Gerland, S., Haas, C., Kaleschke, L., Pavlova, O., Ricker, R., Tian-Kunze, X., Wood, K., and Webster, M.: Arctic Report Card 2020: Sea Ice, Arctic Report Card, https://doi.org/10.25923/N170-9H57, 2020.

Polyakov, I. V., Pnyushkov, A. V., Charette, M., Cho, K.-H., Jung, J., Kipp, L., Muilwijk, M., Whitmore, L., Yang, E. J., and Yoo, J.: Atlantification advances into the Amerasian Basin of the Arctic Ocean, Sci. Adv., 11, eadq7580, https://doi.org/10.1126/sciadv.adq7580, 2025.

Previdi, M., Smith, K. L., and Polvani, L. M.: Arctic amplification of climate change: a review of underlying mechanisms, Environ. Res. Lett., 16, 093003, https://doi.org/10.1088/1748-9326/ac1c29, 2021.

Purich, A. and Doddridge, E. W.: Record low Antarctic sea ice coverage indicates a new sea ice state, Commun. Earth Environ., 4, 314, https://doi.org/10.1038/s43247-023-00961-9, 2023.

Quilestino-Olario, R.: From fossils to conservation: an overview of Antarctic and sub-Antarctic penguins, Polarforschung, 94, 17–41, https://doi.org/10.5194/polf-94-17-2026, 2026.

Rignot, E., Mouginot, J., Scheuchl, B., Van Den Broeke, M., Van Wessem, M. J., and Morlighem, M.: Four decades of Antarctic Ice Sheet mass balance from 1979–2017, P. Natl. Acad. Sci. USA, 116, 1095–1103, https://doi.org/10.1073/pnas.1812883116, 2019.

Rignot, E., Scheuchl, B., Barre, J. B., Brancato, V., Charrier, L., Chen, H., Ciraci, E., Dinh, A., Herreid, S., Jeong, S., Li, X., Mitchell, T., Mohajerani, Y., Shamsian, S., Tolpekin, V., Velicogna, I., and Wollersheim, M.: Thirty years of glacier grounding line retreat in Antarctica, P. Natl. Acad. Sci. USA, 123, e2524380123, https://doi.org/10.1073/pnas.2524380123, 2026.

Riihelä, A., Bright, R. M., and Anttila, K.: Recent strengthening of snow and ice albedo feedback driven by Antarctic sea-ice loss, Nat. Geosci., 14, 832–836, https://doi.org/10.1038/s41561-021-00841-x, 2021.

Sherman, K.: The Large Marine Ecosystem Approach for Assessment and Management of Ocean Coastal Waters, in: Large Marine Ecosystems, vol. 13, Elsevier, 3–16, https://doi.org/10.1016/S1570-0461(05)80025-4, 2005.

Sherman, K.: Toward ecosystem-based management (EBM) of the world×s large marine ecosystems during climate change, Environmental Development, 11, 43–66, https://doi.org/10.1016/j.envdev.2014.04.006, 2014.

Silvano, A., Narayanan, A., Catany, R., Olmedo, E., González-Gambau, V., Turiel, A., Sabia, R., Mazloff, M. R., Spira, T., Haumann, F. A., and Naveira Garabato, A. C.: Rising surface salinity and declining sea ice: A new Southern Ocean state revealed by satellites, P. Natl. Acad. Sci. USA, 122, e2500440122, https://doi.org/10.1073/pnas.2500440122, 2025.

Slater, T., Shepherd, A., McMillan, M., Leeson, A., Gilbert, L., Muir, A., Munneke, P. K., Noël, B., Fettweis, X., Van Den Broeke, M., and Briggs, K.: Increased variability in Greenland Ice Sheet runoff from satellite observations, Nat. Commun., 12, 6069, https://doi.org/10.1038/s41467-021-26229-4, 2021.

SO-CHIC, Sallée, J. B., Abrahamsen, E. P., Allaigre, C., Auger, M., Ayres, H., Badhe, R., Boutin, J., Brearley, J. A., De Lavergne, C., Ten Doeschate, A. M. M., Droste, E. S., Du Plessis, M. D., Ferreira, D., Giddy, I. S., Gülk, B., Gruber, N., Hague, M., Hoppema, M., Josey, S. A., Kanzow, T., Kimmritz, M., Lindeman, M. R., Llanillo, P. J., Lucas, N. S., Madec, G., Marshall, D. P., Meijers, A. J. S., Meredith, M. P., Mohrmann, M., Monteiro, P. M. S., Mosneron Dupin, C., Naeck, K., Narayanan, A., Naveira Garabato, A. C., Nicholson, S.-A., Novellino, A., Ödalen, M., Østerhus, S., Park, W., Patmore, R. D., Piedagnel, E., Roquet, F., Rosenthal, H. S., Roy, T., Saurabh, R., Silvy, Y., Spira, T., Steiger, N., Styles, A. F., Swart, S., Vogt, L., Ward, B., and Zhou, S.: Southern ocean carbon and heat impact on climate, Phil. Trans. R. Soc. A., 381, 20220056, https://doi.org/10.1098/rsta.2022.0056, 2023.

Sørensen, A. M., Lavergne, T., and Eastwood, S.: EU Copernicus Marine Service Product User Manual for Reprocessed Sea Ice Concentration from EUMETSAT OSI SAF SEAICE_GLO_SEAICE_L4_REP_OBSERVATIONS_011_009, Mercator Ocean International, https://documentation.marine.copernicus.eu/PUM/CMEMS-SEAICE-PUM-011-009.pdf (last access: 10 September 2026), 2026.

Spira, T., Du Plessis, M., Haumann, F. A., Giddy, I., Narayanan, A., Silvano, A., and Swart, S.: Wind-triggered Antarctic sea-ice decline preconditioned by thinning Winter Water, Nat. Clim. Chang., 16, 583–590, https://doi.org/10.1038/s41558-026-02601-4, 2026.

Steenhuisen, F. and Wilson, S.: AMAP Area (GIS) – boundary, line and polygon shapefiles, Arctic Monitoring and Assessment Programme (AMAP) [data set], https://www.amap.no/work-area/document/868 (last access: 10 September 2026), 2013.

Steiner, N. S., Bowman, J., Campbell, K., Chierici, M., Eronen-Rasimus, E., Falardeau, M., Flores, H., Fransson, A., Herr, H., Insley, S. J., Kauko, H. M., Lannuzel, D., Loseto, L., Lynnes, A., Majewski, A., Meiners, K. M., Miller, L. A., Michel, L. N., Moreau, S., Nacke, M., Nomura, D., Tedesco, L., Van Franeker, J. A., Van Leeuwe, M. A., and Wongpan, P.: Climate change impacts on sea-ice ecosystems and associated ecosystem services, Elem. Sci. Anth., 9, 00007, https://doi.org/10.1525/elementa.2021.00007, 2021.

Stern, H. L.: Regime Shift in Arctic Ocean Sea-Ice Extent, Geophys. Res. Lett., 52, e2024GL114546, https://doi.org/10.1029/2024GL114546, 2025.

Stokke, O. S.: Introductory essay: Polar regions and multilevel governance, The Polar Journal, 11, 249–268, https://doi.org/10.1080/2154896X.2021.2007460, 2021.

Stroeve, J. and Notz, D.: Changing state of Arctic sea ice across all seasons, Environ. Res. Lett., 13, 103001, https://doi.org/10.1088/1748-9326/aade56, 2018.

Stroh, J. N., Panteleev, G., Kirillov, S., Makhotin, M., and Shakhova, N.: Sea-surface temperature and salinity product comparison against external in situ data in the Arctic Ocean, J. Geophys. Res.-Oceans, 120, 7223–7236, https://doi.org/10.1002/2015JC011005, 2015.

Szkarłat, M., Łuszczuk, M., and Rakowski, P.: Enhancing Science Diplomacy for a Better Arctic Governance, in: GlobalArctic, edited by: Rekvig, G. and Finger, M., Springer Nature Singapore, Singapore, 417–436, https://doi.org/10.1007/978-981-96-4868-9_16, 2025.

Tanguy, R., Bartsch, A., Nitze, I., Irrgang, A., Petzold, P., Widhalm, B., Von Baeckmann, C., Boike, J., Martin, J., Efimova, A., Vieira, G., Whalen, D., Heim, B., Wieczorek, M., and Grosse, G.: Pan-Arctic Assessment of Coastal Settlements and Infrastructure Vulnerable to Coastal Erosion, Sea-Level Rise, and Permafrost Thaw, Earths Future, 12, e2024EF005013, https://doi.org/10.1029/2024EF005013, 2024.

The Antarctic Treaty: The Antarctic Treaty, https://www.ats.aq/e/antarctictreaty.html (last access: 10 September 2026), 1959.

United Nations: United Nations Convention on the Law of the Sea, Montego Bay, https://www.un.org/depts/los/convention_agreements/convention_overview_convention.htm#:~:text=The%20United%20Nations%20Convention%20on,the%20oceans%20and%20their%20resources, (last access: 21 September 2026), 1982a.

United Nations: United Nations Convention on the Law of the Sea, https://www.un.org/depts/los/convention_agreements/texts/unclos/unclos_e.pdf (last access: 10 September 2026), 1982b.

United Nations: Agreement under the United Nations Convention on the Law of the Sea on the Conservation and Sustainable Use of Marine Biological Diversity of Areas beyond National Jurisdiction, https://www.un.org/bbnjagreement/sites/default/files/2024-08/Text%20of%20the%20Agreement%20in%20English.pdf (last access: 10 September 2026), 2023.

von Schuckmann, K., Gues, F., Moreira, L., Liné, A., and de Pascual Collar, Á.: Global ocean change in the era of the triple planetary crisis, in: 9th edition of the Copernicus Ocean State Report (OSR9), edited by: von Schuckmann, K., Moreira, L., de Pascual Collar, Á., Grégoire, M., Brasseur, P., Garric, G., Karstensen, J., Lionello, P., Marcos, M., Poulain, P.-M., and Staneva, J., Copernicus Publications, State Planet, 6-osr9, 2, https://doi.org/10.5194/sp-6-osr9-2-2025, 2025a.

von Schuckmann, K., Gues, F., Moreira, L., Liné, A., and de Pascual Collar, Á.: Ocean change in the northeastern Atlantic and adjacent seas: a multi-dimensional challenge for the environment, society, and economy, in: 9th edition of the Copernicus Ocean State Report (OSR9), edited by: von Schuckmann, K., Moreira, L., de Pascual Collar, Á., Grégoire, M., Brasseur, P., Garric, G., Karstensen, J., Lionello, P., Marcos, M., Poulain, P.-M., and Staneva, J., Copernicus Publications, State Planet, 6-osr9, 3, https://doi.org/10.5194/sp-6-osr9-3-2025, 2025b.

Von Schuckmann, K., Godoy-Faundez, A., Garçon, V., Muller-Karger, F. E., Evans, K., Appeltans, W., Bax, N., Benedetti Cecchi, L., Bernard, A., Bernard, K., Byrnes, J., Canonico, G., Chapuis, L., Clark, M. R., Darnaude, A. M., Davies, C., Englyst, P., Fransson, A., Hallam, S., Heslop, E., Holland, E., Hood, M., Kern, S., Liné, A., Lara-Lopez, A., Loose, N., Martín Míguez, B., McMahon, C. R., Nordlund, L. M., Post, J., Speich, S., Sutton, A., Tanhua, T., Telszewski, M., Poursanidis, D., and Yu, W.: Global ocean indicators: Marking pathways at the science-policy nexus, Mar. Policy, 184, 106922, https://doi.org/10.1016/j.marpol.2025.106922, 2026.

Wang, Q., Shu, Q., and Wang, F.: Recent emergence of Arctic atlantification dominated by climate warming, Sci. Adv., 10, eadq5235, https://doi.org/10.1126/sciadv.adq5235, 2024.

Westermann, S., Barboux, C., Bartsch, A., Delaloye, R., Grosse, G., Heim, B., Hugelius, G., Irrgang, A., Kääb, A. M., Matthes, H., Miesner, F., Nitze, I., Pellet, C., Seifert, F. M., Strozzi, T., Wegmüller, U., Wieczorek, M., and Wiesmann, A.: ESA Permafrost Climate Change Initiative (Permafrost_cci): Permafrost extent for the Northern Hemisphere, v5.0, CEDA archive [data set], https://doi.org/10.5285/D235665772EC4B558E9A89AC85595E71, 2025.

WMO: WMO State of the Climate in 2025, WMO, https://wmo.int/publication-series/state-of-global-climate/state-of-global-climate-2025 (last access: 10 September 2026), 2026.

Wood-Donnelly, C.: Evaluating normative capacity through Arctic environmental governance, Climatic Change, 176, 127, https://doi.org/10.1007/s10584-023-03603-3, 2023.

Worsfold, M., Good, S., Martin, M., McLaren, A., Roberts-Jones, J., and Fiedler, E.: EU Copernicus Marine Service Product User Manual for Global Ocean OSTIA Sea Surface Temperature Reprocessing SST-GLO-SST-L4-REP-OBSERVATIONS-010-011, issue 1.4, Mercator Ocean International, https://documentation.marine.copernicus.eu/PUM/CMEMS-SST-PUM-010-011.pdf (last access: 14 July 2026), 2022.

Worsfold, M., Good, S., McLaren, A., Fiedler, E., Roberts-Jones, J., and Martin, M.: EU Copernicus Marine Service Quality Information Document for Global Ocean OSTIA Sea Surface Temperature Reprocessing SST-GLO-SST-L4-REP-OBSERVATIONS-010-011, issue 3.0, Mercator Ocean International, https://documentation.marine.copernicus.eu/QUID/CMEMS-SST-QUID-010-011.pdf (last access: 14 July 2026), 2026.

Wu, Q., Ma, Y., Hu, A., Rosenbloom, N., Zhang, L., Liu, H., Liu, S., Yang, L., and Yang, C.: Pacific sub-decadal sea surface temperature variations contributed to recent Antarctic Sea ice decline trend, Nat. Commun., 16, 3386, https://doi.org/10.1038/s41467-025-58788-1, 2025.

Young, O. R.: Governing the Arctic Ocean, Mar. Policy, 72, 271–277, https://doi.org/10.1016/j.marpol.2016.04.038, 2016.

Zhang, H., Storto, A., Bai, X., and Yang, C.: Quantifying the interplay of sea ice meltwater and ice–albedo feedbacks in the Arctic ice-ocean system, The Cryosphere, 19, 6807–6826, https://doi.org/10.5194/tc-19-6807-2025, 2025.

Zhang, L., Delworth, T. L., Yang, X., Zeng, F., Lu, F., Morioka, Y., and Bushuk, M.: The relative role of the subsurface Southern Ocean in driving negative Antarctic Sea ice extent anomalies in 2016–2021, Commun. Earth Environ., 3, 302, https://doi.org/10.1038/s43247-022-00624-1, 2022.

Zhou, S., Meijers, A. J. S., Meredith, M. P., Abrahamsen, E. P., Holland, P. R., Silvano, A., Sallée, J.-B., and Østerhus, S.: Slowdown of Antarctic Bottom Water export driven by climatic wind and sea-ice changes, Nat. Clim. Chang., 13, 701–709, https://doi.org/10.1038/s41558-023-01695-4, 2023.

Zhou, W., Leung, L. R., Xie, S.-P., and Lu, J.: An analytic theory for the degree of Arctic Amplification, Nat. Commun., 15, 5060, https://doi.org/10.1038/s41467-024-48469-w, 2024.

State Planet, 7-osr10, 3, 2026
https://doi.org/10.5194/sp-7-osr10-3-2026
© Author(s) 2026. This work is distributed under
the Creative Commons Attribution 4.0 License.

Ocean change in Small Island Developing States

Flora Gues[1], Karina von Schuckmann[2], Mahé Butel[2], Samantha Hallam[3], Alvaro de Pascual[4], Axel Alonso Valle[4], Aurélien Liné[2], and Lorena Moreira Mendez[4]

[1]CELAD, 48 Rte de Lavaur, 31130 Balma, France
[2]Mercator Ocean international, 2 Avenue de l'Aérodrome de Montaudran, 31400 Toulouse, France
[3]Maynooth University, Maynooth, Co. Kildare, Ireland
[4]Nologin Oceanic Weather Systems, Paseo de la Castellana 216, 28046 Madrid, Spain

Correspondence: Karina von Schuckmann (karina.von.schuckmann@mercator-ocean.fr)

Published: 30 September 2026

Abstract. Small Island Developing States (SIDS) depend fundamentally on the ocean for their societies, economies and livelihoods, yet they are among the regions most exposed to ocean changes. Here we present an ocean narrative that quantifies the environmental, economic and societal dimensions of this exposure using a suite of integrated ocean indicators. Through their Exclusive Economic Zones (EEZs), SIDS cover approximately 8 % of the global ocean and 15 % of the tropical ocean (30° S–30° N), encompassing globally important biodiversity hotspots, including coral reefs, mangroves and seagrasses. At the same time, 65 % of their EEZ area is experiencing accelerated sea-level rise, widespread ocean warming, and 56 % of EEZs exhibit rapid (above-global-average) increases in tropical cyclone heat potential since 1960, which represents the ocean heat available to fuel cyclone intensification. Nearly one-third of the SIDS EEZ area contains coral reefs classified as vulnerable, endangered or critically endangered, and one quarter of these reefs have experienced severe accumulated marine heat stress. Coastal hazards are further illustrated by cumulative tropical cyclone damages exceeding 50 % of national GDP in approximately 40 % of assessed SIDS, while nearly 20 % of assessed SIDS have experienced storm surges exceeding 3 m. Nature-based coastal protection also emerges as a critical component of climate resilience, with mangrove ecosystems for example providing annual avoided damages exceeding USD 1 million in 18 SIDS. This ocean narrative highlights the dual role of SIDS as custodians of globally important marine ecosystems and sentinels of ocean and climate change, and demonstrates the need to integrate ocean data and science, ecosystem health and resilience and climate risk assessment into ocean governance.

1 Introduction

Small Island Developing States (SIDS) in all ocean basins share both commonalities in their exposure and vulnerability to ocean changes. The SIDS were recognized as a distinct group of developing countries facing specific social, economic, and environmental vulnerabilities at the United Nations Conference on Environment and Development (Earth Summit, June 1992 in Rio de Janeiro, Brazil, https://www.un.org/en/conferences/small-islands, last access: 16 June 2026). This group of states comprises 40 UN Member States[1] and 20 non-UN members/Associate Members of Regional Commissions[2]. Despite bearing little historical responsibility for

[1]The 40 SIDS that are signatories to the Paris Agreement include: Antigua and Barbuda, Bahamas, Bahrain, Barbados, Belize, Cabo Verde, Comoros, Cook Islands, Cuba, Dominica, Dominican Republic, Fiji, Grenada, Guinea-Bissau, Guyana, Haiti, Jamaica, Kiribati, Maldives, Marshall Islands, Federated States of Micronesia, Mauritius, Nauru, Niue, Palau, Papua New Guinea, Samoa, São Tomé and Príncipe, Singapore, St. Kitts and Nevis, St. Lucia, St. Vincent and the Grenadines, Seychelles, Solomon Islands, Suriname, Timor-Leste, Tonga, Trinidad and Tobago, Tuvalu, and Vanuatu. Source: https://www.undp.org/publications/state-climate-ambition-snapshots-least-developed-countries-ldcs-and-small-island-developing-states-sids (last access: 17 June 2026).

[2]Non UN members/associate members of regional comissions (20): American Samoa, Anguilla, Aruba, Bermuda, British Virgin Islands, Cayman Islands, Commonwealth of Northern Marianas, Cook Islands, Curacao, French Polynesia, Guadeloupe, Guam,

Published by Copernicus Publications.

Table 1. Products used.

Product ref. No.	Product ID and type	Data access	Documentation
1	Fish Stock Status, Environmental Performance Index	SEDAC (2020)	Kleisner and Pauly (2015), UNDP (2026)
2	Small Island Developing States (SIDS)	UN OHRLLS (2026)	UN (1992), UN DESA (2026)
3	ZEE regions	Flanders Marine Institute (2023)	Claus et al. (2014)
4	Species richness in the Oceans	IUCN (2025a)	IUCN (2026)
5	OMI_CLIMATE_SL_GLOBAL_regional_trends Satellite observations	E.U. Copernicus Marine Service (2025)	QUID: Quet et al. (2025) PUM: Pujol et al. (2025)
6	NOAA Optimum Interpolation Sea Surface Temperature (OISST) Satellite observations & in situ observations	Huang et al. (2020)	Huang et al. (2021)
7	IAP global ocean heat content 1° gridded analysis product (IAPv4) Objective analysis from in-situ observations	Cheng et al. (2024a)	Cheng et al. (2024b)
8	INSITU_GLO_PHY_TS_OA_MY_013_052 Objective analysis from in-situ observations	E.U. Copernicus Marine Service (2026)	QUID: Szekely (2026a) PUM: Szekely (2026b)
9	EN4 quality controlled subsurface ocean temperature Objective analyses from in-situ observations	Good et al. (2013a)	Good et al. (2013b)
10	NCEI ocean heat content from 1955 to present calculated from in situ oceanographic subsurface profile data Objective analysis from in-situ observations	Levitus et al. (2017)	Levitus et al. (2012)
11	IUCN endangered and vulnerable coral reefs Expert-derived species range maps	IUCN (2020)	IUCN (2025b)
12	Dollar value of reef tourism	Spalding et al. (2017)	Spalding et al. (2017)
13	Economic Impact of Emergency Events Compiled multi-source disaster impact database	Guha-Sapir (2020)	CRED (2023b)
14	Gros Domestic Products (GDP) by countries Compiled official national statistics	World Bank (2026)	World Bank (2026)
15	Human Impact of Emergency Events Compiled multi-source disaster impact database	Guha-Sapir (2020)	CRED (2023a)
16	Ocean Cyclone Track Observational best-track record	Gahtan et al. (2024)	Knapp et al. (2010)
17	Global Peack Surge Map Compiled historical observational database	Needham and Keim (2015)	Needham and Keim (2012)
18	Mangrove Coastal Protection Benefit Modeling	The Nature Conservancy (2018)	Menéndez et al. (2018)

global warming, SIDS experience its consequences more acutely than most other nations (Martyr-Koller et al., 2021; Mimura et al., 2007; Vousdoukas et al., 2023). Sea-level rise poses an existential threat for many low-lying islands, raising unresolved questions about population displacement, resources rights, and sovereignty in case of territorial loss (Bronen and Chapin, 2013; Green and Wewerinke-Singh, 2025; Marino, 2018; Martyr-Koller et al., 2021; Mimura et al., 2007).

Martinique, Montserrat, New Caledonia, Niue, Puerto Rico, Sint Maarten, Turks and Caicos Islands, U.S. Virgin Islands; Source: https://www.un.org/en/conferences/small-islands.

For SIDS, the Exclusive Economic Zone (EEZ) is, on average, 28 times the country's land mass (https://www.un.org/ohrlls/content/about-small-island-developing-states, last access: 16 June 2026). An illustrative example of this striking contrast is the Marshall Islands, whose land covers only 183 km^2, whereas its EEZ represents around 2 million km^2 (Thorpe, 2005). Thus, for many SIDS, most of the natural resources they have access to come from the ocean. Factors like small population size, remoteness from international markets, high transportation costs, vulnerability to exogenous economic shocks, and fragile land and marine ecosystems, make SIDS particularly vulnerable to biodiversity loss and changes in the ocean, because they lack economic alternatives. Ocean changes already impact SIDS with cascading and compounding risks, and disproportionately higher risks are expected in the course of the 21st century, where vulnerable human communities, especially those in coral reef environments, may exceed adaptation limits well before the end of this century (IPCC, 2019). This emphasizes the need to report on ocean change not only through environmental observations, but also through an understanding of how these changes translate into socioeconomic implications for communities, livelihoods, food security, and sustainable development. Ocean narratives can support this by linking ocean and socioeconomic indicators with scientific evidence, thereby providing a more integrated and societally relevant perspective on ocean change in the areas adjacent to the SIDS.

Here, we provide 3 themes for the ocean narrative with focus on the ocean areas relevant for the SIDS. The first topic puts together information on ocean areas under the jurisdiction, bringing together information on national waters, accelerating sea-level rise, marine species richness, and fisheries. This theme highlights the unique relationship between SIDS and the ocean, emphasizing both the ecological significance of their marine environments and their dependence on ocean resources such as food security, livelihoods, and economic development. The second theme focuses on ocean warming and marine heatwaves in the context of coral reef vulnerability and tourism. Coral reefs provide essential ecosystem services and underpin tourism economies across many SIDS. By linking physical ocean changes with ecosystem impacts and socioeconomic dependence on tourism, this theme explores how increasing thermal stress may affect both marine biodiversity and economic resilience. The third topic examines the role of ocean heat content for fuelling tropical cyclones and discusses the implications for loss and damage in SIDS. It further considers the protective function of mangrove ecosystems, which can reduce coastal exposure to storm surges and flooding. By connecting changes in the ocean climate system with coastal vulnerability and nature-based protection, this narrative highlights the growing importance of adaptation and resilience-building in the face of increasing climate risks.

2 Method

Ocean change is increasingly monitored and reported on through a growing range of physical, biological and chemical ocean indicators, including ocean warming, sea-level rise, deoxygenation, and acidification. At the same time, socioeconomic datasets provide detailed information on, for example, human vulnerability, economic dependence, protection efforts, or governance capacity. However, albeit progress has been achieved for some topics (Gussmann and Hinkel, 2021; Hinkel et al., 2023), these two domains are often analysed separately, making it difficult to understand how changes in the ocean translate into societal impacts and opportunities. The concept of ocean narratives addresses this gap, as they establish scientific linkages between ocean and socioeconomic indicators within a specific thematic context. By combining these datasets and scientific knowledge, the approach helps identify where ocean changes may be having the most impact on human well-being, economic development, and environmental sustainability.

Ocean narratives are a new concept to connect ocean data and indicators to human relevance. The concept has been introduced by an international and multidisciplinary team of scientists (Von Schuckmann et al., 2026), and implemented for the first time in the 8th Copernicus Ocean State Report (von Schuckmann et al., 2025a, b). Ocean narratives create a bridge between ocean science, societal outcomes, and therefore contribute to evidence-based knowledge transfer. They are based on the combination of ocean indicators such as ocean warming, sea level rise, ocean acidification, or sea ice change, together with socioeconomic data relevant to specific themes or regions. Spatial and temporal patterns revealed by indicators can highlight potential relationships and emerging areas of concern, while peer-reviewed scientific literature is used to validate and explain these connections. Therefore, the narrative development follows a strict evidence-based approach: links between ocean change and socioeconomic data are only integrated in the ocean narrative when peer-reviewed literature shows scientifically validated relationships. This ensures that narratives are both scientifically robust and accessible to decision-makers.

The approach offers several benefits. First, ocean narratives translate complex ocean science into societally relevant insights as they provide a transparent framework which connects environmental and socioeconomic data (see Table 1) and information. Second, the approach helps identifying regions, sectors, and communities that may be particularly exposed or resilient to ocean change. Third, ocean narratives can support policy development as they link ocean conditions to tangible societal outcomes. And fourth, they enable communication of ocean knowledge and change through compelling, evidence-based stories, designed to resonate with diverse audiences. In other words, ocean narratives can serve as a bridge between observation and action, helping synthesize large and often disconnected datasets into coherent knowl-

edge that can inform sustainable ocean governance and informed decision-making. By improving the accessibility and relevance of scientific information, ocean narratives can contribute to making data and science more actionable.

The narrative presented here is focussed on the ocean area adjacent to the SIDS in the three ocean basins (Atlantic, Pacific and Indican Ocean), as SIDS are directly positioned at the interface between ocean change and human development: their communities and economies are directly dependent on marine and coastal systems. For SIDS, this approach can help answer critical questions: Which islands may be most exposed to sea-level rise? Where could ocean warming have implications for tourism-dependent economies, for example through impacts on coral reefs? How might changes in marine ecosystems affect food security and livelihoods in communities that depend heavily on fisheries? What is the exposure of SIDS to intense tropical storms, fuelled by the power of the ocean? By connecting ocean conditions to development realities, ocean narratives provide a more integrated understanding of risk, vulnerability, and opportunity. They can help policymakers, practitioners, and communities move beyond isolated indicators toward a clearer picture of how ocean change influences sustainable development pathways in Small Island Developing States. All data used for the narrative are documented in Product Table 1, together with information on data access and related references.

3 The Ocean Narrative

3.1 SIDS: Bound by the ocean, united by climate risk

The SIDS are located in the tropical ocean basins of the world ocean between 30° S–30° N (Fig. 1). The SIDS EEZs cover 8 % of the global ocean, and 15 % of the global tropical ocean (30° S–30° N). For the different basins, the SIDS EEZs cover 18 % of the tropical Pacific Ocean, 8 % of the tropical Atlantic Ocean, and 12 % of the tropical Indian Ocean (Fig. 1). SIDS are widely recognized as stewards of the ocean and leading advocates for ocean sustainability and environmental governance (Hassanali et al., 2026; Keo and Yoona, 2022; Martyr-Koller et al., 2021; Vousdoukas et al., 2023). SIDS have become influential voices in global negotiations on marine conservation, fisheries, and ocean sustainability, as they can shape outcomes through coalition-building, scientific expertise, diplomacy, and normative leadership (Haas et al., 2023; Saddington, 2023). Notably, they played an important role in securing the 1.5 °C degree limit within the Paris Agreement and championed an ambitious BBNJ Agreement (Hassanali et al., 2026). SIDS have also been recognised as Large Ocean States because their identities, economies, and governance are defined more by ocean space than by land (Hume et al., 2021), positioning them as key actors in ocean governance. For example, SIDS are emerging as important innovators in ocean governance, developing integrated approaches that link conservation and biodiversity, fisheries, tourism, and economic development, and hence they play a growing role in shaping sustainable ocean management practices at both national and international scales (Singh et al., 2025). Particularly, SIDS are actively engaged in transformative ocean governance involving key principles such as biodiversity, inclusivity, equity, adaptability, and cross-sectoral coordination, which are key for addressing the interconnected environmental, social, and economic challenges (Lombard et al., 2023). Spalding et al. (2023) argued that strengthening the role of SIDS is essential for more equitable and effective global ocean governance systems as they are well positioned to activate evidence-based and context-specific solutions to ocean-sustainability challenges.

Marine ecosystems hold globally 43 biodiversity hotspots[3] which cover 46 600 000 km^2, representing 9 % of the global ocean area (Costello et al., 2023, their Table CCP1.1; Olson and Dinerstein, 2002), and include coral reef ecosystems, kelp forests, seagrass meadows, polar and upwelling zones. Species in biodiversity hotspots already show changes in response to climate change, and all biodiversity hotspots are impacted, to differing degrees, by human activities (Moonsammy et al., 2024). SIDS are the stewards of a large share of the world's marine biodiversity, and major ecosystems in their EEZ areas include coral reefs, mangrove forests, seagrass meadows, and coastal wetland systems (Brodie et al., 2020; Costello et al., 2023). The tropical ocean, where most of the SIDS are located, contains the highest marine biodiversity on Earth, where most (83 %) species occurred in shallow depths (0 to 500 m) (Saeedi et al., 2019). For example, the tropical and subtropical areas of the west Pacific host the highest number of marine species worldwide (Asaad et al., 2018; Jablonski et al., 2006). The EEZs of all SIDS cover very high species richness in the world ocean (Fig. 1). For example, SIDS host highly valuable coral reefs and mangrove-seagrass systems, which are among the most species-rich marine ecosystems and support biodiversity, underpin fisheries productivity and provide economic resources (e.g., tourism), and coastal protection (Vasileiadou et al., 2024; Costello et al., 2023; Châles, 2023; Yuan et al., 2024). From this perspective, SIDS are not peripheral actors, they are custodians of a substantial share of the world's ocean biodiversity. Hence, effectively protecting SIDS biodiversity means protecting a large fraction of global marine life.

Transformations in the world's ocean due to climate change will disproportionately affect SIDS. Sea level rise, ocean warming, ocean acidification, and declining warm-water coral reefs will all have adverse impacts on SIDS, who often also have the lowest adaptive capacity (IPCC, 2019). Amongst those, sea-level rise constitutes one of the most

[3] Geographic areas that are exceptionally rich in species, ecologically distinct and/or show high endemism (species occurring in that defined geographic area and nowhere else) are broadly recognised as biodiversity hotspots and prioritised for conservation (Costello et al., 2023).

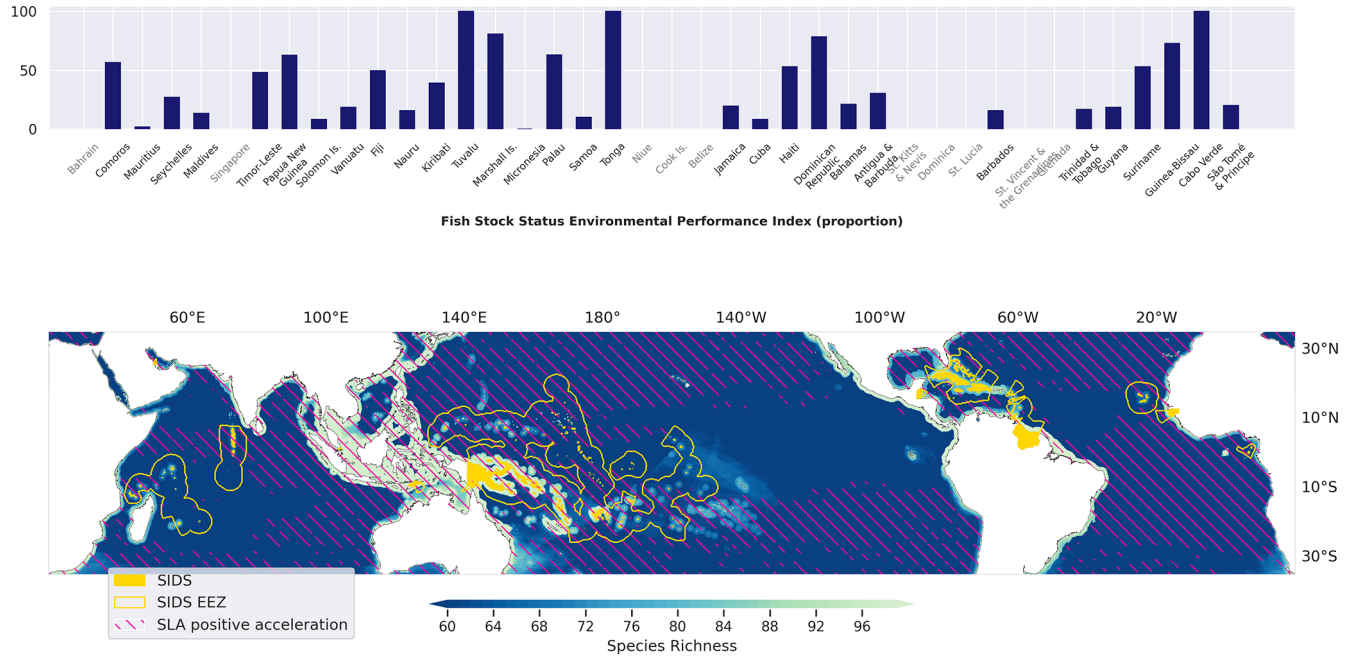


Figure 1. **(a)** Environmental Performance Index (EPI) scores for Fish Stock Status in 2021 of the 40 UN-member Small Island Developing States (SIDS). These scores assess in percentage format the proportion of a country's total catch that comes from overexploited or collapsed stocks, considering all fish stocks within a country's exclusive economic zone (EEZs). A score of 100 % (0 %) for a particular state indicates that none (all) of its catch comes from overexploited or collapsed stocks. Data is based on product ref. no 1. **(b)** Map showing the location of the island countries that make up the SIDS group (solid yellow areas, based on product ref. no. 2) and their corresponding EEZs (yellow contours, based on product ref. no. 3). The richness of species, here provided as the count of the number of species potentially occurring in each grid cell, is represented by the blue-green shaded background (based on product ref. no. 4), whereas the overlaying purple hatched areas mark regions where the rise of sea level has been accelerating in the 1999–2025 period (based on product ref. 5).

significant challenges facing SIDS. Due to the concentration of populations, economic activities, and critical infrastructure within coastal zones, SIDS are disproportionately exposed to the impacts of rising sea levels (Martyr-Koller et al., 2021). Beyond its physical and socioeconomic consequences, sea level rise also raises complex legal and political questions concerning statehood, sovereignty, and the right to self-determination, particularly for low-lying island nations whose territories may become increasingly uninhabitable or submerged (Green and Wewerinke-Singh, 2025; Labh, 2025). Accounting for changes of sea level over the period 1999–2025, 65 % of all SIDS EEZs are directly exposed to sea level acceleration, and 50 % in the Atlantic Ocean, 76 % in the Pacific Ocean, and 33 % in the Indian Ocean (Fig. 1). Adaptation to sea-level rise is therefore a critical component of climate resilience strategies in SIDS.

However, the effectiveness of adaptation measures is constrained by a range of financial, institutional, technical, and geographical barriers (Thomas and Theokritoff, 2024; Robinson et al., 2023). Furthermore, evidence suggests that adaptation limits are likely to be reached in many SIDS under global warming scenarios exceeding 1.5 °C, thereby increasing the risk of irreversible losses and damages (Martyr-Koller et al., 2021). SIDS are hence sentinels for implications of planetary warming, the processes destabilising their coasts today such as from sea level rise are the same processes that will affect low-lying and densely populated coastal areas worldwide. Also, sea-level rise in SIDS raises fundamental questions about adaptation limits, relocation, and even sovereignty, making them key sites where the future of climate governance is already being negotiated in practice.

SIDS are highly dependent on food from aquatic environments (often also named "blue food") for food security, employment, and state revenue, with fisheries forming a core pillar of national economies and diets (Bell et al., 2021; Teneva et al., 2023). For example, fishing for tuna plays a vital role in the economic development and food security of most of the 22 Pacific Island countries and territories (FFA, 2023; Bell et al., 2021), and more than 95 % of all tuna caught from their EEZs comes from almost half (10, from which 9 implemented cooperative management) of the Pacific SIDS, where access fees paid by industrial fishing fleets provide an average of 37 % (range = 4 %–84 %) of their government revenue (excluding grants) (Bell et al., 2021). From 2020 to 2022, the annual value of the tuna catch taken in Forum Fisheries Agency waters (17 members; https://www.ffa.int/, last access: 17 June 2026) averaged USD 2.6 billion (FFA, 2023). Hence, changes in marine

biodiversity and fish stocks are not just ecological loss, but become a direct precursor for inducing food system stress. SIDS have currently overfished their waters to the extent that their current catch is just under 50 % of the maximum catch potential, which results in direct and indirect food security impacts, including losses in healthy, varied and nutrient-rich food, revenues, incomes and economic impacts in SIDS (Sumaila et al., 2013). For the year 2021, 63 % of 30 SIDS[4] obtain their catch from overexploited or collapsed fish stocks (index < 50 %), and 37 % of SIDS obtain their catches from healthy fish stocks (Fig. 1) (Sumaila et al., 2013; Teneva et al., 2023). At global scale, EEZs account for the vast majority (> 90 %) of global marine catch, which are making fisheries status within EEZs a direct reflection of how states exercise marine sovereignty and manage natural capital. SIDS are vulnerable to climate change and global food market price volatility (Campling et al., 2024; Teneva et al., 2023; Englander, 2019). As a result, the fish stock status in SIDS is not merely an ecological indicator, but also a measure of how effectively countries can translate sovereign rights over marine resources into food security, economic benefits, and long-term sustainable ocean stewardship.

3.2 Ocean Warming and Coral Reef Impacts in SIDS

Ocean warming is driven by global warming and has reached record values globally in 2025 (WMO, 2026). For coral reefs, ocean warming disrupts the coral-algae symbiosis, leading to coral bleaching and metabolic stress, which in turn reduce growth and reproduction, increase disease susceptibility, and decrease calcification and reef-building capacity (IPCC, 2023; Pfab et al., 2024; Hughes et al., 2020, 2017). But ocean warming can induce also other implications such as sea level rise, ocean circulation change, increased frequency and intensity of marine heatwaves, reducing carbon uptake capacity, fuel tropical storms, changes in marine ecosystem structure and species distributions, and impacts on fisheries and coastal communities (Cheng et al., 2022). Ocean warming is widespread in the tropical ocean (Pan et al., 2026), and approximately 7 % of all SIDS EEZs are exposed to rapid ocean warming as estimated over the period 1960–2025 (Fig. 2).

Globally, coral reef ecosystems are among the most biologically diverse and economically important marine habitats (Bohorquez et al., 2025). They support an estimated 25 % of all marine species and provide hundreds of billions of dollars annually in goods and services, including coastal protection, fisheries, tourism, and medicine, among other benefits (Beck et al., 2018; Costanza et al., 1997; Spalding et al., 2017; Teh et al., 2013). Beyond their economic value, coral reefs also hold subsistence, cultural and spiritual significance for many islands communities (Cramer et al., 2022; Robles-Zavala and Chang Reynoso, 2018). Climate change, together with pollution and overexploitation, now represents an existential threat to coral reefs (Bhuyan et al., 2026; Bohorquez et al., 2025; Pearce-Kelly et al., 2025), and repeated thermal stress drives widespread bleaching, mortality, and long-term loss of ecosystem function (IPCC, 2019; Hughes et al., 2020). Reefs are currently undergoing rapid global-scale ecological reorganisation, threatening their role as key marine biodiversity reservoirs (Tebbett et al., 2023). Approximately 28 % of the EEZ area of SIDS contains coral reefs classified as vulnerable, endangered or critically endangered, and which amounts to 27 % in the Pacific, 41 % in the Atlantic, and 22 % in the Indian ocean SIDS EEZ areas (Fig. 2).

Between January 2023 and September 2025, 84.4 % of the world's coral reefs have experienced bleaching-level heat stress, exceeding the previous mass bleaching of 68.2 % during 2014–2017 (Lévy et al., 2026). Approximately 25 % of vulnerable, endangered or critically endangered coral reefs[5] in SIDS' EEZs have been exposed to accumulated heat stress conditions (Degree Heating Week (DHW) > 16 °C weeks) for at least one month during the period 1982–2025 (Fig. 2). Although sustained heat stress of this kind remained episodic it affected already about 1/3 of already vulnerable reef systems and the repeated occurrence over four decades signals a growing and cumulative threat to coral reef systems at SIDS EEZ level. Given the diverse and essential contributions provided by tropical reefs to people, degradation at such a scale implies severe consequences for human livelihood and welfare, primarily in developing countries (Pereira et al., 2022; Seguin et al., 2022). Also, coral reef loss is a risk multiplier for SIDS vulnerability, as this amplifies coastal flooding risk, food insecurity, and economic instability (IPCC, 2019). Consequently, SIDS are explicitly highlighted as a priority region in coral reef policy work as they build the natural infrastructure for low-lying island states (https://www.unep.org/topics/ocean-seas-and-coasts/ecosystem-based-approaches/small-grants-programme, last access: 21 September 2026).

Coral reef tourism is a critical ecosystem service, and very high-value reefs in monetary and visitor terms are found in most coral reef jurisdictions, which provides an important incentive for sustainable reef management (Spalding et al., 2017). For 30 % of the world's reefs that are of value in the tourism sector, a total value of nearly USD 36 billion per year has been estimated related to on-reef (e.g., indirect benefits such as the provision of sandy beaches, sheltered water, food and attractive views) and reef adjacent value (in-water activities such as diving and snorkelling) (Spalding et

[4] No data available for Singapore, Niue, Cook Islands, Belize, Saint Kitts and Nevis, Dominica, Saint Lucia, Saint Vincent and the Grenadines, Grenada.

[5] In the IUCN Red List framework, Vulnerable, Endangered and Critically Endangered represent increasing levels of extinction risk, from high to very high and extremely high risk of extinction in the wild, respectively. Source: https://www.iucnredlist.org/ (last access: 17 July 2026).

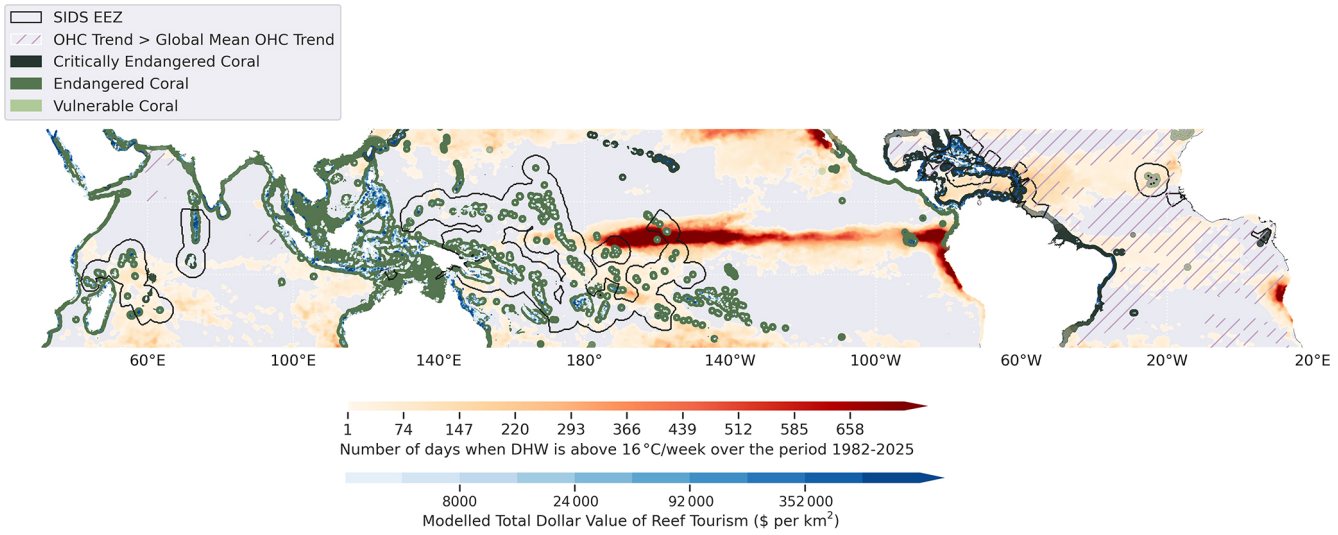


Figure 2. Map displaying combined data about Small Island Developing States' exclusive economic zones (SIDS EEZ, black contours, based on product ref. no. 3), ocean warming trends and coral reefs in order to estimate the potential ecological and socioeconomic impacts on SIDS of coral reefs' bleaching due to extreme temperatures. The yellow-red shading indicates the number of days at each location over the period 1982–2025 in which the Degree Heating Week (DHW) value was over 16 °C weeks (based on product ref. no. 6); beyond this threshold, corals are at risk of severe bleaching and multi-species mortality (> 50 % of corals) (Eakin et al., 2026). The DHW index measures the accumulated heat stress of corals due to positive anomalies in sea surface temperature sustained over periods of several weeks or months (Whitaker and DeCarlo, 2024). Overlaying purple hatched areas highlight regions where at least 95 % of the local Ocean Heat Content (OHC) trend range surpass the global mean OHC trend over period 1960–2025 (trend ranges and averages are computed from an ensemble of product refs. no. 7, 8, 9 and 10). Green shaded areas mark the location of critically endangered, endangered or vulnerable coral reefs (based on product ref. no. 11). The blue dots indicate the estimated monetary values of coral reefs to the local tourism sector, expressed in US dollar revenue per square kilometer and per year. For clarity, the value distribution (based on product ref. no. 12) has been split in deciles, which are differentiated on the map by means of a color gradient; for a full description of the modeling process followed to obtain these estimates, see Spalding et al. (2017).

al., 2017). Globally, SIDS are the most economically dependent states on coral reefs for tourism and fisheries (Bartelet et al., 2024; Teelucksingh et al., 2013). Coral reefs also represent favourable locations for luxury resorts, which play a significant role in the economic development of SIDS (de-Miguel-Molina et al., 2014).

In terms of tourism, coral reefs can account for over 20 % of GDP in some SIDS (OECD, 2020). For the Maldives, Palau, the Turks and Caicos Islands, and the British Virgin Islands in particular, they underpin more than one third of total tourism value (Spalding et al., 2017). In many cases, tourism represents one of the few income sources given the limited availability of alternative livelihoods (Chaijaroen, 2023). Coral reefs also provide coastal protection of tourism infrastructure as they act as natural breakwaters, reducing wave energy and protecting beaches, hotels, resorts, and other coastal infrastructure from erosion and storm damage, which is particularly important for low-lying island nations vulnerable to sea-level rise and extreme weather (Vousdoukas et al., 2023; Ferrario et al., 2014).

3.3 Tropical storms, damages and coastal protection

SIDS are faced with a multitude of disasters, including high vulnerability to cyclones, floods, droughts, earthquakes, tsunamis, and sea-level rise. The disaster mortality rate across SIDS is more than double the global average (IPCC, 2023) associated with high hazard frequency, high concentrations of population in low elevation coastal zones, geographical isolation and lack of economic scale. At the same time, and as of 2023, only 38 % of SIDS reported having multi-hazard early warning systems in place (UNDRR, 2025). According to the Emergency Events Database (EM-DAT), a total of 393 natural hazard-related disasters had been recorded in 2024, which caused 16 753 fatalities, and affected 167.2 million people (CRED, 2025). Regarding tropical cyclones, Hurricane Beryl in 2024, the earliest Category 5 hurricane on record, caused over USD 1 billion in damages across Grenada and Jamaica (Bevan et al., 2025). In the South-West Indian Ocean, Cyclone Belal and Cyclone Hidaya severely affected island nations, such as Réunion, Mauritius and Madagascar, resulting in fatalities, large-scale displacement, and substantial infrastructure damage (CRED, 2025). In 2025, 358 natural hazard-related disasters have been recorded by EM-DAT, which resulted in 16 607 fatal-

ities, affected 110.2 million people, and caused USD 170 billion in economic losses (Delforge et al., 2026). During this year, Hurricane Melissa, for example, affected approximately 7.6 million people across Jamaica Haiti, Cuba, and the Dominican Republic. Jamaica alone, where Hurricane Melissa made landfall as a category 5 hurricane, experienced an estimated USD 10 billion in losses, one of the highest recorded in 2025 (Delforge et al., 2026). Based on available records, cumulative tropical cyclone damage exceeded 50 % of national GDP in approximately 40 % of SIDS with available data, although data availability and record length vary among countries (1903–2026) (Fig. 3).

Key drivers of tropical cyclone intensification include ocean temperature, vertical wind shear and dry air entrainment, with the intensification potential dictated by complex causal chains (Emanuel et al., 2004). These constraints can influence the way the critical thermodynamic interface for ocean-storm interaction evolves, and thus modifies storm intensity (Dzwonkowski et al., 2020). Tropical cyclones intensify by extracting energy from the warm ocean surface with the upper ocean thermal structure critical for their development, and ocean temperature over 26 °C generally regarded a necessary condition (e.g. Gray, 1968). Warm ocean temperatures increase the potential intensity of a tropical cyclone and lead to its intensification (e.g., Dzwonkowski et al., 2020; Jaimes et al., 2015, 2016; Hallam et al., 2019). Tropical Cyclone Heat Potential (TCHP) quantifies the integrated heat content of the upper ocean above the 26 °C isotherm and is widely used as an indicator of the oceanic energy available to support tropical cyclone intensification, as it refers to the subsurface thermal structure as a measure of the potential for cyclone intensification (Momin et al., 2021; Sasaki and Motoi, 2022). Rising ocean temperatures are leading to increases in tropical cyclone intensity (Hallam et al., 2021) and marine heatwaves have shown to increase tropical cyclone intensity, and precipitation richer cyclone conditions (Choi et al., 2024). IPCC (2021) has assessed that the global proportion of Category 3–5 tropical cyclones (TC) has increased over the past four decades, and some studies have linked this increase to an increase in THCP (Liu and Chan, 2022; Song et al., 2021; Wada and Chan, 2021), together with other potential drivers (Wada and Yanase, 2024). Over the period 1960 to 2025, approximately 56 % of the SIDS EEZ areas have experienced above global average increases in tropical cyclone heat potential (Fig. 3), indicating increase in upper-ocean heat availability for tropical cyclone intensification. For the EEZ SIDS areas in the Pacific Ocean, 73 % are exposed to rapid increase in tropical cyclone heat potential, and 32 % in the Atlantic, while EEZs of SIDS in the Indian Ocean are less exposed to this change (1 %) (Fig. 3). There is an increasing number of Category 4 tropical cyclones observed in recent years (Fig. 3), together with high cumulative damages relative to national GDP. Based on available country records, 10 SIDS (Jamaica, St Kitts and Nevis, Grenada, Dominica, Belize, Samoa, Bahamas, Antigua and Barbuda, Vanuatu, and Tonga) have experienced cumulative damages exceeding 50 % of Gross Domestic Product (GDP), although the length of the historical record varies among countries.

As discussed above, increasing tropical cyclone heat potential can intensify tropical cyclones, which in turn enhances storm surge potential through stronger winds and lower atmospheric pressure (Balaguru et al., 2024; Guo and Tan, 2026). For SIDS, storm surge represents one of the most destructive impacts of tropical cyclones, as intensified storms can generate extreme coastal water levels that rapidly inundate densely populated low-lying coastal zones (IPCC, 2023; Irish et al., 2011; Vousdoukas et al., 2023). In addition, rising ocean heat content not only increases tropical cyclone intensity but also contributes to higher baseline sea levels through thermal expansion, amplifying storm surge impacts when cyclones make landfall (Vousdoukas et al., 2023). In SIDS, storm surge impacts are increasingly compounded by heavy rainfall and rising mean sea level, leading to more frequent and severe coastal flooding events during tropical cyclones (Grimley et al., 2024; IPCC, 2023). Nearly 20 % of assessed SIDS (7 out of 40) have experienced tropical cyclone–induced storm surges exceeding 3 m based on historical records spanning 1961–2012 (Fig. 3).

Mangroves provide a critical form of natural coastal protection as they reduce waves and storm surges, and serve as a first line of defence against flooding and erosion (Gedan et al., 2011; Sandi et al., 2018; Thampanya et al., 2006; Krauss et al., 2014). Globally, mangroves provide flood protection benefits exceeding USD 65 billion per year, and if mangroves were lost, 15 million more people would be flooded annually across the world (Menéndez et al., 2020). This demonstrates that the essential value of mangroves as natural coastal defences at global, national, and local scales and can provide incentives for mangrove conservation and restoration in development, climate adaptation, disaster risk reduction, and insurance (Menéndez et al., 2020). Yet, mangroves have experienced significant losses over the last decades with a global loss of 11.8 % since 1970 (Lévy et al., 2026; RAMSAR et al., 2025). The mangrove coastal protection annual expected benefit exceeds USD 1 million in 18 SIDS.

4 Conclusion

Here, we provide an ocean narrative across three themes relevant for SIDS. The first topic highlights the unique relationship between SIDS and the ocean, emphasizing both the ecological significance of their marine environments and their dependence on ocean resources for food security, livelihoods, and economic development. The second theme is linking physical ocean changes with ecosystem impacts and socioeconomic dependence on tourism. The third topic is connecting changes in the ocean climate system with coastal vulnerability and nature-based protection, highlighting the growing importance of adaptation and resilience-building in the face

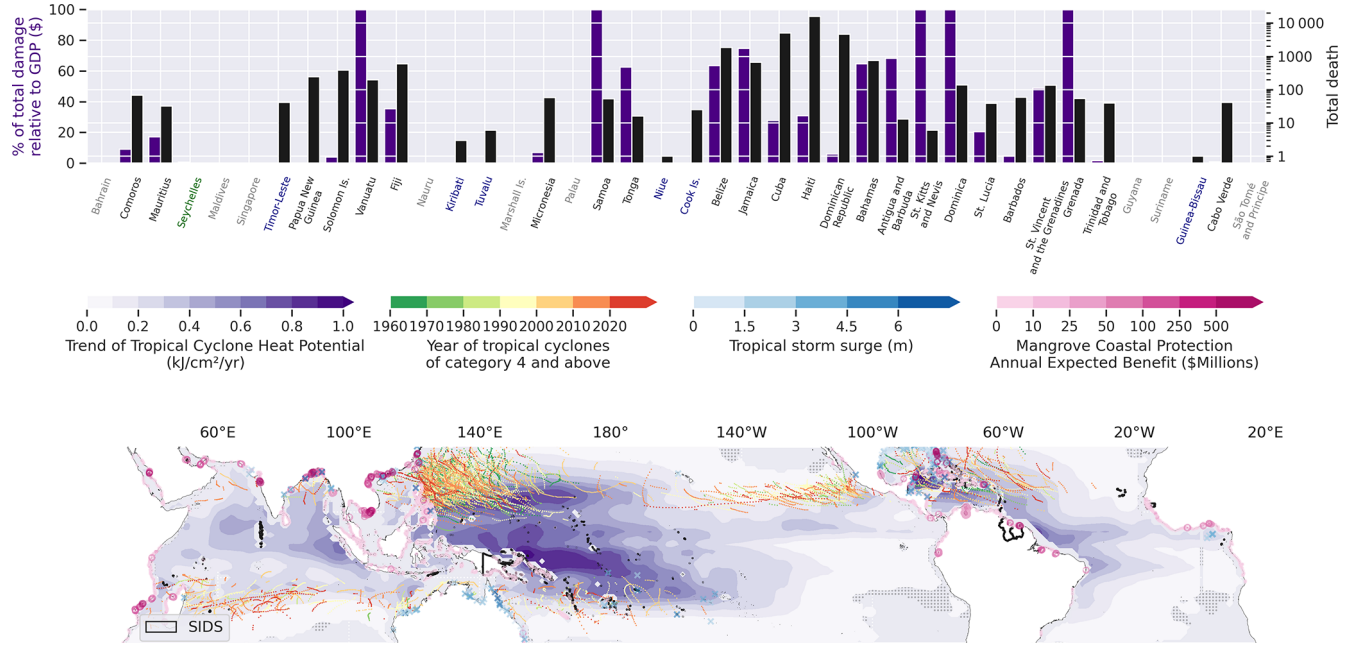


Figure 3. Tropical storms, damages and coastal protection. **(a)** Bar plot summarizing the economic impact and the toll in human lives of cyclones in Small Island Developing States (SIDS). Purple bars represent the percentage of total economic damage (in US dollars) relative to the national Gross Domestic Product (GDP) (based on product refs. no. 13 and 14), whereas black bars indicate the total number of deaths caused by cyclones in each state (product ref. no. 15). Both metrics have been calculated considering all data available since records began. **(b)** Map showing the location of SIDS (black areas, product ref. no. 2) together with different data on tropical storms and coastal protection: local trends in Tropical Cyclone Heat Potential (TCHP) computed over period 1960–2025 (purple shading; based on an average of product refs. no. 7, 8, 9 and 10), with areas dotted in grey indicating a confidence level inferior to 95 % for the trend value (based on product refs. no. 7, 8, 9 and 10); tracks for ocean cyclones of category 4 and above (wind ≧ 113 kn) coloured according to their year of occurrence (green-yellow-red dotted lines, based on product ref no. 16; Saffir-Simpson Hurricane Scale information based on the wind speed provided by the US agency); global peak storm surges registered in situ (blue crosses, based on product ref. no. 17), and annual expected economic benefit from the coastal protection provided by mangroves at marked locations (pink dots, based on product ref. no. 18).

of increasing climate risks. The outcomes can by synthesized as:

- The SIDS EEZs cover 8 % of the global ocean, and 15 % of the global tropical ocean (30° S–30° N), and SIDS are actors in transformative ocean governance. SIDS govern vast marine territories through their EEZs, which place them at the centre of ocean governance debates, where they actively shape and advance discussions on marine conservation, fisheries management, the blue economy, and climate–ocean policy.

- SIDS are custodians of a substantial share of the ocean biodiversity as the EEZs of all SIDS cover very high species richness in the world ocean. SIDS steward a large share of global marine biodiversity through their EEZs, which overlap major tropical biodiversity hotspots including coral reefs, mangroves, seagrass, and coastal wetlands, meaning that protecting SIDS biodiversity is critical to safeguarding a large fraction of the world's ocean life. SIDS provide important insights into the challenges of balancing marine conservation, food security, and economic development under increasing pressures from climate change, globalization, and competing claims on ocean resources.

- SIDS are sentinels for climate change, with 65 % of the EEZ areas of all SIDS directly exposed to sea level acceleration. SIDS are some of the most vulnerable regions to climate change due to high concentration of populations, critical infrastructure within coastal zones, compounded by economic, technological, social, and ecological barriers to adaptation.

- Ocean warming is widespread in the tropical ocean, with approximately 7 % of EEZs of all SIDS exposed to rapid ocean warming over the period 1960–2025. Ocean warming increases the frequency and intensity of marine heatwaves, which adversely impacts coral reef ecosystems. Ocean warming also has many other implications such as sea level rise, ocean circulation change, reduced carbon uptake capacity, increased frequency and strength of tropical storms, changes in marine ecosystem structure and species distributions, and impacts on fisheries and coastal communities.

- Nearly one-third (28 %) of the EEZ area of SIDS contains coral reefs classified as vulnerable, endangered or critically endangered. Coral reef ecosystems are among the most biologically diverse and economically important marine habitats holding unique economic, social and cultural value for SIDS, but climate change, together with pollution and overexploitation, now represents an existential threat to coral reefs.

- Approximately 25 % of vulnerable, endangered or critically endangered coral reefs in SIDS' EEZs have been exposed to accumulated heat stress conditions (DHW > 16 °C weeks) for at least one month during the period 1982–2025. This indicates that while extreme heat stress was episodic in time, it repeatedly impacted a large fraction of coral reef systems already vulnerable at SIDS's EEZ level.

- Based on available records, cumulative tropical cyclone damage exceeded 50 % of national GDP in approximately 40 % of SIDS with available data, although data availability and record length vary among countries (1903–2026). SIDS are faced to a multitude of disasters such as tropical cyclones, but only 38 % of SIDS reported having multi-hazard early warning systems in place.

- Over the period 1960 to 2025, around 56 % of the SIDS EEZ areas have experienced rapid (above global average) increases in tropical cyclone heat potential, indicating increase in upper-ocean heat availability for tropical cyclone intensification.

- Nearly 20 % of assessed SIDS (7 out of 40) have experienced tropical cyclone–induced storm surges exceeding 3 m based on historical records spanning 1961–2012. Storm surge represents one of the most destructive impacts of tropical cyclones, as intensified storms can generate extreme coastal water levels that rapidly inundate densely populated low-lying coastal zones.

- The mangrove coastal protection annual expected benefit exceeds USD 1 million in 18 SIDS. The value of mangroves as natural coastal defences at global, national and local scales is essential and can provide incentives for mangrove conservation and restoration in development, climate adaptation, disaster risk reduction and insurance.

Code availability. All codes are available upon request.

Data availability. All data used are available, and their sources are listed in Table 1.

Author contributions. FG: writing (original draft), conceptualization, methodology and formal analysis. KvS: conceptualization, designing, methodology, writing (original draft), investigation, supervision, and formal analysis. All authors: writing (review and editing).

Competing interests. At least one of the (co-)authors serves as topic editor for the report to which this paper belongs. The peer-review process was guided by an independent editor, and the authors also have no other competing interests to declare.

Disclaimer. The Copernicus Marine Service offering is regularly updated to ensure it remains at the forefront of user requirements. In this process, some products may undergo replacement or renaming, leading to the removal of certain product IDs from the catalogue. If readers have any questions or require assistance regarding these modifications, please feel free to reach out to the Copernicus Marine Service user support team for further guidance. They will be able to provide the necessary information to address concerns and find suitable alternatives.

Publisher's note: Copernicus Publications remains neutral with regard to jurisdictional claims made in the text, published maps, institutional affiliations, or any other geographical representation in this paper. The authors bear the ultimate responsibility for providing appropriate place names. Views expressed in the text are those of the authors and do not necessarily reflect the views of the publisher.

Financial support. This research was carried out as part of the Copernicus Marine Service implemented by MOi under a contributing agreement with the European Commission, and "Ocean observations and indicators for climate and assessments" (ObsSea4Clim) is funded by the European Union Horizon Europe Funding Programme for Research and Innovation under grant no. 101136548.

Review statement. This paper was edited by Marilaure Grégoire.

References

Asaad, I., Lundquist, C. J., Erdmann, M. V., and Costello, M. J.: Delineating priority areas for marine biodiversity conservation in the Coral Triangle, Biol. Conserv., 222, 198–211, https://doi.org/10.1016/j.biocon.2018.03.037, 2018.

Balaguru, K., Chang, C., Leung, L. R., Foltz, G. R., Hagos, S. M., Wehner, M. F., Kossin, J. P., Ting, M., and Xu, W.: A Global Increase in Nearshore Tropical Cyclone Intensification, Earths Future, 12, e2023EF004230, https://doi.org/10.1029/2023EF004230, 2024.

Bartelet, H. A., Barnes, M. L., and Cumming, G. S.: Estimating and comparing the direct economic contributions of reef fisheries and tourism in the Asia-Pacific, Mar. Policy, 159, 105939, https://doi.org/10.1016/j.marpol.2023.105939, 2024.

Beck, M. W., Losada, I. J., Menéndez, P., Reguero, B. G., Díaz-Simal, P., and Fernández, F.: The global flood protection savings provided by coral reefs, Nat. Commun., 9, 2186, https://doi.org/10.1038/s41467-018-04568-z, 2018.

Bell, J. D., Senina, I., Adams, T., Aumont, O., Calmettes, B., Clark, S., Dessert, M., Gehlen, M., Gorgues, T., Hampton, J., Hanich, Q., Harden-Davies, H., Hare, S. R., Holmes, G., Lehodey, P., Lengaigne, M., Mansfield, W., Menkes, C., Nicol, S., Ota, Y., Pasisi, C., Pilling, G., Reid, C., Ronneberg, E., Gupta, A. S., Seto, K. L., Smith, N., Taei, S., Tsamenyi, M., and Williams, P.: Pathways to sustaining tuna-dependent Pacific Island economies during climate change, Nat. Sustain., 4, 900–910, https://doi.org/10.1038/s41893-021-00745-z, 2021.

Bevan, J. L., Fritz, C., and Alaka, L.: Hurricane Beryl 28th June–9th July 2024, National Hurricane Center Tropical Cyclone Report (AL022024), https://www.nhc.noaa.gov/data/tcr/AL022024_Beryl.pdf (last access: 21 September 2026), 2025.

Bhuyan, Md. S., Jenzri, M., Islam, M. T., Adikari, D., and Hoque, M. M.: Climate change impacts on coral reefs and emerging resilience pathways: A systematic review, Ocean Coast. Manage., 276, 108134, https://doi.org/10.1016/j.ocecoaman.2026.108134, 2026.

Bohorquez, J., Fine, M., Grieco, D. I., Gill, D. A., Al-Sawalmih, A., Padilla-Gamiño, J., Bolden, I. W., Hein, M., Backstrom, C., McField, M., Martinez, R., Midberry, B., Al-Guthmy, F., Pikitch, E., Benejam, N., Azulay, C., Ronen, B., Levy, O., McElroy, A., and Kleinhaus, K.: Coral reefs span borders, so must solutions: transboundary conservation in complex political environments, npj Ocean. Sustain., 4, 64, https://doi.org/10.1038/s44183-025-00166-x, 2025.

Brodie, G., Holland, E., N'Yeurt, A. D. R., Soapi, K., and Hills, J.: Seagrasses and seagrass habitats in Pacific small island developing states: Potential loss of benefits via human disturbance and climate change, Mar. Pollut. Bull., 160, 111573, https://doi.org/10.1016/j.marpolbul.2020.111573, 2020.

Bronen, R. and Chapin, F. S.: Adaptive governance and institutional strategies for climate-induced community relocations in Alaska, P. Natl. Acad. Sci. USA, 110, 9320–9325, https://doi.org/10.1073/pnas.1210508110, 2013.

Campling, L., Havice, E., Virdin, J., Carmine, G., Andriamahefazafy, M., Barbesgaard, M., Chakravarty, S., Gorez, B., Hetherington, D., Kim, H., Mfodwo, K., and Standing, A.: A geopolitical-economy of distant water fisheries access arrangements, npj Ocean. Sustain., 3, 26, https://doi.org/10.1038/s44183-024-00060-y, 2024.

Chaijaroen, P.: Coral Reef Deterioration and Livelihoods of Coastal Communities: An Economics Perspective, in: Corals – Habitat Formers in the Anthropocene, edited by: Chimienti, G., IntechOpen, https://doi.org/10.5772/intechopen.105355, 2023.

Châles, F.: A systematic review of coral reef, mangrove, and seagrass ecosystem services in Pacific Small Island Developing States, Mondes Dév., 203, 125–149, https://doi.org/10.3917/e.med.203.0125, 2023.

Cheng, L., Von Schuckmann, K., Abraham, J. P., Trenberth, K. E., Mann, M. E., Zanna, L., England, M. H., Zika, J. D., Fasullo, J. T., Yu, Y., Pan, Y., Zhu, J., Newsom, E. R., Bronselaer, B., and Lin, X.: Past and future ocean warming, Nat. Rev. Earth Environ., 3, 776–794, https://doi.org/10.1038/s43017-022-00345-1, 2022.

Cheng, L., Tan, Z., Pan, Y., Zheng, H., Zhu, Y., Wei, W., Du, J., Li, G., Ye, H., and Gouretski, V.: IAP global ocean heat content 1° gridded analysis product (IAPv4), Marine Science Data Center of the Chinese Academy of Sciences [data set], https://doi.org/10.12157/IOCAS.20240117.001, 2024a.

Cheng, L., Pan, Y., Tan, Z., Zheng, H., Zhu, Y., Wei, W., Du, J., Yuan, H., Li, G., Ye, H., Gouretski, V., Li, Y., Trenberth, K. E., Abraham, J., Jin, Y., Reseghetti, F., Lin, X., Zhang, B., Chen, G., Mann, M. E., and Zhu, J.: IAPv4 ocean temperature and ocean heat content gridded dataset, Earth Syst. Sci. Data, 16, 3517–3546, https://doi.org/10.5194/essd-16-3517-2024, 2024b.

Choi, H.-Y., Park, M.-S., Kim, H.-S., and Lee, S.: Marine heatwave events strengthen the intensity of tropical cyclones, Commun. Earth Environ., 5, 69, https://doi.org/10.1038/s43247-024-01239-4, 2024.

Claus, S., De Hauwere, N., Vanhoorne, B., Deckers, P., Souza Dias, F., Hernandez, F., and Mees, J.: Marine Regions: Towards a Global Standard for Georeferenced Marine Names and Boundaries, Mar. Geod., 37, 99–125, https://doi.org/10.1080/01490419.2014.902881, 2014.

Costanza, R., d'Arge, R., De Groot, R., Farber, S., Grasso, M., Hannon, B., Limburg, K., Naeem, S., O'Neill, R. V., Paruelo, J., Raskin, R. G., Sutton, P., and Van Den Belt, M.: The value of the world's ecosystem services and natural capital, Nature, 387, 253–260, https://doi.org/10.1038/387253a0, 1997.

Costello, M. J., Vale, M. M., Kiessling, W., Maharaj, S., Price, J., and Talukdar, G. H.: Cross-Chapter Paper 1: Biodiversity Hotspots, in: Climate Change 2022: Impacts, Adaptation and Vulnerability. Contribution of Working Group II to the Sixth Assessment Report of the Intergovernmental Panel on Climate Change, 1st edn., Cambridge University Press, Cambridge, UK and New York, NY, USA, https://doi.org/10.1017/9781009325844, 2023.

Cramer, K. L., Bernard, M. L., Bernat, I., Gutierrez, L., Murphy, E. L., Sangolquí, P., Surrey, K. C., and Gerber, L. R.: The Present and Future Status of Ecosystem Services for Coral Reefs, in: Imperiled: The Encyclopedia of Conservation, Elsevier, 46–54, https://doi.org/10.1016/B978-0-12-821139-7.00177-X, 2022.

CRED: Human Impact Variables, EM-DAT, CRED (Centre for Research on the Epidemiology of Disasters), https://doc.emdat.be/docs/data-structure-and-content/impact-variables/human/ (last access: 1 July 2026), 2023a.

CRED: Economic Impact Variables, EM-DAT, CRED (Centre for Research on the Epidemiology of Disasters), https://doc.emdat.be/docs/data-structure-and-content/impact-variables/economic/ (last access: 1 July 2026), 2023b.

CRED: 2024 Disasters in Numbers. Brussels, Centre for Research on the Epidemiology of Disasters (CRED), Belgium, https://files.emdat.be/reports/2024_EMDAT_report.pdf (last access: 21 September 2026), 2025.

Delforge, D., Below, R., Wathelet, V., Tonnelier, M., Alonso, A., and Speybroeck, N.: 2025 Disasters in Numbers, Centre for Research on the Epidemiology of Disasters (CRED), Belgium, https://files.emdat.be/reports/2025_EMDAT_report.pdf (last access: 21 September 2026), 2026.

de-Miguel-Molina, B., de-Miguel-Molina, M., and Rumiche-Sosa, M. E.: Luxury sustainable tourism in Small Island Developing States surrounded by coral reefs, Ocean Coast. Manage., 98, 86–94, https://doi.org/10.1016/j.ocecoaman.2014.06.017, 2014.

Dzwonkowski, B., Coogan, J., Fournier, S., Lockridge, G., Park, K., and Lee, T.: Compounding impact of severe weather events fuels marine heatwave in the coastal ocean, Nat. Commun., 11, 4623, https://doi.org/10.1038/s41467-020-18339-2, 2020.

Eakin, C. M., Heron, S. F., Connolly, S. R., Devotta, D. A., Liu, G., Geiger, E. F., De La Cour, J. L., Gomez, A. M., Skirving, W. J., Baird, A. H., Cantin, N. E., Couch, C. S., Donner, S. D., Gilmour, J., Gonzalez-Rivero, M., Gudka, M., Harrison, H. B., Hodgson, G., Hoegh-Guldberg, O., Hoey, A. S., Hoogenboom, M. O., Hughes, T. P., Johnson, M. E., Kerry, J. T., Kimura, T., Mihaly, J., Muñiz-Castillo, A. I., Obura, D. O., Pratchett, M. S., Rivera-Sosa, A., Ross, C. L., Stein, J., Thompson, A., Torda, G., Viehman, T. S., Walter, C. S., Wilson, S., Marsh, B. L., Spady, B. L., Dyer, N., Adam, T. C., Alcolado, P., Alidoostsalimi, M., Alidoostsalimi, P., Alvarez-Filip, L., Álvarez-Noriega, M., Arias-González, J. E., Bahr, K. D., Barnes, P., Barraza Sandoval, J. E., Baum, J. K., Bauman, A. G., Beger, M., Berry, K., Bessell-Browne, P., Bigot, L., Bonito, V., Brodnicke, O. B., Burdick, D., Burkepile, D. E., Burt, A. J., Burt, J. A., Butler, I. R., Caldwell, J. M., Chancerelle, Y., Chen, C. A., Cherh, K.-L., Childress, M. J., Coker, D. J., Costa, B., Coward, G., Crabbe, M. J. C., Dallison, T., Dalton, S., DeCarlo, T. M., Drury, C., Drysdale, I., Edwards, C. B., Eggertsen, L., Elma, E., Ennis, R. S., Evans, R. D., Eyal, G., Fenner, D., Figueroa-Zavala, B., Fisch, J., Fox, M. D., Gadoutsis, E., Gilbert, A., Halford, A. R., Heintz, T., Hewlett, J., Hobbs, J.-P. A., Hoot, W. C., Houk, P., Johnston, L., Johnston, M. A., Kayanne, H., Kennedy, E. V., Kikuchi, R. K. P. D., Kloiber, U., Koike, H., Kramer, K. L., Kuo, C.-Y., Lang, J., Lawrence, A., Leadbeater, A., Leão, Z. M. A. N., Lee, J. N., Lewis, C., Lirman, D., Longo, G. O., MacDonald, C., Mallela, J., Mangubhai, S., Da Silva, I. M., Mason-Parker, C., McDonough, V., McField, M., Mello, T., Miternique-Agathe, C., Madi, M., Moldzio, S., Monroe, A. A., Montefalcone, M., Moses, K. S., Mostafavi, P. G., Moura, R. L. D., Munasinghe, C. S., Mwaura, J., Nakamura, T., Nicet, J.-B., Nuttall, M. F., Oliveira, M. D. M., Oxenford, H. A., Pandolfi, J. M., Patankar, V., Perez, D., Perera, N., Prabuning, D., Precht, W., Raj, K. D., Reimer, J. D., Richardson, L. E., Rotjan, R., Ryan, N., Salm, R., Sandin, S. A., Schopmeyer, S., Shedrawi, G., Shokri, M. R., Smith, J. E., Smith, K., Smith, S. R., Smith, T. B., Sommer, B., Soto, M., Suckoo, R., Sykes, H., Tagarino, K. A., Teoh, M., Thai, M. Q., Toh, T. C., Tredinnick, A., Tso, A., Tyley, H., Ussi, A. M., Vargas-Angel, B., Vaterlaus, C., Vermeij, M. J. A., Vo, S. T., Voolstra, C. R., Wee, H. B., Weiler, B. A., Williams, D. E., Yahya, S. A. S., Yeemin, T., Ziegler, M., and Manzello, D. P.: Severe and widespread coral reef damage during the 2014–2017 Global Coral Bleaching Event, Nat. Commun., 17, 1318, https://doi.org/10.1038/s41467-025-67506-w, 2026.

Emanuel, K., DesAutels, C., Holloway, C., and Korty, R.: Environmental Control of Tropical Cyclone Intensity, J. Atmos. Sci., 61, 843–858, https://doi.org/10.1175/1520-0469(2004)061<0843:ECOTCI>2.0.CO;2, 2004.

Englander, G.: Property rights and the protection of global marine resources, Nat. Sustain., 2, 981–987, https://doi.org/10.1038/s41893-019-0389-9, 2019.

E.U. Copernicus Marine Service: Global Ocean Mean Sea Level trend map from Observations Reprocessing, Marine Data Store (MDS) [data set], https://doi.org/10.48670/moi-00238, 2025.

E.U. Copernicus Marine Service: Global Ocean in situ – Delayed Mode temperature and salinity CORA – objective analysis, Marine Data Store (MDS) [data set], https://doi.org/10.48670/mds-00383, 2026.

Ferrario, F., Beck, M. W., Storlazzi, C. D., Micheli, F., Shepard, C. C., and Airoldi, L.: The effectiveness of coral reefs for coastal hazard risk reduction and adaptation, Nat. Commun., 5, 3794, https://doi.org/10.1038/ncomms4794, 2014.

FFA: FFA 2023 Tuna Economic Indicators Brochure, Pacific Islands Forum Fisheries Agency, HONIARA, Solomon Islands, https://www.ffa.int/publications-and-statistics/statistics/ (last access: 21 September 2026), 2023.

Flanders Marine Institute: Maritime Boundaries Geodatabase: Maritime Boundaries and Exclusive Economic Zones (200NM), version 12, Flanders Marine Institute [data set], https://doi.org/10.14284/632, 2023.

Gahtan, J., Knapp, K. R., Schreck, C. J. III, Diamond, H. J., Kossin, J. P., and Kruk, M. C.: International Best Track Archive for Climate Stewardship (IBTrACS) Project, Version 4.01, NOAA National Centers for Environmental Information [data set], https://doi.org/10.25921/82ty-9e16, 2024.

Gedan, K. B., Kirwan, M. L., Wolanski, E., Barbier, E. B., and Silliman, B. R.: The present and future role of coastal wetland vegetation in protecting shorelines: answering recent challenges to the paradigm, Climatic Change, 106, 7–29, https://doi.org/10.1007/s10584-010-0003-7, 2011.

Good, S. A., Martin, M. J., and Rayner, N. A.: EN4 quality controlled subsurface ocean temperature and salinity profiles and objective analyses, Met Office Hadley Centre [data set], https://www.metoffice.gov.uk/hadobs/en4/index.html (last access: 1 July 2026), 2013a.

Good, S. A., Martin, M. J., and Rayner, N. A.: EN4: Quality controlled ocean temperature and salinity profiles and monthly objective analyses with uncertainty estimates, J. Geophys. Res.-Oceans, 118, 6704–6716, https://doi.org/10.1002/2013JC009067, 2013b.

Gray, W. M.: Global View Of The Origin Of Tropical Disturbances And Storms, Mon. Wea. Rev., 96, 669–700, https://doi.org/10.1175/1520-0493(1968)096<0669:GVOTOO>2.0.CO;2, 1968.

Green, A. and Wewerinke-Singh, M.: State Continuity, Self-Determination and Sea-Level Rise, Int. Comp. Law Q., 74, 555–585, https://doi.org/10.1017/S0020589325100961, 2025.

Grimley, L. E., Hollinger Beatty, K. E., Sebastian, A., Bunya, S., and Lackmann, G. M.: Climate change exacerbates compound flooding from recent tropical cyclones, npj Nat. Hazards, 1, 45, https://doi.org/10.1038/s44304-024-00046-3, 2024.

Guha-Sapir, D.: EM-DAT, the Emergency Events Database, Centre for Research on the Epidemiology of Disasters (CRED), Université catholique de Louvain, https://www.emdat.be (last access: 1 July 2026), 2020.

Guo, Y.-P. and Tan, Z.-M.: Enhanced global storm surges by tropical cyclone poleward migration, P. Natl. Acad. Sci. USA, 123, e2535524123, https://doi.org/10.1073/pnas.2535524123, 2026.

Gussmann, G. and Hinkel, J.: A framework for assessing the potential effectiveness of adaptation policies: Coastal risks and sea-level rise in the Maldives, Environ. Sci. Policy, 115, 35–42, https://doi.org/10.1016/j.envsci.2020.09.028, 2021.

Haas, B., Jaeckel, A., Pouponneau, A., Sacedon, R., Singh, G. G., and Cisneros-Montemayor, A. M.: The use of influential

power in ocean governance, Front. Mar. Sci., 10, 1045887, https://doi.org/10.3389/fmars.2023.1045887, 2023.

Hallam, S., Marsh, R., Josey, S. A., Hyder, P., Moat, B., and Hirschi, J. J.-M.: Ocean precursors to the extreme Atlantic 2017 hurricane season, Nat. Commun., 10, 896, https://doi.org/10.1038/s41467-019-08496-4, 2019.

Hallam, S., Guishard, M., Josey, S. A., Hyder, P., and Hirschi, J.: Increasing tropical cyclone intensity and potential intensity in the subtropical Atlantic around Bermuda from an ocean heat content perspective 1955–2019, Environ. Res. Lett., 16, 034052, https://doi.org/10.1088/1748-9326/abe493, 2021.

Hassanali, K., Catzim, N., Derrig, R., Harden-Davies, H., Nelson, V. G., and Pouponneau, A.: Big schools of small fish in a big pond – the influence of small-island developing states in the BBNJ process, Front. Mar. Sci., 13, 1762739, https://doi.org/10.3389/fmars.2026.1762739, 2026.

Hinkel, J., Garcin, M., Gussmann, G., Amores, A., Barbier, C., Bisaro, A., Le Cozannet, G., Duvat, V., Imad, M., Khaleel, Z., Marcos, M., Pedreros, R., Shareef, A., and Waheed, A.: Co-creating a coastal climate service to prioritise investments in erosion prevention and sea-level rise adaptation in the Maldives, Climate Services, 31, 100401, https://doi.org/10.1016/j.cliser.2023.100401, 2023.

Huang, B., Liu, C., Banzon, V. F., Freeman, E., Graham, G., Hankins, W., Smith, T. M., and Zhang, H.-M.: NOAA 0.25-degree Daily Optimum Interpolation Sea Surface Temperature (OISST), Version 2.1, NOAA National Centers for Environmental Information [data set], https://doi.org/10.25921/RE9P-PT57, 2020.

Huang, B., Liu, C., Banzon, V., Freeman, E., Graham, G., Hankins, B., Smith, T., and Zhang, H.-M.: Improvements of the Daily Optimum Interpolation Sea Surface Temperature (DOISST) Version 2.1, J. Climate, 34, 2923–2939, https://doi.org/10.1175/JCLI-D-20-0166.1, 2021.

Hughes, D. J., Alderdice, R., Cooney, C., Kühl, M., Pernice, M., Voolstra, C. R., and Suggett, D. J.: Coral reef survival under accelerating ocean deoxygenation, Nat. Clim. Chang., 10, 296–307, https://doi.org/10.1038/s41558-020-0737-9, 2020.

Hughes, T. P., Kerry, J. T., Álvarez-Noriega, M., Álvarez-Romero, J. G., Anderson, K. D., Baird, A. H., Babcock, R. C., Beger, M., Bellwood, D. R., Berkelmans, R., Bridge, T. C., Butler, I. R., Byrne, M., Cantin, N. E., Comeau, S., Connolly, S. R., Cumming, G. S., Dalton, S. J., Diaz-Pulido, G., Eakin, C. M., Figueira, W. F., Gilmour, J. P., Harrison, H. B., Heron, S. F., Hoey, A. S., Hobbs, J.-P. A., Hoogenboom, M. O., Kennedy, E. V., Kuo, C., Lough, J. M., Lowe, R. J., Liu, G., McCulloch, M. T., Malcolm, H. A., McWilliam, M. J., Pandolfi, J. M., Pears, R. J., Pratchett, M. S., Schoepf, V., Simpson, T., Skirving, W. J., Sommer, B., Torda, G., Wachenfeld, D. R., Willis, B. L., and Wilson, S. K.: Global warming and recurrent mass bleaching of corals, Nature, 543, 373–377, https://doi.org/10.1038/nature21707, 2017.

Hume, A., Leape, J., Oleson, K. L. L., Polk, E., Chand, K., and Dunbar, R.: Towards an ocean-based large ocean states country classification, Mar. Policy, 134, 104766, https://doi.org/10.1016/j.marpol.2021.104766, 2021.

IPCC: The Ocean and Cryosphere in a Changing Climate: Special Report of the Intergovernmental Panel on Climate Change, 1st edn., Cambridge University Press, https://doi.org/10.1017/9781009157964, 2019.

IPCC: Climate Change 2021 – The Physical Science Basis: Working Group I Contribution to the Sixth Assessment Report of the Intergovernmental Panel on Climate Change, 1st edn., Cambridge University Press, https://doi.org/10.1017/9781009157896, 2021.

IPCC: Climate Change 2022 – Impacts, Adaptation and Vulnerability: Working Group II Contribution to the Sixth Assessment Report of the Intergovernmental Panel on Climate Change, 1st edn., Cambridge University Press, https://doi.org/10.1017/9781009325844, 2023.

Irish, J. L., Resio, D. T., and Divoky, D.: Statistical properties of hurricane surge along a coast, J. Geophys. Res., 116, C10007, https://doi.org/10.1029/2010JC006626, 2011.

IUCN: Reef-forming Corals (spatial data), The IUCN Red List of Threatened Species, IUCN [data set], https://www.iucnredlist.org/resources/spatial-data-download (last access: 1 July 2026), 2020.

IUCN: Species Richness and Rarity-Weighted Richness spatial data, International Union for Conservation of Nature [data set], https://www.iucnredlist.org/resources/other-spatial-downloads (last access: 1 July 2026), 2025a.

IUCN: Red List Technical Working Group: Mapping Standards and Data Quality for IUCN Red List Spatial Data. Version 1.21, IUCN, https://nc.iucnredlist.org/redlist/content/attachment_files/Mapping_Standards_Version_1.21_Nov2025.pdf (last access: 1 July 2026), 2025b.

IUCN: The IUCN Red List of Threatened Species, Version 2025-2, https://www.iucnredlist.org (last access: 1 July 2026), 2026.

Jablonski, D., Roy, K., and Valentine, J. W.: Out of the Tropics: Evolutionary Dynamics of the Latitudinal Diversity Gradient, Science, 314, 102–106, https://doi.org/10.1126/science.1130880, 2006.

Jaimes, B., Shay, L. K., and Uhlhorn, E. W.: Enthalpy and Momentum Fluxes during Hurricane Earl Relative to Underlying Ocean Features, Mon. Weather Rev., 143, 111–131, https://doi.org/10.1175/MWR-D-13-00277.1, 2015.

Jaimes, B., Shay, L. K., and Brewster, J. K.: Observed air-sea interactions in tropical cyclone Isaac over Loop Current mesoscale eddy features, Dynam. Atmos. Oceans, 76, 306–324, https://doi.org/10.1016/j.dynatmoce.2016.03.001, 2016.

Keo, K. and Yoona, J.: The State of Climate Ambition, UNDP, New York, https://www.undp.org/publications/state-climate-ambition-snapshots-least-developed-countries-ldcs-and-small-island-developing-states-sids (last access: 17 June 2026), 2022.

Kleisner, K. and Pauly, D.: Stock-Status Plots (SSPs), Sea Around Us, https://www.seaaroundus.org/doc/Methods/StockStatusMethod/Method-SSP-new-June-08-2015.pdf (last access: 21 September 2026), 2015.

Knapp, K. R., Kruk, M. C., Levinson, D. H., Diamond, H. J., and Neumann, C. J.: The International Best Track Archive for Climate Stewardship (IBTrACS): Unifying Tropical Cyclone Data, B. Am. Meteorol. Soc., 91, 363–376, https://doi.org/10.1175/2009BAMS2755.1, 2010.

Krauss, K. W., McKee, K. L., Lovelock, C. E., Cahoon, D. R., Saintilan, N., Reef, R., and Chen, L.: How mangrove forests adjust to rising sea level, New Phytol., 202, 19–34, https://doi.org/10.1111/nph.12605, 2014.

Labh, N.: Reconsidering Sovereignty Amid the Climate Crisis, Carnegie Endowment for International Peace Publications, https://assets.carnegieendowment.org/static/files/Labh-Climate%20Sovereignty.pdf (last access: 16 June 2026), 2025.

Levitus, S., Antonov, J. I., Boyer, T. P., Baranova, O. K., Garcia, H. E., Locarnini, R. A., Mishonov, A. V., Reagan, J. R., Seidov, D., Yarosh, E. S., and Zweng, M. M.: World ocean heat content and thermosteric sea level change (0–2000 m), 1955–2010, Geophys. Res. Lett., 39, 2012GL051106, https://doi.org/10.1029/2012GL051106, 2012.

Levitus, S., Antonov, J., Boyer, T., Baranova, O. K., Garcia, H. E., Locarnini, R. A., Mishonov, A. V., Reagan, J. R., Seidov, D., Yarosh, E., and Zweng, M. M.: NCEI ocean heat content, temperature anomalies, salinity anomalies, thermosteric sea level anomalies, halosteric sea level anomalies, and total steric sea level anomalies from 1955 to present calculated from in situ oceanographic subsurface profile data (NCEI Accession 0164586), Version 1.1, NOAA National Centers for Environmental Information [data set], https://doi.org/10.7289/V53F4MVP, 2017.

Lévy, M., von Schuckmann, K., Butel, M., Cheung, W. W. L., Claudet, J., Frölicher, T. L., Guillotreau, P., Haugan, P., Adams, J., Amon, D., Bambridge, T., Barzuna, C., Blanke, B., Cheng, L., Chiba, S., Cortés, J., Friedlingstein, P., Gattuso, J.-P., Gelcich, S., Gephart, J., Greaves, D., Hasson, A., Jolly, C., Li, D., Shin, Y.-J., Slangen, A., Takoko, M., Thébaud, O., Vincent, A., and Vincent, P.: The 2026 Starfish Barometer, in: 10th edition of the Copernicus Ocean State Report (OSR10), edited by: Grégoire, M., Brasseur, P., Garric, G., Karstensen, J., Lionello, P., Marcos, M., Poulain, P.-M., and Staneva, J., Copernicus Publications, State Planet, 7-osr10, 1, https://doi.org/10.5194/sp-7-osr10-1-2026, 2026.

Liu, K. S. and Chan, J. C. L.: Growing Threat of Rapidly-Intensifying Tropical Cyclones in East Asia, Adv. Atmos. Sci., 39, 222–234, https://doi.org/10.1007/s00376-021-1126-7, 2022.

Lombard, A. T., Clifford-Holmes, J., Goodall, V., Snow, B., Truter, H., Vrancken, P., Jones, P. J. S., Cochrane, K., Flannery, W., Hicks, C., Gipperth, L., Allison, E. H., Diz, D., Peters, K., Erinosho, B., Levin, P., Holthus, P., Szephegyi, M. N., Awad, A., Golo, H., and Morgera, E.: Principles for transformative ocean governance, Nat. Sustain., 6, 1587–1599, https://doi.org/10.1038/s41893-023-01210-9, 2023.

Marino, E.: Adaptation privilege and Voluntary Buyouts: Perspectives on ethnocentrism in sea level rise relocation and retreat policies in the US, Global Environ. Chang., 49, 10–13, https://doi.org/10.1016/j.gloenvcha.2018.01.002, 2018.

Martyr-Koller, R., Thomas, A., Schleussner, C.-F., Nauels, A., and Lissner, T.: Loss and damage implications of sea-level rise on Small Island Developing States, Curr. Opin. Env. Sust., 50, 245–259, https://doi.org/10.1016/j.cosust.2021.05.001, 2021.

Menéndez, P., Losada, I. J., Beck, M. W., Torres-Ortega, S., Espejo, A., Narayan, S., Díaz-Simal, P., and Lange, G.-M.: Valuing the protection services of mangroves at national scale: The Philippines, Ecosyst. Serv., 34, 24–36, https://doi.org/10.1016/j.ecoser.2018.09.005, 2018.

Menéndez, P., Losada, I. J., Torres-Ortega, S., Narayan, S., and Beck, M. W.: The Global Flood Protection Benefits of Mangroves, Sci. Rep., 10, 4404, https://doi.org/10.1038/s41598-020-61136-6, 2020.

Mimura, N., Nurse, L. A., McLean, R. F., Agard, J., Briguglio, L., Lefale, P., Payet, R., and Sem, G.: Small islands, in: Climate Change 2007: Impacts, Adaptation and Vulnerability, Contribution of Working Group II to the Fourth Assessment Report of the Intergovernmental Panel on Climate Change, edited by: Parry, M. L., Canziani, O. F., Palutikof, J. P., van der Linden, P. J., and Hanson, C. E., Cambridge University Press, Cambridge, UK and New York, NY, USA, 687–716, https://www.ipcc.ch/site/assets/uploads/2018/02/WGIIAR5-Chap29_FINAL.pdf (last access: 28 September 2026), 2007.

Momin, I. M., Karmakar, A., Gupta, A., and Mitra, A. K.: Tropical Cyclone Heat Potential (TCHP) from the NCMRWF NEMO based global ocean analysis and forecast system, MAUSAM, 72, 207–214, https://doi.org/10.54302/mausam.v72i1.136, 2021.

Moonsammy, S., Boman, M., Ramdhanie, V., and Renn-Moonsammy, D.-M.: State-of-the art valuation of wetland ecosystem services in Small Island Developing States: A systematic review with an emphasis on future research needs, Ecosyst. Serv., 68, 101625, https://doi.org/10.1016/j.ecoser.2024.101625, 2024.

Needham, H. F. and Keim, B. D.: A storm surge database for the US Gulf Coast, Int. J. Climatol., 32, 2108–2123, https://doi.org/10.1002/joc.2425, 2012.

Needham, H. F. and Keim, B. D.: Global Peak Storm Surge Map, SURGEDAT – The World's Storm Surge Information Center, Louisiana State University [data set], https://surge.climate.lsu.edu/data.html (last access: 1 July 2026), 2015.

OECD: Sustainable Ocean for All: Harnessing the Benefits for Developing Countries, OECD Publishing, https://doi.org/10.1787/bede6513-en, 2020.

Olson, D. M. and Dinerstein, E.: The Global 200: Priority Ecoregions for Global Conservation, Ann. MO Bot. Gard., 89, 199, https://doi.org/10.2307/3298564, 2002.

Pan, Y., Cheng, L., Abraham, J., Trenberth, K. E., Reagan, J., Du, J., Wang, Z., Storto, A., Von Schuckmann, K., Zhu, Y., Mann, M. E., Zhu, J., Wang, F., Yu, F., Locarnini, R., Fasullo, J., Huang, B., Graham, G., Yin, X., Gouretski, V., Zheng, F., Li, Y., Zhang, B., Wan, L., Chen, X., Wang, D., Feng, L., Song, X., Liu, Y., Reseghetti, F., Simoncelli, S., Chen, G., Zhang, R., Mishonov, A., Wei, W., Tan, Z., Li, G., Cao, L., Chen, L., Yuan, H., Lyu, K., Sulaiman, A., Mayer, M., Wang, H., Ma, Z., Bao, S., Yan, H., Liu, Z., Yang, C., Liu, X., Hausfather, Z., Gues, F., Song, X., Zhang, M., and Chen, L.: Ocean Heat Content Sets Another Record in 2025, Adv. Atmos. Sci., https://doi.org/10.1007/s00376-026-5876-0, 2026.

Pearce-Kelly, P., Altieri, A. H., Bruno, J. F., Cornwall, C. E., McField, M., Muñiz-Castillo, A. I., Rocha, J., Setter, R. O., Sheppard, C., Roman-Cuesta, R. M., and Yesson, C.: Considerations for determining warm-water coral reef tipping points, Earth Syst. Dynam., 16, 275–292, https://doi.org/10.5194/esd-16-275-2025, 2025.

Pereira, P. H. C., Araujo, J. C., Lima, G. V., Côrtes, L. G. F., Gomes, E., and Magris, R. A.: Effectiveness of management zones for recovering parrotfish species within the largest coastal marine protected area in Brazil, Sci. Rep., 12, 12232, https://doi.org/10.1038/s41598-022-15990-1, 2022.

Pfab, F., Detmer, A. R., Moeller, H. V., Nisbet, R. M., Putnam, H. M., and Cunning, R.: Heat stress and bleaching in corals: a bioenergetic model, Coral Reefs, 43, 1627–1645, https://doi.org/10.1007/s00338-024-02561-1, 2024.

Pujol, M. I., Quet, V., and Legeais, J. F.: EU Copernicus Marine Service Product User Manual for the OMI_CLIMATE_SL_GLOBAL_regional_trends, issue 6.0, Mercator Ocean International, https://documentation.marine.copernicus.eu/PUM/CMEMS-SL-PUM-CLIMATE.pdf (last access: 1 July 2026), 2025.

Quet, V., Taburet, G., and Pujol, M. I.: EU Copernicus Marine Service Quality Information Document for OMI_CLIMATE_SL_GLOBAL_regional_trends, issue 7.0, Mercator Ocean International, EU Copernicus Marine Service, https://documentation.marine.copernicus.eu/QUID/CMEMS-SL-QUID-CLIMATE.pdf (last access: 1 July 2026), 2025.

RAMSAR, Robertson, H., Fennessy, S., Hilton, G., Job, N., Kumar, R., Simpson, M., Aggestam, F., Aldred, M., Chacón, A., Costanza, R., Davidson, N., Field, C., Finlayson, C. M., Gandra, F., Gillis, L. G., Hernández-Blanco, M., Moritsch, M., Thornton, S., Wood, K., and Van'T Hoff, V.: Global Wetland Outlook 2025: Valuing, conserving, restoring and financing wetlands, Convention on Wetlands, https://doi.org/10.69556/GWO-2025-eng, 2025.

Robinson, S., Carlson, D., Bouton, E., Dolan, M., Meakem, A., Messer, A., and Roberts, J. T.: The dynamics of institutional arrangements for climate change adaptation in small island developing states in the Atlantic and Indian Oceans, Sustain. Sci., 18, 251–264, https://doi.org/10.1007/s11625-022-01186-z, 2023.

Robles-Zavala, E. and Chang Reynoso, A. G.: The recreational value of coral reefs in the Mexican Pacific, Ocean Coast. Manage., 157, 1–8, https://doi.org/10.1016/j.ocecoaman.2018.02.010, 2018.

Saddington, L.: Geopolitical imaginaries in climate and ocean governance: Seychelles and the Blue Economy, Geoforum, 139, 103682, https://doi.org/10.1016/j.geoforum.2023.103682, 2023.

Saeedi, H., Costello, M. J., Warren, D., and Brandt, A.: Latitudinal and bathymetrical species richness patterns in the NW Pacific and adjacent Arctic Ocean, Sci. Rep., 9, 9303, https://doi.org/10.1038/s41598-019-45813-9, 2019.

Sandi, S. G., Rodríguez, J. F., Saintilan, N., Riccardi, G., and Saco, P. M.: Rising tides, rising gates: The complex ecogeomorphic response of coastal wetlands to sea-level rise and human interventions, Adv. Water Resour., 114, 135–148, https://doi.org/10.1016/j.advwatres.2018.02.006, 2018.

Sasaki, H. and Motoi, T.: Accelerated Increase in Tropical Cyclone Heat Potential in the Typhoon Rapidly Intensifying Zone during 1955–2020, SOLA, 18, 65–70, https://doi.org/10.2151/sola.2022-011, 2022.

SEDAC: 2020 Environmental Performance Index, NASA Socioeconomic Data and Applications Center (SEDAC), Yale Center for Environmental Law & Policy (YCELP) [data set], https://doi.org/10.7927/F54C-0R44, 2020.

Seguin, R., Mouillot, D., Cinner, J. E., Stuart Smith, R. D., Maire, E., Graham, N. A. J., McLean, M., Vigliola, L., and Loiseau, N.: Towards process-oriented management of tropical reefs in the anthropocene, Nat. Sustain., 6, 148–157, https://doi.org/10.1038/s41893-022-00981-x, 2022.

Singh, P., Linnér, B.-O., and Singh, A. A.: Marine spatial planning and ocean governance in Small Island Developing States, Reg. Environ. Change, 25, 91, https://doi.org/10.1007/s10113-025-02412-x, 2025.

Song, J., Klotzbach, P. J., and Duan, Y.: Increasing lifetime maximum intensity of rapidly intensifying tropical cyclones over the western North Pacific, Environ. Res. Lett., 16, 034002, https://doi.org/10.1088/1748-9326/abdbf1, 2021.

Spalding, A. K., Grorud-Colvert, K., Allison, E. H., Amon, D. J., Collin, R., De Vos, A., Friedlander, A. M., Johnson, S. M., Mayorga, J., Paris, C. B., Scott, C., Suman, D. O., Cisneros-Montemayor, A. M., Estradivari, Giron-Nava, A., Gurney, G. G., Harris, J. M., Hicks, C., Mangubhai, S., Micheli, F., Naggea, J., Obura, D., Palacios-Abrantes, J., Pouponneau, A., and Thurber, R. V.: Engaging the tropical majority to make ocean governance and science more equitable and effective, npj Ocean. Sustain., 2, 8, https://doi.org/10.1038/s44183-023-00015-9, 2023.

Spalding, M., Burke, L., Wood, S. A., Ashpole, J., Hutchison, J., and Zu Ermgassen, P.: Mapping the global value and distribution of coral reef tourism, Mar. Policy, 82, 104–113, https://doi.org/10.1016/j.marpol.2017.05.014, 2017.

Sumaila, U. R., Dyck, A., and Cheung, W. W. L.: Fisheries subsidies and potential catch loss in SIDS Exclusive Economic Zones: food security implications, Envir. Dev. Econ., 18, 427–439, https://doi.org/10.1017/S1355770X13000156, 2013.

Szekely, T.: EU Copernicus Marine Service Quality Information Document for In Situ TAC Objective Analysis product INSITU_GLO_PHY_TS_OA_MY_013_052, issue 1.15, Mercator Ocean International, https://documentation.marine.copernicus.eu/QUID/CMEMS-INS-QUID-013-052.pdf (last access: 1 July 2026), 2026a.

Szekely, T.: EU Copernicus Marine Service Product User Manual for the In Situ TAC objective analysis Products INSITU_GLO_PHY_TS_OA_MY_013_052 and INSITU_GLO_PHY_TS_OA_NRT_013_002, issue 1.13, Mercator Ocean International, https://documentation.marine.copernicus.eu/PUM/CMEMS-INS-PUM-013-002-052.pdf (last access: 1 July 2026), 2026b.

Tebbett, S. B., Connolly, S. R., and Bellwood, D. R.: Benthic composition changes on coral reefs at global scales, Nat. Ecol. Evol., 7, 71–81, https://doi.org/10.1038/s41559-022-01937-2, 2023.

Teelucksingh, S., Nunes, P. A. L. D., and Perrings, C.: Biodiversity-based development in Small Island Developing States, Envir. Dev. Econ., 18, 381–391, https://doi.org/10.1017/S1355770X13000260, 2013.

Teh, L. S. L., Teh, L. C. L., and Sumaila, U. R.: A Global Estimate of the Number of Coral Reef Fishers, PLoS ONE, 8, e65397, https://doi.org/10.1371/journal.pone.0065397, 2013.

Teneva, L., Free, C. M., Hume, A., Agostini, V. N., Klein, C. J., Watson, R. A., and Gaines, S. D.: Small island nations can achieve food security benefits through climate-adaptive blue food governance by 2050, Mar. Policy, 151, 105577, https://doi.org/10.1016/j.marpol.2023.105577, 2023.

Thampanya, U., Vermaat, J. E., Sinsakul, S., and Panapitukkul, N.: Coastal erosion and mangrove progradation of Southern Thailand, Estuarine, Coastal and Shelf Science, 68, 75–85, https://doi.org/10.1016/j.ecss.2006.01.011, 2006.

The Nature Conservancy: Mapping Ocean Wealth – Mangrove Coastal Protection Benefit, The Nature Conservancy [data set],

https://maps.oceanwealth.org/#/data (last access: 1 July 2026), 2018.

Thomas, A. and Theokritoff, E.: Adaptation constraints, limits and enabling conditions in small island developing states, Curr. Opin. Env. Sust., 71, 101488, https://doi.org/10.1016/j.cosust.2024.101488, 2024.

Thorpe, A.: Mainstreaming Fisheries into National Development Plans and Poverty Reduction Strategies: Current Situation and Opportunities, FAO Fisheries Circular No. 997, FAO, Rome, https://openknowledge.fao.org/items/f54a6f47-c723-4f26-b353-274ca8242f42 (last access: 28 September 2026), 2005.

UN: Report of the United Nations Conference on Environment and Development, Rio de Janeiro, 3–14 June 1992, Agenda 21, Chap. 17, Section G, A/CONF.151/26/Rev.1 (Vol. I), United Nations, New York, https://sdgs.un.org/sites/default/files/publications/Agenda21.pdf (last access: 1 July 2026), 1992.

UN DESA: Small Island Developing States, UN DESA, https://sdgs.un.org/topics/small-island-developing-states (last access: 1 July 2026), 2026.

UNDP: Fish Stock Status, Environmental Performance Index, SIDS Data Platform Development Indicators, United Nations Development Programme (UNDP), https://sids.data.undp.org/development-indicators/key-epi-FSS/recentValue/bars (last access: 21 September 2026), 2026.

UNDRR: Gobal Assessment Report on Disaster Risk Reduction. Resilience Pays: Investing and Financing for Our Future, UNDRR, https://www.undrr.org/gar/gar2025#download (last access: 24 June 2026), 2025.

UN OHRLLS: List of SIDS, Office of the High Representative for the Least Developed Countries, Landlocked Developing Countries and Small Island Developing States, UN OHRLLS [data set], https://www.un.org/ohrlls/content/list-sids (last access: 1 July 2026), 2026.

Vasileiadou, K., Chatzinikolaou, E., Klayn, S., Pavloudi, C., and Reizopoulou, S.: Editorial: Marine biodiversity hotspots – challenges and resilience, Front. Mar. Sci., 11, 1338242, https://doi.org/10.3389/fmars.2024.1338242, 2024.

von Schuckmann, K., Gues, F., Moreira, L., Liné, A., and de Pascual Collar, Á.: Global ocean change in the era of the triple planetary crisis, in: 9th edition of the Copernicus Ocean State Report (OSR9), edited by: von Schuckmann, K., Moreira, L., de Pascual Collar, Á., Grégoire, M., Brasseur, P., Garric, G., Karstensen, J., Lionello, P., Marcos, M., Poulain, P.-M., and Staneva, J., Copernicus Publications, State Planet, 6-osr9, 2, https://doi.org/10.5194/sp-6-osr9-2-2025, 2025a.

von Schuckmann, K., Gues, F., Moreira, L., Liné, A., and de Pascual Collar, Á.: Ocean change in the northeastern Atlantic and adjacent seas: a multi-dimensional challenge for the environment, society, and economy, in: 9th edition of the Copernicus Ocean State Report (OSR9), edited by: von Schuckmann, K., Moreira, L., de Pascual Collar, Á., Grégoire, M., Brasseur, P., Garric, G., Karstensen, J., Lionello, P., Marcos, M., Poulain, P.-M., and Staneva, J., Copernicus Publications, State Planet, 6-osr9, 3, https://doi.org/10.5194/sp-6-osr9-3-2025, 2025b.

Von Schuckmann, K., Godoy-Faundez, A., Garçon, V., Muller-Karger, F. E., Evans, K., Appeltans, W., Bax, N., Benedetti Cecchi, L., Bernard, A., Bernard, K., Byrnes, J., Canonico, G., Chapuis, L., Clark, M. R., Darnaude, A. M., Davies, C., Englyst, P., Fransson, A., Hallam, S., Heslop, E., Holland, E., Hood, M., Kern, S., Liné, A., Lara-Lopez, A., Loose, N., Martín Míguez, B., McMahon, C. R., Nordlund, L. M., Post, J., Speich, S., Sutton, A., Tanhua, T., Telszewski, M., Poursanidis, D., and Yu, W.: Global ocean indicators: Marking pathways at the science-policy nexus, Mar. Policy, 184, 106922, https://doi.org/10.1016/j.marpol.2025.106922, 2026.

Vousdoukas, M. I., Athanasiou, P., Giardino, A., Mentaschi, L., Stocchino, A., Kopp, R. E., Menéndez, P., Beck, M. W., Ranasinghe, R., and Feyen, L.: Small Island Developing States under threat by rising seas even in a 1.5 °C warming world, Nat. Sustain., 6, 1552–1564, https://doi.org/10.1038/s41893-023-01230-5, 2023.

Wada, A. and Chan, J. C. L.: Increasing TCHP in the Western North Pacific and Its Influence on the Intensity of FAXAI and HAGIBIS in 2019, SOLA, 17A, 29–32, https://doi.org/10.2151/sola.17A-005, 2021.

Wada, A. and Yanase, W.: Is the Increasing Trend in the Environmental Upper-Ocean Heat Content in the Northwest Pacific Strengthening Tropical Cyclone Intensity?, in: Advances in Hurricane Risk in a Changing Climate, vol. 3, edited by: Collins, J., Done, J., Zhu, Y.-J., and Wilson, P., Springer Nature Switzerland, Cham, 97–124, https://doi.org/10.1007/978-3-031-63186-3_5, 2024.

Whitaker, H. and DeCarlo, T.: Re(de)fining degree-heating week: coral bleaching variability necessitates regional and temporal optimization of global forecast model stress metrics, Coral Reefs, 43, 969–984, https://doi.org/10.1007/s00338-024-02512-w, 2024.

WMO: WMO State of the Climate in 2025, WMO, https://wmo.int/publication-series/state-of-global-climate/state-of-global-climate-2025 (last access: 21 September 2026), 2026.

World Bank: GDP (current US$), World Development Indicators, World Bank [data set], https://data.worldbank.org/indicator/NY.GDP.MKTP.CD?view=map (last access: 1 July 2026), 2026.

Yuan, M.-H., Lin, K.-T., Pan, S.-Y., and Yang, C.-K.: Exploring coral reef benefits: A systematic SEEA-driven review, Sci. Total Environ., 950, 175237, https://doi.org/10.1016/j.scitotenv.2024.175237, 2024.

State Planet, 7-osr10, 1, 2026
https://doi.org/10.5194/sp-7-osr10-1-2026
© Author(s) 2026. This work is distributed under
the Creative Commons Attribution 4.0 License.

The 2026 Starfish Barometer

Marina Lévy[1], Karina von Schuckmann[2], Mahé Butel[2], William W. L. Cheung[3], Joachim Claudet[4], Thomas L. Frölicher[5,6], Patrice Guillotreau[7], Peter Haugan[8], Janine Adams[9], Diva Amon[10], Tamatoa Bambridge[11], Cynthia Barzuna[12], Bruno Blanke[13], Lijing Cheng[14], Sanae Chiba[15], Jorge Cortés[16], Pierre Friedlingstein[17,18], Jean-Pierre Gattuso[19,20], Stefan Gelcich[21], Jessica Gephart[22], Deborah Greaves[23], Audrey Hasson[2], Claire Jolly[24], Daoji Li[25], Yunne-Jai Shin[26], Aimée Slangen[27,28], Mere Takoko[29], Olivier Thébaud[30], Adrien Vincent[31], and Patrick Vincent[2]

[1]Sorbonne Université, LOCEAN-IPSL, CNRS, IRD, MNHN, Paris, France
[2]Mercator Ocean International, Toulouse, France
[3]Institute for the Oceans and Fisheries, The University of British Columbia, Vancouver, Canada
[4]CNRS, PSL-EPHE-UPVD, CRIOBE, Paris, France
[5]Climate and Environmental Physics, Physics Institute, University of Bern, Bern, Switzerland
[6]Oeschger Centre for Climate Change Research, University of Bern, Bern, Switzerland
[7]MARBEC, Université de Montpellier, CNRS, Ifremer, IRD, Sète, France
[8]Institute of Marine Research, Bergen, Norway
[9]Department of Botany, Institute for Coastal and Marine Research, Nelson Mandela University, Gqeberha, South Africa
[10]Marine Science Institute, University of California, Santa Barbara, Santa Barbara, CA, USA
[11]Centre de Recherches Insulaires et Observatoire de l'Environnement, Moorea, Polynésie Française
[12]World Resources Institute, Washington, DC, United States
[13]Laboratoire d'Océanographie Physique et Spatiale (LOPS), Université de Brest, CNRS, Ifremer, IRD, IUEM, Plouzané, France
[14]State Key Laboratory of Earth System Numerical Modeling and Application, Institute of Atmospheric Physics, Chinese Academy of Sciences, Beijing, China
[15]North Pacific Marine Science Organization, Sidney, British Columbia, Canada
[16]Department of Mechanical and Aerospace Engineering, University of California San Diego, San Diego, USA
[17]Faculty of Environment, Science and Economy, University of Exeter, Exeter, UK
[18]Laboratoire de Météorologie Dynamique, Institut Pierre-Simon Laplace, CNRS, ENS, Université PSL, Sorbonne Université, Ecole Polytechnique, Paris, France
[19]Laboratoire d'Océanographie de Villefranche, CNRS, Sorbonne Université, Villefranche-sur-Mer, France
[20]Institute for Sustainable Development and International Relations, Sciences Po, Paris, France
[21]Instituto Milenio en Socio-Ecología Costera (SECOS), Santiago, Chile
[22]School of Aquatic and Fishery Sciences, University of Washington, Seattle, WA, USA
[23]University of Oxford, Oxford, UK
[24]OECD, Directorate on Science, Technology and Innovation, Paris, France
[25]State Key Laboratory of Estuarine and Coastal Research, East China Normal University, Shanghai, China
[26]MARBEC, IRD, Université de Montpellier, IFREMER, CNRS, Montpellier, France
[27]Department of Estuarine and Delta Systems, NIOZ Royal Netherlands Institute for Sea Research, Yerseke, the Netherlands
[28]Department of Physical Geography, Faculty of Geosciences, Utrecht University, Utrecht, the Netherlands
[29]Pacific Whale Fund, Gisborne, New Zealand
[30]Ifremer, Université de Brest, CNRS, IRD, UMR 6308, AMURE, Unité d'Économie Maritime, IUEM, Plouzané, France
[31]Albatros Advisory, Bordeaux, France

Correspondence: Marina Lévy (marina.levy@sorbonne-universite.fr)

Published by Copernicus Publications.

Received: 12 March 2026 – Discussion started: 17 March 2026
Revised: 17 April 2026 – Accepted: 27 April 2026 – Published: 8 June 2026

Abstract. The Ocean plays a central role in regulating climate, sustaining biodiversity, and supporting human societies, yet it is experiencing increasing environmental change driven by human activities. The Starfish Barometer provides an annual, science-based synthesis of global Ocean-related developments. It does not generate new data, but brings together already available siloed information. It is structured around five interconnected dimensions – the five arms of the Starfish: Ocean state, human pressures, societal harms, protection efforts, and opportunities for humanity. This article presents the second edition of the Barometer, released each year on World Ocean Day (8 June). In the 2026 Barometer, key highlights confirm the consequences and intensification of human pressures on the Ocean. Global sea-level rise and Ocean warming are accelerating; the number of identified threatened marine species continues to rise, and the level of threat they experience is intensifying. Over 84 % of global coral reefs are at risk, exposed to bleaching-level heat stress. Annual plastic waste generation reached 130 million t, with up to 10 % potentially reaching the Ocean. Global shipping emissions remain stable indicating limited decarbonization progress. Economic losses from tropical storms and floods were particularly high in 2024, illustrating how human pressures are translating into material costs for societies. Geopolitical instability has increased maritime insurance costs, and half of the social cost of climate change falls on the Ocean economy. Major in-situ ocean observing systems are shrinking reducing Ocean protection capacity. In parallel, protection efforts continue to expand. Stronger protection rules for rays and sharks have been adopted, reflecting gradual progress in conservation ambition. A treaty for the High Seas has been adopted, providing a legal framework to protect and govern the Ocean. More than 2000 Ocean startups worldwide are also contributing to innovation, with a growing will for sustainable Ocean development and Ocean-focused environmentally beneficial investments. Taken together, these signals show a growing gap between increasing human pressures on the Ocean and the efforts being made to protect it and drive change. While governance frameworks, financial commitments, and innovation ecosystems are advancing, current trajectories remain insufficient to meet global biodiversity, climate and Ocean sustainability objectives, as reflected for example in SDG 14, the link to other SDGs, and related international frameworks (von Schuckmann et al., 2020). By compiling robust, evidence-based information within a consistent annual framework guided by international and multidisciplinary expertise, the Starfish Barometer provides a transparent and evidence-based foundation to support accountability for a sustainable Ocean.

1 Introduction

The Ocean is essential to life on Earth. It regulates the climate, sustains biodiversity, supports livelihoods, and shapes cultures worldwide. But it is undergoing rapid changes driven by human activities, with consequences for both marine ecosystems and human societies. Keeping track of these changes and their socioeconomic implications, and making them understandable beyond scientific and expert communities, are a growing need.

The Starfish Barometer was established to address this need by providing a yearly synthesis of the most recent, robust, and evidence-based scientific knowledge on the Ocean for a broad audience. This article presents the second edition of the Starfish Barometer, published on World Ocean Day (8 June), one year after its initial release (Lévy et al., 2025). While the first edition marked the creation of the Barometer, this new edition confirms its role as a recurring tool designed to update, year after year, information on the state of the Ocean and on its interactions with Humanity.

Indeed, the Starfish Barometer adopts a perspective centered on the interdependence between Humanity and the Ocean. Human activities generate pressures on the Ocean, but also drive protection efforts. In return, the Ocean provides essential benefits to societies while also posing risks and constraints. By presenting these interactions in a balanced and integrated manner, the Barometer aims to support informed public understanding and long-term engagement with Ocean issues.

An annual update is essential. The Ocean's state, the pressures it faces, and the efforts to protect it evolve continuously, as do scientific understanding and governance frameworks. Over the past year, new evidence, assessments, and policy developments have refined our knowledge of Ocean changes and their implications. The Starfish Barometer aims to capture these developments in a consistent way from one year to the next, contributing to a sustained narrative on the importance of the Ocean for society.

The Starfish Barometer does not generate new data. Instead, it brings together evidence-based information already published and validated in the peer-reviewed scientific literature as well as in institutional and international reports. Its added value lies in synthesizing this dispersed knowledge into an integrated overview, while keeping in sight the tar-

gets identified under the United Nations Sustainable Development Goal dedicated to the Ocean, SDG 14 (UN, 2015). The Barometer is designed for a non-specialist audience – including policy makers, educators, civil society actors, and the general public – while remaining grounded in established scientific evidence.

This second edition provides an overview of the information released in the year following the previous Starfish Barometer. It highlights key developments and new information, focusing on global rather than regional information, and on historical changes, current status, and ongoing trends, rather than future projections. The selection of Ocean-related developments – ranging from updated scientific findings to governance and policy milestones – is not exhaustive, but reflects globally relevant signals based on the best available updates or new knowledge at the time of publication. This article provides the peer-reviewed scientific foundation underpinning the release of the 2026 Starfish Barometer to the general public and all stakeholders, scheduled on 8 June 2026 (http://www.starfishbarometer.org, last access: 12 March 2026).

2 Methods

Each annual edition of the Starfish Barometer follows the same symbolic and structural framework, organised around five thematic arms (Fig. 1): Ocean state, human pressures, societal harms, protection efforts, and opportunities for Humanity. Key information is presented as concise, evidence-based summaries of key developments, highlighted through clear and accessible headlines. In the following, we refer to these as items. While this structure remains constant, items evolve from one edition to the next to reflect the most recent and relevant developments. Rather than systematically updating a fixed set of indicators, the Barometer offers a curated, narrative-based synthesis aimed at capturing a selection of policy-relevant Ocean signals of the year at the global scale, without seeking to provide an exhaustive account of Ocean-related developments. This curation relies on collective expert judgement within the scientific committee, guided by the availability of new evidence.

2.1 Structural framework

The structure of the Starfish Barometer is represented by a five-armed Starfish. The upper arm provides a global view of the Ocean's state. The two left arms represent negative dynamics, from human-induced pressures to societal harms, while the two right arms reflect positive dynamics, from protection efforts to opportunities the Ocean offers to Humanity. The Starfish can be read horizontally, from negative to positive, or vertically, from human actions to societal consequences. Four items are attached to each arm.

2.2 Expert group

The content of the Starfish Barometer was curated by a multidisciplinary and international group of experts, substantially expanded compared to the first edition. This enlarged group brings together a wide range of scientific expertise covering most Ocean-related themes, as well as diverse geographic backgrounds, ensuring global coverage of Ocean issues. This writing committee was also designed to increase gender and geographical diversity, including experts from both the Global North and the Global South. Bringing diverse perspectives is a key aspiration of the Barometer's methodology, supporting a comprehensive and integrated view of the Ocean-human relationship.

The overall coordination of the article was ensured by two chairs assisted by a project manager. The five thematic arms of the Starfish Barometer were each coordinated by an arm leader. All other members of the expert group contributed to at least two arms, a structure deliberately chosen to foster cross-fertilisation across themes and to avoid siloed analyses.

2.3 Context of the second edition

This second edition of the Starfish Barometer was developed during the year that followed the United Nations Ocean Conference (UNOC-3) and its associated One Ocean Science Congress. This period was marked by particularly intense multilateral activity related to Ocean governance and protection, alongside the continued degradation of Ocean systems. The Barometer was therefore developed in a context of both heightened political momentum and persistent environmental pressures, reinforcing the importance of a yearly, structured assessment of Ocean-related developments. In practice, the analysis draws on the information and knowledge available at the time of writing.

2.4 Selection of items

For this second edition, the selection of items builds explicitly on last year's edition whenever possible. When updated information was available, these updates were prioritised and incorporated into the 2026 edition. As a result, a substantial share of the items presented this year, approximately between one half and three quarters, correspond to follow-ups of themes highlighted last year, reflecting the Barometer's objective of tracking Ocean-related signals over time.

Importantly, an item often encompasses several pieces of information related to a common topic. In such cases, continuity was ensured at the thematic level rather than through the systematic update of all associated figures or indicators. An item was retained from one year to the next when at least one relevant and meaningful element had evolved or been updated, even if other aspects of the topic remained unchanged. This approach allows the Barometer to follow key issues over time without implying that all quantitative elements are monitored or updated annually.

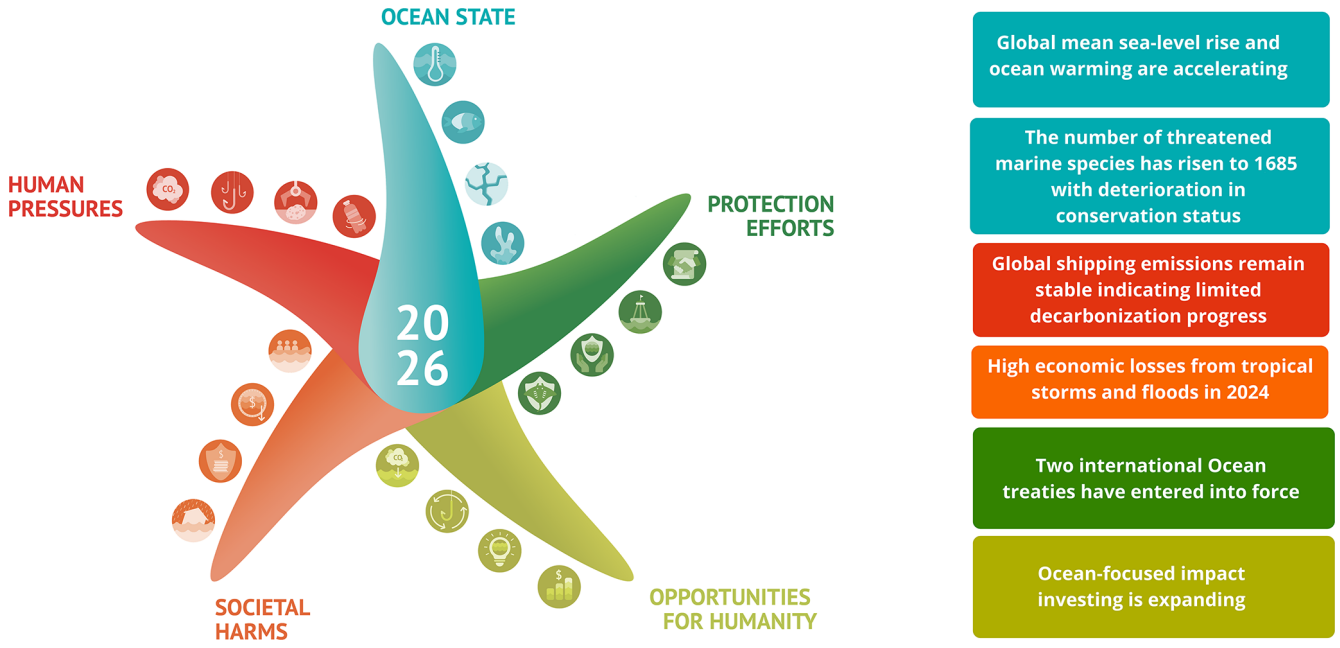


Figure 1. Schematic representation of the five arms of the Starfish Barometer and six global key developments chosen for 2026. At the top, the blue arm represents the current state of the Ocean. The four other arms can be read horizontally, from red tones on the left to green tones on the right (negative to positive), or vertically, from darker tones at the top to lighter tones at the bottom (human actions to societal consequences).

When no significant updated information was available for previously featured topics, new items were identified to reflect developments that became particularly relevant that year, even if they had not been highlighted in the previous edition. The Barometer should therefore be considered across successive editions, as developments highlighted in earlier years remain relevant and may not be repeated unless new information or updates become available.

This balance between continuity and renewal is a deliberate methodological choice. The Starfish Barometer acknowledges that Ocean-related data, assessments, and policy developments evolve at different paces across domains. Its non-exhaustive and adaptive framework allows certain key themes to be followed across successive editions when meaningful updates exist, while leaving room to introduce new information when warranted by the most recent scientific or governance context.

Candidate items – both follow-ups and new developments – were proposed by experts within each arm based on shared criteria, including global-scale relevance, robustness of the underlying data, significance of the development, and relevance to the Ocean-human relationship. Proposed items were first discussed within arm-specific subgroups and subsequently reviewed during plenary meetings involving the full expert group. These collective discussions ensured consistency across arms, facilitated cross-arm comparisons, and supported the final selection of items that best capture the most meaningful Ocean-related signals of the year. Together, these principles define how continuity and renewal are balanced across editions.

2.5 Arm allocation of items

The allocation of items to specific arms is guided by thematic relevance but is not exclusive, as many Ocean-related developments span multiple dimensions. For example, some services offered by the Ocean, presented as opportunities for Humanity, can simultaneously represent human pressures on the Ocean and drivers of societal harm. In such cases, items were assigned to the arm most closely aligned with their primary emphasis, following a consistent editorial framework rather than rigid topical boundaries.

This reflects the inherently interconnected nature of the Ocean–human system, in which processes and impacts often span multiple dimensions of the Barometer. While these interconnections are acknowledged, they are not systematically developed within the Barometer, as its objective is to present a set of robust, evidence-based signals rather than to establish explicit causal relationships between dimensions, which should also strictly be based on scientific evidence (von Schuckmann et al., 2026).

To maintain concision and balance across arms, each arm of the Starfish Barometer is limited in length and presents four key messages, one per item, anchored in recent developments and supported, in most cases, by figures and trend analyses. No explicit logical or causal links are imposed be-

tween individual items within or across arms. Instead, each item stands as an independent, robust signal from the year.

2.6 Data sources

All figures presented in the Starfish Barometer are drawn directly from authoritative sources and are reported as published, ensuring transparency and traceability. Readers seeking further methodological detail or information on associated uncertainties are referred to the original sources provided in the reference list.

3 2026 Starfish Barometer

3.1 Ocean state

Global mean sea-level rise and Ocean warming are accelerating. Global mean sea-level rise is a consequence of Ocean warming and land ice melt (Wang et al., 2024; Dangendorf et al., 2024; Mu et al., 2025). While global mean sea level rise was estimated at $2.6 \pm 0.3\,\mathrm{mm\,yr^{-1}}$ over the period 1993 to 2011 (WMO, 2026), this rate has increased to $4.2 \pm 0.3\,\mathrm{mm\,yr^{-1}}$ over the period 2012–2025 (Leclercq et al., 2026), consistent with an acceleration in sea-level rise over the last 30 years. Global mean Ocean warming is also since 1960 (Minière et al., 2023; Storto and Yang, 2024), and reached record values in 2025 (Pan et al., 2026; WMO, 2026). In addition to these long-term trends, recent years have been consecutively marked by particularly high values. In 2025, global mean temperatures at the sea surface reached their third highest levels on record, at 0.49 °C above the 1981–2010 baseline slightly below the peaks observed in 2023 and 2024 (Pan et al., 2026), with 20 % of the Global Ocean experiencing strong marine heatwave conditions in June 2025 (Mercator Ocean International, 2025a, b). Warming is a climate change stressor to marine ecosystems that adds to other climate change stressors such as changes in salinity, deoxygenation and acidification. About 25 % of the top 1000 m of the Ocean is now affected by more than two climate change stressors simultaneously (Tan et al., 2025).

Global sea ice extent reached its second lowest annual maximum at 32.1 million km^2 since 1982. Sea ice is frozen seawater that forms in autumn and winter in both polar Ocean basins and progressively melts in spring and summer. It is important because it helps regulate Earth's climate and supports polar ecosystems. With climate change, the maximum extent reached by sea ice in winter continues to rapidly shrink in the Arctic (Meier et al., 2025; Roach and Meier, 2024; von Schuckmann et al., 2024; Walsh et al., 2022), and since 2015 also in the Antarctic (IPCC, 2019; Hobbs et al., 2024). Annual maximum sea ice extent reached 14.3 million km^2 in March 2025 in the Arctic (Howell et al., 2025; Meier et al., 2025) and 17.8 million km^2 in September 2025 in the Antarctic (Bliss et al., 2025), adding up (asynchronous sum) to 32.1 million km^2 taken together. The Annual minimum was 4.6 million km^2 in September 2025 in the Arctic and 2.0 million km^2 in March 2025 in the Antarctic. This is the fourth consecutive year that Antarctic sea ice has reached a minimum below 2.0 million km^2 (Bliss et al., 2025). Declining sea ice is increasing the accessibility of trans-arctic shipping routes (PAME, 2026).

The number of threatened marine species has risen to 1685 with deterioration in conservation status. As of the most recent update (April 2026), 1685 (8.6 %) of the 19 508 marine species assessed by the International Union for Conservation of Nature worldwide are classified as threatened with extinction on their Red List (IUCN, 2026). This indicator provides a broad signal of the status of assessed marine biodiversity, although it also reflects the evolving coverage and completeness of species assessments over time. Compared with the value reported in the previous edition of the Barometer, the current assessment includes eight additional threatened marine species (Starfish, 2025: Lévy et al., 2025). Of the threatened species, 293 are classified as Critically Endangered, 660 as Endangered, and 732 as Vulnerable. This corresponds to a deterioration in conservation status for 30 species since last year. Population trends reinforce this assessment: 1224 threatened species are experiencing population declines, 13 more than last year, while only 28 species show increasing populations (one fewer than in 2024). Beyond extinction risk, the IUCN Red List also reports 1631 threats to ecosystems such as invasive and other problematic species, genes and diseases affecting marine ecosystems, further undermining ecosystem stability and resilience.

84.4 % of coral reefs experience heat stress severe enough to cause bleaching. Warm-water coral reefs are among the most diverse and valuable ecosystems on Earth. They occupy nearly 0.2 % of the global seafloor, support at least 25 % of all marine species, and underpin coastal protection, food security, livelihoods, cultural values and human wellbeing for hundreds of millions of people worldwide (Souter et al., 2020). Climate change now represents an existential threat to coral reefs (Pearce-Kelly et al., 2025), and repeated thermal stress drives widespread bleaching, mortality and long-term loss of ecosystem function (IPCC, 2019). Between January 2023 and September 2025, 84.4 % of the world's coral reefs have experienced bleaching-level heat stress, exceeding the previous global record of 68.2 % during 2014–2017 and far surpassing the 1998 and 2010 mass bleaching episodes (Coral Reef Watch, 2026). Coral reef degradation is also influenced by additional stressors such as eutrophication, acidification and overfishing, which can act in synergy with climate change (Bhuyan et al., 2026). All wetland ecosystems are losing surface area since 1970, coral reefs (−26.4 %) but also mangroves (−11.8 %), salt marshes (−14 %), kelp forests (−48.1 %), and seagrass (−16.3 %) (Ramsar, 2025).

3.2 Human pressures

Global shipping emissions remain stable indicating limited decarbonisation progress. Fossil fuel CO_2 emissions are the main contributor to recent climate change (IPCC, 2021). Global fossil carbon dioxide (CO_2) emissions have increased by 1.1 % between 2024 and 2025, and reached a record high of 38.1 billion t CO_2 in 2025, with 2025 emissions from international shipping at 0.6 billion t CO_2 similar to their 2024 value (Andrew and Peters, 2025; Friedlingstein et al., 2025). A Net-Zero framework, proposing a USD 100 t^{-1} CO_2 fee on vessels exceeding emission thresholds, was developed by the International Maritime Organization but stalled in 2025 and is rescheduled for 2026.

67 % of industrial fishing vessels in large coastal marine protected areas are untracked. Between 2022 and 2024, an estimated 67 % of industrial fishing vessels operating in coastal Marine Protected Areas (MPAs) larger than 1 km^2 were not publicly tracked, highlighting widespread unsustainable fishing practices and major shortcomings in transparency and governance (Paolo et al., 2024; Basurto et al., 2025; Seguin et al., 2025). These MPAs represent 17.4 % of global marine protection, yet industrial fishing pressure remains largely untracked. In contrast, industrial fishing activity is close to zero in fully and highly protected MPAs, which currently cover only about 2.2 % of the global Ocean (Raynor et al., 2025), underscoring the effectiveness of strong protection measures when properly implemented and enforced. Climate change further exacerbates these governance challenges by shifting fish distributions and fishing effort (Pinsky et al., 2020; Dahms and Killen, 2023). Expanding marine protection under the Kunming-Montreal Global Biodiversity Framework target to conserve 30 % of marine and coastal areas by 2030, coupled with effective monitoring, enforcement, and climate-adapted governance, is critical to reducing unsustainable fishing as a direct human pressure on Ocean ecosystems. The proportion of overfished stocks has been increasing at a rate of approximately 1 % yr^{-1} over the past two decades (Sharma et al., 2025).

31 exploration contracts for deep-sea mineral resources are currently active. The deep sea is the largest and least understood biome on Earth, it holds a remarkable diversity of life forms adapted to extreme conditions, it is important for global biodiversity and function, including fisheries support and climate regulation (Sánchez et al., 2024). A total of thirty-one contracts lasting 15 years each are currently ongoing in areas beyond national jurisdictions, issued by the International Seabed Authority, including 19 contracts for polymetallic nodules, 7 for polymetallic sulphides and 5 for cobalt-rich ferromanganese crusts (International Seabed Authority, 2026). Exploration activities consist of geological studies, mineral resource assessments, bathymetric measurements and environmental surveys and sampling. They can also include the development and testing of mining technology and mineral processing techniques (Hilmi et al., 2026). If scaled up to industrial levels without effective environmental safeguards, deep-sea mining could have severe long-term impacts on deep-Ocean ecosystems due to their slow recovery rates (Amon et al., 2022). In 2026, eight new countries opposed deep-seabed mining, bringing the global total to 40 countries (Deep Sea Conservation Coalition, 2026).

A record 130 Mt of plastic waste was produced, with up to 10 % potentially reaching the Ocean. Global plastic production continues to rise, and annual plastic waste polluting the environment reached 130 Mt yr^{-1} in 2025 (The Pew Charitable Trusts, 2025). Due to the lack of global monitoring, the proportion of total waste that reaches the Ocean remains highly uncertain, likely between 1 and 14 Mt yr^{-1} (Lebreton et al., 2017; The Pew Charitable Trusts, 2025; UNEP, 2021). The main sources of marine litter are land-based and plastics constitute 85 % of total marine litter (UNEP, 2021). The seafloor is the primary sink for large plastic debris, with approximately 11 million Mt accumulated globally (Zhu et al., 2024), where recovery is neither technically nor financially feasible. More than 2800 marine species are impacted by plastic pollution through entanglement, ingestion, chemical contamination and other processes (Tekman et al., 2022). While an agreement for an International Plastics Treaty failed in 2025, a Global Plastic Action Partnership is advancing systemic and circular-economy solutions to reduce plastic pollution (Global Plastic Action Partnership, 2026).

3.3 Societal harms

High economic losses from tropical storms and floods in 2024. Economic losses from tropical storms and floods can vary greatly from one year to another. Tropical storms draw their energy from warm Ocean waters making the Ocean a key driver of storm intensity and frequency (Guan et al., 2026). Over the long term, related economic losses have increased decade by decade since the early 1980s, with an acceleration during the past two decades (WMO, 2021). In 2024, damage costs due to tropical storms and flood surges were nearly twice as high as in 2023, reaching USD 212 billion (inflation-adjusted, Munich RE, 2026), of which only 34 % were insured. This high level is largely explained by two strong hurricanes. Other long-term consequences add to the direct economic damage of tropical cyclones, such as 79 000 children prevented from accessing education between 2000 and 2020 (Jing et al., 2025). Monetary valuation of losses from tropical storms and floods can shape decisions and actions to reduce exposure to risk, but these effects occur within broader socio-economic systems where underinvestment persists and losses from extreme events can reinforce vulnerability, inequality, and instability (Hallegatte et al., 2020; Weerasinghe et al., 2025; Fischer and Patterson, 2026).

Geopolitical instability has increased maritime insurance costs to USD 39.9 billion. The global marine insur-

ance premium base reached USD 39.9 billion in 2024, representing a 1.5 % increase from 2023, and a 21 % increase since 2021 (IUMI, 2025). The largest share of risk is held by cargo (57 %), followed by hull (24 %), offshore energy (12 %) and marine liability (7 %). While expanding trade has contributed to insurance premium growth, geopolitical instability and international conflicts have emerged as major additional drivers, creating uncertainty across global trade and becoming critical factors of risk (Chi et al., 2025; Cong et al., 2024; Kotenko et al., 2022).

Half of the social cost of climate change falls on the Ocean economy. The social cost of carbon estimates the economic damages caused by emitting one additional tonne of CO_2 into the atmosphere. For the Ocean, climate damages to fisheries and mariculture, coral reefs, mangroves, and ports were estimated at USD 48 t^{-1} of CO_2 in 2020, equalling all other carbon social costs including those on health, agriculture and infrastructure and highlighting the importance of including Ocean impacts in carbon pricing and climate policy to fully capture societal harms (Bastien-Olvera et al., 2026). Much of this increase comes from declining fisheries and the degradation of coastal protection and biodiversity. Despite its importance for guiding policy, only 28 % of global emissions are currently covered by a carbon price (World Bank, 2025).

8260 migrants lost their lives at sea. In 2025, the number of dead or missing migrants at sea stands at high levels (8260 fatalities, IOM, 2026), highlighting that the Ocean remains an important and unsafe route for human mobility. This reflects the Ocean as a space of transit, risk, and human activity, where significant humanitarian challenges persist. The drivers of migration are complex and multifaceted. Economic and political insecurity due to resource grabbing and severe climatic conditions, including extreme weather events, sea-level rise, desertification, and water scarcity, are among the factors that push people to leave their countries (Maatouk et al., 2025; Yang et al., 2025).

3.4 Protection efforts

Marine protected areas cover 10.01 % of the global Ocean, with 3.2 % fully or highly protected. Global Ocean protection has reached the 10 % milestone but remains far from the Kunming-Montreal Global Biodiversity Framework target to conserve 30 % of marine and coastal areas by 2030. Marine Protected Area (MPA) coverage has increased from 8.34 % in 2024 to 10.01 % of the global Ocean in mid-2026 (Lévy et al., 2025; ProtectedPlanet, 2026). The global Ocean can be divided into areas within national jurisdiction, and international waters beyond national jurisdiction. A total of 22.54 % of national waters and 1.45 % of international waters are designated as MPAs. Actively managed MPAs, with evidence of monitoring and enforcement, have more positive ecological outcomes than those that are only designated (Horta e Costa et al., 2025). Despite this recent progress, the extent of effectively protected areas remains limited at the global scale, and their outcomes depend on implementation, monitoring, and broader enabling conditions, such as governance arrangements and incentive structures (Barzuna et al., 2025): 3.2 % of the Ocean is fully or highly protected (Marine Protection Atlas, 2026).

Major in-situ Ocean observing systems are shrinking reducing Ocean protection capacity. Effective protection requires sustained measurement to anticipate risks and respond effectively. The number of in-situ Ocean observations on the physical and chemical state of the Ocean is estimated at 120 000 d^{-1} in 2025 (GOOS, 2025). This number is primarily driven by autonomous networks such as drifting buoys with high-frequency observations. The number of Argo profiling floats reached 4166 in December 2025 (Argo, 2026). Some major networks such as moored buoys and ship-based observations are shrinking since the pandemic (Boyer et al., 2023). Part of the observation decline is due to global budget constraints, reduced ship-time and reduced number of experienced personnel, reflecting broader constraints on ocean science capacity (Tanhua et al., 2024; von Jackowski, 2025; GOOS, 2025). Taken together this threatens international Ocean science and diplomacy (Gattuso et al., 2025). Ocean observing is a critical infrastructure for climate resilience, disaster risk reduction, Ocean health, sustainable development, and economic stability. They are the feeding ground for operational systems to monitor and forecast changing Ocean conditions.

Two international Ocean treaties have entered into force. Global governance of the High Seas has gained momentum with the Agreement on the Conservation and Sustainable Use of Marine Biological Diversity Beyond National Jurisdiction (BBNJ) entering into force on 17 January 2026. This treaty provides a shared legal framework to protect and govern the 61 % of the Ocean beyond national jurisdiction. It sets the foundation for establishing marine protected areas in international waters, for environmental impact assessments, for fairer rules for sharing benefits from marine genetic resources, and for giving a voice to indigenous and local communities and ensuring equity through capacity building and technology transfer. A treaty to ban harmful fisheries subsidies came into force in September 2025 (WTO, 2026). This treaty prohibits government support to illegal fishing activities, a key factor in the widespread depletion of the world's fish stocks and human trafficking (Selig et al., 2022). It commits members of the World Trade Organization to curbing billions of dollars in annual spending on the most harmful subsidies. Subsidies that lower the cost of fishing can fuel overfishing and illegal fishing where management is weak. An estimated 65 % of government fisheries support carries this risk (OECD, 2025a).

Stronger international protections for sharks and rays adopted. A decision regarding international trade protections for several marine species was adopted by parties of the Convention on International Trade in Endangered Species of Wild Fauna and Flora (CITES) in December 2025 (IISD,

2025). Oceanic whitetip sharks, whale sharks, and manta and devil rays were upgraded to the highest levels of protection, taking a significant step toward curbing the overexploitation of these vulnerable marine species. Wedgefishes and giant guitarfish were assigned zero export quotas, effectively halting all legal international trade in these wild-caught species (CITES, 2026a). Gulper, tope, and smoothhound sharks were listed for the first time under CITES trade controls. Trade bans do not stop overexploitation and illegal trade, but contribute to closing major loopholes in the global fin, meat, and cartilage trades that drive population collapses. To date, international commercial trade is highly restricted or prohibited for more than 1500 marine species under CITES (e.g. corals, giant clams, seahorses) (CITES, 2026b).

3.5 Opportunities for Humanity

Global nutrition from fisheries increasingly relies on circular economy practices. In 2023, global marine animal production, including both fisheries and aquaculture, stalled at 115 million t (FAO FishStatJ, 2026), a number comparable to last year (Lévy et al., 2025). In addition, the global production of marine aquatic plants was 39 million t (FAO FishStatJ, 2026). Thus global marine production, including animals and plants, reached a total of 154 million t. Aquaculture production represented 48 % of this global marine production (FAO FishStatJ, 2026). Marine animal production is an important source of nutrition for people around the world, with around 89 % of all aquatic animal production destined for direct human consumption in 2022 (FAO SOFIA, 2024). Beyond direct consumption, a significant share of marine animal production is used to produce fishmeal and fish oil, which are primarily used in animal feed, largely driven by growing demand for aquaculture (FAO SOFIA, 2024). By-products of marine fisheries have supplied an increasing share of fishmeal and fish oil production, with 34 % of fishmeal and 53 % of fish oil sourced from by-products in 2022. This increasing use of fisheries by-products represents an opportunity for advancing circular economy practices (FAO SOFIA, 2024).

Over 2000 startups drive Ocean innovations. The Ocean is increasingly recognised as a driver of innovation, particularly in food and energy systems, climate change mitigation and adaptation, human health, and coastal resilience. Over the past decade, more than 2000 startups have emerged worldwide across the Ocean economy (Katapult Ocean, 2024) and more are coming (Chang et al., 2026). Their role in driving digital transformation and cleaner energy adoption can help Ocean industries shift away from harmful business-as-usual practices and ease current Ocean economy productivity stagnation and decline (Jolliffe and Jolly, 2025). However, the external conditions under which businesses operate remain insufficiently aligned with sustainability goals and continue to perpetuate systemic risks. Addressing these challenges requires collaboration and coordinated collective and individual action to create an enabling environment in which businesses can contribute to a just and sustainable future (Jones et al., 2025), alongside the establishment of rigorous standards and science-based regulatory pathways (Doney et al., 2025).

Ocean-focused impact investing is expanding. In 2018, four environmentally beneficial investment funds were dedicated to Ocean health and sustainability worldwide (WEF, 2025). By 2025, more than 40 venture and impact funds were active or in fundraising across the Ocean economy (WEF, 2025). These investments cover a range of sectors, including sustainable seafood, seaweed production, Ocean pollution mitigation, coastal resilience, and Ocean data. Financial commitments to Ocean-related activities have increased accordingly. Official development assistance for the Ocean economy reached USD 3.5 billion in 2022, a 45 % increase from 2021 (OECD, 2024). Of this, USD 2.4 billion (69 %) supported initiatives that promote sustainable Ocean activities and protect marine ecosystems. Stakeholders announced EUR 8.7 billion in firm financial commitments for Ocean-related projects by 2030, comprising EUR 4.7 billion from philanthropies and private investors and EUR 4 billion from public financial institutions (BEFF, 2025). These amounts remain below estimates of the annual investment required to achieve SDG 14, which are approximately USD 175 billion yr^{-1} by 2030, indicating a gap between current financial commitments and the scale of transformation required (Johansen and Vestvik, 2020; OECD, 2025b).

The Ocean buffers climate change. The Ocean has a natural capacity to remove and store heat and carbon away from the atmosphere and, as such, is crucial in mitigating climate change. It has absorbed about 12 billion t CO_2 yr^{-1} on average over the last decade, roughly 29 % of human-caused CO_2 emissions (Friedlingstein et al., 2025), resulting in Ocean acidification. This Ocean sink has been stagnant since 2016, largely in response to climate variability modulating the expected sink growth due to the atmospheric CO_2 increase. The 2023/2024 sink strength was further affected by the El Niño conditions and the near-global marine heatwave (Li et al., 2024; Müller et al., 2025). Greenhouse gas emissions have caused an Earth energy imbalance, leading to heat accumulation in the climate system that has reached its highest levels in modern records over the past two decades (Forster et al., 2025; WMO, 2026). The Ocean absorbs roughly 90 % of this excess heat (von Schuckmann et al., 2023), resulting in Ocean warming, while the remaining 10 % warms the continents and atmosphere and melts ice on the planet.

4 Conclusions

Building on the first edition released in 2025, the 2026 Barometer introduces several new thematic areas, including deep-sea mining exploration contracts, the social costs of Ocean-related climate change, the capacity of Ocean observing systems, strengthened protection for sharks and rays, cir-

cular economy practices in fisheries, and the Ocean's role as a carbon and heat sink. It also brings new perspectives on issues already tracked in the previous edition, including global sea-ice extent, industrial fishing activities within marine protected areas, and key dimensions of the blue economy.

Most of all, the 2026 Starfish Barometer confirms an Ocean system under intensifying stress. Intensification is the dominant signal, with indication of acceleration in some cases: global mean sea-level rise and Ocean warming are accelerating; sea-ice extent is reaching historically low levels at both poles; the number of identified threatened marine species continues to climb; an unprecedented share of coral reefs are under severe heat stress. In parallel, human pressures remain high: shipping emissions show limited signs of decarbonisation, industrial fishing is still insufficiently transparent, deep-sea mining exploration contracts are being granted, and plastic waste has reached record levels while the fraction reaching the Ocean remains poorly evaluated due to the absence of global monitoring. These pressures translate into rising societal harms, highlighting that the Ocean-human relationship is not only ecological, but profoundly social, economic, and geopolitical: the sharp long-term increase in economic losses from storms and floods, the growing costs of maritime insurance, the high toll of migration fatalities at sea, and new estimates showing that Ocean-related damages represent a major share of the total socioeconomic cost of climate change, overexploitation, biodiversity loss and pollution.

At the same time, 2026 also reflects tangible momentum for protection and transformation. Marine protected areas have expanded, and evidence continues to show that strong, fully or highly protected areas deliver the most effective outcomes – yet still cover only a small fraction of the Ocean. In-situ observations are critical infrastuctures, but show signs of decline due to budget constraints even as societal demand for Ocean information rises. Critically, the entry into force of major international agreements – including the High Seas treaty and the ban on harmful fisheries subsidies – marks a step change in the legal and institutional conditions for action, alongside strengthened trade protections for threatened sharks and rays. On the opportunity side, circular economy gains in fisheries and aquaculture, a rapidly growing innovation ecosystem, and expanding Ocean-focused investing illustrate the potential for solutions, while also underscoring that current financial commitments remain far below estimated needs.

The Starfish Barometer highlights the importance of bringing together robust evidence from across the vast, often siloed network of Ocean science, policy, and practice. By integrating evidence-based knowledge into a coherent global picture across Ocean state, human pressures, societal harms, protection efforts, and opportunities for Humanity – and updating it annually – it provides a clear view of trends, emerging risks and multilateral advances. This global perspective makes it evident that Ocean change is inherently transboundary and requires coordinated international action.

Data availability. No data sets were used in this article.

Author contributions. ML co-developed the concept of the starfish barometer, provided overall leadership and led the writing of the manuscript. KvS served as co-lead on scientific directions and played a central role in shaping the manuscript's final writing. MB coordinated the project, facilitated collaboration across all contributors, and organized the meetings and workflow that enabled the integration of the Barometer. The Barometer arms were led by TF (Ocean State), WC (Human Pressures), PG (Societal Harms), JC (Protection Efforts), and PH (Opportunities for Humanity). All coauthors contributed to content curation and manuscript preparation.

Competing interests. At least one of the (co-)authors serves as topic editor for the report to which this paper belongs. The peer-review process was guided by an independent editor, and the authors also have no other competing interests to declare.

Disclaimer. Publisher's note: Copernicus Publications remains neutral with regard to jurisdictional claims made in the text, published maps, institutional affiliations, or any other geographical representation in this paper. The authors bear the ultimate responsibility for providing appropriate place names. Views expressed in the text are those of the authors and do not necessarily reflect the views of the publisher.

Acknowledgements. We wish to honor the memory of Kristina Gjerde, who warmly supported the first edition of the Starfish Barometer. The Starfish barometer is an outcome of the 3rd United Nations Ocean Conference. This Starfish edition was greatly facilitated by Laurence Collet (communication), Xi Ruan (production support) and Pierre Bahurel (operational leadership). We thank François Houllier and Olivier Poivre d'Arvor for their support. This article has been reviewed by Corinne Le Quéré and Elva Escobar-Briones, whose thoughtful and constructive comments have substantially supported the improvement of this edition of the Starfish Barometer.

Review statement. This paper was edited by Marilaure Grégoire and reviewed by Elva Escobar-Briones and Corinne Le Quéré.

References

Amon, D. J., Levin, L. A., Metaxas, A., Mudd, G. M., and Smith, C. R.: Heading to the deep end without knowing how to swim: Do we need deep-seabed mining?, One Earth, 5, 220–223, https://doi.org/10.1016/j.oneear.2022.02.013, 2022.

Andrew, R. M. and Peters, G. P.: The Global Carbon Project's fossil CO2 emissions dataset (2025v15), Zenodo [data set], https://doi.org/10.5281/zenodo.17417124, 2015.

Argo: https://argo.ucsd.edu, last access: 2 April 2026.

Barzuna, C., Haugan, P., Barbière, J., Swift, A., Khan, M., Ansong, J. O., James, P. A. S., Scherer, M., Thiele, T., von Schuckmann, K., Abramic, A., Barrowclough, D., Cisneros-Montemayor, A., Girón, A., Heaps, L., Koirala, S., Lyons, M., Paul, K., Priyanto, A. T., Randone, M., Rosado, S., Santos, C. F., Savoldelli, C., Spalding, A. K., Strand, M., Sumaila, U. R., Swaddling, A., Turner, J., Vestergaard, O., and Yulianto, I.: Handbook on Sustainable Ocean Plans: A practitioners' guide, World Resources Institute, Washington, DC, https://oceanpanel.org/publication/sop-handbook/ (last access: 12 March 2026), 2025.

Bastien-Olvera, B. A., Aburto-Oropeza, O., Brander, L. M., Cheung, W. W., Emmerling, J., Free, C. M., Granella, F., Tavoni, M., Verschuur, J., and Ricke, K.: Accounting for ocean impacts nearly doubles the social cost of carbon, Nat. Clim. Chang., https://doi.org/10.1038/s41558-025-02533-5, 2026.

Basurto, X., Gutierrez, N. L., Franz, N., Mancha-Cisneros, M. D. M., Gorelli, G., Aguión, A., Funge-Smith, S., Harper, S., Mills, D. J., Nico, G., and Tilley, A.: Illuminating the multidimensional contributions of small-scale fisheries, Nature, 637, 875–884, https://doi.org/10.1038/s41586-024-08448-z, 2025.

BEFF: Blue Economy and Finance Forum, https://beff2025monaco.org/images/BilanBlue%20Economy%20and%20Finance%20ForumVDEF_11.06.pdf (last access: 12 March 2026), 2025.

Bhuyan, M. S., Jenzri, M., Islam, M. T., Adikari, D., and Hoque, M. M.: Climate change impacts on coral reefs and emerging resilience pathways: A systematic review, Ocean Coast. Manag., 276, 108134, https://doi.org/10.1016/j.ocecoaman.2026.108134, 2026.

Bliss, A. C., Comiso, J. C., Parkinson, C. L., Gersten, R., and Markus, T.: Current State of Sea Ice Cover, https://earth.gsfc.nasa.gov/cryo/data/current-state-sea-ice-cover (last access: 2 April 2026), 2025

Boyer, T., Zhang, H., O'Brien, K., Reagan, J., Diggs, S., Freeman, E., Garcia, H., Heslop, E., Hogan, P., Huang, B., Jiang, L., Kozyr, A., Liu, C., Locarnini, R., Mishonov, A., Paver, C., Wang, Z., Zweng, M., Alin, S., Barbero, L., Barth, J., Belbeoch, M., Cebrian, J., Connell, K., Cowley, R., Dukhovskoy, D., Galbraith, N., Goni, G., Katz, F., Kramp, M., Kumar, A., Legler, D., Lumpkin, R., McMahon, C., Pierrot, D., Plueddemann, A., Smith, E., Sutton, A., Turpin, V., Jiang, L., Suneel, V., Wanninkhof, R., Weller, R., and Wong, A.: Effects of the Pandemic on Observing the Global Ocean, B. Am. Meteorol. Soc., 104, E389–E410, https://doi.org/10.1175/BAMS-D-21-0210.1, 2023.

Chang, L., Giron, C., and Tardiff, R.: The Ocean Economy Imperative: Defining Value, Managing Risk and Mobilizing Investment, World Economic Forum, https://reports.weforum.org/docs/WEF_Ocean_Economy_Imperative_2026.pdf (last access: 12 March 2026), 2026.

Chi, X., Zheng, R., Chen, Y., and Xiao, G.: Research on the volatility spillover effects of geopolitical conflict risks on international shipping and crude oil markets, Front. Mar. Sci., 12, 1647599, https://doi.org/10.3389/fmars.2025.1647599, 2025.

CITES: Amendments to Appendices I and II of the Convention adopted by the Conference of the Parties at its 20th meeting, Samarkand, 24 November–5 December 2025, Notification To The Parties, No. 2026/005, Geneva, https://cites.org/sites/default/files/notifications/E-Notif-2026-005_0.pdf (last access: 12 March 2026), 2026a.

CITES: Convention on International Trade in Endangered Species of Wild Fauna and Flora, https://cites.org/eng, last access: 2 April 2026b.

Cong, L., Zhang, H., Wang, P., Chu, C., and Wang, J.: Impact of the Russia-Ukraine Conflict on Global Marine Network Based on Massive Vessel Trajectories, Remote Sens., 16, 1329, https://doi.org/10.3390/rs16081329, 2024.

Coral reef Watch: https://coralreefwatch.noaa.gov/satellite/research/coral_bleaching_report.php, last access: 2 April 2026.

Dahms, C. and Killen, S. S.: Temperature change effects on marine fish range shifts: A meta-analysis of ecological and methodological predictors, Glob. Change Biol., 29, 4459–4479, https://doi.org/10.1111/gcb.16770, 2023.

Dangendorf, S., Sun, Q., Wahl, T., Thompson, P., Mitrovica, J. X., and Hamlington, B.: Probabilistic reconstruction of sea-level changes and their causes since 1900, Earth Syst. Sci. Data, 16, 3471–3494, https://doi.org/10.5194/essd-16-3471-2024, 2024.

Deep Sea Conservation Coalition: https://deep-sea-conservation.org/solutions/no-deep-sea-mining/momentum-for-a-moratorium/, last access: 2 April 2026.

Doney, S., Lebling, K., Ashford, O. S., Pearce, C. R., Burns, W., Nawaz, S., Satterfield, T., Findlay, H. S., Gallo, N. D., Gattuso, J. P., and Halloran, P.: Principles for responsible and effective marine carbon dioxide removal development and governance, World Resources Institute, hal-05121256, https://doi.org/10.69902/84b3a9a8, 2025.

FAO FishStatJ: Software for Fishery and Aquaculture Statistical Time Series, Food and Agriculture Organization of the United Nations, https://www.fao.org/fishery/en/topic/166235/en, last access: 2 April 2026.

FAO SOFIA: Blue Transformation in action, The State of World Fisheries and Aquaculture (SOFIA) 2024, Rome, https://doi.org/10.4060/cd0683en, 2024.

Fischer, S. and Patterson, L.: Natural disasters, environmental values, and the importance of politics: Empirical evidence from worldwide survey data, J. Econ. Psychol., 114, 102890, https://doi.org/10.1016/j.joep.2026.102890, 2026.

Forster, P. M., Smith, C., Walsh, T., Lamb, W. F., Lamboll, R., Cassou, C., Hauser, M., Hausfather, Z., Lee, J.-Y., Palmer, M. D., von Schuckmann, K., Slangen, A. B. A., Szopa, S., Trewin, B., Yun, J., Gillett, N. P., Jenkins, S., Matthews, H. D., Raghavan, K., Ribes, A., Rogelj, J., Rosen, D., Zhang, X., Allen, M., Aleluia Reis, L., Andrew, R. M., Betts, R. A., Borger, A., Broersma, J. A., Burgess, S. N., Cheng, L., Friedlingstein, P., Domingues, C. M., Gambarini, M., Gasser, T., Gütschow, J., Ishii, M., Kadow, C., Kennedy, J., Killick, R. E., Krummel, P. B., Liné, A., Monselesan, D. P., Morice, C., Mühle, J., Naik, V., Peters, G. P., Pirani, A., Pongratz, J., Minx, J. C., Rigby, M., Rohde, R., Savita, A., Seneviratne, S. I., Thorne, P., Wells, C.,

Western, L. M., van der Werf, G. R., Wijffels, S. E., Masson-Delmotte, V., and Zhai, P.: Indicators of Global Climate Change 2024: annual update of key indicators of the state of the climate system and human influence, Earth Syst. Sci. Data, 17, 2641–2680, https://doi.org/10.5194/essd-17-2641-2025, 2025.

Friedlingstein, P., O'Sullivan, M., Jones, M. W., Andrew, R. M., Bakker, D. C. E., Hauck, J., Landschützer, P., Le Quéré, C., Li, H., Luijkx, I. T., Peters, G. P., Peters, W., Pongratz, J., Schwingshackl, C., Sitch, S., Canadell, J. G., Ciais, P., Aas, K., Alin, S. R., Anthoni, P., Barbero, L., Bates, N. R., Bellouin, N., Benoit-Cattin, A., Berghoff, C. F., Bernardello, R., Bopp, L., Brasika, I. B. M., Chamberlain, M. A., Chandra, N., Chevallier, F., Chini, L. P., Collier, N. O., Colligan, T. H., Cronin, M., Djeutchouang, L., Dou, X., Enright, M. P., Enyo, K., Erb, M., Evans, W., Feely, R. A., Feng, L., Ford, D. J., Foster, A., Fransner, F., Gasser, T., Gehlen, M., Gkritzalis, T., Goncalves De Souza, J., Grassi, G., Gregor, L., Gruber, N., Guenet, B., Gürses, Ö., Harrington, K., Harris, I., Heinke, J., Hurtt, G. C., Iida, Y., Ilyina, T., Ito, A., Jacobson, A. R., Jain, A. K., Jarníková, T., Jersild, A., Jiang, F., Jones, S. D., Kato, E., Keeling, R. F., Klein Goldewijk, K., Knauer, J., Kong, Y., Korsbakken, J. I., Koven, C., Kunimitsu, T., Lan, X., Liu, J., Liu, Z., Liu, Z., Lo Monaco, C., Ma, L., Marland, G., McGuire, P. C., McKinley, G. A., Melton, J., Monacci, N., Monier, E., Morgan, E. J., Munro, D. R., Müller, J. D., Nakaoka, S.-I., Nayagam, L. R., Niwa, Y., Nutzel, T., Olsen, A., Omar, A. M., Pan, N., Pandey, S., Pierrot, D., Qin, Z., Regnier, P. A. G., Rehder, G., Resplandy, L., Roobaert, A., Rosan, T. M., Rödenbeck, C., Schwinger, J., Skjelvan, I., Smallman, T. L., Spada, V., Sreeush, M. G., Sun, Q., Sutton, A. J., Sweeney, C., Swingedouw, D., Séférian, R., Takao, S., Tatebe, H., Tian, H., Tian, X., Tilbrook, B., Tsujino, H., Tubiello, F., van Ooijen, E., van der Werf, G., van de Velde, S. J., Walker, A., Wanninkhof, R., Yang, X., Yuan, W., Yue, X., and Zeng, J.: Global Carbon Budget 2025, Earth Syst. Sci. Data Discuss. [preprint], https://doi.org/10.5194/essd-2025-659, in review, 2025.

Gattuso, J.-P., Houllier, F., Adams, J., Amon, D., Bambridge, T., Cheung, W., Chiba, S., Cortés, J., Duarte, C. M., Frölicher, T., Gelcich, S., Gjerde, K., Greaves, D., Haugan, P. M., Li, D., and Tuda, A.: US federal cuts threaten international ocean science and diplomacy, Nature Ecology and Evolution, 9, 1079–1080, https://doi.org/10.1038/s41559-025-02750-3, 2025.

Global Plastic Action Partnership: https://www.globalplasticaction.org/home, last access: 2 April 2026.

GOOS: Global Ocean Observing System Status Report 2025, No. GOOS-310, https://www.ocean-ops.org/goosreport/#home, 2025.

Guan, S., Huang, M., Cai, W., Zhang, Z., Lin, I. I., Kim, H. S., Zhou, L., Lin, X., Xu, Z., Jin, F. F., and Mei, W.: Weak self-induced cooling of tropical cyclones amid fast sea surface warming, Nat. Geosci., 19, 153–158, https://doi.org/10.1038/s41561-025-01879-x, 2026.

Hallegatte, S., Vogt-Schilb, A., Rozenberg, J., Bangalore, M., and Beaudet, C.: From Poverty to Disaster and Back: a Review of the Literature, Econ. Disasters Clim. Chang., 4, 223–247, https://doi.org/10.1007/s41885-020-00060-5, 2020.

Horta e Costa, B., de Benito-Abelló, C., Pike, E., Turnbull, J., MacCarthy, J., Harasta, N., Fragkopoulou, E., Roessger, J., Sullivan-Stack, J., Grorud-Colvert, K., and Gill, D.: Marine protected areas stage of establishment and level of protection are good predictors of their conservation outcomes, Cell Rep. Sustain., 2, https://doi.org/10.1016/j.crsus.2025.100345, 2025.

Hilmi, N., Dbouk, W., Crisóstomo, M., Couvreur, C., Arruda, G., Aziza, A., and Bax, N.: Governing the deep: Economic, ecological, and legal perspectives on deep-sea mining in areas beyond national jurisdiction, Mar. Policy, 183, 106887, https://doi.org/10.1016/j.marpol.2025.106887, 2026.

Hobbs, W., Spence, P., Meyer, A., Schroeter, S., Fraser, A. D., Reid, P., Tian, T. R., Wang, Z., Liniger, G., Doddridge, E. W., and Boyd, P. W.: Observational evidence for a regime shift in summer Antarctic sea ice, J. Climate, 37, 2263–2275, https://doi.org/10.1175/JCLI-D-23-0479.1, 2024.

Howell, S. E. L., Cabaj, A., Babb, D. G., Landy, J. C., Dawson, J., Mahmud, M., and Brady, M.: Near sea ice-free conditions in the northern route of the Northwest Passage at the end of the 2024 melt season, The Cryosphere, 19, 6711–6725, https://doi.org/10.5194/tc-19-6711-2025, 2025.

IISD: Summary of the 20th Meeting of the CITES Conference of the Parties, 24 November–5 December 2025, Earth Negotiations Bulletin, https://enb.iisd.org/sites/default/files/2025-12/enb21124e.pdf (last access: 12 March 2026), 2025.

International Seabed Authority: https://isa.org.jm/exploration-contracts/, last access: 2 April 2026.

IOM: Missing Migrants Project by International Organization for Migration, https://missingmigrants.iom.int/data, last access: 25 February 2026.

IPCC: IPCC Special Report on the Ocean and Cryosphere in a Changing Climate, Cambridge University Press, https://doi.org/10.1017/9781009157964, 2019.

IPCC: Climate Change 2021: The Physical Science Basis, Contribution of Working Group I to the Sixth Assessment Report of the Intergovernmental Panel on Climate Change, Cambridge University Press, https://doi.org/10.1017/9781009157896, 2021.

IUCN: The IUCN Red List of Threatened Species: https://www.iucnredlist.org/en, last access: 2 April 2026.

IUMI: IUMI STATS Report 2025, International Union of Marine Insurance, Germany, https://iumi.com/wp-content/uploads/2026/02/IUMI-Stats-Report-2025-2.pdf (last access: 12 March 2026), 2025.

Jing, R., Heft-Neal, S., Wang, Z., Chen, J., Qiu, M., Opper, I. M., Wagner, Z., and Bendavid, E.: Decreased likelihood of schooling as a consequence of tropical cyclones: Evidence from 13 low- and middle-income countries, P. Natl. Acad. Sci. USA, 122, e2413962122, https://doi.org/10.1073/pnas.2413962122, 2025.

Johansen, D. F. and Vestvik, R. A.: The cost of saving our ocean-estimating the funding gap of sustainable development goal 14, Mar. Policy, 112, 103783, https://doi.org/10.1016/j.marpol.2019.103783, 2020.

Jolliffe J. and Jolly C.: Why ocean economy productivity is declining and what policymakers can do about it, OECD Blog, https://www.oecd.org/en/blogs/2025/09/why-ocean-economy-productivity-is-declining-and-what-policymakers-can-do-about-it.html (last access: 12 March 2026), 2025.

Jones, M., Polasky, S., Rueda, X., Brooks, S., Ingram, J. C., von Hase, A., Egoh, B., Kohsaka, R., Kulak, M., Leach, K., Loyola, R., Mandle, L., Rodriguez Osuna, V., Schaafsma, M., and Sonter, L.: IPBES Business and Biodiversity Assessment: Summary for Policymakers, Zenodo, https://doi.org/10.5281/zenodo.19705111, 2025.

Katapult Ocean: BlueInvest Investor Report 2024 Unlocking the potential of the Blue Economy, https://blueinvest-community.converve.io/upload/fck/file/Report_Blue_Invest_FINAL_7march-compressed.pdf (last access: 12 March 2026), 2024.

Kotenko, S., Ilchenko, S., Kasianova, V., Diakov, V., Mashkantseva, S., and Nitsenko, V.: Determination of the Expected Value of Losses Caused by the Cargo Transportation Insurance Risks by Water Transport, Inventions, 7, 81, https://doi.org/10.3390/inventions7030081, 2022.

Lebreton, L. C., van der Zwet, J., Damsteeg, J. W., Slat, B., Andrady, A., and Reisser, J.: River plastic emissions to the world's ocean, Nat. Commun., 8, 15611, https://doi.org/10.1038/ncomms15611, 2017.

Leclercq, L., Oelsmann, J., Cazenave, A., Passaro, M., Jevrejeva, S., Connors, S., Legeais, J.-F., Birol, F., and Abarca-del-Rio, R.: Abrupt trend change in global mean sea level and its components in the early 2010s, Commun. Earth Environ., 7, 130, https://doi.org/10.1038/s43247-025-03149-5, 2026.

Lévy, M., von Schuckmann, K., Vincent, P., Blanke, B., Claudet, J., Guillotreau, P., Hasson, A., Jolly, C., Shin, Y., Thébaud, O., Vincent, A., and Bahurel, P.: The 2025 Starfish Barometer, in: 9th edition of the Copernicus Ocean State Report (OSR9), edited by: von Schuckmann, K., Moreira, L., de Pascual Collar, Á., Grégoire, M., Brasseur, P., Garric, G., Karstensen, J., Lionello, P., Marcos, M., Poulain, P.-M., and Staneva, J., Copernicus Publications, State Planet, 6-osr9, 1, https://doi.org/10.5194/sp-6-osr9-1-2025, 2025.

Li, C., Burger, F. A., Raible, C. C., and Frölicher, T. L.: Observed regional impacts of marine heatwaves on sea-air CO2 exchange, Geophys. Res. Lett., 51, e2024GL110379, https://doi.org/10.1029/2024GL110379, 2024.

Maatouk, C., Germanos, O., Khattab, Y., Aad, A. M., Aboelhassan, Y. M. E. I., Gandour, G., Hafeez, H. S., Vicerra, P. M. M., Budhathoki, S. S., Lucas, D., and Canals, M. L.: Migration and health policy: Applying the nexus to safety issues of migrants crossing the Mediterranean Sea, Public Health Chall., 4, e70023, https://doi.org/10.1002/puh2.70023, 2025.

Marine Protection Atlas: https://mpatlas.org, last access: 25 February 2026.

Meier, W. N., Petty, A., Hendricks, S., Bliss, A., Kaleschke, L., Divine, D., Farrell, S., Gerland, S., Perovich, D., Ricker, R., Tian-Kunze, X., and Webster, M.: NOAA Arctic Report Card 2025: Sea Ice, NOAA technical report OAR ARC 25-06 (Arctic Report Card), https://doi.org/10.25923/mmxf-0r86, 2025.

Mercator Ocean International: Marine Heatwave Forecasts – 28 June 2025: https://www.mercator-ocean.eu/bulletin/marine-heatwave-forecasts-28-june-2025/ (last access: 2 March 2026), 2025a.

Mercator Ocean International: June 2025 is the 3rd warmest June for the global Ocean following 2023 and 2024, https://www.mercator-ocean.eu/june-2025-marks-third-warmest-june-on-record-globally-following-2023-and-2024-record-high-intensity-marine-heatwaves-impact-62-of-the-mediterranean-sea/ (last access: 2 March 2026), 2025b.

Minière, A., von Schuckmann, K., Sallée, J. B., and Vogt, L.: Robust acceleration of Earth system heating observed over the past six decades, Sci. Rep., 13, 22975, https://doi.org/10.1038/s41598-023-49353-1, 2023.

Mu, D., Huang, R., Yin, P., Yan, H., and Xu, T.: Reconstructing sea level rise from global 945 tide gauges since 1900, Earth Syst. Sci. Data, 17, 5507–5528, https://doi.org/10.5194/essd-17-5507-2025, 2025.

Müller, J. D., Gruber, N., Schneuwly, A., Bakker, D. C., Gehlen, M., Gregor, L., Hauck, J., Landschützer, P., and McKinley, G. A.: Unexpected decline in the ocean carbon sink under record-high sea surface temperatures in 2023, Nat. Clim. Chang., 15, 978–985, https://doi.org/10.1038/s41558-025-02380-4, 2025.

Munich RE: https://www.munichre.com/en/risks/natural-disasters/hurricanes.html, last access: 25 February 2026.

OECD: Development co-operation for a sustainable ocean economy in 2022: A snapshot, https://one.oecd.org/document/DCD%282024%2921/en/pdf (last access: 12 March 2026), 2024.

OECD: Review of Fisheries 2025, OECD Publishing, Paris, https://doi.org/10.1787/560cd8fc-en, 2025a.

OECD: Promoting Sustainable Ocean Economies, OECD Publishing, Paris, https://www.oecd.org/content/dam/oecd/en/publications/reports/2025/06/promoting-sustainable-ocean-economies_07f85c4d/72055d7f-en.pdf (last access: 12 March 2026), 2025b.

PAME: The Increase In Arctic Shipping 2013–2025, Arctic Shipping Status Report #1 (updated February 2026), https://oaarchive.arctic-council.org/bitstreams/61870641-ba6a-4e1d-8e71-be201713a27f/download, last access: 12 March 2026.

Pan, Y., Cheng, L., Abraham, J., Trenberth, K. E., Reagan, J., Du, J., Wang, Z., Storto, A., Von Schuckmann, K., Zhu, Y., and Mann, M. E.: Ocean Heat Content Sets Another Record in 2025, Adv. Atmos. Sci., https://doi.org/10.1007/s00376-026-5876-0, 2026.

Paolo, F. S., Kroodsma, D., Raynor, J., Hochberg, T., Davis, P., Cleary, J., Marsaglia, L., Orofino, S., Thomas, C., and Halpin, P.: Satellite mapping reveals extensive industrial activity at sea, Nature, 625, 85–91, https://doi.org/10.1038/s41586-023-06825-8, 2024.

Pearce-Kelly, P., Altieri, A. H., Bruno, J. F., Cornwall, C. E., McField, M., Muñiz-Castillo, A. I., Rocha, J., Setter, R. O., Sheppard, C., Roman-Cuesta, R. M., and Yesson, C.: Considerations for determining warm-water coral reef tipping points, Earth Syst. Dynam., 16, 275–292, https://doi.org/10.5194/esd-16-275-2025, 2025.

Pinsky, M. L., Selden, R. L., and Kitchel, Z. J.: Climate-driven shifts in marine species ranges: scaling from organisms to communities, Annu. Rev. Mar. Sci., 12, 153–179, https://doi.org/10.1146/annurev-marine-010419-010916, 2020.

Protected Planet: Marine Protected Areas, Protected Planet, https://www.protectedplanet.net/en/thematic-areas/marine-protected-areas, last access: 25 February 2026.

Ramsar: Global Wetland Outlook 2025: Valuing, conserving, restoring and financing wetlands, Secretariat of the Convention on Wetlands, Gland, Switzerland, https://doi.org/10.69556/GWO-2025-eng, 2005.

Raynor, J., Orofino, S., Costello, C., McDonald, G., Mayorga, J., and Sala, E.: Little-to-no industrial fishing occurs in fully and highly protected marine areas, Science, 389, 392–395, https://doi.org/10.1126/science.adt9009, 2025.

Roach, L. A. and Meier, W. N.: Sea ice in 2023, Nat. Rev. Earth Environ., 5, 235–237, https://doi.org/10.1038/s43017-024-00542-0, 2024.

Sánchez, O., Stefanni, S., and Bhadury, P: The deep sea biodiversity and conservation collection, Sci. Rep., 14, 27559, https://doi.org/10.1038/s41598-024-77742-7, 2024.

Seguin, R., Le Manach, F., Devillers, R., Velez, L., and Mouillot, D.: Global patterns and drivers of untracked industrial fishing in coastal marine protected areas, Science, 389, 396–401, https://doi.org/10.1126/science.ado9468, 2025.

Selig, E. R., Nakayama, S., Wabnitz, C. C. C., Österblom, H., Spijkers, J., Miller, N. A., Bebbington, J., and Decker Sparks, J. L.: Revealing global risks of labor abuse and illegal, unreported, and unregulated fishing, Nat. Commun., 13, 1612, https://doi.org/10.1038/s41467-022-28916-2, 2022.

Sharma, R., Barange, M., Agostini, V., Barros, P., Gutierrez, N. L., Vasconcellos, M., Fernandez Reguera, D., Tiffay, C., and Levontin, P. (Eds.): Review of the state of world marine fishery resources – 2025, FAO Fisheries and Aquaculture Technical Papers, No. 721, Rome, https://doi.org/10.4060/cd5538en, 2025.

Souter, D., Planes, S., Wicquart, J., Logan, M., Obura, D., and Staub, F. (Eds.): Status of Coral Reefs of the World: 2020, Global Coral Reef Monitoring Network (GCRMN), Australian Institute of Marine Science, https://gcrmn.net/2020-report/ (last access: 12 March 2026), 2020.

Storto, A. and Yang, C.: Acceleration of the ocean warming from 1961 to 2022 unveiled by large-ensemble reanalyses, Nat. Commun., 15, 545, https://doi.org/10.1038/s41467-024-44749-7, 2024.

Tan, Z., Von Schuckmann, K., Speich, S., Bopp, L., Zhu, J., and Cheng, L.: Observed large-scale and deep-reaching compound ocean state changes over the past 60 years, Nat. Clim. Chang, 16, 58–68, https://doi.org/10.1038/s41558-025-02484-x, 2025.

Tanhua, T., Traon, P.-Y. L., Köstner, N., Eparkhina, D., Navarro, G., Dunbar, M. B., Speich, S., Pascual, A., von Schuckmann, K., Liguori, G., Karstensen, J., Hassoun, A. E. R., Doorn, E. van, Barceló-Llull, B., Gómez, B. P., Cusack, C., Heslop, E., Lara-Lopez, A., Petihakis, G., Telszewski, M., Palacz, A. P., Wilmer-Becker, K., Pearlman, J., Piniella, Á. M., Heymans, J. J., and Lips, I.: Towards a sustained and fit-for-purpose European ocean observing and forecasting system, Front. Mar. Sci., 11, 1394549, https://doi.org/10.3389/fmars.2024.1394549, 2024.

Tekman, M. B., Walther, B. A., Peter, C., Gutow, L., and Bergmann, M.: Impacts of plastic pollution in the oceans on marine species, biodiversity and ecosystems, WWF Germany, Berlin, https://doi.org/10.5281/zenodo.5898684, 2022.

The Pew Charitable Trusts: Breaking the Plastic Wave 2025, https://www.pew.org/en/research-and-analysis/reports/2025/12/breaking-the-plastic-wave-2025 (last access: 2 April 2026), 2025.

UN: 2030 Agenda for Sustainable Development, https://sdgs.un.org/2030agenda (last access: 2 April 2026), 2015.

UNEP: From Pollution to Solution: A global assessment of marine litter and plastic pollution, Nairobi, United Nations Environment Programme, https://wedocs.unep.org/handle/20.500.11822/36963 (last access: 12 March 2026), 2021.

von Jackowski, A.: Navigating the current landscape of ocean observations: an overview from platform infrastructures to networks related to ocean time series, Front. Mar. Sci., 11, 1363863, https://doi.org/10.3389/fmars.2024.1363863, 2025.

von Schuckmann, K., Holland, E., Haugan, P., and Thomson, P.: Ocean science, data, and services for the UN 2030 Sustainable Development Goals, Mar. Polic., 121, 104154, https://doi.org/10.1016/j.marpol.2020.104154, 2020.

von Schuckmann, K., Minière, A., Gues, F., Cuesta-Valero, F. J., Kirchengast, G., Adusumilli, S., Straneo, F., Ablain, M., Allan, R. P., Barker, P. M., Beltrami, H., Blazquez, A., Boyer, T., Cheng, L., Church, J., Desbruyeres, D., Dolman, H., Domingues, C. M., García-García, A., Giglio, D., Gilson, J. E., Gorfer, M., Haimberger, L., Hakuba, M. Z., Hendricks, S., Hosoda, S., Johnson, G. C., Killick, R., King, B., Kolodziejczyk, N., Korosov, A., Krinner, G., Kuusela, M., Landerer, F. W., Langer, M., Lavergne, T., Lawrence, I., Li, Y., Lyman, J., Marti, F., Marzeion, B., Mayer, M., MacDougall, A. H., McDougall, T., Monselesan, D. P., Nitzbon, J., Otosaka, I., Peng, J., Purkey, S., Roemmich, D., Sato, K., Sato, K., Savita, A., Schweiger, A., Shepherd, A., Seneviratne, S. I., Simons, L., Slater, D. A., Slater, T., Steiner, A. K., Suga, T., Szekely, T., Thiery, W., Timmermans, M.-L., Vanderkelen, I., Wjiffels, S. E., Wu, T., and Zemp, M.: Heat stored in the Earth system 1960–2020: where does the energy go?, Earth Syst. Sci. Data, 15, 1675–1709, https://doi.org/10.5194/essd-15-1675-2023, 2023.

von Schuckmann, K., Moreira, L., Grégoire, M., Marcos, M., Staneva, J., Brasseur, P., Garric, G., Lionello, P., Karstensen, J., and Neukermans, G. (Eds.): 8th edition of the Copernicus Ocean State Report (OSR8), Copernicus Publications, State Planet, 4-osr8, 10.5194/sp-4-osr8, 2024.

von Schuckmann, K., Godoy-Faundez, A., Garçon, V., Muller-Karger, F. E., Evans, K., Appeltans, W., Bax, N., Cecchi, L. B., Bernard, A., Bernard, K., Byrnes, J., Canonico, G., Chapuis, L., Clark, M. R., Darnaude, A. M., Davies, C., Englyst, P., Fransson, A., Hallam, S., Heslop, E., Holland, E., Hood, M., Kern, S., Liné, A., Lara-Lopez, A., Loose, N., Míguez, B. M., McMahon, C. R., Nordlund, L. M., Post, J., Speich, S., Sutton, A., Tanhua, T., Telszewski, M., Poursanidis, D., and Yu, W.: Global ocean indicators: Marking pathways at the science-policy nexus, Mar. Polic., 184, 106922, https://doi.org/10.1016/j.marpol.2025.106922, 2026.

Walsh, J. E., Eicken, H., Redilla, K., and Johnson, M.: Sea ice breakup and freeze-up indicators for users of the Arctic coastal environment, The Cryosphere, 16, 4617–4635, https://doi.org/10.5194/tc-16-4617-2022, 2022.

Wang, J., Church, J. A., Zhang, X. and Chen, X.: Improved Sea Level Reconstruction from 1900 to 2019, J. Clim., 37, 6453–6474, https://doi.org/10.1175/JCLI-D-23-0410.1, 2024.

Weerasinghe, T., Amaratunga, D., and Haigh, R.: Appraising investments in Disaster Risk Reduction (DRR): A systematic literature review, Prog. Disaster Sci., 26, 100438, https://doi.org/10.1016/j.pdisas.2025.100438, 2025.

WEF: Making Waves in the Regenerative & Sustainable Ocean Economy: Transformative Ocean Investment Opportunities, https://reports.weforum.org/docs/WEF_Transformative_Ocean_Investment_Opportunities_2025.pdf (last access: 12 March 2026), 2025.

WMO: State of the Global Climate 2021, WMO-No. 1290, ISBN 978-92-63-11290-3, https://library.wmo.int/idurl/4/56300 (last access: 12 March 2026), 2021.

World Meteorological Organization (WMO): State of the Global Climate 2025 (WMO-No. 1342), Geneva, ISBN 978-92-63-11299-7, https://doi.org/10.59327/WMO/S/CRI/SOC/1, 2026.

World Bank: State and Trends of Carbon Pricing 2025, World Bank, Washington, DC, https://hdl.handle.net/10986/43277 (last access: 19 May 2026), 2025.

WTO (World Trade Organization): https://www.wto.org/english/news_e/news25_e/fish_15sep25_e.htm, last access: 2 April 2026.

Yang, X., Chen, D., Wahab, I., and Burman, A.: Evidence of climate and economic drivers affecting migration in an unequal and warming world, Commun. Earth Environ., 6, 782, https://doi.org/10.1038/s43247-025-02811-2, 2025.

Zhu, X., Rochman, C. M., Hardesty, B. D., and Wilcox, C.: Plastics in the deep sea – A global estimate of the ocean floor reservoir, Deep-Sea Res.-Pt. I, 206, 104266, https://doi.org/10.1016/j.dsr.2024.104266, 2024.

State Planet, 7-osr10, 4, 2026
https://doi.org/10.5194/sp-7-osr10-4-2026
© Author(s) 2026. This work is distributed under
the Creative Commons Attribution 4.0 License.

Three decades of marine bioregions evolution through analysis of phytoplankton phenology

Wilhem Riom[1], Nicolas Mayot[1,2], Alexandre Mignot[3], Vincent Taillandier[1], and Fabrizio D'Ortenzio[1]

[1]Sorbonne Université & CNRS, Laboratoire d'Océanograpie de Villefranche, UMR 7093 LOV, 06230 Villefranche-sur-mer, France
[2]Centre National d'Études Spatiales (CNES), 75001 Paris, France
[3]Mercator Ocean International, 31400 Toulouse, France

Correspondence: Wilhem Riom (wilhem.riom@imev-mer.fr)

Received: 30 July 2025 – Discussion started: 15 September 2025
Revised: 27 February 2026 – Accepted: 8 March 2026 – Published: 30 September 2026

Abstract. Ocean biogeochemistry is undergoing significant modification in response to climate change. To better track these evolutions, we present a novel ocean monitoring indicator that follows the temporal evolution of marine bioregions of similar phytoplankton phenologies. Chlorophyll *a* concentration observations from remotely sensed ocean color describe seven distinct marine bioregions characterized by their unique patterns of phytoplankton biomass seasonality. The sizes and locations of these bioregions are monitored from 1998 to 2024 using a multi-sensor merged L4 ocean color product. While the bioregions' extents appear to follow interannual and decadal climate variability, their long term evolution suggests a poleward extension of less seasonal phytoplankton phenology, which is generally characteristic of the tropical and subtropical bands. This innovative approach allows the systematic monitoring of how phytoplankton adapt their seasonal cycle in response to changes in environmental conditions, hence giving valuable insights into the evolution of marine ecosystems over the past three decades and helping advance our understanding of global ocean biological responses to environmental change.

1 Introduction

Phytoplankton, the main primary producers in the ocean, sustain marine food webs (Fenchel, 1988; Kiørboe, 1993) and play a central role in regulating oceanic carbon fluxes (Falkowski, 1994). Environmental conditions shape phytoplankton growth and losses through "bottom-up" (e.g., light and nutrients availability) and "top-down" (e.g., grazing) processes. Over the past three decades, satellite ocean color measurements make it possible to estimate phytoplankton biomass (Behrenfeld et al., 2005) proxied by chlorophyll *a* concentration (Huot et al., 2007). This, in turn, has enabled the study of phytoplankton phenology (i.e. the temporal succession of main biological events) (Longhurst, 2007; Racault et al., 2012; Sapiano et al., 2012; Boyce et al., 2017). Climate influences the distribution of environmental factors that, in turn, regulate the spatiotemporal dynamics of phytoplankton biomass (Falkowski and Oliver, 2007). Distinct seasonal patterns emerge along latitudinal gradients, from the equator to the poles (Longhurst, 1995). At high latitudes, primary production is mainly light limited, whereas in tropical and subtropical regions, phytoplankton production is essentially nutrient limited (Boyce et al., 2017). Like the marine environment itself, phytoplankton biomass responds to both annual and decadal climate variability (Li et al., 2024).

Climate change is altering oceanic ecosystems (see OSR10 Chap. 1.3 by Lévy et al.), with complex impacts on phytoplankton growth. For instance, rising sea temperatures might directly affect metabolism (O'Connor et al., 2009) but also environmental conditions through enhanced water column stratification (Yamaguchi and Suga, 2019), which in turn might further limit growth by hindering upward transport of nutrients to the sunlit layers (Sarmiento et al., 2004; Fernández-González et al., 2022). As for terrestrial plants

Published by Copernicus Publications.

Table 1. Product table.

Product ref. no.	Product Id & type	Data access	Documentation
1	OCEANCOLOUR_GLO_BGC_L4_MY_009_104, Satellite observations	EU Copernicus Marine Service Product (2022)	Quality Information Document (QUID): Garnesson et al. (2025) Product User Manual (PUM): Colella et al. (2024)

(Cleland et al., 2007; Inouye, 2022), marine phytoplankton are expected to respond to these environmental changes by adjusting their seasonal cycles (Winder and Sommer, 2012). Most of the documentation effort focused on variations in the onset, duration, and intensity of bloom events (e.g., Sommer and Lengfellner, 2008; Martinez et al., 2011; Henson et al., 2018; Salgado-Hernanz et al., 2019). These changes may cause phenological mismatches hence disrupting energy transfer to higher trophic levels (Visser and Both, 2005; Asch et al., 2019) and have broader implications for the global carbon cycle (Fisher et al., 2025). Consequently, establishing robust indicators monitoring interannual to decadal changes in phytoplankton phenology is critical to better address the evolution of the marine ecosystem with climate change.

With the large amount of remotely sensed ocean color observations, numerical clustering methods emerged as key tools to identify regions with similar seasonal dynamics of phytoplankton (hereafter referred to as bioregions) (International Ocean Color Coordinating Group; IOCCG et al., 2009). Several studies (e.g. D'Ortenzio and Ribera d'Alcalà, 2009; Lacour et al., 2015; Ardyna et al., 2017; Boyer et al., 2017; Kheireddine et al., 2021; Baudena et al., 2025) have applied such methods to partition oceanic domains into bioregions characterized by similar seasonal patterns of chlorophyll *a* concentration, which are often used as a basis for inferring provinces of similar biogeochemical functioning. Similarly to how Mayot et al. (2016) extended D'Ortenzio and Ribera d'Alcalà (2009) climatological partitioning of the Mediterranean Sea, this study presents an ocean monitoring approach built on Baudena et al. (2025) climatological bioregionalization of the global ocean. This method tracks variations in the extension of the bioregions in respect of time to reveal the trends in geographical changes of phytoplankton phenology. The main idea behind our approach is that tracking these variations may serve as a relevant proxy for assessing changes of phytoplankton dynamics, which, in turn, could inform on main variations of environmental factors of the marine ecosystem.

We introduce here a proof of concept for such an approach using the supervised clustering method introduced in Baudena et al. (2025). Annual partition of the global ocean (56° S–56° N) from 1998 to 2024 is obtained by classifying annual time series of remotely sensed chlorophyll *a* concentration (Copernicus-GlobColor) into bioregions. After presenting the mean climatological state of the bioregions, we investigate their change in surface area over the last three decades. Then, building on D'Ortenzio et al. (2012) and adapting methods from Higgins et al. (2016), originally applied to terrestrial biomes, we compare the geographical extension of the bioregions between two decadal periods at the greatest extent of our dataset, (1998–2007 and 2015–2024) to identify the main trends in the reorganization of phytoplankton phenology. Finally, possible correlation with environmental changes and method limitations are evoked in the discussion section.

2 Material and methods

2.1 Data

Chlorophyll *a* concentrations data were retrieved from the merged multi-sensor ocean color product ref. no. 1 (see Table 1). This product offers cloud free remotely sensed surface chlorophyll *a* concentration at a 4 km spatial resolution and daily intervals. Using such a L4 product (an optimally interpolated, merged satellite dataset), as compared to L3 (merged product) in Baudena et al. (2025), compensates for the lack of observation inherent to satellite ocean color (Stock et al., 2020) and ensures a maximal spatialization of the bioregions at an annual temporal resolution.

2.2 Supervised Clustering

Annual ensembles of seasonal time series of chlorophyll *a* concentration were built from 1998 to 2024. The time series composing them were all processed similarly to allow subsequent classification according to Baudena et al. (2025) supervised clustering method. In short, within each annual ensemble, each individual time series characterizes the seasonal evolution of chlorophyll *a* concentration over a $1° \times 1°$ grid. Following the method detailed in Sect. S1 in the Supplement, the time series were obtained averaging all available observations within each $1 \times 1°$ pixel over a 8 d temporal window. To dampen sub-seasonal variations, time series were all smoothed with a 5 weeks centered rolling average method. Finally, all annual time series were normalized by their maximum to ensure that the clustering method focuses on their shape rather than on their magnitude.

CHAPTER 2.1

Time series associated with pixels in the Arctic and Southern Oceans (respectively above 56° N and below 56° S) were removed from every annual ensemble due to lack of continuous satellite observation through winter in relation to permanent cloud presence and polar night. Coastal pixels located within 111 km (∼ 1°) from the coast were also discarded due to the uncertainty in chlorophyll *a* concentration estimations within optically complex waters (Case 2 waters). As a result 80 % of the global ocean area is considered. In the southern hemisphere, time series were all shifted six months backward, to ensure identical sequencing of seasons in the time series of all pixels.

Each annual ensemble was then partitioned into the seven clusters of Baudena et al. (2025) based on their seasonality patterns. These seven clusters were found to optimally partition open ocean seasonal cycles of surface chlorophyll *a* concentration in respect of multiple statistical tests discussed in the companion study. The assignment of a given time serie into one of the clusters was done according to its minimal euclidean distance (maximal similarity) with the central time series of Baudena et al. (2025) clusters. To prevent assignment of too dissimilar seasonal patterns, a threshold distance was considered to accept (distance below the threshold) or refuse (distance above the threshold) an assignment. To account for the method's sensitivity to this hyperparameter, we discretized a range of possible values, defined by the minimum and maximum classification distances found among the most deviating elements of any cluster, from 1.33 (cluster 1) to 2.60 (cluster 7), based on the unsupervised clustering of Baudena et al. (2025). Each annual ensemble was partitioned several times from a low (strict definition of the clusters) to high threshold values (lax definition of the clusters) selected within this range with a regular step of 0.05 (see sensitivity analysis in Sect. S2). At least 88 % of the time series were always successfully sorted within the seven clusters (see Fig. S2b). Unclassified time series, mostly located in regions of low satellite data availability region (see Fig. S2a), were all excluded from ulterior analysis.

2.3 Bioregions

The spatial projection of each pixel's membership over the global ocean forms large coherent spatial domains similarly classified. These oceanic domains correspond to the bioregions as defined by Baudena et al. (2025). As a reminder, bioregions share similar seasonal patterns in phytoplankton phenology suggesting a common biogeochemical functioning (Longhurst, 1995). Over time, the spatial definition of the bioregion might change with annual time series characteristic of a given pixel being attributed to different clusters over different years. A change of phytoplankton phenology is attributed to a pixel when its bioregion changes from one year to another. For a given pixel, the frequency of phenology change is defined as the total sum of these changes over the study period. These changes might present oscillating patterns from annual to decadal period or long term trends.

Three climatological partitions of the global ocean were considered hereafter. They were constructed by keeping, in each pixel, the most frequent bioregion over the selected temporal extent. The three considered periods are: from 1998 to 2024 and two decadal periods from 1998 to 2007 and from 2015 to 2024. The former climatological period supports the documentation of the average bioregion extent while the latter two decadals periods were chosen at the edge of the temporal span to support the documentation of long term changes in the bioregion's extent. The use of decadal bioregions also dampens interannual variability.

When comparing the decadal bioregions' extent between the 1998–2007 and the 2015–2024, we attribute a stable phenology change to a given pixel when its classification changed between the two periods and if this assignment remained identical for more than six years in each of the two decades. This temporal criterion was chosen strictly above half a decade to grant a reasonable and robust indicator of the bioregion persistence while remaining permissive in respect of inter annual climate variability.

To assess phytoplanktonic biomass across the bioregions, we analyzed their chlorophyll *a* concentrations, presented as probability distribution functions in Fig. 1b. The distribution for bioregion 1 is notably bimodal, showing a minor peak near 0.03 mg m^{-3} and a dominant one just above 0.1 mg m^{-3}. This finding prompted us to subdivide bioregion 1, after the clustering, based on a threshold of 0.06 mg m^{-3} for yearly average chlorophyll *a*, creating an oligotrophic group (below the threshold) and a mesotrophic group (above the threshold). Although both sub-regions exhibit a similar non-seasonal pattern, this subdivision reveals distinct phenologies, suggesting they are controlled by different environmental forcings that either sustain or inhibit year-round phytoplankton growth.

2.4 Uncertainties estimation

Following the set of threshold distance, each annual ensemble is partitioned twenty six times (see Sect. 2.2). In each of these partitions, the distribution of the bioregion surface area relative to the set of threshold distances is characterised hereafter by its central value (the median) within its interquartile range (Q1–Q3). The interquartile range of surface area estimates accounts for the bioregionalization method uncertainty. All surface areas are reported relative to the total global ocean area. To identify long-term changes, we fitted a linear model to the central surface area estimates in respect of time. The statistical significance of these linear trends was determined using a Spearman rank correlation, with a trend considered significant at $p < 0.1$.

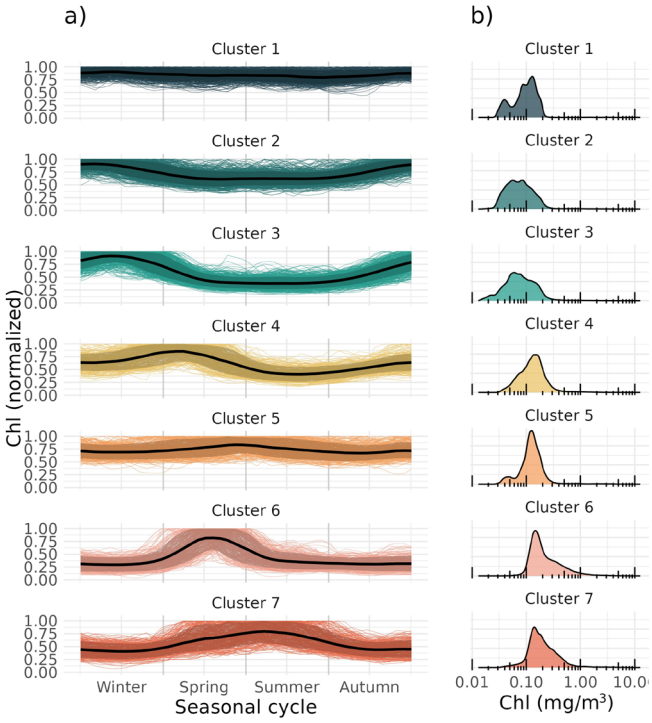


Figure 1. Clusters resulting from the supervised clustering of the ensemble of year 2024 from product ref. no. 1 according to the strictest threshold. The left panel **(a)** shows the mean normalized seasonal cycles within each cluster (thick continuous black line) within its 10 % and 90 % percentiles (transparent black bands). In the background, examples of time series within that cluster are represented. The right panel **(b)**, displays the distribution of chlorophyll concentration within each cluster.

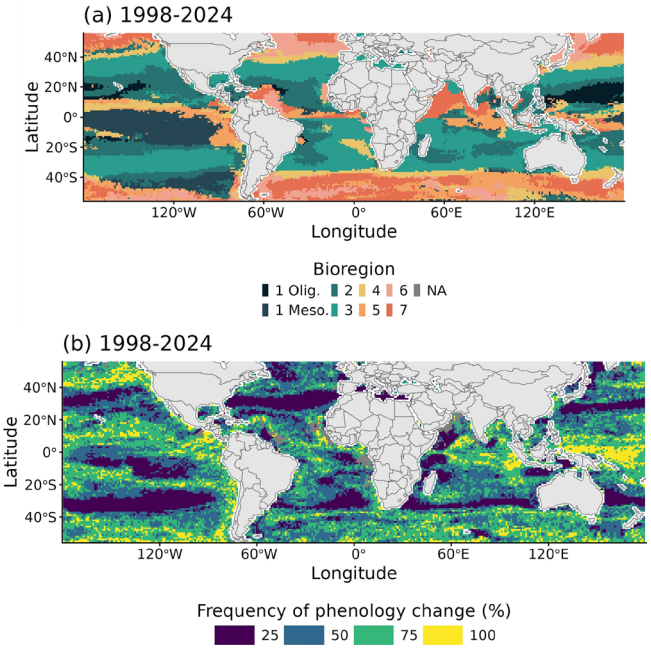


Figure 2. **(a)** Climatological distribution of the bioregions in the 1998–2024 period. **(b)** Amount of phenology change per pixel over the 1998–2024 period given in % of the total number of considered years. Both panels display the results obtained using the least strict clustering criteria on the ensemble processed from product ref. no. 1. Pixels designated as NA (in grey) refer to the position of the time series that were not successfully classified.

3 Results

Our analysis is presented in three parts. First, we recall the phytoplankton phenology and climatological repartition of the seven marine bioregions (described in more details in Baudena et al., 2025). Second, we assess the interannual variability and long-term trends in the surface area evolution of each bioregion from 1998 to 2024. Finally, we identify the locations of stable phenological changes by comparing two distinct decades at the edges of the period.

3.1 Bioregion and phytoplankton phenology

For each year, the supervised clustering method subdivides the ensemble into the seven clusters identified in Baudena et al. (2025). These clusters outline specific phenological patterns inferred from the mean seasonal cycle of chlorophyll *a* concentration (Fig. 1a). These patterns, corresponding to the bioregions in Fig. 2a, range from no clear seasonality (bioregion 1) to those with pronounced single or double peak events (bioregions 7–6–4), which are typical of blooms in temperate and high-latitude systems, as we found in Fig. 2a.

In agreement with Baudena et al. (2025), the climatological distribution of the related bioregions over the 1998–2024 period (Fig. 2a) follows a meridional distribution sketching coherent, large-scale structures corresponding to major oceanic domains, such as the subtropical gyres (bioregions 1 Olig., 2 and 3) and convergences zones (bioregion 4). The biogeochemical relevance of this partitioning is reinforced by the distribution of chlorophyll *a* concentrations within each bioregion (Fig. 1b). A clear poleward productivity gradient emerges, with the lowest surface biomass in the perpetually stratified regimes of the subtropical band and the highest in the high-latitude bloom regions (bioregion 6–7). This aligns with established knowledge of global ocean productivity patterns (Behrenfeld et al., 2005).

Baudena et al. (2025) offered a biogeochemical interpretation of the bioregions, summarized as follows. Bioregions 6 and 7 correspond to Longhurst (1995)'s model 1 (*polar, irradiance-limited*). Bioregion 5 exhibits features of both model 1 and model 2 (*mid-latitude, nutrient-limited spring production peak*). Bioregion 4 closely aligns with the Bloom bioregion identified by D'Ortenzio et al. (2012). Bioregion 3 matches Longhurst (1995)'s model 3 (*subtropical, winter nutrient-limited*), whereas Bioregion 2 closely resembles the Tropical bioregion described by D'Ortenzio et al. (2012). Finally, Bioregion 1 corresponds to Longhurst's model 4

CHAPTER 2.1

(*tropical*). Its additional subdivision, introduced here, produces spatially coherent domains that distinguish between oligotrophic regions in the centers of subtropical gyres and mesotrophic regions primarily distributed around the equator.

3.2 Temporal evolution of the bioregions

The boundaries of bioregions in Fig. 2a are not static. Figure 2b displays the frequency of changes in each pixel bioregion's affiliation, interpreted as changes in phytoplankton phenology, over the 1998–2024 period. These changes occur most frequently in transitional areas in-between major bioregions, as well as in coastal zones, over the equatorial band, and over high-latitude regions of the northern Pacific and Southern Ocean (Fig. 2b). Bioregion 3, centered at 30° in both hemispheres, appears as the most stable bioregion.

A visual analysis of the temporal evolution of each bioregion's surface area (Fig. 3) reveals strong interannual variabilities (time evolution of black dots) in all bioregions. Bioregions 1, 2, 3 and 6 also display high decadal variability (black lines). Linear trend analysis ($p < 0.1$) indicates a significant reduction in the global surface area of bioregion 3 and bioregion 4. Conversely, the mesotrophic bioregion 1 shows a significant expansion. While surface areas of bioregions 6 and 7 exhibit large changes from one year to the other, their surface area estimates are associated with large method uncertainties ($\sim 50\,\%$), precluding the consideration of the trend significance.

3.3 Stable changes of phenology

To isolate long-term trends from interannual variability, we identified areas with stable phenological changes between the 1998–2007 and 2015–2024 decadal periods. As highlighted in Fig. 4a, these regions are mostly located within the tropical and subtropical band. Overall 4.93 % [4.56 %, 5.06 %] of the global ocean is affected suggesting slow transitions in essentially steady conditions. The dominant pathways in phenology transition are summarized in Table 2. The most prominent change (1.82 % of the global ocean) is the transition from bioregion 3 to the less seasonal bioregion 2, occurring primarily in the subtropical Pacific and Indian Oceans. Other significant shifts include the expansions at lower latitude of bioregion 1 at the expense of bioregion 2 (0.62 %) and of bioregion 3 at the expense of bioregion 4 (0.27 %). In the North Atlantic's temperate band, a notable net transition from bioregion 7 to 6 also occurred (0.09 %). As summarized by Fig. 4b, the most prominent trend is a poleward expansion of bioregions of weaker seasonality. These spatial patterns of change correspond to the surface area trends observed over the full time series (Fig. 3).

Table 2. Major pathways among stable phenology changes. Changes in surface area from one bioregion to another are given relatively to the global ocean. Estimates are given within their first and third quartiles and grouped by oceanographic basins. Minor changes, associated with an area inferior to 0.01 % of the global ocean, are not represented. Estimates highlighted in bold indicate values greater than 0.1 % of the global ocean.

		Oceanic Basins					Total
		Indian Ocean	North Pacific Ocean	South Pacific Ocean	North Atlantic Ocean	South Atlantic Ocean	
Pathways of stable phenology changes	2 to 1 Olig.	–	**0.12 % [0.12, 0.12]**	0.01 % [0.01, 0.01]	0.03 % [0.03, 0.03]	–	**0.16 % [0.16, 0.16]**
	2 to 1 Meso.	0.03 % [0.03, 0.03]		**0.36 % [0.36, 0.36]**	0.07 % [0.07, 0.07]	–	**0.46 % [0.46, 0.46]**
	3 to 2	**0.67 % [0.66, 0.67]**	**0.55 % [0.52, 0.55]**	**0.15 % [0.15, 0.15]**	**0.19 % [0.18, 0.19]**	**0.21 % [0.21, 0.21]**	**1.82 % [1.78, 1.83]**
	4 to 3	0.01 % [0.01, 0.01]	**0.16 % [0.14, 0.16]**	0.02 % [0.01, 0.02]	0.02 % [0.02, 0.02]	0.06 % [0.06, 0.06]	**0.27 % [0.24, 0.27]**
	6 to 7	–	0.03 % [0.02, 0.06]	0.02 % [0.01, 0.02]	0.08 % [0.03, 0.10]	0.01 % [0.001, 0.10]	**0.13 % [0.06, 0.19]**
	7 to 6	0.01 % [0.01, 0.01]	0.01 % [0.01, 0.02]	–	**0.17 % [0.13, 0.19]**	**0.23 % [0.19, 0.24]**	**0.43 % [0.33, 0.47]**

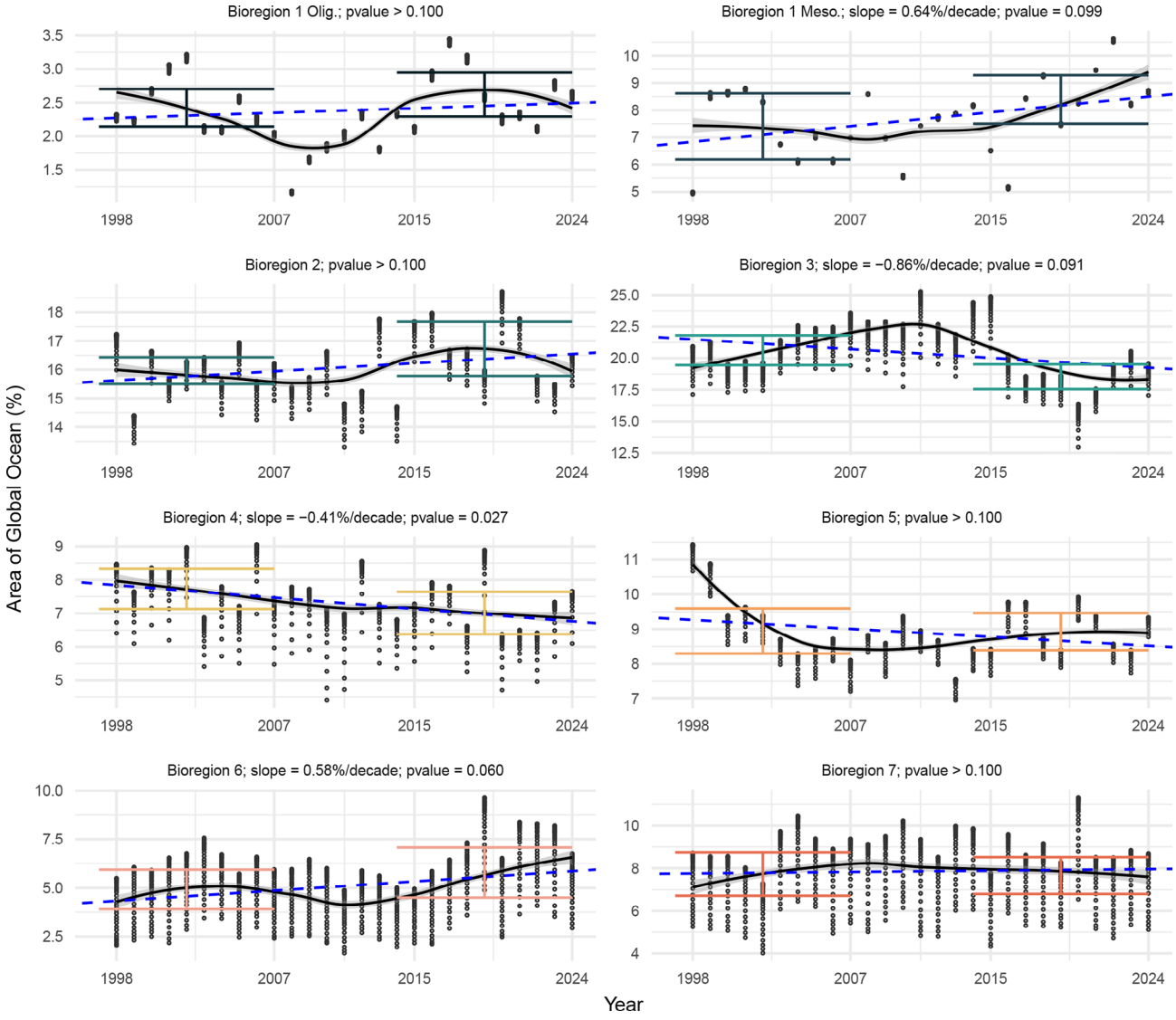


Figure 3. Evolution of bioregions' surface area from 1998 to 2024. The time evolution of black dots represent estimates of the areas following the varying acceptance thresholds. The black trend line displays the smoothed centered 10-year rolling average, the blue dotted line corresponds to the linear tendency of the annual median area estimate. Panels' titles show the linear trends on the condition that it was found significant ($p < 0.1$). First and third quartiles of the decadal bioregions (1998–2007 and 2015–2024) are indicated as colored error bars. Note the varying y-scale across panels.

4 Discussion and conclusion

Our analysis introduces a novel ocean indicator approach that distinguishes between intermittent, year-to-year variability and persistent, long-term shifts in phytoplankton phenology. While boundary regions exhibit frequent intermittent changes (Fig. 2b), our decadal analysis finds that nearly 5 % (see Table 2) of the global ocean experienced a displacement of phytoplankton phenology suggesting persistent ecosystem reorganization over the past three decades. The cascading changes (i.e., transitions from bioregion 4 to 3, bioregion 3 to 2, and 2 to 1) identified above, are possibly driven by an intensification of upper-ocean stratification in relation to climate warming (Capotondi et al., 2012). At these low latitudes (30° S–30° N), a shallower vertical mixing prevents entrainment of deeper nutrients (Vereshchaka and Shatravin, 2025) therefore hindering biomass accumulation of surface waters (Sarmiento et al., 2004; Polovina et al., 2008). The robustness of our ocean indicator approach is further validated in the temperate North Atlantic, where despite high method uncertainties, the documented shift from a double to a single bloom phenology (bioregion 7 to 6) linked to delayed autumnal mixing in Martinez et al. (2011) is successfully captured. The documented changes also echo the variations of

CHAPTER 2.1

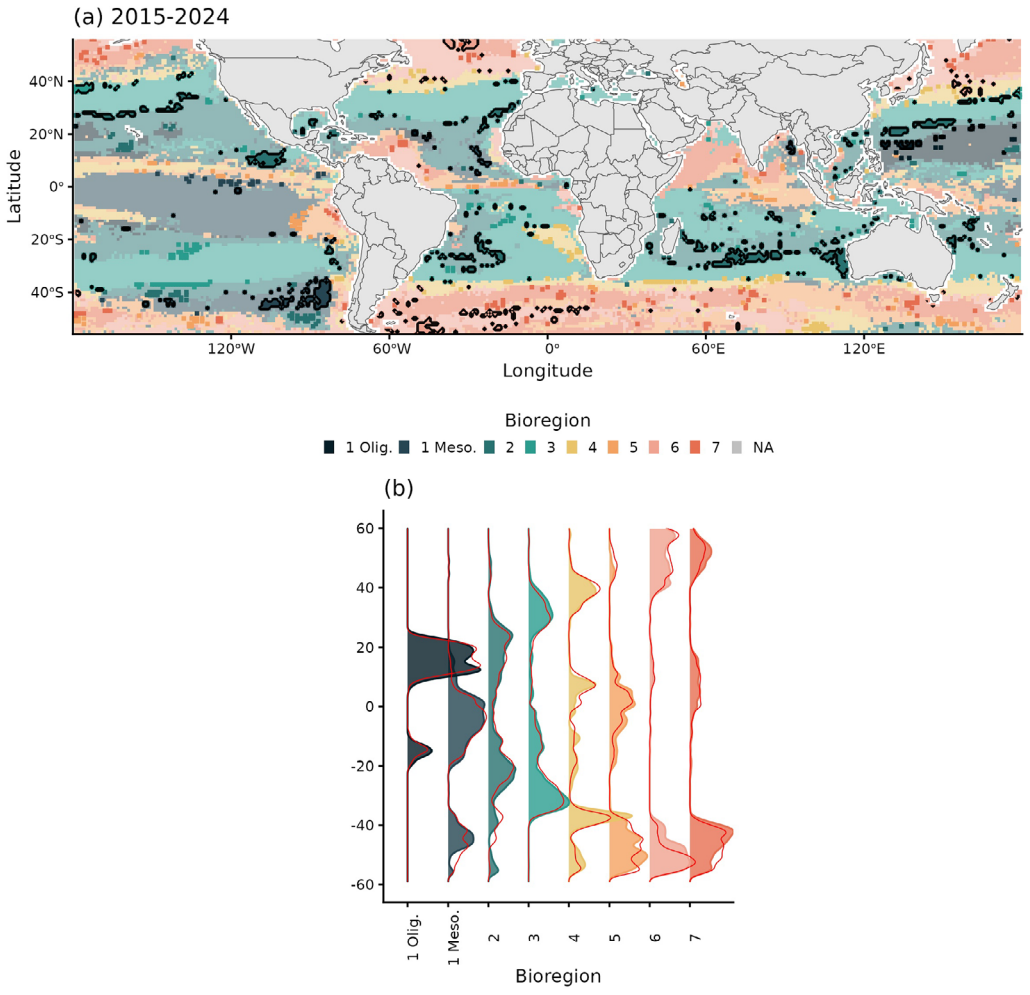


Figure 4. **(a)** Bioregions in the 2015–2024 decadal period with stable changes identified by black contours. **(b)** Latitudinal distribution of bioregions for the 2015–2024 decadal period (filled), compared with the 1998–2007 decadal period (red line).

micronekton habitats provinces monitored from sea surface temperature, stratification index and net primary production evolution in Albernhe et al. (2025).

The proposed ocean monitoring approach is nevertheless subject to several limitations. First, satellite ocean color observations are sparse at high latitudes inducing increasing method uncertainties poleward and the exclusion of the subpolar and polar domains (above 60°). In these domains significant and rapid phenological changes are already documented (Kahru et al., 2011; Thomalla et al., 2023; Manizza et al., 2023), with potential propagating effects on higher trophic levels (Fossheim et al., 2015). Second, because satellites only measure the ocean surface, our analysis cannot capture changes in subsurface productivity patterns, such as the deepening of the deep chlorophyll maximum (Mignot et al., 2014, Cornec et al., 2021). Finally, while the twenty seven year long time series is substantial, it remains challenging to definitively disentangle long-term climate-driven trends from the influence of natural decadal-scale climate modes (e.g., D'Ortenzio et al., 2012; Zhai et al., 2013; Li et al., 2024).

Despite these limitations, the ocean indicator approach presented here provides a powerful and pragmatic tool to effectively map the locations of potential long-term ecosystem shifts. This makes it a crucial complement to established indicators, such as the ocean indicator method for chlorophyll *a* concentration (EU Copernicus Marine Service Information, 2020). While such concentration-based indicators quantify how much biomass is present, our phenology-based approach reveals how the ecosystem's seasonal dynamics are unfolding. It can therefore detect critical shifts in ecosystem structure and function even when the total annual biomass remains unchanged. Furthermore, identifying long term trends in the distribution of chlorophyll *a* concentration was shown to be dependent on the type of ocean color product (Zhai et al., 2024, Pauthenet et al., 2024). Investigating the presence and variability of the bioregions based on ESA's Ocean Color Climate Change Initiative (Sathyen-

dranath et al., 2019) would further consolidate (invalidate) the highlighted trends. In this paper, we mainly propose an approach, a proof-of-concept, that could be further applied to other ocean colors time-series.

Future work could integrate Global ocean hindcast, to overcome the limitations of remotely sensed ocean color and extend monitoring to regions with poor satellite coverage (EU Copernicus Marine Service Information, 2024) and other four dimensional products (EU Copernicus Marine Service Information, 2025) to account for in-depth process. Earth system models can also help predict future states according to climatic projections (Yamaguchi et al., 2022; Fisher et al., 2025). The partitioning could also be refined by incorporating additional variables (e.g., the particulate backscattering coefficient) to better delineate bioregions. However, the current method's simplicity remains its main asset, ensuring a broad application range, ease of use, and making it an ideal candidate for immediate operational implementation.

Code and data availability. Ocean color data were collected from the OCEANCOLOUR_GLO_BGC_L4_MY_009_104 product, provided by the Copernicus Marine Environment Monitoring Service (CMEMS, http://marine.copernicus.eu/, last access: 22 May 2025). Cluster centroids resulting from Baudena et al. (2025) were obtained directly from the author. Code is available upon request from the corresponding author.

Supplement. The supplement related to this article is available online at https://doi.org/10.5194/sp-7-osr10-4-2026-supplement.

Author contributions. WR: Conceptualization, Data Curation, Formal Analysis, Investigation, Methodology, Visualization, Writing – Original Draft Preparation. NM: Conceptualization, Investigation, Methodology, Writing – Original Draft Preparation, Visualization, Writing – Review & Editing. AM: Conceptualization, Formal Analysis, Visualization, Writing – Review & Editing. VT: Conceptualization, Supervision, Writing – Review & Editing. FDO: Conceptualization, Funding Acquisition, Supervision, Writing – Review & Editing.

Competing interests. The contact author has declared that none of the authors has any competing interests.

Disclaimer. The Copernicus Marine Service offering is regularly updated to ensure it remains at the forefront of user requirements. In this process, some products may undergo replacement or renaming, leading to the removal of certain product IDs from the catalogue. If readers have any questions or require assistance regarding these modifications, please feel free to reach out to the Copernicus Marine Service user support team for further guidance. They will be able to provide the necessary information to address concerns and find suitable alternatives.

Publisher's note: Copernicus Publications remains neutral with regard to jurisdictional claims made in the text, published maps, institutional affiliations, or any other geographical representation in this paper. The authors bear the ultimate responsibility for providing appropriate place names. Views expressed in the text are those of the authors and do not necessarily reflect the views of the publisher.

Acknowledgements. The authors gratefully acknowledge Karina von Schuckmann for her insightful guidance and valuable contributions throughout all stages of the present study. They also sincerely thank the reviewers for their constructive comments and valuable feedback, which significantly enhanced the clarity and quality of this manuscript. During the preparation of this work the authors used ChatGPT-4 from OpenAI (https://chat.openai.com, last access: July 2025) in order to improve the readability and language of the manuscript. After using this tool/service, the authors reviewed and edited the content as needed and take full responsibility for the content of the publication.

Financial support. NM received in 2025 a postdoctoral research grant from the CNES (Centre National d'Etudes Spatiales). WR acknowledges the financial support from the CNES through the APR – 2022 (project SEASONS) and BRIDGES-AVATAR (grant no. ANR-22-EXBR-0004) integrated in France (2030) and managed by Agence Nationale de la Recherche.

Review statement. This paper was edited by Marilaure Grégoire and reviewed by Hongyan Xi and one anonymous referee.

References

Albernhe, S., Gorgues, T., Titaud, O., Lehodey, P., Menkes, C., and Conchon, A.: Micronekton indicators evolution based on biophysically defined provinces, in: 9th edition of the Copernicus Ocean State Report (OSR9), edited by: von Schuckmann, K., Moreira, L., de Pascual Collar, Á., Grégoire, M., Brasseur, P., Garric, G., Karstensen, J., Lionello, P., Marcos, M., Poulain, P.-M., and Staneva, J., Copernicus Publications, State Planet, 6-osr9, 4, https://doi.org/10.5194/sp-6-osr9-4-2025, 2025.

Ardyna, M., Claustre, H., Sallée, J., D'Ovidio, F., Gentili, B., Van Dijken, G., D'Ortenzio, F., and Arrigo, K. R.: Delineating environmental control of phytoplankton biomass and phenology in the Southern Ocean, Geophys. Res. Lett., 44, 5016–5024, https://doi.org/10.1002/2016GL072428, 2017.

Asch, R. G., Stock, C. A., and Sarmiento, J. L.: Climate change impacts on mismatches between phytoplankton blooms and fish spawning phenology, Glob. Change Biol., 25, 2544–2559, https://doi.org/10.1111/gcb.14650, 2019.

Baudena, A., Riom, W., Taillandier, V., Mayot, N., Mignot, A., and D'Ortenzio, F.: Comparing satellite and BGC-Argo chlorophyll estimation: A phenological study, Remote Sens. Environ., 326, 114743, https://doi.org/10.1016/j.rse.2025.114743, 2025.

Behrenfeld, M. J., Boss, E., Siegel, D. A., and Shea, D. M.: Carbon-based ocean productivity and phytoplankton physiology from space, Global Biogeochem. Cy., 19, 2004GB002299, https://doi.org/10.1029/2004GB002299, 2005.

Boyce, D. G., Petrie, B., Frank, K. T., Worm, B., and Leggett, W. C.: Environmental structuring of marine plankton phenology, Nat. Ecol. Evol., 1, 1484–1494, https://doi.org/10.1038/s41559-017-0287-3, 2017.

Capotondi, A., Alexander, M. A., Bond, N. A., Curchitser, E. N., and Scott, J. D.: Enhanced upper ocean stratification with climate change in the CMIP3 models, J. Geophys. Res., 117, https://doi.org/10.1029/2011jc007409, 2012.

Cleland, E., Chuine, I., Menzel, A., Mooney, H., and Schwartz, M.: Shifting plant phenology in response to global change, Trends Ecol. Evol., 22, 357–365, https://doi.org/10.1016/j.tree.2007.04.003, 2007.

Colella, S., Böhm, E., Cesarini, C., Jutard, Q., and Brando, V. E.: EU Copernicus Marine Service Product User Manual for Ocean Colour Products, OCEANCOLOUR_GLO_BGC_L4_MY_009_104, Issue 5.0, Mercator Ocean International, https://documentation.marine.copernicus.eu/PUM/CMEMS-OC-PUM.pdf (last access: 22 May 2025), 2024.

Cornec, M., Claustre, H., Mignot, A., Guidi, L., Lacour, L., Poteau, A., D'Ortenzio, F., Gentili, B., and Schmechtig, C.: Deep Chlorophyll Maxima in the Global Ocean: Occurrences, Drivers and Characteristics, Global Biogeochem. Cy., 35, https://doi.org/10.1029/2020gb006759, 2021.

D'Ortenzio, F. and Ribera d'Alcalà, M.: On the trophic regimes of the Mediterranean Sea: a satellite analysis, Biogeosciences, 6, 139–148, https://doi.org/10.5194/bg-6-139-2009, 2009.

D'Ortenzio, F., Antoine, D., Martinez, E., and Ribera d'Alcalà, M.: Phenological changes of oceanic phytoplankton in the 1980s and 2000s as revealed by remotely sensed ocean-color observations, Global Biogeochem. Cy., 26, 2011GB004269, https://doi.org/10.1029/2011GB004269, 2012.

EU Copernicus Marine Service Information: Global Ocean Chlorophyll-a trend map from Observations Reprocessing, omi_health_chl_global_oceancolour_trend, Mercator Ocean International [data set], https://doi.org/10.48670/moi-00230, 2020.

EU Copernicus Marine Service Information: Global Ocean Biogeochemistry Hindcast, cmems_mod_glo_bgc_my_0.25deg_P1D-m, Mercator Ocean International [data set], https://doi.org/10.48670/moi-00019, 2024.

EU Copernicus Marine Service Information: Global Ocean 3D Chlorophyll-a concentration, Particulate Backscattering coefficient, Particulate Organic Carbon, Downwelling Photosynthetic Available Radiation and downwelling irradiance at three different wavelengths (ED380, ED412 and ED490), cmems_obs-mob_glo_bgc-chl-poc_my_0.25deg_P7D-m, Mercator Ocean International [data set], https://doi.org/10.48670/moi-00046, 2025.

EU Copernicus Marine Service Product: Global Ocean Colour (Copernicus-GlobColour), Bio-Geo-Chemical, L4 (monthly and interpolated) from Satellite Observations (1997–ongoing), cmems_obs-oc_glo_bgc-plankton_my_l4-gapfree-multi-4km_P1D, Mercator Ocean International [data set], https://doi.org/10.48670/moi-00281, 2022.

Falkowski, P. G.: The role of phytoplankton photosynthesis in global biogeochemical cycles, Photosynth. Res., 39, 235–258, https://doi.org/10.1007/bf00014586, 1994.

Falkowski, P. G. and Oliver, M. J.: Mix and match: how climate selects phytoplankton, Nat. Rev. Microbiol., 5, 813–819, https://doi.org/10.1038/nrmicro1751, 2007.

Fenchel, T.: Marine Plankton Food Chains, Annu. Rev. Ecol. Syst., 19, 19–38, 1988.

Fernández-González, C., Tarran, G. A., Schuback, N., Woodward, E. M. S., Arístegui, J., and Marañón, E.: Phytoplankton responses to changing temperature and nutrient availability are consistent across the tropical and subtropical Atlantic, Commun. Biol., 5, 1035, https://doi.org/10.1038/s42003-022-03971-z, 2022.

Fisher, B. J., Poulton, A. J., Meredith, M. P., Baldry, K., Schofield, O., and Henley, S. F.: Climate-driven shifts in Southern Ocean primary producers and biogeochemistry in CMIP6 models, Biogeosciences, 22, 975–994, https://doi.org/10.5194/bg-22-975-2025, 2025.

Fossheim, M., Primicerio, R., Johannesen, E., Ingvaldsen, R. B., Aschan, M. M., and Dolgov, A. V.: Recent warming leads to a rapid borealization of fish communities in the Arctic, Nat. Clim. Change, 5, 673–677, https://doi.org/10.1038/nclimate2647, 2015.

Garnesson, P., Mangin, A., and Jutard, Q.: EU Copernicus Marine Service Quality Information Document for the Global Ocean Colour (Copernicus-GlobColour), Bio-Geo-Chemical, L4 from Satellite Observations, OCEANCOLOUR_GLO_BGC_L4_MY_009_104, Issue 5.1, Mercator Ocean International, https://documentation.marine.copernicus.eu/QUID/CMEMS-OC-QUID-009-101to104-111-113-116-118.pdf (last access: 22 May 2025), 2025.

Henson, S. A., Cole, H. S., Hopkins, J., Martin, A. P., and Yool, A.: Detection of climate change-driven trends in phytoplankton phenology, Glob. Change Biol., 24, https://doi.org/10.1111/gcb.13886, 2018.

Higgins, S. I., Buitenwerf, R., and Moncrieff, G. R.: Defining functional biomes and monitoring their change globally, Glob. Change Biol., 22, 3583–3593, https://doi.org/10.1111/gcb.13367, 2016.

Huot, Y., Babin, M., Bruyant, F., Grob, C., Twardowski, M. S., and Claustre, H.: Relationship between photosynthetic parameters and different proxies of phytoplankton biomass in the subtropical ocean, Biogeosciences, 4, 853–868, https://doi.org/10.5194/bg-4-853-2007, 2007.

Inouye, D. W.: Climate change and phenology, WIREs Climate Change, 13, e764, https://doi.org/10.1002/wcc.764, 2022.

IOCCG, Dowell, M., and Platt, T.: Partition of the Ocean into Ecological Provinces: Role of Ocean-Colour Radiometry., International Ocean Colour Coordinating Group (IOCCG), https://doi.org/10.25607/OBP-99, 2009.

Kahru, M., Brotas, V., Manzano-Sarabia, M., and Mitchell, B. G.: Are phytoplankton blooms occurring earlier in the Arctic?: Phytoplankton Blooms In The Arctic, Glob. Change Biol., 17, 1733–1739, https://doi.org/10.1111/j.1365-2486.2010.02312.x, 2011.

Kiørboe, T.: Turbulence, Phytoplankton Cell Size, and the Structure of Pelagic Food Webs, in: Advances in Marine Biology, Elsevier, 1–72, https://doi.org/10.1016/s0065-2881(08)60129-7, 1993.

Kheireddine, M., Mayot, N., Ouhssain, M., and Jones, B. H.: Regionalization of the Red Sea Based on Phytoplankton Phenology: A Satellite Analysis, J. Geophys. Res.-Oceans, 126, https://doi.org/10.1029/2021jc017486, 2021.

Lacour, L., Claustre, H., Prieur, L., and D'Ortenzio, F.: Phytoplankton biomass cycles in the North Atlantic subpolar gyre: A similar mechanism for two different blooms in the Labrador Sea, Geophys. Res. Lett., 42, 5403–5410, https://doi.org/10.1002/2015gl064540, 2015.

Li, Z., Sun, D., Wang, S., Huan, Y., Zhang, H., Yuan, Y., and He, Y.: Ocean-scale patterns of environment and climate changes driving global marine phytoplankton biomass dynamics, Sci. Adv., 10, https://doi.org/10.1126/sciadv.adm7556, 2024.

Longhurst, A.: Seasonal cycles of pelagic production and consumption, Prog. Oceanogr., 36, 77–167, https://doi.org/10.1016/0079-6611(95)00015-1, 1995.

Longhurst, A. R.: Ecological Geography of the Sea, 2nd edn., Elsevier, https://doi.org/10.1016/b978-0-12-455521-1.x5000-1, 2007.

Manizza, M., Carroll, D., Menemenlis, D., Zhang, H., and Miller, C. E.: Modeling the Recent Changes of Phytoplankton Blooms Dynamics in the Arctic Ocean, J. Geophys. Res.-Oceans, 128, e2022JC019152, https://doi.org/10.1029/2022JC019152, 2023.

Martinez, E., Antoine, D., D'Ortenzio, F., and De Boyer Montégut, C.: Phytoplankton spring and fall blooms in the North Atlantic in the 1980s and 2000s, J. Geophys. Res., 116, 2010JC006836, https://doi.org/10.1029/2010JC006836, 2011.

Mayot, N., D'Ortenzio, F., Ribera d'Alcalà, M., Lavigne, H., and Claustre, H.: Interannual variability of the Mediterranean trophic regimes from ocean color satellites, Biogeosciences, 13, 1901–1917, https://doi.org/10.5194/bg-13-1901-2016, 2016.

Mignot, A., Claustre, H., Uitz, J., Poteau, A., D'Ortenzio, F., and Xing, X.: Understanding the seasonal dynamics of phytoplankton biomass and the deep chlorophyll maximum in oligotrophic environments: A Bio-Argo float investigation, Global Biogeochem. Cy., 28, 856–876, https://doi.org/10.1002/2013gb004781, 2014.

O'Connor, M. I., Piehler, M. F., Leech, D. M., Anton, A., and Bruno, J. F.: Warming and Resource Availability Shift Food Web Structure and Metabolism, PLoS Biol., 7, e1000178, https://doi.org/10.1371/journal.pbio.1000178, 2009.

Pauthenet, E., Martinez, E., Gorgues, T., Roussillon, J., Drumetz, L., Fablet, R., and Roux, M.: Contrasted Trends in Chlorophyll-*a* Satellite Products, Geophys. Res. Lett., 51, e2024GL108916, https://doi.org/10.1029/2024GL108916, 2024.

Polovina, J. J., Howell, E. A., and Abecassis, M.: Ocean's least productive waters are expanding, Geophys. Res. Lett., 35, 2007GL031745, https://doi.org/10.1029/2007GL031745, 2008.

Racault, M.-F., Le Quéré, C., Buitenhuis, E., Sathyendranath, S., and Platt, T.: Phytoplankton phenology in the global ocean, Ecol. Indic., 14, 152–163, https://doi.org/10.1016/j.ecolind.2011.07.010, 2012.

Salgado-Hernanz, P. M., Racault, M.-F., Font-Muñoz, J. S., and Basterretxea, G.: Trends in phytoplankton phenology in the Mediterranean Sea based on ocean-colour remote sensing, Remote Sens. Environ., 221, 50–64, https://doi.org/10.1016/j.rse.2018.10.036, 2019.

Sapiano, M. R. P., Brown, C. W., Schollaert Uz, S., and Vargas, M.: Establishing a global climatology of marine phytoplankton phenological characteristics, J. Geophys. Res., 117, 2012JC007958, https://doi.org/10.1029/2012JC007958, 2012.

Sarmiento, J. L., Slater, R., Barber, R., Bopp, L., Doney, S. C., Hirst, A. C., Kleypas, J., Matear, R., Mikolajewicz, U., Monfray, P., Soldatov, V., Spall, S. A., and Stouffer, R.: Response of ocean ecosystems to climate warming, Global Biogeochem. Cy., 18, 2003GB002134, https://doi.org/10.1029/2003GB002134, 2004.

Sathyendranath, S., Brewin, R., Brockmann, C., Brotas, V., Calton, B., Chuprin, A., Cipollini, P., Couto, A., Dingle, J., Doerffer, R., Donlon, C., Dowell, M., Farman, A., Grant, M., Groom, S., Horseman, A., Jackson, T., Krasemann, H., Lavender, S., Martinez-Vicente, V., Mazeran, C., Mélin, F., Moore, T., Müller, D., Regner, P., Roy, S., Steele, C., Steinmetz, F., Swinton, J., Taberner, M., Thompson, A., Valente, A., Zühlke, M., Brando, V., Feng, H., Feldman, G., Franz, B., Frouin, R., Gould, R., Hooker, S., Kahru, M., Kratzer, S., Mitchell, B., Muller-Karger, F., Sosik, H., Voss, K., Werdell, J., and Platt, T.: An Ocean-Colour Time Series for Use in Climate Studies: The Experience of the Ocean-Colour Climate Change Initiative (OC-CCI), Sensors, 19, 4285, https://doi.org/10.3390/s19194285, 2019.

Sommer, U. and Lengfellner, K.: Climate change and the timing, magnitude, and composition of the phytoplankton spring bloom, Glob. Change Biol., 14, 1199–1208, https://doi.org/10.1111/j.1365-2486.2008.01571.x, 2008.

Stock, A., Subramaniam, A., Van Dijken, G. L., Wedding, L. M., Arrigo, K. R., Mills, M. M., Cameron, M. A., and Micheli, F.: Comparison of Cloud-Filling Algorithms for Marine Satellite Data, Remote Sens., 12, 3313, https://doi.org/10.3390/rs12203313, 2020.

Thomalla, S. J., Nicholson, S.-A., Ryan-Keogh, T. J., and Smith, M. E.: Widespread changes in Southern Ocean phytoplankton blooms linked to climate drivers, Nat. Clim. Chang., 13, 975–984, https://doi.org/10.1038/s41558-023-01768-4, 2023.

Vereshchaka, A. L. and Shatravin, A. V.: Chlorophyll dynamics in low latitudes unveils a new partition of the ocean, Sci. Total Environ., 966, 178697, https://doi.org/10.1016/j.scitotenv.2025.178697, 2025.

Visser, M. E. and Both, C.: Shifts in phenology due to global climate change: the need for a yardstick, Proc. R. Soc. B., 272, 2561–2569, https://doi.org/10.1098/rspb.2005.3356, 2005.

Winder, M. and Sommer, U.: Phytoplankton response to a changing climate, Hydrobiologia, 698, 5–16, https://doi.org/10.1007/s10750-012-1149-2, 2012.

Yamaguchi, R. and Suga, T.: Trend and Variability in Global Upper-Ocean Stratification Since the 1960s, J. Geophys. Res.-Oceans, 124, 8933–8948, https://doi.org/10.1029/2019jc015439, 2019.

Yamaguchi, R., Rodgers, K. B., Timmermann, A., Stein, K., Schlunegger, S., Bianchi, D., Dunne, J. P., and Slater, R. D.: Trophic level decoupling drives future changes in phytoplankton bloom phenology, Nat. Clim. Chang., 12, 469–476, https://doi.org/10.1038/s41558-022-01353-1, 2022.

Zhai, D., Beaulieu, C., and Kudela, R. M.: Long-Term Trends in the Distribution of Ocean Chlorophyll, Geophys. Res. Lett., 51, e2023GL106577, https://doi.org/10.1029/2023GL106577, 2024.

Zhai, L., Platt, T., Tang, C., Sathyendranath, S., and Walne, A.: The response of phytoplankton to climate variability associated with the North Atlantic Oscillation, Deep-Sea Res. Pt. II, 93, 159–168, https://doi.org/10.1016/j.dsr2.2013.04.009, 2013.

State Planet, 7-osr10, 5, 2026
https://doi.org/10.5194/sp-7-osr10-5-2026
© Author(s) 2026. This work is distributed under
the Creative Commons Attribution 4.0 License.

Establishing a monitoring approach for marine heatwaves in the Black and Mediterranean Seas

Leonardo Lima[1], Rafael Gomes de Menezes[1], Ehsan Sadighrad[1], Ronan McAdam[1], Filipe Costa[1], Pietro Miraglio[1], Mehmet Ilicak[2,1], Eric Jansen[1], Ali Aydogdu[1], Francesco Maicu[1], and Emanuela Clementi[1]

[1]CMCC Foundation – Euro-Mediterranean Center on Climate Change, Lecce 73100, LE, Italy
[2]Eurasia Institute of Earth Sciences, Istanbul Technical University, Istanbul, Turkey

Correspondence: Leonardo Lima (leonardo.lima@cmcc.it)

Received: 31 July 2025 – Discussion started: 30 September 2025
Revised: 2 February 2026 – Accepted: 8 March 2026 – Published: 30 September 2026

Abstract. Increased frequency and intensity of marine heatwaves (MHWs) are contributing to cumulative thermal stress on marine systems, as extreme temperature events interact with long-term ocean warming. These impacts are particularly relevant in semi-enclosed basins such as the Mediterranean and Black Seas, where surface warming and rising ocean heat content (OHC) have been especially pronounced over the past decade. While MHW-related effects have been documented in the Mediterranean Sea, assessments remain limited for the Black Sea. Most studies to date have focused on sea surface manifestations of MHWs, although it is well established that such extremes can also extend into near-surface layers below the mixed layer. However, the vertical structure and persistence of MHWs beneath the surface remain less understood, particularly in the Black Sea. In this context, this study aims to identify and characterize MHWs in both surface and subsurface waters in the Mediterranean and Black Seas, and to provide a framework for monitoring MHWs within the upper water column. To this end, MHWs were detected using both sea surface temperature (SST) and OHC anomalies down to 40 m depth, allowing for the assessment of their spatial structure and vertical consistency. SST- and OHC-derived metrics generally show good agreement, particularly in the event's duration and frequency. Seasonal analysis further reveals that summer MHWs are typically more intense and show weaker surface–subsurface correlations, whereas winter events are more vertically coherent. Discrepancies between surface and subsurface MHW metrics are particularly evident in the Black Sea, where circulation patterns associated with the Rim Current appear to influence the vertical structure of heat extremes, leading to subsurface events that are not captured by surface-based metrics. In the Adriatic Sea, enhanced MHW occurrence promotes persistent stratification and reduced winter mixing, affecting both surface and subsurface layers. In 2024, both the Black Sea and Mediterranean Sea experienced record-high MHW intensities and durations, with events lasting over 30 d and temperature anomalies exceeding 4.6 °C in key regions such as the Anatolian coast, where summer upwelling commonly influences local ocean conditions. To improve MHW monitoring, we recommend integrating both SST- and OHC-based methods to capture surface and subsurface events in these regions. Nevertheless, due to regional variability, multiple MHW definitions such as threshold-based approaches, including the Hobday framework which also defines MHW categories, are necessary to accommodate diverse monitoring objectives and management strategies.

Published by Copernicus Publications.

1 Introduction

The rapid rise in ocean temperature due to global warming has led to a significant increase in the frequency and intensity of marine heatwaves (MHWs) in recent decades (Oliver et al., 2018; Fox-Kemper et al., 2021; Cooley et al., 2022). These extreme thermal events are typically characterized as periods lasting at least 5 d, during which sea surface temperatures (SSTs) exceed the 90th percentile relative to a historical baseline (Hobday et al., 2016; HD2016 hereafter). In recent years, favorable atmospheric conditions, such as weakened winds, increased shortwave radiation and reduced heat losses from the ocean, have contributed to the increased frequency and spatial extent of MHWs, resulting in severe disruptions to marine ecosystems and global biodiversity (Tan et al., 2022; Smith et al., 2023; Darmaraki et al., 2024). Large-scale climate modes, most notably the El Niño–Southern Oscillation (ENSO), also play a central role in driving prolonged MHW conditions, particularly when remote anomalies are reinforced by local atmospheric and oceanographic processes (Holbrook et al., 2019; Dutheil et al., 2024; Gregory et al., 2024). At the local scale, oceanographic mechanisms are also significant, as reduced upwelling limits the supply of cooler waters and enhanced eddy activity traps heat and prolongs events (Izquierdo et al., 2022; Su et al., 2025). The combined influence of large-scale climate modes and local ocean-atmosphere interactions has been recognized as a key driver of extreme events, as detailed by Sen Gupta et al. (2020) in their review of the most impactful MHWs globally.

In the Mediterranean Sea, Marullo et al. (2023) investigated the role of atmospheric forcing and linked the development of SST anomalies to the prevalence of anticyclonic atmospheric conditions during the well-known MHW event of 2022–2023. Pastor et al. (2024) revealed the co-occurrence of marine and atmospheric heatwaves, with their relationship exhibiting spatial variability throughout the region. Moreover, correlations of MHWs with large-scale climate modes, such as the East Atlantic and East Atlantic–West Russian patterns, combined with their concurrence with atmospheric heatwaves, may amplify intensity and spatial extent of MHWs in this region (Hamdeno and Alvera-Azcaráte, 2023). Darmaraki et al. (2024) provide a comprehensive overview of the local and large-scale mechanisms driving Mediterranean MHWs, which result in ecological consequences. These events are associated with the onset of mass mortality events in the regional ecosystem (Garrabou et al., 2022). In line with these ecological effects, a recent study demonstrated that they may also disrupt essential ecosystem processes, such as inhibiting the spring phytoplankton bloom in the northwestern Mediterranean (Li et al., 2024). During summer 2022, MHWs severely impacted benthic communities in the northwestern Mediterranean, causing extensive mortality of gorgonians and red corals in the Calanques National Park (Estaque et al., 2023) and pronounced subsurface warming down to 30–40 m in the northeastern Gulf of Lion, affecting gorgonian populations (Estournel et al., 2025). The potential to cause significant changes in ecosystems and biota, with vast socio-economic impacts, makes the research on MHWs indispensable.

From HD2016's MHW definition, several variants have been developed to define extreme sea temperature events. These typically vary in the way temperature anomalies are identified. For instance, some definitions use fixed SST thresholds, while others rely on climatology-based percentiles, which may be calculated using either a fixed baseline or a moving average (Rosselló et al., 2023). Higher thresholds (e.g. 99th percentile) detect fewer but more extreme MHW events (Cheng et al., 2023). To separate long-term ocean warming from short-term extremes, detrending methods are often used (Martínez et al., 2023; Capotondi et al., 2024). In a similar way, moving-average climatologies – which consider years close to the target year – can reduce the imprint of the warming trend. There are also approaches that include spatial characteristics to better reflect the extent and ecological importance of these temperature events (Bonino et al., 2023). However, when considering ecological impacts specifically, it remains challenging to adopt a single MHW definition that applies across all regions, ecosystems, and species, as temperature thresholds and biological responses can vary widely (Amaya et al., 2023).

Recent studies have characterized MHWs in the Mediterranean Sea, highlighting their spatial features, temporal evolution, and representation in observational and reanalysis datasets (e.g. Dayan et al., 2022, 2023; Marullo et al., 2023; Rossellò et al., 2023; Darmaraki et al., 2024; Pastor et al., 2024). For example, Dayan et al. (2022) have demonstrated the relevance of regional high-resolution reanalysis data for representing MHW statistics, showing high-skills of the regional reanalysis as compared to the remote sensing data.

In a subsequent study, Dayan et al. (2023) examined subsurface MHWs by employing an ocean heat content (OHC) indicator that integrates temperature across different depths and found that subsurface MHWs occur less frequently but with longer duration than surface events. Monitoring MHWs below the surface is essential because subsurface anomalies can persist longer than surface events and affect ecological and socio-economic systems, including fisheries, aquaculture, and biogeochemical cycles. Developing indicators which cover depth ranges therefore provides critical information beyond what is captured by SST alone, and the prolonged subsurface persistence may be linked to wind-driven processes that facilitate the downward propagation of thermal anomalies (Darmaraki et al., 2024). Similarly, McAdam et al. (2023) defined subsurface MHWs using OHC integrated over the upper 0–40 m and demonstrated that seasonal indicators of subsurface MHWs are predicted with greater accuracy than the more commonly-used surface-focused indicators, highlighting the added value of considering subsurface events.

Table 1. Product table.

Product ref. no.	Product ID & type	Data access	Documentation
1	SST_BS_SST_L4_REP_OBSERVATIONS_010_022; satellite observations	EU Copernicus Marine Service Product (2024a)	Quality Information Document (QUID): Pisano et al. (2024a) Product User Manual (PUM): Pisano et al. (2024b)
2	SST_MED_SST_L4_REP_OBSERVATIONS_010_021; satellite observations	EU Copernicus Marine Service Product (2024b)	QUID: Pisano et al. (2024c) PUM: Pisano et al. (2024d)
3	BLKSEA_MULTIYEAR_PHY_007_004 (BLKREA); numerical models	EU Copernicus Marine Service Product (2024c)	QUID: Lima et al. (2024) PUM: Lecci et al. (2024a)
4	MEDSEA_MULTIYEAR_PHY_006_004 (MEDREA); numerical models	EU Copernicus Marine Service Product (2024d)	QUID: Escudier et al. (2024) PUM: Lecci et al. (2024b)
5	GLOBAL_MULTIYEAR_PHY_001_030 (GLOREA); numerical models	EU Copernicus Marine Service Product (2024e)	QUID: Drévillon et al. (2024a) PUM: Drévillon et al. (2024b)

While studies on MHWs are extensive in the Mediterranean Sea, comparable research in the Black Sea remains limited. To our knowledge, Mohamed et al. (2022) is the only study to date that specifically investigates MHWs in this region using satellite data. Their analysis examined trends in MHW frequency in relation to the rate of SST warming. The new Copernicus Black Sea reanalysis (product ref. no. 3 in Table 1; Lima et al., 2026), configured at a horizontal resolution of $1/40°$ with 121 vertical levels, has served as the foundation for developing Ocean Monitoring Indicators (OMIs) for the region. In particular, the OHC OMI indicates a warming trend of approximately $0.77 \pm 0.07\,\mathrm{W\,m^{-2}}$ (2005–2022) in the Black Sea (EU Copernicus Marine Service Information, 2024a). This ocean warming signal, which has also impacted the formation of its cold intermediate layer (CIL) in recent years (Stanev et al., 2019; Lima et al. 2021, 2026), emphasizes the importance of studying MHWs in Black Sea.

We focus on OHC integrated over the upper 0–40 m layer, which encompasses the biologically productive epipelagic zone and the upper mixed layer in both the Mediterranean and Black Seas. This depth range is particularly relevant for ecology and coastal management, as it includes the main habitat of commercially important species and most aquaculture operations, where organisms are directly exposed to heat anomalies (Granata et al., 2011; Cheminée et al., 2021; Macias et al., 2019; Nenciu et al., 2023). Building on earlier efforts, this study revisits work on the Mediterranean Sea (e.g., Dayan et al., 2022, 2023) using an updated reference climatology and extends them by applying a consistent monitoring framework to both the Mediterranean and Black Seas. It includes an uncertainty assessment of key MHW metrics based on multiple datasets and provides insights into historical MHW characteristics in the less-studied Black Sea. Additionally, SST and upper-OHC indicators are integrated within a unified monitoring perspective, allowing the surface and subsurface expressions of MHWs to be jointly assessed. While the use of multiple observational and reanalysis products has been previously explored for the Mediterranean Sea, this multi-dataset approach is here applied consistently to both basins, providing new insights into historical MHW characteristics. The primary objective is to develop a comprehensive monitoring approach for MHWs in both regional seas.

The manuscript is structured as follows: Sect. 2 describes the datasets and methodologies used to detect MHWs across both basins. Section 3 presents and discusses key MHW metrics derived from the standard definition, applied to SST as well as OHC for subsurface detection. MHW metrics are subsequently examined with respect to the water mass structures in the Mediterranean and Black Seas. Section 4 concludes the study and proposes an OMI for tracking MHWs in these regions. The comparison between standard MHW metrics and those obtained using a detrending approach is presented exclusively in the Appendix as supplementary material.

2 Data and methods

We follow the definition of MHWs from HD2016, originally formulated for SST, and extend it here to upper-OHC. The HD2016 detection framework is applied independently to each selected thermal field. A MHW is defined as a period in which the selected thermal field exceeds a set threshold for at least five consecutive days. This threshold corresponds to the 90th percentile of the local daily mean value computed over the long-term reference period (1993–2022), which was selected to ensure consistency across all datasets, as the Black Sea regional reanalysis starts in 1993, thereby accounting for the long-term warming signal present in each field. If two MHW events are separated by a gap of 2 d or fewer during which the selected field remains below the threshold, they

are merged and treated as a single continuous event. In addition to the standard approach, we perform a separate analysis to examine how removing long-term trends affects MHW detection, applying a detrending method to Mediterranean subregions and to the Black Sea as a whole (Appendix A). Specifically, we remove the linear trend of SST or OHC individually at each grid point before applying the detection algorithm. Table 2 presents the MHW metrics analyzed and discussed in this study.

We detect MHWs using both SST and upper-OHC integrated over the 0–40 m layer, based on regional and global reanalysis datasets, and additionally using observational SST products for SST-based analyses. The choice of the 0–40 m layer is primarily motivated by its biological relevance, as it represents the upper portion of the epipelagic zone, which concentrates most biological productivity and socioeconomic activities in the Mediterranean and Black Sea (Kubryakov et al., 2020; Konsta et al., 2025), and therefore constitutes a relevant layer for assessing the biogeochemical impacts of MHWs. From a physical perspective, MLD is typically much shallower than 40 m in the Mediterranean Sea, particularly between spring and autumn (Houpert et al., 2015), and during surface MHWs (Darmaraki et al., 2024). Therefore, the 0–40 m range can also be used to identify upper ocean events which are not reflected by surface-only monitoring (Juza et al., 2022; Dayan et al., 2023). In this work, we further explore this assumption, for example during winter when MLD extends to depths beyond 40 m. Identifying extremes in heat content over a depth range is favoured over focusing on specific depth levels, given that many marine species migrate vertically throughout the day and to avoid surface-only extremes (Ma and Chen, 2025).

The Mediterranean Sea regional reanalysis (product ref. no. 4 in Table 1) is configured with a horizontal grid resolution of $1/24°$ (approximately 4–5 km) and 141 unevenly spaced vertical levels (Escudier et al., 2021). In contrast, the Black Sea regional reanalysis (product ref. no. 3 in Table 1) employs a finer horizontal resolution of $1/40°$ and 121 unevenly spaced vertical levels (Lima et al., 2026). Both regional reanalyses are forced with atmospheric data from the ERA5 reanalysis (Hersbach et al., 2020), assimilate in situ temperature and salinity profiles, along-track sea level anomaly observations, and apply SST relaxation to correct surface heat fluxes. They serve as the basis for MHW detection in this study. For broader comparison, MHWs are also identified using a global reanalysis product (product ref. no. 5 in Table 1), which has a coarser horizontal resolution of $1/12°$ and includes 50 vertical levels (Lellouche et al., 2021). This global product is forced with ERA-Interim atmospheric reanalysis (Dee et al., 2011) until end of 2018 and ERA5 reanalysis thereafter and assimilates in situ observations, along-track SLA, and SST data. Additionally, for validation and complementarity, we compare reanalysis-derived MHW metrics based on SST with those obtained from an observational-based Level 4 SST product (product refs. no. 1 and 2 in Table 1; Pisano et al., 2016; Embury et al., 2024). All datasets can be accessed through the Copernicus Marine Service catalogue, which provides comprehensive documentation on their specifications and quality assessments.

For evaluating the OHC anomaly, we apply a formula similar to that used by Lima et al. (2020, 2021), which has also been adopted for calculating the OHC OMI for the Black and Mediterranean Seas within the Copernicus Marine Service framework (EU Copernicus Marine Service Information, 2024a, b). The OHC anomaly is defined here as the deviation from the long-term reference period and is closely proportional to the average temperature change from $z_1 = 0$ m to $z_2 = 40$ m depth:

$$\mathrm{OHC} = \int_{z_1}^{z_2} \rho_0 c_p \left(T_\mathrm{m} - T_\mathrm{clim}\right) \mathrm{d}z \tag{1}$$

with a reference density $\rho_0 = 1020\,\mathrm{kg\,m^{-3}}$ and a specific heat capacity $c_p = 3980\,\mathrm{J\,kg^{-1}\,°C^{-1}}$; T_m corresponds to the daily average temperature and T_clim denotes the climatological temperature for the corresponding day, calculated over a 30-year period (1993–2022), consistent with the baseline period used to define MHWs.

3 Results and discussion

3.1 SST-Derived Surface Marine Heatwave Characterization

The surface MHW metrics in the regional reanalyses (product refs. no. 3 and 4 in Table 1) over the period 1993–2024 (Fig. 1) confirm and update the basin-scale patterns of the Mediterranean Sea previously reported (e.g. Dayan et al., 2022, 2023). The average number of MHW events is slightly lower along certain coastal regions of North Africa, particularly between 10 and 35° E (Fig. 1a). Despite this lower frequency, the average duration of events in these areas is relatively high, exceeding 30 d (Fig. 1b), suggesting fewer but more persistent heatwaves. Mignot et al. (2022) define persistent MHWs as events lasting over 38 d with SST anomalies above 2.3 °C at the global ocean scale. In contrast, most of the Adriatic Sea, as well as the Ionian Sea, Gulf of Lion, and the area extending from the Algerian current to Crete exhibit higher average numbers of events (e.g. > 2.4 per year), but shorter durations (< 18 d), indicating frequent but brief MHW occurrences (Fi. 1a–b).

A similar spatial pattern is observed in the northern Black Sea, particularly in the area near the Kerch Strait, where MHWs occur more frequently but are shorter in duration, with approximately 2.6 events per year lasting between 10 to 14 d (Fig. 1a–b). In contrast, the central and southern regions of the basin, highlighted by green shading in both the spatial maps of mean frequency and duration, exhibit a lower frequency of events, ranging from around 1.8 to 2.2 events

CHAPTER 2.2

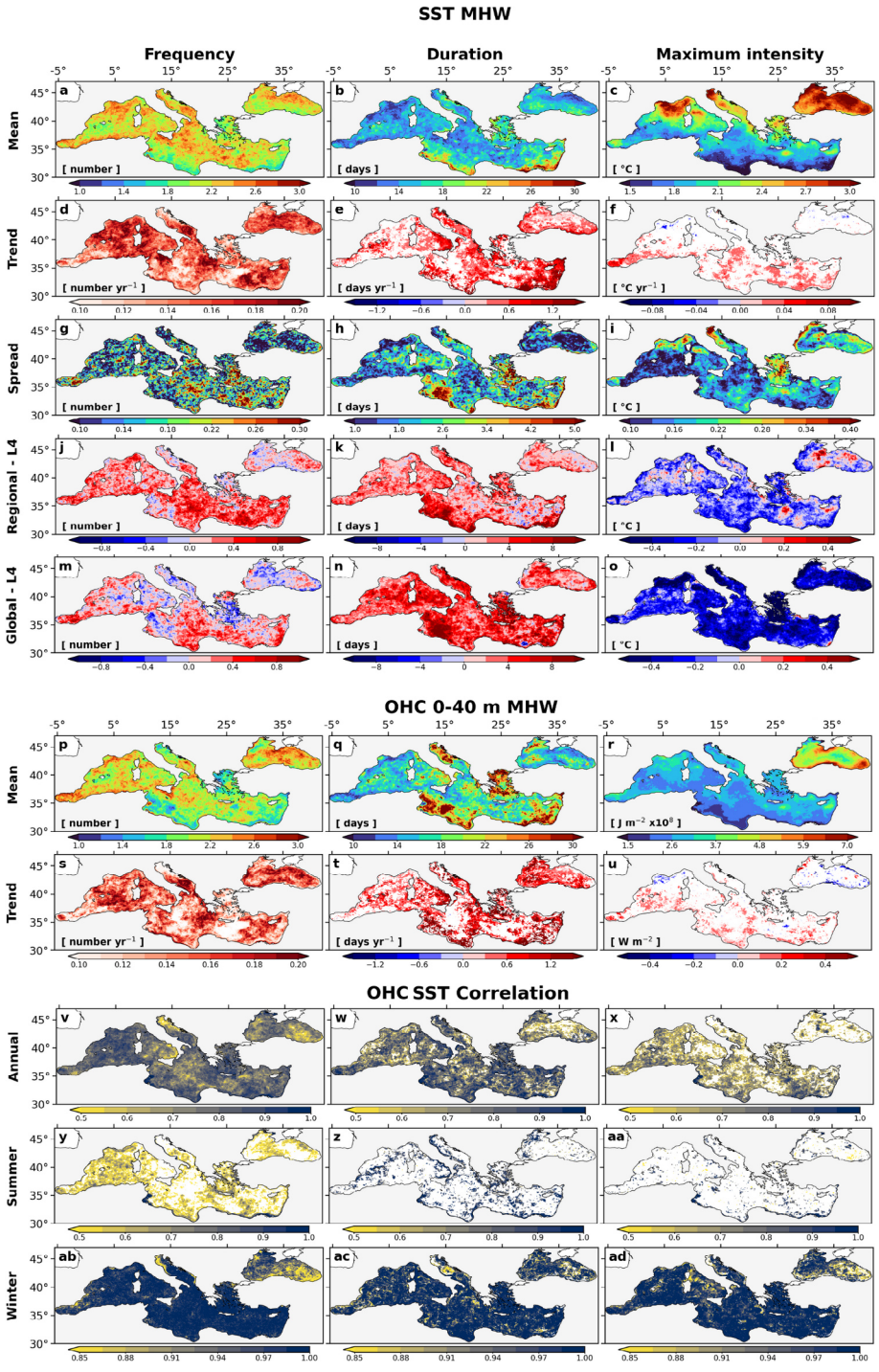


Figure 1. Spatial distribution of MHW metrics derived from SST and upper OHC (0–40 m) in the regional reanalyses (product refs. no. 3 and 4 in Table 1) for the period 1993–2024. Panels **(a)**–**(c)** show the spatial patterns of mean values of annual MHW metrics based on the SST definition, while panels **(d)**–**(f)** display the corresponding statistically significant trends of annual MHW metrics ($p < 0.05$). Panels **(g)**–**(i)** present the spread of annual MHW metrics based on the SST definition across the regional reanalysis, global reanalysis (product ref. no. 5 in Table 1), and SST-L4 observational products (product refs. no. 1 and 2 in Table 1). Panels **(j)**–**(l)** and **(m)**–**(o)** show the differences in annual SST-derived MHW metrics between the regional and global reanalyses relative to the SST-L4 observational product. Panels **(p)**–**(r)** display the spatial patterns of mean values of annual MHW metrics derived from OHC in the regional reanalysis, while panels **(s)**–**(u)** show the corresponding statistically significant trends of annual MHW metrics ($p < 0.05$). Panels **(v)**–**(x)** shows the significant Pearson correlation ($p < 0.05$) between MHW metrics estimated from SST and OHC. Panels **(y)**–**(aa)** show the Pearson correlation between SST- and OHC-derived MHW metrics computed for summer, while panels **(ab)**–**(ad)** show the corresponding Pearson correlation based on winter MHW metrics ($p < 0.05$).

Table 2. MHW metrics following Hobday et al. (2016) and Dayan et al. (2022), including additional diagnostic metrics used in this study.

Frequency	Number of discrete events
Duration	Consecutive period of time during which the temperature exceeds the 90th percentile
Maximum intensity	Highest temperature anomaly value relative to the climatology
Trends	Least-squares regression of all metrics with 95 % of confidence interval
Ensemble spread	The variability of each MHW metric among ensemble members, calculated as the standard deviation of that metric
Percentage discrepancy	Relative difference between reanalysis-derived MHW metrics and observation-based reference values, computed from basin-averaged differences and expressed as a percentage of the reference

per year, but with longer average durations of approximately 18 to 22 d (Fig. 1a–b). This spatial differentiation is generally consistent with the findings of Mohamed et al. (2022), especially regarding the northern sector.

The mean intensity of MHWs is notably high in the Black Sea, exceeding 2.85 °C relative to the daily climatology for 1993–2022 in specific areas such as the northwestern shelf, the Anatolian and Caucasian coasts (Fig. 1c). In the Mediterranean Sea, similarly elevated intensities are observed in the northern Adriatic Sea and the Gulf of Lion, extending offshore towards the regions surrounding Corsica. In these areas, the results suggest that MHWs tend to be short and frequent but exhibit relatively high intensity.

The number of MHW events has increased over time, showing positive trends of similar magnitude in both the Mediterranean and Black Seas (considering only statistically significant trends, $p < 0.05$) (Fig. 1d). Notably, in the Mediterranean Sea the highest increases – exceeding 2 events per decade – are observed south of Sicily, in the southern Adriatic Sea, Cretan Passage (south of Greece and east of Ionian Sea), parts of the Balearic Sea, and east of Corsica and Sardinia. Regarding event duration, the most pronounced positive trends are observed in the eastern Mediterranean Sea, exceeding 12 d per decade ($p < 0.05$) (Fig. 1e). Meanwhile, intensity trends are strongest near the Alboran Sea, increasing around 0.5 °C per decade, and extending across the central and eastern Mediterranean with generally positive values ($p < 0.05$) (Fig. 1f). However, this spatial extension is irregular and lacks a coherent pattern that would suggest a continuous or regionally connected increase. In the Black Sea, significant trends exceeding 1.5 events per decade ($p < 0.05$) cover much of the basin, with the highest values observed south of the Crimean Peninsula (Fig. 1d). Duration trends reach maximum values between 6 and 12 d per decade, particularly in peripheral zones of the basin and over the northwestern shelf (Fig. 1e). In contrast, intensity trends are predominantly non-significant throughout the region (Fig. 1f).

We compute the spread of the main MHW metrics using the regional and global reanalyses (product refs. no. 3, 4 and 5 in Table 1) alongside the SST-L4 observational products (product refs. no. 1 and 2 in Table 1). For the number of events, relatively high spread values are observed throughout the domain (Fig. 1g); notably, the highest values, exceeding 0.3, are found in the Aegean Sea, the Alboran Sea, the eastern Mediterranean Sea. For event duration, the largest spread is observed in parts of the Aegean Sea and along the southern Mediterranean, particularly near the African coast south of Sicily, where values exceed 5 d (Fig. 1h). In comparison, the spread in duration values is generally lower across the Black Sea. The highest spread in MHW intensity, above 0.34 °C, is observed in localized areas within the Gulf of Lion and continues along the coasts surrounding Corsica into the Tyrrhenian Sea, as well as in the northern part of the Adriatic Sea and in the Aegean Sea (Fig. 1i). In the Black Sea, intensity spread values of similar magnitude are found along the western coast and west of the Crimean Peninsula.

For validation, we computed the differences between metrics derived from both regional and global reanalysis data with respect to observed SST-L4 data (Fig. 1j–o), while percentage discrepancies are used to summarize basin-averaged results in Table 3. The MHW metrics derived from the regional reanalysis generally exhibit positive biases relative to the SST-L4 product in terms of number and duration, while MHW intensity from both reanalyses is lower than the observed one (Fig. 1j–o). For a more specific assessment, the Mediterranean Sea is divided into geographic subregions as proposed by Dayan et al. (2022) (Table 3). Overall, the regional reanalysis demonstrates superior performance compared to the global reanalysis, producing results that more closely match the SST-L4 reference data, as reported for the Mediterranean Sea in previous analyses by Dayan et al. (2022). An exception is observed in the number of detected events in the whole Mediterranean Sea (MED) and the West and East Mediterranean regions (WMED and EMED), where the global reanalysis typically outperforms the regional analysis.

Table 3. Percentage discrepancies (%) based on basin-averaged differences in MHW metrics of the regional and global reanalyses (product refs. no. 3, 4 and 5 in Table 1) relative to the SST-L4 observational product (product refs. no. 1 and 2 in Table 1) for the period 1993–2024. Percentage discrepancies are derived from basin-averaged differences and are reported for MHW metrics at the annual scale (number of events per year, mean duration, and mean intensity), as well as for seasonal MHW metrics computed separately for summer and winter. Reanalysis products that produce MHW metrics closest to the observational SST-L4 product are highlighted in bold. The subdomain definition follows Dayan et al. (2022) and considers metrics for the entire Mediterranean (MED), as well as for the western (WMED) and eastern (EMED) Mediterranean basins, in addition to the Adriatic, Aegean, and Black Seas.

	Frequency (number)		Duration (days)		Maximum intensity (°C)	
	Regional	Global	Regional	Global	Regional	Global
Annual						
MED	10.58	**3.01**	**18.15**	32.41	**8.65**	17.60
WMED	8.99	**2.98**	**19.89**	31.07	**9.58**	16.42
EMED	13.80	**5.60**	**17.13**	31.00	**8.75**	18.23
Adriatic Sea	**2.24**	5.40	**21.44**	40.06	**6.20**	19.46
Aegean Sea	**2.22**	8.42	**15.11**	45.38	**10.35**	25.11
Black Sea	**0.53**	4.72	**6.89**	19.04	**1.69**	14.81
Summer						
MED	12.89	**6.45**	**13.34**	25.05	**6.88**	21.78
WMED	8.79	**4.72**	**7.36**	15.33	**6.58**	17.53
EMED	17.64	**9.95**	**21.08**	34.69	**8.06**	19.82
Adriatic Sea	7.13	**5.30**	**9.82**	29.94	**6.86**	24.09
Aegean Sea	8.24	**5.52**	**10.39**	39.21	**4.68**	28.88
Black Sea	5.14	**0.28**	**3.84**	4.66	**5.77**	14.82
Winter						
MED	10.37	**2.41**	**36.05**	64.23	**7.08**	13.09
WMED	7.36	**1.52**	**33.75**	51.86	**8.24**	11.58
EMED	16.86	**1.87**	**33.73**	61.20	**3.85**	15.56
Adriatic Sea	**1.42**	18.24	**35.55**	62.87	4.55	**0.53**
Aegean Sea	**8.95**	21.63	**27.87**	62.91	10.25	**3.60**
Black Sea	**2.15**	14.41	**8.38**	34.71	9.34	**8.16**

Based on the annual SST-based MHW metrics summarized in Table 3, the overall mean percentage discrepancies in the number of MHWs per year across the entire Mediterranean and Black Seas are 10.58 % and 0.53 %, respectively, for the regional reanalysis, and 3.01 % and 4.72 % for the global reanalysis. While the regional reanalysis exhibits higher discrepancies for this metric in the Mediterranean Sea, it performs comparably overall and clearly outperforms the global reanalysis for other MHW characteristics, including duration and maximum intensity, with lower discrepancies in both basins. When considering summer MHW metrics, percentage discrepancies in the number of events are larger for the regional reanalysis across all subdomains, whereas the regional reanalysis outperforms the global reanalysis for all subdomains in terms of MHW duration and intensity (Table 3). Winter results are generally similar, with the regional reanalysis outperforming the global product across most of the domain (Table 3). Exceptions occur for frequency when considering either the Mediterranean basin as a whole or the western and eastern Mediterranean individually, and also for MHW intensity over the Adriatic, Aegean and Black Seas, where the ensemble spread of SST-derived intensity metrics is relatively high (Fig. 1i).

An overview of surface MHWs, highlighting the key findings, follows.

- Based on annual average metrics, MHWs show clear spatial differences: the northern Mediterranean and northern Black Sea generally experience frequent but short events, while the southern Mediterranean and central-southern Black Sea generally have fewer but longer-lasting heatwaves.

- According to annual average intensities, intensity hotspots are identified, with the strongest heatwaves in the northwestern Black Sea, Anatolian and Caucasian coasts, northern Adriatic, Gulf of Lion, and areas surrounding Corsica.

– Trends calculated from annual averages generally show significant increases in the number and duration of MHWs in both seas, with regional differences in intensity trends.

3.2 OHC-Derived Subsurface Marine Heatwave Characterization

We also compute analogous MHW metrics based on upper OHC (0–40 m; Fig. 1p–u). In the Mediterranean Sea, the average number of MHW events decreases compared to those derived from SST, particularly along the African coast (from 10 to 35° E), in the Adriatic Sea, around the Gulf of Lion, and throughout much of the central basin between 15 and 30° E (Fig. 1p). These results are consistent with the conclusions of Dayan et al. (2023). In contrast, the number of subsurface MHW events increases in certain regions, such as parts of the Alboran Sea, though this increase is spatially limited, and across most of the Black Sea.

Unlike the number of events, the mean duration of subsurface MHWs is generally longer as compared to the events observed at the sea surface across many regions in both the Mediterranean and Black Seas (Fig. 1q). In the Mediterranean Sea, notable increases in event duration are observed in the Aegean Sea, the northern and central Adriatic Sea, and the central basin – particularly between 10 and 20° E. This includes the Gulf of Gabès and the adjacent coasts of Tunisia and Libya, where average event durations can exceed 28 d. In the Black Sea, duration increases are observed particularly in the western part, between 25 and 35° E, with values exceeding 24 d along the northwestern coast.

For intensity, the OHC-based results reveal patterns (Fig. 1r) that are not captured by the SST-based definition (Fig. 1c). A shared feature of both SST- and OHC-derived MHW intensity is the elevated values consistently observed in the Black Sea relative to most of the Mediterranean Sea. Notably, in the Black Sea, the mean intensity from OHC shows distinct signals associated with the Rim Current and mesoscale eddies. For example, values exceed 7.0×10^8 J m^{-2} in the Batumi region, located in the southeastern part of the basin, and reach approximately 6.0×10^8 J m^{-2} west of Crimea, near the Sevastopol eddy region. Similar to the SST-derived metric, the OHC-derived intensity also shows relatively higher values in the northern Mediterranean, particularly over the Gulf of Lion, Strait of Otranto, the Crete gyre, southeast of Cyprus (Latakia eddies), Antalya Bay (Asia minor current) and the Alboran Sea. In these regions, the mean intensity can reach values above 3.7×10^8 J m^{-2}.

Similarly to the SST-derived metric, the OHC-based trends show positive values for both the number and duration of MHW events (Fig. 1s–t). In the Mediterranean Sea, strong trends, exceeding 2 events per decade, are observed in the central and south Adriatic Sea, Cretan Passage (east of the Ionian Sea and south of Greece), parts of the Balearic Sea and Algerian basin (Fig. 1s). These regions coincide with areas where the SST-based trends in the number of events are also elevated (Fig. 1d). In contrast, the OHC-derived trends are relatively lower in regions such as the southern coast of Sicily and the eastern coasts of Corsica and Sardinia, when compared to the corresponding SST-derived trends. In the Black Sea, the number of events exhibits stronger increasing trends along the Rim Current, a signal not captured by the SST-based metric. For event duration, the OHC-based trends display more spatial gaps (areas with no statistically significant trend), particularly in the eastern Mediterranean (Fig. 1t), where trend values are also slightly lower compared to those derived from SST (Fig. 1e). An interesting finding emerges for MHW intensity: OHC-based trends show localized negative values along the Rim Current pathway, especially near the Anatolian coast and in areas adjacent to the Kerch Strait (Fig. 1u). In the Mediterranean Sea, small areas of negative trends in intensity are observed in regions such as the Gulf of Lion and the Crete gyre (Fig. 1u). Among these, only the Gulf of Lion also exhibits similar negative trends in the SST-based definition (Fig. 1f).

Correlation maps for the period 1993–2024 show statistically significant agreement between annual-average MHW metrics derived from SST and OHC in the upper 0–40 m throughout large areas of the western and central Mediterranean Sea (Fig. 1v–x). Considering the number of events, significant correlations are observed in most of the Mediterranean, but this decreases toward the central and eastern basins and in the Black Sea. Event duration exhibits generally stronger and more spatially consistent correlations, particularly in the Mediterranean Sea, with r values often exceeding 0.8, while correlations in the Black Sea are weaker overall. Correlations for event intensity tend to be lower and more variable, with non-significant values covering nearly the entire Black Sea and the central and northern Adriatic Sea.

While correlations indicate agreement between surface and subsurface MHW metrics on an annual scale (particularly for frequency and duration; Fig. 1v–x), they may mask differences in timing, depth structure, or seasonal behavior. To partially address this limitation, we further examine seasonal correlations, which reveal marked contrasts between summer and winter conditions. During summer (Fig. 1y–aa), correlations are generally weaker, which is consistent with enhanced upper-ocean stratification and a shallower mixed layer. Given that OHC is defined over the upper 0–40 m and that summer mixed-layer depths are typically shallower than 40 m in both basins (Kara et al., 2009; Houpert et al., 2015), SST- and OHC-derived MHW metrics tend to diverge, suggesting that additional subsurface processes below the mixed layer may contribute to summer MHW development. This seasonal decoupling highlights the relevance of a combined detection approach using both surface and subsurface indicators. In contrast, during winter (Fig. 1ab–ad), increased vertical mixing and convective processes deepen the mixed

layer, in some regions exceeding 70 m, resulting in consistently high significant correlations between SST- and OHC-based MHW metrics across most of the Mediterranean and Black Seas, with values above 0.85 ($p < 0.05$). Overall, these seasonal correlation patterns are consistent with the findings of Juza et al. (2022), who associated shallow, intense MHWs during summer with strong stratification and deeper penetration of thermal anomalies in winter when vertical mixing is enhanced.

The following highlights summarize the main patterns and trends of MHWs identified using the upper-OHC (0–40 m) definition:

- Subsurface MHWs generally last longer than surface events. The average number of events is lower in some Mediterranean regions (e.g., African coast, Adriatic Sea, central basin) and higher across most of the Black Sea.
- Subsurface MHW intensities are highest in the Black Sea, particularly near the Rim Current and mesoscale eddies. In the Mediterranean, average intensities are lower, with relatively elevated values in some regions such as the Gulf of Lion, Crete gyre, and Alboran Sea.
- Trends calculated from annual averages show increasing numbers and durations of subsurface MHWs, with the strongest increases in the central and south Adriatic Sea and Cretan Passage for the number of events (Mediterranean), and along the Rim Current for the number of events and in the western Black Sea for duration; very localized negative intensity trends occur in both seas.
- Correlations between SST- and upper-OHC-derived MHW metrics increase in winter with deeper mixing and convection, but are weaker in summer due to stratification and shallow mixed layers, highlighting the added value of combining surface and subsurface indicators.

3.3 Sensitivity of SST- and OHC-Based MHW Metrics and Water Mass Structure

The objective of this section is to characterize MHW events using both definitions and to assess the sensitivity of each approach to the vertical structure of water masses. This section does not explore causal relationships or feedbacks between MHWs and water mass formation. Instead, it provides a descriptive evaluation of how different MHW definitions respond to varying water mass structures.

3.3.1 Black Sea Cold Intermediate Layer

In the Black Sea, a prominent feature is the CIL, a subsurface cold water mass that forms during winter through surface cooling and convective mixing. The CIL, typically characterized by temperatures below 8 °C and found at depths of 30 and 80 m (Ivanov et al., 2001), contributes significantly to subsurface ventilation (Özsoy and Ünlüata, 1997). Its seasonal formation is driven by dense surface waters sinking during cold winters, and it can modulate heat distribution in the upper ocean. The warming of the Black Sea has led to an increased occurrence and intensity of MHWs and has significantly contributed to the gradual disappearance of the CIL, as evidenced by both observational and reanalysis datasets (Stanev et al., 2019; Lima et al., 2021, 2026).

In the Black Sea, the detection of MHWs differs significantly between surface- and subsurface-based metrics, particularly in years marked by the formation of the CIL (e.g. 2012) which alters the thermal structure of the water column. Figure 2 shows MHWs intensity and duration evaluated using both SST-based (left) and OHC-based (right) definitions for selected years: 2011 is included due to a pronounced negative surface temperature anomaly. The years 2012 and 2017 feature the presence of the CIL, with 2012 showing a well-developed CIL and 2017 a less pronounced presence (Stanev et al., 2019; Lima et al., 2026). The year 2024 is included as it exhibited record breaking MHW intensity. In 2011, reanalysis data revealed negative temperature anomalies confined to the near-surface layers, promoting the subduction of cold water and contributing to the development of a well-defined CIL in 2012 (Lima et al., 2026). These thermal structures influence MHWs detection differently depending on the metric applied. In 2011, SST-based metrics indicate limited MHW coverage due to cooler surface conditions. However, in 2012, OHC-based metrics show significantly reduced MHW spatial extent compared to SST-based estimates (see also Fig. 4, discussed in a later section), highlighting the importance of vertical heat distribution in accurately characterizing MHWs. In 2017, another year marked by the presence of the CIL, cold temperatures were more uniformly distributed throughout the upper layers in the Black Sea. In this case, SST- and OHC-based definitions produced closely aligned metrics, both indicating diminished MHW coverage, particularly in the western Black Sea. These findings demonstrate how the presence and vertical structure of the CIL influence the detection and apparent intensity of MHWs, depending on whether surface or subsurface indicators are used.

In 2017 and 2024, the OHC-based metric detected a more pronounced signal, with intensified MHW events notably concentrated along the Rim Current and in eddy-dominated areas, such as the Sevastopol eddy located west of Crimea. This spatial distribution aligns with the long-term pattern observed in OHC-derived metrics over the period 1993–2024 (Fig. 1r), reinforcing the consistency of subsurface-driven MHW signals in these dynamically active regions. In contrast, the SST-based approach does not completely capture these features, highlighting the added value of incorporating subsurface heat content to more accurately represent MHW intensity and spatial variability. In 2024, surface MHW intensity increased substantially, surpassing 4.6 °C along the

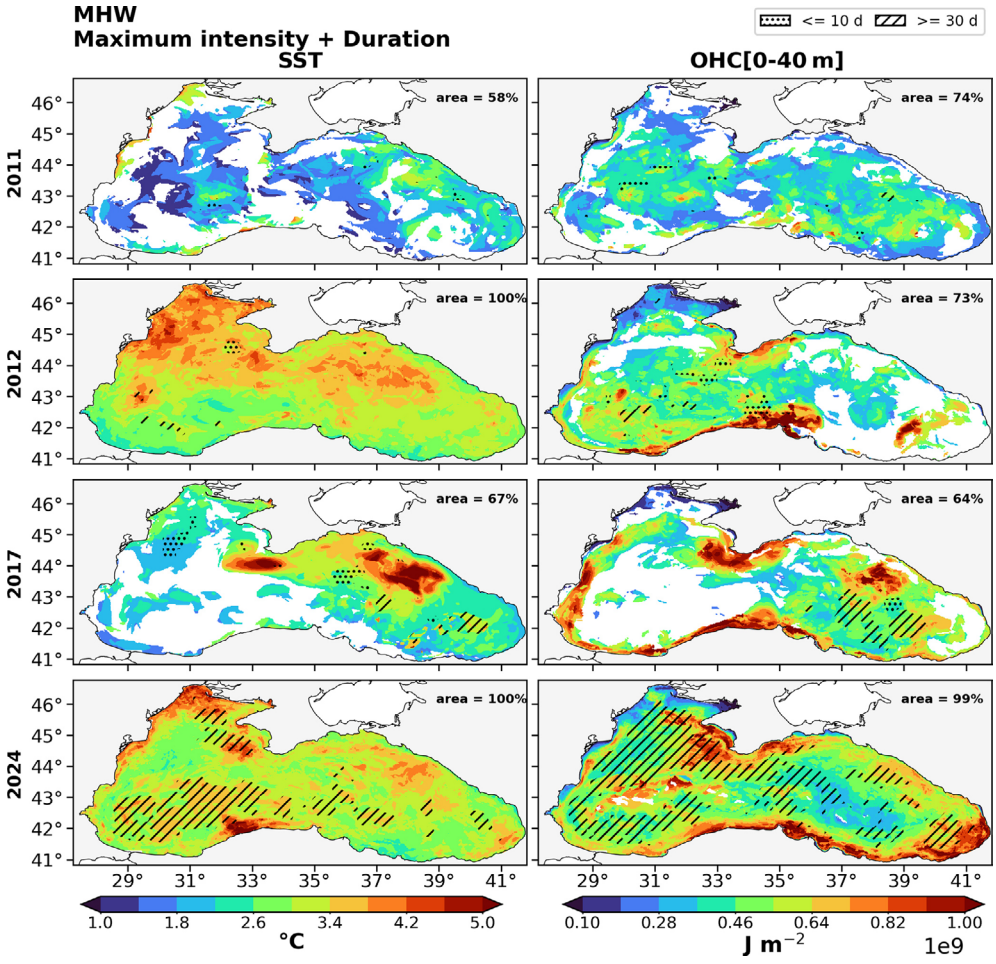


Figure 2. Spatial distribution of the yearly average of maximum intensity of MHW events for selected years in the Black Sea using SST-based (left) and OHC-based (right) definition. Hatched areas highlight regions where events lasted less than 10 d or more than 30 d. Results are derived from the Black Sea regional reanalysis (product ref. no. 3 in Table 1).

Anatolian coast, a region influenced by summer upwelling (Gunduz et al., 2022), and reaching up to 1×10^9 J m^{-2} in areas along both the southern and northern branches of the Rim Current. Furthermore, both SST- and OHC-based definitions identify events with durations exceeding 30 d, with consistent detections particularly evident west of Crimea and in the central and southwestern parts of the basin.

To summarize the interaction between MHWs and the CIL in the Black Sea:

- Long-term warming has led to an increased occurrence of MHWs and to a progressive reduction or even absence of the CIL in recent years (see also Fig. 4 later).

- Nevertheless, in years characterized by more severe winters (e.g., 2012 and 2017), the CIL can still develop, altering the upper-ocean thermal structure and leading to substantial differences between SST- and OHC-based metrics when the CIL is well developed (e.g., 2012), and to more convergent estimates when subsurface cooling is more vertically uniform (e.g., 2017).

- OHC-based metrics consistently emphasize dynamically active regions, such as the Rim Current and associated eddies, highlighting the importance of subsurface heat content for resolving the spatial structure and intensity of Black Sea MHWs.

3.3.2 Southern Adriatic Sea Pit and the Eastern Mediterranean Deep Water

To better understand how MHW metrics respond to changes in water mass structure in the Mediterranean Sea, we focus on the Southern Adriatic Sea Pit (SAP), a key area for the formation of Eastern Mediterranean Deep Water (EMDW), which occurs during winter. Since this process affects how deep the surface layer mixes, it can influence how MHWs are detected.

The Adriatic Deep Water (ADW), along with the North Adriatic Dense Water (NAdDW), is identified as one of the main sources of EDMW (Gačić et al., 2001; Paladini de Mendoza et al., 2022; Parras-Berrocal et al., 2023). The southward spread of NAdDW along the western Adriatic coast, together with open-ocean convection in the center of the permanent cyclonic gyre over the SAP, contributes to the formation of ADW (Denamiel et al., 2025). ADW plays a significant role in maintaining the overturning circulation of the Mediterranean Sea.

Figure 3 presents a time series of wintertime mean values for the number, duration, and intensity of MHW events evaluated using both SST-based and OHC-based approaches, together with the winter mean MLD, defined as the depth where potential density increases by 0.01 kg m^{-3} relative to 10 m, all averaged over the SAP basin. In most years, lower MHW frequency and shorter event durations are associated with deeper MLDs, typically exceeding 100 m. An interesting observation occurs in 2014, when relatively higher MHW metrics – exceeding two events with durations longer than 15 d based on both SST- and OHC-derived estimates – coincide with a relatively shallow winter MLD, averaging approximately 50 m. This suggests that the increased presence of MHWs may have contributed to a more stratified winter, a behavior that may be partly explained by anomalous atmospheric forcing, consistent with the findings of Le Meur et al. (2025), who reported positive wintertime heat flux anomalies from ERA5 reanalysis in the South Adriatic during 2014.

Similarly, data from the Copernicus OMI on Mediterranean Water Mass Formation Rates (EU Copernicus Marine Service Information, 2024c) indicate an abrupt decline in EMDW formation, with notably low transport (in Sverdrups), during the 2014–2016 period. Kokkini et al. (2020) reported that 2014 was characterized by less saline water dominating the upper layers across the entire pit, accompanied by a significant heat gain in the whole Adriatic Sea. These conditions likely suppressed winter convection, leading to weakened ADW formation, while the associated heat gain may have contributed to the observed increase in MHW activity. In 2017, EMDW formation was reestablished, consequently accompanied by a marked increase in winter MLD and a sharp decline in MHW events.

The Hovmöller diagrams in Fig. 3 presents the wintertime EMDW formation rates for key years, illustrating a significant increase in 2017 compared to 2014. The methodology for estimating EMDW formation follows Simoncelli and Pinardi (2018), consistent with the approach applied in the OMI analysis described in the paragraph above. These years were selected to illustrate contrasting MHW detection patterns under varying deep-water formation regimes (see spatial maps in Fig. 3). In 2014, widespread MHWs across the Adriatic Sea, particularly in the SAP, indicate inhibited convective mixing, leading to weaker EMDW formation and a shallower winter MLD. Conversely, in 2017, stronger convective conditions prevailed, reflected in deeper MLDs and higher EMDW formation rates, coinciding with a substantial reduction in MHW activity.

We also present the results for 2024, when the MHW assumed a higher intensity in the Adriatic Sea and events lasted more than 30 d in the SAP region (Fig. 3; top). In that year, the time series also indicates a reduction in winter MLD, which is accompanied by elevated MHW metrics, underscoring how MHWs influence the ocean's stratified state. Unlike in 2014, when vertical convection ceased, the Hovmöller diagram for 2024 reveals signs of vertical convection that may be influenced by regional salinity.

Overall, time series of wintertime MHW estimates derived from both SST- and OHC-based definitions demonstrate strong spatial agreement in the Adriatic Sea, although intensity maps reveal differing spatial patterns, with distinct regions of higher intensity depending on the metric used (Fig. 3). To summarize, the wintertime interaction between MHWs, upper-ocean stratification, and deep-water formation in the Southern Adriatic Sea reveals that:

- Enhanced wintertime MHW activity is associated with increased upper-ocean stratification, expressed by a shallower MLD, whereas deeper winter mixing is consistently linked to reduced or absent MHW occurrence.
- High wintertime MHW activity and associated heat gain (e.g., 2014) coincide with weakened winter convection and reduced EMDW formation, while years characterized by stronger convection (e.g., 2017) exhibit deeper mixed layers and suppressed MHW activity.

3.4 Intensity-Based Analysis of MHW in the Black and Mediterranean Seas

Our findings indicate that the use of a single method for monitoring MHWs, whether based exclusively on SST or OHC, is insufficient to fully characterize and monitor MHWs across both the Black and Mediterranean Seas. Each index reflects different aspects of ocean warming and is influenced by distinct physical drivers, with SST closely linked to atmospheric conditions and OHC representing heat stored beneath the surface. When applied separately, these indices may offer an incomplete representation of thermal anomalies, limiting their effectiveness in capturing the full scope and variability of MHWs in both seas. Our results support previous findings (e.g., McAdam et al., 2023) that highlight the importance of incorporating subsurface information into monitoring strategies. Therefore, we recommend a combined approach that integrates SST- and OHC-based definitions, including event intensity levels based on the categorization framework such as established by Hobday et al. (2018). Figures 4 and 5 show this combined approach applied to the Black Sea and Mediterranean Sea respectively.

In the Black Sea, both the average spatial extent and basin-average number of days of moderate MHW events have increased over time, with recent years showing coverage ex-

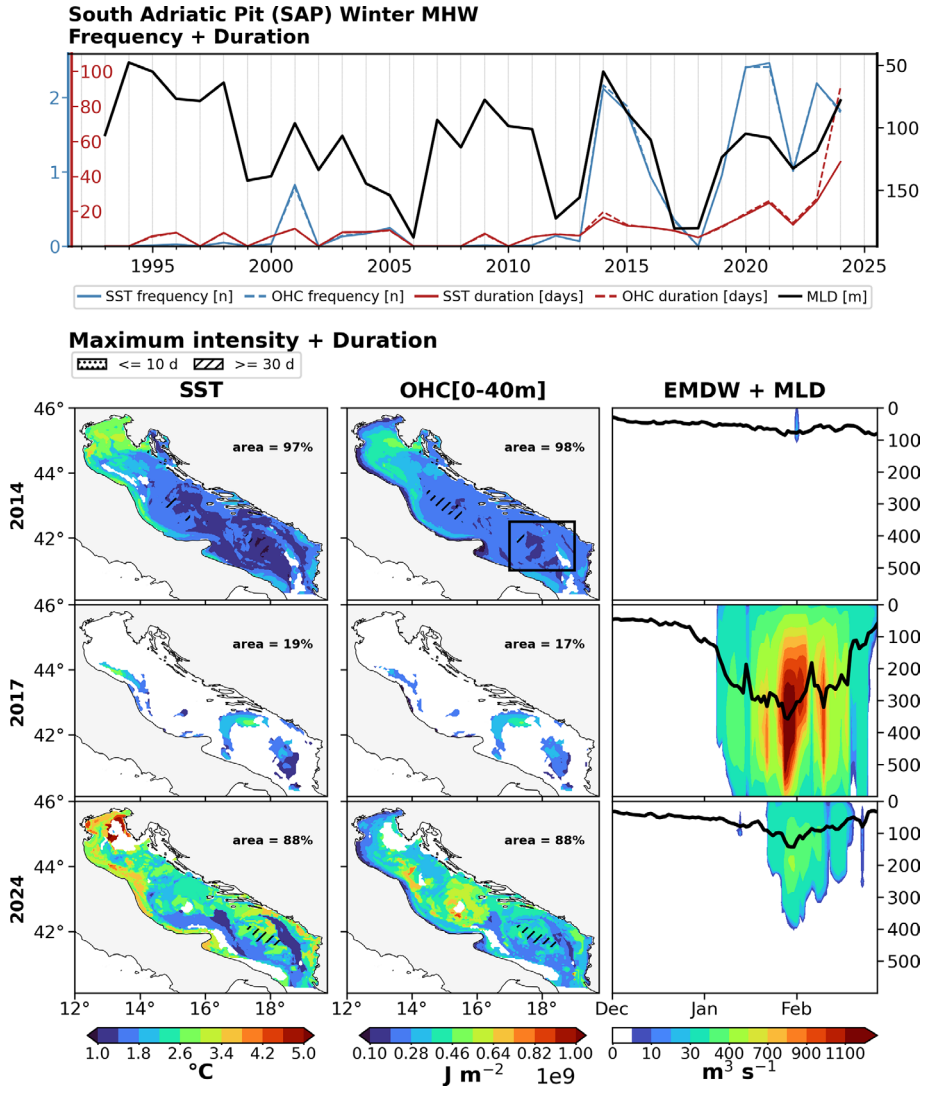


Figure 3. Upper plot: Time series show basin-averaged MHW frequency and duration (days) from two definitions based on SST and OHC, together with mean MLD during winter (1993–2024) in the SAP region. Lower plot: Spatial maps exhibit MHW maximum intensity based on SST (°C) on the left and OHC (0–40 m, J m^{-2}) in the middle for 2014, 2017, and 2024 in the Adriatic Sea. The black rectangle on the 2014 OHC map indicates the SAP region. Hatched areas highlight regions where events lasted less than 10 d or more than 30 d. Hovmöller diagrams on the right panels reveal water mass formation rates of the EMDW (m^3 s^{-1}) overlapped by daily mean MLD values for the winter months in the SAP region. Results are derived from the Mediterranean Sea regional reanalysis (product ref. no. 4 in Table 1).

tending across nearly the entire basin (Fig. 4). A notable result is found in 1994, when the SST-based definition indicates that moderate events cover almost the entire sea, with the basin-average number of days exceeding 25. By comparison, the OHC-based definition for the same year shows spatial coverage of about 60 % and a slightly lower basin-average number of days, just below 25. As discussed in the previous section, years marked by the presence of the CIL can exhibit distinct behavior depending on the MHW definition applied. In 2012, the SST-based definition indicates nearly complete basin-wide coverage of moderate MHWs on an annual scale, whereas the OHC-based definition shows less than 80 % coverage. In contrast, during 2017, when the cold signal associated with the CIL was more uniformly distributed throughout the water column, both definitions produced similar metrics for moderate events, with spatial coverage around 60 % and a basin-average of approximately 25 d. The correlation between moderate MHW metrics derived from SST and OHC definitions is 0.89 for spatial coverage and 0.88 for the basin-average number of days, both statistically significant ($p < 0.05$).

The spatial coverage of strong MHW events shows a positive trend over time for both definitions. In contrast, no clear trend is observed in the basin-averaged number of days, al-

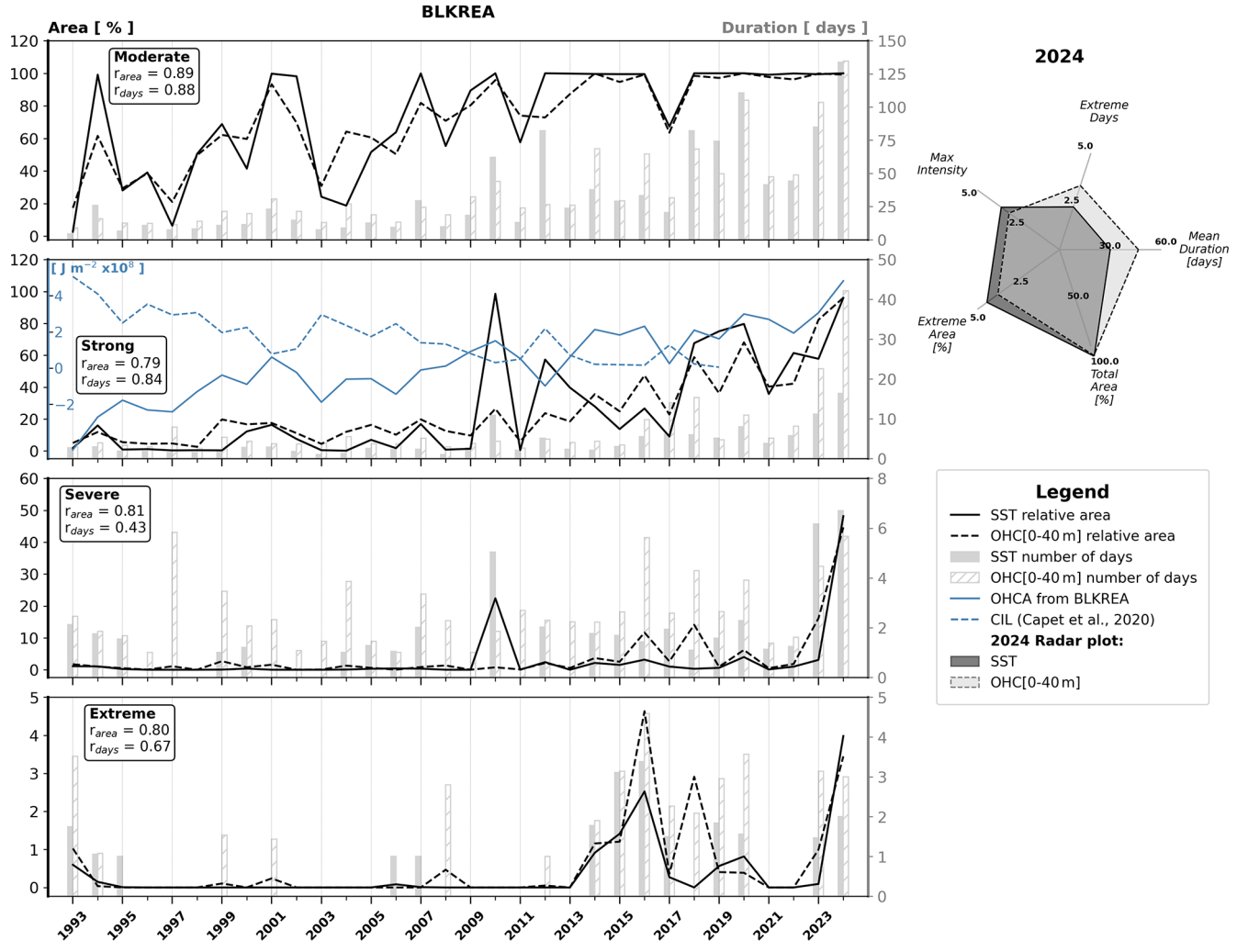


Figure 4. Time series of the temporal and basin-wide mean spatial coverage of MHW events in the Black Sea based on SST (solid line) and OHC (dashed line) definitions. Results are derived from the Black Sea regional reanalysis (product ref. no. 3 in Table 1). The bars show the mean number of days of events for each category over the years, with SST-based values in grey and OHC-based values shown with hatching. On the right, the radar chart summarizes selected MHW metrics using both definitions for the year 2024. Events are categorized as moderate, strong, severe, or extreme, following the classification by Hobday et al. (2018). The correlations between the spatial coverage (r_{area}) and number of days (r_{days}) are also presented for each category. For the "strong" category, blue curves show the time series of OHC anomalies within 0–100 m (solid blue line) and CIL cold content from observations (dashed blue line; Capet et al., 2020).

though elevated values are noted in recent years, particularly in 2023 and 2024. The year 2010 is particularly notable, with the SST-based definition indicating that strong events affect nearly the entire basin and the basin-average number of days exceeded 10. This signal is not captured by the OHC-based definition. Similarly, SST-based metrics indicate that more than 20 % of the basin was affected by severe events in 2010, a pattern not detected using the OHC approach. Mohamed et al. (2022) associated the exceptionally high MHW activity in 2010 with the influence of El Niño, suggesting a potential link between large-scale climate variability and surface heatwave manifestations in the Black Sea. The presence of the CIL is also reflected in the detection of strong events in 2012, when the SST-based definition shows a wider spatial extent than the OHC-based definition, further highlighting the impact of subsurface thermal structure on MHW detection in the Black Sea. To further illustrate this, we include the 0–100 m OHC anomaly from the Black Sea regional reanalysis, together with observational estimates of CIL cold content from Capet et al. (2020). These datasets respectively show a decline in OHC and an increase in CIL cold content in both 2012 and 2017, consistent with a more pronounced CIL presence during those years, which may have affected the detection of MHWs using the OHC-based definition. Correlation coefficients between SST- and OHC-based metrics are statistically significant ($p < 0.05$). For spatial coverage, the coef-

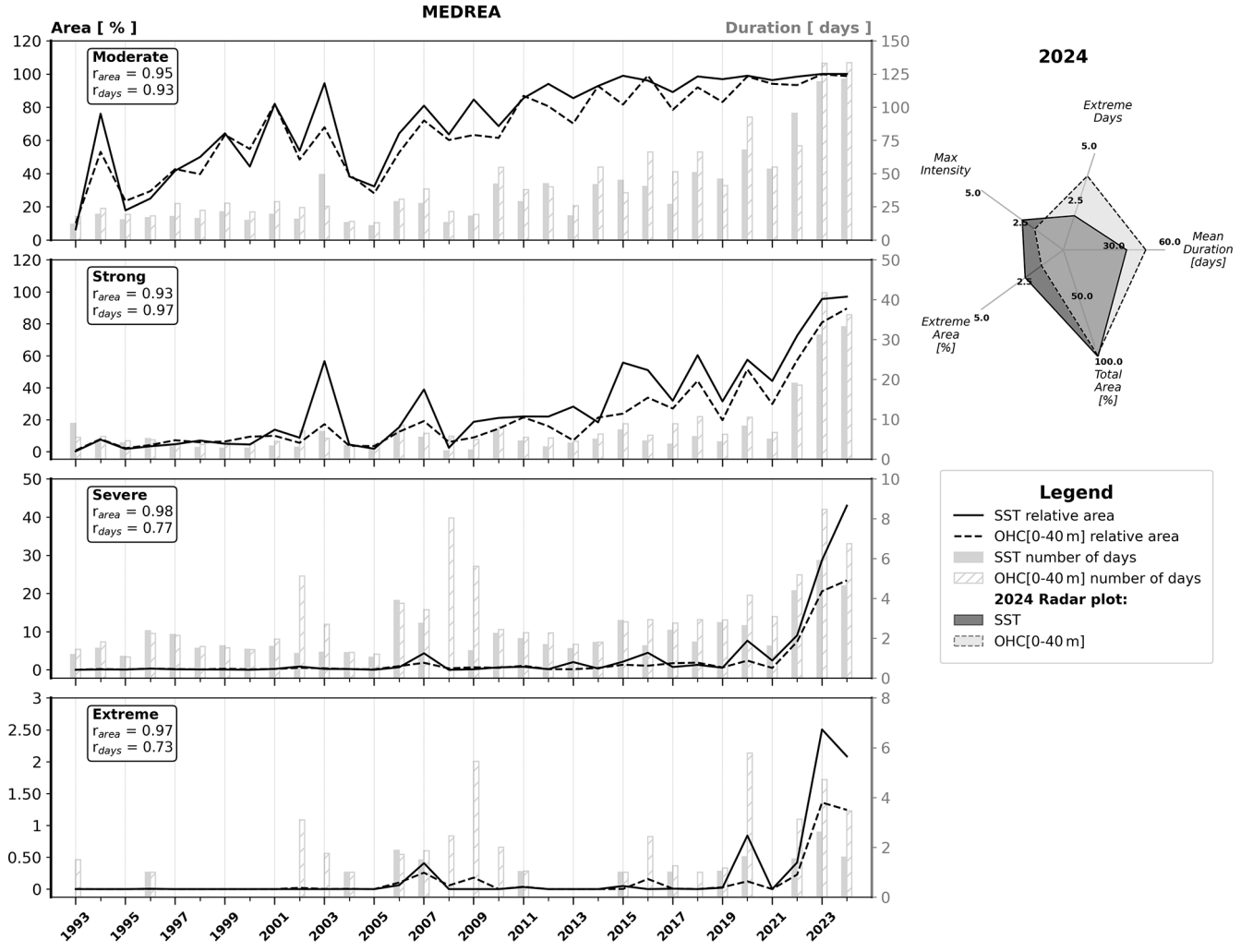


Figure 5. Time series of the temporal and basin-wide mean spatial coverage of MHW events in the Mediterranean Sea based on SST (solid line) and OHC (dashed line) definitions. Results are derived from the Mediterranean Sea regional reanalysis (product ref. no. 4 in Table 1). The bars show the mean number of days of events for each category over the years, with SST-based values in grey and OHC-based values shown with hatching. On the right, the radar chart summarizes selected MHW metrics using both definitions for the year 2024. Events are categorized as moderate, strong, severe, or extreme, following the classification by Hobday et al. (2018). The correlations between the spatial coverage (r_{area}) and number of days (r_{days}) are also presented for each category.

ficients are 0.79, 0.81, and 0.80 for the strong, severe, and extreme categories, respectively. For the basin-average number of days, the corresponding correlations are 0.84, 0.43, and 0.67.

Considering all categories, the year 2024 exhibits record-high values in both spatial coverage and basin-average number of days for MHW events, based on both SST- and OHC-based definitions. In this year, moderate events were detected on more than 125 d according to both definitions, while the OHC-based definition indicates that strong events occurred with a basin-average duration of approximately 40 d. Detection based on either SST or OHC reveals spatial coverage exceeding 80 % for strong events and approaching 50 % for severe events. Although extreme events covered a smaller area in 2024, their occurrence remains relatively high compared to previous years in the time series. Additional MHW metrics for 2024 are summarized in the radar chart (Fig. 4, right).

In the Mediterranean Sea (Fig. 5), both the basin-averaged number of days and spatial extent of moderate and strong MHW events have increased in recent years, with peaks occurring in 2023 or 2024 depending on the metric and definition used. In 2023 and 2024, moderate events nearly cover the entire basin, with the mean number of days exceeding 100. Although strong events occur less frequently and affect smaller areas, their spatial extent and mean total days have increased significantly since 2021, peaking in 2024 with values exceeding 80 % coverage and approximately 40 d. An exception to this overall increasing trend occurred in 2005,

when a notable decline in the spatial extent of both moderate and strong MHWs was observed. This anomaly coincides with an abrupt disruption in the long-term warming trend reported in the Mediterranean Sea that year, which had consequences for the formation of Western Mediterranean Deep Water (López-Jurado et al., 2005; Beuvier et al., 2012).

When comparing definitions, OHC-based metrics generally indicate lower spatial coverage for both moderate and strong MHW events relative to SST-based estimates. Severe events cover less than 10 % of the basin for most years in the study period, although recent years show an increase, with SST- and OHC-based values reaching approximately 40 % and 20 %, respectively, in 2024. Despite this expansion in spatial extent, the frequency of severe events remains low, with these events typically occurring on fewer than 7 d.

Overall, metrics derived from SST- and OHC-based definitions exhibit strong and statistically significant correlations ($r > 0.9$, $p < 0.05$). However, the mean total days of severe and extreme events show lower correlations of 0.77 and 0.73, respectively. The year 2024 displays notably high values across multiple MHW metrics, as illustrated in the radar chart (Fig. 5, right).

To synthesize the intensity-based analysis of MHWs in the Black and Mediterranean Seas, the main findings are summarized as follows:

- SST- and OHC-based definitions provide complementary information, and their combined use is required to robustly characterize MHW intensity, duration, and spatial extent across both basins.
- Subsurface thermal structure, particularly the presence of the CIL, strongly modulates MHW detection in the Black Sea.
- The Mediterranean Sea exhibits recent MHW intensification consistent with the Black Sea. The year 2024 represents an unprecedented MHW year, with record-high spatial coverage and basin-averaged duration across multiple intensity categories in both seas.

4 Conclusions

We update and expand the analysis of MHW metrics in the Mediterranean Sea and apply a similar assessment to the Black Sea, following HD2016. For both regions, we estimate the uncertainty of SST-based MHW metrics using three different products and extend the analysis to sub-surface MHWs by means of an OHC-based formulation. This ensemble-based approach can be further strengthened by including additional reanalyses and observational datasets, thereby allowing for a more robust quantification of uncertainties. The regional reanalysis provides more reliable estimates than the global reanalysis, closely aligning MHW metrics with observational SST data. MHW metrics derived from SST and OHC are generally consistent, with high correlation in event duration ($r > 0.8$, $p < 0.05$) across the central and eastern Mediterranean. The number of MHW events also exhibits generally high correlations, though values decline toward the central and eastern Mediterranean and parts of the Black Sea, where correlation coefficients fall below 0.6 ($p < 0.05$) and become non-significant ($p > 0.05$) over a more extensive area (Fig. 1v–x). However, substantial differences also emerge, including variations in intensity patterns and cases where surface anomalies are not accompanied by subsurface warming, and vice versa. These contrasts highlight the importance of using SST- and OHC-based formulations as complementary sub-indicators to better characterize the full vertical structure and spatial complexity of MHWs.

Our seasonal analysis further refines these conclusions by showing that the agreement between surface and subsurface MHW metrics is strongly season-dependent. Although annual correlations are generally high, they mask pronounced summer–winter contrasts. During summer, enhanced upper-ocean stratification and shallow mixed-layer depths lead to weaker correlations between SST- and OHC-derived metrics, indicating that surface-only definitions do not fully capture the subsurface structure of MHWs (and vice versa). This limitation is particularly relevant because summer MHWs are typically more intense and associated with the strongest ecological and socio-economic impacts (Wang and Zhou, 2024). In contrast, winter conditions are characterized by deeper mixed layers and enhanced vertical mixing, resulting in consistently high and significant correlations between SST- and OHC-based metrics across most of the Mediterranean and Black Seas. Together, these results demonstrate that while surface and subsurface indicators converge under well-mixed winter conditions, a combined SST–OHC monitoring approach is essential to adequately characterize the vertical structure and impacts of MHWs, particularly during summer.

In the Black Sea, OHC-derived MHW intensity highlights subsurface processes associated with the Rim Current, capturing localized maxima that are absent in SST-based estimates. In 2012, the presence of a well-developed CIL led to subsurface cooling, which masked the MHW signal in OHC, while surface temperature anomalies remained detectable using the SST-based definition. In the Adriatic Sea, surface and subsurface MHWs show generally consistent frequency and duration over time, particularly in the SAP region. However, the spatial distribution of maximum intensity often diverges between SST- and OHC-based definitions, with peak values located in different areas depending on the definition used. These variations highlight the limitations of using either SST- or OHC-based definitions alone. Radar plots that integrate intensity, duration, and spatial extent are useful for monitoring the temporal evolution of MHW characteristics. They serve as synthetic indicators for ocean monitoring and help synthesize interannual differences as well as those arising from the use of SST versus OHC definitions.

In 2024, both the Black Sea and Mediterranean Sea experienced record-high MHW intensities and durations, with events lasting over 30 d and temperature anomalies exceeding 4.6 °C in key regions such as the Anatolian coast (Fig. 2, bottom left), where summer upwelling commonly influences local ocean conditions. These extreme recent events underscore the urgency of refining monitoring strategies and understanding the mechanisms behind MHW development in these semi-enclosed basins.

Our findings provide valuable insights for monitoring MHWs in both seas. We recommend a MHW OMI that integrates both SST and OHC definitions to capture surface and subsurface heatwave signals in the Mediterranean and Black Seas. While the HD2016 definition remains practical for current monitoring, future studies may benefit from refined methods such as higher percentiles, moving average climatologies, or detrending to better separate extremes from long-term warming (Appendix A). Since the 90th percentile may be less restrictive for some regions, categorizing MHWs according to their intensity remains essential, and the Hobday framework provides a robust basis by classifying events as moderate, strong, severe, or extreme.

While the need to provide information on both surface and subsurface characteristics of MHWs is made clear in this study for the Mediterranean and Black Sea, and in Sun et al. (2023) at global scale, the depth ranges of interest depend greatly on region and application. The 0–40 m layer was selected here to capture the biologically productive upper epipelagic zone, which supports key ecological functions and socio-economic activities. Incorporating a subsurface MHW indicator provides valuable insights for ecosystem management and early warning systems. Monitoring OHC-based heat anomalies can help anticipate thermal stress on sensitive habitats, aquaculture sites, or commercial fisheries before surface signals appear, enabling timely management actions and reducing the impacts of mass mortality events and disruptions in biological productivity. Future studies should therefore explore region-specific depth thresholds that account for local oceanographic dynamics and ecological sensitivities.

Appendix A: Effect of SST and OHC Detrending on MHW Metrics

An additional analysis is performed to assess the impact of using a detrending approach for MHW detection by removing the mean trend value over the full spatial domain of each product from the original SST and OHC time series before applying the detection algorithm. Specifically, the linear trend is removed individually at each grid point to account for local variations in long-term change.

According to the standard SST-based definition, basin-averaged values for both the number and duration of MHW events exhibit marked interannual variability in both the Black and Mediterranean Seas, with particularly pronounced fluctuations in the former. For example, the number of events in the Black Sea ranged from fewer than one to nearly five per year during relatively short intervals, such as between 2009 and 2013. Additional peaks approaching or exceeding five events were observed in 2018, 2020, and 2024. In recent years, the number of events has increased in both basins, with 2024 marking a record year for both. Elevated frequency in 2024 also extends to event duration, highlighting it as an exceptionally warm year in both regions. In that year, the spatially averaged duration of extreme temperatures exceeds 30 d in the Mediterranean Sea and approaches 30 d in the Black Sea. In the first part of the analyzed period, the detrended metrics are larger until around 2007–2008, then they become lower than the "reference" metrics. Instead, the intensity of events is not significantly influenced by detrending over the years. The intensity time series begins with elevated values exceeding 5 °C in 1993 in the Black Sea and over time, intensity decreases and stabilizes around 3 °C, whereas in the Mediterranean Sea, values consistently remain close to 2 °C.

The analysis is further extended beyond regional reanalysis products to assess the impact of detrending within a multi-product framework (Fig. A1, right and Table A1). We first describe the results obtained using the formulation without detrending the SST. Considering the number of events, regional reanalysis products always show higher trends with respect to the global reanalysis and satellite observations. In contrast, the global reanalysis exhibits the highest trends in event duration, surpassing both regional reanalysis and the observed SST except for the Adriatic and Black Seas, where the duration trend is higher in the regional reanalysis. In these two regions, however, no product shows a statistically significant intensity trend. After detrending SST, most trends in the number and duration of events become non-significant (Fig. A1 and Table A1 exclude trends that are not statistically significant). Exceptions include the regional reanalysis in the western, eastern, and entire Mediterranean Sea, where the duration of events shows small and negative trends. In the Aegean Sea, the duration trend derived from the global reanalysis remains positive, although its magnitude is reduced to approximately half of that observed under the standard (non-detrended) definition. Regarding MHW intensity, either the global or regional reanalysis indicates increasing trends across most of the Mediterranean Sea. Again, in the Adriatic and Black Seas, no product shows a statistically significant trend.

To distinguish the warming signal, Martínez et al. (2023) analyzed MHW metrics in the Mediterranean Sea by applying detections to the SST-L4 observational product and comparing results from the standard definition with those obtained after detrending. Similarly, their findings reveal positive trends using the standard method, whereas the detrended approach shows no statistically significant trends. Consistent with our findings, their results indicate that the occurrence of

Table A1. Long-term trends (1993–2024) with 95 % confidence interval indicated in brackets of MHW number, duration, and maximum intensity per year, derived from regional and global reanalysis (product refs. no. 3, 4 and 5 in Table 1) as well as the SST-L4 observation products (product refs. no. 1 and 2 in Table 1), for selected (sub)regions. The subdomain definition follows Dayan et al. (2022) and considers metrics for the entire Mediterranean (MED), as well as for the western (WMED) and eastern (EMED) Mediterranean basins, in addition to the Adriatic, Aegean, and Black Seas. Non-significant trends ($p \geq 0.05$) are indicated by hyphens. Both SST (top) and OHC (bottom) derived metrics are presented. Trends calculated from the detrended approach are highlighted in bold.

SST-derived metrics

	MED				WMED			EMED			Adriatic			Aegean			Black Sea		
	MEDREA	GLOREA	L4	Martínez et al. (2023)	MEDREA	GLOREA	L4	MEDREA	GLOREA	L4	MEDREA	GLOREA	L4	MEDREA	GLOREA	L4	BLKREA	GLOREA	L4
Number events	0.143 (0.032)	0.117 (0.029)	0.105 (0.048)	0.074	0.131 (0.050)	0.124 (0.039)	0.103 (0.043)	0.142 (0.043)	0.111 (0.038)	0.095 (0.051)	0.140 (0.050)	0.111 (0.041)	0.128 (0.059)	0.127 (0.049)	0.090 (0.047)	0.103 (0.058)	0.134 (0.058)	0.117 (0.047)	0.126 (0.063)
per year	–	–	–	–	–	–	–	–	–	–	–	–	–	–	–	–	–	–	–
Duration d yr^{-1}	0.263 (0.173)	0.367 (0.180)	0.190 (0.136)	0.154	0.189 (0.226)	0.269 (0.202)	0.169 (0.151)	0.300 (0.197)	0.401 (0.188)	0.177 (0.173)	0.359 (0.213)	0.325 (0.321)	0.213 (0.169)	0.404 (0.313)	0.461 (0.225)	0.306 (0.254)	0.394 (0.224)	0.356 (0.270)	0.308 (0.212)
	−0.154 (0.130)	–	–	–	**−0.142 (0.187)**	–	–	**−0.165 (0.143)**	–	–	–	–	–	–	**0.202 (0.228)**	–	–	–	–
Intensity °C yr^{-1}	0.015 (0.009)	0.014 (0.008)	0.012 (0.010)	0.036	0.022 (0.016)	0.022 (0.013)	–	0.013 (0.008)	0.013 (0.007)	0.013 (0.009)	–	–	–	–	0.015 (0.008)	–	–	–	–
	0.011 (0.009)	–	–	–	**0.015 (0.015)**	**0.012 (0.010)**	–	**0.007 (0.007)**	–	–	–	–	–	–	**0.007 (0.008)**	–	–	–	–

OHC-derived metrics

	MED		WMED		EMED		Adriatic		Aegean		Black Sea	
	MEDREA	GLOREA	MEDREA	GLOREA	MEDREA	GLOREA	MEDREA	GLOREA	MEDREA	GLOREA	BLKREA	GLOREA
Number events	0.121 (0.031)	0.091 (0.039)	0.125 (0.045)	0.093 (0.044)	0.123 (0.041)	0.084 (0.043)	0.132 (0.039)	0.085 (0.039)	0.105 (0.048)	0.054 (0.058)	0.128 (0.043)	0.099 (0.054)
per year	–	**−0.140 (0.080)**	–	**−0.135 (0.068)**	–	**−0.132 (0.085)**	–	**−0.128 (0.058)**	–	**−0.126 (0.085)**		**−0.112 (0.059)**
Duration d yr^{-1}	0.306 (0.168)	0.345 (0.273)	0.275 (0.260)	0.303 (0.243)	0.327 (0.201)	0.346 (0.310)	0.415 (0.251)	0.373 (0.465)	0.504 (0.336)	0.317 (0.397)	0.317 (0.122)	0.367 (0.275)
	–	**−0.298 (0.193)**	–	**−0.334 (0.223)**	**−0.113 (0.113)**	**−0.395 (0.286)**	–	**−0.292 (0.351)**	–	**−0.338 (0.254)**	–	**−0.181 (0.193)**
Intensity W m^{-2}	–	–	–	–	–	0.001 (0.002)	–	–	–	–	−0.117 (0.080)	–
	0.022 (0.021)	–	**0.048 (0.039)**	–	–	**−0.005 (0.004**	–	–	–	–	–	**−0.003 (0.004)**

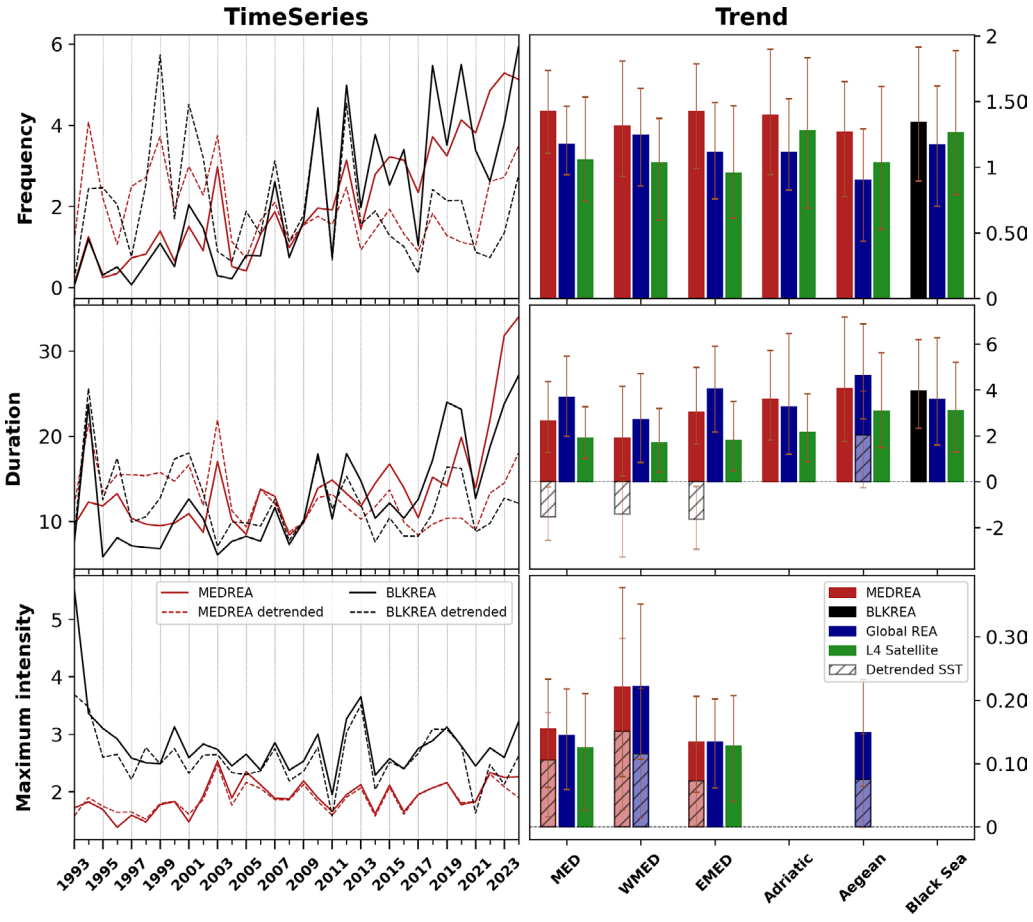


Figure A1. Left: Time series of annual MHWs metrics – number, duration (in days), and maximum intensity (in °C) – averaged over the entire Mediterranean (red lines) and Black Seas (black lines), comparing the SST definition (solid lines) with the detrended approach (dashed lines), based on the regional reanalysis (product refs. no. 3 and 4 in Table 1). Right: significant ($p < 0.05$) long-term trends (1993–2024) in MHWs number (events per decade), duration (days per decade), and maximum intensity (°C per decade), derived from regional and global reanalysis (product ref. no. 3, 4 and 5 in Table 1) as well as the SST-L4 observation product (product refs. no. 1 and 2 in Table 1), for selected (sub)regions following Dayan et al. (2022): the entire Mediterranean (MED), the western (WMED) and eastern (EMED) Mediterranean basins, and the Adriatic, Aegean, and Black Seas. Brown lines indicate the 95 % confidence interval. Solid bars show standard metrics definition, striped bars show SST de-trended metrics.

MHWs is predominantly driven by the underlying temperature trend.

A similar pattern is observed using the OHC-based definition, with the number of MHWs exhibiting interannual variability (Fig. A2 and Table A1). The annual count ranges from 1 event to a peak of over 5 events in 2020 in the Black Sea and in 2023 in both basins. When the time series is detrended, high MHW frequencies are also evident at the beginning of the period, with more than 4 events occurring in 1999 and 2001 in the Black Sea, compared to less than 3 events in the non-detrended data. Regarding the duration, maximum values of approximately 40 d are observed in both seas in 2024, whereas the detrended data consistently show durations below 20 d. When considering MHWs intensity, consistently with SST-based metrics, the Black Sea constantly shows larger values with respect to the Mediterranean Sea.

After removing the warming trend, the number of MHW events shows negative trends in all regions, with statistically significant values observed in the global reanalysis (Fig. A2, right and Table A1). In contrast, most trends from the regional reanalysis become non-significant after detrending. The global reanalysis also shows lower event frequency trends compared to the regional reanalysis across the study areas. Event duration exhibits the strongest trend of 5 d per decade in the Aegean Sea. In some areas, such as the entire Mediterranean, the WMED and EMED, and the Black Sea, duration trends from the global reanalysis are higher than those evaluated from the regional datasets. Furthermore, all duration trends become negative, or not significant, after detrending. Considering the MHWs intensity, most of the analyzed regions show not statistically significant values, with

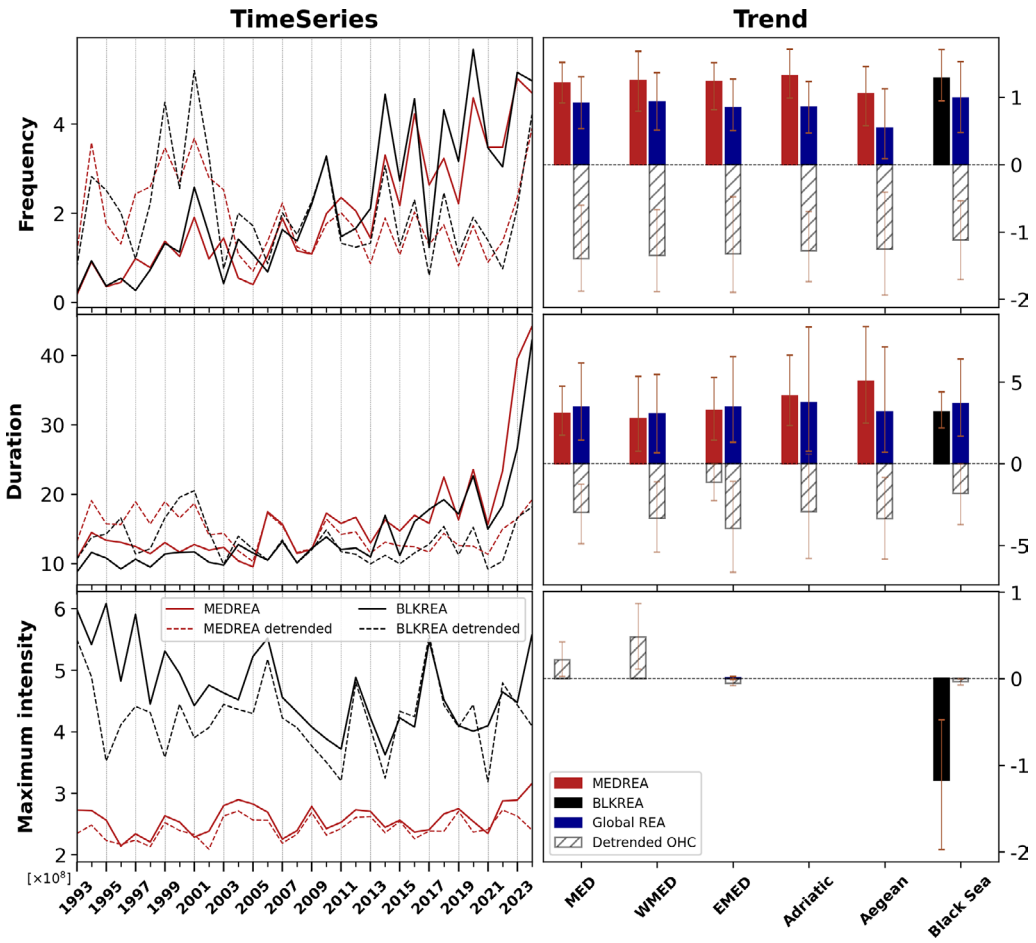


Figure A2. Left: time series of annual MHWs metrics number, duration (in days), and maximum intensity (in J m^{-2}) – averaged over the entire Mediterranean (red lines) and Black (black lines) Seas, comparing the OHC (0–40 m) definition without detrending (solid lines) with the OHC-detrended approach (dashed lines), based on regional reanalysis data (product refs. no. 3 and 4 in Table 1). Right: long-term trends (1993–2024) in MHWs number (events per decade), duration (days per decade), and maximum intensity (W m^{-2}), derived from regional and global reanalyses (product ref. no. 3, 4 and 5 in Table 1), for selected (sub)regions following Dayan et al. (2022): the entire Mediterranean (MED), the western (WMED) and eastern (EMED) Mediterranean basins, and the Adriatic, Aegean, and Black Seas. Brown lines indicate the 95 % confidence interval. Solid bars show standard metrics definition, striped bars show SST de-trended metrics.

positive trends in the Mediterranean Sea and especially in the WMED basin when detrended OHC values are used.

Code and data availability. This study is based on public databases, and their references are listed in Table 1. For marine heatwave detection, this study employs the Python-based toolbox available at https://github.com/ecjoliver/marineHeatWaves (Oliver, 2016).

Author contributions. LL led the organization of the study, prepared the manuscript, defined plots and figure layout, participated in code implementation, and presented the results during meetings. RM contributed to key decisions and analysis discussions, which were essential to shaping the final form of the manuscript, worked on the code, especially for figure preparation, and reviewed the manuscript. ES provided useful input to the analyses throughout the study, contributed to the understanding of the code, and played a very important role in analyses related to the Mediterranean Sea, particularly the Adriatic Sea. He also reviewed the manuscript. RMcA provided scientific guidance from the early stages, helped define objectives and conclusions, contributed with the initial analysis using the original code, and revised the manuscript, including scientific content and English writing. FC parallelized the processing code for MHW detection, which was crucial in accelerating the analyses, and actively contributed to scientific discussions. EC revised the manuscript in depth, improved analyses, results presentation, and conclusions, and contributed to leadership and planning. MI, EJ, and PM participated in technical discussions, supported the interpretation of results, and reviewed the manuscript. AA contributed to specific analyses and helped improve the manuscript. FM participated in meetings where key aspects were discussed and followed the manuscript development.

Competing interests. The contact author has declared that none of the authors has any competing interests.

Disclaimer. The Copernicus Marine Service offering is regularly updated to ensure it remains at the forefront of user requirements. In this process, some products may undergo replacement or renaming, leading to the removal of certain product IDs from the catalogue. If readers have any questions or require assistance regarding these modifications, please feel free to reach out to the Copernicus Marine Service user support team for further guidance. They will be able to provide the necessary information to address concerns and find suitable alternatives.

Publisher's note: Copernicus Publications remains neutral with regard to jurisdictional claims made in the text, published maps, institutional affiliations, or any other geographical representation in this paper. The authors bear the ultimate responsibility for providing appropriate place names. Views expressed in the text are those of the authors and do not necessarily reflect the views of the publisher.

Acknowledgements. The authors thank the coordination team of the *Copernicus Ocean State Report* issue 10 (*OSR10*), especially Karina Von Schuckmann, for her valuable suggestions that significantly improved the manuscript at all levels. We also acknowledge Lorena Moreira Mendez and Alvaro de Pascual for their technical support and for organizing the *OSR10* meetings, which provided a very fruitful environment for discussion with a group of researchers. The authors thank Urmas Raudsepp and other anonymous referees for their constructive comments that improved the manuscript.

Financial support. This research was funded by the Copernicus Marine Service through the Black Sea Monitoring and Forecasting Centre (Contract No. 2425L04-COP-MFC BLK-5400) and the Mediterranean Sea Monitoring and Forecasting Centre (Contract No. 2425L05-COP-MFC MED-5500). RMcA was supported by ObsSea4Clim "Ocean observations and indicators for climate and assessments" funded by the European Union, grant agreement number: 101136548, contribution number 43.

Review statement. This paper was edited by Pierre-Marie Poulain and reviewed by Urmas Raudsepp, Mélanie Juza, and two anonymous referees.

References

Amaya, D. J., Jacox, M. G., Fewings, M. R., Saba, V. S., Stuecker, M. F., Rykaczewski, R. R., Ross, A. C., Stock, C. A., Capotondi, A., Petrik, C. M., Bograd, S. J., Alexander, M. A., Cheng, W., Hermann, A. J., Kearney, K. A., and Powell, B. S.: Marine heatwaves need clear definitions so coastal communities can adapt, Nature, 616, 29–32, https://doi.org/10.1038/d41586-023-00924-2, 2023.

Beuvier, J., Béranger, K., Lebeaupin Brossier, C., Somot, S., Sevault, F., Drillet, Y., Bourdallé-Badie, R., Ferry, N., and Lyard, F.: Spreading of the Western Mediterranean Deep Water after winter 2005: Time scales and deep cyclone transport, J. Geophys. Res.-Oceans, 117, https://doi.org/10.1029/2011JC007679, 2012.

Bonino, G., Masina, S., Galimberti, G., and Moretti, M.: Southern Europe and western Asian marine heatwaves (SEWA-MHWs): a dataset based on macroevents, Earth Syst. Sci. Data, 15, 1269–1285, https://doi.org/10.5194/essd-15-1269-2023, 2023.

Capet, A., Vandenbulcke, L., and Grégoire, M.: A new intermittent regime of convective ventilation threatens the Black Sea oxygenation status, Biogeosciences, 17, 6507–6525, https://doi.org/10.5194/bg-17-6507-2020, 2020.

Capotondi, A., Rodrigues, R. R., Sen Gupta, A., Benthuysen, J. A., Deser, C., Frölicher, T. L., Lovenduski, N. S., Amaya, D. J., Le Grix, N., Xu, T., Hermes, J., Holbrook, N. J., Martinez-Villalobos, C., Masina, S., Koll Roxy, M., Schaeffer, A., Schlegel, R. W., Smith, K. E., and Wang, C.: A global overview of marine heatwaves in a changing climate, Commun. Earth Environ., 5, 701, https://doi.org/10.1038/s43247-024-01806-9, 2024.

Cheminée, A., Le Direach, L., Rouanet, E., Astruch, P., Goujard, A., Blanfuné, A., Bonhomme, D., Chassaing, L., Jouvenel, J.-Y., Ruitton, S., Thibaut, T., and Harmelin-Vivien, M.: All shallow coastal habitats matter as nurseries for Mediterranean juvenile fish, Sci. Rep., 11, 14631, https://doi.org/10.1038/s41598-021-93557-2, 2021.

Cheng, Y., Zhang, M., Song, Z., Wang, G., Zhao, C., Shu, Q., Zhang, Y., and Qiao, F.: A quantitative analysis of marine heatwaves in response to rising sea surface temperature, Sci. Total Environ., 881, 163396, https://doi.org/10.1016/j.scitotenv.2023.163396, 2023.

Cooley, S., D. Schoeman, L. Bopp, P. Boyd, S. Donner, D. Y. Ghebrehiwet, S.-I. Ito, W. Kiessling, P. Martinetto, E. Ojea, M.-F. Racault, B. Rost, and M. Skern-Mauritzen: Oceans and Coastal Ecosystems and Their Services, In: Climate Change 2022: Impacts, Adaptation and Vulnerability. Contribution of Working Group II to the Sixth Assessment Report of the Intergovernmental Panel on Climate Change, edited by: Pörtner, H.-O., Roberts, D. C., Tignor, M., Poloczanska, E. S., Mintenbeck, K., Alegría, A., Craig, M., Langsdorf, S., Löschke, S., Möller, V., Okem, A., and Rama, B., Cambridge University Press, Cambridge, UK and New York, NY, USA, 379–550, https://doi.org/10.1017/9781009325844.005, 2022.

Darmaraki, S., Denaxa, D., Theodorou, I., Livanou, E., Rigatou, D., Raitsos, D. E., Stavrakidis-Zachou, O., Dimarchopoulou, D., Bonino, G., McAdam, R., Organelli, E., Pitsouni, A., and Parasyris, A.: Marine heatwaves in the Mediterranean Sea: A literature review, Mediterr. Mar. Sci., 25, 586–620, https://doi.org/10.12681/mms.38392, 2024.

Dayan, H., McAdam, R., Masina, S., and Speich, S.: Diversity of marine heatwave trends across the Mediterranean Sea over the last decades, Copernicus Marine Service Ocean State Report, 6, 205–210, https://doi.org/10.1080/1755876X.2022.2095169, 2022.

Dayan, H., McAdam, R., Juza, M., Masina, S., and Speich, S.: Marine heat waves in the Mediterranean Sea: An assessment from the surface to the subsurface to meet national needs, Frontiers in Marine Science, 10, 1045138, https://doi.org/10.3389/fmars.2023.1045138, 2023.

Dee, D. P., Uppala, S. M., Simmons, A. J., Berrisford, P., Poli, P., Kobayashi, S., Andrae, U., Balmaseda, M. A., Balsamo, G., Bauer, P., Bechtold, P., Beljaars, A. C. M., van de Berg, L., Bidlot, J., Bormann, N., Delsol, C., Dragani, R., Fuentes, M., Geer, A. J., Haimberger, L., Healy, S. B., Hersbach, H., Hólm, E. V., Isaksen, L., Kållberg, P., Köhler, M., Matricardi, M., McNally, A. P., Monge-Sanz, B. M., Morcrette, J.-J., Park, B.-K., Peubey, C., de Rosnay, P., Tavolato, C., Thépaut, J.-N., and Vitart, F.: The ERA-Interim reanalysis: Configuration and performance of the data assimilation system, Q. J. R. Meteorol. Soc., 137, 553–597, https://doi.org/10.1002/qj.828, 2011.

Denamiel, C., Tojčić, I., and Pranić, P.: A new vision of the Adriatic Dense Water future under extreme warming, Ocean Sci., 21, 37–62, https://doi.org/10.5194/os-21-37-2025, 2025.

Drévillon, M., Lellouche, J.-M., Régnier, C., Garric, G., Bricaud, C., Hernandez, O., and Bourdallé-Badie, R.: EU Copernicus Marine Service Quality Information Document for the Global Ocean Physics Reanalysis, GLOBAL_MULTIYEAR_PHY_001_030, issue 1.6, Mercator Ocean International, https://documentation.marine.copernicus.eu/QUID/CMEMS-GLO-QUID-001-030.pdf (last access: 31 October 2025), 2024a.

Drévillon, M., Fernandez, E., and Lellouche, J.-M.: EU Copernicus Marine Service Product User Manual for the Global Ocean Physics Reanalysis, GLOBAL_MULTIYEAR_PHY_001_030, issue 1.6, Mercator Ocean International, https://documentation.marine.copernicus.eu/PUM/CMEMS-GLO-PUM-001-030.pdf (last access: 31 October 2025), 2024b.

Dutheil, C., Lal, S., Lengaigne, M., Cravatte, S., Menkès, C., Receveur, A., Börgel, F., Gröger, M., Houlbreque, F., Le Gendre, R., Mangolte, I., Peltier, A., and Meier, H. E. M.: The massive 2016 marine heatwave in the Southwest Pacific: An "El Niño–Madden-Julian Oscillation" compound event, Sci. Adv., 10, https://doi.org/10.1126/sciadv.adp2948, 2024.

Embury, O., Merchant, C. J., Good, S. A., Rayner, N. A., Høyer, J. L., Atkinson, C., Block, T., Alerskans, E., Pearson, K. J., Worsfold, M., McCarroll, N., and Donlon, C.: Satellite-based time-series of sea-surface temperature since 1980 for climate applications, Sci. Data, 11, 326, https://doi.org/10.1038/s41597-024-03147-w, 2024.

Escudier, R., Clementi, E., Cipollone, A., Pistoia, J., Drudi, M., Grandi, A., Lyubartsev, V., Lecci, R., Aydoğdu, A., Delrosso, D., Omar, M., Masina, S., Coppini, G., and Pinardi, N.: A high resolution reanalysis for the Mediterranean Sea, Front. Earth Sci., 9, 702285, https://doi.org/10.3389/feart.2021.702285, 2021.

Escudier, R., Clementi, E., Nigam, T., Aydogdu, A., Fini, E., Pistoia, J., Grandi, A., and Miraglio, P.: EU Copernicus Marine Service Quality Information Document for the Mediterranean Sea Physics Reanalysis, MEDSEA_MULTIYEAR_PHY_006_004, issue 2.4, Mercator Ocean International, https://documentation.marine.copernicus.eu/QUID/CMEMS-MED-QUID-006-004.pdf (last access: 31 October 2025), 2024.

Estaque, T., Richaume, J., Bianchimani, O., Schull, Q., Mérigot, B., Bensoussan, N., Bonhomme, P., Vouriot, P., Sartoretto, S., Monfort, T., Basthard-Bogain, S., Fargetton, M., Gatti, G., Barth, L., Cheminée, A., and Garrabou, J.: Marine heatwaves on the rise: One of the strongest ever observed mass mortality event in temperate gorgonians, Glob. Change Biol., 29, 6159–6162, https://doi.org/10.1111/gcb.16931, 2023.

Estournel, C., Estaque, T., Ulses, C., Barral, Q.-B., and Marsaleix, P.: Extreme sensitivity of the northeastern Gulf of Lion (western Mediterranean) to subsurface heatwaves: physical processes and insights into effects on gorgonian populations in the summer of 2022, Ocean Sci., 21, 1487–1503, https://doi.org/10.5194/os-21-1487-2025, 2025.

EU Copernicus Marine Service Product: Black Sea – High Resolution L4 Sea Surface Temperature Reprocessed, Mercator Ocean International [data set], https://doi.org/10.48670/moi-00160, 2024a.

EU Copernicus Marine Service Product: Mediterranean Sea – High Resolution L4 Sea Surface Temperature Reprocessed, Mercator Ocean International [data set], https://doi.org/10.48670/moi-00173, 2024b.

EU Copernicus Marine Service Product: Black Sea Physics Reanalysis, Mercator Ocean International [data set], https://doi.org/10.48670/mds-00356, 2024c.

EU Copernicus Marine Service Product: Mediterranean Sea Physics Reanalysis, Mercator Ocean International [data set], https://doi.org/10.25423/CMCC/MEDSEA_MULTIYEAR_PHY_006_004_E3R1, 2024d.

EU Copernicus Marine Service Product: Global Ocean Physics Reanalysis, Mercator Ocean International [data set], https://doi.org/10.48670/moi-00021, 2024e.

EU Copernicus Marine Service Information: Black Sea Ocean Heat Content Anomaly (0–300 m) time series and trend from Reanalysis & Multi-Observations Reprocessing, Mercator Ocean International, https://doi.org/10.48670/moi-00306, 2024a.

EU Copernicus Marine Service Information: Mediterranean Ocean Heat Content Anomaly (0–700 m) time series and trend from Reanalysis & Multi-Observations Reprocessing, Mercator Ocean International, https://doi.org/10.48670/moi-00261, 2024b.

EU Copernicus Marine Service Information: Mediterranean Water Mass Formation Rates from Reanalysis, Mercator Ocean International, https://doi.org/10.48670/mds-00318, 2024c.

Fox-Kemper, B., Hewitt, H. T., Xiao, C., Aðalgeirsdóttir, G., Drijfhout, S. S., Edwards, T. L., Golledge, N. R., Hemer, M., Kopp, R. E., Krinner, G., Mix, A., Notz, D., Nowicki, S., Nurhati, I. S., Ruiz, L., Sallée, J.-B., Slangen, A. B. A., and Yu, Y.: Ocean, Cryosphere and Sea Level Change, In: Climate Change 2021: The Physical Science Basis. Contribution of Working Group I to the Sixth Assessment Report of the Intergovernmental Panel on Climate Change, edited by: Masson-Delmotte, V., Zhai, P., Pirani, A., Connors, S. L., Péan, C., Berger, S., Caud, N., Chen, Y., Goldfarb, L., Gomis, M. I., Huang, M., Leitzell, K., Lonnoy, E., Matthews, J. B. R., Maycock, T. K., Waterfield, T., Yelekçi, O., Yu, R., and Zhou, B., Cambridge University Press, Cam-

bridge, United Kingdom and New York, NY, USA, 1211–1362, https://doi.org/10.1017/9781009157896.011, 2021.

Gačić, M., Lascaratos, A., Manca, B. B., and Mantziafou, A.: Adriatic deep water and interaction with the Eastern Mediterranean Sea, in: Physical oceanography of the Adriatic Sea: Past, present and future, Springer Netherlands, Dordrecht, 111–142, https://doi.org/10.1007/978-94-015-9819-4_4, 2001.

Garrabou, J., Gómez-Gras, D., Medrano, A., Cerrano, C., Ponti, M., Schlegel, R., Bensoussan, N., Turicchia, E., Sini, M., Gerovasileiou, V., Teixido, N., Mirasole, A., Tamburello, L., Cebrian, E., Rilov, G., Ledoux, J.-B., Ben Souissi, J., Khamassi, F., Ghanem, R., Benabdi, M., Grimes, S., Ocaña, O., Bazairi, H., Hereu, B., Linares, C., Kersting, D. K., la Rovira, G., Ortega, J., Casals, D., Pagès-Escolà, M., Margarit, N., Capdevila, P., Verdura, J., Ramos, A., Izquierdo, A., Barbera, C., Rubio-Portillo, E., Anton, I., López-Sendino, P., Díaz, D., Vázquez-Luis, M., Duarte, C., Marbà, N., Aspillaga, E., Espinosa, F., Grech, D., Guala, I., Azzurro, E., Farina, S., Gambi, M. C., Chimienti, G., Montefalcone, M., Azzola, A., Pulido Mantas, T., Fraschetti, S., Ceccherelli, G., Kipson, S., Bakran-Petricioli, T., Petricioli, D., Jimenez, C., Katsanevakis, S., Kizilkaya, I. T., Kizilkaya, Z., Sartoretto, S., Elodie, R., Ruitton, S., Comeau, S., Gattuso, J.-P., and Harmelin, J.-G.: Marine heatwaves drive recurrent mass mortalities in the Mediterranean Sea, Glob. Change Biol., 28, 5708–5725, https://doi.org/10.1111/gcb.16301, 2022.

Granata, A., Cubeta, A., Minutoli, R., Bergamasco, A., and Guglielmo, L.: Distribution and abundance of fish larvae in the northern Ionian Sea (Eastern Mediterranean), Helgoland Mar. Res., 65, 381–398, https://doi.org/10.1007/s10152-010-0231-2, 2011.

Gregory, C. H., Artana, C., Lama, S., León-FonFay, D., Sala, J., Xiao, F., Xu, T., Capotondi, A., Martinez-Villalobos, C., and Holbrook, N. J.: Global marine heatwaves under different flavors of ENSO, Geophys. Res. Lett., 51, e2024GL110399, https://doi.org/10.1029/2024GL110399, 2024.

Gunduz, G., Causio, S., Bonino, G., Vandenbulcke, L., Gregorie, M., Lima, L., Ciliberti, S., Ilicak, M., Aydogdu, A., Masina, S., Coppini, G., and Pinardi, N.: Coastal upwelling along the Turkish coast of the Black Sea: Its role in the distribution of the hydrographic properties, in: Copernicus Ocean State Report, issue 6, J. Oper. Oceanogr., 15, s205–s211, https://doi.org/10.1080/1755876X.2022.2095169, 2022.

Hamdeno, M. and Alvera-Azcaráte, A.: Marine heatwaves characteristics in the Mediterranean Sea: Case study the 2019 heatwave events, Front. Mar. Sci., 10, 1093760, https://doi.org/10.3389/fmars.2023.1093760, 2023.

Hersbach, H., Bell, B., Berrisford, P., Hirahara, S., Horányi, A., Munoz-Sabater, J., Nicolas, J., Peubey, C., Radu, R., Schepers, D., Simmons, A., Soci, C., Abdalla, S., Abellan, X., Balsamo, G., Bechtold, P., Biavati, G., Bidlot, J., Bonavita, M., De Chiara, G., Dahlgren, P., Dee, D., Diamantakis, M., Dragani, R., Flemming, J., Forbes, R., Fuentes, M., Geer, A., Haimberger, L., Healy, S., Hogan, R. J., Hólm, E. V., Janisková, M., Keeley, S., Laloyaux, P., Lopez, P., Lupu, C., Radnoti, G., de Rosnay, P., Rozum, I., Vamborg, F., Villaume, S., and Thépaut, J.-N.: The ERA5 global reanalysis, Q. J. R. Meteorol. Soc., 146, 1999–2049, https://doi.org/10.1002/qj.3803, 2020.

Hobday, A. J., Alexander, L. V., Perkins, S. E., Smale, D. A., Straub, S. C., Oliver, E. C. J., Benthuysen, J. A., Burrows, M. T., Donat, M. G., Feng, M., Holbrook, N. J., Moore, P. J., Scannell, H. A., Sen Gupta, A., and Wernberg, T.: A hierarchical approach to defining marine heatwaves, Prog. Oceanogr., 141, 227–238, https://doi.org/10.1016/j.pocean.2015.12.014, 2016.

Hobday, A. J., Oliver, E. C. J., Sen Gupta, A., Benthuysen, J. A., Burrows, M. T., Donat, M. G., Holbrook, N. J., Moore, P. J., Thomsen, M. S., Wernberg, T., and Smale, D. A.: Categorizing and naming marine heatwaves, Oceanography, 31, 162–173, https://doi.org/10.5670/oceanog.2018.205, 2018.

Holbrook, N. J., Scannell, H. A., Sen Gupta, A., Benthuysen, J. A., Feng, M., Oliver, E. C. J., Alexander, L. V., Burrows, M. T., Donat, M. G., Hobday, A. J., Moore, P. J., Perkins-Kirkpatrick, S. E., Smale, D. A., Straub, S. C., and Wernberg, T.: A global assessment of marine heatwaves and their drivers, Nat. Commun., 10, 2624, https://doi.org/10.1038/s41467-019-10206-z, 2019.

Houpert, L., Testor, P., Durrieu de Madron, X., Somot, S., D'Ortenzio, F., Estournel, C., and Lavigne, H.: Seasonal cycle of the mixed layer, the seasonal thermocline and the upper-ocean heat storage rate in the Mediterranean Sea derived from observations, Prog. Oceanogr., 132, 333–352, https://doi.org/10.1016/j.pocean.2014.11.004, 2015.

Ivanov, L. I., Backhaus, J. O., Özsoy, E., and Wehde, H.: Convection in the Black Sea during cold winters, J. Marine Syst., 31, 65–76, https://doi.org/10.1016/S0924-7963(01)00047-1, 2001.

Izquierdo, P., González Taboada, F., González-Gil, R., Arrontes, J., and Rico, J. M.: Alongshore upwelling modulates the intensity of marine heatwaves in a temperate coastal sea, Sci. Total Environ., 835, 155478, https://doi.org/10.1016/j.scitotenv.2022.155478, 2022.

Juza, M., Fernández-Mora, À., and Tintoré, J.: Sub-regional marine heat waves in the Mediterranean Sea from observations: Long-term surface changes, sub-surface and coastal responses, Front. Mar. Sci., 9, 785771, https://doi.org/10.3389/fmars.2022.785771, 2022.

Kara, A. B., Helber, R. W., Boyer, T. P., and Elsner, J. B.: Mixed layer depth in the Aegean, Marmara, Black and Azov Seas: Part I: General features, J. Marine Syst., 78, S169–S180, https://doi.org/10.1016/j.jmarsys.2009.01.022, 2009.

Kokkini, Z., Mauri, E., Gerin, R., Poulain, P. M., Simoncelli, S., and Notarstefano, G.: On the salinity structure in the South Adriatic as derived from float and glider observations in 2013–2016, Deep-Sea Res. Pt. II, https://doi.org/10.1016/j.dsr2.2019.07.013, 2020.

Konsta, K., Doxa, A., Katsanevakis, S., and Mazaris, A. D.: Projected marine heatwaves over the Mediterranean Sea and the network of marine protected areas: A three-dimensional assessment, Climatic Change, 178, https://doi.org/10.1007/s10584-025-03860-4, 2025.

Kubryakov, A. A., Mikaelyan, A. S., Stanichny, S. V., and Kubryakova, E. A.: Seasonal stages of chlorophyll-a vertical distribution and its relation to the light conditions in the Black Sea from Bio-Argo measurements, J. Geophys. Res.-Oceans, 125, e2020JC016790, https://doi.org/10.1029/2020JC016790, 2020.

Lecci, R., Lima, L., Cretì, S., and Jansen, E.: EU Copernicus Marine Service Product User Manual for the Black Sea Physics Reanalysis, BLKSEA_MULTIYEAR_PHY_007_004, issue 4.0, Mercator Ocean International, https://documentation.marine.copernicus.eu/PUM/CMEMS-BLK-PUM-007-004.pdf (last access: 31 October 2025), 2024a.

Lecci, R., Drudi, M., Grandi, A., and Clementi, E.: EU Copernicus Marine Service Product User Manual for the Black Sea Physics Reanalysis, MEDSEA_MULTIYEAR_PHY_006_004, issue 2.4, Mercator Ocean International, https://documentation.marine.copernicus.eu/PUM/CMEMS-MED-PUM-006-004.pdf (last access: 31 October 2025), 2024b.

Lellouche, J.-M., Greiner, E., Bourdallé-Badie, R., Garric, G., Melet, A., Drévillon, M., Bricaud, C., Hamon, M., Le Galloudec, O., Regnier, C., Candela, T., Testut, C.-E., Gasparin, F., Ruggiero, G., Benkiran, M., Drillet, Y., and Le Traon, P.-Y.: The Copernicus Global 1/12° oceanic and sea ice GLORYS12 reanalysis, Front. Earth Sci., 9, 698876, https://doi.org/10.3389/feart.2021.698876, 2021.

Le Meur, J., Wirth, A., Paladini de Mendoza, F., Miserocchi, S., and Cardin, V.: Intermittent supply of dense water to the deep South Adriatic Pit: An observational study, Front. Mar. Sci., 12, https://doi.org/10.3389/fmars.2025.1516780, 2025.

Li, M., Organelli, E., Serva, F., Bellacicco, M., Landolfi, A., Pisano, A., Marullo, S., Shen, F., Mignot, A., van Gennip, S., and Santoleri, R.: Phytoplankton spring bloom inhibited by marine heatwaves in the north-western Mediterranean Sea, Geophys. Res. Lett., 51, https://doi.org/10.1029/2024GL109141, 2024.

Lima, L., Peneva, E., Ciliberti, S., Masina, S., Lemieux, B., Storto, A., and Chtirkova, B.: Section 2.6: Ocean heat content in the Black Sea, in: Copernicus Marine Service Ocean State Report, Issue 4, J. Oper. Oceanogr., 13, s41–s47, https://doi.org/10.1080/1755876X.2020.1785097, 2020.

Lima, L., Ciliberti, S. A., Aydoğdu, A., Masina, S., Escudier, R., Cipollone, A., Azevedo, D., Causio, S., Peneva, E., Lecci, R., Clementi, E., Jansen, E., Ilicak, M., Cretì, S., Stefanizzi, L., Palermo, F., and Coppini, G.: Climate signals in the Black Sea from a multidecadal eddy-resolving reanalysis, Front. Mar. Sci., 8, 710973, https://doi.org/10.3389/fmars.2021.710973, 2021.

Lima, L., Azevedo, D., Ilicak, M., Jansen, E., Costa, F., Causio, S., Cretí, S., and Clementi, E.: EU Copernicus Marine Service Quality Information Document for the Black Sea Physics Reanalysis, BLKSEA_MULTIYEAR_PHY_007_004, issue 5.0, Mercator Ocean International, https://documentation.marine.copernicus.eu/QUID/CMEMS-BLK-QUID-007-004.pdf (last access: 31 October 2025), 2024.

Lima, L., Azevedo, D., Ilicak, M., Jansen, E., Costa, F., Sozer, A., Miraglio, P., and Clementi, E.: Advances in monitoring the Black Sea: a new regional multidecadal ocean reanalysis at 1/40° resolution, Ocean Sci., 22, 1051–1072, https://doi.org/10.5194/os-22-1051-2026, 2026.

López-Jurado, J.-L., González-Pola, C., and Vélez-Belchi, P.: Observation of an abrupt disruption of the long-term warming trend at the Balearic Sea, western Mediterranean Sea, in summer 2005, Geophys. Res. Lett., 32, L24606, https://doi.org/10.1029/2005GL024430, 2005.

Ma, X. and Chen, G.: Marine heatwaves are shaping the vertical structure of phytoplankton in the global ocean, Commun. Earth Environ., 6, 715, https://doi.org/10.1038/s43247-025-02718-y, 2025.

Macias, J. C., Avila Zaragozá, P., Karakassis, I., Sanchez-Jerez, P., Massa, F., Fezzardi, D., Yücel Gier, G., Franičević, V., Borg, J. A., Chapela Pérez, R. M., Tomassetti, P., Angel, D. L., Marino, G., Nhhala, H., Hamza, H., Carmignac, C., and Fourdain, L.: Allocated zones for aquaculture: A guide for the establishment of coastal zones dedicated to aquaculture in the Mediterranean and the Black Sea, General Fisheries Commission for the Mediterranean: Studies and Reviews, 97, 1–90, FAO, https://openknowledge.fao.org/server/api/core/bitstreams/5c494a74-d1f9-4f9d-9b26-9ff8f3b0f634/content (last access: 21 January 2026), 2019.

Martínez, J., Leonelli, F. E., García-Ladona, E., Garrabou, J., Kersting, D. K., Bensoussan, N., and Pisano, A.: Evolution of marine heatwaves in warming seas: The Mediterranean Sea case study, Front. Mar. Sci., 10, https://doi.org/10.3389/fmars.2023.1193164, 2023.

Marullo, S., Serva, F., Iacono, R., Napolitano, E., di Sarra, A., Meloni, D., Monteleone, F., Sferlazzo, D., De Silvestri, L., and de Toma, V.: Record-breaking persistence of the 2022/23 marine heatwave in the Mediterranean Sea, Environ. Res. Lett., 18, 114041, https://doi.org/10.1088/1748-9326/ad02ae, 2023.

McAdam, R., Masina, S., and Gualdi, S.: Seasonal forecasting of subsurface marine heatwaves, Commun. Earth Environ., 4, 225, https://doi.org/10.1038/s43247-023-00892-5, 2023.

Mignot, A., von Schuckmann, K., Landschützer, P., Gasparin, F., van Gennip, S., Perruche, C., Lamouroux, J., and Amm, T.: Decrease in air-sea CO2 fluxes caused by persistent marine heatwaves, Nat. Commun., 13, 4300, https://doi.org/10.1038/s41467-022-31983-0, 2022.

Mohamed, B., Ibrahim, O., and Nagy, H.: Sea Surface temperature variability and marine heatwaves in the Black Sea, Remote Sens., 14, 2383, https://doi.org/10.3390/rs14102383, 2022.

Nenciu, M., Ni?ă, V., Lazăr, L., Spînu, A., and Vlăsceanu-Mateescu, E.: Fostering the Development of Western Black Sea Aquaculture: A Scientific Case Study for Finfish Cage Farming Allocated Zone Designation, Fishes, 8, 104, https://doi.org/10.3390/fishes8020104, 2023.

Oliver, E. C. J.: marineHeatWaves, GitHub [code], https://github.com/ecjoliver/marineHeatWaves (last access: 1 April 2026), 2016.

Oliver, E. C. J., Donat, M. G., Burrows, M. T., Moore, P. J., Smale, D. A., Alexander, L. V., Benthuysen, J. A., Feng, M., Sen Gupta, A., Hobday, A. J., Holbrook, N. J., Perkins-Kirkpatrick, S. E., Scannell, H. A., Straub, S. C., and Wernberg, T.: Longer and more frequent marine heatwaves over the past century, Nat. Commun., 9, 1324, https://doi.org/10.1038/s41467-018-03732-9, 2018.

Özsoy, E. and Ünlüata, Ü.: Oceanography of the Black Sea: a review of some recent results, Earth-Sci. Rev., 42, 231–272, https://doi.org/10.1016/S0012-8252(97)81859-4, 1997.

Paladini de Mendoza, F., Schroeder, K., Langone, L., Chiggiato, J., Borghini, M., Giordano, P., Verazzo, G., and Miserocchi, S.: Deep-water hydrodynamic observations of two moorings sites on the continental slope of the southern Adriatic Sea (Mediterranean Sea), Earth Syst. Sci. Data, 14, 5617–5635, https://doi.org/10.5194/essd-14-5617-2022, 2022.

Parras-Berrocal, I. M., Vázquez, R., Cabos, W., Sein, D. V., Álvarez, O., Bruno, M., and Izquierdo, A.: Dense water formation in the eastern Mediterranean under a global warming scenario, Ocean Sci., 19, 941–952, https://doi.org/10.5194/os-19-941-2023, 2023.

Pastor, F., Paredes-Fortuny, L., and Khodayar, S.: Mediterranean marine heatwaves intensify in the presence of concur-

rent atmospheric heatwaves, Commun. Earth Environ., 5, 797, https://doi.org/10.1038/s43247-024-01982-8, 2024.

Pisano, A., Nardelli, B. B., Tronconi, C., and Santoleri, R.: The new Mediterranean optimally interpolated pathfinder AVHRR SST dataset (1982–2012), Remote Sens. Environ., 176, 107–116, https://doi.org/10.1016/j.rse.2016.01.019, 2016.

Pisano, A., Fanelli, C., Massi, A., Tronconi, C., Cesarini, C., La Padula, F., Buongiorno Nardelli, B., and Ciani, D.: EU Copernicus Marine Service Quality Information Document for the Black Sea – High Resolution L4 Sea Surface Temperature Reprocessed, SST_BS_SST_L4_REP_OBSERVATIONS_010_022, Issue 4.0, Mercator Ocean International, https://documentation.marine.copernicus.eu/QUID/CMEMS-SST-QUID-010-021-022-041-042.pdf (last access: 31 October 2025), 2024a.

Pisano, A., Fanelli, C., Massi, A., Tronconi, C., Cesarini, C., La Padula, F., Buongiorno Nardelli, B., and Ciani, D.: EU Copernicus Marine Service Product User Manual for the Black Sea - High Resolution L4 Sea Surface Temperature Reprocessed, SST_BS_SST_L4_REP_OBSERVATIONS_010_022, Issue 4.0, Mercator Ocean International, https://documentation.marine.copernicus.eu/PUM/CMEMS-SST-PUM-010-021-022-041-042.pdf (last access: 31 October 2025), 2024b.

Pisano, A., Fanelli, C., Massi, A., Tronconi, C., Cesarini, C., La Padula, F., Buongiorno Nardelli, B., and Ciani, D.: EU Copernicus Marine Service Quality Information Document for the Mediterranean Sea – High Resolution L4 Sea Surface Temperature Reprocessed, SST_MED_SST_L4_REP_OBSERVATIONS_010_021, Issue 4.0, Mercator Ocean International, https://documentation.marine.copernicus.eu/QUID/CMEMS-SST-QUID-010-021-022-041-042.pdf (last access: 31 October 2025), 2024c.

Pisano, A., Fanelli, C., Massi, A., Tronconi, C., Cesarini, C., La Padula, F., Buongiorno Nardelli, B., and Ciani, D.: EU Copernicus Marine Service Product User Manual for the Mediterranean Sea - High Resolution L4 Sea Surface Temperature Reprocessed, SST_MED_SST_L4_REP_OBSERVATIONS_010_021, Issue 4.0, Mercator Ocean International, https://documentation.marine.copernicus.eu/PUM/CMEMS-SST-PUM-010-021-022-041-042.pdf (last access: 31 October 2025), 2024d.

Rosselló, P., Pascual, A., and Combes, V.: Assessing marine heat waves in the Mediterranean Sea: A comparison of fixed and moving baseline methods, Front. Mar. Sci., 10, 1168368, https://doi.org/10.3389/fmars.2023.1168368, 2023.

Sen Gupta, A., Thomsen, M., Benthuysen, J. A., Hobday, A. J., Oliver, E., Alexander, L. V., Burrows, M. T., Donat, M. G., Feng, M., Holbrook, N. J., Perkins-Kirkpatrick, S., Moore, P. J., Rodrigues, R. R., Scannell, H. A., Taschetto, A. S., Ummenhofer, C. C., Wernberg, T., and Smale, D. A.: Drivers and impacts of the most extreme marine heatwave events, Sci. Rep., 10, 19359, https://doi.org/10.1038/s41598-020-75445-3, 2020.

Simoncelli, S. and Pinardi, N.: Water mass formation processes in the Mediterranean Sea over the past 30 years, in: Copernicus Marine Service Ocean State Report, Issue 2, J. Oper. Oceanogr., 11, s13–s16, https://doi.org/10.1080/1755876X.2018.1489208, 2018.

Smith, K. E., Burrows, M. T., Hobday, A. J., King, N. G., Moore, P. J., Sen Gupta, A., Thomsen, M. S., Wernberg, T., and Smale, D. A.: Biological impacts of marine heatwaves, Annu. Rev. Mar. Sci., 15, 119–145, https://doi.org/10.1146/annurev-marine-032122-121437, 2023.

Stanev, E. V., Peneva, E., and Chtirkova, B.: Climate change and regional ocean water mass disappearance: Case of the Black Sea, J. Geophys. Res.-Oceans, 124, 4803–4819, https://doi.org/10.1029/2019JC015076, 2019.

Su, S., Fu, Y.-X., Sun, W., and Dong, J.: Marine heatwaves and cold spells accompanied by mesoscale eddies globally, Remote Sens., 17, 2468, https://doi.org/10.3390/rs17142468, 2025.

Sun, D., Li, F., Jing, Z., Hu, S., and Zhang, B.: Frequent marine heatwaves hidden below the surface of the global ocean, Nat. Geosci., 16, 1099–1104, 2023.

Tan, H. J., Cai, R. S., and Wu, R. G.: Summer marine heatwaves in the South China Sea: Trend, variability and possible causes, Advances in Climate Change Research, 13, 323–332, https://doi.org/10.1016/j.accre.2022.04.003, 2022.

Wang, Y. and Zhou, Y.: Seasonal dynamics of global marine heatwaves over the last four decades, Front. Mar. Sci., 11, https://doi.org/10.3389/fmars.2024.1406416, 2024.

State Planet, 7-osr10, 6, 2026
https://doi.org/10.5194/sp-7-osr10-6-2026
© Author(s) 2026. This work is distributed under
the Creative Commons Attribution 4.0 License.

Freshening of the Barents Sea during the recent decade and its impact on the outflow of dense waters

Roshin P. Raj[1,2], **Vidar S. Lien**[3], **Sourav Chatterjee**[4,5], **Saradhy Surendran**[6], **Antonio Bonaduce**[1,2], **and Laurent Bertino**[1,2]

[1]Nansen Environmental and Remote Sensing Center, Bergen, Norway
[2]Bjerknes Center for Climate Research, Bergen, Norway
[3]Institute of Marine Research, Bergen, Norway
[4]National Centre for Polar and Ocean Research, Ministry of Earth Sciences, Goa, India
[5]Centre for Climate Change Research, Indian Institute of Tropical Meteorology, Ministry of Earth Sciences, Pune, India
[6]Nansen Environmental Research Center, Cochin, India

Correspondence: Roshin P. Raj (roshin.raj@nersc.no)

Received: 5 September 2025 – Discussion started: 29 September 2025
Revised: 27 June 2026 – Accepted: 13 July 2026 – Published: 30 September 2026

Abstract. Dense water formed in the shallow Barents Sea feeds the deep branch of the Atlantic Meridional Overturning Circulation and is therefore an important part of the global climate system. The properties of dense waters in the Barents Sea are sensitive to the temperature and salinity of Atlantic Water (AW) advected into the region, as well as to the interaction with sea ice. Here, using a suite of satellite, reanalysis and in situ data for the time-period 1991–2024, we investigate the drivers of the interannual variability and recent changes in the hydrographic properties of the dense waters exiting the Barents Sea. Statistical analysis of the data shows that the freshening in the southern Barents Sea during the recent years, is primarily associated with decreased salinity of the inflowing AW. In contrast, freshening in the northern Barents Sea reflects the combined influence of fresher AW and enhanced import of sea ice from the central Arctic, driven by changes in atmospheric circulation, which temporarily halted the long-term Atlantification trend. The combination of reduced salinity and persistently warm conditions produced the lowest density of dense waters exiting the Barents Sea in the last three decades, with implications for downstream overturning circulation.

1 Introduction

The advection of Atlantic Water (AW) into the Arctic Ocean and its transformation into dense water through heat and freshwater exchanges constitute a major component of the thermohaline circulation (Aagaard, 1981; Rudels et al., 2015; Raj and Halo, 2016; Bashmachnikov et al., 2023). The shallow Barents Sea shelf (mean depth of 230 m) located along the advective path of AW (Furevik, 2001; Sundby and Drinkwater, 2007; Årthun and Eldevik, 2016) accounts for a substantial part of the dense water that is formed within the Arctic (Martin and Cavalieri, 1989). The AW entering the Barents Sea from the southwest through the Barents Sea Opening (BSO) is a major source of interannual variability in the region's hydrography (Årthun et al., 2012; Lien et al., 2024). After entering the southern Barents Sea (SBS), a large amount of the heat carried by the AW is released to the atmosphere (Serreze et al., 2007; Smedsrud et al., 2010), before travelling further north and setting the southward limit of sea ice extent in the northern Barents Sea (NBS) (Barton et al., 2018). In comparison to the SBS, the hydrographic variability in the NBS is shaped not only by variations in the AW entering from the south and north (see Fig. 1; Lind and Ingvaldsen, 2012), but also by the import of sea ice and less saline Arctic Water from the polar basin (Lind et al., 2018). After undergoing considerable modifications within the Barents Sea, the poleward flowing AW enters the polar

Published by Copernicus Publications.

Table 1. Product ID & Type, data access and documentation details of different datasets used in this study.

Product ref. no.	Product ID & Type	Data access	Documentation
1	ARCTIC_MULTIYEAR_PHY_002_003, numerical models	EU Copernicus Marine Service Product (2025)	Quality Information Document (QUID): Xie and Bertino (2025) Product User Manual (PUM): Ali et al. (2025)
2	ESA CCI SSS, satellite observations	NERC EDS Centre for Environmental Data Analysis	Boutin et al. (2025)
3	In-situ Observations (CTD)	ICES Report on Ocean Climate (IROC)	González-Pola et al. (2023)
4	ERA-5 MSLP, numerical models	Copernicus Climate Change Service (C3S): ERA5 monthly averaged data on single level	Hersbach et al. (2020)

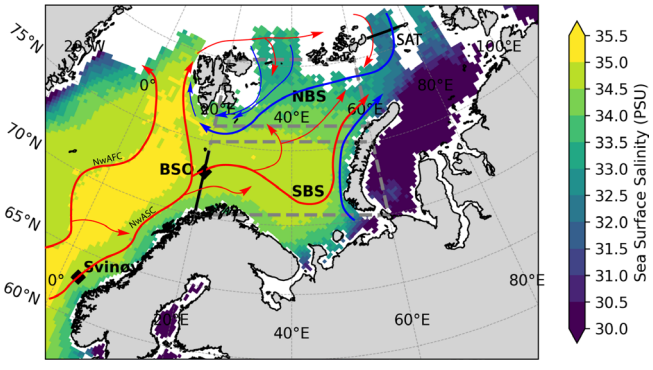


Figure 1. Mean sea surface salinity (SSS) in the eastern Nordic Seas and the Barents Sea (2010–2023) from ESA CCI SSS satellite database (see Table 1 for details). Thick black lines indicate the location of sections, Barents Sea Opening (BSO) and St. Anna Trough (SAT) shown in Fig. 6. Two black square boxes represent the locations of Svinøy and BSO shown in Fig. 2. The main circulation features of the region are overlayed (Red: Atlantic Water; Blue: Arctic Water) on the mean SSS. The Norwegian Atlantic Slope Current (NwASC; Orvik et al., 2001) and Norwegian Atlantic Front Current (NwAFC; Raj et al., 2019) transporting warm AW poleward are also indicated. The location of the NBS and SBS are represented by two dashed grey boxes.

basin through the St. Anna Trough (SAT) (e.g., Schauer et al., 2002), thereby contributing to the renewal of the intermediate and deep water in the Arctic Ocean (Rudels et al., 1994; Jones et al., 1995; Rudels et al., 2000).

Within the Barents Sea, several processes contribute to the water mass modification (Pfirman et al., 1994; Rudels et al., 1994; Ozhigin and Ivshin, 1999; Rudels et al., 2004). These processes include freshwater input from river runoff, sea-ice melting and net precipitation (Coachman and Barnes, 1963; Steele et al., 1995), wind and tidal mixing (Sundfjord et al., 2007), atmospheric cooling and subsequent sea-ice formation (Aagaard et al., 1981; Smedsrud et al., 2013; Skagseth et al., 2020). The dense water formed within, exits the Barents Sea through the northern BSO into the Nordic Seas, and through the St. Anna Trough into the central Arctic (Fig. 1). Given its contribution to the overflow waters that feed the lower limb of the Atlantic Meridional Overturning Circulation (AMOC), variability in dense-water formation within the Barents Sea is of high importance (Smedsrud et al., 2013; Lind et al., 2018).

During recent years, the Barents Sea has experienced rapid changes driven by complex feedback mechanisms, making the region a focal point for understanding ongoing and future Arctic climate change and its implications (Lind et al., 2018; Chatterjee et al., 2024; Challet et al., 2025). An example is the reduced atmospheric heat loss in the SBS (Skagseth et al., 2020) that is found to impact the outflow of dense waters entering the Nordic Seas through the northern part of the BSO (Skagseth et al., 2020). The dense waters exiting the Barents Sea at BSO and SAT can also be affected by changes in salinity due to sea ice import from the north (Lind et al., 2018), as well as by the downstream impact of the freshwater anomalies from the northern North Atlantic. In this context, a large salinity anomaly observed during 2012–2016 stands out, representing the most anomalous event recorded during the past 120 years in the northern North Atlantic (Holliday et al., 2020; Kenigson and Timmermans, 2021). While, Holliday et al. (2020) attributed this freshening to anomalous winter wind patterns rerouting Arctic-origin water in the Labrador Current into the northern North Atlantic, Kenigson and Timmermans (2021) linked it to the wind-driven displacements of the Subpolar Front. This event also coincided with the decadal variability in the subpolar gyre circulation, which has strengthened since the mid-2000s (Chafik et al., 2019) and exerts a strong influence on the properties of AW entering the Nordic Seas (Hatun et al., 2005). Even though the subsequent northward propagation of these negative salinity

CHAPTER 2.3

anomalies has been documented (Mork et al., 2019), their downstream impacts, particularly on dense water formation in the Barents Sea, remain poorly understood. In here, we combine regional ocean reanalysis, in situ observations, and satellite remote sensing datasets to investigate recent changes in Barents Sea salinity, identify the mechanisms driving these changes, and assess their influence on the properties of dense waters exiting the Barents Sea.

2 Data & Methods

Details of the model data, satellite data obtained from the Climate Change Initiative (CCI) of the European Space Agency (ESA), ECMWF Reanalysis Version5 (ERA5) atmospheric reanalysis and in situ data from International Council for the Exploration of the Sea (ICES), is given below and in Table 1. Different acronyms used are listed in the Appendix.

TOPAZ4 Reanalysis: TOPAZ4 is a regional ocean-sea ice reanalysis product and represents Arctic Ocean Physics Reanalysis in the Copernicus Marine Service (product ref. no. 1, Table 1). The TOPAZ4b version used here is a coupled ocean and sea ice data assimilation system for the Arctic based on the HYbrid Coordinate Ocean Model (HYCOM), with 50 hybrid z-isopycnal layers at a horizontal resolution of 12 to 16 km, uses the ensemble Kalman filter method (EnKF; Evensen, 2003; Ali et al., 2019; Raj et al., 2020) to assimilate consistently multiple types of observations in the ocean and sea ice (Xie et al., 2016, 2019). Forced by ERA5 reanalysis, it assimilates observations, including along-track altimetry data, sea surface temperature, sea ice concentration, and sea ice drift from satellites, along with in situ temperature and salinity profiles. The detailed setup of the TOPAZ4 reanalysis and its performance is detailed in Sakov et al. (2012) and Xie et al. (2023).

ESA CCI SSS data: The CCI+SSS project aims to generate improved calibrated global SSS fields from all available satellite L-band radiometer measurements, with regional extensions utilising C-band radiometer data. This initiative seeks to leverage the full potential of the ESA/Earth Explorer Soil Moisture and Ocean Salinity (SMOS), in conjunction with the Soil Moisture Active Passive (SMAP) and AQUARIUS satellite missions, by assembling expert teams in earth observation, satellite data validation, and the study of climate variability. Monthly sea surface salinity product (product ref. no. 2, Table 1) for the Northern Hemisphere on a 25 km EASE grid, v5.5, available for the time-period 2010 to 2023 is used here (Boutin et al., 2025).

ERA-5: Monthly mean sea level pressure (MSLP; $0.25° \times 0.25°$ spatial grid) data (product ref. no. 4, Table 1) for the time-period (1991–2024) is used in this study to investigate the role of large-scale atmospheric forcing.

ICES data: The temperature, salinity, and density data (product ref. no. 3, Table 1) at BSO and Svinøy sections are obtained from the ICES database (https://ocean.ices.dk/core/iroc, last access: August 2025).

Lead–lag correlations were calculated from detrended monthly salinity anomalies after removing the climatological seasonal cycle. The significance of the correlations was evaluated using a two-sided Student's t-test based on the effective sample size, estimated from the lag-1 autocorrelation of the two time series to account for serial dependence.

3 Results

3.1 Southern Barents Sea

Reanalysis data averaged over the full Barents Sea domain (20 to 60° E; 70 to 80° N) and from surface to bottom show a rapid decline in the overall salinity in the Barents Sea after 2016–2017, followed by a salinity minimum in 2021–2022 (trend, 2016–2022: -0.07 ± 0.01 psu per decade). The salinity decline followed a period of gradual salinity increase (1991–2015; trend: 0.01 ± 0.002 psu per decade; Fig. 2a). This salinity minimum aligns with the freshening in the North Atlantic during the period 2012–2016 (Holliday et al., 2020), and subsequently in the Norwegian Sea (Mork et al., 2019), consistent with an advection time of a few years from the North Atlantic to the BSO (Furevik, 2001; Årthun and Eldevik, 2016). To understand the regional drivers of this salinity change, we further focus our analysis on the southern (SBS; 20 to 60° E; 70 to 75° N) and northern (NBS; 20 to 60° E; 76 to 80° N) Barents Sea separately (Fig. 1). The spatial variability of mean SSS, shown in Fig. 1, is used to qualitatively separate the BS into the AW dominated SBS and the Arctic Water dominated NBS. In general, from visual analysis, the long-term variability in the salinity of the two regions shows a positive trend followed by a sudden drop in salinity since the mid 2010s (Fig. 2a).

The propagation of salinity anomalies from the Nordic Seas into the SBS via BSO is visible in Fig. 2b. In accordance with findings reported in the literature, the salinity variability (upper ocean, 200 m) in SBS follows that at the BSO and Svinøy, located further upstream along the advection path of AW in the Norwegian Sea (Fig. 1). The positive trend in salinity followed by an abrupt drop is also seen at BSO and Svinøy, but with a lag. The minimum in salinity at Svinøy is found during 2018, while at BSO and SBS it is at around the time-periods 2019–2020 and 2021–2022 respectively (Fig. 2a, b). To further confirm the propagation of the salinity anomalies, we performed a lagged correlation analysis using monthly mean data from the TOPAZ reanalysis. Note that the correlation between annual mean salinity from in-situ and TOPAZ salinity data is 0.9 for both Svinøy and BSO. The lagged correlation analysis (detrended and deseasoned) shows a maximum significant correlation ($r = 0.6$) at 16-months lag between Svinøy and BSO (Svinøy leads BSO). Even though the mean speed of the Norwegian Atlantic Slope Current (NwASC; Fig. 1) is around 30 cm s^{-1}

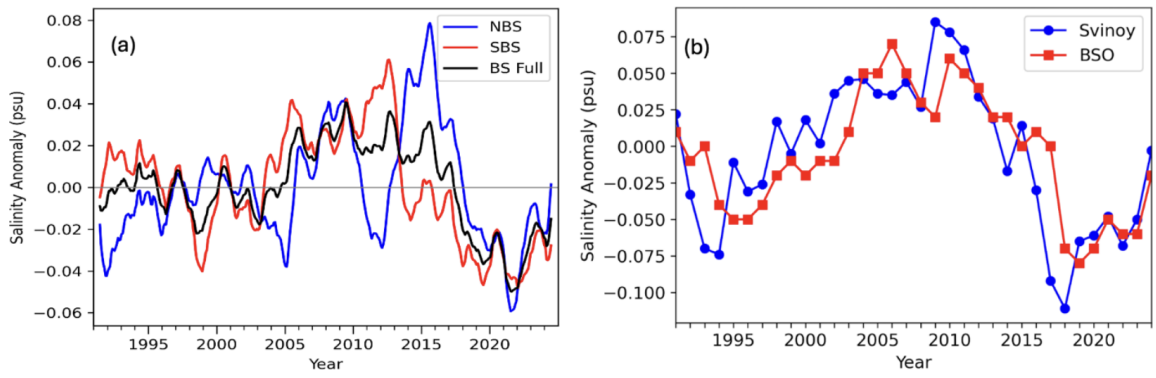


Figure 2. **(a)** Interannual (12 month running mean) variability of depth-averaged salinity anomaly in the southern Barents Sea (SBS; red), northern Barents Sea (NBS; blue) and the full Barents Sea (BS_Full; black) obtained from TOPAZ reanalysis. **(b)** Time series showing annual averaged salinity anomaly in the upper 200 m depth at the Svinøy (63° N, 3° E; Fig. 1) and Barents Sea Opening (BSO; Fig. 1; 73° N, 20° E), from in situ observations (ICES data) during the TOPAZ time period (1991–2024).

(Orvik et al., 2001) with a variability of $\pm 10\,\mathrm{cm\,s^{-1}}$ (Raj et al., 2018), the hydrographic anomalies propagating along with the NwASC are much slower, roughly an order of magnitude lower than its core speed (Broomé and Nilsson, 2018). This accounts for a travel time, consistent with our result, to cover a distance of around 1300 km between Svinøy (63° N, 3° E) and BSO (73° N, 20° E).

Extending the analysis to the 1970s using observations from the BSO (Blindheim and Loeng, 1981; González-Pola et al., 2020; Fig. 3b) reveals that the salinity anomaly during 1978–1979 has been more pronounced than the one during 2018–2019. On the other hand, the salinity anomaly of the latest event is more pronounced than that during the late 1980s and late 1990s. Notably the temperature remained relatively high during the latest salinity anomaly event (Fig. 3c). The lower temperature during those earlier low salinity periods compensated for the lower salinity with respect to density changes. A consequence of the warming in recent decades is therefore an unprecedented (in the instrumental record) low AW density observed since 2016 in the Barents Sea (Fig. 3a).

3.2 Northern Barents Sea

We now shift our focus to the NBS, which, in addition to being influenced by AW, also is dominated by the exchanges of sea ice and less saline and colder Arctic Water from the Polar Basin (Pfirman et al., 1994; Lind et al., 2018). Moreover, the NBS has two sources of AW; inflow of AW from the SBS (Schauer et al., 2002), and the onshelf intrusion of AW flowing eastward along the northern Barents Sea shelf slope in the Polar Basin (Fig. 1, Lind and Ingvaldsen, 2012; Lundesgaard et al., 2022). Our analysis showed an increasing salinity in the NBS, especially during mid-2000s to mid-2010s (trend, 2004–2015: 0.05 ± 0.01 psu per decade, $p < 0.05$), followed by a rapid decline from 2016 onwards until 2022 (trend, 2016–2022: -0.11 ± 0.02 psu per decade, $p < 0.05$; Fig. 2a). A lag correlation analysis (deseasoned and detrended) found a correlation ($r = 0.4$) between the salinity variability of BSO and NBS at a lag of 16 months, which is consistent with the travel time reported by Årthun and Eldevik (2016). Although the relationship becomes more pronounced ($r = 0.5$) during 2016–2024 when salinity is declining, it is not significant ($r = 0.2$) during 2004–2015 with increasing salinity in the NBS. This suggests that different processes govern salinity variability in the NBS during that time. Notably, Lind et al. (2018) has attributed the increased salinity in the NBS during the mid-2000 to mid-2010 to the reduced sea ice import from the central Arctic. As sea-ice import is anticipated to exert its strongest influence on regional SSS, we analyzed satellite-derived SSS data, which also showed a decrease in surface salinity after 2016 (figure not shown). A negative SSS anomaly is also evident during 2013 in the satellite-derived salinity data, likely linked to the exceptional sea-ice melt of 2012 (Parkinson and Comiso, 2013). Further analysis of TOPAZ4b reanalysis SSS for a longer time period (1991–2024) found an increase in SSS from the mid-2000s to mid-2010s. The positive trend is consistent with the results of Lind et al. (2018), who showed a similar trend during the time-period due to a decrease in sea ice import from the central Arctic. Our analysis further shows that in recent times (after 2016), this trend has changed due to a change in the atmospheric circulation pattern in the central Arctic (Fig. 4). The recent freshening in NBS is consistent with a stronger southward sea ice drift into the region from the central Arctic (Fig. 4a). When comparing the difference in MSLP during the time-period with increasing salinity in the northern Barents Sea (1993–2015) and the period of rapid decline and lower salinity (2016–2024), we find anomalous northwesterly geostrophic winds that favour increased sea ice import from the central Arctic into the NBS during the latter period (Fig. 4b). Furthermore, the period of increasing salinity (mid-2000s to mid-2010s) is also consistent with the negative trend in fresher Arctic water import from the eastern Barents Sea, which increased thereafter (Chatterjee et al., 2024).

CHAPTER 2.3

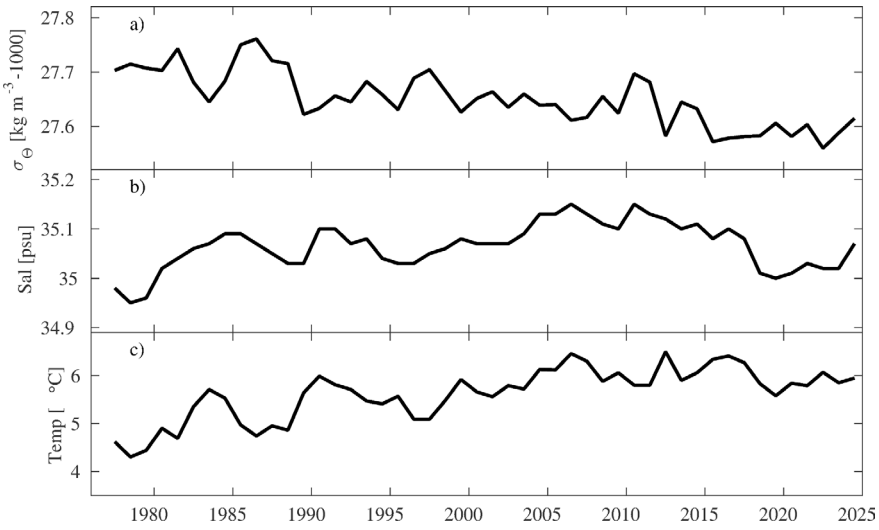


Figure 3. Time series showing annual average **(a)** density, **(b)** salinity, and **(c)** temperature averaged over 50–200 m depth in the Barents Sea Opening section, based on CTD observations during the period 1978–2024.

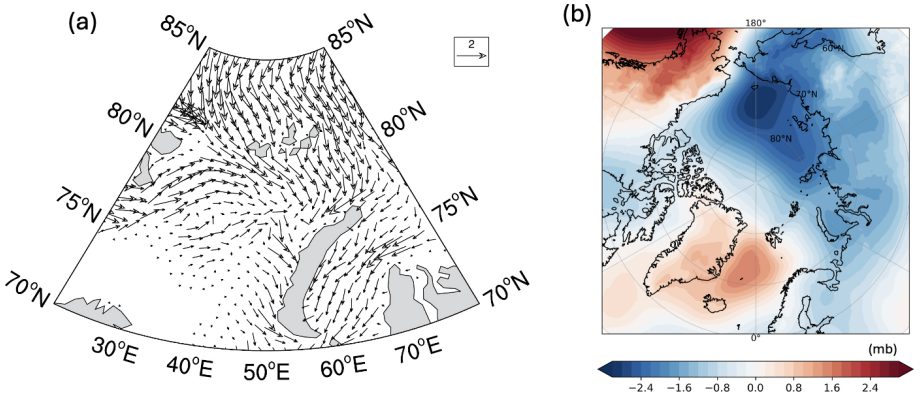


Figure 4. **(a)** Difference in winter-mean (NDJFM) sea-ice drift velocity (cm s^{-1}) from TOPAZ4b, defined as the mean over 2016–2024 minus the mean over 1993–2015. **(b)** Same as panel **(a)** but for MSLP difference from ERA-5.

3.3 Downstream effects

In the following, we investigate the downstream effects of the changes in the salinity of the Barents Sea on the dense outflow waters exiting the Barents Sea into the Nordic Seas and the central Arctic. Figure 5 shows the annually averaged temperature and salinity of the densest 5 % of the water masses in sections crossing the outflow of dense water from the Barents Sea into the Nordic Seas and into the central Arctic respectively at BSO and SAT (see Fig. 1 for locations). At BSO, the increase in temperature during the 2000s was partly offset in terms of density change by an increase in salinity. In the last ten years, however, the drop in salinity has further reduced density to levels unprecedented within the entire time-period (Fig. 5a, c). At SAT (Fig. 5b, d) the variability of the density of dense waters is in general dominated by temperature, however, in recent years the sharp drop in salinity contributed to form record low density. The cooling of the AW en route through the Barents Sea has been reported to decline in recent decades (Skagseth et al., 2020). A warming trend is also reflected in the reanalysis results, with the temperatures of the densest water being below 0 °C before 2005 and around or above 0 °C in all years after 2005 (Fig. 5b).

4 Summary and Discussion

In this study, we present the evidence of the recent freshening in the Barents Sea resulting from the unprecedented salinity anomaly observed in the northern North Atlantic during 2012–2016 (e.g., Holliday et al., 2020). The recent salinity anomaly transported into the SBS differs from previous low salinity anomalies (late 1970s and 1980s). During the recent salinity event, the temperature remained relatively high, whereas the temperature and salinity previously covaried (e.g., Furevik, 2001; Mork et al., 2019). A possi-

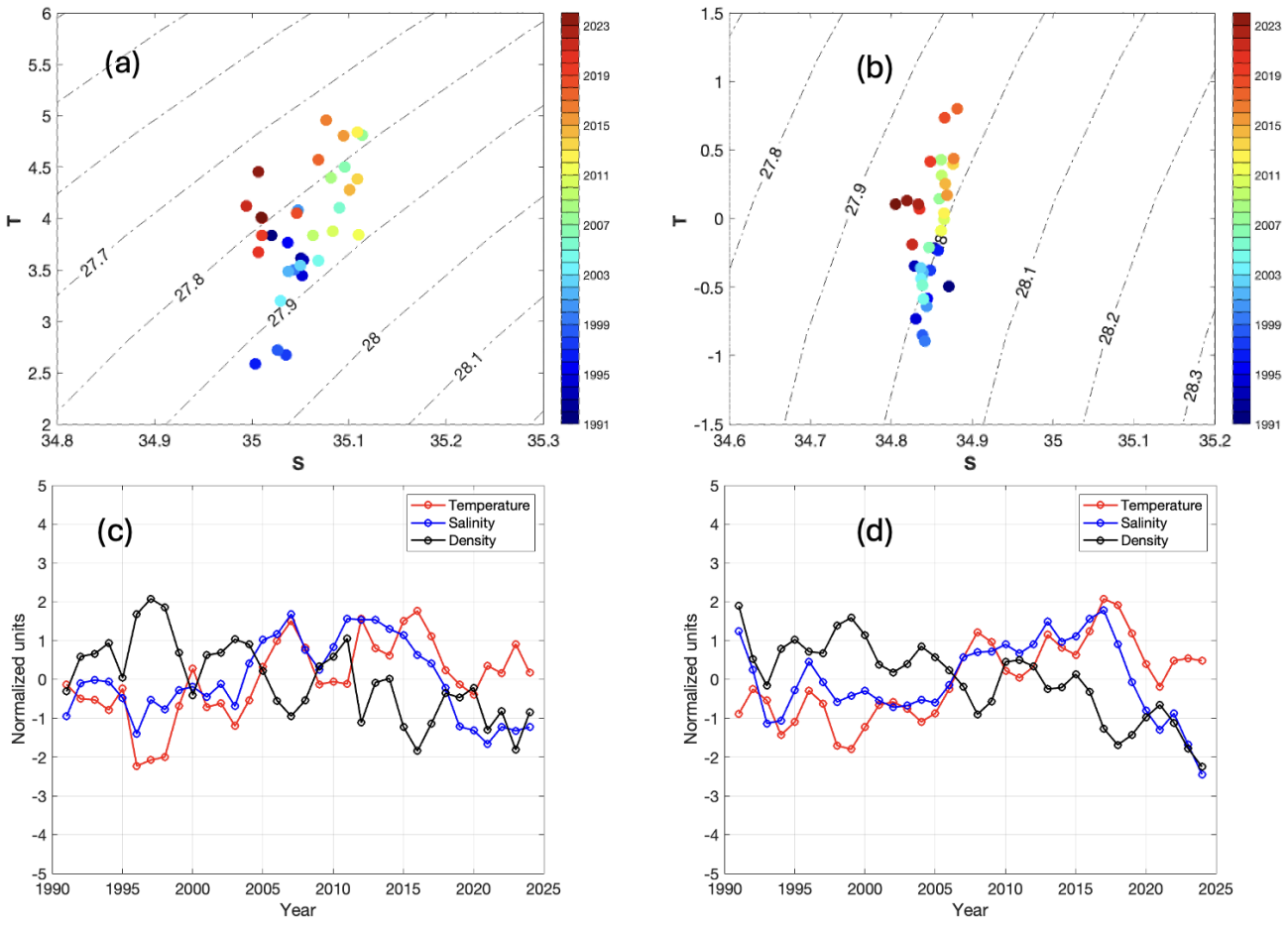


Figure 5. Temperature-salinity diagram showing the hydrographic properties of the densest 5 % of the water masses in **(a)** BSO and **(b)** SAT. The data represent TOPAZ reanalysis annual averages. Color denotes the year of the annual average. The temporal evolution of temperature, salinity and density, shown in panels **(a)** and **(b)**, after applying z-score normalisation are presented in panels **(c)** and **(d)** respectively.

ble mechanism for the positive correlation between temperature and salinity was proposed by Sundby and Drinkwater (2007), suggesting that atmospheric conditions favoring (working against) increased flow along the Norwegian coast push the temperature and salinity gradients downstream (upstream), causing both temperature and salinity to locally increase (decrease). However, the most recent salinity anomaly was caused by lower salinity entering the Nordic Seas from the North Atlantic. This is further underpinned by the observation that while the 2012–2016 salinity anomaly in the North Atlantic was unprecedented for the last 120 years, direct hydrographic observations from the BSO (Blindheim and Loeng, 1981; González-Pola et al., 2020) dating back to the late 1970s, show that the negative salinity anomaly in the Barents Sea during 1977–1979 was even stronger (Fig. 3). Moreover, although relatively colder AW has intruded into the Norwegian Sea from the North Atlantic since the mid-2000s, a reduced heat loss from the ocean surface has helped in sustaining the temperature anomalies and thereby decoupling the temperature and salinity signal in the Nordic Seas (e.g. Skagseth et al., 2020; Mork and Skagseth et al., 2019; Chatterjee et al., 2024).

The salinity variability in the NBS is found to be more complex and is influenced by both the sea ice import from the central Arctic as well as the AW salinity variability transported from the SBS. The reduction in sea-ice import into the NBS, and associated weakened stratification and increased penetration of AW to the surface has been found to increase the salinity of the region during the time period 2003–2016 (e.g., Lind et al., 2018). Our study showed that the positive trend in the salinity of the NBS no longer exists after 2016; in fact, the salinity of the region has shown a rapid freshening since then. In addition to low saline waters from SBS, this drop in the salinity variability is also linked to the increased transport of sea ice into the region, an opposite scenario to that reported by Lind et al. (2018). During this time period after 2016, anomalous northwesterly geostrophic winds are found to favour increased sea ice import from the central Arctic to the NBS. An increased sea ice import and associated enhanced stratification of the upper ocean in NBS inhibits

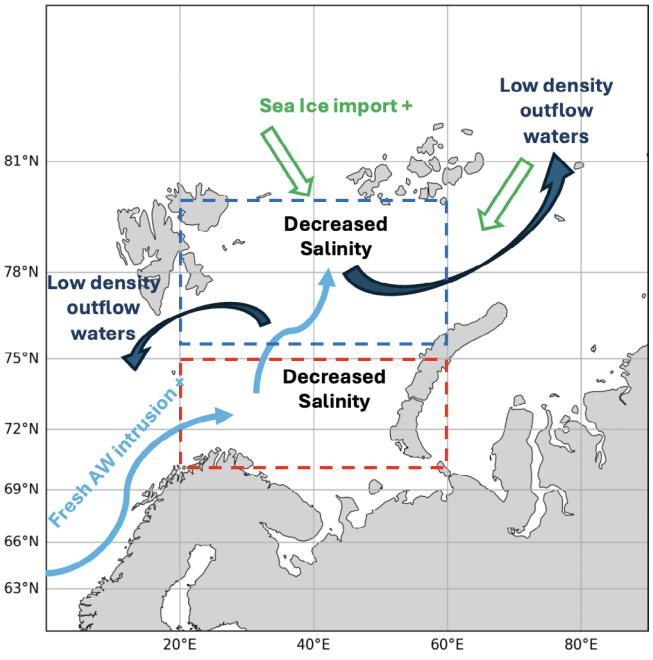


Figure 6. Summary diagram of the mechanisms involved in the recent freshening in the NBS (dashed blue box) and SBS (dashed red box) and its implications on the outflow waters. The figure summarizes the influence of fresh water intrusion into the SBS and NBS via the BSO, the increased sea ice import into the NBS from the central Arctic that in turn impacts the stratification and dampens the surfacing of AW thereby affecting the salinity of the region.

penetration of AW to the surface, pausing the Atlantication trend, and in turn favors a more direct downstream impact of SBS salinity anomaly through lateral advection (Fig. 6). Whereas, with reduced sea ice import during 2003–2016, as reported in Lind et al. (2018), the weakened stratification in the NBS region favours local vertical mixing, which may play a larger role in driving the NBS salinity over the lateral transport from SBS, as also confirmed by the weaker correlation between BSO and NBS salinity variability during 2003–2016.

Results (Fig. 5) show that in both outflow regions from the Barents Sea, the densest water masses were warming from 1993 to 2016 (BSO) and 2018 (SAT). Concurrent with the warming, the salinity was also increasing, partly offsetting the density decrease due to the warming. Then, during the most recent years, the temperature has declined, but a strong decline in salinity offset the increase in density from the cooling, resulting in the density being at the lowest for the full model timeseries. These hydrographic changes are in agreement with findings based on observations both in the BSO (Skagseth et al., 2020) and the SAT (Zabudkina et al., 2025). Moreover, our results indicate that the trends in the hydrographic properties of the dense water exiting the Barents Sea mainly reflect the trend in the hydrographic properties of the AW entering through the BSO. Historical records, however, indicate this has not always been the case. In the proximity of the Novaya Zemlya Bank, where polynya activity causes strong cooling and sea-ice formation and subsequent brine release, dense water with high salinity may form in winter (Nansen, 1906). Indeed, during the period of unprecedented low salinity of the inflowing AW in 1978–1979 (Fig. 3b), water with salinity exceeding 35.1 was observed near the bottom in the northeastern Barents Sea, yielding densities $\sigma_\Theta > 28.2$ (Midttun, 1985). In 2008, during the period of maximum AW salinity in the BS, no brine-enriched bottom water was observed close to the Novaya Zemlya Bank and the maximum observed density of $\sigma_\Theta = 28.09$ (Lien and Trofimov, 2013) was less than the $\sigma_\Theta > 28.2$ observed in 1979 (Midttun, 1985). These observations suggest that in today's warmer climate with strongly reduced sea-ice formation in the Barents Sea, the density of the bottom water in the Barents Sea is likely insufficiently large to contribute to intermediate and deep-water renewal during periods of anomalously low salinity.

Appendix A: List of acronyms and definitions used in this study

AW	Atlantic Water
AMOC	Atlantic Meridional Overturning Circulation
BS	Barents Sea
BSO	Barents Sea Opening
CCI	Climate Change Initiative
ESA	European Space Agency
ERA5	ECMWF Reanalysis Version5
ICES	International Council for the Exploration of the Sea
MSLP	mean sea level pressure
NAO	North Atlantic Oscillation
NBS	Northern Barents Sea
NwAFC	Norwegian Atlantic Front Current
NwASC	Norwegian Atlantic Slope Current
SAT	St.Anna Trough
SBS	Southern Barents Sea
SMAP	Soil Moisture Active Passive
SMOS	Soil Moisture and Ocean Salinity
SSS	Sea surface salinity

Code and data availability. Details of data avaibility are listed in Table 1. Codes used will be made accessible upon request.

Author contributions. RR, VSL, SC were involved in the intial study design, analysis, discussion and writing the manuscript. SS was involved in the analysis, while AB and LB were involved in discussions and the writing phase.

Competing interests. The contact author has declared that none of the authors has any competing interests.

Disclaimer. The Copernicus Marine Service offering is regularly updated to ensure it remains at the forefront of user requirements. In this process, some products may undergo replacement or renaming, leading to the removal of certain product IDs from the catalogue. If readers have any questions or require assistance regarding these modifications, please feel free to reach out to the Copernicus Marine Service user support team for further guidance. They will be able to provide the necessary information to address concerns and find suitable alternatives.

Publisher's note: Copernicus Publications remains neutral with regard to jurisdictional claims made in the text, published maps, institutional affiliations, or any other geographical representation in this paper. The authors bear the ultimate responsibility for providing appropriate place names. Views expressed in the text are those of the authors and do not necessarily reflect the views of the publisher.

Acknowledgements. Authors acknowledge the computational support provided by the Norwegian Sigma2 infrastructure under project NS2993K. We also thank the two anonymous reviewers for their valuable comments and suggestions, which helped improve the manuscript.

Financial support. This research was supported by the ObsSea4Clim project funded by the European Union, Horizon Europe Funding Programme for Research and Innovation (grant no. 101136548, ObsSea4Clim contribution no. 59), the Copernicus Marine Environment Monitoring Service (CMEMS) Arctic Marine Forecasting Centre project (ARC MFC; contract no. 21002L1), ESA CCI+SSS project (grant no. 4000123663/18/I-NB), ESA Dragon 6 Program (grant no. 95451), and ESA SLBC project (grant no. 4000140620/23/IBN).

Review statement. This paper was edited by Pierre Brasseur and reviewed by two anonymous referees.

References

Aagaard, K.: On the deep circulation of the Arctic Ocean, Deep-Sea Res., 28, 251–268, https://doi.org/10.1016/0198-0149(81)90066-2, 1981.

Aagaard, K., Coachman, L. K., and Carmack, E.: On the halocline of the Arctic Ocean, Deep-Sea Res. Pt. A, 28, 529–545, https://doi.org/10.1016/0198-0149(81)90115-1, 1981.

Ali, A., Christensen, K. H., Breivik, Ø., Malila, M., Raj, R. P., Bertino, L., Chassignet, E. P., and Bakhoday-Paskyabi, M.: A comparison of Langmuir turbulence parameterizations and key wave effects in a numerical model of the North Atlantic and Arctic Oceans, Ocean Model., 137, 76–97, https://doi.org/10.1016/j.ocemod.2019.02.005, 2019.

Ali, A., Burud, A., Williams, T., Xie, J., Yumruktepe, C., Wakamatsu, T., Melsom, A., Bertino, L., and Gao, S.: EU Copernicus Marine Service Product User Manual for the Arctic Ocean Physics Reanalysis, ARCTIC_MULTIYEAR_PHY_002_003, issue 5.20, Mercator Ocean International, https://documentation.marine.copernicus.eu/PUM/CMEMS-ARC-PUM-002-ALL.pdf (last access: August 2025), 2025.

Årthun, M. and Eldevik, T.: On Anomalous ocean heat transport toward the Arctic and associated climate predictability, J. Clim., 29, 689–704, https://doi.org/10.1175/JCLI-D-15-0448.1, 2016.

Årthun, M., Eldevik, T., Smedsrud, L. H., Skagseth, Ø., and Ingvaldsen, R. B.: Quantifying the Influence of Atlantic Heat on Barents sea ice variability and retreat, J. Climate, 25, 4736–4743, https://doi.org/10.1175/JCLI-D-11-00466.1, 2012.

Barton, B. I., Lenn, Y., and Lique, C.: Observed Atlantification of the Barents Sea Causes the Polar Front to Limit the Expansion of Winter Sea Ice, J. Phys. Oceanogr., 48, 1849–1866, https://doi.org/10.1175/JPO-D-18-0003.1, 2018.

Bashmachnikov, I. L., Raj, R. P., Golubkin, P., and Kozlov, I. E.: Heat Transport by mesoscale eddies in the Norwegian and Greenland Seas, J. Geophys. Res.-Oceans, 128, e2022JC018987, https://doi.org/10.1029/2022JC018987, 2023.

Blindheim, J. and Loeng, H.: On the variability of Atlantic influence in the Norwegian and Barents Seas, Fiskeridirektoratets Skrevne Serie for Havundersøkelser, 17, 161–189, 1981.

Boutin, J., Vergely, J. L., Reul, N., Catany, R., Jouanno, J., Martin, A., Rouffi, F., Bertino, L., Bonjean, F., Corato, G., Gévaudan, M., Guimbard, S., Khvorostyanov, D., Kolodziejczyk, N., Matthews, M., Olivier, L., Raj, R., Rémy, E., Reverdin, G., Supply, A., Thouvenin-Masson, C., Vialard, J., Sabia, R., and Mecklenburg, S.: ESA Sea Surface Salinity Climate Change Initiative (Sea_Surface_Salinity_cci): Monthly sea surface salinity product for the Southern Hemisphere on a 25km EASE grid, v5.5, for 2010 to 2023, NERC EDS Centre for Environmental Data Analysis [data set], https://catalogue.ceda.ac.uk/uuid/0397ca6f625e47f489684bad2bd533bb (last access: August 2025), 2025.

Broomé, S. and Nilsson, J.: Shear dispersion and delayed propagation of temperature anomalies along the Norwegian Atlantic Slope Current, Tellus, 70, 1453215, https://doi.org/10.1080/16000870.2018.1453215, 2018.

Chafik, L., Nilsen, J. E. Ø., Dangendorf, S., Reverdin, G., and Frederikse, T.: North Atlantic Ocean Circulation and Decadal Sea Level Change During the Altimetry Era, Sci. Rep., 9, 1041, https://doi.org/10.1038/s41598-018-37603-6, 2019.

Challet, F., Raj, R. P., Chatterjee, S., Herbaut, C., and Bonaduce, A.: Weakening of the Arctic water outflow from the Barents Sea and consequences on the Fram Strait warming, J. Geophys. Res.-Oceans, 130, e2024JC021054, https://doi.org/10.1029/2024JC021054, 2025.

Chatterjee, S., Semmler, T., Screen, J. A., Furevik, T., Selivanova, J., Raj, R. P., Murukesh, N., and Ravichandran, M.: Atmosphere–Ocean–Sea Ice Feedbacks Sustain Recent Barents Sea Ice Loss despite Cooler Atlantic Water Inflow, J. Clim., 37, 6519–6532, https://doi.org/10.1175/JCLI-D-24-0020.1, 2024.

Coachman, L. K. and Barnes, C. A.: Surface waters in the Eurasian Basin of the Arctic Ocean, Arctic, 15, 251–277, https://doi.org/10.14430/arctic3581, 1963.

EU Copernicus Marine Service Product: Arctic Ocean Physics Reanalysis, Mercator Ocean International [data set], https://doi.org/10.48670/moi-00007, 2025.

Evensen, G.: The Ensemble Kalman Filter: theoretical formulation and practical implementation, Ocean Dynam., 53, 343–367, 2003.

Furevik, T.: Annual and interannual variability of Atlantic Water temperatures in the Norwegian and Barents Seas: 1980–1996, Deep-Sea Res. Pt.I, 48, 383–404, https://doi.org/10.1016/S0967-0637(00)00050-9, 2001.

González-Pola, C., Larsen, K. M. H., Fratantoni, P., and Beszczynska-Möller, A.: ICES Report on Ocean Climate 2019, ICES Cooperative Research Reports (CRR), https://doi.org/10.17895/ices.pub.7537, 2020.

González-Pola, C., Larsen, K. M. H., Fratantoni, P., and Beszczynska-Möller, A.: ICES Report on ocean climate, ICES Cooperative Research Reports (CRR), Vol. 358, https://doi.org/10.17895/ices.pub.24755574, 2023.

Hatun, H., Sandø, A. B., Drange, H., Hansen, B., and Valdimarsson, H.: Influence of the Atlantic subpolar gyre on the thermohaline circulation, Science, 309, 1841–1844, https://doi.org/10.1126/science.1114777, 2005.

Hersbach, H., Bell, B., Berrisford, P., Hirahara, S., Horányi, A., Muñoz-Sabater, J., Nicolas, J., Peubey, C., Radu, R., Schepers, D., Simmons, A., Soci, C., Abdalla, S., Abellan, X., Balsamo, G., Bechtold, P., Biavati, G., Bidlot, J., Bonavita, M., De Chiara, G., Dahlgren, P., Dee, D., Diamantakis, M., Dragani, R., Flemming, J., Forbes, R., Fuentes, M., Geer, A., Haimberger, L., Healy, S., Hogan, R. J., Hólm, E., Janisková, M., Keeley, S., Laloyaux, P., Lopez, P., Lupu, C., Radnoti, G., de Rosnay, P., Rozum, I., Vamborg, F., Villaume, S., and Thépaut, J.-N.: The ERA5 global reanalysis, Q. J. R. Meteorol. Soc., 146, 1999–2049, https://doi.org/10.1002/qj.3803, 2020.

Holliday, N. P., Bersch, M., Berx, B., Chafik, L., Cunningham, S., Florindo-López, C., Hátún, H., Johns, W., Josey, S. A., Larsen, K. M. H., Mulet, S., Oltmanns, M., Reverdin, G., Rossby, T., Thierry, V., Valdimarsson, H., and Yashayaev, I.: Ocean circulation causes the largest freshening event for 120 years in eastern subpolar North Atlantic, Nat. Commun., 11, 585, https://doi.org/10.1038/s41467-020-14474-y, 2020.

Jones, E. P., Rudels, B., and Anderson, L. G.: Deep waters of the Arctic Ocean: origins and circulation, Deep-Sea Res. Part I, 42, 737–760, https://doi.org/10.1016/0967-0637(95)00013-V, 1995.

Kenigson, J. S. and Timmermans, M.: Nordic Seas Hydrography in the Context of Arctic and North Atlantic Ocean Dynamics, J. Phys. Oceanogr., 51, 101–114, https://doi.org/10.1175/JPO-D-20-0071.1, 2021.

Lien, V. S. and Trofimov, A. G.: Formation of Barents Sea Branch Water in the north-eastern Barents Sea, Polar Res., 32, https://doi.org/10.3402/polar.v32i0.18905, 2013.

Lien, V. S., Raj, R. P., and Chatterjee, S.: Surface and bottom marine heatwave characteristics in the Barents Sea: a model study, in: 8th edition of the Copernicus Ocean State Report (OSR8), edited by: von Schuckmann, K., Moreira, L., Grégoire, M., Marcos, M., Staneva, J., Brasseur, P., Garric, G., Lionello, P., Karstensen, J., and Neukermans, G., Copernicus Publications, State Planet, 4-osr8, 8, https://doi.org/10.5194/sp-4-osr8-8-2024, 2024.

Lind, S. and Ingvaldsen, R. B.: Variability and Impacts of Atlantic Water Entering the Barents Sea from the North, Deep-Sea Res. Pt. I, 62, 70–88, https://doi.org/10.1016/j.dsr.2011.12.007, 2012.

Lind, S., Ingvaldsen, R. B., and Furevik, T.: Arctic warming hotspot in the northern Barents Sea linked to declining sea-ice import, Nat. Clim. Change, 8, 634–639, https://doi.org/10.1038/s41558-018-0205-y, 2018.

Lundesgaard, Ø., Sundfjord, A., Lind, S., Nilsen, F., and Renner, A. H. H.: Import of Atlantic Water and sea ice controls the ocean environment in the northern Barents Sea, Ocean Sci., 18, 1389–1418, https://doi.org/10.5194/os-18-1389-2022, 2022.

Martin, S. and Cavalieri, D. J.: Contributions of the Siberian shelf polynyas to the Arctic Ocean Intermediate and Deep Water, J. Geophys. Res.-Oceans, 94, 12725–12738, https://doi.org/10.1029/JC094iC09p12725, 1989.

Midttun, L.: Formation of dense bottom water in the Barents Sea, Deep-Sea Res Pt. A, 32, 1233–1241, https://doi.org/10.1016/0198-0149(85)90006-8, 1985.

Mork, K. A., Skagseth, Ø., and Søiland, H.: Recent warming and freshening of the Norwegian Sea observed by Argo data, J. Clim., 32, 3695–3705, https://doi.org/10.1175/JCLI-D-18-0591.1, 2019.

Nansen, F.: Northern Waters: Captain Roald Amundsen's Oceanographic Observations in the Arctic Seas in 1901, with a Discussion of the Origin of the Bottom Waters of the Northern Seas, Jacob Dybwad, Christiania, Norway, ISBN 9781107281035, https://doi.org/10.1017/CBO9781107281035, 1906.

Orvik, K. A., Skagseth, Ø., and Mork, M.: Atlantic in inflow to the Nordic Seas: current structure and volume fluxes from moored current meters, VM-ADCP and SeaSoar-CTD observations, 1995–1999, Deep-Sea Res. Pt. I, 48, 937–957, https://doi.org/10.1016/S0967-0637(00)00038-8, 2001.

Ozhigin, V. K. and Ivshin, V. A.: Water masses of the Barents Sea, PINRO Press, Murmansk, Russia, 48 pp., ISBN 5-86349-064-0, 1999 (in Russian).

Parkinson, C. L. and Comiso, J. C.: On the 2012 record low Arctic sea ice cover: Combined impact of preconditioning and an August storm, Geophys. Res. Lett., 40, 1356–1361, https://doi.org/10.1002/grl.50349, 2013.

Pfirman, S. L., Bauch, D., and Gammelsrød, T.: The Northern Barents Sea: Water Mass Distribution and Modification, in: The Role of the Polar Oceans in Shaping the Global Environment, edited by: Johannessen, O. M., Muench, R. D., and Overland, J. E., Geophys. Monogr. Ser., 85, 77–94, https://doi.org/10.1029/GM085p0077, 1994.

Raj, R. P. and Halo, I.: Monitoring the mesoscale eddies of the Lofoten Basin: Importance, progress, and challenges, Int. J. Remote Sens., 37, 3712–3728,https://doi.org/10.1080/01431161.2016.1201234, 2016.

Raj, R. P., Nilsen, J. E. Ø., Johannessen, J. A., Furevik, T., Andersen, O. B., and Bertino, L.: Quantifying Atlantic Water transport to the Nordic Seas by remote sensing, Remote Sens. Environ., 216, 758–769, https://doi.org/10.1016/j.rse.2018.04.055, 2018.

Raj, R. P., Chatterjee, S., Bertino, L., Turiel, A., and Portabella, M.: The Arctic Front and its variability in the Norwegian Sea, Ocean Sci., 15, 1729–1744, https://doi.org/10.5194/os-15-1729-2019, 2019.

Raj, R. P., Halo, I., Chatterjee, S., Belonenko, T., Bakhoday-Paskyabi, M., Bashmachnikov, I., Fedorov, A., and Xie, J.: Inter-

action between mesoscale eddies and the gyre circulation in the Lofoten Basin, J. Geophys. Res.-Oceans, 125, e2020JC016102, https://doi.org/10.1029/2020JC016102, 2020.

Rudels, B., Jones, E. P., Anderson, L. G., and Kattner, G.: On the Intermediate depth waters of the Arctic Ocean, in: The Role of the Polar Oceans in Shaping the Global Environment, edited by: Johannessen, O. M., Muench, R. D., and Overland, J. E., Geophys. Monogr. Ser., 85, 33–46, https://doi.org/10.1029/GM085p0033, 1994.

Rudels, B., Muench, R. D., Gunn, J., Schauer, U., and Friedrich, H. J.: Evolution of the Arctic boundary current north of the Siberian shelves. J. Mar. Sys., 25, 77–99, https://doi.org/10.1016/S0924-7963(00)00009-9, 2000.

Rudels, B., Jones, E. P., Schauer, U., and Eriksson, P.: Atlantic sources of the Arctic Ocean surface and halocline waters, Polar Res., 23, 181–208, https://doi.org/10.1111/j.1751-8369.2004.tb00007.x, 2004.

Rudels, B., Korhonen, M., Schauer, U., Pisarev, S., Rabe, B., and Wisotzki, A.: Circulation and transformation of Atlantic water in the Eurasian Basin and the contribution of the Fram Strait inflow branch to the Arctic Ocean heat budget, Prog. Oceanogr., 132, 128–152, https://doi.org/10.1016/j.pocean.2014.04.003, 2015.

Sakov, P., Counillon, F., Bertino, L., Lisæter, K. A., Oke, P. R., and Korablev, A.: TOPAZ4: an ocean-sea ice data assimilation system for the North Atlantic and Arctic, Ocean Sci., 8, 633–656, https://doi.org/10.5194/os-8-633-2012, 2012.

Schauer, U., Loeng, H., Rudels, B., Ozhigin, V. K., and Dieck, W.: Atlantic water inflow through the Barents and Kara Seas, Deep-Sea Res. Pt. I, 49, 2281–2298, https://doi.org/10.1016/S0967-0637(02)00125-5, 2002.

Serreze, M. C., Holland, M. M., and Stroeve, J.: Perspectives on the Arctic's shrinking sea-ice cover, Science, 315, 1533–1536, https://doi.org/10.1126/science.1139426, 2007.

Skagseth, Ø., Eldevik, T., Årthun, M., Asbjørnsen, H., Lien, V. S., and Smedsrud, L. H.: Reduced efficiency of the Barents Sea cooling machine, Nat. Clim. Change, 10, 661–666, https://doi.org/10.1038/s41558-020-0772-6, 2020.

Smedsrud, L. H., Ingvaldsen, R., Nilsen, J. E. Ø., and Skagseth, Ø.: Heat in the Barents Sea: transport, storage, and surface fluxes, Ocean Sci., 6, 219–234, https://doi.org/10.5194/os-6-219-2010, 2010.

Smedsrud, L. H., Esau, I., Ingvaldsen, R. B., Eldevik, T., Haugan, P. M., Li, C., Lien, V. S., Olsen, A., Omar, A. M., Otterå, O. H., Risebrobakken, B., Sandø, A. B., Semenov, V. A., and Sorokina, S. A.: The role of the Barents Sea in the climate system, Rev. Geophys., 51, 415–449, https://doi.org/10.1002/rog.20017, 2013.

Steele, M., Morison, J. H., and Curtin, T. B.: Halocline water formation in the Barents Sea, J. Geophys. Res., 100, 881–894, https://doi.org/10.1029/94JC02310, 1995.

Sundby, S. and Drinkwater, K.: On the mechanisms behind salinity anomaly signals of the northern North Atlantic, Prog. Oceanogr., 73, 190–202, https://doi.org/10.1016/j.pocean.2007.02.002, 2007.

Sundfjord, A., Fer, I., Kasajima, Y., and Svendsen, H.: Observations of turbulent mixing and hydrography in the marginal ice zone of the Barents Sea, J. Geophys. Res., 112, C05008, https://doi.org/10.1029/2006JC003524, 2007.

Xie, J. and Bertino, L.: EU Copernicus Marine Service Quality Information Document for the Arctic Ocean Physics Reanalysis, ARCTIC_MULTIYEAR_PHY_002_003, issue 1.5, Mercator Ocean International, https://documentation.marine.copernicus.eu/QUID/CMEMS-ARC-QUID-002-003.pdf (last access: 5 August 2025), 2025.

Xie, J., Counillon, F., Bertino, L., Tian-Kunze, X., and Kaleschke, L.: Benefits of assimilating thin sea ice thickness from SMOS into the TOPAZ system, The Cryosphere, 10, 2745–2761, https://doi.org/10.5194/tc-10-2745-2016, 2016.

Xie, J., Raj, R. P., Bertino, L., Samuelsen, A., and Wakamatsu, T.: Evaluation of Arctic Ocean surface salinities from the Soil Moisture and Ocean Salinity (SMOS) mission against a regional reanalysis and in situ data, Ocean Sci., 15, 1191–1206, https://doi.org/10.5194/os-15-1191-2019, 2019.

Xie, J., Raj, R. P., Bertino, L., Martínez, J., Gabarró, C., and Catany, R.: Assimilation of sea surface salinities from SMOS in an Arctic coupled ocean and sea ice reanalysis, Ocean Sci., 19, 269–287, https://doi.org/10.5194/os-19-269-2023, 2023.

Zabudkina, Z., Osadchiev, A., Ivanov, V., Makhotin, M., and Merkulov, V.: Interannual variability of the Barents Sea branch water in the northeastern part of the Barents Sea and the St. Anna Trough, Front. Mar. Sci., 12, 1569186, https://doi.org/10.3389/fmars.2025.1569186, 2025.

State Planet, 7-osr10, 7, 2026
https://doi.org/10.5194/sp-7-osr10-7-2026
© Author(s) 2026. This work is distributed under
the Creative Commons Attribution 4.0 License.

Towards a multi-product methodology for calculating the ocean monitoring indicator of SST extremes in the IBI region

Álvaro de Pascual Collar[1], Axel Alonso Valle[1], Alex Gallardo[1], Marta de Alfonso Alonso-Muñoyerro[2], Begoña Pérez Gómez[2], Stefania Ciliberti[1], and Marcos G. Sotillo[1]

[1]Nologin Oceanic Weather Systems, Madrid, 28045, Spain
[2]Puertos del Estado, Madrid, 28042, Spain

Correspondence: Álvaro de Pascual Collar (alvaro.depascual@nowsystems.eu)

Received: 22 August 2025 – Discussion started: 22 September 2025
Revised: 8 June 2026 – Accepted: 14 June 2026 – Published: 30 September 2026

Abstract. The ongoing evaluation and refinement of the Copernicus Ocean Monitoring Indicators (OMIs) is essential to ensure their scientific robustness and operational relevance. This process takes place within a context of continuous advances in upstream products and the need to adapt methodologies to evolving scientific priorities and decision-making requirements. In this framework, the release of new Copernicus products and the growing demand for quantifying uncertainty in indicator results are particularly relevant.

Among the operational OMIs produced by the Iberia–Biscay–Ireland (IBI) Monitoring and Forecasting Center is the Sea Surface Temperature (SST) extremes indicator, which assesses the intensity of extreme thermal events in the region. This study proposes two methodological improvements to it: first, replacing the near real-time data product currently used to compute the indicator with the recently developed Interim extension of its multi-year counterpart; and second, exploring the use of a multi-product ensemble approach that integrates regional and global model outputs with satellite-based observations to provide a first-order measure of inter-product spread.

The methodology focuses on comparing the 2024 SST extremes OMI, computed using the existing approach, with outputs generated by the revised methodologies. The evaluation uses the observationally based SST extremes OMI as a reference (currently available in the Copernicus Marine catalog), and the analysis examines spatial patterns and local behaviors, highlighting consistencies and discrepancies across products.

The results show that both the Interim dataset and the multi-product approach improve the robustness and consistency of the SST extremes indicator. While the Interim dataset enhances internal coherence by reducing heterogeneity in data sources, the ensemble method provides a more reliable assessment by incorporating inter-product spread information. Together, these advances strengthen the scientific maturity and operational value of SST extremes monitoring in the IBI region.

1 Introduction

Ocean indicators can be defined as measures based on scientifically validated data and methodologies that enable the assessment of the state of ocean phenomena across various temporal and spatial scales, in a manner that is accessible and meaningful to end users. These indicators are derived from environmental variables (e.g., temperature, salinity, sea level), processes (such as primary productivity), or events (such as algal blooms or marine heatwaves) (von Schuckmann et al., 2026). Given that operational Ocean Monitoring Indicators (OMIs) are developed within a dynamic and evolving framework of oceanographic data production, their underlying methodologies must be periodically reviewed and updated. These continuous methodological refinements are essential to ensure that OMIs remain aligned with the current state of scientific knowledge, incorporate the best avail-

Published by Copernicus Publications.

Table 1. List of datasets used in this work referencing the source and documentation.

Product ref. no.	Product ID Acronym Type	Data access	Documentation
1	OMI_CLIMATE_TEMPSAL_IBI_extreme_var_mean_and_anomaly (OMI-NRT) Numerical models	EU Copernicus Marine Service Product (2021)	Quality Information Document (QUID): de Pascual Collar et al. (2021a) Product User Manual (PUM): de Pascual Collar et al. (2021b)
2	IBI_MULTIYEAR_PHY_005_002 (IBI-REA for Reanalysis dataset, IBI-INT for Interim dataset) Numerical models	EU Copernicus Marine Service Product (2024a)	QUID: Levier et al. (2024a) PUM: Castrillo-Acuña et al. (2024a)
3	IBI_ANALYSISFORECAST_PHY_005_001 (IBI-NRT) Numerical models	EU Copernicus Marine Service Product (2024b)	QUID: Levier et al. (2024b) PUM: Castrillo-Acuña et al. (2024b)
4	GLOBAL_MULTIYEAR_PHY_001_030 (GLO-REA) Numerical models	EU Copernicus Marine Service Product (2023)	QUID: Drévillon et al. (2023) PUM: Drévillon et al. (2024)
5	GLOBAL_ANALYSISFORECAST_PHY_001_024 (GLO-NRT) Numerical models	EU Copernicus Marine Service Product (2024c)	QUID: Lellouche et al. (2024) PUM: Le Galloudec et al. (2024)
6	SST_ATL_SST_L4_REP_OBSERVATIONS_010_026 (SAT-REP) Satellite observations	EU Copernicus Marine Service Product (2024d)	QUID: Autret et al. (2024) PUM: Autret et al. (2023)
7	SST_ATL_SST_L4_NRT_OBSERVATIONS_010_025 (SAT-NRT) Satellite observations	EU Copernicus Marine Service Product (2022a)	QUID: Piollé et al. (2022a) PUM: Piollé et al. (2022b)
8	OMI_EXTREME_SST_IBI_sst_mean_and_anomaly_obs (OMI-OBS) In-situ observations	EU Copernicus Marine Service Product (2022b)	QUID: de Alfonso et al. (2022a) PUM: de Alfonso et al. (2022b)

able upstream data, and maximize their accuracy, reliability, and operational relevance.

Among the operational OMIs maintained by the Iberia–Biscay–Ireland Monitoring and Forecasting Centre (IBI-MFC) is the Sea Surface Temperature (SST) extremes indicator (listed as OMI-NRT in Table 1, product ref. no. 1). This OMI provides an assessment of extreme SST events in the IBI region by quantifying the annual anomaly of the 99th percentile of SST. The indicator is derived by calculating the difference between the 99th percentile value for a given year and the climatological mean of the 99th percentile, obtained from a multi-decadal model reanalysis time series over its full temporal coverage. To minimize the latency of the operational product, the indicator is computed by combining outputs from both reanalysis and near real-time (NRT) Copernicus Marine products (referenced in Table 1 as IBI-REA and IBI-NRT, product refs. no. 2 and 3, respectively). While the IBI-REA is used to estimate the climatological 99th percentile mean, the IBI-NRT dataset provides the corresponding value for the target year. This methodological combination ensures that the indicator remains both scientifically robust and operationally relevant. Its consistency is evaluated through comparisons with in situ observations, as documented in Álvarez Fanjul et al. (2019).

The OMI-NRT indicator demonstrates both scientific maturity and operational readiness in alignment with the GOOS (Global Ocean Observing System: https://goosocean.org/, last access: 20 July 2026) framework (von Schuckmann et al., 2026). Scientifically, the indicator is verified through a robust methodology based on peer-reviewed percentile analysis of SST extremes (Pérez Gómez et al., 2018), using the 99th percentile to capture high-impact thermal events. It provides significant and policy-relevant information on marine heat extremes, which are known to be associated with a wide range of ecological and socioeconomic impacts (Oliver et al., 2021; Smith et al., 2021), grounded in a multi-decadal model reanalysis and operational NRT datasets from the Copernicus Marine Service. The approach is scalable and adaptable to

other ocean regions, supporting consistent and reproducible implementation. From an operational standpoint, the indicator is justified by its relevance to coastal and marine impact assessments and is measurable through Essential Ocean Variables using standardized Copernicus data products. It is accessible via the Copernicus Marine platform, updated annually, and compliant with FAIR principles. These attributes collectively position the SST extremes indicator as a mature product according to GOOS quality criteria.

Nevertheless, the current indicator could benefit from two methodological improvements, which are explored in the present work. First, the incorporation of the recently released Interim dataset from the Copernicus IBI Multiyear product (referenced as IBI-INT in Table 1, product ref. no. 2) may enhance the consistency of the upstream data used in the calculation of the indicator. This is due to the reduction of heterogeneity in the modeling systems involved and the exclusive use of outputs derived from the IBI Multiyear system itself. This refinement would improve the "Verified" criterion of the GOOS framework by strengthening the traceability and scientific coherence of the data sources underpinning the indicator.

Second, the availability of multiple SST datasets in the Copernicus Marine Data Store opens the possibility of applying a multi-product ensemble methodology to calculate the same indicator across different Copernicus Marine products. This would allow for the characterization of inter-product spread associated with the indicator values, offering a more robust interpretation of results. Incorporating such ensemble-based estimates would directly contribute to enhancing the "Significant" and "Scalable" criteria, by improving the indicator's robustness and enabling its comparison across regions and systems.

To assess the sensitivity of the proposed methodological refinements, their results will be evaluated and discussed in light of independent observational evidence, using in situ datasets provided by the Copernicus observational OMI product for SST extremes (referenced in Table 1 as OMI-OBS, product ref. no. 8). This validation step will allow for a critical comparison of performance and consistency between the existing and alternative approaches, supporting the long-term goal of improving the scientific and operational maturity of the SST extremes indicator within the IBI region and beyond.

2 Data and methods

The present study aims to assess two potential modifications to the operational procedures for computing the SST extremes indicator in the IBI region. The baseline indicator taken as the starting point is that listed in Table 1 as OMI-NRT, whose methodology is described in detail below.

The OMI-NRT indicator evaluates SST extremes for a given target year by quantifying the anomaly of the 99th percentile of SST, computed as the difference between the 99th percentile of SST for the target year and the climatological mean of the 99th percentile derived from a multi-decadal reanalysis. The climatological baseline is obtained from the Copernicus IBI reanalysis product (referenced in Table 1 as IBI-REA), computed over the full extent of the multi-year product period (in this study, 1993–2023) in order to provide the most robust climatological reference possible at each indicator update, while the SST values for the target year (in this study, 2024) are drawn from the IBI near-real-time product (referenced in Table 1 as IBI-NRT).

The methodology proceeds in two main steps. In the first step, the annual 99th percentile of SST is computed for each individual year of the multi-year product (IBI-REA):

$$P_{99}^{\mathrm{MYP}}(x,y) = \mathrm{perc}_{99}\left(\left\{T^{\mathrm{MYP}}(x,t)\,|t \in y\right\}\right) \tag{1}$$

where $T^{\mathrm{MYP}}(x,t)$ is the SST field from the multi-year product at spatial location x and time t, and perc_{99} denotes the 99th percentile computed over all temporal instances within year y. These annual 99th percentiles are subsequently averaged over the full reference period to obtain the climatological mean of the 99th percentile, which serves as the reference climatology:

$$\overline{P}_{99}^{\mathrm{MYP}}(x) = \frac{1}{N}\sum_{y=y_1}^{y_N} P_{99}^{\mathrm{MYP}}(x,y) \tag{2}$$

In the second step, the 99th percentile for the target year y^* is computed using the near-real-time product (IBI-NRT):

$$P_{99}^{\mathrm{NRT}}\left(x,y^*\right) = \mathrm{perc}_{99}\left(\left\{T^{\mathrm{NRT}}(x,t)\,|t \in y^*\right\}\right) \tag{3}$$

where $T^{\mathrm{NRT}}(x,t)$ is the SST field from the near-real-time product at spatial location x and time t, including all available time steps within the target year y^*.

Finally, the annual anomaly map of the 99th percentile for the target year is obtained by subtracting the climatological mean of the 99th percentile from the near-real-time-derived 99th percentile:

$$A_{99}\left(x,y^{/\mathrm{Yr}}\right) = P_{99}^{\mathrm{NRT}}\left(x,y^{/\mathrm{Yr}}\right) - \overline{P}_{99}^{\mathrm{MYP}}(x) \tag{4}$$

Positive values of A_{99} indicate that the 99th percentile of SST for the target year exceeds the climatological reference, reflecting anomalously high extreme SST conditions, whereas negative values indicate that the 99th percentile falls below the climatological reference, suggesting a relative attenuation of SST extremes during that year.

The first methodological modification evaluated in this study involves the replacement of the datasets currently used in the computation of the OMI-NRT indicator. This reassessment is motivated by the recent inclusion in the Copernicus Marine catalogue of a new interim dataset, part of the IBI multiyear product (referenced in Table 1 as IBI-INT). This new dataset is suitable for the calculation of the SST

extremes indicator for two main reasons. First, it is generated using the same ocean model configuration as the IBI reanalysis (IBI-REA), which ensures greater homogeneity between the computational systems involved and reduces potential biases in the indicator's estimation. Second, the IBI-INT dataset is updated on a monthly basis with a latency of 4 months relative to real time, offering a compromise between timeliness and data consistency. Based on this, the present work defines OMI-INT as an SST extremes indicator analogous to OMI-NRT, but with the IBI-NRT dataset replaced by IBI-INT. This alternative formulation seeks to balance the trade-off between the update frequency of the indicator and the homogeneity of the upstream data used in its computation.

The second methodological modification addressed in this study involves the implementation of a multi-product approach for calculating the SST extremes indicator in the IBI region. To this end, a systematic review of the Copernicus Marine catalogue was conducted to identify products suitable for applying the same percentile-based methodology used in the operational OMI-NRT indicator. For each selected product, an independent estimation of the SST extremes indicator was computed, which is subsequently treated as a member of an ensemble. Several inclusion criteria were defined to ensure methodological consistency and scientific robustness across the ensemble members: (i) products must provide gridded SST data covering the IBI region; (ii) daily temporal resolution is required to compute annual 99th percentile anomalies; (iii) the time series must be long enough to support the construction of a robust climatology of the 99th percentile; and (iv) the product must be updated with a latency that ensures sufficient proximity to real time.

Based on these criteria, two additional product pairs from the Copernicus catalogue were identified as suitable for ensemble integration. First, the Global Ocean Physics modelling system provides both a reanalysis product (referenced in Table 1 as GLO-REA, product ref. no. 4) and a near real-time forecast product (referenced as GLO-NRT in Table 1, product ref. no. 5) that meet all necessary conditions. Second, satellite-derived SST observations from the European North West Shelf/Iberia-Biscay-Irish Seas High-Resolution L4 SST dataset are available in both a reprocessed delayed mode (referenced in Table 1 as SAT-REP, product ref. no. 6) and a near real-time version (referenced as SAT-NRT in Table 1, product ref. no. 7), both of which satisfy the requirements for computing the indicator.

In both cases, as with the previously defined OMI-NRT and OMI-INT indicators, the methodology involves calculating the 99th percentile anomaly of SST for the target year using near real-time products (GLO-NRT and SAT-NRT), referenced to the corresponding climatological 99th percentile derived from the respective multiyear products (GLO-REA and SAT-REP).

Accordingly, this study defines the MULTI-OMI as the ensemble SST extremes indicator, computed using the same methodology as OMI-NRT but incorporating multiple Copernicus products. The ensemble comprises three members derived from: (i) IBI regional modelling data (IBI-REA and IBI-INT), (ii) global ocean modelling data (GLO-REA and GLO-NRT), and (iii) satellite-derived SST observations (SAT-REP and SAT-NRT). Each member anomaly is initially computed at the native spatial resolution of its corresponding NRT product. Prior to the ensemble aggregation, all individual anomaly fields are remapped to the IBI-NRT grid using a conservative interpolation method, ensuring a consistent spatial framework for the intercomparison of OMI-NRT, OMI-INT, and MULTI-OMI. The ensemble mean is then obtained as the simple arithmetic mean of the three regridded member anomalies, while the associated inter-product spread is quantified through the standard deviation computed across the three ensemble members. This ensemble-based approach enables an uncertainty-aware interpretation of the results by providing, alongside the central estimate, a measure of inter-product spread that informs on the reliability of the indicator. Following the methodology of the baseline indicator (OMI-NRT), the climatological 99th percentiles are computed over the longest period commonly available across all multi-year and reprocessed datasets. Since the different products considered present slight differences in their temporal coverage, a common reference period of 1993–2023 is adopted for all ensemble members, as this interval is fully covered by all multi-year and reprocessed products (IBI-REA, GLO-REA, and SAT-REP), ensuring methodological consistency and comparability across ensemble members and the operational baseline indicator (OMI-NRT).

Since this study aims to assess the sensitivity of the SST extremes indicator to the methodological modifications proposed above, it is necessary to establish a common reference dataset against which the results of each variant can be evaluated. For this purpose, the Copernicus Marine SST extremes indicator derived from observational data (referenced in Table 1 as OMI-OBS, product ref. no. 8) is used as the benchmark. This indicator follows the same percentile-based methodology as OMI-NRT, with the key difference that it is computed using non-gridded in situ data provided by the Copernicus Marine In Situ Thematic Assembly Centre. These observational datasets are derived from quality-controlled measurements collected by fixed stations and provide an independent and realistic representation of SST conditions in the IBI region. However, the reference period of OMI-OBS is subject to additional constraints imposed by the nature of the in situ data. Since observational records from fixed stations may contain temporal gaps, only stations with a minimum of 10 years of data and a minimum annual data coverage of 70 % are retained for the computation of the climatological 99th percentile. These quality thresholds follow the criteria established in the original OMI-OBS methodology and are necessary to ensure the statistical robustness of the climatology derived from non-gridded in situ observations.

3 Results of indicator using interim and near real-time products

The first objective of this study is to assess how the substitution of near real-time SST data with the recently released Interim dataset from Copernicus affects the estimation of the SST extremes indicator in the IBI region. As described in Sect. 2 (Data and Methods), this analysis is conducted by comparing two configurations: the current operational setup (OMI-NRT), which uses near real-time data (IBI-NRT) for the target year, and an alternative formulation (OMI-INT), which replaces it with the Interim dataset (IBI-INT). Both configurations apply the same methodological framework, differing only in the input dataset used for 2024. This comparison allows us to evaluate the sensitivity of the indicator to upstream data choices and to explore whether the use of a more homogeneous modeling framework improves internal consistency and overall robustness.

Figure 1 presents the results of the SST extremes indicator for the year 2024, computed using the OMI-NRT and OMI-INT configurations. The anomaly maps displayed include shaded regions that indicate areas where the absolute value of the 2024 anomaly exceeds one or two standard deviations of the interannual distribution of the 99th percentile, as derived from the IBI-REA climatological reference (1993–2023). This visualization allows for the identification of regions where the anomalies are unusually high relative to the historical variability of SST extremes.

The anomaly fields from both OMI configurations consistently reveal that 2024 was characterized by predominantly positive SST anomalies across the IBI region, with broad agreement between products in highlighting widespread warm signals. Both configurations identify a continuous tongue of positive anomalies extending from approximately 36 to 48° N, strongly impacting the Cantabrian coast and large portions of the French Atlantic coastline, where anomalies frequently exceed one standard deviation and locally surpass the two-standard-deviation threshold, pointing to exceptionally intense events. A similar coherent pattern is observed in the Mediterranean, where both products display dominant positive anomalies, most pronounced in the Alboran Sea. However, notable differences emerge in regions of high natural variability and in the spatial extent and intensity of anomalies. Along the Portuguese coast and Gulf of Cádiz, OMI-NRT tends to produce broader and more intense negative anomalies compared to OMI-INT, while in the northeastern Atlantic near 54° N, negative anomalies exceeding one standard deviation in the OMI-NRT configuration represent the most pronounced discrepancies. Conversely, positive anomaly regions exhibit opposite behavior, with both the Atlantic anomaly tongue extending toward the Bay of Biscay and Mediterranean warm anomalies appearing more extensive and generally stronger in the OMI-INT configuration. These systematic differences suggest the presence of biases between the IBI-NRT and IBI-INT datasets relative to the climatological reference provided by IBI-REA, which will be examined in detail in Sect. 5 (Assessment of SST indicator configurations using in situ observations).

4 Analysis of multi-product indicator results

The second improvement explored in this work is the adoption of a multi-product ensemble approach, referred to as MULTI-OMI. As described in the Data and Methods section, this configuration combines three independent estimates of the 2024 SST extremes indicator derived from distinct Copernicus datasets: regional model outputs, global model outputs, and satellite-based SST observations. The ensemble mean provides a consolidated estimate of SST anomalies, while the ensemble spread serves as an indicator of the robustness of the results across the different upstream data sources. Figure 2 shows both the ensemble mean of the anomaly in the 99th percentile of SST for 2024 and the corresponding ensemble standard deviation, allowing for the identification of regions with high inter-product agreement, as well as those with greater sensitivity to the choice of data product. Areas with elevated standard deviation values indicate reduced inter-product consistency and therefore require more cautious interpretation. The ensemble spread thus provides a practical measure of the indicator's robustness, helping to identify regions where the signal is most reliable and where it should be interpreted with greater care.

The spatial distribution of SST anomalies in the ensemble mean (Fig. 2a) reproduces the main patterns identified in the OMI-NRT and OMI-INT configurations, particularly in regions where the anomaly signal clearly exceeds climatological variability (exceedance of the one- and two-standard-deviation thresholds). In particular, a tongue of positive anomalies extends across the open Atlantic and reaches into the Gulf of Biscay, affecting the Cantabrian coast of the Iberian Peninsula. Similarly, widespread positive anomalies dominate the Mediterranean basin, especially in the Alboran Sea. Negative anomalies along the Portuguese coast and the Gulf of Cádiz also closely match those obtained from the OMI-NRT configuration, confirming the dominance of this cold signal across different datasets.

It is worth noting that the adoption of the MULTI-OMI configuration represents a fundamental shift in the nature of the indicator, moving from a single-product to a multi-source ensemble framework. While OMI-NRT and OMI-INT each produce a single estimate of the SST extremes indicator, MULTI-OMI provides a range of outcomes reflecting the sensitivity of the indicator to the choice of upstream data source; in this context, the ensemble mean should not be interpreted merely as a more accurate single estimate, but as the central tendency across the contributing observational or modelling system. The ensemble spread, quantified here through the standard deviation across members, thus serves as a practical first-order measure of inter-product

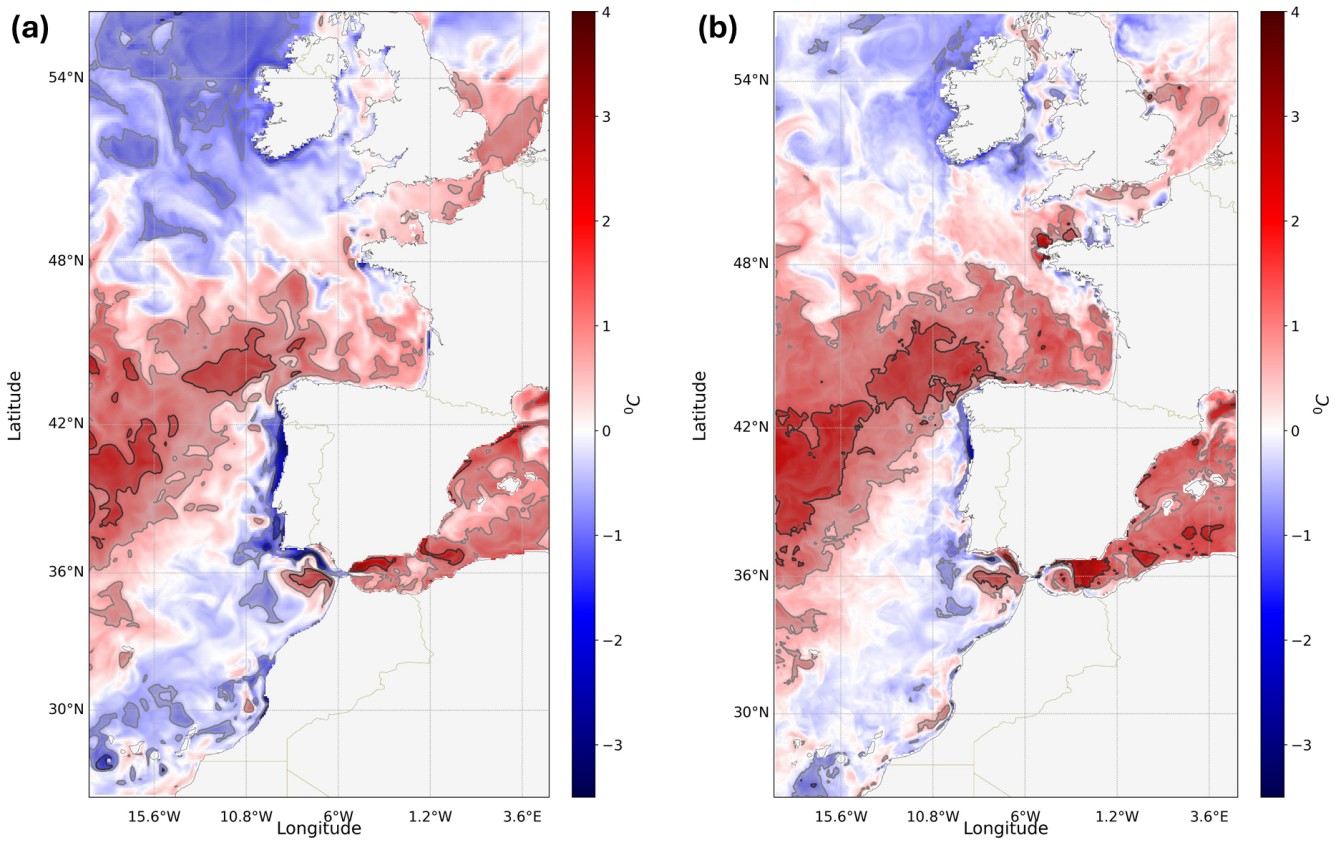


Figure 1. Anomaly in 2024 of the 99th percentile of the annual SST distribution (blue/red shading), referenced to the climatological mean for the period 1993–2023 derived from the IBI reanalysis product (IBI-REA). Panel **(a)** shows results obtained using the OMI-NRT configuration, which combines IBI-REA and the near real-time product IBI-NRT, while panel **(b)** displays results using the OMI-INT configuration, which replaces IBI-NRT with the Interim dataset IBI-INT. Grey and black contour lines, along with partial grey shading, indicate regions where the absolute anomaly exceeds one and two standard deviations, respectively, of the interannual distribution of the 99th percentile during the reference period.

spread, providing users with actionable insight into the reliability of the indicator estimates. In this regard, Fig. 2a also includes a significance criterion based on the sign agreement across ensemble members, which allows for the identification of regions where the indicator should be interpreted with particular caution. Regions where the anomaly signal is not considered significant – shaded in grey – are those where at least one ensemble member shows an opposite sign of the SST anomaly, indicating a lack of agreement among members on the direction of the anomaly. These regions are generally confined to areas with low anomaly magnitudes, where, according to the applied criteria, even small discrepancies among members can result in a non-significant outcome. Additionally, three notable coastal areas of non-significant anomalies are observed, where the weak anomaly signal coincides with greater discrepancies among ensemble members. The first region is located along the northwestern African coast, in the vicinity of the Saharan upwelling system, an area known to be characterized by high high-frequency variability due to the interaction between coastal upwelling dynamics and mesoscale processes (Desbiolles et al., 2014; Barton et al., 2004). Here, the strong short-term variability characteristic of coastal upwelling likely contributes to the divergence in ensemble estimates. The second area extends along the French Atlantic coast, from the Spanish border to the Brittany Peninsula, where model disagreement may stem from complex coastal dynamics, the influence of shallow nearshore waters, and variable spatial resolution among products. The entire Irish Sea appears as a region of non-significant anomalies, likely reflecting the heightened uncertainty in resolving fine-scale variability within shallow, semi-enclosed waters, which in turn amplifies discrepancies across ensemble members.

Figure 2b shows the standard deviation of the ensemble, which highlights areas where discrepancies between ensemble members are largest, indicating a potential decrease in the reliability of the indicator estimates. The highest values are predominantly concentrated along coastal areas and the continental slope. The most pronounced maxima appear in regions where strong coastal dynamics and sharp bathy-

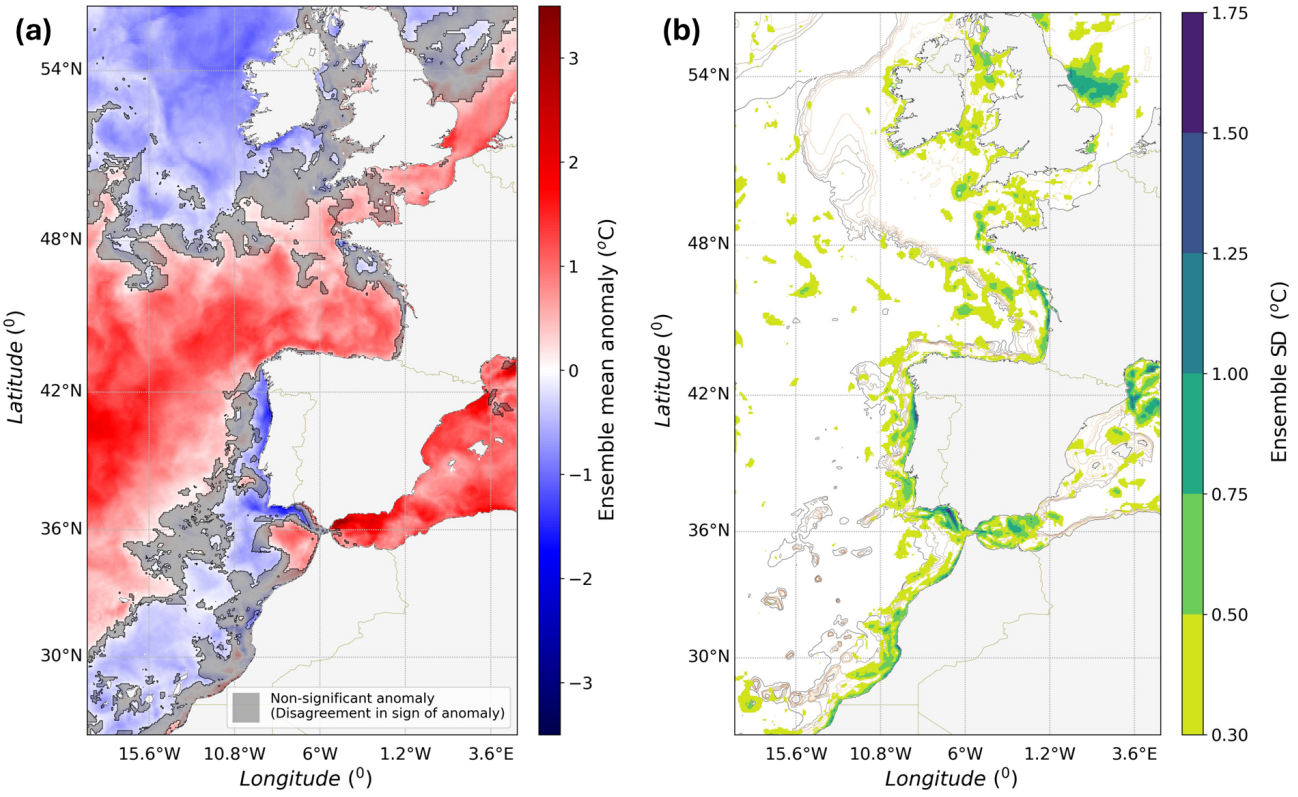


Figure 2. Results of the multi-product SST extremes indicator computed using the MULTI-OMI configuration. **(a)** Ensemble mean of the 2024 anomaly of the 99th percentile of annual SST (blue/red shading) computed with respect to the reference period 1993–2023. Grey shading indicates regions where at least one ensemble member shows an opposite sign of the SST anomaly, in which case the anomaly sign is considered non-significant. **(b)** Standard deviation (SD) of the ensemble. Only SD values above 0.3 °C are shown (contour shading), along with bathymetric contour lines at 50, 100, 500, 1000, 1500, 2000, and 3000 m depth (contour lines over ocean areas).

metric gradients coincide, such as the Gulf of Cádiz and the upwelling zones off both the Iberian Peninsula and the northwestern African coast. A well-defined band of increased discrepancy is also evident along the Armorican Slope in the Bay of Biscay, as well as in the coastal margins of the French Atlantic façade. In these areas, the magnitude of inter-member differences is such that it can render the anomaly sign non-significant near the coast. In the Mediterranean, particularly in the Alboran Sea, elevated discrepancies are observed in association with mesoscale structures and gyres generated by the inflow of Atlantic water through the Strait of Gibraltar (Macias et al., 2016).

5 Assessment of SST indicator configurations using in situ observations

The results of the three SST extremes indicator configurations (OMI-NRT, OMI-INT, and MULTI-OMI) are now compared with in situ observational data from the Copernicus product OMI-OBS for 2024. The objective is to evaluate the degree of agreement between the gridded indicator estimates and observed SST extremes, and to understand how methodological choices influence the consistency and reliability of the results (see Fig. 3).

Figure 3a displays the spatial distribution of the 2024 SST anomaly in the 99th percentile, as estimated by the MULTI-OMI ensemble mean, overlaid with anomaly values derived from in situ observations (OMI-OBS). Observational points are categorized according to whether they fall within or outside the inter-product spread range defined by the ensemble mean ± standard deviation. The results reveal a widespread agreement in the sign of the anomalies between MULTI-OMI and OMI-OBS, indicating consistency in the detection of warm and cold events. However, the inclusion of observed values within the ensemble uncertainty range reveals instances in which they fall outside the bounds defined by the ensemble standard deviation, even when the sign of the anomaly matches. This behavior does not display a clear spatial distribution and is more clearly illustrated (and commented) in Fig. 3b.

Figure 3b presents a Taylor diagram (Taylor, 2001) comparing the performance of the three indicator configurations, using OMI-OBS as the reference. The results for OMI-INT show that replacing near real-time data with the Interim

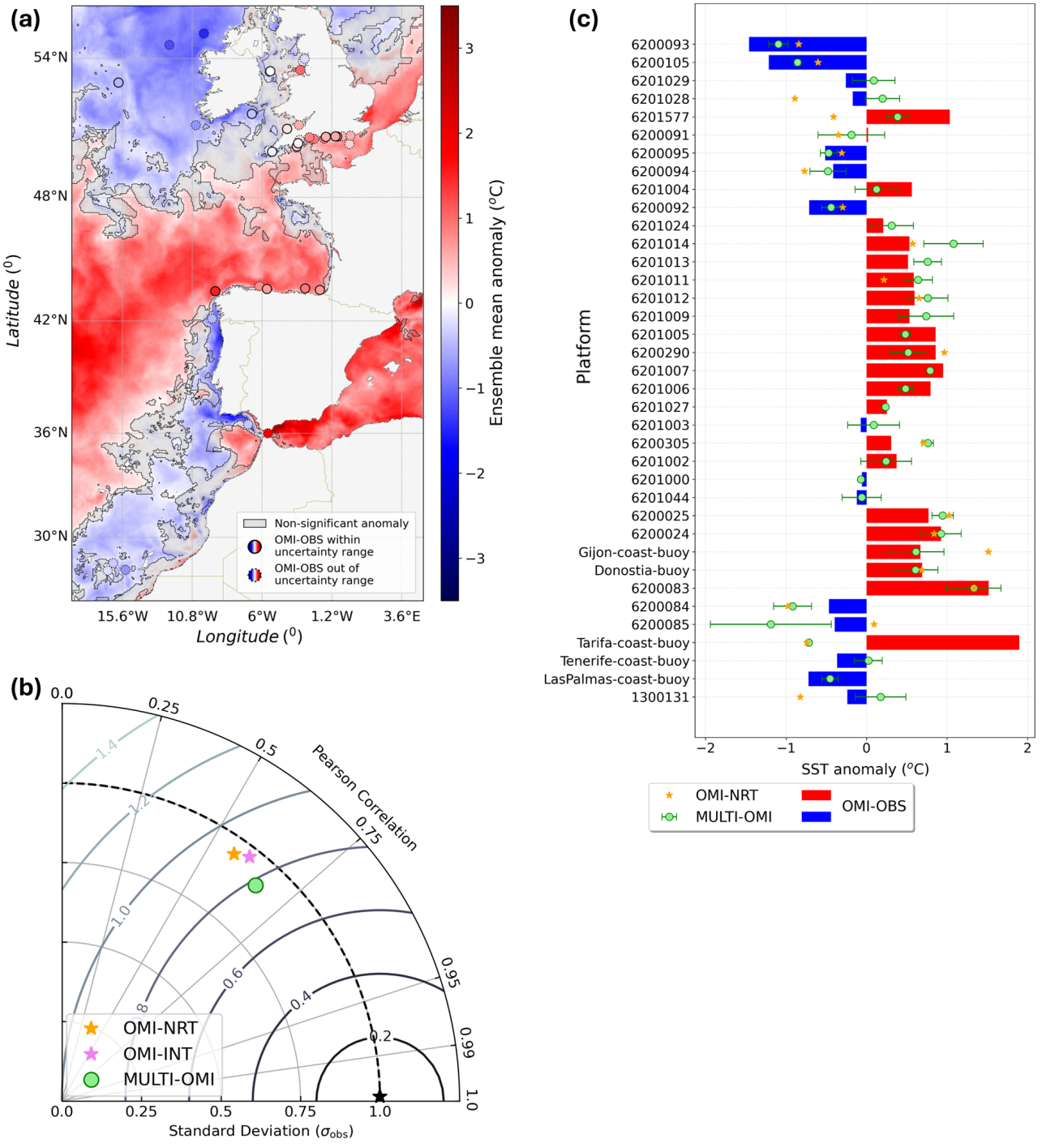


Figure 3. **(a)** Anomaly in 2024 of the 99th percentile of the annual SST distribution from the MULTI-OMI configuration (shading, same as in Fig. 2a), shown alongside corresponding anomalies computed from in situ observations provided by the OMI-OBS product (colored circles). Circles with solid black outlines indicate locations where the observed anomaly lies within the inter-product spread range defined by the MULTI-OMI ensemble mean ± standard deviation. Circles with dashed outlines represent locations where the observed anomaly falls outside this range. **(b)** Taylor diagram showing the performance of the three configurations (OMI-NRT, OMI-INT, and MULTI-OMI) relative to in situ observations (OMI-OBS). **(c)** Anomaly values for the 99th percentile of the annual SST distribution in 2024 computed from OMI-OBS (blue and red horizontal bars, indicating negative and positive anomalies, respectively), compared with estimates from MULTI-OMI (green circles with uncertainty bars) and OMI-NRT (orange stars). The OMI-OBS values are displayed using bars just to facilitate the visualization and identification of the reference data. Platforms are ordered by decreasing latitude along the vertical axis.

dataset yields a modest improvement in overall performance. This improvement is particularly evident in the spatial standard deviation ratio, which in OMI-INT lies closer to unity than in OMI-NRT, indicating that the former provides a more accurate estimation of the spatial variability of the 99th percentile anomaly, along with a slight enhancement in spatial correlation. The superior performance of OMI-INT over OMI-NRT supports the inclusion of the former as the IBI regional modelling member of the MULTI-OMI ensemble, while OMI-NRT is consequently discarded as an ensemble member. In light of this, the remainder of the analysis focuses on the MULTI-OMI configuration, which incorporates OMI-INT as its regional modelling component.

Regarding the MULTI-OMI configuration, it is important to interpret the results within the context of applying single-value metrics to an ensemble-based product. In this case, the Taylor diagram was computed using the ensemble mean as a single representative estimate of the indicator. From this perspective, the MULTI-OMI configuration behaves as expected for ensemble-based methodologies. On the one hand, the ensemble mean yields a higher correlation with observations, likely due to a more accurate representation of average anomaly values across the region. On the other hand, this increase in correlation comes at the expense of a reduced ability to capture variability. Since the ensemble mean averages out the anomaly fields of its members, the spatial variability of the resulting field is inherently reduced compared to that of any individual member. This smoothing effect leads to a spatial standard deviation of the ensemble mean that is lower than that of the observations, which is reflected in the Taylor diagram as a displacement of the MULTI-OMI point away from the reference standard deviation line. Nevertheless, despite this limitation, the ensemble mean of the MULTI-OMI configuration achieves a noticeable reduction in the centered root-mean-squared error (RMSE), as shown in the Taylor diagram, which is consistent with a reduction in the RMSE computed directly from the data, decreasing from 0.76 °C for OMI-NRT to 0.65 °C for MULTI-OMI. This highlights that, even when using only the ensemble mean as a single representative estimate, the multi-product approach yields a net improvement in performance, demonstrating its potential to enhance the accuracy of SST extremes indicators.

Figure 3c presents the same comparison as in Fig. 3a, using a representation that facilitates the identification of discrepancies in the magnitude of the estimated anomalies. Several mismatches can be observed, which may be partly attributed to the use of the ensemble spread as a proxy for uncertainty. While the computation of formally robust confidence intervals would require the generation of long-term simulations for the interim and reprocessed systems, which currently fall outside the scope of this contribution, the ensemble standard deviation provides a practical first-order estimate of inter-product spread that is sufficient to identify regions of reduced inter-product agreement and to motivate further in-depth analysis. Additionally, many observational platforms are located near the coast, where gridded products (regardless of whether they originate from models or satellite observations) often exhibit higher uncertainty due to complex dynamics and limited spatial resolution. This is also evident in the absence of OMI-NRT values at some coastal stations, a limitation caused by land-sea masking and insufficient data coverage close to the shoreline. Likewise, the absence of uncertainty bars for MULTI-OMI at certain locations indicates that only one ensemble member contributed data at those stations, preventing the estimation of an uncertainty range.

Table 2. Confusion matrix comparing the performance of the MULTI-OMI and OMI-NRT configurations against in situ observations (OMI-OBS) for the estimation of the sign (positive or negative) of the 99th percentile SST anomaly in 2024. Each cell shows the number of stations and the corresponding percentage (relative to the total of 22 stations with valid OMI-NRT data) for which the estimated anomaly sign matches or deviates from the observed sign. In the MULTI-OMI results, the "non-significant" category refers to cases where the ensemble anomaly is not statistically significant, i.e., where at least one ensemble member disagrees on the sign of the anomaly. Bold values indicate correct classifications (true positives or true negatives), italic values indicate incorrect classifications (false positives or false negatives), and non-significant cases, which are not considered either correct or incorrect, are shown without special formating.

Sign of the estimated/ observed anomaly		OMI-OBS +	OMI-OBS −
OMI-NRT	+	**10 (45.4 %)**	*1 (4.6 %)*
	−	*3 (13.6 %)*	**8 (36.4 %)**
MULTI-OMI	+	**11 (50.0 %)**	*0 (0.0 %)*
	−	*1 (4.6 %)*	**7 (31.8 %)**
	Non-significant	1 (4.6 %)	2 (9.1 %)

Beyond the improvement in single-estimate accuracy achieved through the multi-product approach (Fig. 3c), it is also important to evaluate other advantages offered by adopting an ensemble-based approach. Table 2 summarizes the confusion matrices for the OMI-NRT and MULTI-OMI configurations, comparing their estimates of the sign (positive or negative) of the 99th percentile SST anomaly in 2024 against in situ observations provided by OMI-OBS. The analysis is restricted to the 22 observational stations for which valid OMI-NRT data are available. In the case of MULTI-OMI, instances classified as "non-significant", i.e., where the ensemble members disagree on the sign of the anomaly, are reported separately and not considered either correct or incorrect estimates.

Overall, the MULTI-OMI configuration demonstrates a high level of agreement with observations, correctly predicting the anomaly sign at 18 out of 22 stations (81.8 %), matching the performance of OMI-NRT in terms of total correct

classifications. However, the nature of the errors differs between the two configurations. MULTI-OMI does not produce any false positives and only one false negative, whereas OMI-NRT yields both false positives (1) and false negatives (3). This suggests that MULTI-OMI is more conservative in regions of uncertainty, likely due to its ensemble-based structure, which avoids assigning a sign when model agreement is insufficient. This cautious behavior is reflected in the "non-significant" category, which accounts for 3 out of 22 stations (13.6 %) in the MULTI-OMI configuration.

In summary, although both configurations achieve the same overall accuracy with respect to the observed anomaly signs, the MULTI-OMI configuration enables the identification of areas of high uncertainty that, through their exclusion, support the reliability of the anomalies in the rest of areas, even if these have low magnitudes. Accuracy ratio for the MULTI-OMI configuration in areas with anomalies that are considered significant is 94.7 % (18 out of 19), which is higher than the 81.8 % reached in the OMI-NRT configuration (18 out of 22).

6 Conclusions

The continuous evolution of the Copernicus Marine catalogue, with the incorporation of new and improved modelling and observational products, provides both the motivation and the opportunity for periodic methodological reassessment of existing Ocean Monitoring Indicators. In this context, the present study has evaluated two methodological alternatives to the operational OMI for SST extremes in the IBI region (OMI-NRT): (i) the replacement of the near-real-time IBI dataset with the interim version of the IBI multiyear product (OMI-INT), and (ii) the development of a multi-product ensemble approach integrating regional model, global model, and satellite-derived SST estimates (MULTI-OMI). Both modifications were designed to reduce potential biases in the original product while providing enhanced robustness and user-oriented inter-product spread information.

To achieve this, three indicator configurations were compared: the operational baseline (OMI-NRT), an alternative configuration using the Interim dataset (OMI-INT), and a multi-product ensemble approach (MULTI-OMI). The performance of these three configurations was assessed using standard statistical metrics, including mean bias and RMSE, and classification-based validation techniques. All comparisons were made with respect to the OMI-OBS product, which derives SST extremes from in situ observational data, providing an independent and robust benchmark evaluating each configuration's ability to reproduce the magnitude and sign of 99th percentile SST anomalies for the year 2024.

The results obtained in this study lead to several relevant conclusions regarding the methodological alternatives analyzed. First, the OMI-INT configuration shows a moderate improvement over the current operational configuration (OMI-NRT). This improvement is probably associated with the greater consistency of the upstream data, since in the OMI-INT configuration both the climatological baseline and the target-year data are derived from products generated using the same ocean model configuration (IBI-REA and IBI-INT, respectively), thereby reducing potential biases introduced by the use of heterogeneous modeling configurations, i.e. the combination of data generated with IBI-REA and IBI-NRT. Beyond the numerical improvements, the methodological coherence offered by using a single modeling system justifies the adoption of the Interim dataset in future operational contexts.

The MULTI-OMI configuration has also provided valuable insights through its multi-product *approach*. The spatial distribution of SST anomalies for 2024, as estimated by MULTI-OMI, confirms the presence of strong positive anomalies in the Mediterranean and across the open Atlantic toward the Bay of Biscay. At the same time, MULTI-OMI identifies several regions – particularly along the northwestern African coast, the Atlantic coast of France, and the entire Irish Sea – where the anomaly is classified as non-significant due to disagreement among ensemble members. These areas are associated with high dynamical variability, such as coastal upwelling systems, complex shelf dynamics, or limited model agreement in semi-enclosed basins. Moreover, the spatial distribution of ensemble spread highlights regions of elevated inter-product discrepancy, which tend to concentrate along continental slopes, coastal upwelling systems, and mesoscale gyre structures, such as those found in the Gulf of Cadiz, the Portuguese coast and the Alboran Sea.

Regarding the benefits of applying a multi-product methodology, the use of the ensemble mean in MULTI-OMI demonstrates that its advantages outweigh the minor limitations observed. While ensemble averaging tends to dampen extreme values – reducing the amplitude of high or low anomalies – it leads to a net reduction in overall error, as evidenced by the decrease in RMSE from 0.76 °C (OMI-NRT) to 0.65 °C (MULTI-OMI). This makes the MULTI-OMI configuration clearly superior in the metrics evaluated through the Taylor diagram. The improvement indicates greater accuracy in estimating anomalies near the mean. Furthermore, beyond improvements in single-estimate accuracy, the ensemble-based nature of MULTI-OMI allows inter-product spread information to be directly incorporated into the indicator. This type of information can be essential for decision-making, as it helps reduce classification errors – particularly false positives and false negatives – when determining the sign of the anomaly.

Another advantage of the multi-product approach lies in its capacity to improve spatial coverage, especially in coastal zones. The use of multiple gridded data sources with differing resolutions and origins (e.g., numerical models and satellite products) increases the likelihood of capturing valid in-

formation in regions where a single product might offer limited or no coverage.

The present work left open some new paths to be explored, for example it encourages the analysis of the multi-product methodology over decadal time scales. Such a study would allow for the statistical characterization of error distributions and the estimation of uncertainty intervals with controlled confidence levels. This would enable the generation of statistically consistent uncertainty ranges for the SST extremes indicator. Additionally, analyzing the temporal variability of SST maxima would provide insight into the climatic variability of extreme thermal events and support the development of trend analyses and spatial maps of SST extremes in the IBI region.

Since the goal of this study is to improve the original operational indicator for SST extremes, it is important to reflect on the operational implications of the proposed multi-product approach, as illustrated in Fig. 2. This figure shows the type of outputs that can be delivered by a modified operational OMI based on ensemble methods. However, if the underlying philosophy of a multi-product methodology is to consolidate all available sources of information, then the configuration shown in Fig. 2 has an important limitation: it excludes one of the key datasets available in the Copernicus Marine catalogue – namely, the in situ observational product used to compute OMI-OBS.

While the ideal solution would be to incorporate OMI-OBS directly as an additional member of the ensemble, the integration of non-gridded in situ data into a gridded multi-product framework presents significant methodological challenges. These include spatial interpolation, and ensemble consistency, all of which require careful treatment and lie beyond the scope of the present study.

As a practical compromise, a hybrid approach is proposed and illustrated in Fig. 4. In this solution, the ensemble-based map from MULTI-OMI is retained as the primary product, but in regions where the anomaly is classified as non-significant, the corresponding observational value from OMI-OBS is overlaid, provided such data are available. This strategy allows for the integration of observational insight precisely in the areas where model-based uncertainty is highest.

Such an approach enables the retention of meaningful information in regions where ensemble uncertainty prevents a reliable interpretation, thereby improving the utility of the indicator in operational contexts without compromising the methodological integrity of the ensemble system.

The results of this study demonstrate that the MULTI-OMI configuration provides methodological and operational improvements over the current OMI-NRT framework, as evaluated through the GOOS quality criteria. By integrating multiple independent gridded datasets – including both model-based and satellite-derived sources – MULTI-OMI enhances the traceability, robustness, and coverage of the indicator. It improves the reliability of SST extreme estimates, reduces

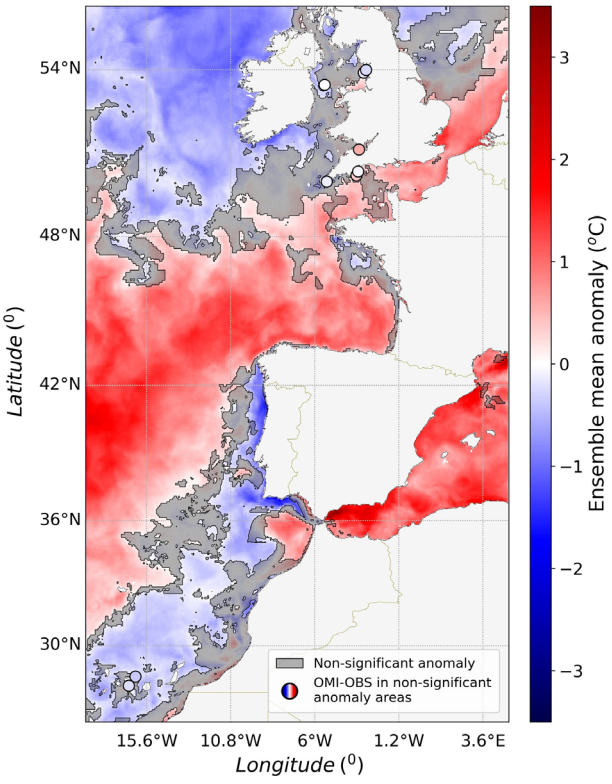


Figure 4. Map of the 2024 SST anomaly in the 99th percentile with respect to the reference period 1993–2023 as estimated by the MULTI-OMI ensemble mean (color shading), combined with in situ observational data from OMI-OBS (red and blue circles) in regions where the ensemble anomaly is classified as non-significant (grey shading) by MULTI-OMI.

overall errors, and incorporates uncertainty in a way that directly supports informed decision-making. Additionally, its greater adaptability to coastal regions and varied spatial contexts strengthens both its scalability and accessibility. Taken together, these advancements position MULTI-OMI as a significant step forward toward a more scientifically mature and operationally relevant OMI, aligned with the evolving needs of climate monitoring and marine risk assessment.

Code availability. The software used for this work is the property of NOW Systems S.L. The methodology strictly describes all the steps followed to develop this code. Anyone interested in accessing this software should contact the corresponding author.

The Taylor diagram in Fig. 3b was generated using the Python implementation by Calim Costa (2021), based on Taylor (2001), freely available on GitHub (https://github.com/mabelcalim/Taylor_diagram).

Data availability. The data used in this work have been obtained from the Copernicus Marine Service. All the mentioned databases

are accessible through the Copernicus Marine Service. Their references can be found in the product tables (Table 1).

Author contributions. APC led the manuscript writing and revisions, and contributed to data analysis and generation of the OMI-INT and MULTI-OMI indicator configurations. AAV performed the main data analysis across all indicator configurations and contributed to manuscript writing and revisions. AG, MAAM and BPG contributed to the generation of the OMI-OBS indicator data and participated in the conceptualization of the study and manuscript revisions. SC and MGS contributed to manuscript revisions.

Competing interests. At least one of the (co-)authors serves as topic editor for the report to which this paper belongs. The peer-review process was guided by an independent editor, and the authors also have no other competing interests to declare.

Disclaimer. The Copernicus Marine Service offering is regularly updated to ensure it remains at the forefront of user requirements. In this process, some products may undergo replacement or renaming, leading to the removal of certain product IDs from the catalogue. If readers have any questions or require assistance regarding these modifications, please feel free to reach out to the Copernicus Marine Service user support team for further guidance. They will be able to provide the necessary information to address concerns and find suitable alternatives.

Publisher's note: Copernicus Publications remains neutral with regard to jurisdictional claims made in the text, published maps, institutional affiliations, or any other geographical representation in this paper. The authors bear the ultimate responsibility for providing appropriate place names. Views expressed in the text are those of the authors and do not necessarily reflect the views of the publisher.

Acknowledgements. The authors gratefully acknowledge the Copernicus Marine Service for providing free and open access to all the datasets used in this study. These data products were essential for the computation and validation of the SST extremes indicators presented in this work.

We also thank Calim Costa (2021) for making available the Python implementation of the Taylor diagram.

Review statement. This paper was edited by Marta Marcos and reviewed by two anonymous referees.

References

Álvarez Fanjul, E., de Pascual Collar, A., Pérez Gómez, B., de Alfonso, M., García Sotillo, M., Staneva, J., Clementi, E., Grandi, A., Zacharioudaki, A., Korres, G., Ravdas, M., Renshaw, R., Tinker, J., Raudsepp, U., Lagemaa, P., Maljutenko, I., Geyer, G., Müller, M., and Çağlar Yumruktepe, V.: Sea level, sea surface temperature and SWH extreme percentiles: combined analysis from model results and in situ observations, Section 2.7, S31, in: Copernicus Marine Service Ocean State Report, Issue 3, edited by: von Schuckmann, K., Le Traon, P.-Y., Smith, N., Pascual, A., Djavidnia, S., Gattuso, J.-P., Grégoire, M., and Nolan, G., J. Oper. Oceanogr., 12, S1–S123, https://doi.org/10.1080/1755876X.2019.1633075, 2019.

Autret, E., Tandéo, P., and Piollé, J.-F.: EU Copernicus Marine Service Product User Manual for the European North West Shelf/Iberia Biscay Irish Seas - High Resolution L4 Sea Surface Temperature Reprocessed, SST_ATL_SST_L4_REP_OBSERVATIONS_010_026, Issue 1.5, Mercator Ocean International, https://documentation.marine.copernicus.eu/PUM/CMEMS-SST-PUM-010-026.pdf (last access: 9 April 2025), 2023.

Autret, E., Piollé, J.-F., and Tandéo, P.: EU Copernicus Marine Service Quality Information Document for the European North West Shelf/Iberia Biscay Irish Seas - High Resolution L4 Sea Surface Temperature Reprocessed, SST_ATL_SST_L4_REP_OBSERVATIONS_010_026, Issue 1.0, Mercator Ocean International, https://documentation.marine.copernicus.eu/QUID/CMEMS-SST-QUID-010_026_038_039_044.pdf (last access: 9 April 2025), 2024.

Barton, E. D., Arístegui, J., Tett, P., and Navarro-Pérez, E.: Variability in the Canary Islands area of filament-eddy exchanges, Prog. Oceanogr., 62, 71–94, https://doi.org/10.1016/j.pocean.2004.07.003, 2004.

Calim Costa, M.: Taylor diagram in python based on Taylor (2001), GitHub [code], https://github.com/mabelcalim/Taylor_diagram, 2021.

Castrillo-Acuña, L., Levier, B., Aznar, R., and Sotillo, M. G.: EU Copernicus Marine Service Product User Manual for the Atlantic-Iberian Biscay Irish-Ocean Physics Reanalysis, IBI_MULTIYEAR_PHY_005_002, Issue 4.2, Mercator Ocean International, https://documentation.marine.copernicus.eu/PUM/CMEMS-IBI-PUM-005-002.pdf (last access: 18 March 2025), 2024a.

Castrillo-Acuña, L., Reffray, G., Levier, B., Escudier, R., Gutknecht, E., Aznar, R., Sotillo, M. G., and Cailleau, S.: EU Copernicus Marine Service Product User Manual for the Atlantic-Iberian Biscay Irish-Ocean Physics Analysis and Forecast, IBI_ANALYSISFORECAST_PHY_005_001, Issue 8.2, Mercator Ocean International, https://documentation.marine.copernicus.eu/PUM/CMEMS-IBI-PUM-005-001.pdf (last access: 18 March 2025), 2024b.

de Alfonso, M., Gallardo, A., Manzano, F., and Pérez Gómez, B.: EU Copernicus Marine Service Quality Information Document for the Iberia Biscay Ireland sea surface temperature extreme variability mean and anomaly (observations), OMI_EXTREME_SST_IBI_sst_mean_and_anomaly_obs, Issue 2.0, Mercator Ocean International, https://documentation.marine.copernicus.eu/QUID/CMEMS-OMI-QUID-EXTREME-SST-OBS.pdf (last access: 5 June 2025), 2022a.

de Alfonso, M., Gallardo, A., Manzano, F., and Pérez Gómez, B.: EU Copernicus Marine Service Product User Manual for the Iberia Biscay Ireland sea surface temperature extreme variability mean and anomaly (observations),

OMI_EXTREME_SST_IBI_sst_mean_and_anomaly_obs, Issue 2.0, Mercator Ocean International, https://documentation.marine.copernicus.eu/PUM/CMEMS-OMI-PUM-EXTREME-SST-OBS.pdf (last access: 5 June 2025), 2022b.

de Pascual Collar, A., Sotillo, M. G., De Alfonso, M., Pérez Gómez, B., and Álvarez Fanjul, E.: EU Copernicus Marine Service Quality Information Document for the Iberia Biscay Ireland Sea Surface Temperature extreme from Reanalysis, IBI_OMI_TEMPSAL_extreme_var_temp_mean_and_anomaly, Issue 1.2, Mercator Ocean International, https://documentation.marine.copernicus.eu/QUID/CMEMS-OMI-QUID-TEMPSAL-EXTREME-VAR-TEMP.pdf (last access: 16 June 2025), 2021a.

de Pascual Collar, A., Sotillo, M. G., De Alfonso, M., Pérez Gómez, B., and Álvarez Fanjul, E.: EU Copernicus Marine Service Product User Manual for the Iberia Biscay Ireland Sea Surface Temperature extreme from Reanalysis, IBI_OMI_TEMPSAL_extreme_var_temp_mean_and_anomaly, Issue 1.2, Mercator Ocean International, https://documentation.marine.copernicus.eu/PUM/CMEMS-OMI-PUM-TEMPSAL-EXTREME-VAR-TEMP.pdf (last access: 5 June 2025), 2021b.

Desbiolles, F., Blanke, B., and Bentamy, A.: Short-term upwelling events at the western African coast related to synoptic atmospheric structures as derived from satellite observations. J. Geophys. Res.-Oceans, 119, 461–483, https://doi.org/10.1002/2013JC009278, 2014.

Drévillon, M., Lellouche, J. M., Régnier, C., Garric, G., Bricaud, C., Hernandez, O., and Bourdallé-Badie, R.: EU Copernicus Marine Service Quality Information Document for the Global Ocean Physics Reanalysis, GLOBAL_MULTIYEAR_PHY_001_030, Issue 1.6, Mercator Ocean International, https://documentation.marine.copernicus.eu/QUID/CMEMS-GLO-QUID-001-030.pdf (last access: 18 March 2025), 2023.

Drévillon, M., Fernandez, E., and Lellouche, J. M.: EU Copernicus Marine Service Product User Manual for the Global Ocean Physics Reanalysis, GLOBAL_MULTIYEAR_PHY_001_030, Issue 1.6, Mercator Ocean International, https://documentation.marine.copernicus.eu/PUM/CMEMS-GLO-PUM-001-030.pdf (last access: 18 March 2025), 2024.

EU Copernicus Marine Service Product: Iberia Biscay Ireland Sea Surface Temperature extreme from Reanalysis, Mercator Ocean International [data set], https://doi.org/10.48670/moi-00254, 2021.

EU Copernicus Marine Service Product: European North West Shelf/Iberia Biscay Irish Seas – High Resolution ODYSSEA L4 Sea Surface Temperature Analysis, Mercator Ocean International [data set], https://doi.org/10.48670/moi-00152, 2022a.

EU Copernicus Marine Service Product: Iberia Biscay Ireland sea surface temperature extreme variability mean and anomaly (observations), Mercator Ocean International [data set], https://doi.org/10.48670/moi-00255, 2022b.

EU Copernicus Marine Service Product: Global Ocean Physics Reanalysis, Mercator Ocean International [data set], https://doi.org/10.48670/moi-00021, 2023.

EU Copernicus Marine Service Product: Atlantic-Iberian Biscay Irish-Ocean Physics Reanalysis, Mercator Ocean International [data set], https://doi.org/10.48670/moi-00029, 2024a.

EU Copernicus Marine Service Product: Atlantic-Iberian Biscay Irish-Ocean Physics Analysis and Forecast, Mercator Ocean International [data set], https://doi.org/10.48670/moi-00027, 2024b.

EU Copernicus Marine Service Product: Global Ocean Physics Analysis and Forecast, Mercator Ocean International [data set], https://doi.org/10.48670/moi-00016, 2024c.

EU Copernicus Marine Service Product: European North West Shelf/Iberia Biscay Irish Seas – High Resolution L4 Sea Surface Temperature Reprocessed, Mercator Ocean International [data set], https://doi.org/10.48670/moi-00153, 2024d.

Le Galloudec, O., Law Chune, S., Nouel, L., Fernandez, E., Derval, C., Tressol, M., Dussurget, R., Biardeau, A., and Tonani, M.: EU Copernicus Marine Service Product User Manual for the Global Ocean Physics Analysis and Forecast, GLOBAL_ANALYSISFORECAST_PHY_001_024, Issue 2.1, Mercator Ocean International, https://documentation.marine.copernicus.eu/PUM/CMEMS-GLO-PUM-001-024.pdf (last access: 18 March 2025), 2024.

Lellouche, J. M., Le Galloudec, O., Regnier, C., Van Gennip, S., Law Chune, S., Levier, B., Greiner, E., Drevillon, M., and Szczypta, C.: EU Copernicus Marine Service Quality Information Document for the Global Ocean Physics Analysis and Forecast, GLOBAL_ANALYSISFORECAST_PHY_001_024, Issue 1.1, Mercator Ocean International, https://documentation.marine.copernicus.eu/QUID/CMEMS-GLO-QUID-001-024.pdf (last access: 18 March 2025), 2024.

Levier, B., Reffray, G., Aznar, R., Ciliberti, S., Sotillo, M. G., and Cailleau, S.: EU Copernicus Marine Service Quality Information Document for the Atlantic-Iberian Biscay Irish-Ocean Physics Reanalysis, IBI_MULTIYEAR_PHY_005_002, Issue 5.2, Mercator Ocean International, https://documentation.marine.copernicus.eu/QUID/CMEMS-IBI-QUID-005-002.pdf (last access: 18 March 2025), 2024a.

Levier, B., Reffray, G., Escudier, R., Gutknecht, E., Amo-Baladrón, A., Ciliberti, S., Aznar, R., and Sotillo, M. G.: EU Copernicus Marine Service Quality Information Document for the Atlantic-Iberian Biscay Irish-Ocean Physics Analysis and Forecast, IBI_ANALYSISFORECAST_PHY_005_001, Issue 6.2, Mercator Ocean International, https://documentation.marine.copernicus.eu/QUID/CMEMS-IBI-QUID-005-001.pdf (last access: 18 March 2025), 2024b.

Macias, D., Garcia-Gorriz, E., and Stips, A.: The seasonal cycle of the Atlantic Jet dynamics in the Alboran Sea: direct atmospheric forcing versus Mediterranean thermohaline circulation, Ocean Dynam., 66, 137–151, https://doi.org/10.1007/s10236-015-0914-y, 2016.

Oliver, E. C. J., Benthuysen, J. A., Darmaraki, S., Donat, M. G., Hobday, A. J., Holbrook, N. J., Schlegel, R. W., and Sen Gupta, A.: Marine heatwaves, Annu. Rev. Mar. Sci., 13, 313–342, https://doi.org/10.1146/annurev-marine-032720-095144, 2021.

Pérez Gómez, B., de Alfonso, M., Zacharioudaki, A., Pérez González, I., Álvarez Fanjul, E., Müller, M., Marcos, M., Manzano, F., Korres, G., Ravdas, M., and Tamm, S.: Sea level, SST and waves: extremes variability, Chap. 3.1, in: Copernicus Marine Service Ocean State Report, Issue 2, J. Oper. Oceanogr.,

11, s79–s88, https://doi.org/10.1080/1755876X.2018.1489208, 2018.

Piollé, J.-F., Autret, E., and Briand, D.: EU Copernicus Marine Service Quality Information Document for the European North West Shelf/Iberia Biscay Irish Seas – High Resolution ODYSSEA L4 Sea Surface Temperature Analysis, SST_ATL_SST_L4_NRT_OBSERVATIONS_010_025, Issue 2.0, Mercator Ocean International, https://documentation.marine.copernicus.eu/QUID/CMEMS-SST-QUID-010-025.pdf (last access: 9 April 2025), 2022a.

Piollé, J.-F., Autret, E., Prévost, C., and Briand, D.: EU Copernicus Marine Service Product User Manual for the European North West Shelf/Iberia Biscay Irish Seas – High Resolution ODYSSEA L4 Sea Surface Temperature Analysis, SST_ATL_SST_L4_NRT_OBSERVATIONS_010_025, Issue 2.0, Mercator Ocean International, https://documentation.marine.copernicus.eu/PUM/CMEMS-SST-PUM-010-025.pdf (last access: 9 April 2025), 2022b.

Smith, K. E., Burrows, M. T., Hobday, A. J., Sen Gupta, A., Moore, P. J., Thomsen, M., Wernberg, T., and Smale, D. A.: Socioeconomic impacts of marine heatwaves: Global issues and opportunities, Science, 374, eabj3593, https://doi.org/10.1126/science.abj3593, 2021.

Taylor, K. E.: Summarizing multiple aspects of model performance in a single diagram, J. Geophys. Res.-Atmos., 106, 7183–7192, https://doi.org/10.1029/2000JD900719, 2001.

von Schuckmann, K., Godoy-Faundez, A., Garçon, V., Muller-Karger, F. E., Evans, K., Appeltans, W., Bax, N., Benedetti Cecchi, L., Bernard, A., Bernard, K., Byrnes, J., Canonico, G., Chapuis, L., Clark, M. R., Darnaude, A. M., Davies, C., Englyst, P., Fransson, A., Hallam, S., Heslop, E., Holland, E., Hood, M., Kern, S., Liné, A., Lara-Lopez, A., Loose, N., Martín Míguez, B., McMahon, C. R., Nordlund, L. M., Post, J., Speich, S., Sutton, A., Tanhua, T., Telszewski, M., Poursanidis, D., and Yu, W.: Global ocean indicators: Marking pathways at the science-policy nexus, Mar. Policy, 184, 106922, https://doi.org/10.1016/j.marpol.2025.106922, 2026.

State Planet, 7-osr10, 8, 2026
https://doi.org/10.5194/sp-7-osr10-8-2026
© Author(s) 2026. This work is distributed under
the Creative Commons Attribution 4.0 License.

New insights on mesoscale activity in the western Mediterranean Sea

Laura Gómez-Navarro[1,2], Maxime Ballarotta[3], Diego Cortés-Morales[1], Marie-Isabelle Pujol[3], Laura Fortunato[4], Baptiste Mourre[1], and Ananda Pascual[1]

[1]IMEDEA (UIB-CSIC), Esporles, 07190, Spain
[2]ICM (CSIC), Barcelona, 08003, Spain
[3]CLS, Ramonville-Saint-Agne, 31520, France
[4]Dipartimento di Scienze e tecnologie, Università degli studi di Napoli Parthenope, 80143, Naples, Italy

Correspondence: Laura Gómez-Navarro (laura.gomez@icm.csic.es)

Received: 25 August 2025 – Discussion started: 6 October 2025
Revised: 8 September 2026 – Accepted: 9 September 2026 – Published: 30 September 2026

Abstract. Mesoscale ocean variability plays a crucial role in regional circulation, heat transport, and the distribution of tracers such as nutrients, biological material, and pollutants. Mesoscale eddies are key drivers of these ocean dynamics, and their observation (particularly of small-scale and coastal structures) has been limited by the resolution of conventional altimetry products. The Surface Water and Ocean Topography (SWOT) mission provides unprecedented high-resolution sea surface height data, offering new opportunities to refine mesoscale observations and improve our understanding of their impact on surface ocean dynamics. In this study, we assess the potential of a new gridded altimetry product that incorporates SWOT wide-swath data (MIOST-K) and its differences with respect to the reference and widely used Copernicus Marine Environment Monitoring Service (CMEMS) product DUACS-OI, based solely in nadir altimetry. We analyze the eddy field in the western Mediterranean region, important for many different socio-economic activities like tourism, maritime transport, and fisheries and aquaculture. Compared to DUACS-OI, MIOST-K identifies a larger number of mesoscale eddies, particularly in coastal regions, and generally exhibits higher eddy kinetic energy (EKE) associated with the detected structures. We identify differences not only in the number of eddies, but also in their characteristics: e.g. size and associated EKE. This is relevant for defining optimum marine traffic routes, but also for operational activities such as marine pollution management. To evaluate the implications of these differences for transport and retention processes, we analyse the retention capacity of Algerian Eddies, which in the past have been found relevant in the transport of marine debris between the North African coast and the Balearic Islands. MIOST-K leads to substantially different particle retention estimates for some eddies, highlighting the sensitivity of transport processes to mesoscale circulation representation. Our findings evaluate how well SWOT-enhanced data affects the representation of mesoscale eddies and their velocity structures, showing important implications for ocean monitoring, climate studies, and marine ecosystem management.

1 Introduction

As the ocean continues to undergo rapid physical and ecological change, the ability to monitor and understand its dynamics at finer scales is increasingly critical. This study presents emerging approaches and technologies that are advancing our capacity to observe ocean processes. Among these, the enhanced detection and characterization of mesoscale features (such as eddies) represents an unprecedented leap forward, particularly in regions like the western Mediterranean Sea, where such structures strongly influence circulation, ecosystem connectivity, and pollutant dispersion (e.g. Suaria and Aliani, 2014; Cotroneo et al., 2021).

Conventional mesoscale monitoring has relied primarily on satellite altimetry products such as the Copernicus Ma-

Published by Copernicus Publications.

Table 1. Product table.

Product ref. no.	Product ID & type	Data access	Documentation
1	SEALEVEL_EUR_PHY_L4_NRT_008_060; satellite observations	EU Copernicus Marine Service Product (2025a)	Quality Information Document (QUID): Ballarotta et al. (2025a) Product User Manual (PUM): Pujol (2025a)
2	SEALEVEL_EUR_PHY_L4_MY_008_068; satellite observations	EU Copernicus Marine Service Product (2025b)	QUID: Ballarotta et al. (2025b) PUM: Pujol (2025b)
3	Gridded Sea Level Height and geostrophic velocities computed with Multiscale Interpolation; MIOST-K v2.0.1; satellite observations	AVISO/DUACS (2025)	PUM: Ballarotta (2025)

rine Environment Monitoring Service (CMEMS), Sea Level – Thematic Assembly Centre (SL-TAC) dataset (e.g. Le Traon et al., 1998; Sánchez-Román et al., 2023). However, the launch of the Surface Water and Ocean Topography (SWOT) mission, and its Ka-band Radar Interferometer (KaRIn) instrument, has opened new observational pathways (Morrow et al., 2019; Fu et al., 2024). Recent studies have demonstrated that mesoscale eddies can be directly identified from SWOT wide-swath SSH observations, particularly in regions with small Rossby radius of deformation (e.g., Verger-Miralles et al., 2025; de Marez et al., 2026; Han et al., 2026; Fu et al., 2026). However, direct swath-based detection is more limited for larger mesoscale eddies extending beyond the instantaneous SWOT swath coverage. Gridded products integrating SWOT observations, provide a complementary approach by reconstructing spatially continuous fields, allowing both smaller-scale structures and larger mesoscale eddies to be characterized. This study evaluates the added value of a new pre-operational Level-4 (L4) surface product (MIOST with KaRIn; Ballarotta et al., 2025c), which integrates SWOT KaRIn data during the science phase (September 2023–December 2024), by comparing it with existing CMEMS products based solely on nadir altimetry.

Using an eddy detection method based on Mason et al. (2014), we assess differences in the eddy field across both products. We focus on key properties of eddies detected in both datasets, particularly Eddy Kinetic Energy (EKE). We center our comparison in a case study focused on the Algerian eddies and their potential to transport floating marine debris towards environmentally vulnerable areas of high biodiversity importance, such as the Cabrera National Park marine protected area (Compa et al., 2020) and nearby regions (e.g. Ruiz-Orejón et al., 2019). In this region, mesoscale dynamics have been identified as key facilitators of plastic pollution transport from the southern Mediterranean coast (Compa et al., 2020). Several media reports (e.g. 20minutos, 2015; Última Hora, 2015; Diario de Mallorca, 2022) have documented large quantities of marine debris reaching Cabrera National Park, underscoring the vulnerability of this protected area to the spread of pollution. As bio-physical hotspots, eddies with longer retention times may enhance exposure risks for sensitive ecosystems. The important role of Algerian eddies in transport and retention processes makes them a compelling target for evaluating the added value of high-resolution SWOT-based surface current products in tracking and forecasting marine debris transport. Therefore, we evaluate the retention rate of particles inside Algerian eddies and thus the risk of marine debris reaching the park's vicinity. Algerian eddies have been found to also be a very important dynamic structure for heat, water masses and matter transport in the basin (e.g. Taupier-Letage et al., 2003; Escudier et al., 2016). In contrast to cyclonic eddies, anticyclonic Algerian eddies last longer and are known to travel farther from their origin and play a stronger role in regional connectivity (Pessini et al., 2018; Cotroneo et al., 2021). Their ability to trap and retain floating material has important implications for both ecological impact and the dispersion of pollutants (Suaria and Aliani, 2014).

This study evaluates how SWOT KaRIn observations affect the representation of surface mesoscale activity in gridded altimetric products over the western Mediterranean. By comparing eddy fields derived from legacy and SWOT-enhanced datasets, we assess differences in the representation of surface circulation, focusing particularly on EKE and eddy retention capacity. More accurate surface mesoscale information can support route planning strategies aimed at reducing ship emissions (e.g. Wang et al., 2023) and improve the identification of pollutant transport pathways toward ecologically sensitive areas such as Cabrera National Park. Beyond improving our understanding of mesoscale dynamics, the overarching objective is to evaluate the added value of high-resolution SWOT-enhanced altimetry for applications ranging from marine pollution mitigation to improved maritime operations and ecosystem management.

2 Data

2.1 DUACS optimal interpolation (DUACS-OI)

The *European Seas Gridded L4 Sea Surface Height* dataset (Table 1, product reference 1 and 2) from the Copernicus Marine Service, provides Sea Level Anomaly (SLA) fields at 1/8° resolution over European regional seas, at a daily temporal frequency. The product is generated by the Data Unification and Altimeter Combination System (DUACS) system (*Centre National d'Etudes Spatiales/Collecte Localisation Satellites*; CNES/CLS) using optimal interpolation of along-track altimeter measurements from multiple satellites (Le Traon et al., 1998). It includes SLA, Absolute Dynamic Topography (ADT), and derived surface geostrophic currents. ADT is obtained by adding the Mean Dynamic Topography (MDT) to SLA. The MDT used is the Mediterranean 2020 product (MDT_CMEMS_2020_MED, EU Copernicus Marine Service Product, 2024). The dataset, is available in Near-Real-Time (NRT, product reference 1) and delayed-time (DT, product reference 2), and supports studies of mesoscale and large-scale sea level variability (e.g. Pascual et al., 2007, 2009; Marcos et al., 2015; Taburet et al., 2019; Ballarotta et al., 2019; Sánchez-Román et al., 2023). The NRT data is updated daily, and at the moment of the study had a temporal coverage from 4 October 2022 to 25 November 2024, while the delayed-time data from 1 January 1992 to 31 December 2023. Therefore, the DT product is only used for the analysis of the mean circulation (Fig. 1), and the NRT product is used for the rest of analyses as it covers 2024.

2.2 MIOST with SWOT KaRIn (MIOST-K)

The Multiscale Inversion of Ocean Surface Topography (MIOST) product (Table 1, product reference 3) is a new-generation gridded altimetry dataset that incorporates SWOT KaRIn data, i.e., two-dimensional swath (SSHA) observations. This global product is available at a spatial resolution of 1/8° and at daily temporal frequency. We utilized the experimental L4 multimission sea level product distributed by AVISO v2.0.1, which combines SWOT swath altimetry with conventional nadir altimeter measurements. The dataset relies on the MIOST method (Ubelmann et al., 2021, 2022), a statistical technique that reconstructs sea surface height fields by decomposing variability across multiple spatial and temporal scales. The reconstruction combines SWOT KaRIn wide-swath observations, SWOT nadir data, and conventional nadir altimeter measurements within broad spatio-temporal windows around the target date. In Delayed-Time (DT) mode, both past and future observations are incorporated to constrain the interpolation process, with decreasing weights assigned to observations farther away in time. This allows mesoscale structures sampled during nearby overpasses to contribute to the reconstructed daily fields beyond the instantaneous SWOT and nadir ground-track coverage (see Fig. A1 for an example of the SWOT coverage contributing to the reconstruction of day 20 April 2024) (Ballarotta et al., 2025c). The MDT product used is also the MDT_CMEMS_2020_MED (EU Copernicus Marine Service Product, 2024). More details can be found in Ballarotta et al. (2025c) and Ballarotta (2025). These products were processed by SSALTO/DUACS and distributed by AVISO (https://www.aviso.altimetry.fr, last access: 22 April 2026) supported by CNES.

The inclusion of SWOT's Ka-band Radar Interferometer (KaRIn) observations improves the resolution of SSH fields, allowing finer-scale ocean dynamics (such as mesoscale and submesoscale structures) to be resolved. This experimental product (from hereinafter MIOST-K) provides daily gridded maps of SSH and derived geostrophic velocities, offering new opportunities to study ocean surface variability at unprecedented detail (Ballarotta et al., 2025c).

3 Methods

3.1 Py-eddy tracker

The py-eddy-tracker is an eddy tracking algorithm based on geometric and physical techniques. It was firstly developed by Mason et al. (2014) and later updated by Delepoulle et al. (2022). Since then, it has been widely used to study eddies and for the generation of updated eddy field datasets (e.g. Pegliasco et al. 2022). In this study, we use version 3.6.1 of the algorithm (Delepoulle et al., 2022) to identify eddies from daily snapshots of Absolute Dynamic Topography (ADT) fields. Two types of contours are identified by the algorithm: the effective contour (outermost closed contour defining the eddy extent) and the speed contour (inner contour corresponding to the region of maximum mean azimuthal geostrophic velocity). Further details can be found in Mason et al. (2014). Compared to SLA, ADT provides more reliable eddy identification, especially in the Mediterranean Sea (Pegliasco et al., 2021, 2022), because it includes both the mean dynamic topography and its temporal variability, helping distinguish mesoscale eddies from variations in persistent jets and recurrent circulation patterns included in the MDT. A pre-processing and set of parameterizations are necessary to implement the py-eddy tracker (see Mason et al., 2014; Pegliasco et al., 2022 for further details):

1. The ADT fields are filtered with a Bessel high-pass filter of 500 km to remove the background large-scale signal and isolate the eddies (Pegliasco et al., 2022).

2. A detection step of 0.002 m was used between consecutive isolines. This corresponds to the height difference between contour levels used to identify eddy boundaries. Starting from the eddy center (defined by a minimum value for cyclonic eddies and a maximum value for anticyclonic eddies), closed ADT isolines are identi-

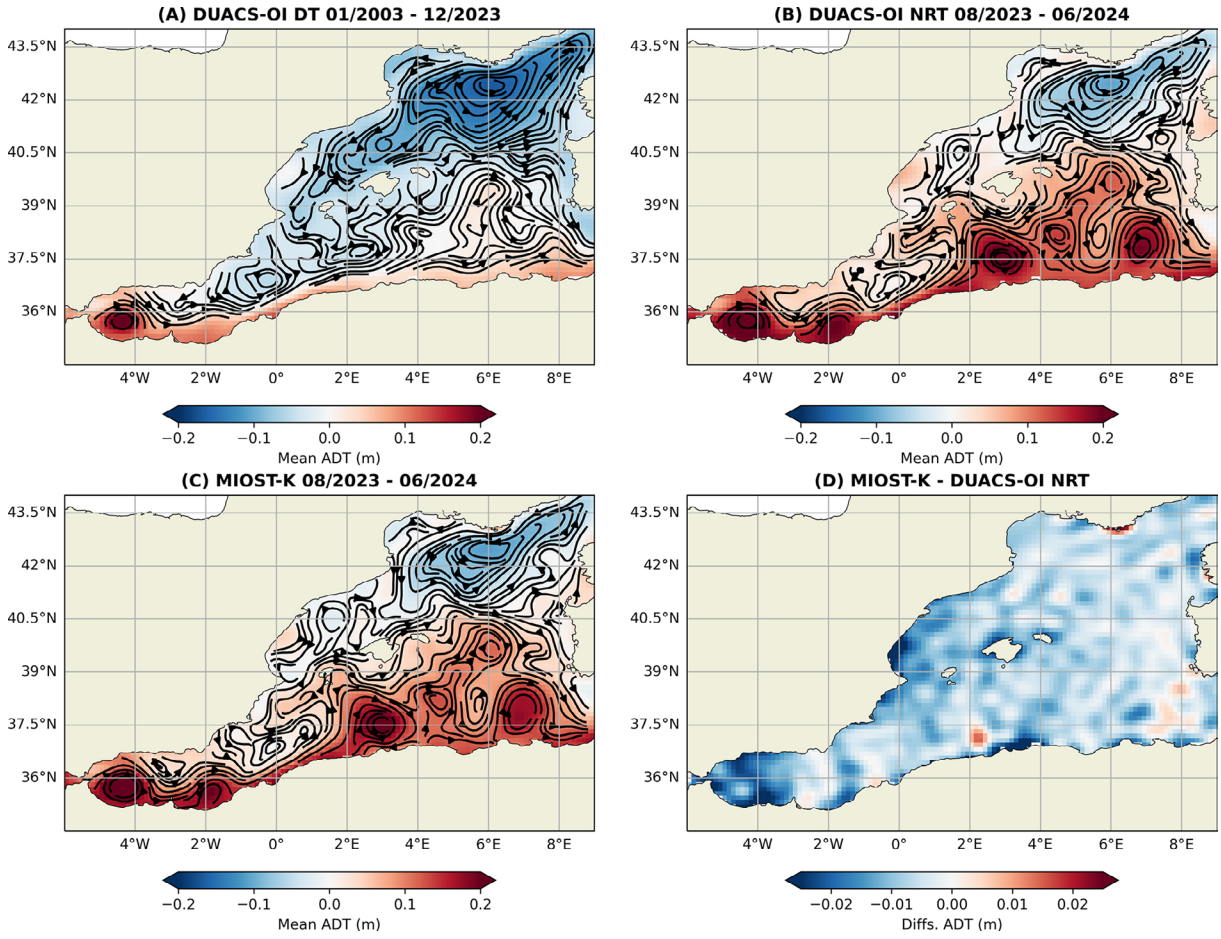


Figure 1. General circulation represented by the mean Absolute Dynamic Topography (ADT) and the mean velocity field (streamlines) calculated from the different altimetric products: **(A)** 20 years mean from DUACS-DT (product reference 2), **(B)** 11 months mean of DUACS-NRT (product reference 1), **(C)** 11 months mean of MIOST-K (product reference 3) and **(D)** mean ADT difference between MIOST-K and DUACS-OI (**C** − **B**).

fied outward at intervals of 0.002 m until the eddy edge is reached (Cui et al., 2025).

3. A maximum shape error of 55 % is allowed for a detected contour to be identified as an effective eddy. This metric is defined as the ratio between the circle fit and identified outermost contour. This shape error (Kurian et al., 2011) limits the identification to eddies, and removes other elongated closed-contour structures like filaments (Mason et al., 2019).

3.2 Particle simulations and eddy retention calculation

We calculate the eddy particle retention to quantify how differences in eddy properties, such as size, intensity, and associated EKE, influence particle transport and trapping. For this analysis, Lagrangian simulations are performed using the OceanParcels Lagrangian framework v2.4.2 (Delandmeter and van Sebille, 2019) to simulate 2D trajectories of virtual particles at the sea surface. Particles are advected using the velocity fields of the two datasets (DUACS-OI and MIOST-K). A fourth order Runge-Kutta particle advection scheme is used with a run-time time-step (dt) of 25 min. Particles are treated as infinitesimal, passive and buoyant tracers transported exclusively by horizontal advection, with no additional physical processes included. Simulations are performed with particles released within a 2 by 2° box around identified Algerian eddies' contours separated by 1/30° (∼ 3.5 km) with an advection time (T) of 20 d. The inner (speed) eddy contour is used here, to keep the eddy's more coherent inner core. This timescale represents a trade-off between the minimum lifetime of the Algerian eddies (∼ 60 d) and the requirement that enough particles remain within the eddy core during the simulation. Particles which leave the domain are removed from the analysis. Here we showcase the impact on the retention capacity by selecting 3 Algerian eddies as representative examples. Further details are shown in Table C1.

Next, the eddy retention is calculated as the relative difference in the number of particles enclosed by the eddy contour between the release day and 20 d later. The Eddy Retention Percentage (ERP) is then calculated as:

$$\mathrm{ERP} = \frac{N_T - N_0}{N_0} \times 100, \quad (1)$$

where N_T and N_0 are the number of particles at the final and the release days, respectively.

4 Results

The general circulation of the western Mediterranean has been thoroughly studied in the past. The new SWOT data is unveiling smaller oceanic scales and partially or even unobserved dynamics, but the impact of this on the general circulation patterns will be better understood when we have more years of SWOT data. Currently, with more than one year of SWOT data during the science phase, we can already infer a first estimate of how and if these general circulation patterns are affected by this new dataset, and thus the consequences this could have for different monitoring efforts (Fig. 1). Figure 1A is included as a reference representation of the mean circulation over 20 years in the western Mediterranean. The main circulation features shown in Fig. 1A are also observed in the shorter-term averages shown in Fig. 1B and C, indicating that the large-scale circulation is consistently represented in both datasets. Differences between Fig. 1B and C arise mainly at the smaller-scale features and in the characteristics of the mesoscale structures, already suggesting that the inclusion of SWOT observations impacts the representation of mesoscale circulation. Although part of these differences may also arise from intrinsic methodological differences between the DUACS-OI and MIOST reconstruction approaches, previous comparisons based solely on nadir altimetry showed relatively small differences between the two products in the Mediterranean (Ballarotta et al., 2023; Verbrugge et al., 2024). This suggests that the higher differences observed here are strongly influenced by the inclusion of SWOT wide-swath observations in MIOST-K. These differences are further highlighted in the mean ADT difference field shown in Fig. 1D, particularly in coastal regions and along energetic circulation pathways (e.g. Alboran Sea and Algerian Current). However, the magnitude of these differences is about an order of magnitude smaller than the values in the ADT field (note the limits of colorbar in Fig. 1B, C and D). This is expected from the enhanced spatial sampling provided by SWOT wide-swath observations compared to conventional nadir altimetry (e.g. Lopez-Radcenco et al., 2019; Ballarotta et al., 2025c), particularly for mesoscale and coastal structures (e.g. Dibarboure et al., 2025). In contrast to the effectively one-dimensional along-track sampling of nadir altimeters, SWOT provides two-dimensional swath measurements, and the implications of these differences are further explored through the analysis of daily eddy variability in the following sections.

We obtain the daily eddy identification fields for both datasets from August 2023 to June 2024 (inclusive), and calculate the total number of cyclonic (blue) and anticyclonic (red) eddies. An example of all the eddies identified daily during April 2024 is shown in Fig. 2A and B for DUACS-OI and MIOST-K, respectively. The spatial distribution of eddy centre counts, computed in 1 by 1° bins over the full study period, is shown in Fig. 2C and D. Both products identify high eddy activity in the central and northwestern Mediterranean, and the Alboran Sea, although MIOST-K generally detects a larger number of eddies, particularly in coastal regions such as west of Corsica (also observed in Fig. 2A and B). Complementary observations, including satellite chlorophyll data, support the presence of coastal eddies in this region (Fig. B1; Fortunato et al., 2025). Moreover, the DUACS-OI product appears to merge multiple nearby cyclonic eddies into one larger structure, particularly in areas such as the Gulf of Lion, thereby reducing the number of identified eddies. The daily temporal variability of anticyclonic and cyclonic eddy counts is shown in Fig. 2E and F, respectively. Despite high temporal variability, MIOST-K consistently identifies a larger number of eddies than DUACS-OI throughout most of the analysis period. For anticyclonic eddies, MIOST-K detects on average 19.0 ± 2.0 eddies per day (mean $\pm$ standard deviation), compared to 12.5 ± 2.0 for DUACS-OI. For cyclonic eddies, the mean daily counts are 20.4 ± 3.1 and 16.6 ± 2.4 for MIOST-K and DUACS-OI, respectively. The temporal correlation between the two daily eddy-count time series is low for both anticyclonic ($r = 0.253$) and cyclonic eddies ($r = 0.165$). This likely reflects the sensitivity of daily eddy counts to product-dependent differences not only in eddy detection, but also splitting, merging, and lifetime, rather than fundamental differences in the temporal variability of mesoscale activity.

With the inclusion of the SWOT data, we also observe changes in the already observed big mesoscale eddies of the DUACS-OI product. An important change is in the EKE associated with these eddies. Firstly, the EKE field is retrieved (Delepoulle et al., 2022; py-eddy-tracker, 2022) for each daily field (Fig. 3A and C). Then we find the eddies that match for both datasets and calculate the mean EKE associated to these eddies. i.e., the eddy-averaged EKE (Fig. 3B and D). Figure 3E shows the temporal variability of the daily mean of eddy-averaged EKE (daily mean EKE) of all the matching eddies identified. MIOST-K shows a higher daily mean throughout the majority of the study's time period. Both datasets reach their maximum during the same energetic event on 25 April 2024, although the MIOST-K value is approximately 6 % higher than in DUACS-OI. More importantly, specific daily differences between the products can be substantially larger, with MIOST-K exhibiting increases of up to 78 % relative to DUACS-OI during certain energetic mesoscale events, such as on 16 September 2023. On 96 % of the days, the daily mean in MIOST-K is

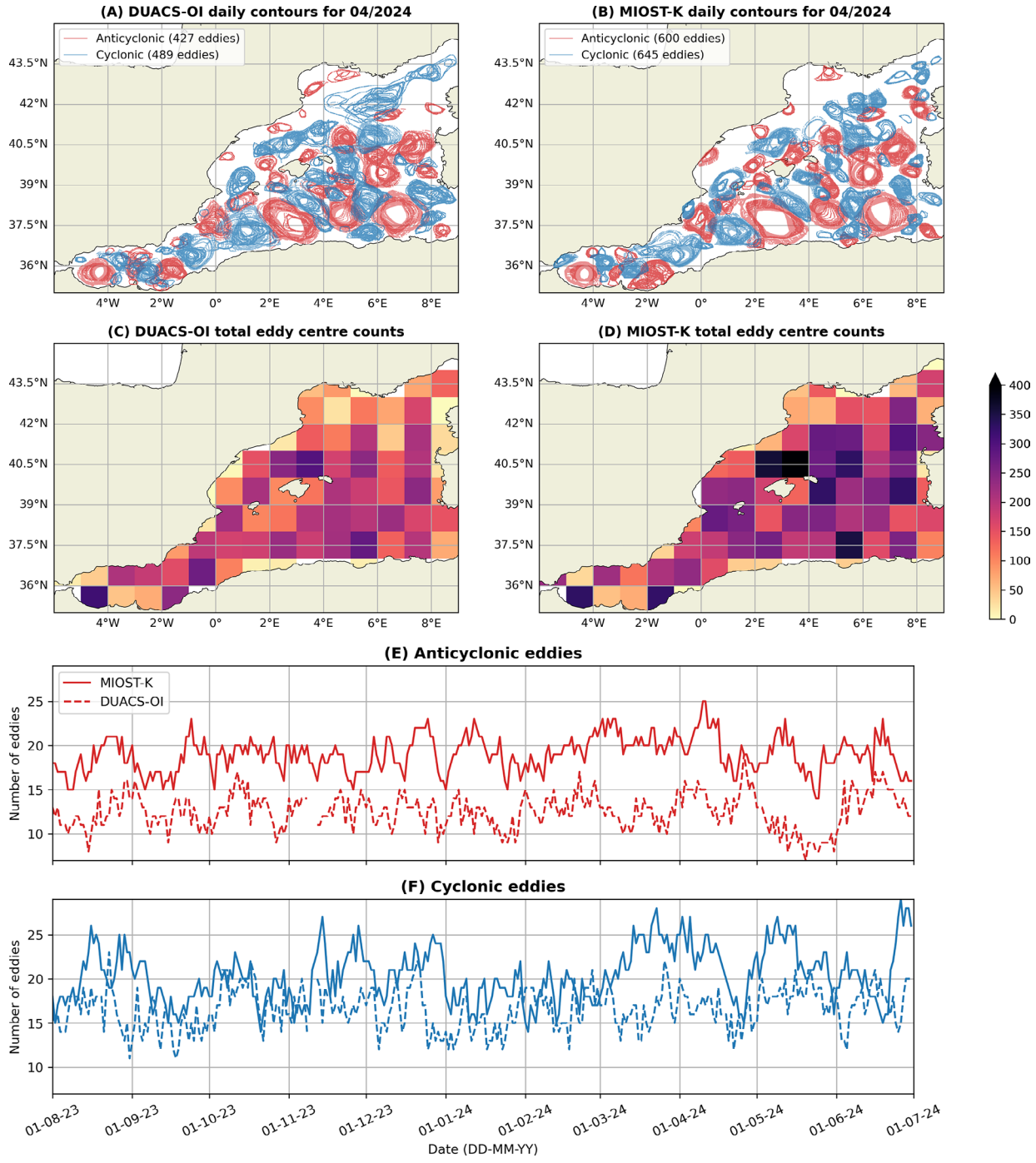


Figure 2. Number of daily eddy identifications. Panels **(A)** and **(B)** show all the daily eddies (outer contours) identified during April 2024 for DUACS-OI (product reference 1) and MIOST-K (product reference 3), respectively. Panels **(C)** and **(D)** show the eddy centre counts in $1 \times 1°$ bins, for DUACS-OI and MIOST-K, respectively. Panels **(E)** and **(F)** show the temporal variability of the anticyclones and cyclones, respectively, identified throughout the study period.

higher than in DUACS-OI (we also checked the differences in the daily maximum of eddy-averaged EKE, and these are higher 93 % of the time). This enhanced EKE representation is likely associated with the improved spatial sampling, two-dimensional swath geometry, and enhanced representation of higher-wavenumber variability enabled by SWOT observations. Furthermore, SWOT observations are expected to exhibit substantially lower noise levels than conventional nadir altimeters (Vergara et al., 2023), which may also contribute to the differences observed. This has important im-

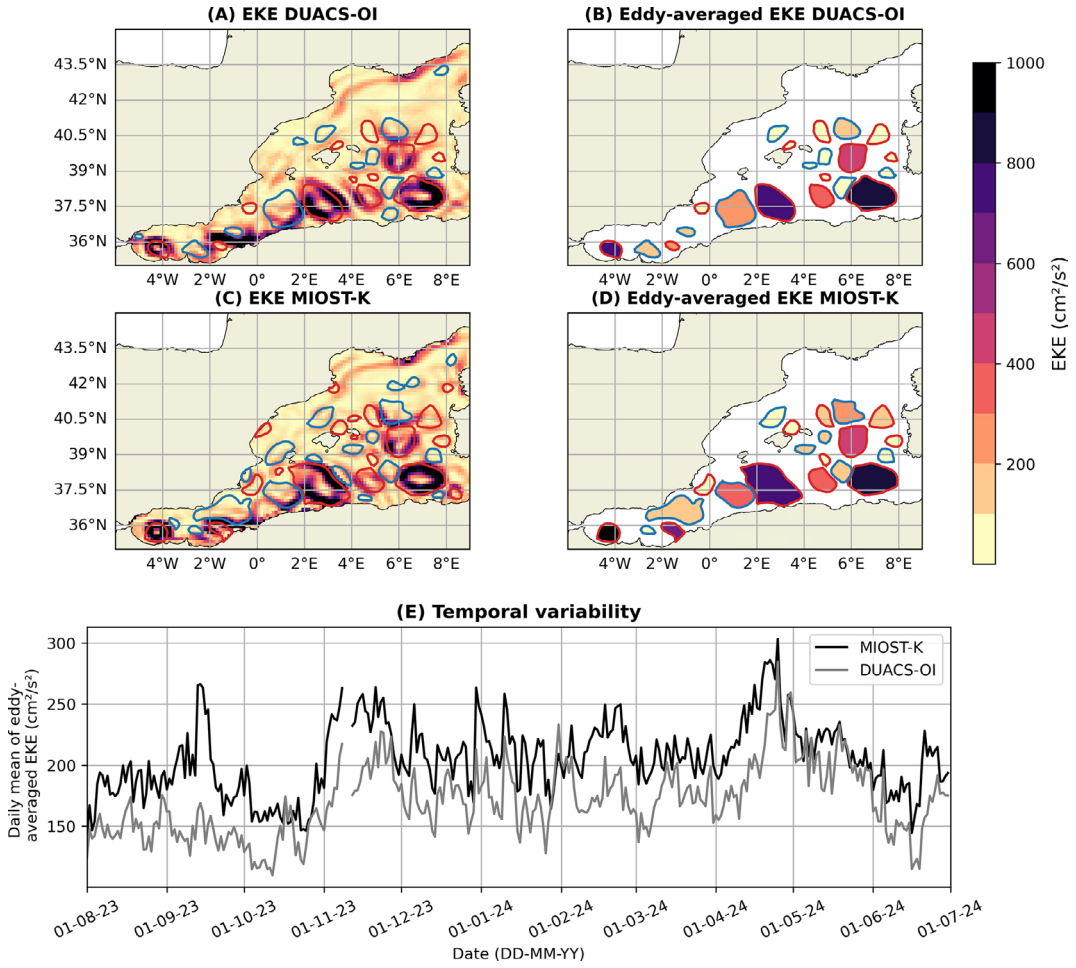


Figure 3. Temporal variability of Eddy Kinetic Energy (EKE) associated with the detected eddies. Panels **(A)** and **(C)** show the EKE field on 20 April 2024 and all the identified anticyclonic (red) and cyclonic (blue) outer eddy contours, for DUACS-OI (product reference 1) and MIOST-K (product reference 3), respectively. Panels **(B)** and **(D)** show the individual eddy-averaged EKE of only the eddies identified in both datasets on that date. Panel **(E)** shows the temporal variability of the spatially averaged EKE within detected, matching eddy contours and averaged across all eddies for each day for DUACS-OI (dashed) and MIOST-K (solid).

plications for KE trend studies (e.g. Martínez-Moreno et al., 2019; Barceló-Llull et al., 2025), which in turn also can mean a challenge for current climate model projections (Barceló-Llull et al., 2025). For example, Hogg et al. (2015) mention the significant impact EKE trend variations have on the ocean's carbon and heat sinks in regions like the Southern Ocean, where increasing EKE has been associated with changes in the efficacy of these sinks and the consequent global climatic implications. In the western Mediterranean Sea, where mesoscale eddies strongly influence transport and exchanges between subbasins, the enhanced EKE representation identified in MIOST-K may similarly have important implications for regional heat, salt, and carbon-related transport processes. For example, the higher EKE observed in the energetic Alboran Sea eddies shown in Fig. 3 could affect the representation of heat and salt exchanges through the Strait of Gibraltar (e.g. Bryden et al., 1994; Tsimplis and Bryden, 2000; Sánchez-Román et al., 2009; Hargous et al., 2026). Such differences in EKE and mesoscale structure representation may also influence particle transport and retention estimates, with implications for marine pollution management and offshore spatial planning, as explored in the Algerian eddy case study presented in the following section.

Figure 4 illustrates three examples of Algerian Eddies and their retention capacity. All three eddies were observed in different regions of the Algerian Basin during multiple SWOT KaRIn overpasses throughout their respective 20 d advection periods (approximately five overpasses for each case), supporting the use of these examples to assess the influence of SWOT-enhanced reconstruction on particle retention estimates. After 20 d, the eddies retain substantially different percentages of particles, reflecting the strong variability in mesoscale transport and retention processes across the subbasin. Such differences are expected between Algerian

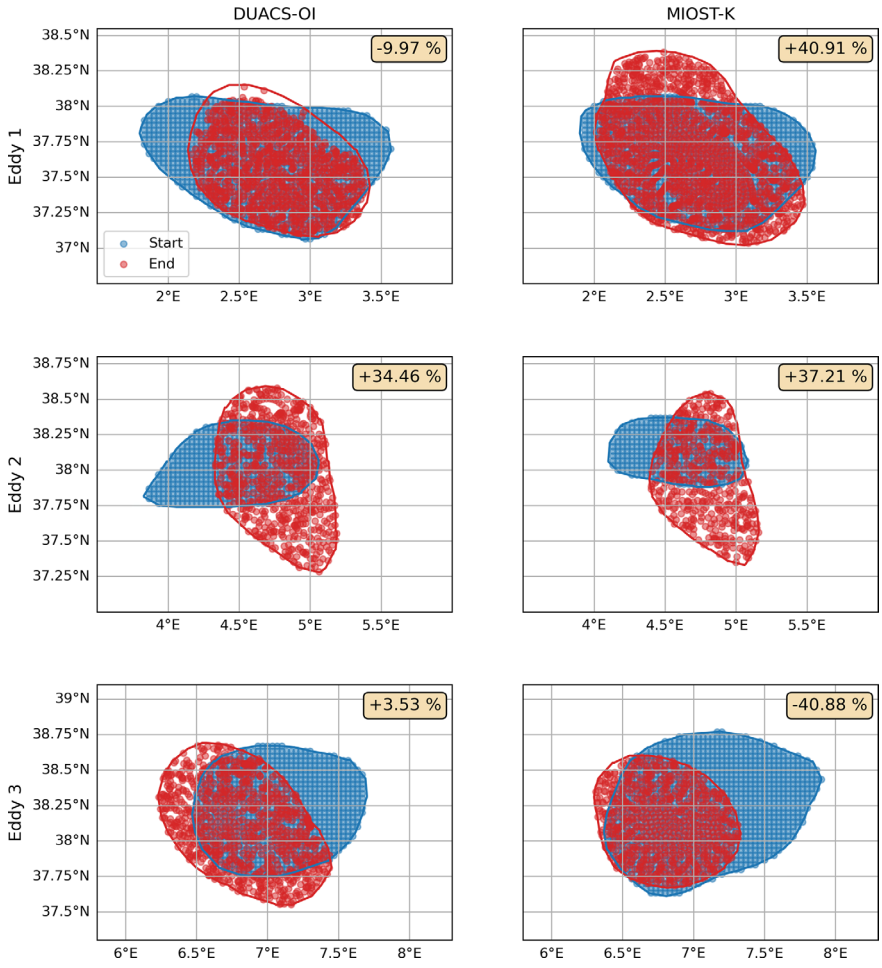


Figure 4. Eddy retention capacity of three Algerian Eddies examples for DUACS-OI (left panels, product reference 1) and MIOST-K (right panels, product reference 3). Blue (red) particles and contours (inner eddy contours) correspond to the initial (final) dates (see Table C1). Only particles inside the eddy contours are shown. The top right box indicates the eddy retention percentage, with positive (negative) values indicating retention (leakage).

eddies, as their retention capacity can depend on their dynamical state, including eddy intensity, coherence, deformation, interaction with the surrounding circulation, and eddy lifetime stage. We therefore consider three different eddy examples to illustrate how differences in mesoscale representation between DUACS-OI and MIOST-K can impact transport and retention estimates under different dynamical conditions. In Eddy 1, the DUACS-OI eddy shows leakage, while the MIOST-K eddy retains and even increases the number of particles inside the eddy contour. In Eddy 2, both products retain more particles, although retention is slightly higher in MIOST-K. In contrast, Eddy 3 exhibits stronger leakage in MIOST-K, while DUACS-OI retains slightly more particles. This demonstrates an important impact of the differences in eddy properties identified between the operational DUACS-OI and the new dataset, MIOST-K. Despite only subtle qualitative differences in eddy contours (Fig. 2), the particle retention over just 20 d shows high variability, likely linked to the higher EKE structures observed in the SWOT-enhanced product (Fig. 3). These differences are not only scientifically relevant but may also have practical implications for environmental monitoring and marine spatial planning. The same eddy can exhibit opposite retention and leakage behaviours depending on the product used. If applied operationally, such contrasting representations could lead to substantially different estimates of the transport and accumulation of pollutants, marine litter, nutrients, fish larvae, or aquaculture-derived waste, potentially influencing pollutant dispersion assessments, aquaculture site suitability, or ecosystem management strategies.

5 Discussion

In this study, we highlight the value of incorporating wide-swath altimetric observations for advancing the representation of mesoscale ocean dynamics. A key dynamic property

of mesoscale eddies is their associated EKE. Results indicate a notable increase in signal strength, with MIOST-K capturing regional means of daily EKE up to 1.8 times greater than DUACS-OI. This result is important due to its link with the understanding of atmosphere-ocean interactions, especially in the current climate change scenario. Better monitoring these structures, not only their occurrence, but their characteristics, is key for related monitoring studies of for example sea surface temperature, and marine operational activities such as forecasts of extreme events and marine fisheries management.

The increase in eddy detections with MIOST-K is more pronounced for anticyclonic eddies than for cyclonic eddies. Although the origin of this eddy asymmetry was not specifically investigated here, it may be related to the improved detection of smaller-scale and coastal eddies, where the differences between the products are strongest. In the western Mediterranean, anticyclonic eddies tend to be more persistent, coherent, and longer-lived than cyclonic eddies (Stegner et al., 2021), potentially increasing their detectability in SWOT products. Similar asymmetries have also been observed by SWOT in other regions, and are generally explained by the greater stability and propagation capacity of anticyclonic eddies, allowing them to persist longer and propagate farther (de Marez et al., 2026). This enhanced detection of anticyclonic eddies may also be relevant for the monitoring of long-lasting surface temperature anomalies associated with these structures, which could contribute to the development of local marine heatwaves (Aguiar et al., 2022).

We also observe clear changes in the retention capacity of Algerian eddies with MIOST-K over a 20 d period. This result has important consequences for marine pollution management strategies, namely those that can affect marine protected areas like the Cabrera National Park (Compa et al., 2020). This also influences the transport properties of these eddies related to the redistribution of temperature, salinity and nutrients, which influence the circulation of the area, and the nutrient inputs in other regions of the western Mediterranean Sea (e.g. Bryden et al., 1994; Hargous et al., 2026).

The eddy identification algorithm used to identify eddies is quite sensitive to pre-processing choices and parameterizations (e.g. Pegliasco et al., 2021), and could be refined in follow-up studies. Here it is used to compare 2 datasets, so the impact on the conclusions obtained should be minimal. The Eulerian method used here is commonly implemented in the community, namely in altimetry. Many other eddy identification and tracking techniques exist which use an Eulerian framework (e.g. Ioannou et al., 2024), but also Lagrangian ones, which could help to better capture retention capabilities, as Lagrangian structures could assess material coherence in space and time simultaneously (e.g. Beron-Vera et al., 2013; Haller et al., 2016; Liu et al., 2019). To further validate the robustness of our retention findings, future work could extend the Lagrangian analysis to a larger ensemble of eddies. Statistical comparison across datasets would help quantify whether observed differences are consistent and significant, and whether eddy properties such as size or eccentricity correlate with retention efficiency. This would also support the operational use of eddy-based transport estimates in pollution risk forecasting and coastal marine management. Lastly, we take advantage of a very novel dataset (MIOST-K), but it is under continuous improvement due to the young age of SWOT. It will be interesting to continue this study with a longer series of data to further evaluate these mesoscale eddies in the Mediterranean region and look further into the improvement of the coastal eddy field in the region (Fortunato et al., 2025).

It is worth mentioning that, by design, conventional interpolation methods tend to filter out small-scale features detected by SWOT, leading to an underrepresentation of fine-scale eddies (typically around 50 km in diameter, or < 100 km in wavelength) in Level-4 products such as DUACS and MIOST. Moreover, SWOT captures a broader range of high-resolution ocean dynamics, including nonlinear eddies and internal waves, that are beyond the reach of nadir altimeters and not resolved by current mapping techniques. Recent studies have shown that mesoscale eddies can be identified directly from SWOT wide-swath SSH observations (e.g. Verger-Miralles et al., 2025; de Marez et al., 2026; Han et al., 2026; Fu et al., 2026). This direct approach is less suited to larger eddies that extend beyond the swath, but preserves the fine-scale information contained in SWOT observations and avoids the smoothing introduced by Level-4 mapping. However, a key limitation lies in the coarse temporal sampling imposed by the 21 d repeat cycle of the science phase, which hinders the analysis of rapidly evolving fine-scale dynamics (Archer et al., 2025). To fully exploit SWOT's potential, especially at submesoscales, new frameworks are needed. Promising advances in this direction are emerging from data- and model-driven mapping approaches (e.g., Fablet et al., 2021; Le Guillou et al., 2023, 2025) and in the development of robust validation strategies tailored to SWOT observations (Coadou-Chaventon et al., 2025; Verger-Miralles et al., 2025).

6 Conclusions

This study provides new insights on how the monitoring capabilities of surface circulation, namely mesoscale activity, will improve with the new wide-swath satellites such as SWOT. This is relevant to improve operational oceanography services, for example in managing and forecasting marine pollution events. The objective is to assess changes in the mesoscale eddy field by quantifying eddy count, variability, and associated kinetic energy. We then examine how the detected eddy properties affect their retention capacity. While this study is not intended as a comprehensive intercomparison of the DUACS-OI and MIOST-K products, it does show how the surface currents monitoring scenario might change

in the near future, opening the door to a better representation of the different processes involved and its implications.

The results show the promising potential of new wide-swath products to better understand the eddy field, achieving specific capacities, particularly for observing small mesoscale eddies and resolving features in coastal areas. We also find that the already observed mesoscale eddy field by conventional products (DUACS-OI) has notable differences when compared to new products including SWOT (MIOST-K). An increase in Eddy Kinetic Energy (EKE) is found, which plays a vital role in the Mediterranean Sea by driving the variability of ocean circulation, redistributing heat, salt, and nutrients, and supporting marine productivity in this climatically sensitive region. Mesoscale eddies, which contribute to EKE, influence biological hotspots, the dispersion of pollutants, marine heatwaves and local weather patterns such asMediterranean cyclones. Monitoring EKE is therefore essential for improving ocean forecasting, managing fisheries, and understanding the impacts of climate change. This requires high-resolution observations from satellites, autonomous platforms, and regional cooperation to effectively track these dynamic processes and inform environmental management and policy. With this new dataset, the gap of high-resolution satellite data is further filled. The retention capacity of the eddies is strongly affected with this new data, meaning that once this data is incorporated into the operational products, a better estimation of marine pollution impacts will be possible. This will be of importance for different marine management strategies, especially those related to marine pollution and fisheries management.

Our findings demonstrate that incorporating SWOT wide-swath observations affects the representation of surface mesoscale features in the western Mediterranean, including in regions where conventional altimetry has limitations. By comparing eddy characteristics such as associated EKE and retention capacity, we show how these improvements can directly support marine applications such as pollution risk assessment for the protection of marine reserves. Looking ahead, the integration of next-generation satellite technologies and data-processing methodologies will be essential to further refine surface current products. This work contributes to a framework for ongoing monitoring and evaluation of regional circulation patterns, and underscores the importance of sustained innovation in ocean observing systems.

Appendix A

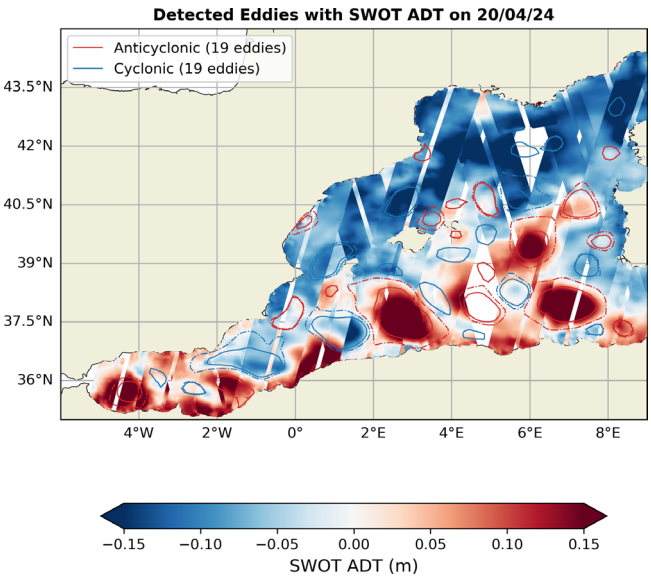


Figure A1. Outer (dashed) and inner (solid) eddy contours identified with MIOST-K on 20 April 2024. The background fields are all the SWOT L3 ADT (filtered) [m] observations on 20 April 2024 ± 10 d. SWOT L3 LR ADT 2 km (Expert v2.0.1) data was obtained from AVISO (AVISO/DUACS, 2024).

Appendix B

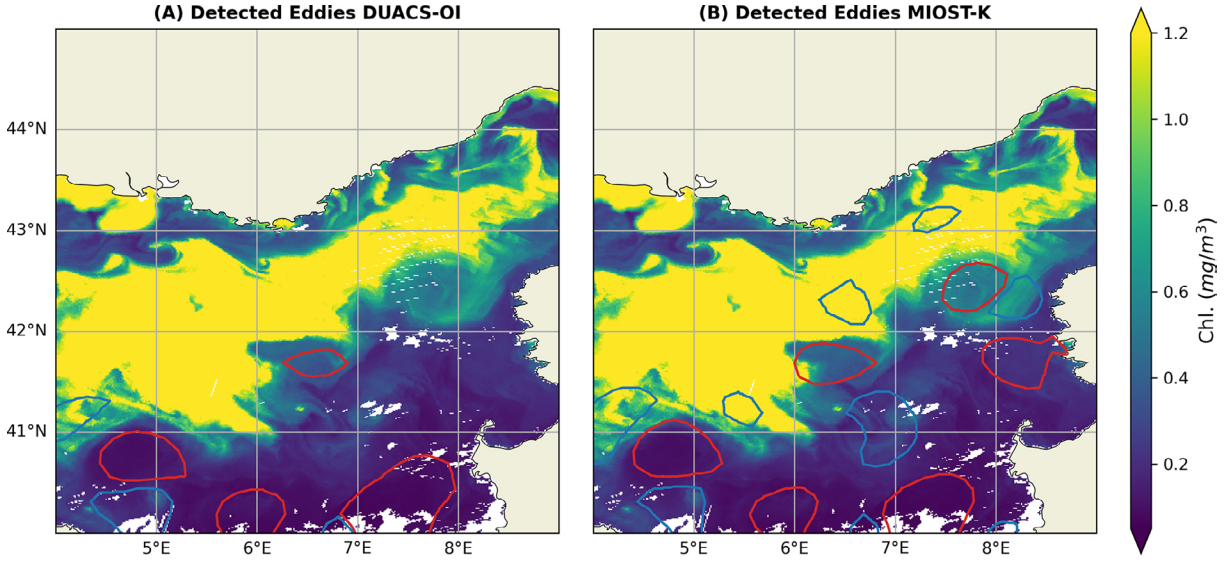


Figure B1. Chlorophyll fields (Chl.) on 2 April 2024 with the corresponding eddy outer contours (anticyclonic red, cyclonic blue) for DUACS-OI **(A)** and MIOST-K **(B)**. Daily level-3 chlorophyll *a* concentrations at 1 km spatial resolution were obtained from the multi-sensor dataset cmems_obs-oc_med_bgc-plankton_my_l3-multi-1km_P1D (E.U. Copernicus Marine Service Information, 2023; Berthon and Zibordi, 2004; Volpe et al., 2019).

Appendix C

Table C1. Eddy retention information.

	Date		Number of particles (DUACS-OI; **MIOST-K**)	
	Initial	End	Initial	End
Eddy 1	1 April 2024	21 April 2024	1123; **1078**	1011; **1519**
Eddy 2	1 February 2024	21 February 2024	502; **344**	675; **472**
Eddy 3	1 February 2024	21 February 2024	821; **1140**	850; **674**

Code availability. The codes used in this study are available on GitHub: https://github.com/LauraGomezNavarro/paper-OSR10_Gomez-Navarro_etal_2026 (last access: 14 September 2026), and the version used for the manuscript is published on Zenodo: https://doi.org/10.5281/zenodo.22725565 (Gómez-Navarro, 2026).

Data availability. The data used in this study can be downloaded directly from the Copernicus Marine Service and the AVISO websites. The exact product names are given in Table 1, and the associated DOIs are indicated in the references.

Author contributions. LGN, AP, MIP, MB, DCM, and LF contributed to the conceptualization of the study. LGN carried out the formal analysis, investigation, and prepared the original draft of the manuscript. DCM, AP, and LGN developed the methodology. MIP and MB curated the data. All authors contributed to the review and editing of the manuscript.

Competing interests. The contact author has declared that none of the authors has any competing interests.

Disclaimer. The Copernicus Marine Service offering is regularly updated to ensure it remains at the forefront of user requirements. In this process, some products may undergo replacement or renaming, leading to the removal of certain product IDs from the catalogue. If readers have any questions or require assistance regarding these modifications, please feel free to reach out to the Copernicus Marine Service user support team for further guidance. They will be able to provide the necessary information to address concerns and find suitable alternatives.

Publisher's note: Copernicus Publications remains neutral with regard to jurisdictional claims made in the text, published maps, institutional affiliations, or any other geographical representation in this paper. The authors bear the ultimate responsibility for providing appropriate place names. Views expressed in the text are those of the authors and do not necessarily reflect the views of the publisher.

Acknowledgements. The authors gratefully acknowledge the helpful comments of the OSR coordination team, Karina von Schuckmann, Lorena Moreira and Alvaro de Pascual during the definition, implementation and writing of this study, and the feedback of the two anonymous reviewers. Additionally, the Copernicus Marine Service and AVISO are acknowledged for access to the datasets used for this work.

Financial support. This study is funded by the Copernicus Marine Service (Sea-Level Thematic Center 24251L02-COP-TAC SL-2100). We also acknowledge funding from the Spanish Ministry of Science, Innovation, and Universities, the Spanish Research Agency, the European Regional Development Fund (MCIN/AEI/10.13039/501100011033/FUE) under Grant PID2021-122417NB-I00 (FaSt-SWOT project). LGN is also grateful for current funding under the Marie Sklodowska-Curie Actions programme, funded by the European Union (HORIZON-MSCA-2023-PF RELACS, grant agreement no. 101155713), and funding from the Spanish government through the "Severo Ochoa Centre of Excellence" accreditation (CEX2019-000928-S).

Review statement. This paper was edited by Gilles Garric and reviewed by two anonymous referees.

References

20minutos: El GOB denuncia la presencia de numerosos residuos plásticos en aguas del parque Nacional de Cabrera, https://www.20minutos.es/noticia/2517637/0/gob-denuncia-presencia-numerosos-residuos-plasticos-aguas-parque-nacional-cabrera/ (last access: 9 July 2025), 2015.

Aguiar, E., Mourre, B., Alvera-Azcárate, A., Pascual, A., Mason, E., and Tintoré, J.: Strong Long-Lived Anticyclonic Mesoscale Eddies in the Balearic Sea: Formation, Intensification, and Thermal Impact, J. Geophys. Res.-Oceans, 127, e2021JC017589, https://doi.org/10.1029/2021JC017589, 2022.

Archer, M., Wang, J., Klein, P., Dibarboure, G., and Fu, L.-L.: Wide-swath satellite altimetry unveils global submesoscale ocean dynamics, Nature, 640, 691–696, https://doi.org/10.1038/s41586-025-08722-8, 2025.

AVISO/DUACS: SWOT level-3 KaRIn low rate SSH expert (v2.0.1) dataset, CNES [data set], https://doi.org/10.24400/527896/A01-2023.018, 2024.

AVISO/DUACS: SALTO/DUACS Mutlimission Experimental Level-4 maps, computed with SWOT Level-3 products (using both KaRIn and nadir instruments) (v2.0.1), CNES [data set], https://doi.org/10.24400/527896/a01-2025.001, 2025.

Ballarotta, M.: SSALTO/DUACS Experimental Product Handbook: Gridded Sea Level Heights and geostrophic velocities computed with SWOT Level-3 products (using both KaRIn and nadir instruments) with MIOST Version 2.0.1., Issue 2.1, AVISO, https://www.aviso.altimetry.fr/fileadmin/documents/data/tools/hdbk_duacs_experimental_miost_swot_v2.1.pdf (last access: 22 April 2026), 2025.

Ballarotta, M., Ubelmann, C., Pujol, M.-I., Taburet, G., Fournier, F., Legeais, J.-F., Faugère, Y., Delepoulle, A., Chelton, D., Dibarboure, G., and Picot, N.: On the resolutions of ocean altimetry maps, Ocean Sci., 15, 1091–1109, https://doi.org/10.5194/os-15-1091-2019, 2019.

Ballarotta, M., Ubelmann, C., Veillard, P., Prandi, P., Etienne, H., Mulet, S., Faugère, Y., Dibarboure, G., Morrow, R., and Picot, N.: Improved global sea surface height and current maps from remote sensing and in situ observations, Earth Syst. Sci. Data, 15, 295–315, https://doi.org/10.5194/essd-15-295-2023, 2023.

Ballarotta, M., Pujol, M.-I., and SL-TAC team: EU Copernicus Marine Service Quality Information Document for the European Seas Gridded L4 Sea Surface Heights And Derived Variables NRT, SEALEVEL_EUR_PHY_L4_NRT_008_060, Issue 13.0, Mercator Ocean International, https://documentation.marine.copernicus.eu/QUID/CMEMS-SL-QUID-008-032-068.pdf (last access: 16 July 2025), 2025a.

Ballarotta, M., Pujol, M.-I., and SL-TAC team: EU Copernicus Marine Service Quality Information Document for the European Seas Gridded L4 Sea Surface Heights And Derived Variables Reprocessed 1993 Ongoing, SEALEVEL_EUR_PHY_L4_MY_008_068, Issue 13.0, Mercator Ocean International, https://documentation.marine.copernicus.eu/QUID/CMEMS-SL-QUID-008-032-068.pdf (last access: 16 July 2025), 2025b.

Ballarotta, M., Ubelmann, C., Bellemin-Laponnaz, V., Le Guillou, F., Meda, G., Anadon, C., Laloue, A., Delepoulle, A., Faugère, Y., Pujol, M.-I., Fablet, R., and Dibarboure, G.: Integrating wide-swath altimetry data into Level-4 multi-mission maps, Ocean Sci., 21, 63–80, https://doi.org/10.5194/os-21-63-2025, 2025c.

Barceló-Llull, B., Rosselló, P., Combes, V., Sánchez-Román, A., Pujol, M. I., and Pascual, A.: Kuroshio Extension and Gulf Stream dominate the Eddy Kinetic Energy intensification observed in the global ocean, Sci. Rep., 15, https://doi.org/10.1038/s41598-025-06149-9, 2025.

Beron-Vera, F. J., Wang, Y., Olascoaga, M. J., Goni, G. J., and Haller, G.: Objective Detection of Oceanic Eddies and the Agulhas Leakage, J. Phys. Oceanogr., 43, https://doi.org/10.1175/JPO-D-12-0171.1, 2013.

Berthon, J.-F. and Zibordi, G.: Bio-optical relationships for the northern Adriatic Sea, Int. J. Remote Sens., 25, 1527–1532, https://doi.org/10.1080/01431160310001592544, 2004.

Bryden, H. L., Candela, J., and Kinder, T. H.: Exchange through the Strait of Gibraltar, Prog. Oceanogr., 33, 201–248, https://doi.org/10.1016/0079-6611(94)90028-0, 1994.

Coadou-Chaventon, S., Swart, S., Novelli, G., and Speich, S.: Resolving Sharper Fronts of the Agulhas Current Retroflection Using SWOT Altimetry, Geophys. Res. Lett., 52, https://doi.org/10.1029/2025gl115203, 2025.

Compa, M., Alomar, C., Mourre, B., March, D., Tintoré, J., and Deudero, S.: Nearshore spatio-temporal sea surface trawls of plastic debris in the Balearic Islands, Mar. Environ. Res., 158, 104945, https://doi.org/10.1016/j.marenvres.2020.104945, 2020.

Cotroneo, Y., Celentano, P., Aulicino, G., Perilli, A., Olita, A., Falco, P., Sorgente, R., Ribotti, A., Budillon, G., Fusco, G., and Pessini, F.: Connectivity Analysis Applied to Mesoscale Eddies in the Western Mediterranean Basin, Remote Sensing, 13, 4228, https://doi.org/10.3390/rs13214228, 2021.

Cui, A., Zhang, Z., Yan, H., and Han, B.: Spatial and Temporal Characteristics of Mesoscale Eddies in the North Atlantic Ocean Based on SWOT Mission, Remote Sens., 17, 1469, https://doi.org/10.3390/rs17081469, 2025.

Delandmeter, P. and van Sebille, E.: The Parcels v2.0 Lagrangian framework: new field interpolation schemes, Geosci. Model Dev., 12, 3571–3584, https://doi.org/10.5194/gmd-12-3571-2019, 2019.

Delepoulle, A., Mason, E., Busché, C., Pegliasco, C., Capet, A., Troupin, C., and Koldunov, N.: AntSimi/pyeddy-tracker: v3.6.1, Zenodo [code], https://doi.org/10.5281/zenodo.6333988, 2022.

de Marez, C., Bendinger, A., and Dilmahamod, A. F.: High-latitude eddy statistics from SWOT compared with in situ observations, Ocean Sci., 22, 1515–1528, https://doi.org/10.5194/os-22-1515-2026, 2026.

Diario de Mallorca: Casi la totalidad de los residuos de Cabrera son plásticos, https://www.diariodemallorca.es/mallorca/2022/04/18/totalidad-residuos-cabrera-son-plasticos-65095274.html (last access: 9 July 2025), 2022.

Dibarboure, G., Anadon, C., Briol, F., Cadier, E., Chevrier, R., Delepoulle, A., Faugère, Y., Laloue, A., Morrow, R., Picot, N., Prandi, P., Pujol, M.-I., Raynal, M., Tréboutte, A., and Ubelmann, C.: Blending 2D topography images from the Surface Water and Ocean Topography (SWOT) mission into the altimeter constellation with the Level-3 multi-mission Data Unification and Altimeter Combination System (DUACS), Ocean Sci., 21, 283–323, https://doi.org/10.5194/os-21-283-2025, 2025.

Escudier, R., Mourre, B., Juza, M., and Tintoré, J.: Subsurface circulation and mesoscale variability in the Algerian subbasin from altimeter-derived eddy trajectories, J. Geophys. Res.-Oceans, 121, 6310–6322, https://doi.org/10.1002/2016JC011760, 2016.

E.U. Copernicus Marine Service Information (CMEMS): Mediterranean Sea, Bio-Geo-Chemical, L3, daily Satellite Observations (1997–ongoing), Marine Data Store (MDS) [data set], https://doi.org/10.48670/moi-00299, 2023.

EU Copernicus Marine Service Product: Mediterranean Sea Mean Dynamic Topography, Mercator Ocean International [data set], https://doi.org/10.48670/moi-00151, 2024.

EU Copernicus Marine Service Product: European Seas Gridded L4 Sea Surface Heights And Derived Variables NRT, Mercator Ocean International [data set], https://doi.org/10.48670/moi-00142, 2025a.

EU Copernicus Marine Service Product: European Seas Gridded L4 Sea Surface Heights And Derived Variables Reprocessed 1993 Ongoing, Mercator Ocean International [data set], https://doi.org/10.48670/moi-00141, 2025b.

Fablet, R., Beauchamp, M., Drumetz, L., and Rousseau, F.: Joint Interpolation and Representation Learning for Irregularly Sampled Satellite-Derived Geophysical Fields, Front. Appl. Math. Stat., 7, 655224, https://doi.org/10.3389/fams.2021.655224, 2021.

Fortunato, L., Gómez-Navarro, L., Combes, V., Cotroneo, Y., Aulicino, G., and Pascual, A.: Coastal Eddy Detection in the Balearic Sea: SWOT Capabilities, Remote Sens., 17, 2552, https://doi.org/10.3390/rs17152552, 2025.

Fu, C., Han, X., Wang, Q., Pennelly, C., and Myers, P. G.: Wide-swath satellite altimetry reveals hotspots of small mesoscale eddies in the western Arctic Ocean, Commun. Earth Environ., 7, 344, https://doi.org/10.1038/s43247-026-03498-9, 2026.

Fu, L., Pavelsky, T., Cretaux, J., Morrow, R., Farrar, J. T., Vaze, P., Sengenes, P., Vinogradova-Shiffer, N., Sylvestre-Baron, A., Picot, N., and Dibarboure, G.: The Surface Water and Ocean Topography Mission: A Breakthrough in Radar Remote Sensing of the Ocean and Land Surface Water, Geophys. Res. Lett., 51, e2023GL107652, https://doi.org/10.1029/2023GL107652, 2024.

Gómez-Navarro, L.: LauraGomezNavarro/paper-OSR10_Gomez-Navarro_etal_2026: First release update (Version v1.0.2), Zenodo [code], https://doi.org/10.5281/zenodo.22725565, 2026.

Haller, G., Hadjighasem, A., Farazmand, M., and Huhn, F.: Defining coherent vortices objectively from the vorticity, J. Fluid Mech., 795, 136–173, https://doi.org/10.1017/jfm.2016.151, 2016.

Han, X., Wang, Q., Stewart, A. L., Wang, Z., Yang, Q., Ni, Q., Liu, C., and Chen, D.: High coastal eddy activity around Antarctica revealed by SWOT, Natl. Sci. Rev., 13, nwag181, https://doi.org/10.1093/nsr/nwag181, 2026.

Hargous, P., Combes, V., Barceló-Llull, B., and Pascual, A.: Eddy kinetic energy variability from 30 years of altimetry in the Mediterranean Sea, Ocean Sci., 22, 549–564, https://doi.org/10.5194/os-22-549-2026, 2026.

Hogg, A. M., Meredith, M. P., Chambers, D. P., Abrahamsen, E. P., Hughes, C. W., and Morrison, A. K.: Recent trends in the Southern Ocean eddy field, J. Geophys. Res.-Oceans, 120, 257–267, https://doi.org/10.1002/2014JC010470, 2015.

Ioannou, A., Guez, L., Laxenaire, R., and Speich, S.: Global Assessment of Mesoscale Eddies with TOEddies: Comparison Between Multiple Datasets and Colocation with In Situ Measurements, Remote Sens., 16, 4336, https://doi.org/10.3390/rs16224336, 2024.

Kurian, J., Colas, F., Capet, X., McWilliams, J. C., and Chelton, D. B.: Eddy properties in the California Current System, J. Geophys. Res., 116, C08027, https://doi.org/10.1029/2010JC006895, 2011.

Le Guillou, F., Gaultier, L., Ballarotta, M., Metref, S., Ubelmann, C., Cosme, E., and Rio, M.-H.: Regional mapping of energetic short mesoscale ocean dynamics from altimetry: performances from real observations, Ocean Sci., 19, 1517–1527, https://doi.org/10.5194/os-19-1517-2023, 2023.

Le Guillou, F., Chapron, B., and Rio, M.: VarDyn: Dynamical Joint-Reconstructions of Sea Surface Height and Temperature From

Multi-Sensor Satellite Observations, J. Adv. Model. Earth Sy., 17, e2024MS004689, https://doi.org/10.1029/2024MS004689, 2025.

Le Traon, P. Y., Nadal, F., and Ducet, N.: An Improved Mapping Method of Multisatellite Altimeter Data, J. Atmos. Ocean. Tech., 15, 522–534, https://doi.org/10.1175/1520-0426(1998)015<0522:AIMMOM>2.0.CO;2, 1998.

Lopez-Radcenco, M., Pascual, A., Gómez-Navarro, L., Aissa-El-Bey, A., Chapron, B., and Fablet, R.: Analog Data Assimilation of Along-Track Nadir and Wide-Swath SWOT Altimetry Observations in the Western Mediterranean Sea, IEEE J. Sel. Top. Appl., 12, 2530–2540, https://doi.org/10.1109/JSTARS.2019.2903941, 2019.

Liu, T., Abernathey, R., Sinha, A., and Chen, D.: Quantifying Eulerian Eddy Leakiness in an Idealized Model, J. Geophys. Res.-Oceans, 124, 8869–8886, https://doi.org/10.1029/2019JC015576, 2019.

Marcos, M., Pascual, A., and Pujol, I.: Improved satellite altimeter mapped sea level anomalies in the Mediterranean Sea: A comparison with tide gauges, Adv. Space Res., 56, 596–604, https://doi.org/10.1016/j.asr.2015.04.027, 2015.

Martínez-Moreno, J., Hogg, A. M., Kiss, A. E., Constantinou, N. C., and Morrison, A. K.: Kinetic Energy of Eddy-Like Features From Sea Surface Altimetry, J. Adv. Model. Earth Sy., 11, 3090–3105, https://doi.org/10.1029/2019MS001769, 2019.

Mason, E., Pascual, A., and McWilliams, J. C.: A New Sea Surface Height–Based Code for Oceanic Mesoscale Eddy Tracking, J. Atmos. Ocean. Tech., 31, 1181–1188, https://doi.org/10.1175/JTECH-D-14-00019.1, 2014.

Mason, E., Ruiz, S., Bourdalle-Badie, R., Reffray, G., García-Sotillo, M., and Pascual, A.: New insight into 3-D mesoscale eddy properties from CMEMS operational models in the western Mediterranean, Ocean Sci., 15, 1111–1131, https://doi.org/10.5194/os-15-1111-2019, 2019.

Morrow, R., Fu, L.-L., Ardhuin, F., Benkiran, M., Chapron, B., Cosme, E., d'Ovidio, F., Farrar, J. T., Gille, S. T., Lapeyre, G., Le Traon, P.-Y., Pascual, A., Ponte, A., Qiu, B., Rascle, N., Ubelmann, C., Wang, J., and Zaron, E. D.: Global Observations of Fine-Scale Ocean Surface Topography With the Surface Water and Ocean Topography (SWOT) Mission, Front. Mar. Sci., 6, 232, https://doi.org/10.3389/fmars.2019.00232, 2019.

Pascual, A., Pujol, M.-I., Larnicol, G., Le Traon, P.-Y., and Rio, M.-H.: Mesoscale mapping capabilities of multisatellite altimeter missions: First results with real data in the Mediterranean Sea, J. Mar. Syst., 211, 65, https://doi.org/10.1016/j.jmarsys.2004.12.004, 2007.

Pascual, A., Boone, C., Larnicol, G., and Le Traon, P.-Y.: On the Quality of Real-Time Altimeter Gridded Fields: Comparison with In Situ Data, J. Atmos. Ocean. Tech., 26, 556–569, https://doi.org/10.1175/2008jtecho556.1, 2009.

Pegliasco, C., Chaigneau, A., Morrow, R., and Dumas, F.: Detection and tracking of mesoscale eddies in the Mediterranean Sea: A comparison between the Sea Level Anomaly and the Absolute Dynamic Topography fields, Adv. Space Res., 68, 401–419, https://doi.org/10.1016/j.asr.2020.03.039, 2021.

Pegliasco, C., Delepoulle, A., Mason, E., Morrow, R., Faugère, Y., and Dibarboure, G.: META3.1exp: a new global mesoscale eddy trajectory atlas derived from altimetry, Earth Syst. Sci. Data, 14, 1087–1107, https://doi.org/10.5194/essd-14-1087-2022, 2022.

Pessini, F., Olita, A., Cotroneo, Y., and Perilli, A.: Mesoscale eddies in the Algerian Basin: do they differ as a function of their formation site?, Ocean Sci., 14, 669–688, https://doi.org/10.5194/os-14-669-2018, 2018.

Pujol, M.-I.: EU Copernicus Marine Service Product User Manual for the European Seas Gridded L4 Sea Surface Heights And Derived Variables NRT, SEALEVEL_EUR_PHY_L4_NRT_008_060, Issue 10.0, Mercator Ocean International, https://documentation.marine.copernicus.eu/PUM/CMEMS-SL-PUM-008-032-068.pdf (last access: 16 July 2025), 2025a.

Pujol, M.-I.: EU Copernicus Marine Service Product User Manual for the European Seas Gridded L 4 Sea Surface Heights And Derived Variables Reprocessed 1993 Ongoing, SEALEVEL_EUR_PHY_L4_MY_008_068, Issue 10.0, Mercator Ocean International, https://documentation.marine.copernicus.eu/PUM/CMEMS-SL-PUM-008-032-068.pdf (last access: 16 July 2025), 2025b.

py-eddy-tracker: Welcome to py-eddy-tracker's documentation!, https://py-eddy-tracker.readthedocs.io/en/v3.6.1/ (last access: 8 July 2025), 2022.

Ruiz-Orejón, L. F., Mourre, B., Sardá, R., Tintoré, J., and Ramis-Pujol, J.: Quarterly variability of floating plastic debris in the marine protected area of the Menorca Channel (Spain), Environ. Pollut., 252, 1742–1754, https://doi.org/10.1016/j.envpol.2019.06.063, 2019.

Sánchez-Román, A., Sannino, G., García-Lafuente, J., Carillo, A., and Criado-Aldeanueva, F.: Transport estimates at the western section of the Strait of Gibraltar: A combined experimental and numerical modeling study, J. Geophys. Res.-Oceans, 114, https://doi.org/10.1029/2008JC005023, 2009.

Sánchez-Román, A., Pujol, M. I., Faugère, Y., and Pascual, A.: DUACS DT2021 reprocessed altimetry improves sea level retrieval in the coastal band of the European seas, Ocean Sci., 19, 793–809, https://doi.org/10.5194/os-19-793-2023, 2023.

Stegner, A., Vu, B. L., Dumas, F., Ghannami, M. A., Nicolle, A., Durand, C., and Faugere, Y.: Cyclone-Anticyclone asymmetry of eddy detection on gridded altimetry product in the Mediterranean Sea, J. Geophys. Res.-Oceans, 126, e2021JC017475, https://doi.org/10.1029/2021JC017475, 2021.

Suaria, G. and Aliani, S.: Floating debris in the Mediterranean Sea, Mar. Pollut. Bull., 86, 494–504, https://doi.org/10.1016/j.marpolbul.2014.06.025, 2014.

Taburet, G., Sanchez-Roman, A., Ballarotta, M., Pujol, M.-I., Legeais, J.-F., Fournier, F., Faugere, Y., and Dibarboure, G.: DUACS DT2018: 25 years of reprocessed sea level altimetry products, Ocean Sci., 15, 1207–1224, https://doi.org/10.5194/os-15-1207-2019, 2019.

Taupier-Letage, I., Puillat, I., Millot, C., and Raimbault, P.: Biological response to mesoscale eddies in the Algerian Basin, J. Geophys. Res., 108, https://doi.org/10.1029/1999JC000117, 2003.

Tsimplis, M. and Bryden, H.: Estimation of the transports through the Strait of Gibraltar, Deep-Sea Res. Pt. I, 47, 2219–2242, https://doi.org/10.1016/S0967-0637(00)00024-8, 2000.

Ubelmann, C., Dibarboure, G., Gaultier, L., Ponte, A., Ardhuin, F., Ballarotta, M., and Faugère, Y.: Reconstructing Ocean Surface Current Combining Altimetry and Future Spaceborne Doppler Data, J. Geophys. Res.-Oceans, 126, e2020JC016560, https://doi.org/10.1029/2020JC016560, 2021.

Ubelmann, C., Carrere, L., Durand, C., Dibarboure, G., Faugère, Y., Ballarotta, M., Briol, F., and Lyard, F.: Simultaneous estimation of ocean mesoscale and coherent internal tide sea surface height signatures from the global altimetry record, Ocean Sci., 18, 469–481, https://doi.org/10.5194/os-18-469-2022, 2022.

Última Hora: Un mar de plásticos, https://www.ultimahora.es/noticias/local/2015/07/23/157489/mar-plasticos.html (last access: 22 July 2025), 2015.

Verbrugge, N., Greiner E., Augot, J., Sammartino, M., Colella, S., Buongiorno-Nardelli, B., Hernandez-Carrasco, I., Falcini, F., Rossi, V., and Lacorata, G.: Algorithm Theoretical Baseline Document for 4DMED-SEA Project, version 2, ESA, http://ricerca.ismar.cnr.it/4DMED/docs/4DMED-SEA-D2_ATBD_v2.0-signed.pdf (last access: 15 June 2026), 2024.

Vergara, O., Morrow, R., Pujol, M.-I., Dibarboure, G., and Ubelmann, C.: Global submesoscale diagnosis using along-track satellite altimetry, Ocean Sci., 19, 363–379, https://doi.org/10.5194/os-19-363-2023, 2023.

Verger-Miralles, E., Mourre, B., Gómez-Navarro, L., Barceló-Llull, B., Casas, B., Cutolo, E., Díaz-Barroso, L., d'Ovidio, F., Tarry, D. R., Zarokanellos, N. D., and Pascual, A.: SWOT Enhances Small-Scale Eddy Detection in the Mediterranean Sea, Geophys. Res. Lett., 52, e2025GL116480, https://doi.org/10.1029/2025GL116480, 2025.

Volpe, G., Colella, S., Brando, V. E., Forneris, V., La Padula, F., Di Cicco, A., Sammartino, M., Bracaglia, M., Artuso, F., and Santoleri, R.: Mediterranean ocean colour Level 3 operational multi-sensor processing, Ocean Sci., 15, 127–146, https://doi.org/10.5194/os-15-127-2019, 2019.

Wang, H., Liu, Y., Yang, Y., Yan, R., and Wang, S.: Optimal Shipping Route under the Designation of the Mediterranean Sulfur Emission Control Area: Mathematical Models and Applications, Mathematics, 11, 4897, https://doi.org/10.3390/math11244897, 2023.

State Planet, 7-osr10, 9, 2026
https://doi.org/10.5194/sp-7-osr10-9-2026
© Author(s) 2026. This work is distributed under
the Creative Commons Attribution 4.0 License.

Space-time variability of phytoplankton biomass, diversity and production over the last 27 years in the Mediterranean Sea

Simone Colella, Vittorio Ernesto Brando, Annalisa Di Cicco, and Gianluca Volpe

Consiglio Nazionale delle Ricerche, Istituto di Scienze Marine,
Via Fosso del Cavaliere 100, 00133, Rome, Italy

Correspondence: Simone Colella (simone.colella@cnr.it)

Received: 15 September 2025 – Discussion started: 2 October 2025
Revised: 4 September 2026 – Accepted: 8 September 2026 – Published: 30 September 2026

Abstract. Phytoplankton dynamics in the Mediterranean Sea were investigated over the period 1998–2025 using a suite of Copernicus Marine Environment Monitoring Service satellite products, jointly analysing surface phytoplankton biomass (CHL), phytoplankton size classes (PSC), and integrated primary production (PP) alongside key physical drivers such as sea surface temperature (SST), photosynthetically available radiation (PAR), and mixed layer depth (MLD). Empirical Orthogonal Function (EOF) analysis was applied independently to each variable to characterize variable-specific modes of variability, and in a multivariate configuration (MEOF) to identify coherent modes of shared physical–biological variability. The dominant univariate EOF patterns capture the basin-scale annual cycle and reveal a light–temperature-driven control: PP peaks in summer in phase with PAR and SST, while CHL and MLD peak in winter, reflecting the nutrient–light trade-off characteristic of oligotrophic systems. Secondary univariate modes highlight the sub-basin spring bloom dynamics of the northwestern Mediterranean, associated with episodic deep convection in the Gulf of Lion and the ensuing nutrient supply, with biomass accumulation as the downstream biological response. The MEOF analysis identifies two physically coherent modes of coupled variability: a dominant annual light–temperature mode and a secondary spring-bloom mode linking winter mixing, spring restratification, and enhanced biological production.

1 Introduction

Marine ecosystems are undergoing rapid changes under the combined influence of natural climate variability and anthropogenic forcing (Halpern et al., 2015; IPCC, 2021). Detecting and understanding these changes requires long, continuous, and consistent observational records that span multiple decades (Doney et al., 2012). In the ocean, such records allow scientists to separate short-term variability from persistent trends, attribute changes to their physical and biogeochemical drivers, and assess the resilience of ecosystems to environmental perturbations (Behrenfeld et al., 2006; Boyce et al., 2010).

Phytoplankton, the microscopic photosynthetic organisms that form the base of the marine food web, play a fundamental role in biogeochemical cycles. Phytoplankton biomass and size structure are recognized as Essential Ocean Variables (EOVs) by the Global Ocean Observing System (GOOS), and as Essential Biodiversity Variables (EBVs) by the Group on Earth Observations Biodiversity Observation Network (GEO BON), reflecting their relevance for ecosystem monitoring and climate studies (Muller-Karger et al., 2018). Understanding the spatiotemporal variability of phytoplankton is therefore crucial to monitor ecosystem functioning, assess environmental status, and forecast ecological responses to climate change. In the European context, assessing primary production is also directly relevant to policy frameworks such as the Marine Strategy Framework Directive (MSFD), which requires indicators of ecosystem productivity and resilience to achieve and monitor Good Environmental Status. Satellite ocean-colour observations have revolutionized our ability to monitor phytoplankton dynamics,

Published by Copernicus Publications.

Table 1. List of Marine Copernicus products used in this work and available from https://marine.copernicus.eu (last access: 18 September 2026). Documentation column refers to relevant Quality Information Document (QUID) and Product User Manual (PUM) also available on CMEMS website.

Product ref. no.	Product ID and type	Data access	Documentation
1	OCEANCOLOUR_MED_BGC_L4_MY_009_144, satellite observations	EU Copernicus Marine Service Product (2025a)	QUID: Colella et al. (2025) PUM: Colella et al. (2026)
2	SST_MED_SST_L4_REP_OBSERVATIONS_010_021, satellite observations	EU Copernicus Marine Service Product (2024a)	QUID: Pisano et al. (2024a) PUM: Pisano et al. (2024b)
3	MEDSEA_MULTIYEAR_PHY_006_004, numerical model	EU Copernicus Marine Service Product (2025b)	QUID: Escudier et al. (2025) PUM: Lecci et al. (2025)

providing consistent, synoptic estimates of surface chlorophyll concentration over the past three decades. Chlorophyll concentration (CHL) is widely used as a proxy for phytoplankton biomass, and thanks to the development of regionally-tuned algorithms, its accuracy has significantly improved (Volpe et al., 2007, 2019; Ciancia et al., 2021).

Beyond phytoplankton biomass, robust ecosystem assessments benefit from the joint analysis of complementary biological indicators, such as phytoplankton size classes (PSC) and primary production (PP), together with physical drivers that regulate upper-ocean dynamics (Halpern et al., 2012; Borja et al., 2013; Piroddi et al., 2015). Phytoplankton size structure provides insight into community organization and trophic pathways, while primary production links biomass to carbon fluxes and ecosystem functioning (Behrenfeld and Boss, 2014; Kostadinov et al., 2010). Physical variables such as sea surface temperature (SST) and mixed layer depth (MLD) describe the environmental forcing that shapes oceanic biological patterns in both space and time (Mantua and Hare, 2002; de Boyer Montégut et al., 2004). SST and MLD act as integrative proxies of surface heating, stratification and nutrient entrainment, and therefore provide a mechanistic link between atmospheric forcing and biological response. In addition, light availability, expressed in terms of photosynthetically available radiation (PAR), represents a fundamental driver of phytoplankton production and modulates the seasonal expression of biomass and productivity (Behrenfeld and Falkowski, 1997; Arteaga et al., 2020). Considering biological and physical variables together enables the identification of mechanistic links and feedbacks, helping to disentangle the natural climate variability from the anthropogenic influences (Boyce et al., 2010; Polovina et al., 2008).

For many years, the Mediterranean Sea has been recognized as an ideal natural laboratory for studying coupled physical–biological processes (Bethoux et al., 1999; Robinson and Golnaraghi, 1994). It is a semi-enclosed basin with strong environmental gradients, marked seasonality, and distinct trophic regimes, ranging from mesotrophic in the western waters to ultra-oligotrophic in the eastern gyres (Siokou-Frangou et al., 2010). Its small size, high sensitivity to atmospheric forcing, and rapid response to climatic anomalies make it an excellent testbed for climate-related ecosystem studies (Malanotte-Rizzoli and Robinson, 1994; Lejeusne et al., 2010). Previous satellite-based studies have documented the dominant patterns of chlorophyll variability and their relationship with physical forcing, highlighting the role of seasonal water column stratification, mesoscale dynamics, and deep convection in shaping phytoplankton variability (D'Ortenzio and Ribera d'Alcalà, 2009; Volpe et al., 2012; Mayot et al., 2016). However, most basin-scale analyses have focused primarily on CHL (e.g. Bosc et al., 2004; D'Ortenzio and Ribera d'Alcalà, 2009; Volpe et al., 2012), while none, to the best of our knowledge, have jointly examined biomass, size structure, and primary production within a unified, long-term observational framework over the Mediterranean Sea.

Over the last decade, the Copernicus Marine Environment Monitoring Service (CMEMS) has provided continuous, high-quality satellite ocean colour products (Le Traon et al., 2019, 2021). Unlike other global satellite data providers, CMEMS has progressively specialized in delivering regionally optimized products for the pan-European seas (Brando et al., 2024). In particular, recent developments include gap-free multi-sensor chlorophyll field, phytoplankton size classes and a Mediterranean-specific, wavelength-resolved primary production model integrated into the operational CMEMS processing chain (Brando et al., 2024). These advances enable, for the first time, the construction of coherent, multi-decadal time series of CHL, PSC, and PP that are mutually consistent and suitable for basin-scale variability analyses.

In this study, we explicitly build on the methodological framework introduced by Volpe et al. (2012), extending it in three main directions. First, to provide a more comprehensive description of ecosystem functioning, we include phytoplankton size classes and primary production, in addition to surface chlorophyll, extending the analysis period to 27 years. Second, we exploit improved physical proxies, replacing sea level anomaly with mixed layer depth to better represent upper-ocean dynamics controlling nutrient availabil-

ity. Third, we extend the univariate EOF framework to a multivariate approach, simultaneously decomposing biological and physical variables to directly capture their coupled modes of variability. Empirical Orthogonal Function (EOF) analysis is applied both independently to each variable, to identify the dominant modes of seasonal to interannual variability, and in a joint multivariate configuration, to identify coherent patterns of co-variability across the biological–physical system. This dual approach allows us to infer the main mechanisms governing phytoplankton variability and to quantify the degree of coupling between ecosystem and physical forcing.

The objectives of this work are therefore to:

i. identify the dominant seasonal and interannual modes of the space–time variability of phytoplankton biomass, size structure, and primary production in the Mediterranean Sea over the period 1998–2025;

ii. investigate their relationship with key physical drivers, such as SST and MLD, within a coherent multivariate framework.

By focusing on variability rather than long-term trends, this study aims to provide a robust baseline for interpreting Mediterranean phytoplankton dynamics and to set the stage for future assessments of long-term ecosystem change.

2 Data and Method

2.1 Phytoplankton biomass (CHL) and phytoplankton size classes (PSC)

Phytoplankton biomass is represented by CHL (product ref. no. 1 in Table 1). CHL fields are derived from a gap-free Level-4 multi-sensor satellite product specifically developed for the Mediterranean Sea and provided by CMEMS. This product blends regionally optimized algorithms across open-ocean and coastal waters as a function of optical water types, ensuring long-term consistency over the period 1998–2025 (Volpe et al., 2019; Colella et al., 2025; Brando et al., 2024).

Phytoplankton size structure is described in terms of three PSC: pico- ($< 2\,\mu m$), nano- (2–20 µm), and microphytoplankton ($> 20\,\mu m$), following the dimensional classification of Sieburth et al. (1978). PSC, expressed as fraction of total CHL, are derived from chlorophyll field using the Mediterranean-specific algorithm by Di Cicco et al. (2025), which relates total chlorophyll concentration to the relative contribution of each size class based on diagnostic pigment relationships and regional bio-optical characteristics. PSC fields are distributed by CMEMS as Level-3 products, with gaps mainly due to cloud contamination. Here, PSC was instead derived directly from the CHL gap-filled product.

CHL is used throughout this study as a proxy for surface phytoplankton biomass. While seasonal photo-acclimation effects may modulate chlorophyll concentration independently of biomass (Bellacicco et al., 2016), CHL remains a robust indicator of phytoplankton variability at seasonal to interannual scales in the Mediterranean Sea, as demonstrated in previous studies (e.g., Volpe et al., 2012).

2.2 Sea Surface Temperature (SST) and Mixed Layer Depth (MLD)

To characterize the physical forcing to phytoplankton variability, we use SST (product ref. no. 2 in Table 1) and MLD (product ref. no. 3 in Table 1).

SST is derived from an optimally interpolated Level-4 multi-sensor satellite product providing a stable and homogeneous time series at approximately 4 km spatial resolution over the period 1998–2025. SST is used here as a proxy for surface heating and seasonal stratification, and as an indicator of the thermal environment influencing phytoplankton metabolic rates.

MLD is obtained from the Mediterranean Monitoring and Forecasting Centre (Med-MFC) physical reanalysis (January 1998–May 2023) and near-real-time (June 2023–February 2025) products. MLD is used as a proxy of upper-ocean mixing and nutrient entrainment and represents a more direct indicator of the physical processes controlling nutrient supply to the euphotic zone than surface variables alone. The use of MLD replaces the sea level anomaly variable adopted in Volpe et al. (2012), benefiting from the improved representation of vertical mixing available in recent reanalysis products.

2.3 Primary production (PP) and photosynthetically available radiation (PAR)

PP (product ref. no. 1 in Table 1) is derived from a Mediterranean-specific, wavelength-resolved bio-optical model integrated into the CMEMS operational processing chain. PP, as provided by CMEMS, represents the production throughout the full euphotic zone, including subsurface features such as the deep chlorophyll maximum.

The PP model builds on the formulation of Antoine and Morel (1996) which linked satellite chlorophyll observations to PP through the coupling of an atmospheric radiative transfer model (Tanré et al., 1979) with a bio-optical representation of phytoplankton absorption and scattering properties (Morel, 1991), at global scale. Here, the Mediterranean implementation refines these components to account for the peculiar bio-optical properties of the basin and benefits from improved atmospheric and bio-optical parameterizations and the availability of recent high-resolution satellite and in situ datasets. In this context, daily column-integrated PP is computed as:

$$\mathrm{PP} = 12 \int_{z=0}^{\mathrm{Depth}} \int_{t=0}^{24} \int_{\lambda=400}^{700} \mathrm{Chl}(z)\, a^{*}_{\mathrm{Chl}} \mathrm{PAR}(z,t,\lambda)\, \varphi_{\mu} \times (\mathrm{Chl}, T)(z)\, \mathrm{d}\lambda \mathrm{d}z \mathrm{d}t \quad (1)$$

where 12 is the Carbon molar weight to express PP as mass of Carbon; Chl(z) is the chlorophyll concentration profile; a^{*}_{Chl} is the chlorophyll-specific absorption coefficient, expressed as a function of chlorophyll concentration; PAR(z, t, λ) is the photosynthetically available radiation at depth z, time t, and wavelength λ; and $\varphi_{\mu}(\mathrm{Chl}, T)$ is the photosynthetic quantum yield, formulated as a function of chlorophyll and temperature, which expresses the efficiency of converting captured energy into Carbon. The daily PP was computed as the triple integral of the production rate with respect to wavelength (over the band, 400–700 nm), time (over 24 h), and depth.

A major advancement of the Mediterranean configuration is the adoption of the revised Ocean Atmosphere Spectral Irradiance Model (OASIM; Gregg and Casey, 2009), which provides direct and diffuse irradiance at 5 nm spectral resolution between 400 and 700 nm, on a daily 4 km grid. In addition to its role in driving the primary production model, light availability was explicitly analysed using PAR derived from OASIM. PAR was considered as an independent driver of phytoplankton production variability, allowing the contribution of light-driven processes to seasonal and interannual changes in primary production to be assessed in a manner fully consistent with the modelling framework. This irradiance field, combined with the reparametrized bio-optical module, enables the computation of light penetration through the water column, with updated absorption (Bricaud et al., 1998) and scattering (Morel et al., 2002) coefficients.

OASIM-derived irradiance was used instead of satellite-derived PAR to ensure consistency with the wavelength-resolved PP model, which requires spectral direct and diffuse irradiance to compute light absorption, scattering and propagation through the water column. This choice also provides a homogeneous radiative forcing over the full 27-year period, avoiding potential inter-sensor discontinuities in multi-sensor satellite PAR records, and the Mediterranean implementation has been evaluated with good results against in situ radiometric observations (Lazzari et al., 2021).

Since remote sensing observations provide chlorophyll information only for the surface layer, vertical distributions must be reconstructed to compute depth-integrated production. This follows the empirical approach of Morel and Berthon (1989), which relates satellite-derived surface pigment concentration to euphotic zone chlorophyll content and profile shape. For the Mediterranean Sea, this approach has been revisited using the MedBiOp in situ dataset (Volpe et al., 2019). Applying k-means clustering to vertical chlorophyll profiles, the in situ dataset was partitioned into seven groups, each representing a trophic regime and used to associate the surface observations to the vertical distribution.

Temperature effects on phytoplankton physiology are accounted for using vertical temperature profiles from the Mediterranean Monitoring and Forecasting Centre (Med-MFC) physical reanalysis (product ref. no. 3 in Table 1). Temperature modulates the photosynthetic quantum yield, thereby influencing primary production without directly altering biomass. The PP model is primarily optimized for optically simple (Case I) open waters. In optically complex coastal waters (Case II), such as river-influenced and shallow regions, PP estimates are associated with higher uncertainty and should be interpreted with caution. Thus, areas permanently classified as Case II waters, such as the northern Adriatic coastal strip and the mouth of the Nile River (characterized by strong riverine inputs and turbid plumes; Brando et al., 2015; Masoud, 2022), along with the Gulf of Gabès (a shallow and highly turbid system; Katlane et al., 2013), are masked and excluded from the data analysis.

Further details on the PP calculation, including the use of OASIM, are provided in Appendix A.

2.4 Spatio-temporal harmonization and preprocessing

To ensure consistency among variables, all datasets were resampled onto a common monthly grid with 4 km spatial resolution. Spatial regridding was performed using the nearest-neighbour approach, followed by the computation of monthly averages. The monthly temporal resolution minimizes the influence of high-frequency variability, thereby emphasizing seasonal and interannual signals.

The choice of a 4 km spatial resolution is consistent with the adopted monthly time scale and allows the permanent or semi-permanent mesoscale features to be retained while filtering out finer-scale variability that is incompatible with monthly sampling. All variables were analysed over the period January 1998 to February 2025.

2.5 Empirical Orthogonal Function analysis

As stated in the introduction, the objectives of this work are, on the one hand, to address the phytoplankton variability per se, in terms of biomass, size distribution, and productivity, and, on the other hand, to link this variability to key physical drivers. To this end, we perform both univariate and multivariate analyses of a consistent dataset including physical (MLD, PAR, SST) and biological (CHL, PP, PSC) variables. The univariate Empirical Orthogonal Functions (EOFs) were used to describe the dominant spatial and temporal patterns of each field independently, without imposing any a priori coupling among variables. Comparisons among univariate EOF modes are therefore used only as an interpretative tool, based on similarities in spatial structure, temporal phasing, and lagged correlations. The multivariate EOF (MEOF) analysis (applied only to the five core variables MLD, SST, PAR,

CHAPTER 2.6

CHL, and PP, since PSC fields are diagnostically derived from CHL) was then used to identify the modes of variability that are shared by the core physical and biological variables. In contrast to the univariate EOFs, each MEOF mode is characterized by a single temporal amplitude common to all variables and therefore provides a more formal estimate of their coupled variability. Because univariate EOFs maximize the variance of each variable separately, whereas MEOF maximizes the variance of the entire standardized dataset, the ordering and spatial structure of the modes are not expected to coincide exactly between the two approaches. The two analyses should therefore be regarded as complementary: univariate EOFs diagnose variable-specific variability, while MEOFs identify basin-scale coupled modes of the physical–biological system.

Spatio-temporal variability is analysed following the methodology of Volpe et al. (2012). EOFs summarize the dominant modes of variability of a field and are interpreted as the product between the spatial pattern and the corresponding temporal amplitude. The closer to zero either of these two components is, the less relevant the associated variability of that mode will be at that specific location and time. An important aspect for interpreting the results is the sign agreement between spatial and temporal components: when they have the same sign, the mode variability follows the spatial pattern and its associated temporal amplitude as shown, whereas when their signs differ, the variability is reversed. Analogously, if the spatial pattern presents regions with positive and negative values, these regions vary in opposition of phase.

Univariate EOFs are computed independently for each variable based on the singular value decomposition of anomaly fields. No temporal filtering is applied, and the analysis therefore focuses on mean fields and dominant seasonal to interannual modes of variability. For each variable, long-term mean fields were computed and removed from the corresponding time series. The resulting anomaly fields describe deviations from the climatological mean state and constitute the input for the subsequent EOF analysis. EOF spatial patterns thus describe the characteristic structures of variability around the mean state, while the associated temporal amplitudes represent the evolution of these patterns over time.

A multivariate EOF (MEOF) analysis was then applied to the same anomaly fields, using the same spatial and temporal resolution. As in the univariate EOF analysis, the mean value of each variable was removed from the time series. In addition, each variable was divided by its standard deviation before the MEOF decomposition, so that variables with different units and variability ranges contributed comparably to the analysis.

2.6 Statistical correlation analysis

Correlation analysis is used here to support the interpretation of the dominant modes of variability; however, statistical correlation alone does not imply strict causality, and results are interpreted in the context of physical and biogeochemical processes known to occur in the Mediterranean Sea. The Pearson linear correlation was computed either between the temporal amplitudes of selected EOF modes or, where appropriate, between mean spatial fields. Moreover, to account for potential phase shifts between different phenomena, the temporal cross-correlation was computed also considering a variable time lag up to one year.

3 Results and discussion

This section presents the mean spatial fields and the dominant modes of spatio-temporal variability, explored through both univariate and multivariate EOF analyses, derived from 27 years of satellite observations of biological and physical variables.

3.1 Mean fields

The average surface mixed layer thickness (Fig. 1a) is generally thinner than 50 m, apart from the Aegean Sea, the south Adriatic and in particular the Gulf of Lion where it presents values twice as large as the rest of the basin. MLD pattern confirms the dynamic nature of the cold-water spot in the Gulf of Lion where it exceeds 125 m and represents one of the most energetic water mass formation sites in the Mediterranean (Marshall and Schott, 1999). The MLD signature in the Gulf of Lion leaves a clear imprint on phytoplankton abundance and productivity, as discussed below.

The average SST values (Fig. 1b) show a NW-SE gradient in all sub-basins, with the Alboran Sea, the Gulf of Lion, the North Adriatic and Aegean seas to be the cold end of the range of variability. This thermal structure is consistent with the MLD pattern described above and is likely driven by dynamical factors such as river outflows (Struglia et al., 2004), water mass formation (Marshall and Schott, 1999) or wind forcing (Millot, 1999) rather than due to insolation, only.

Figure 1c shows the basin-scale average PAR field. The southeastern basin receives approximately double the solar radiation compared to the northern part, reflecting both the expected meridional gradient and the longitudinal asymmetry visible in the image. This pattern also reflects the spatial distribution of cloudiness across the basin (Enriquez-Alonso et al., 2016).

Figure 1d shows the average CHL concentration over the entire period, revealing the well-known west-east gradient characteristic of the Mediterranean, with higher phytoplankton biomass in the western basin. The most phytoplankton-rich areas are the bloom region of the Gulf of Lion (Marty et al., 2002; D'Ortenzio and Ribera d'Alcalà, 2009) and the African coast, where Atlantic surface waters entering through the Gibraltar Strait drive the Algerian current (Millot, 1999; Bosc et al., 2004) and, together with Mediterranean intermediate waters, give rise to the western Alboran Gyre

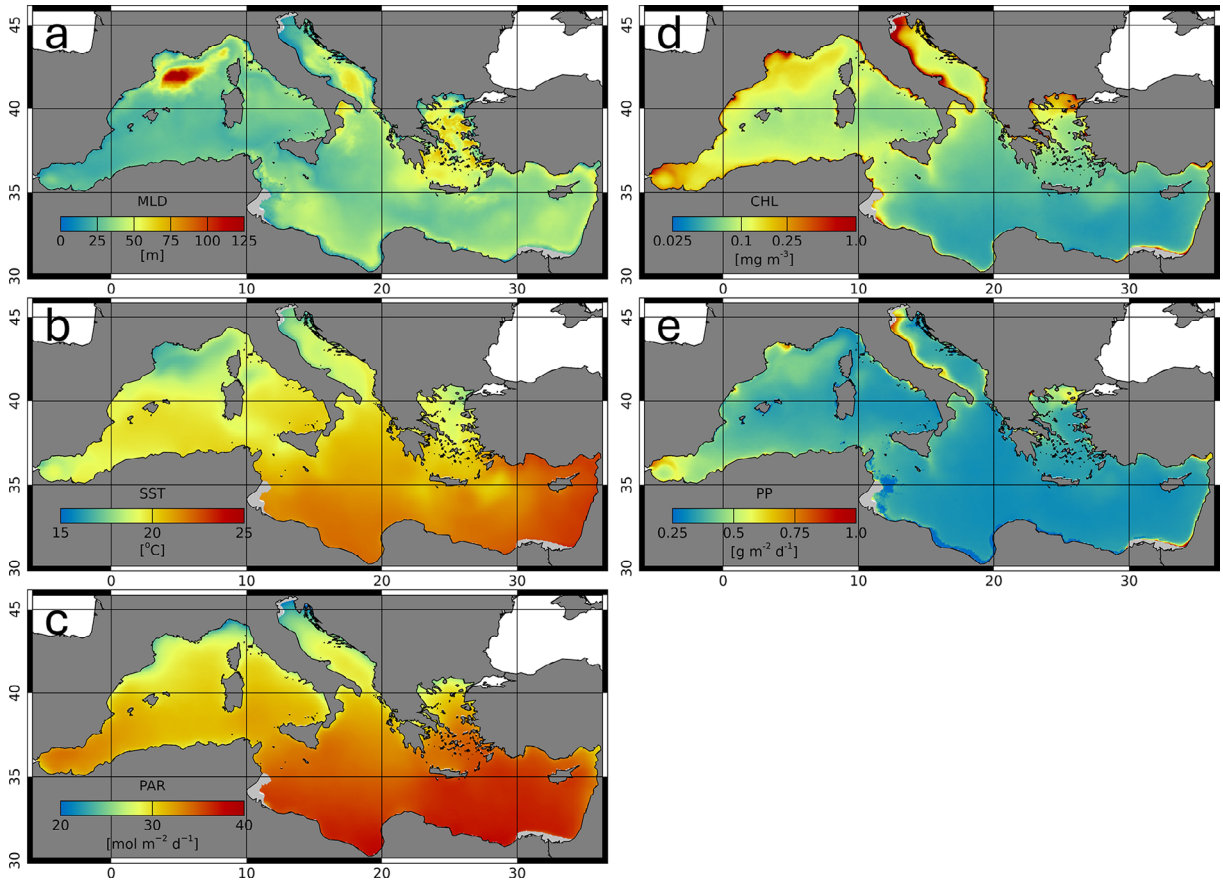


Figure 1. Mean time averages (1998–2025) of MLD **(a)**, SST **(b)**, PAR **(c)**, CHL **(d)**, and PP **(e)**. Light grey indicates the areas permanently masked out because of persistent or recurrent Case II water conditions.

(Gascard and Richez, 1985), whose signature is clearly visible across all fields. Coastal areas are on average more enriched in phytoplankton than open waters, likely due to riverine nutrient inputs and coastal upwelling.

The average PP (Fig. 1e) spans approximately one order of magnitude, ranging from roughly 0.25 to 1.0 g m^{-2} d^{-1}. Although PP broadly mirrors the spatial patterns seen in CHL (Fig. 1d), with higher values in the western basin and along coastal areas, its basin-scale gradients are comparatively less pronounced.

Not surprisingly, CHL and SST mean fields (Fig. 1d–b) here computed with 27 years of observations appear at first sight very similar to those previously computed with only nine years of observations as shown in Volpe et al. (2012, Fig. 3). However, a closer look at the data in the two reference periods reveals a general warming (Pisano et al., 2020; EU Copernicus Marine Service Product, 2024b) consistent with a basin-scale tendency toward upper-layer oligotrophication and reduced phytoplankton abundance (Colella et al., 2016; EU Copernicus Marine Service Product, 2024c). These differences can locally account for as much as 5 % increase in SST and 20 % decrease in CHL (Fig. B1). This SST-CHL inverse relationship can be broken locally where river inputs (north Adriatic Sea), coastal dynamics (north Aegean Sea) or permanent mesoscale features (Rhodes Gyre) play a major role in regulating both the thermal and phytoplankton fields.

Table 2. Pearson spatial correlation coefficient computed between the various variables.

	MLD	SST	PAR	CHL	PP
MLD	–	0.03	0.06	−0.29	−0.18
SST	–	–	0.71	−0.57	−0.31
PAR	–	–	–	−0.67	−0.39
CHL	–	–	–	–	0.80
PP	–	–	–	–	–

Table 2 shows the outcome of the correlation analysis between the mean fields of Fig. 1. High correlation is here reported for SST-PAR, SST-CHL, PAR-CHL and CHL-PP. The other spatial correlation can be considered negligible.

As expected from their functional forms and from being derived as a direct function of CHL (Di Cicco et al., 2017, 2025), the mean fields of PSC (Fig. B2) spatially show

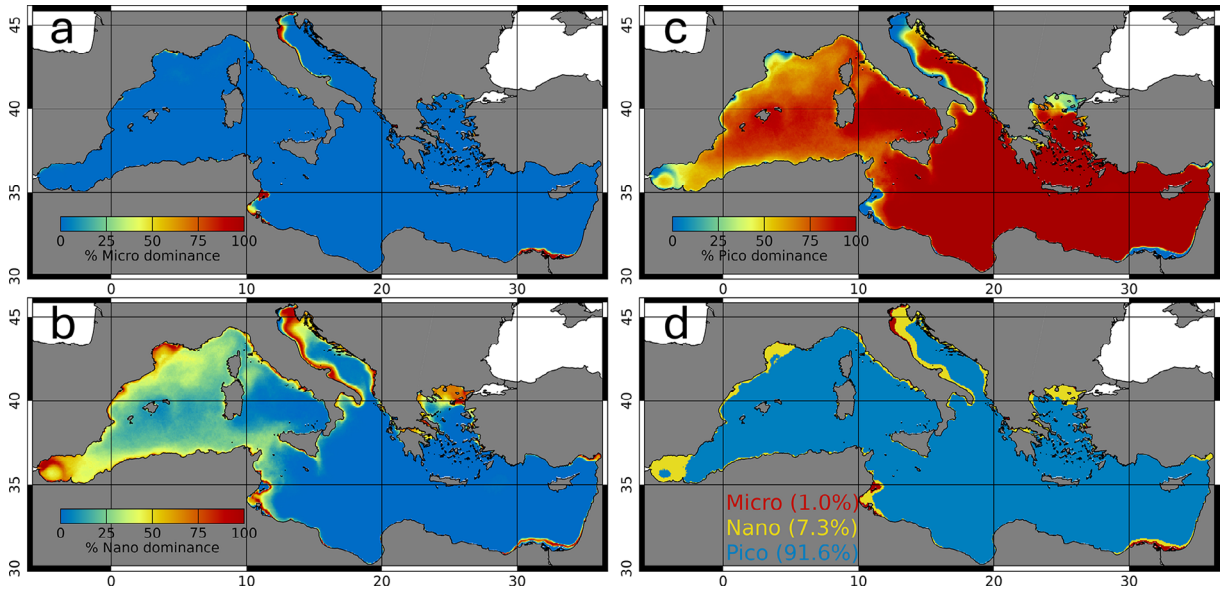


Figure 2. Percent dominance of PSC size classes (Micro, Nano and Pico in panels **a**, **b** and **c**, respectively) over time. Panel **(d)** shows the overall temporal dominance of each size class in percent over the entire time series.

patterns very close to CHL. By design and because of the known co-variability between phytoplankton accessory pigments associated with each fraction and total CHL concentration (Chisholm, 1992; Hirata et al., 2011), the three size classes individually highly correlate with CHL: r^2 equals 0.99, 0.97 and 0.99 for pico, nano and micro, respectively. The mean fields of the three PSC are characterized by different intensity, each being relevant in specific areas of the range of variability.

To achieve the percent PSC pixel dominance (Fig. 2), we counted, for each pixel, the number of months in which a given PSC showed a higher value than all the others. The resulting map was then normalized by the total number of months in the time series. Figure 2a, d show that microphytoplankton is the most abundant class only over 1 % of the basin in correspondence with coastal waters and the main river outflows. Thus, the terrigenous origin of the high nutrient levels in these areas sustains the development of larger phytoplankton cells throughout the time series, a condition otherwise rarely observed in the basin except in the deep-water formation region associated with the intense spring bloom in the northwestern Mediterranean (Marty et al., 2002; Uitz et al., 2006; D'Ortenzio and Ribera d'Alcalà, 2009; Siokou-Frangou et al., 2010; Volpe et al., 2012). Nanophytoplankton predominance is more widespread in both space and time (Fig. 2b), significantly contributing to the size distribution of the entire western basin, in the Adriatic and in the north Aegean Sea. The relevance of its contribution reflects the trophism of the areas, as clearly shown by the yellow areas in Fig. 2d where nano class is shown to be dominant. Figure 2c shows that the entire eastern basin along with the Tyrrhenian and the deep-bottom open waters of the Adriatic Sea are nearly always dominated by pico phytoplankton, consistently with in situ observations (Marty et al., 2002; Siokou-Frangou et al., 2010). The occurrence of this size class remains relevant also over the western basin where it dominates the size spectrum 75 % of the time. The dominance of the smallest size class is once more the fingerprint of the oligotrophic nature of the surface Mediterranean open waters.

3.2 Variability

3.2.1 Basin-scale annual variability

Figures 3 and 4 show the spatial pattern and temporal amplitudes of the first EOF modes computed over MLD, SST, CHL, PAR and PP.

The first MLD mode accounts for 61.7 % of the total variance and is dominated by the Gulf of Lion, where values are two to three times larger than the rest of the basin (Fig. 3a), consistent with its role as the primary deep-water formation site in the Mediterranean (MEDOC Group, 1970; Marshall and Schott, 1999). Large variability is also found in the south Adriatic and in the Aegean Sea, both of which are subject to recurrent deep convection events. On the other hand, reduced variability is found in correspondence of permanent current systems such as the Algerian current in the western basin which splits into two branches: one in the Tyrrhenian and the other following the Atlantic Ionian Stream (AIS) towards the Levantine Basin. The temporal evolution of this mode (Fig. 4a) shows a pulsed sinusoidal signal with sharp maxima during winter mixing, much more pronounced than the low background value characteristic of the rest of the strati-

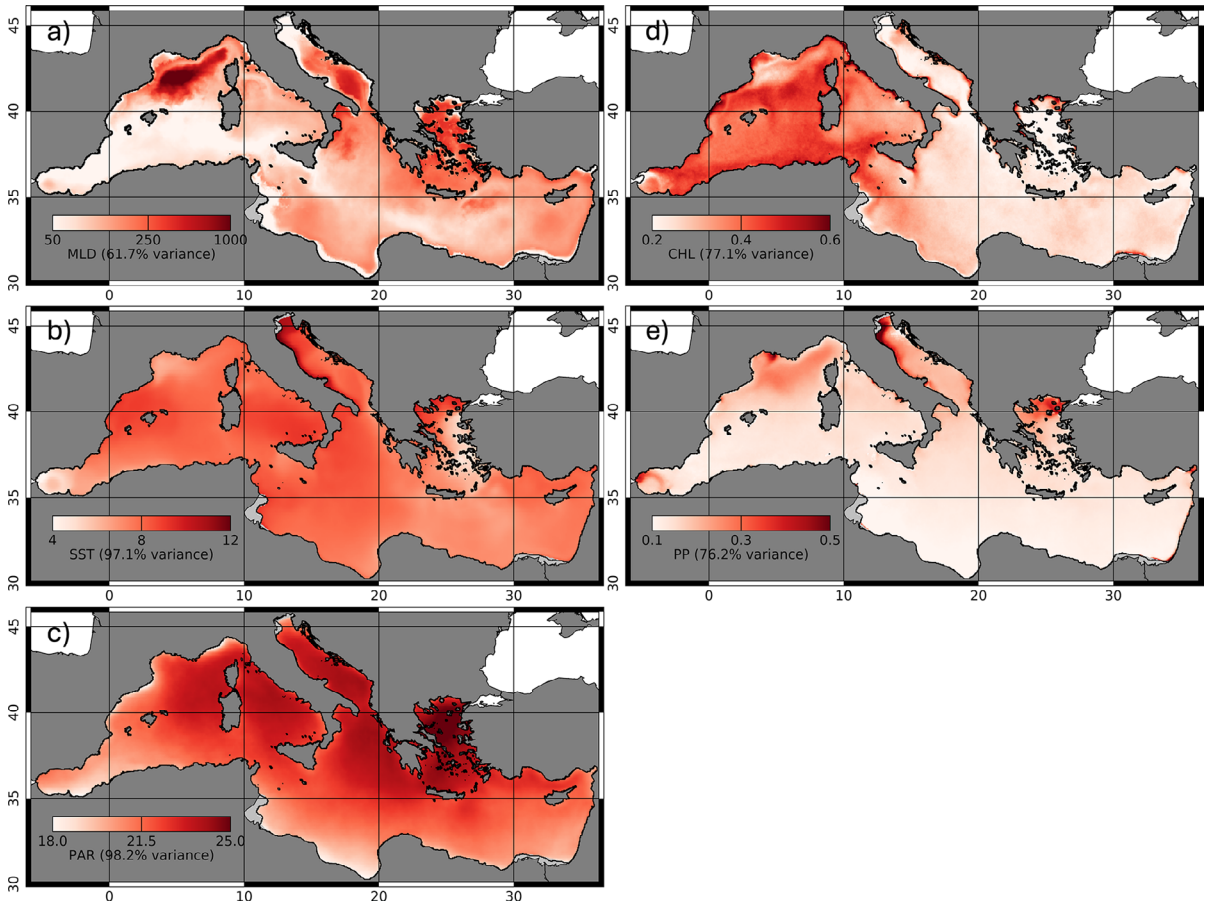


Figure 3. Spatial patterns of the first mode of EOF for MLD **(a)**, SST **(b)**, PAR **(c)**, CHL **(d)**, and PP **(e)**. Light grey indicates the areas permanently masked out because of persistent or recurrent Case II water conditions.

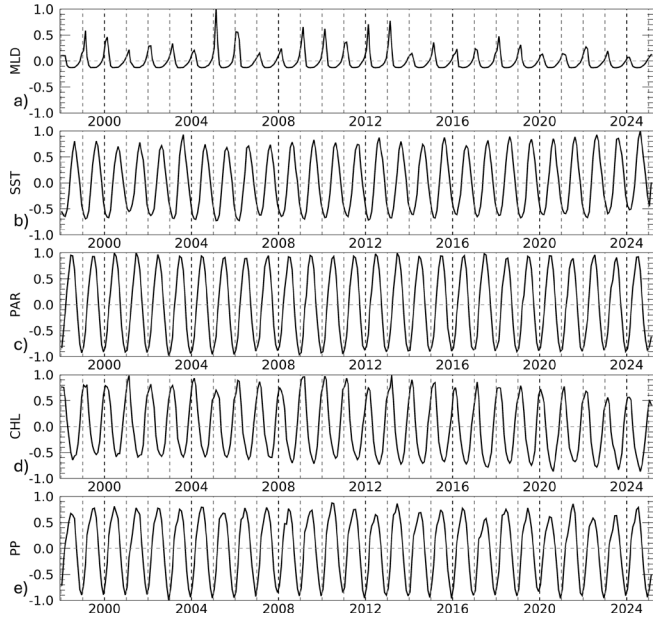


Figure 4. First mode of EOF MLD **(a)**, SST **(b)**, PAR **(c)**, CHL **(d)**, and PP **(e)** temporal evolutions.

fied period. Unlike the temporal evolutions of the first mode of the other variables (Fig. 4b–e), the one associated with the first mode of MLD shows a pronounced interannual variability with values spanning over one order of magnitude and with lower amplitudes during the last decade. The combination of the spatial pattern and temporal evolution indicates that the first MLD mode primarily represents the dominant basin-scale seasonal cycle of winter mixed-layer deepening, with the largest amplitude in the Gulf of Lion.

Figure 3b shows the SST first mode (97 % of the total variance) with three main patterns of homogeneous variability. The highest pattern of variability is associated with coastal areas of the western Adriatic Sea. The lowest SST variability is found at Gibraltar, in the Gulf of Lion, in the Aegean Sea and south of Crete Island, and to a lesser extent, in the Sicily Channel. These areas are affected by distinct physical mechanisms that attenuate the amplitude of the seasonal warming and cooling cycle driven by solar shortwave radiation. At Gibraltar, the continuous inflow of cooler Atlantic waters mitigates surface warming and reduces the seasonal thermal range (Harzallah et al., 2014). In the Sicily Channel, the AIS-driven upwelling system brings colder waters to the

surface preferentially during summer (Bosc et al., 2004; Bonanno et al., 2014) dampening the seasonal SST signal. In the Aegean Sea and the Gulf of Lion, the dominant seasonal wind regimes (the Meltemi and the Mistral, respectively) drive enhanced turbulent heat loss and vertical mixing that limit surface ocean warming (Ziv et al., 2004; Millot, 1999; Herrmann and Somot, 2008). The temporal evolution of the SST mode (Fig. 4b) is a smooth, nearly symmetric sinusoid with positive values in summer (August) and negative values in winter (January–February), consistent with the annual cycle of solar heating.

The first PAR mode explains 98 % of its total variance (Fig. 3c). The highest variability is found in the northern and central parts of the basin, with the Aegean Sea standing out as a clear maximum. This is physically consistent with the larger seasonal swing of day length and solar zenith angle at higher latitudes, which drives a pronounced contrast between low winter PAR and high summer PAR values. The Aegean is further enhanced by the persistent clear-sky conditions maintained by the Meltemi wind regime (Tyrlis and Lelieveld, 2013), which removes clouds and aerosols and thus could maximise the amplitude of the seasonal PAR signal. Analogously, the African coast is characterized by lower variability. A band of lower variability is also visible along the northern coastlines, the Gulf of Lion, the Ligurian Sea and the northern Adriatic, where high frequency in cloud cover due to the orography of the region (Houze, 2012) could play an important role to reduce insolation and to moderate seasonal PAR variations. The temporal amplitude (Fig. 4c) is a near-perfect sinusoid with minima in December–January and maxima in June–July, similar to the SST first mode (Fig. 4b). This tight phase coherence reflects the well-established coupling between sea surface heating and incoming solar irradiance at the annual timescale, with PAR driving SST with only a slight lag (1–2 months) due to the ocean's thermal inertia.

Figure 3d shows the CHL first mode (77.1 % of the total variance). The highest CHL variability is found in the western basin, with special reference to the Balearic front area and the Algerian Current system. Variability decreases progressively eastward, reaching minima near river mouths and straits. A notable feature is the tongue of elevated variability extending from the Algerian Current toward the Tyrrhenian Sea and further into the eastern basin, closely resembling the corresponding signature in the MLD field (Fig. 3a). This spatial analogy is not coincidental: the winter reinforcement of the Algerian Current drives mesoscale instabilities that promote vertical mixing, leading to MLD deepening and the subsequent nutrient enrichment of the surface layer, which in turn enhances phytoplankton biomass and the associated chlorophyll signal. Furthermore, maximum positive values generally occur in February when cold nutrient-rich waters reach the surface through a deeper mixed layer, stimulating phytoplankton growth. CHL minima are associated with the summer stratification period (July–August, Fig. 4d). However, photo-acclimation has been claimed to explain this CHL annual cycle which is dominated by low light conditions and nutrient enhancement during winter and the opposite during summer (Behrenfeld et al., 2005; Bellacicco et al., 2016).

The first PP mode explains 76.2 % of its total variance (Fig. 3e), with areas of distinct variability. The highest variability is found in the coastal northern Adriatic Sea, where allochthonous nutrient inputs from rivers are well known to sustain elevated coastal productivity (Penna et al., 2004; Nixon, 2003; Cossarini et al., 2020). However, the PP signal in this region should be regarded with care because this area is characterized by optically complex waters and the PP model bio-optical parameterization derives from open-ocean conditions. Other coastal areas of significant variability are the straits of Gibraltar and the Dardanelles, where lateral advection of nutrient-enriched waters drives a clear seasonal signal, and with the open waters of the Ligurian Sea and the Gulf of Lion, reflecting the influence of winter convective mixing and the ensuing nutrient supply to the euphotic zone. This interpretation is consistent with Mediterranean biogeochemical studies showing that nutrient availability and primary production patterns are strongly shaped by hydrodynamic forcing, riverine inputs, and mixed-layer dynamics in key productive and convective regions of the basin (Cossarini et al., 2020; Reale et al., 2020). The remaining basin presents comparatively low annual PP variability. This pattern is modulated by a marked temporal amplitude, oscillating sinusoidally with positive values during summer, reaching maxima generally in July, and minima in winter, typically in December or January (Fig. 4e). This seasonal phasing perfectly matches PAR annual cycle (Fig. 4c) and SST (Fig. 4b), but in striking opposition of phase with CHL (Fig. 4d), whose maxima occur in late winter. This apparent paradox, maximum primary production when chlorophyll concentration is at its annual minimum, and vice versa, is a well-documented characteristic of the Mediterranean Sea and of oligotrophic gyres (Behrenfeld et al., 2005; Mignot et al., 2014; Bellacicco et al., 2016). The mechanistic explanation for this decoupling lies in the contrasting seasonal forcings that govern CHL and PP. In winter, deep convective mixing entrains nutrient-rich subsurface waters into the euphotic zone, stimulating phytoplankton growth and elevating bulk CHL concentrations. However, the concurrent low irradiance, as captured by the PAR minimum, limits the rate of photosynthetic carbon fixation, keeping PP suppressed despite high CHL values. Conversely, in summer, the development of strong thermal stratification reduces the vertical supply of nutrients to the euphotic layer, in agreement with Mediterranean biogeochemical studies linking nutrient availability to mixed-layer dynamics, and CHL declines to its seasonal minimum (Reale et al., 2020). Yet the high irradiance characteristic of the Mediterranean summer (PAR maximum) drives intense photosynthetic activity per unit biomass, sustaining elevated PP under otherwise oligotrophic conditions. This light-driven enhancement of summer PP is compatible

with the process of cellular photo-acclimation: under high irradiance, phytoplankton reduce their cellular chlorophyll-to-carbon ratio, so that bulk CHL decreases even if photosynthetic rates remain elevated (Behrenfeld et al., 2005; Bellacicco et al., 2016). The first EOF mode of PP therefore captures a predominantly light-driven signal rather than one driven by nutrient or biomass dynamics, with PAR emerging as the primary modulator of the annual PP cycle at the Mediterranean basin scale. The alignment between the PP and PAR temporal amplitudes (Fig. 4e and c) directly reflects this dominant physical control.

It is worth mentioning that nearly the total variability of light (98 %) and temperature (97 %) is linked to the annual cycle while there is still a substantial part of variability to be explained for MLD, CHL and PP.

The first mode of phytoplankton CHL (Fig. 4d) presents high correlation values at lag zero with both SST (Fig. 4b, $r = -0.93$) and MLD (Fig. 4a, $r = 0.8$). Although part of this variability can surely be explained in terms of photo-acclimation (Bellacicco et al., 2016), it is likewise a clear sign of the winter cooling that deepens the MLD in turn favouring nutrients into the upper water column. This promotes biomass accumulation. Analogously, the first mode of PP (Fig. 4e) is highly correlated with the first mode of PAR (Fig. 4c, $r = 0.98$, at lag zero) which in turn also drives the SST first mode with two months lag (Fig. 4b, $r = 0.97$).

Phytoplankton size diversity (PSC) is perfectly in line with CHL (Figs. 3d and 4d), as shown in Figs. B3a, b, c and B4a, b, c, with maxima in winter and minima in summer. We did use the same colorbar range in Fig. B3, just to show that Micro, being the less dominant and frequent (Fig. 2), shows the most pronounced variability. Variability reduces with the dominance of the cell size with Pico being the most stable, still with the very same space-time pattern as the others, including total CHL.

3.2.2 Sub-basin seasonal variability: spring bloom and deep-water formation

The second EOF mode computed over the MLD (Fig. 5a) explains 14 % of its total variability and presents two spatially distinct regions in opposition of phase: the Gulf of Lion on one side and the rest of the basin on the other. This spatial opposition suggests that this mode captures localised deep convection dynamics rather than the basin-scale annual signal dominated by the first EOF mode. The temporal amplitude (Fig. 6a) shows recurrent negative pulses during winter and positive values throughout the rest of the year, although occasional winter maxima can be observed in 2005, 2006, 2009, 2010, 2012, and 2013. These anomalous years have already been correlated with positive-to-negative North Atlantic Oscillation (NAO) transition (Basterretxea et al., 2018) which intensify northerly winds over the Gulf of Lion and favour deep-water formation events. Taken together, the spatial and temporal signals of this mode can be interpreted as representing sub-basin scale deep-water formation, with the Gulf of Lion as the primary driver, largely decoupled from the smoother seasonal pattern described by the first mode.

Figure 5b displays the second EOF mode of SST (1.2 % of the total variance) with a clear northwest–southeast gradient, with predominantly positive anomalies in the western Mediterranean and negative values over the Levantine Basin. The northern Aegean Sea constitutes an exception within the eastern sub-basin, showing positive variability. This spatial pattern closely resembles that reported by Volpe et al. (2012), despite the longer time series used here. The corresponding temporal amplitude (Fig. 6b) shows a regular seasonal cycle, with positive values typically from January to August–September and negative values during the remaining months. Nevertheless, the amplitude of both maxima and minima varies considerably from year to year, reflecting interannual modulation likely linked to large-scale atmospheric forcing such as the NAO, consistent with the variability identified in the MLD second mode.

The second EOF mode of PAR (Fig. 5c) explains only 0.6 % of the total variance, confirming that PAR variability is largely dominated by the annual cycle. Its spatial pattern shows a weak dipole-like structure between the northwestern Mediterranean and the Levantine sub-basin. This residual signal may partly reflect non-seasonal modulation of cloud cover and surface shortwave radiation by atmospheric circulation patterns, but its physical interpretation remains uncertain and a contribution from noise cannot be excluded. Therefore, the second mode of PAR is not considered a robust component of the deep-water formation and spring bloom mechanism discussed in this section.

The second EOF mode of CHL (Fig. 5d) explains 5.6 % of the total variance and is spatially coherent with the MLD and SST second modes and aligns well with the results of Volpe et al. (2012). Pronounced positive anomalies are found in the northwestern Mediterranean, particularly in the Gulf of Lion, the Ligurian Sea, and to a lesser extent around the Bonifacio Gyre, while the rest of the basin shows limited variability. This pattern is clearly linked to spring bloom dynamics: the deep winter mixing captured by the MLD second mode in the Gulf of Lion supplies nutrients to the euphotic zone, and the subsequent restratification in spring, consistent with the SST second mode gradient, triggers intense phytoplankton growth. The temporal amplitude (Fig. 6d) confirms this interpretation, displaying recurring positive peaks during the spring months and negative values throughout winter and summer, with an interannual variability in bloom intensity.

The PP second EOF mode (Fig. 5e) explains 7.6 % of the variance and exhibits widespread positive variability throughout the Mediterranean basin, with negative values confined to the Adriatic Sea, Aegean Sea and along African coasts of the Levantine basin. This broader spatial signature, compared to the more localised chlorophyll second mode, suggests that PP integrates the regional bloom signal of the northwestern Mediterranean with a diffuse positive response

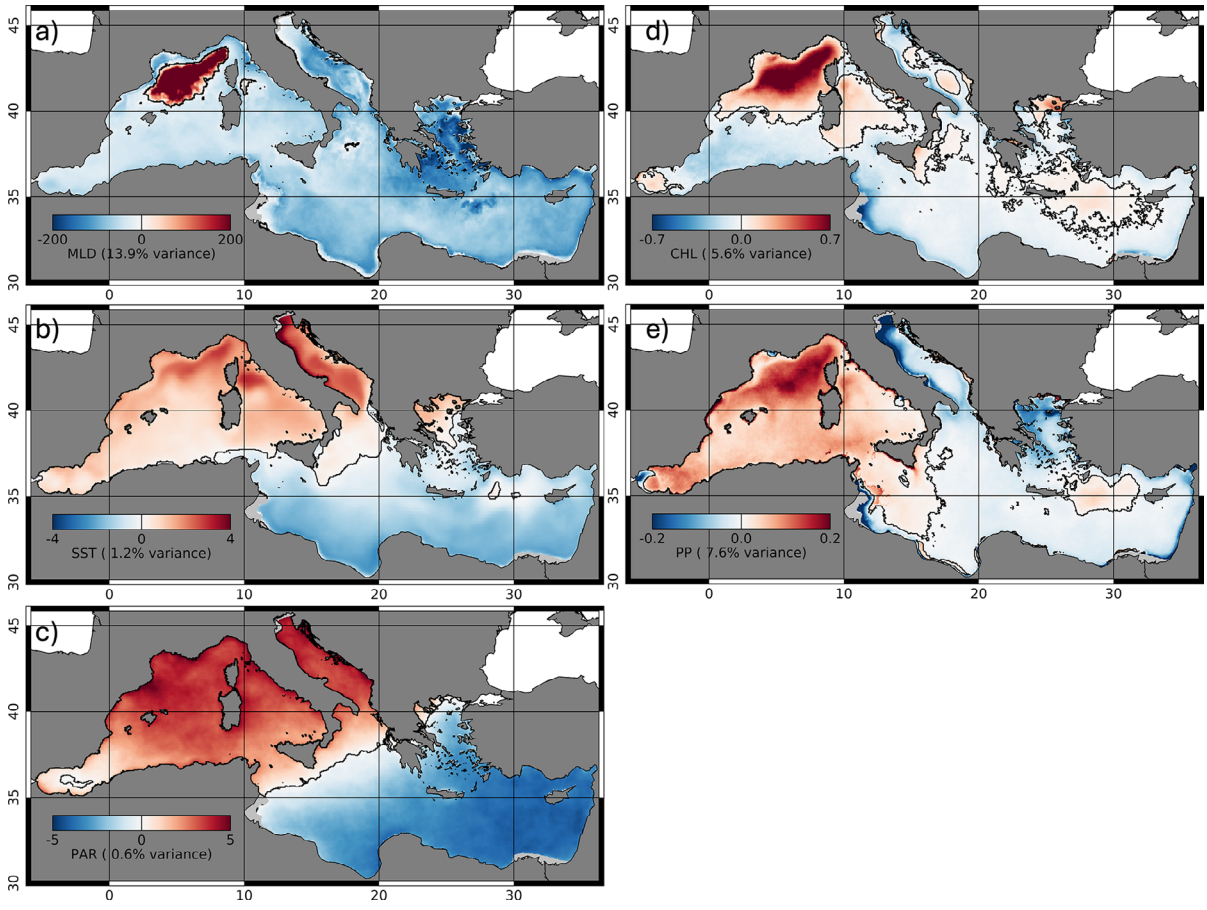


Figure 5. Second mode of EOF variability for MLD **(a)**, SST **(b)**, PAR **(c)**, CHL **(d)** and PP **(e)** spatial patterns. Light grey indicates the areas permanently masked out because of persistent or recurrent Case II water conditions.

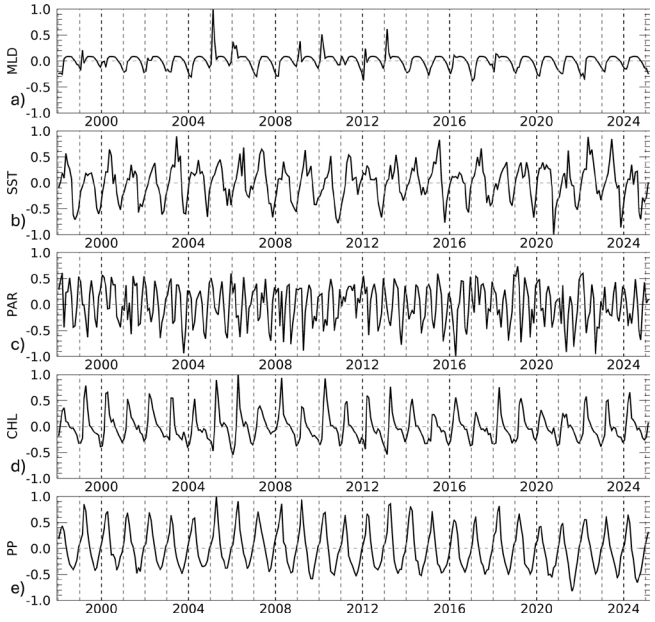


Figure 6. Second mode of EOF MLD **(a)**, SST **(b)**, PAR **(c)**, CHL **(d)**, and PP **(e)** temporal evolutions.

across the open basin, possibly linked to the increased light availability. The temporal amplitude (Fig. 6e) follows CHL maxima in correspondence of the spring months but exhibits a faster and deeper decay during summer, with more intense negative minima than those observed in the CHL temporal signal. This asymmetry indicates that PP is more sensitive than CHL to the combined effect of nutrient depletion and reduced mixing in the post-bloom period.

Consistently with previous findings (Volpe et al., 2012), minima in the second mode of SST (Fig. 6b), that are likely associated with the pre-conditioning phase to deep-water formation in the Gulf of Lion, have the potential to drive the late-winter bloom in PP (Fig. 6e, $r = -0.8$ with four months lag) in turn sustaining phytoplankton CHL accumulation (Fig. 6d, $r = 0.74$) with one month lag with respect to PP peaks.

PSC second modes (Figs. B3d, e, f and B4d, e, f) perfectly align with the CHL second mode (Figs. 5d and 6d), exhibiting the dynamics of the spring bloom in response to the deep convection. This is consistent with the considerations expressed for both the average fields and the annual cycle variability. As in the first mode, the spatial intensity expressed

by the second mode increases with the size classes, although less evidently. This indicates that during deep mixing nutrient abundance sustains the entire phytoplankton community. This is consistent with classical and trait-based phytoplankton size theory, according to which larger cells, particularly diatoms, are generally favoured under nutrient-rich and turbulent conditions, whereas smaller cells are more competitive under stratified and oligotrophic conditions (Margalef, 1978; Litchman and Klausmeier, 2008; Finkel et al., 2010). This is reflected here in the increasing extension of the blooming area with phytoplankton size.

3.2.3 Multivariate EOF (MEOF) analysis

The first MEOF mode (Fig. 7) represents 68 % of the total multivariate variance and identifies the dominant shared variability across the physical and biological variables. The temporal component (Fig. 7f) is a nearly perfect sinusoid with an annual period (summer maxima in July), stable amplitude, and no appreciable long-term trend across the entire 1998–2025 record, confirming that the dominant mode of co-variability across all five variables is the annual cycle driven by solar radiation and surface heating. Variance of this mode is however notably lower than the variance explained by the first modes of the univariate EOFs of PAR and SST (98 % and 97 %, respectively), which almost entirely capture the annual cycle of their respective fields. In the multivariate framework, a single temporal amplitude must simultaneously represent all five variables, and since MLD and CHL exhibit annual cycles that differ in phase and shape from those of PAR and SST, a fraction of the total variance is necessarily redistributed to higher MEOF modes.

MLD and CHL spatial variabilities are uniformly negative across the basin, confirming that these two variables are in anti-phase with the seasonal solar-thermal forcing embedded in the temporal amplitude: MLD deepens and CHL peaks in winter, when the amplitude is negative. MLD shows the highest variability in the deep-water formation areas (Gulf of Lion and south Adriatic Sea) while CHL variability is larger in the western than in the Levantine basin. Notably, as in the univariate first EOF modes, the signature of the Algerian Current splitting into two branches is clearly recognizable here in both the MLD and CHL spatial patterns.

SST, PAR and PP variabilities are everywhere positive and in phase with temporal amplitude. Their spatial patterns are consistent with the dominant seasonal structures described by the univariate analyses, indicating that PP is organized around a physically coherent seasonal cascade: solar radiation heats the surface, stratifies the water column, suppresses deep mixing and nutrient supply, reduces phytoplankton biomass, yet sustains high photosynthetic rates per unit biomass, producing the summer PP maximum under oligotrophic conditions.

The second MEOF mode (Fig. 8) accounts for 22 % of the total multivariate variance and identifies the main secondary mode of shared variability across the physical–biological system. This mode is associated with the coupled spring-bloom response. Although several features are consistent with those found in the univariate second EOFs, the MEOF mode reflects shared covariance among variables rather than a direct correspondence with individual univariate EOF modes.

The temporal amplitude (Fig. 8f) displays a regular seasonal cycle with positive values in spring and negative values in late summer through winter, with clear interannual variability in peak shape and magnitude. This temporal structure is consistent with the springtime variability described by CHL and PP, indicating that this MEOF mode is mainly associated with the spring bloom signal and its interannual modulation.

The MLD (Fig. 8a) shows positive variability concentrated in the Gulf of Lion and Ligurian Sea but extends more broadly into the Aegean Sea and parts of the eastern Mediterranean. This spatial footprint suggests that, within the multivariate mode, MLD contributes through a broader mixing/preconditioning signal across multiple convection-prone areas of the basin, rather than through a signal confined to the Gulf of Lion.

The SST (Fig. 8b) is negative across the whole basin, with the largest anomalies in the western Mediterranean and northwestern coastal areas. This pattern is physically consistent with post-convection cooling and with the seasonal thermal preconditioning that precedes the spring bloom.

The PAR (Fig. 8c) is positive across the entire basin, with highest values in the western and central Mediterranean. The positive PAR values, in phase with the positive MLD and the negative SST, suggest that the second MEOF mode represents the transition from winter deep mixing to spring restratification, during which increasing irradiance acts as the trigger for phytoplankton growth.

CHL variability (Fig. 8d) shows pronounced positive anomalies in the Gulf of Lion and surrounding northwestern Mediterranean regions, indicating that spring bloom dynamics strongly contribute to this multivariate mode.

The PP variability in the second MEOF mode (Fig. 8e) shows high variability mainly in the Gulf of Lion, emphasizing the productive bloom response of the northwestern Mediterranean and its tight link with CHL, in contrast with the more stable oligotrophic conditions of the eastern basin.

4 Summary and Conclusions

This study presented a comprehensive analysis of the physical–biological coupling in the Mediterranean Sea over the period 1998–2025, characterising the space-time variability of phytoplankton biomass, size structure, and primary production and their relationships with sea surface tempera-

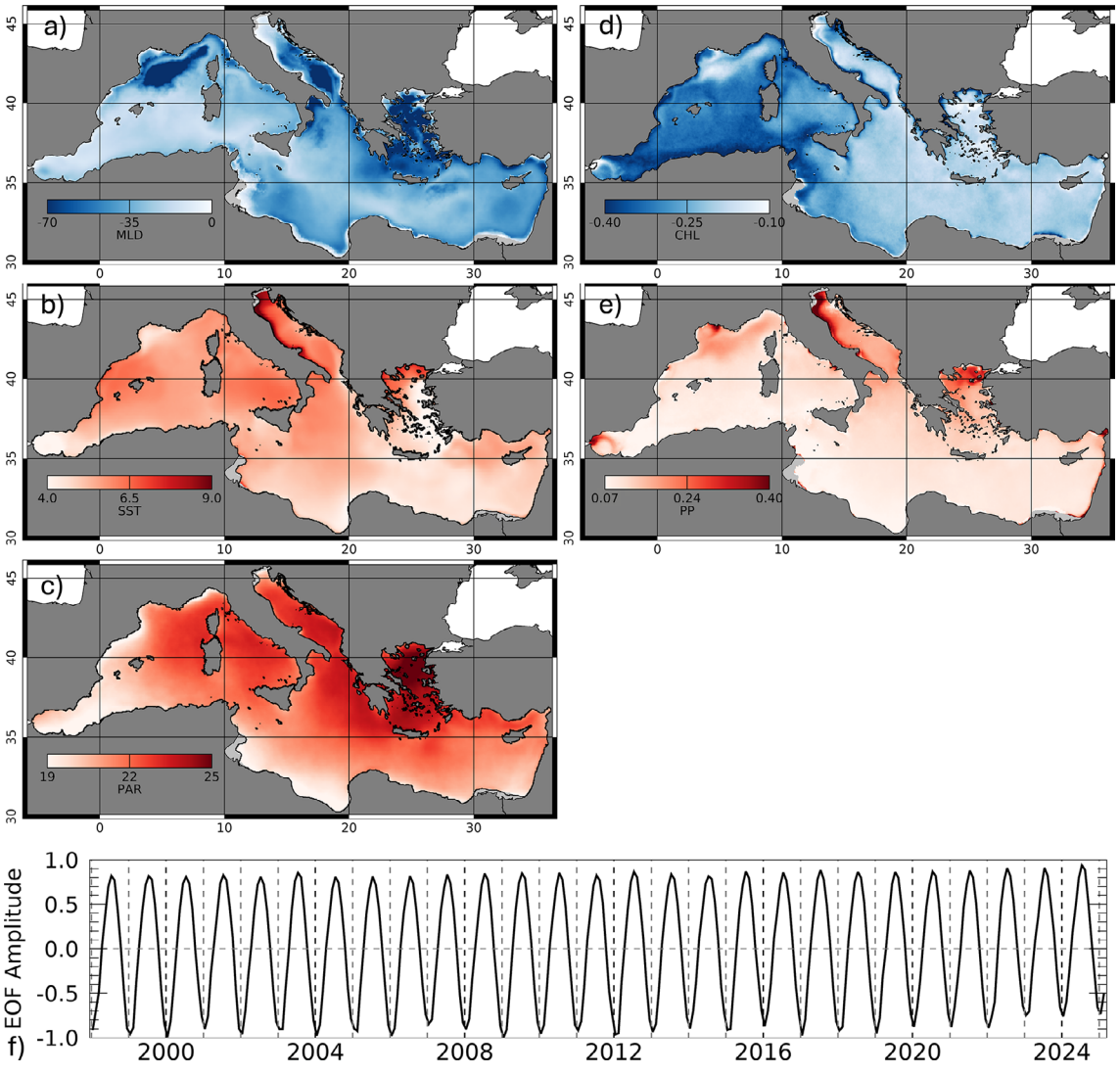


Figure 7. First mode of MEOF of MLD **(a)**, SST **(b)**, PAR **(c)**, CHL **(d)** and PP **(e)** spatial patterns and temporal evolution **(f)**. Light grey indicates the areas permanently masked out because of persistent or recurrent Case II water conditions.

ture, photosynthetically available radiation, and mixed layer depth. Building on the methodological framework of Volpe et al. (2012), the analysis was extended in several main directions: the extension of the time series until 2025, the inclusion of PP and PSC alongside CHL, the replacement of sea level anomaly with mixed layer depth as a proxy for upper-ocean dynamics, and the addition of a multivariate EOF approach to simultaneously decompose the coupled biological-physical system. The combined univariate and multivariate framework enabled a robust characterisation of the dominant modes of seasonal and interannual variability and of the mechanistic links between physical forcing and ecosystem response.

The mean fields computed over the full 27-year record confirm the well-established physical–biological structure of the Mediterranean basin. A pronounced west-east gradient characterises CHL and PP, with higher values in the western basin driven by enhanced vertical mixing and nutrient supply, and progressively oligotrophic conditions toward the Levantine basin. MLD confirmed the Gulf of Lion as the dominant deep-water formation site of the basin, whose mixing signal leaves a clear imprint on phytoplankton abundance and productivity. Phytoplankton size structure is consistent with regional trophic conditions: microphytoplankton dominance is confined to river-influenced coastal areas and the deep-mixing zone of the northwestern Mediterranean, nanophytoplankton is widespread in the western basin and semi-enclosed seas, while picophytoplankton dominates the oligotrophic open waters of the eastern Mediterranean more than 75 % of the time. A direct comparison with Volpe et al. (2012), whose climatology spanned only nine years, reveals a detectable basin-scale warming of up to 5 % in SST (with

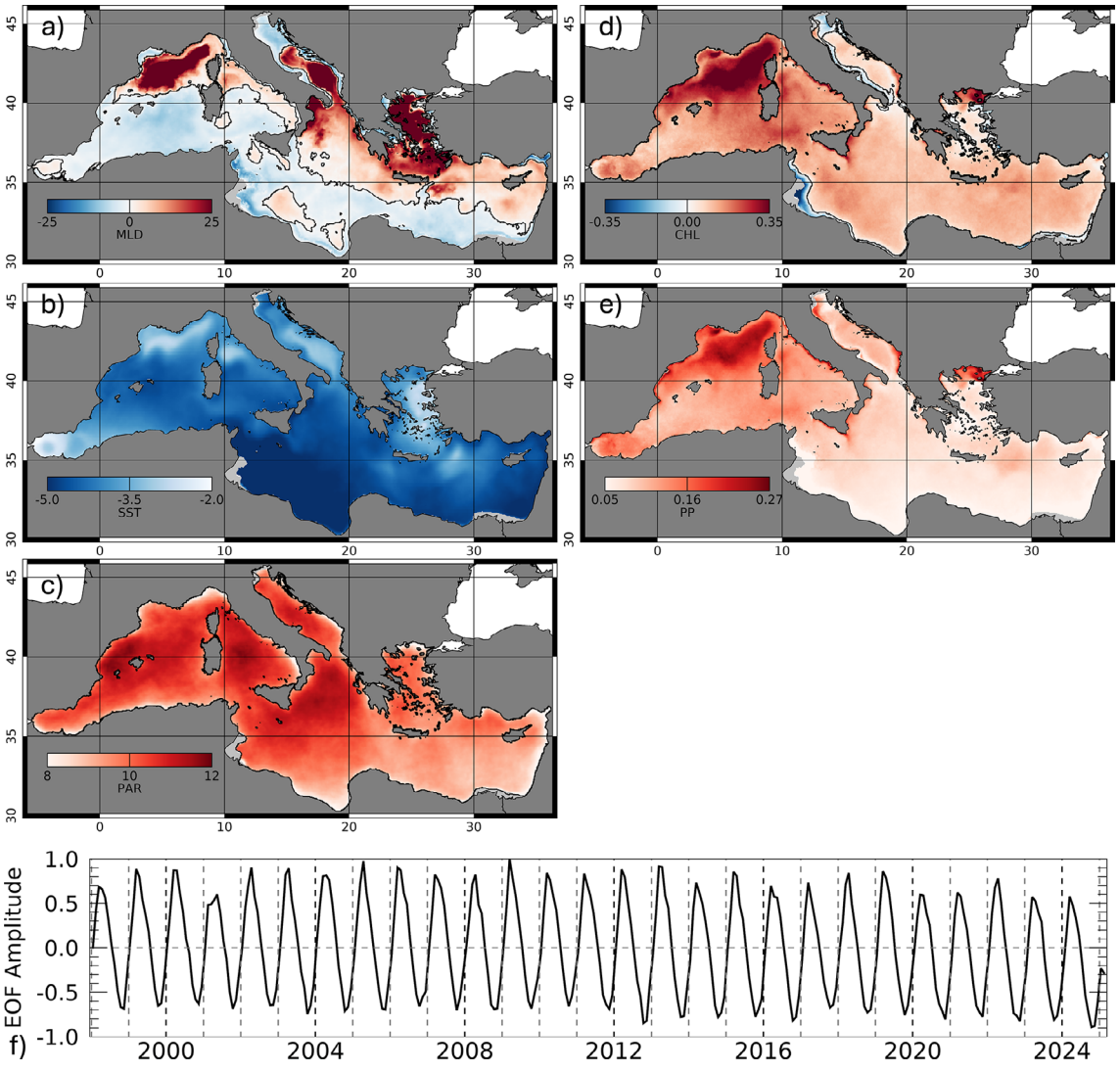


Figure 8. Second mode of MEOF of MLD **(a)**, SST **(b)**, PAR **(c)**, CHL **(d)** and PP **(e)** spatial patterns and temporal evolution **(f)**. Light grey indicates the areas permanently masked out because of persistent or recurrent Case II water conditions.

possible links to the higher frequency of the marine heatwaves) accompanied by a corresponding decrease in CHL of up to 20 %, consistent with a long-term oligotrophication driven by intensified thermal stratification.

The EOF and MEOF analyses consistently identified two dominant modes of variability in the Mediterranean physical-biological system. The first mode represents the basin-scale annual cycle and explains most of the total variance. It reflects the seasonal interplay between solar radiation, surface heating, stratification, mixed-layer dynamics, and biological response, highlighting the contrasting seasonal behaviour of phytoplankton biomass and primary production. In particular, primary production follows light availability more closely than chlorophyll concentration, consistent with the role of photo-acclimation in shaping the seasonal chlorophyll cycle in oligotrophic environments.

The second mode captures the sub-basin spring-bloom dynamics of the northwestern Mediterranean and its interannual modulation. This mode links winter deep convection, nutrient replenishment, spring restratification, and the subsequent enhancement of phytoplankton biomass and primary production. While chlorophyll and primary production exhibit different relationships at the annual scale, they become more closely coupled during bloom conditions, when biological variability is more directly associated with biomass accumulation.

The multivariate EOF analysis further demonstrates that these annual-cycle and spring-bloom regimes are coherent coupled modes emerging from the covariance between physical forcing and biological response, thereby providing an integrated description of Mediterranean ecosystem variability.

Despite the robustness of the framework adopted, several limitations should be acknowledged. The present analysis is deliberately centred on the abiotic forcing of phytoplankton variability, and biotic processes, such as top-down grazing control by zooplankton, inter-specific competition among phytoplankton functional types, and nutrient recycling mediated by the microbial loop, are not explicitly represented. This is an inherent constraint of the adopted method. As a consequence, a fraction of the residual variability, particularly at sub-seasonal timescales and at the local scale, may reflect biological processes that remain hidden in higher modes and outside the explanatory reach of the variables considered.

Taken together, the results establish a robust observational baseline for the interpretation of Mediterranean phytoplankton dynamics at seasonal to interannual scales. The analysis reveals a clear separation in the dominant controls of variability: the first mode, accounting for the bulk of the seasonal signal, is primarily driven by the light-temperature cascade (solar irradiance heating the surface, suppressing vertical mixing, and modulating photosynthetic rates) whereas the second mode, linked to the spring bloom dynamics of the northwestern Mediterranean, is driven by nutrient supply through episodic deep convection, with biomass accumulation as the downstream biological response. The consistency between the univariate and multivariate frameworks, and the agreement with previous satellite-based studies, reinforce the reliability of the CMEMS multi-decadal products for ecosystem monitoring. At the same time, the emerging signals of warming-driven oligotrophication in the long-term mean fields underscore the need for continued observation and dedicated trend analyses. Future work should extend the present variability-focused approach to explicitly quantify long-term trends in CHL, PP, and PSC and their attributable physical drivers, while also exploring the role of interannually varying atmospheric modes such as the NAO and East Atlantic Pattern in modulating the spring bloom intensity. Beyond these scientific directions, the results also point to potential improvements to the operational CMEMS processing chain. In particular, it would be valuable to incorporate phytoplankton size class information directly into the PP model parameterisation, given that larger and smaller cells differ substantially in their chlorophyll-specific absorption properties and photosynthetic quantum yields, a refinement that could improve the accuracy of satellite-derived PP estimates across the trophic gradients of the Mediterranean basin.

Appendix A

The primary production (PP) model adopted in this study is based on the formulation originally developed by Antoine and Morel (1996), which links satellite-derived chlorophyll concentration to phytoplankton primary production through the coupling of an atmospheric radiative transfer model (Tanré et al., 1979) with a bio-optical representation of phytoplankton absorption and scattering processes (Morel, 1991).

Primary production is computed on a daily basis as a column-integrated quantity through the explicit resolution of spectral, temporal, and vertical variability of photosynthesis. Daily PP is expressed as:

$$\mathrm{PP} = 12 \int_{z=0}^{\mathrm{Depth}} \int_{t=0}^{24} \int_{\lambda=400}^{700} \mathrm{Chl}(z)\, a^{*}_{\mathrm{Chl}} \mathrm{PAR}(z,t,\lambda)\, \varphi_{\mu} \times (\mathrm{Chl}, T)(z)\, \mathrm{d}\lambda \mathrm{d}z \mathrm{d}t \quad \text{(A1)}$$

where the factor 12 represents the Carbon molar mass, allowing PP to be expressed as mass of Carbon per square meter per day; Chl(z) is the vertical chlorophyll concentration profile; a^{*}_{Chl} is the chlorophyll-specific absorption coefficient, parameterized as a function of chlorophyll concentration; PAR(z, t, λ) is the photosynthetically available radiation at depth z, time t, and wavelength λ; and ϕ_{μ}(Chl, T) is the photosynthetic quantum yield, formulated as a function of chlorophyll concentration and temperature and expressing the efficiency of conversion of absorbed light into fixed carbon.

While initially conceived for global-scale applications, this framework has been specifically adapted to the Mediterranean Sea to account for the basin's distinctive bio-optical characteristics.

The computation of primary production relies on an accurate description of the spectral, spatial, and temporal variability of solar radiation reaching the ocean surface. In the Mediterranean configuration adopted here, atmospheric forcing is provided by the revised Ocean Atmosphere Spectral Irradiance Model (OASIM; Gregg and Casey, 2009), which represents the atmospheric radiative transfer component of the bio-optical framework.

OASIM is a physically based radiative transfer model that simulates the propagation of solar radiation through the atmosphere by accounting for absorption and scattering by atmospheric gases, aerosols, and clouds. The model resolves both direct and diffuse downwelling irradiance and provides spectrally resolved fluxes over the PAR range. In the CMEMS Mediterranean processing chain, OASIM delivers daily fields of downwelling spectral irradiance at 5 nm resolution between 400 and 700 nm, on a 4 km spatial grid, ensuring full consistency with satellite ocean-colour products and allowing an explicit coupling with wavelength-dependent bio-optical properties.

The Mediterranean implementation of OASIM has been specifically validated against independent in situ radiometric observations from the BOUSSOLE mooring and Biogeochemical Argo floats, demonstrating good skill in reproducing surface and subsurface irradiance across the PAR spectrum and supporting its suitability for regional applications (Lazzari et al., 2021). The model is forced with ancillary atmospheric data including cloud properties (cloud cover, liquid water path and optical thickness), surface meteorological variables (sea-level pressure, wind speed and humidity), atmospheric absorbing gases (notably ozone and water vapour), and aerosol optical properties. These inputs are derived from a combination of operational atmospheric reanalyses (e.g. ECMWF products) and satellite-based climatologies, ensuring temporally resolved (daily) forcing consistent with the ocean-colour and bio-optical datasets used in the primary production model.

The marine bio-optical component of the primary production model describes how solar radiation, once transmitted through the atmosphere, is attenuated and spectrally transformed within the water column and made available to phytoplankton photosynthesis. It follows the spectral light–photosynthesis framework originally developed by Antoine and Morel (1996), which provides a mechanistic coupling between underwater light fields, phytoplankton biomass distribution, and photosynthetic response.

In this framework, PAR is explicitly resolved as a function of wavelength, depth, and time. Light propagation within the water column is governed by absorption and scattering by water itself and by optically active constituents, primarily phytoplankton pigments and associated particles. As a result, the vertical chlorophyll concentration profile plays a dual role: it quantifies phytoplankton biomass and simultaneously controls the attenuation and spectral composition of light with depth.

The interaction between the underwater spectral irradiance field and phytoplankton biomass is mediated by the chlorophyll-specific absorption coefficient, a^*_{Chl}, which determines the chlorophyll efficiency in absorbing photons at each wavelength. The absorbed radiant energy is then converted into fixed carbon through photosynthesis, with an efficiency described by the photosynthetic quantum yield, ϕ_μ. Together, a^*_{Chl} and ϕ_μ link light availability to local photosynthetic rates, ensuring consistency between optical conditions and phytoplankton physiological response.

Following the original formulation, the realized quantum yield is expressed as a fraction of its maximum value, $\phi_{\mu,\max}$, through a dimensionless light-response function:

$$\phi_\mu = \phi_{\mu,\max}\, f(x), \tag{A2}$$

where $x = \mathrm{PUR}/K_{\mathrm{PUR}}$, PUR is the photosynthetically usable radiation, and K_{PUR} is a scaling irradiance controlling the transition between light-limited and light-saturated photosynthesis. The function $f(x)$ follows the formulation of Platt et al. (1980), accounting for saturation and photoinhibition effects. Temperature influences photosynthesis indirectly through its effect on K_{PUR}, which is parameterized using an Eppley-type formulation:

$$K_{\mathrm{PUR}}(T) = K_{\mathrm{PUR}}(20\,^\circ\mathrm{C})\, 1.065^{(T-20)}. \tag{A3}$$

Through this mechanism, temperature modulates the photosynthesis–irradiance response without altering either the functional form of $f(x)$ or the definition of $\phi_{\mu,\max}$.

In the original model, the $\phi_{\mu,\max}$ and the maximum chlorophyll-specific absorption coefficient $a_{\max}$ were assumed constant under the hypothesis that opposite variations of the two quantities compensate each other. Consistently with this assumption, the spectral shape and magnitude of the chlorophyll-specific absorption coefficient were also treated as invariant. In the present study, following Bricaud et al. (1998), chlorophyll-specific absorption spectra are instead allowed to vary in both magnitude and spectral shape as a function of chlorophyll concentration, thereby breaking the assumption of a constant $\phi_{\mu,\max}\, a_{\max}$ product and requiring an explicit representation of their variability. Following Morel et al. (1996), the maximum quantum yield is therefore expressed as a function of chlorophyll concentration:

$$\phi_{\mu,\max} = 0.05 \frac{\mathrm{Chl}^{0.66}}{0.44 + \mathrm{Chl}^{0.66}}. \tag{A4}$$

This formulation accounts for observed photo-physiological adaptations across trophic regimes while preserving the original representation of light and temperature effects on photosynthesis. By explicitly introducing chlorophyll dependencies in both $a_{\max}$ and $\phi_{\mu,\max}$, the present model makes explicit the physiological variability that was implicitly embedded in their constant product in the original formulation.

Since remote sensing observations provide chlorophyll information only for the surface layer, vertical chlorophyll distributions must be reconstructed in order to compute depth-integrated primary production. This reconstruction follows the empirical approach of Morel and Berthon (1989), which relates satellite-derived surface pigment concentration to both the total chlorophyll content within the euphotic zone and the shape of the vertical chlorophyll profile.

For the Mediterranean Sea, the empirical reconstruction of vertical chlorophyll structure has been revisited using the MedBiOp in situ dataset (Volpe et al., 2019). Each measured vertical chlorophyll profile is first normalized by dividing chlorophyll concentration at each depth by the mean chlorophyll concentration within the euphotic zone, while depth is normalized by the euphotic depth. This normalization places all profiles on a common, dimensionless vertical coordinate, allowing structures with different magnitudes and depth ranges to be directly compared.

The normalized profiles are then classified using a k-means clustering technique, resulting in seven groups representative of distinct Mediterranean trophic regimes. For

CHAPTER 2.6

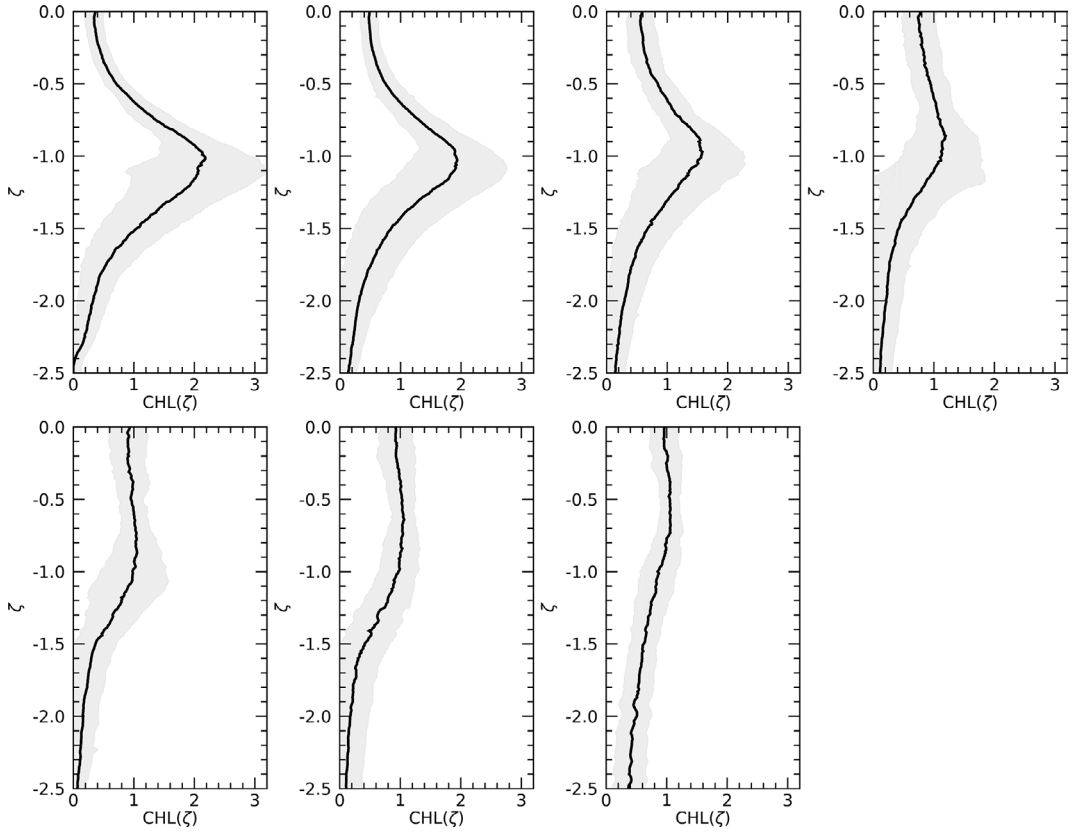


Figure A1. Normalized mean chlorophyll profiles for each cluster and their standard deviation (grey shadow).

each cluster, a mean normalized vertical chlorophyll profile is computed (Fig. A1) and subsequently parameterized using the analytical function:

$$\mathrm{CHL}(\zeta) = A - B\zeta + C \cdot \exp\left[-\frac{(\zeta - D)^2}{2E^2}\right], \tag{A5}$$

where CHL(ζ) is chlorophyll normalized by the euphotic zone mean and ζ is normalized depth (depth divided by euphotic depth). This formulation captures both monotonic decay and the possible occurrence of a subsurface chlorophyll maximum.

To enable application to satellite data, the parameters A, B, C, D, and E are expressed as fourth-degree polynomial functions of the logarithm of surface chlorophyll concentration. The polynomial relationships are derived during the calibration phase using the mean surface chlorophyll concentration associated with each trophic class identified through clustering:

$$\begin{aligned}\mathrm{Param} = &a + b\log\mathrm{Chl} + c\log\mathrm{Chl}^2 + d\log\mathrm{Chl}^3 \\ &+ e\log\mathrm{Chl}^4\end{aligned} \tag{A6}$$

where Param represents each of the five parameters A–E and a–e are polynomial regression coefficients (Table A1).

Once the polynomial coefficients are determined, the relationships are applied operationally using satellite-derived surface chlorophyll concentration to estimate the corresponding set of parameters A–E for each pixel. Through this two-step parameterization, functional representation of mean normalized profiles and polynomial linkage to surface chlorophyll, a continuous vertical chlorophyll profile can be reconstructed on a pixel-by-pixel basis. The method therefore provides pixel-specific estimates of vertical chlorophyll structure consistent with observed Mediterranean trophic regimes.

Figure A2 compares the Mediterranean reconstructed vertical chlorophyll profiles with the global parameterizations of Morel and Berthon (1989) and Uitz et al. (2006), highlighting systematic regional differences in profile shape and ver-

Table A1. Coefficients (a–e) as derived by the polynomial regression (Eq. A6) to estimate the five parameters (A–E) to be used in Eq. (A5) to obtain the chlorophyll vertical profile from satellite observation.

	A	B	C	D	E
a	0.8755	0.3540	0.4556	0.8229	0.3827
b	−0.0544	−0.1707	0.0235	−0.1910	0.1297
c	−0.1769	−0.5926	−0.1879	−0.3334	−0.0333
d	0.4562	−0.1325	−1.812	−0.5699	−0.1379
e	0.2654	0.0744	0.8461	−0.2413	−0.0474

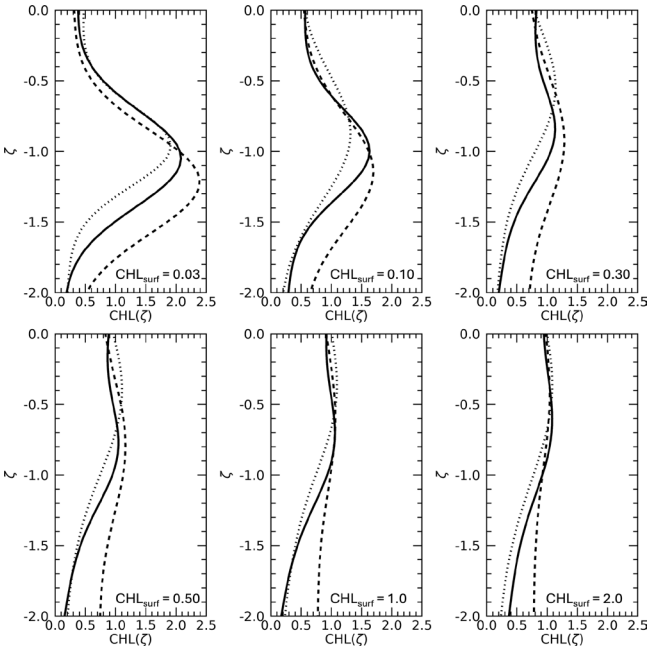


Figure A2. Reconstructed vertical chlorophyll profiles from the Mediterranean model (solid lines), Morel and Berthon (1989) (dashed lines) and Uitz et al. (2006) (dotted lines). The surface chlorophyll concentration (CHLsurf) is indicated in the bottom-right corner of each panel.

tical structure. The Mediterranean profiles exhibit subsurface chlorophyll maxima that are generally shallower and less pronounced than those predicted by the Morel and Berthon formulation, while remaining deeper and more intense than those derived from the Uitz et al. (2006). The normalized depth of the maximum tends to occupy an intermediate position between the two global parameterizations.

In oligotrophic conditions (low surface chlorophyll), the near-surface structure of the Mediterranean profiles is broadly consistent with global reconstructions. However, as surface chlorophyll increases toward mesotrophic and eutrophic regimes, Mediterranean profiles display comparatively lower chlorophyll concentrations in the upper layer and a reduced vertical contrast between surface waters and the deep chlorophyll maximum, suggesting a more vertically distributed biomass structure.

Since primary production estimates rely on different input datasets, the model's response may vary depending on the specific parameter considered. To investigate how individual inputs affect primary production (PP) variability, we performed a sensitivity analysis following the approach of Tilstone et al. (2015). Mean values and natural variability ranges were first defined for all model input parameters based on the observational and climatological datasets used in the primary production computation. PP was then estimated by varying each parameter independently across its range while maintaining all other variables fixed at their mean values.

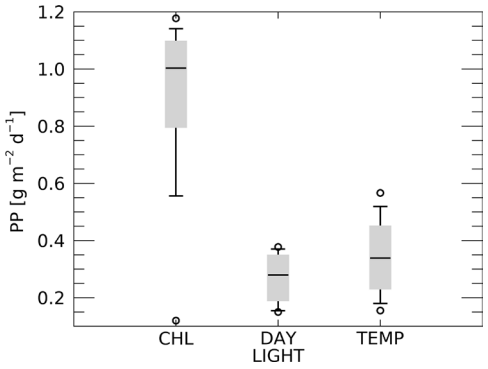


Figure A3. Sensitivity analysis of PP. The grey rectangles represent the interquartile range (25th–75th percentiles) of PP estimates obtained by varying each parameter individually. The horizontal line within each box marks the median (50th percentile). Whiskers denote the 10th and 90th percentiles, while circles indicate the minimum and maximum PP values. The abscissa indicates the input parameters analysed.

This one-at-a-time (OAT) approach allows the relative contribution of each driver to PP variability to be isolated and quantified.

The resulting spread in modelled PP provides a measure of the sensitivity of primary production to each parameter. As shown in Fig. A3, the largest variability in PP is associated with chlorophyll concentration, followed by temperature and, to a lesser extent, daylight duration (photoperiod).

The strong sensitivity to chlorophyll reflects the central role of phytoplankton biomass in determining primary production, as chlorophyll directly controls both light absorption and the magnitude of photosynthetic carbon fixation. Temperature exerts a secondary influence by modulating the photosynthesis–irradiance response through its effect on physiological rates, while variations in daylight primarily affect the temporal integration of photosynthesis rather than its instantaneous efficiency.

Overall, this ranking highlights phytoplankton biomass as the dominant predictor of primary production variability in the model, with physical drivers such as temperature and light acting mainly as modulators that regulate the efficiency and seasonal expression of photosynthetic activity.

Appendix B

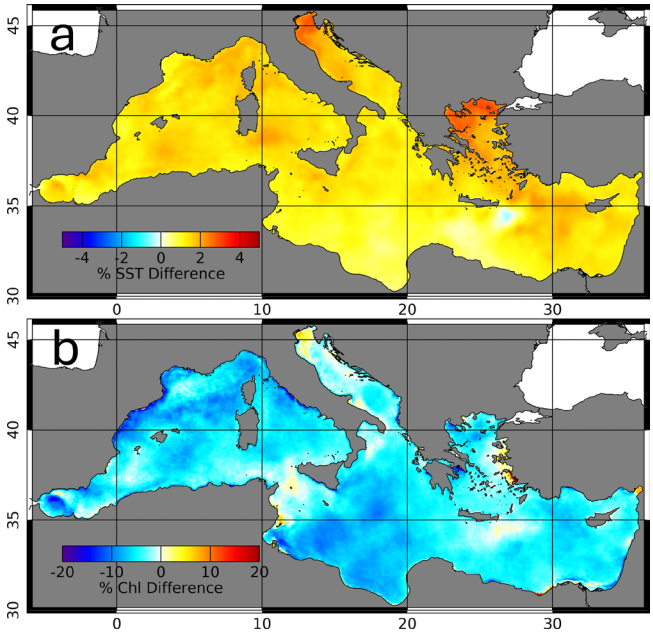


Figure B1. Relative percent difference $\mathrm{RPD} = 100\frac{X-Y}{Y}$, with Y being the mean time average (1998–2006) of SST and CHL for the same period as Volpe et al. (2012). X is the mean time average of SST **(a)** or CHL **(b)** computed over the full time range (1998–2025).

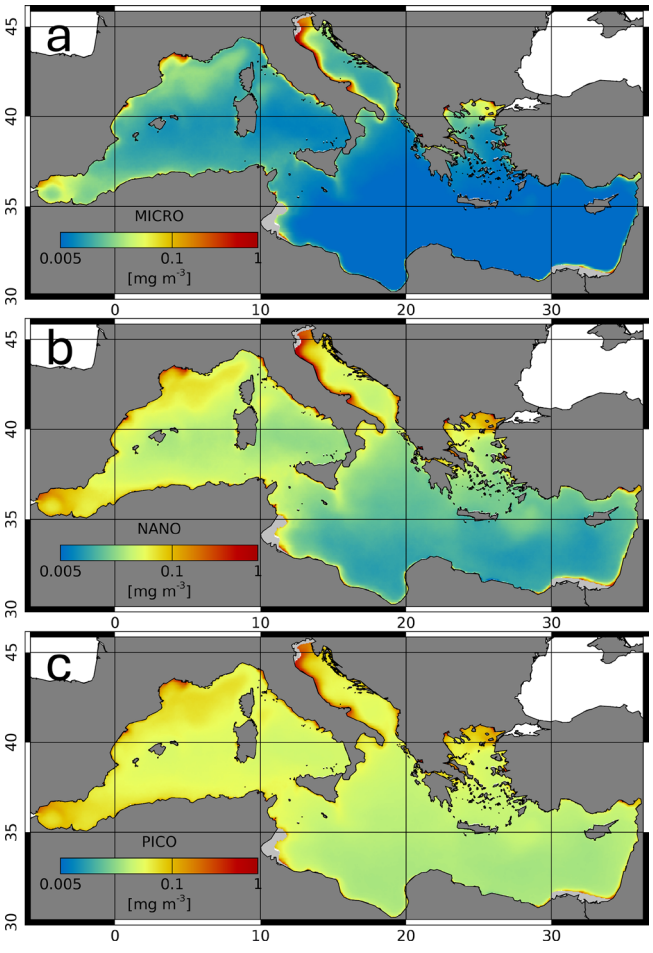


Figure B2. Mean time averages (1998–2025) of Microphytoplankton chlorophyll **(a)**, Nanophytoplankton chlorophyll **(b)** and Picophytoplankton chlorophyll **(c)**. Light grey indicates the areas permanently masked out because of persistent or recurrent Case II water conditions.

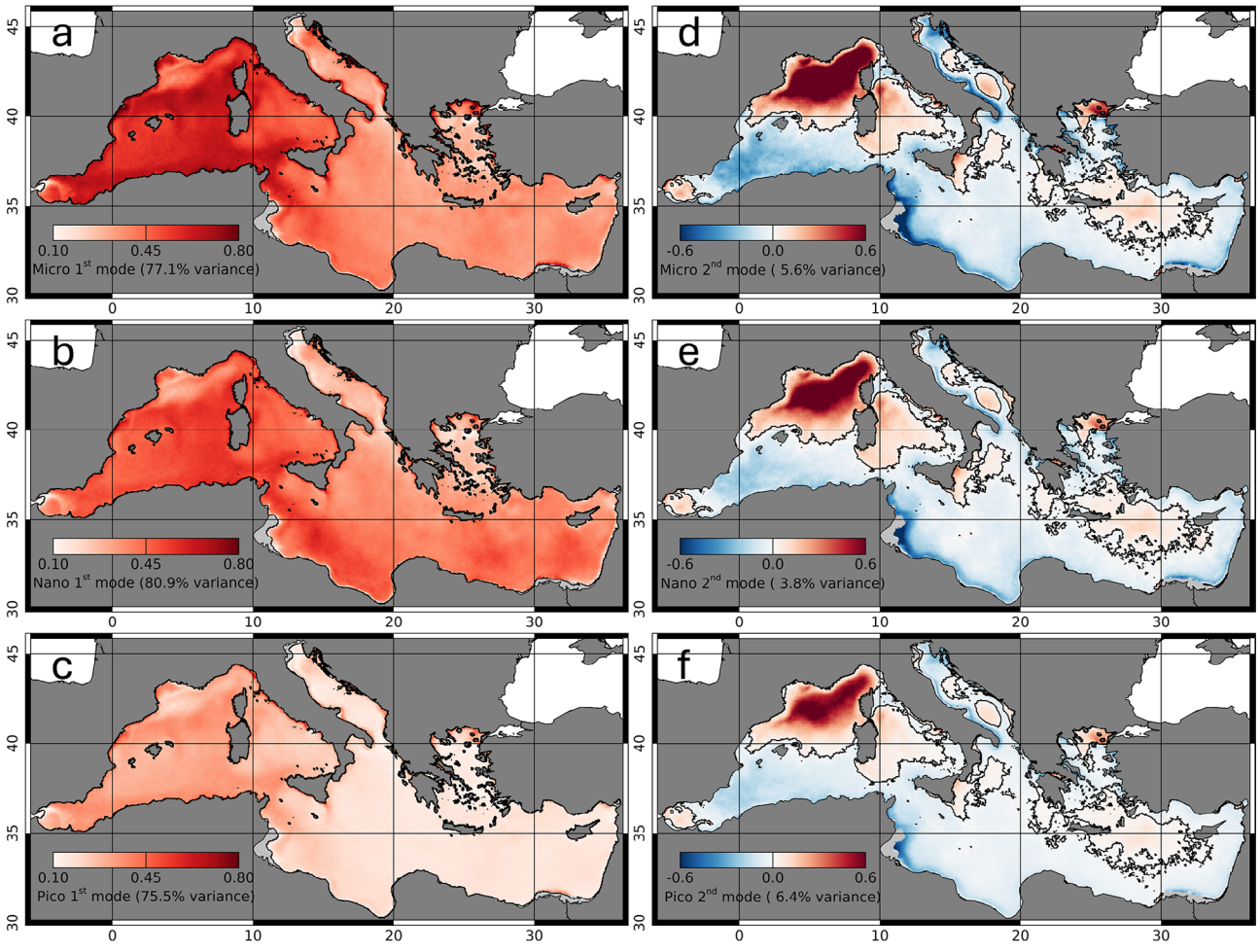


Figure B3. First two EOF spatial patterns computed over Micro- **(a–d)**, Nano- **(b–e)** and Pico-phytoplankton **(c–f)**. Light grey indicates the areas permanently masked out because of persistent or recurrent Case II water conditions.

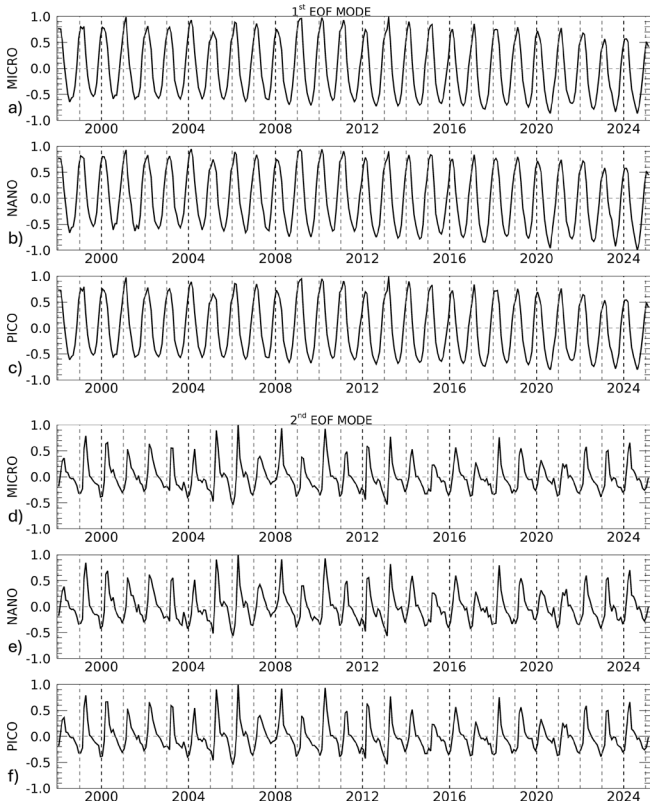


Figure B4. First two EOF temporal evolutions computed over Micro- **(a–d)**, Nano- **(b–e)** and Pico-phytoplankton **(c–f)**.

Data availability. All the datasets used for this work that are not available on the Copernicus Marine Service (Table 1) can be provided by the corresponding authors upon request.

Author contributions. SC: Writing – original draft, Writing – review & editing, Visualization, Validation, Software, Methodology, Investigation, Formal analysis, Conceptualization.

GV: Writing – original draft, Writing – review & editing, Visualization, Validation, Software, Methodology, Investigation, Formal analysis, Conceptualization.

ADC: Writing – review & editing, Investigation, Validation.

VEB: Writing – review & editing, Investigation, Validation, Supervision.

Competing interests. The contact author has declared that none of the authors has any competing interests.

Disclaimer. The Copernicus Marine Service offering is regularly updated to ensure it remains at the forefront of user requirements. In this process, some products may undergo replacement or renaming, leading to the removal of certain product IDs from the catalogue. If readers have any questions or require assistance regarding these modifications, please feel free to reach out to the Copernicus Marine Service user support team for further guidance. They will be able to provide the necessary information to address concerns and find suitable alternatives.

Publisher's note: Copernicus Publications remains neutral with regard to jurisdictional claims made in the text, published maps, institutional affiliations, or any other geographical representation in this paper. The authors bear the ultimate responsibility for providing appropriate place names. Views expressed in the text are those of the authors and do not necessarily reflect the views of the publisher.

Acknowledgements. We thank the European Copernicus Marine Service for satellite data and model output. We are enormously grateful to Flavio La Padula, Filippo Manfredonia, Luis Gonzales Villas, Lorenzo Amodio, Vega Forneris, Emanuele Bohm and Chiara Lapucci for running and maintaining operational services and processing chains within the Ocean Colour Thematic Assembly Center. A special and warm thank goes to Rosalia Santoleri for her pioneering contribution to the European satellite operational oceanography. We also thank the reviewers whose detailed and constructive comments stimulated valuable scientific reflection and significantly improved the quality and clarity of the manuscript.

Review statement. This paper was edited by Marilaure Grégoire and reviewed by two anonymous referees.

References

Antoine, D. and Morel, A.: Oceanic primary production: 1. Adaptation of a spectral light-photosynthesis model in view of application to satellite chlorophyll observations, Global Biogeochem. Cy., 10, 43–55, 1996.

Arteaga, L. A., Boss, E., Behrenfeld, M. J., Westberry, T. K., and Sarmiento, J. L.: Seasonal modulation of phytoplankton biomass in the Southern Ocean, Nat. Commun., 11, 5364, https://doi.org/10.1038/s41467-020-19157-2, 2020.

Basterretxea, G., Font-Muñoz, J. S., Salgado-Hernanz, P. M., Arrieta, J., and Hernández Carrasco, I.: Patterns of chlorophyll interannual variability in Mediterranean biogeographical regions, Remote Sens. Environ., 215, 7–17, https://doi.org/10.1016/j.rse.2018.05.027, 2018.

Behrenfeld, M. J. and Boss, E. S.: Resurrecting the ecological underpinnings of ocean plankton blooms, Annu. Rev. Mar. Sci., 6, 167–194, https://doi.org/10.1146/annurev-marine-052913-021325, 2014.

Behrenfeld, M. J. and Falkowski, P. G.: Photosynthetic rates derived from satellite-based chlorophyll concentration, Limnol. Oceanogr., 42, 1–20, https://doi.org/10.4319/lo.1997.42.1.0001, 1997.

Behrenfeld, M. J., Boss, E., Siegel, D. A., and Shea, D. M.: Carbon-based ocean productivity and phytoplankton physiology from space, Global Biogeochem. Cy., 19, https://doi.org/10.1029/2004GB002299, 2005.

Behrenfeld, M. J., O'Malley, R. T., Siegel, D. A., McClain, C. R., Sarmiento, J. L., Feldman, G. C., Milligan, A. J., Falkowski, P. G., Letelier, R. M., and Boss, E. S.: Climate-driven trends

in contemporary ocean productivity, Nature, 444, 752–755, https://doi.org/10.1038/nature05317, 2006.

Bellacicco, M., Volpe, G., Colella, S., Pitarch, J., and Santoleri, R.: Influence of photoacclimation on the phytoplankton seasonal cycle in the Mediterranean Sea as seen by satellite, Remote Sens. Environ., 184, 595–604, https://doi.org/10.1016/j.rse.2016.08.004, 2016.

Bethoux, J. P., Gentili, B., Morin, P., Nicolas, E., Pierre, C., and Ruiz-Pino, D.: The Mediterranean Sea: a miniature ocean for climatic and environmental studies and a key for the climatic functioning of the North Atlantic, Prog. Oceanogr., 44, 131–146, https://doi.org/10.1016/S0079-6611(99)00023-3, 1999.

Bonanno, A., Placenti, F., Basilone, G., Mifsud, R., Genovese, S., Patti, B., Di Bitetto, M., Aronica, S., Barra, M., Giacalone, G., Ferreri, R., Fontana, I., Buscaino, G., Tranchida, G., Quinci, E., and Mazzola, S.: Variability of water mass properties in the Strait of Sicily in summer period of 1998–2013, Ocean Sci., 10, 759–770, https://doi.org/10.5194/os-10-759-2014, 2014.

Borja, A., Elliott, M., Andersen, J. H., Cardoso, A. C., Carstensen, J., Ferreira, J. G., Heiskanen, A.-S., Marques, J. C., Neto, J. M., Teixeira, H., Uusitalo, L., Uyarra, M. C., and Zampoukas, N.: Good environmental status of marine ecosystems: what is it and how do we know when we have attained it?, Mar. Pollut. Bull., 76, 16–27, https://doi.org/10.1016/j.marpolbul.2013.08.042, 2013.

Bosc, E., Bricaud, A., and Antoine, D.: Seasonal and interannual variability in algal biomass and primary production in the Mediterranean Sea, as derived from 4 years of SeaWiFS observations, Global Biogeochem. Cy., 18, https://doi.org/10.1029/2003GB002034, 2004.

Boyce, D. G., Lewis, M. R., and Worm, B.: Global phytoplankton decline over the past century, Nature, 466, 591–596, https://doi.org/10.1038/nature09268, 2010.

Brando, V. E., Braga, F., Zaggia, L., Giardino, C., Bresciani, M., Matta, E., Bellafiore, D., Ferrarin, C., Maicu, F., Benetazzo, A., Bonaldo, D., Falcieri, F. M., Coluccelli, A., Russo, A., and Carniel, S.: High-resolution satellite turbidity and sea surface temperature observations of river plume interactions during a significant flood event, Ocean Sci., 11, 909–920, https://doi.org/10.5194/os-11-909-2015, 2015.

Brando, V. E., Santoleri, R., Colella, S., Volpe, G., Di Cicco, A., Sammartino, M., González Vilas, L., Lapucci, C., Böhm, E., Zoffoli, M. L., Cesarini, C., Forneris, V., La Padula, F., Mangin, A., Jutard, Q., Bretagnon, M., Bryère, P., Demaria, J., Calton, B., Netting, J., Sathyendranath, S., D'Alimonte, D., Kajiyama, T., Van der Zande, D., Vanhellemont, Q., Stelzer, K., Böttcher, M., and Lebreton, C.: Overview of Operational Global and Regional Ocean Colour Essential Ocean Variables Within the Copernicus Marine Service, Remote Sens., 16, 4588, https://doi.org/10.3390/rs16234588, 2024.

Bricaud, A., Morel, A., Babin, M., Allali, K., and Claustre, H.: Variations of light absorption by suspended particles with chlorophyll a concentration in oceanic (case 1) waters: Analysis and implications for bio-optical models, J. Geophys. Res., 103, 31033–31044, https://doi.org/10.1029/98JC02712, 1998.

Chisholm, S. W.: Phytoplankton Size, in: Primary Productivity and Biogeochemical Cycles in the Sea, edited by: Falkowski, P. G., Woodhead, A. D., and Vivirito, K., Environmental Science Research, vol. 43, Springer, Boston, MA, https://doi.org/10.1007/978-1-4899-0762-2_12, 1992.

Ciancia, E., Lacava, T., Pergola, N., Vellucci, V., Antoine, D., Satriano, V., and Tramutoli, V.: Quantifying the Variability of Phytoplankton Blooms in the NW Mediterranean Sea with the Robust Satellite Techniques (RST), Remote Sens., 13, 5151, https://doi.org/10.3390/rs13245151, 2021.

Colella, S., Falcini, F., Rinaldi, E., Sammartino, M., and Santoleri, R.: Mediterranean ocean colour chlorophyll trends, PloS one, 11, e0155756, https://doi.org/10.1371/journal.pone.0155756, 2016.

Colella, S., Brando, V. E., Cicco, A. D., D'Alimonte, D., Forneris, V., and Bracaglia, M.: EU Copernicus Marine Service Product, Quality Information Document for Mediterranean Sea, Bio-Geo-Chemical, L4, monthly means, daily gapfree and climatology Satellite Observations (1997–ongoing), OCEANCOLOUR_MED_BGC_L4_MY_009_144, Issue 4.1, Mercator Ocean International, https://documentation.marine.copernicus.eu/QUID/CMEMS-OC-QUID-009-141to144-151to154.pdf (last access: 10 September 2026), 2025.

Colella, S., Böhm, E., Cesarini, C., Jutard, Q., and Brando, V. E.: EU Copernicus Marine Service Product, Product User Manual for Mediterranean Sea, Bio-Geo-Chemical, L4, monthly means, daily gapfree and climatology Satellite Observations (1997–ongoing), OCEANCOLOUR_MED_BGC_L4_MY_009_144, Issue 5.0, Mercator Ocean International, https://documentation.marine.copernicus.eu/PUM/CMEMS-OC-PUM.pdf (last access: 10 September 2026), 2026.

Cossarini, G., Bretagnon, M., Di Biagio, V., Fanton d'Andon, O., Garnesson, P., Mangin, A., and Solidoro, C.: Primary production, in: Copernicus Marine Service Ocean State Report, Issue 4, J. Oper. Oceanogr., 13, S16, https://doi.org/10.1080/1755876X.2020.1785097, 2020.

de Boyer Montégut, C., Madec G., Fischer A. S., Lazar A., and Iudicone D.: Mixed layer depth over the global ocean: An examination of profile data and a profile-based climatology, J. Geophys. Res.-Oceans, 109, C12003, https://doi.org/10.1029/2004JC002378, 2004.

Di Cicco, A., Sammartino, M., Marullo, S., and Santoleri, R.: Regional Empirical Algorithms for an Improved Identification of Phytoplankton Functional Types and Size Classes in the Mediterranean Sea Using Satellite Data, Front. Mar. Sci., 4, 126, https://doi.org/10.3389/fmars.2017.00126, 2017.

Di Cicco, A., Sammartino, M., Brando, V. E., Artuso, F., Lai, A., Giardina, I., Volpe, G., Palamara, G. M., Lapucci, C., and Colella, S.: Ocean Colour Estimates of Phytoplankton Diversity in the Mediterranean Sea: Update of the Operational Regional Algorithms Within the Copernicus Marine Service, Remote Sens., 17, 3586, https://doi.org/10.3390/rs17213586, 2025.

Doney, S. C., Ruckelshaus, M., Duffy, J. E., Barry, J. P., Chan, F., English, C. A., Galindo, H. M., Grebmeier, J. M., Hollowed, A. B., Knowlton, N., Polovina, J., Rabalais, N. N., Sydeman, W. J., and Talley, L. D.: Climate change impacts on marine ecosystems, Annu. Rev. Mar. Sci., 4, 11–37, https://doi.org/10.1146/annurev-marine-041911-111611, 2012.

D'Ortenzio, F. and Ribera d'Alcalà, M.: On the trophic regimes of the Mediterranean Sea: a satellite analysis, Biogeosciences, 6, 139–148, https://doi.org/10.5194/bg-6-139-2009, 2009.

Enriquez-Alonso, A., Sanchez-Lorenzo, A., Calbó, J., González, J. A., and Norris, J.: Cloud cover climatologies in the Mediter-

ranean obtained from satellites, surface observations, reanalyses, and CMIP5 simulations: validation and future scenarios, Clim. Dyn., 47, 249–269, https://doi.org/10.1007/s00382-015-2834-4, 2016.

Escudier, R., Clementi, E., Nigam, T., Aydogdu, A., Fini, E., Pistoia, J., Grandi, A., and Miraglio, P.: EU Copernicus Marine Service Product, Quality Information Document for Mediterranean Sea Physics Reanalysis, MEDSEA_MULTIYEAR_PHY_006_004, Issue 2.4, Mercator Ocean International, https://documentation.marine.copernicus.eu/QUID/CMEMS-MED-QUID-006-004.pdf (last access: 10 September 2026), 2025.

EU Copernicus Marine Service Product: Mediterranean Sea – High Resolution L4 Sea Surface Temperature Reprocessed, Mercator Ocean International [data set], https://doi.org/10.48670/moi-00173, 2024a.

EU Copernicus Marine Service Product: Mediterranean Sea Surface Temperature time series and trend from Observations Reprocessing, Mercator Ocean International [OMI], https://doi.org/10.48670/moi-00268, 2024b.

EU Copernicus Marine Service Product: Mediterranean Sea Chlorophyll-a time series and trend from Observations Reprocessing, Mercator Ocean International [OMI], https://doi.org/10.48670/moi-00259, 2024c.

EU Copernicus Marine Service Product: Mediterranean Sea, Bio-Geo-Chemical, L4, monthly means, daily gapfree and climatology Satellite Observations (1997–ongoing), Mercator Ocean International [data set], https://doi.org/10.48670/moi-00300, 2025a.

EU Copernicus Marine Service Product: Mediterranean Sea Physics Reanalysis, Mercator Ocean International [data set], https://doi.org/10.48670/mds-00375, 2025b.

Finkel, Z. V., Beardall, J., Flynn, K. J., Quigg, A., Rees, T. A. V., and Raven, J. A.: Phytoplankton in a changing world: cell size and elemental stoichiometry, J. Plankton Res., 32, 119–137, https://doi.org/10.1093/plankt/fbp098, 2010.

Gascard, J. C. and Richez, C.: Water Masses and Circulation in the Western Alboran Sea and in the Straits of Gibraltar, Prog. Oceanogr., 15, 157–216, https://doi.org/10.1016/0079-6611(85)90031-X, 1985.

Gregg, W. W. and Casey, N. W.: Skill assessment of a spectral ocean–atmosphere radiative model, J. Marine Syst., 76, 49–63, 2009.

Halpern, B. S., Longo, C., Hardy, D., McLeod, K. L., Samhouri, J. F., Katona, S. K., Kleisner, K., Lester, S. E., O'Leary, J., Ranelletti, M., Rosenberg, A. A., Scarborough, C., Selig, E. R., Best, B. D., Brumbaugh, D. R., Chapin, F. S., Crowder, L. B., Daly, K. L., Doney, S. C., Elfes, C., Fogarty, M. J., Gaines, S. D., Jacobsen, K. I., Karrer, L. B., Leslie, H. M., Neeley, E., Pauly, D., Polasky, S., Ris, B., Martin, K. S., Stone, G. S., Sumaila, U. R., and Zeller D.: An index to assess the health and benefits of the global ocean, Nature, 488, 615–620, https://doi.org/10.1038/nature11397, 2012.

Halpern, B. S., Frazier, M., Potapenko, J., Casey, K. S., Koenig, K., Longo, C., Lowndes, J. S., Rockwood, R. C., Selig, E. R., Selkoe, K. A., and Walbridge, S.: Spatial and temporal changes in cumulative human impacts on the world's ocean, Nat. Commun., 6, 7615, https://doi.org/10.1038/ncomms8615, 2015.

Harzallah, A., Alioua, M., and Li, L.; Mass exchange at the Strait of Gibraltar in response to tidal and lower frequency forcing as simulated by a Mediterranean Sea model, Tellus A, 66, https://doi.org/10.3402/tellusa.v66.23871, 2014.

Herrmann, M. and Somot, S.: Relevance of ERA40 dynamical downscaling for modeling deep convection in the Mediterranean Sea, Geophys. Res. Lett., 35, L04607, https://doi.org/10.1029/2007GL032442, 2008.

Hirata, T., Hardman-Mountford, N. J., Brewin, R. J. W., Aiken, J., Barlow, R., Suzuki, K., Isada, T., Howell, E., Hashioka, T., Noguchi-Aita, M., and Yamanaka, Y.: Synoptic relationships between surface Chlorophyll-*a* and diagnostic pigments specific to phytoplankton functional types, Biogeosciences, 8, 311–327, https://doi.org/10.5194/bg-8-311-2011, 2011.

Houze Jr., R. A.: Orographic effects on precipitating clouds, Rev. Geophys., 50, RG1001, https://doi.org/10.1029/2011RG000365, 2012.

IPCC: Climate Change 2021: The Physical Science Basis, Contribution of Working Group I to the Sixth Assessment Report of the Intergovernmental Panel on Climate Change, Cambridge University Press, https://doi.org/10.1017/9781009157896, 2021.

Katlane, R., Nechad, B., Ruddick, K., and Zargouni, F.: Optical remote sensing of turbidity and total suspended matter in the Gulf of Gabes, Arab. J. Geosci., 6, 1527–1535, https://doi.org/10.1007/s12517-011-0438-9, 2013.

Kostadinov, T. S., Siegel, D. A., and Maritorena, S.: Global variability of phytoplankton functional types from space: assessment via the particle size distribution, Biogeosciences, 7, 3239–3257, https://doi.org/10.5194/bg-7-3239-2010, 2010.

Lazzari, P., Salon, S., Terzić, E., Gregg, W. W., D'Ortenzio, F., Vellucci, V., Organelli, E., and Antoine, D.: Assessment of the spectral downward irradiance at the surface of the Mediterranean Sea using the radiative Ocean-Atmosphere Spectral Irradiance Model (OASIM), Ocean Sci., 17, 675–697, https://doi.org/10.5194/os-17-675-2021, 2021.

Lecci, R., Drudi, M., Grandi, A., and Clementi, E.: EU Copernicus Marine Service Product, Product User Manual for Mediterranean Sea Physics Reanalysis, MEDSEA_MULTIYEAR_PHY_006_004, Issue 2.4, Mercator Ocean International, https://documentation.marine.copernicus.eu/PUM/CMEMS-MED-PUM-006-004.pdf (last access: 10 September 2026), 2025.

Lejeusne, C., Chevaldonné, P., Pergent-Martini, C., Boudouresque, C. F., and Pérez, T.: Climate change effects on a miniature ocean: the highly diverse, highly impacted Mediterranean Sea, Trend. Ecol. Evol., 25, 250–260, https://doi.org/10.1016/j.tree.2009.10.009, 2010.

Le Traon, P., Abadie, V., Ali, A., Behrens, A., Staneva, J., Hieronymi, M., and Krasemann, H.: The Copernicus Marine Service from 2015 to 2021: Six years of achievements, Mercat. Ocean. J, https://doi.org/10.48670/moi-cafr-n813, 2021.

Le Traon, P. Y., Reppucci, A., Alvarez Fanjul, E., Aouf, L., Behrens, A., Belmonte, M., Bentamy, A., Bertino, L., Brando, V. E., Kreiner, M. B., Benkiran, M., Carval, T., Ciliberti, S. A., Claustre, H., Clementi, E., Coppini, G., Cossarini, G., De Alfonso Alonso-Muñoyerro, M., Delamarche, A., Dibarboure, G., Dinessen, F., Drevillon, M., Drillet, Y., Faugere, Y., Fernández, V., Fleming, A., Garcia-Hermosa, M. I., Sotillo, M. G., Garric, G., Gasparin, F., Giordan, C., Gehlen, M., Gregoire, M. L.,

Guinehut, S., Hamon, M., Harris, C., Hernandez, F., Hinkler, J. B., Hoyer, J., Karvonen, J., Kay, S., King, R., Lavergne, T., Lemieux-Dudon, B., Lima, L., Mao, C., Martin, M. J., Masina, S., Melet, A., Buongiorno Nardelli, B., Nolan, G., Pascual, A., Pistoia, J., Palazov, A., Piolle, J. F., Pujol, M. I., Pequignet, A. C., Peneva, E., Pérez Gómez, B., Petit de la Villeon, L., Pinardi, N., Pisano, A., Pouliquen, S., Reid, R., Remy, E., Santoleri, R., Siddorn, J., She, J., Staneva, J., Stoffelen, A., Tonani, M., Vandenbulcke, L., von Schuckmann, K., Volpe, G., Wettre, C., and Zacharioudaki, A.: From Observation to Information and Users: The Copernicus Marine Service Perspective, Front. Mar. Sci., 6, 234, https://doi.org/10.3389/fmars.2019.00234, 2019.

Litchman, E. and Klausmeier, C. A.: Trait-based community ecology of phytoplankton, Annu. Rev. Ecol. Evol. S., 39, 615–639, https://doi.org/10.1146/annurev.ecolsys.39.110707.173549, 2008.

Malanotte-Rizzoli, P. and Robinson, A. R. (Eds.): Ocean Processes in Climate Dynamics: Global and Mediterranean Examples, NATO ASI Series, vol. 419. Springer, Dordrecht, https://doi.org/10.1007/978-94-011-0870-6_11, 1994.

Mantua, N. J. and Hare, S. R.: The Pacific Decadal Oscillation, J. Oceanogr., 58, 35–44, https://doi.org/10.1023/A:1015820616384, 2002.

Margalef, R.: Life-forms of phytoplankton as survival alternatives in an unstable environment, Oceanol. Acta, 1, 493–509, 1978.

Marshall, J. and Schott, F.: Open-ocean convection: Observations, theory, and models, Rev. Geophys., 37, 1–64, https://doi.org/10.1029/98RG02739, 1999.

Marty, J. C., Chiavérini, J., Pizay, M. D., and Avril, B.: Seasonal and interannual dynamics of nutrients and phytoplankton pigments in the western Mediterranean Sea at the DYFAMED time-series station (1991–1999). Deep-Sea Res. Pt. II, 49, 1965–1985, https://doi.org/10.1016/S0967-0645(02)00022-X, 2002.

Masoud, A. A.: On the Retrieval of the Water Quality Parameters from Sentinel-3/2 and Landsat-8 OLI in the Nile Delta's Coastal and Inland Waters, Water, 14, 593, https://doi.org/10.3390/w14040593, 2022.

Mayot, N., D'Ortenzio, F., Ribera d'Alcalà, M., Lavigne, H., and Claustre, H.: Interannual variability of the Mediterranean trophic regimes from ocean color satellites, Biogeosciences, 13, 1901–1917, https://doi.org/10.5194/bg-13-1901-2016, 2016.

MEDOC Group: Observation of formation of deep water in the Mediterranean Sea, 1969, Nature, 227, 1037–1040, https://doi.org/10.1038/2271037a0, 1970.

Mignot, A., Claustre, H., Uitz, J., Poteau, A., d'Ortenzio, F., and Xing, X.: Understanding the seasonal dynamics of the deep chlorophyll maximum in oligotrophic environments: A bio-argo float investigation, Global Biogeochem. Cy., 28, 856–876, https://doi.org/10.1002/2013GB004781, 2014.

Millot, C.: Circulation in the Western Mediterranean Sea, J. Marine Syst., 20, 423–442, https://doi.org/10.1016/S0924-7963(98)00078-5, 1999.

Morel, A.: Light and marine photosynthesis: a spectral model with geochemical and climatological implications, Prog. Oceanogr., 26, 263–306, 1991.

Morel, A. and Berthon, J. F.: Surface pigments, algal biomass profiles, and potential production of the euphotic layer: Relationships reinvestigated in view of remote-sensing applications, Limnol. Oceanogr., 34, 1545–1562, 1989

Morel, A., Antoine, D., Babin, M., and Dandonneau, Y.: Measured and modeled primary production in the northeast Atlantic (EUMELI JGOFS program): the impact of natural variations in photosynthetic parameters on model predictive skill, Deep-Sea Res. Pt. I, 43, 1273–1304, https://doi.org/10.1016/0967-0637(96)00059-3, 1996.

Morel, A., Antoine, D., and Gentili, B.: Bidirectional reflectance of oceanic waters: accounting for Raman emission and varying particle scattering phase function, Appl. Optics, 41, 6289–6306, https://doi.org/10.1364/AO.41.006289, 2002.

Muller-Karger, F. E., Miloslavich, P., Bax, N. J., Simmons, S., Costello, M. J., Sousa Pinto, I., Canonico, G., Turner, W., Gill, M., Montes, E., Best, B. D., Pearlman, J., Halpin, P., Dunn, D., Benson, A., Martin, C. S., Weatherdon, L. V., Appeltans, W., Provoost, P., Klein, E., Kelble, C. R., Miller, R. J., Chavez, F. P., Iken, K., Chiba, S., Obura, D., Navarro, L. M., Pereira, H. M., Allain, V., Batten, S., Benedetti-Checchi, L., Duffy, J. E., Kudela, R. M., Rebelo, L.-M., Shin, Y., and Geller, G.: Advancing Marine Biological Observations and Data Requirements of the Complementary Essential Ocean Variables (EOVs) and Essential Biodiversity Variables (EBVs) Frameworks, Front. Mar. Sci., 5, 211, https://doi.org/10.3389/fmars.2018.00211, 2018.

Nixon, S. W.: Replacing the Nile: are anthropogenic nutrients providing the fertility once brought to the Mediterranean by a great river?, AMBIO, 32, 30–39, https://doi.org/10.1579/0044-7447-32.1.30, 2003.

Penna, N., Capellacci, S., and Ricci, F.: The influence of the Po River discharge on phytoplankton bloom dynamics along the coastline of Pesaro (Italy) in the Adriatic Sea, Mar. Pollut. Bull., 48, 321–326, https://doi.org/10.1016/j.marpolbul.2003.08.007, 2004.

Piroddi, C., Teixeira, H., Lynam, C. P., Smith, C., Alvarez, M. C., Mazik, K. Andonegi, E., Churilova, T., Tedesco, L., Chifflet, M., Chust, G., Galparsoro, I., Garcia, A. C., Kämäri, M., Kryvenko, O., Lassalle, G., Neville, S., Niquil, N., Papadopoulou, N., Rossberg, A. G., Suslin, V., and Uyarra, M. C.: Using ecological models to assess ecosystem status in support of the European Marine Strategy Framework Directive, Ecol. Indic., 58, 175–191, https://doi.org/10.1016/j.ecolind.2015.05.037, 2015.

Pisano, A., Marullo, S., Artale, V., Falcini, F., Yang, C., Leonelli, F. E., Santoleri, R., and Buongiorno Nardelli, B.: New Evidence of Mediterranean Climate Change and Variability from Sea Surface Temperature Observations, Remote Sens., 12, 132, https://doi.org/10.3390/rs12010132, 2020.

Pisano, A., Fanelli, C., Cesarini, C., La Padula, F., and Buongiorno Nardelli, B.: EU Copernicus Marine Service Product, Quality Information Document for Mediterranean Sea – High Resolution L4 Sea Surface Temperature Reprocessed, SST_MED_SST_L4_REP_OBSERVATIONS_010_021, Issue 5.0, Mercator Ocean International, https://documentation.marine.copernicus.eu/QUID/CMEMS-OMI-QUID-MEDSEA-SST.pdf (last access: 10 September 2026), 2024a.

Pisano, A., Fanelli, C., Cesarini, C., La Padula, F., and Buongiorno Nardelli, B.: EU Copernicus Marine Service Product, Product User Manual for Mediterranean Sea – High Resolution L4 Sea Surface Temperature Reprocessed, SST_MED_SST_L4_REP_OBSERVATIONS_010_021, Issue 5.0, Mercator Ocean International,

https://documentation.marine.copernicus.eu/PUM/CMEMS-SST-PUM-010-021-042.pdf (last access: 10 September 2026), 2024b.

Platt, T. G., Gallegos, C. L., and Harrison, W. G.: Photoinhibition of photosynthesis in natural assemblages of marine phytoplankton, J. Mar. Res., 38, https://elischolar.library.yale.edu/journal_of_marine_research/1525 (last access: 18 September 2026), 1980.

Polovina, J. J., Howell, E. A., and Abecassis, M.: Ocean's least productive waters are expanding, Geophys. Res. Lett., 35, L03618, https://doi.org/10.1029/2007GL031745, 2008.

Reale, M., Salon, S., Somot, S., Solidoro, C., Giorgi, F., Crise, A., Cossarini, G., Lazzari, P., and Sevault, F.: Influence of large-scale atmospheric circulation patterns on nutrient dynamics in the Mediterranean Sea in the extended winter season (October–March) 1961–1999, Clim. Res., 82, 117–136, https://doi.org/10.3354/cr01620, 2020.

Robinson, A. R. and Golnaraghi, M.: The Physical and Dynamical Oceanography of the Mediterranean Sea, in: Ocean Processes in Climate Dynamics: Global and Mediterranean Examples, edited by: Malanotte-Rizzoli, P. and Robinson, A. R., NATO ASI Series, vol. 419, Springer, Dordrecht, https://doi.org/10.1007/978-94-011-0870-6_12, 1994.

Sieburth, J. M., Smetacek, V., and Lenz, J.: Pelagic ecosystem structure: Heterotrophic compartments of the plankton and their relationship to plankton size fractions 1, Limnol. Oceanogr., 23, 1256–1263, https://doi.org/10.4319/lo.1978.23.6.1256, 1978.

Siokou-Frangou, I., Christaki, U., Mazzocchi, M. G., Montresor, M., Ribera d'Alcalá, M., Vaqué, D., and Zingone, A.: Plankton in the open Mediterranean Sea: a review, Biogeosciences, 7, 1543–1586, https://doi.org/10.5194/bg-7-1543-2010, 2010.

Struglia, M. V., Mariotti, A., and Filograsso, A.: River discharge into the Mediterranean Sea: Climatology and aspects of the observed variability, J. Climate, 17, 4740–4751, https://doi.org/10.1175/JCLI-3225.1, 2004.

Tanré, D., Herman, M., Deschamps, P. Y., and De Leffe, A.: Atmospheric modeling for space measurements of ground reflectances, including bidirectional properties, Appl. Optics, 18, 3587–3594, 1979.

Tilstone, G. H., Taylor, B. H., Blondeau-Patissier, D., Powell, T., Groom, S. B., Rees, A. P., and Lucas, M. I.: Comparison of new and primary production models using SeaWiFS data in contrasting hydrographic zones of the northern North Atlantic, Remote Sens. Environ., 156, 473–489, https://doi.org/10.1016/j.rse.2014.10.013, 2015.

Tyrlis, E. and Lelieveld, J.: Climatology and dynamics of the summer Etesian winds over the eastern Mediterranean, J. Atmos. Sci., 70, 3374–3396, https://doi.org/10.1175/JAS-D-13-035.1, 2013.

Uitz, J., Claustre, H., Morel, A., and Hooker, S. B.: Vertical distribution of phytoplankton communities in open ocean: An assessment based on surface chlorophyll, J. Geophys. Res.-Oceans, 111, C08005, https://doi.org/10.1029/2005JC003207, 2006.

Volpe, G., Santoleri, R., Vellucci, V., Ribera d'Alcalà, M., Marullo, S., and D'Ortenzio, F.: The Mediterranean ocean colour chlorophyll variability: Regionalization and mesoscale patterns, Remote Sens. Environ., 107, 625–638, https://doi.org/10.1016/j.rse.2006.10.017, 2007.

Volpe, G., Nardelli, B. B., Cipollini, P., Santoleri, R., and Robinson, I. S.: Seasonal to interannual phytoplankton response to physical processes in the Mediterranean Sea from satellite observations, Remote Sens. Environ., 117, 223–235, https://doi.org/10.1016/j.rse.2011.09.020, 2012.

Volpe, G., Colella, S., Brando, V. E., Forneris, V., La Padula, F., Di Cicco, A., Sammartino, M., Bracaglia, M., Artuso, F., and Santoleri, R.: Mediterranean ocean colour Level 3 operational multi-sensor processing, Ocean Sci., 15, 127–146, https://doi.org/10.5194/os-15-127-2019, 2019.

Ziv, B., Saaroni, H., and Alpert, P.: The factors governing the summer regime of the eastern Mediterranean, Int. J. Climatol., 24, 1859–1871, https://doi.org/10.1002/joc.1113, 2004.

State Planet, 7-osr10, 10, 2026
https://doi.org/10.5194/sp-7-osr10-10-2026
© Author(s) 2026. This work is distributed under
the Creative Commons Attribution 4.0 License.

Assessing temporal trends in ocean transparency using GlobColour products from the Copernicus Marine Service and accounting for associated uncertainties

Aurélien Prat[1,★], **Marine Bretagnon**[1,★], **Philippe Bryère**[1], **Quentin Jutard**[1], **and Antoine Mangin**[1]

[1]ACRI-ST, 06904 Sophia-Antipolis, France

★These authors contributed equally to this work.

Correspondence: Aurélien Prat (aurelien.prat@acri-st.fr)

Received: 15 September 2025 – Discussion started: 14 October 2025
Revised: 7 August 2026 – Accepted: 1 September 2026 – Published: 30 September 2026

Abstract. Ocean transparency refers to the ability of water to transmit light, which directly influences the depth to which sunlight penetrates the water column. This parameter is crucial for marine ecosystems, as it determines the availability of light for photosynthesis, a process vital for phytoplankton, the primary producers of the ocean. Phytoplankton not only form the base of the marine food web but also contribute significantly to biogeochemical cycles, including the carbon cycle. A decline in transparency can limit photosynthesis by reducing the depth of the euphotic zone, potentially disrupting ecosystems and impacting carbon sequestration.

Transparency has traditionally been measured using the Secchi disk, a simple yet effective tool for assessing water clarity. More recently, satellite-derived products have revolutionized the study of transparency, enabling large-scale and long-term observations. But whatever the method employed to measure transparency, robust evaluation of long-term trends depends on properly accounting for the inherent uncertainties of the observations. This issue is especially critical for remote sensing datasets, as the succession of sensors across two decades can introduce biases in long-term trend detection.

In this study, we accounted for observational uncertainties in the products by using a Monte Carlo approach, which incorporates the Seasonal Mann–Kendall test to evaluate trend detection reliability and the Theil–Sen slope estimator to quantify trend magnitude. In parallel, seasonal and inter-annual variability in transparency were also examined in relation to in situ data of water discharge, providing insights of riverine influences on transparency dynamics. Study areas include turbid French estuaries (Gironde and Loire), the semi-sheltered Gulf of Morbihan waters, tropical waters around Mayotte, and the oligotrophic North-East Atlantic, representing a broad range of hydrographic and climatic regimes.

The results reveal pronounced spatial contrasts: strong variability and decreasing transparency linked to high-flow events in the Gironde estuary, weaker but noticeable trends in the Loire estuary, no significant changes observed in the North-East Atlantic, and stable conditions for clear waters off Mayotte. The gulf of Morbihan exhibited strong variability that prevailed any trend detection from the long-term signal. Resolution analyses highlighted the importance of finer-scale products for capturing local estuarine processes, while coarser resolution provided more robust basin-scale patterns. This study confirms the value of satellite-derived transparency indicators and highlights the need to integrate uncertainties, resolution effects and call for synergies with in situ data to improve water quality assessments.

Published by Copernicus Publications.

1 Introduction

Water transparency is a critical indicator of coastal ecosystem health, as it governs light availability for primary productivity and shapes the habitat conditions for a wide range of marine organisms. Transparency is influenced by both natural processes and human-induced pressures, including sediment inputs, nutrient enrichment, and physical disturbances. Monitoring transparency across diverse marine environments is essential for understanding the impacts of environmental change and anthropogenic activity on coastal and oceanic systems.

Satellite-derived Secchi depth (ZSD) has been widely used as a proxy for water transparency across a broad range of aquatic environments, including coastal waters (Harvey et al., 2015), estuaries (Son et al., 2025), lakes (Gomes et al., 2020), and the open ocean. Various approaches have been developed to retrieve ZSD from satellite observations. Among them, the method proposed by Morel et al. (2007) provides a theoretical framework that has been implemented in a global product distributed through the Copernicus Marine Service (Garnesson et al., 2025a). This product (product ref. no. 1, Table 1) enables consistent, large-scale, and long-term assessments of water transparency variability.

In this study, we analyse long-term and seasonal variability in ZSD across a set of contrasted marine and coastal environments using satellite-derived estimates from 1998 to 2022. The study sites include the estuary of Gironde and Loire rivers, the Gulf of Morbihan, the coastal waters around Mayotte in the Indian Ocean, and the broader region of the North-East Atlantic basin. These regions span a range of climatic and hydrographic regimes, from turbid estuarine systems subject to strong riverine influence and seasonal variability, to tropical reef ecosystems under increasing anthropogenic pressure, and oligotrophic offshore waters. This spatial diversity allows for a comprehensive evaluation of the natural and anthropogenic drivers of the transparency variability.

While many previous studies have focused on spatial patterns, seasonal variability, or mean temporal changes, the role of observational uncertainty in trend assessment has received comparatively less attention. In most cases, trend significance is inferred primarily from the temporal structure of the time series itself , rather than being explicitly derived from the uncertainties associated with the observations (Franzke, 2012; Hughes and Williams, 2010). As a result, the measurement uncertainty inherent to satellite products is often not propagated into the trend estimation process. We address this limitation by incorporating pixel-level product uncertainty into a Monte-Carlo framework, thereby generating a distribution of possible trend slopes rather than a single deterministic estimate. This approach provides a more robust assessment of trend significance and confidence, especially where signal amplitudes are small relative to observation error or where data density is uneven. In that sense, the proposed framework advances current practice by explicitly distinguishing apparent trends from trends that remain robust after observation uncertainty is taken into account.

The objectives of this study are threefold. First, we investigate seasonal and interannual variability in each study area and explore correlations with environmental drivers such as river discharge, extreme weather events and climatic fluctuations. Second, we assess long-term trends in Secchi depth over the 1998–2022 period, placing particular emphasis on the role of the uncertainty in the trend detection process. Uncertainty from satellite products is explicitly integrated in the trend estimation to improve the robustness of the analysis. Third, we examine how spatial resolution (1 km vs. 4 km) influences the characterisation of these trends and evaluate the implications for monitoring in coastal environments. Together, these analyses aim to enhance our understanding of transparency dynamics in diverse marine settings and contribute to the development of reliable, satellite-based indicators for long-term water quality assessment.

2 Material and Methods

To assess the influence of environmental and anthropogenic drivers on water transparency, five regions were selected to represent a range of contrasting marine environments (Fig. 1). These include: (1) the coastal waters off Morbihan, a semi-sheltered temperate system influenced by moderate urban and agricultural pressures; (2) the Gironde and (3) Loire estuaries, characterized by strong fluvial inputs, seasonal turbidity maxima, and intensive land use in their catchments; (4) Mayotte, a tropical coral reef lagoon system subject to both oceanic conditions and increasing anthropogenic stress; and (5) a broader domain encompassing the North-East Atlantic basin, which enables the analysis of spatial gradients and large-scale trends in transparency from coastal to open-ocean environments.

Water transparency was analysed using satellite-derived Secchi depth (ZSD) estimates from the Copernicus Marine Service. For the regions of interest (1), (2), (3), and (5), the dataset used was the North Atlantic ocean colour multi-sensor merged product (product ref. no. 1, Table 1), which provides daily composites at 1 km spatial resolution. For Mayotte (4), we used the global ocean colour multi-sensor merged product (product ref. no. 2, Table 1), which directly provides monthly composites at 4 km resolution. In both cases, ZSD estimates were derived using the algorithm of Morel et al. (2007), which links chlorophyll *a* concentrations to water clarity through bio-optical relationships. A detailed description of the datasets, their processing chain, and associated quality assessment is available in the corresponding Copernicus Marine Service Quality Information Documents (QUID) (Garnesson et al., 2025a). Note that the studied regions exhibit relatively low CDOM absorption (mean $a_{\mathrm{CDOM}} < 0.3\,\mathrm{m}^{-1}$), suggesting a limited influence of

Table 1. Product table.

Product ref. no.	Product ID & type	Data access	Documentation
1	OCEANCOLOUR_ATL_BGC_L3_MY_009_113, Satellite observations	EU Copernicus Marine Service Product (2025a)	Quality Information Document (QUID): Garnesson et al. (2025a); Product User Manual (PUM): Colella et al. (2024a)
2	OCEANCOLOUR_GLO_BGC_L3_MY_009_103, Satellite observations	EU Copernicus Marine Service Product (2025b)	Quality Information Document (QUID): Garnesson et al. (2025b); Product User Manual (PUM): Colella et al. (2024b)
3	Mean monthly river discharge data product, In-situ observations	HydroPortail – Eau France, French national hydrological database	Practical Guide to Intercomparisons of River Discharge Measurements: Bertrand et al. (2016)

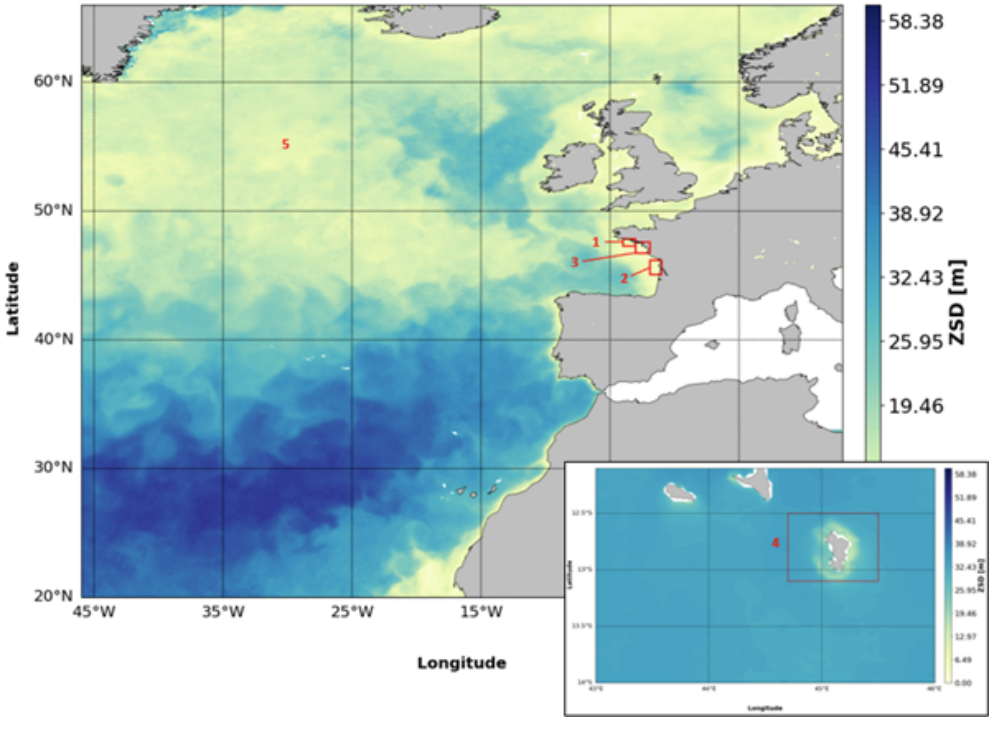


Figure 1. Map of Secchi disk depths for July 2020, showing the locations of the selected sites.

coloured dissolved organic matter on the optical properties. In this context, the assumptions underlying the Morel-based algorithm are likely to be reasonably satisfied. In addition to the satellite datasets, mean monthly river discharge data products (product ref. no. 3, Table 1) were obtained from the SANDRE Hydrologic Service through the Eau France HydroPortail, in order to evaluate the potential influence of freshwater inputs on transparency.

Prior to analysis, the daily satellite products were aggregated into monthly composites, using the arithmetic mean for both the ZSD values and the associated uncertainties. This choice reflects a conservative worst-case assumption of correlated uncertainties across daily observations, which we adopted because the true covariance structure is unknown and cannot be estimated robustly from the available information. Monthly products were preferred as they reduce short-term noise, mitigate data gaps from cloud cover, and enhance the robustness of long-term trend detection by averaging out high-frequency variability and emphasizing persistent signals. For the Atlantic study sites, monthly means were computed based only on pixels with at least 30 % revisit coverage over the entire time series, ensuring sufficient

temporal consistency. This threshold reflects a compromise between temporal data availability and spatial representativeness and avoid trends driven by sparse observations. Comparisons with unfiltered datasets (not shown) suggest that the main conclusions are robust to this choice.

To assess trends in ocean transparency while accounting for observational uncertainty, a Monte Carlo framework was implemented, combined with the Seasonal Mann–Kendall (SMK) test (Hirsch et al., 1982) and Theil–Sen's slope estimator (Hipel and McLeod, 1994). The Theil–Sen estimator was chosen for its robustness to outliers and its nonparametric nature, as it does not rely on distributional assumptions, unlike ordinary least squares regression. This property is particularly suitable for environmental time series, which often include extreme values. Although that estimator can be sensitive to missing data, this limitation is not relevant here due to the completeness of the monthly time series.

The uncertainty metric used in this study corresponds to the per-pixel relative uncertainty provided in the Copernicus products. These uncertainties are derived from comparisons with in situ reference measurements and from the multisensor merging approach, as described in the Copernicus Quality Information Document (QUID) (Garnesson et al., 2025a). Consequently, they are intrinsically linked to the magnitude of the ZSD variable and may exhibit moderate seasonal and spatial variability. However, this variability is not expected to bias the results, as uncertainty is explicitly incorporated into the trend detection framework. Specifically, the Monte Carlo approach propagates the reported uncertainties into ensembles of synthetic time series, enabling the assessment of trend significance under realistic, observation-dependent noise conditions. As such, spatial and temporal variations in uncertainty are inherently accounted for in the trend statistics, rather than treated as fixed or external perturbations.

For each time step, normally distributed synthetic values were generated based on the reported relative uncertainties of the ZSD measurements, with a standard deviation derived from the reported relative uncertainty. A Gaussian approximation is justified here because the reported uncertainty reflects the combined effect of multiple independent error sources (e.g., reprojection, multi-sensor merging, temporal averaging), following the central limit theorem. This procedure was repeated 5000 times to produce ensembles of time series that reflect the inherent uncertainty in the observations. The choice of 5000 Monte Carlo realizations was supported by a convergence analysis showing that the estimated trend statistics stabilized beyond this number of iterations. The SMK test was applied to each realization to assess trend significance, while Theil–Sen's slope provided an estimate of the trend magnitude. By aggregating the outputs, we derived robust confidence intervals for the trend slope and calculated the frequency of statistically significant outcomes, thereby quantifying both the strength and reliability of observed trends in transparency. In parallel, the SMK test and Theil–Sen's slope estimator were also applied directly to the original time series at each study site without incorporating uncertainties, in order to provide a baseline reference for comparison with the Monte Carlo-based results.

3 Results and discussion

3.1 Seasonal variability and climatic driver

Time series of Secchi disk depth (ZSD) provide valuable insights into both the seasonal variability of water transparency and its interannual variability across the study regions.

A first-order analysis reveals that among the regions considered (Northeast Atlantic, Gulf of Morbihan, Loire Estuary, Gironde Estuary, and Mayotte), the deepest ZSD values are observed at the Northeast Atlantic site. This high transparency is explained by the predominance of offshore conditions, where sediment inputs and terrigenous influence are minimal, yielding an average ZSD of 26 m. Mayotte ranks second, with an average ZSD of 24 m. This is consistent with its clear, oligotrophic waters, which are not influenced by major river inputs. In contrast, water transparency is lower in coastal sites, with average ZSD values of 7, 5.6, and 7.9 m in the Gironde Estuary, Loire Estuary, and Gulf of Morbihan, respectively.

Each of the studied regions exhibits its own characteristic seasonal pattern (Fig. 2). To quantify this variability, a climatology of ZSD was constructed for each site (monthly means over the entire archive). The amplitude of the seasonal cycle varies across regions. All regions exhibit low interannual variability. Mayotte shows the highest interannual variability among them and is also associated with the second highest ZSD values. The most pronounced seasonal signal is observed in the Atlantic, where the transparency depth varies by up to 8 m between its maximum in August and minimum in March.

Mayotte exhibits the second strongest seasonal variability, with an amplitude of 6.4 m between the month of maximum ZSD (December) and minimum ZSD (July). The highest ZSD values, indicative of greater water transparency, occur at the onset of the rainy season (November–April), prior to significant water discharge, whereas the lowest transparency is observed during the middle of the dry season (May–October), likely driven by intensified wind conditions.

While both the Atlantic region and the Mayotte site display the largest absolute seasonal variability, the Gulf of Morbihan shows the strongest relative seasonal signal. There, ZSD varies by up to 62 % relative to the annual mean between the most transparent and least transparent months (August and March, respectively). The seasonal cycle of ZSD in the Gulf of Morbihan closely follows that of surface salinity, with maximum transparency coinciding with higher salinity levels. This relationship suggests a strong influence of winter freshwater discharge on water transparency, likely through

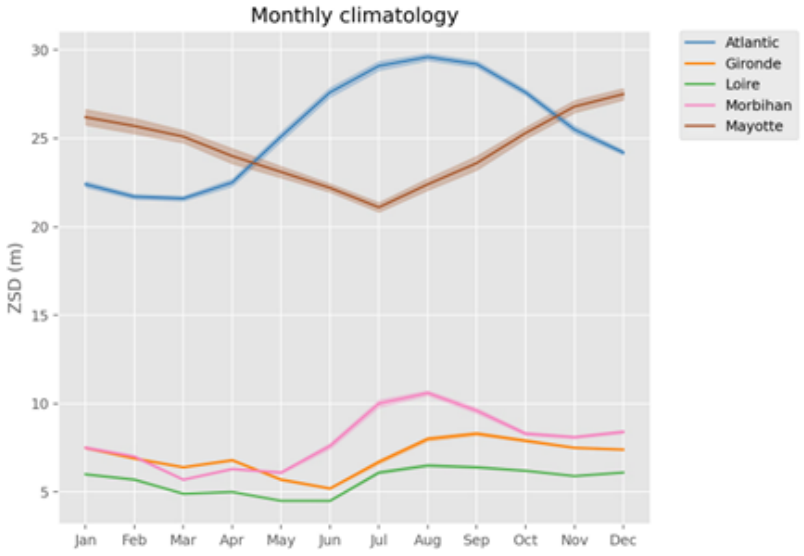


Figure 2. Monthly climatology of ZSD over the archive 1998–2022 for the region of interest. The shaded contours correspond to the standard deviation of each month.

increased water inflow and wind-driven resuspension of particles.

By contrast, the Loire Estuary exhibits the weakest absolute seasonal variability, with an average difference of only 2 m between seasons (or 35 % relative to the annual mean ZSD). The lowest ZSD values are observed in late spring (May–June), whereas the highest values occur in August. Reduced transparency during late spring likely results from a combination of increased river discharge and phytoplankton bloom. However, due to the inherent correlation between ZSD and chlorophyll retrieval algorithms, this interpretation remains uncertain. The peak ZSD observed in August (6.5 m) may reflect nutrient depletion in the surface layer, leading to reduced chlorophyll *a* concentrations as well as a minimum of river discharge.

A similar seasonal pattern is observed in the Gironde Estuary, where minimum ZSD values (5.2 m) occur in May–June and maximum values (8.3 m) in August–September. This site exhibits intermediate seasonal variability (44 %), higher than that of the broader Atlantic region but lower than that observed in the Gulf of Morbihan.

The correspondence between river discharge and precipitation data may provide valuable insights into interannual variability and the occurrence of significant climatic events. For instance, in the Gironde Estuary (Fig. 3b), a pronounced minimum in water transparency (< 4 m) was recorded in June 2004, following a high discharge of the Garonne River ($> 2000\,m^3\,s^{-1}$), which transported large amounts of suspended sediments into the coastal zone. A similar situation occurred in May 2020, when sustained high river discharge during the preceding winter also resulted in reduced transparency.

Comparable events are observed in other regions. In the Loire Estuary (Fig. 3c), strong discharges appear to explain the transparency minima (< 4 m) recorded in May 2001. Conversely, river discharge time series can also shed light on periods of unusually high transparency. For example, during spring–summer 2011, the Loire River discharge remained low for several consecutive months, reflecting reduced rainfall. Consequently, particle input to the coastal zone was lower than in other years, leading to increased water transparency (ZSD > 8 m).

However, there are also periods when high river discharge does not coincide with marked minima in transparency. This suggests that, while river flow plays a key role in shaping seasonal variability, its influence on extreme transparency events is less consistent across the studied regions.

3.2 Long-term trend analysis

As detailed in the methods, long-term trends in water transparency were assessed using the Seasonal Mann–Kendall (SMK) test combined with Theil–Sen's slope estimator, applied both directly to the ZSD time series and within a Monte Carlo framework that accounted for observational uncertainties (Fig. 3). This dual approach allowed us to estimate trend magnitudes, test their statistical significance, and evaluate their robustness under uncertainty.

Long-term trend analysis revealed contrasting patterns across the study areas. In the Atlantic zone, no significant trend was detected, regardless of whether uncertainties were considered (p-value $= 0.3874$, fraction of significant simulations $= 5$ %) (Fig. 3a). This lack of trend is consistent with the area being dominated by open waters, which are largely unaffected by external natural or anthropogenic inputs.

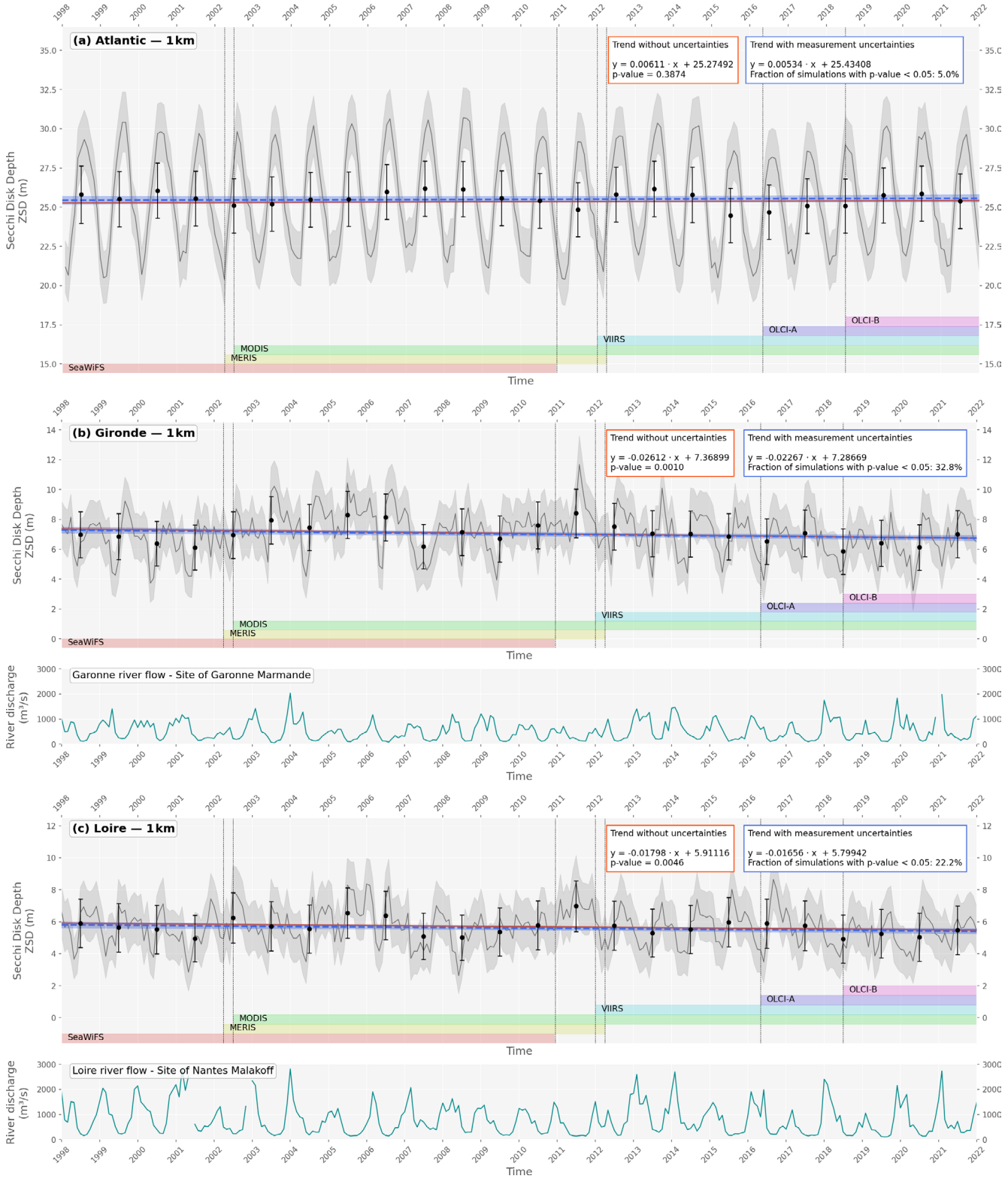

(a) Atlantic — 1km
Trend without uncertainties
y = 0.00611 · x + 25.27492
p-value = 0.3874
Trend with measurement uncertainties
y = 0.00534 · x + 25.43408
Fraction of simulations with p-value < 0.05: 5.0%
Secchi Disk Depth ZSD (m)
Time
SeaWiFS
MERIS
MODIS
VIIRS
OLCI-A
OLCI-B
(b) Gironde — 1km
Trend without uncertainties
y = -0.02612 · x + 7.36899
p-value = 0.0010
Trend with measurement uncertainties
y = -0.02267 · x + 7.28669
Fraction of simulations with p-value < 0.05: 32.8%
Garonne river flow - Site of Garonne Marmande
River discharge (m³/s)
(c) Loire — 1km
Trend without uncertainties
y = -0.01798 · x + 5.91116
p-value = 0.0046
Trend with measurement uncertainties
y = -0.01656 · x + 5.79942
Fraction of simulations with p-value < 0.05: 22.2%
Loire river flow - Site of Nantes Malakoff

Figure 3.

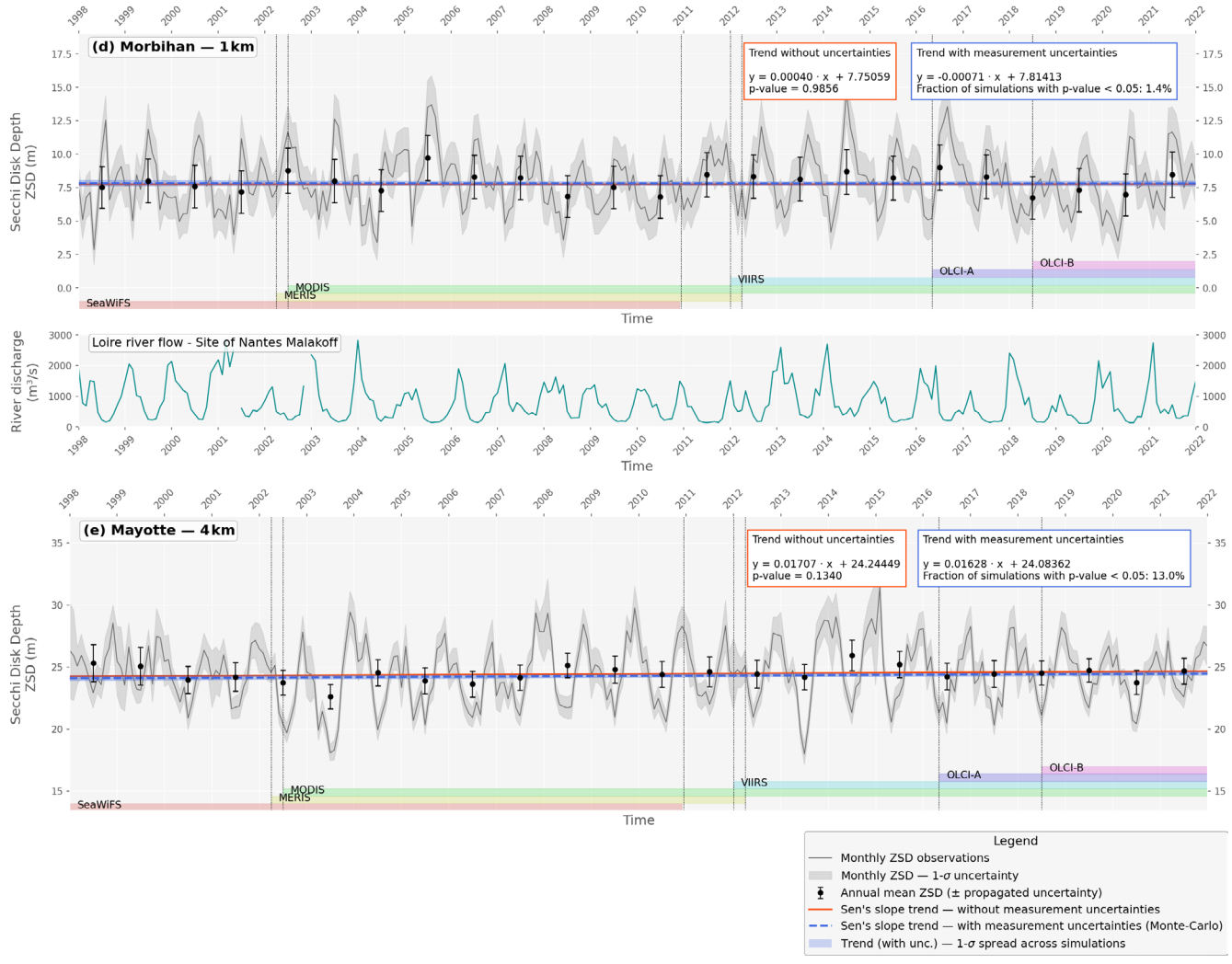


Figure 3. Secchi disk depth (ZSD) time series from 1998 to 2022 across all regions of interest (grey), with trend estimates derived with (blue) and without (red) consideration of observational uncertainties.

In both the Gironde and Loire estuaries, decreasing trends in ZSD were identified when observational uncertainties were not considered; however, accounting for uncertainty substantially altered the assessment of their statistical significance. In the Gironde estuary, a decline of 2.6 cm yr^{-1} was detected using the deterministic approach (p-value = 0.001), whereas incorporating uncertainties yielded a lower proportion of significant simulations (32.8 % of significant simulations) (Fig. 3b). A similar pattern was observed in the Loire estuary, where a decreasing trend was significant only in the absence of uncertainty (p-value = 0.0046), while the Monte Carlo framework reduced the fraction of significant simulations to 22.2 % (Fig. 3c). This discrepancy illustrates how failing to account for uncertainties may lead to overconfident interpretations of trend significance. It also suggests that, although a potential decrease in transparency is plausible, the signal remains close to the detection threshold, and conclusions should therefore be drawn with caution. Despite these differences in statistical robustness, the decreasing trends can be linked to the increasing frequency of flood events observed in the monthly mean discharge of both the Garonne (Gironde estuary) and Loire rivers, which are the main source of sediment inputs in the study areas. Specifically for the Garonne site, five flood-related events with average monthly discharges exceeding 1200 $m^3 s^{-1}$ were recorded between 2010 and 2022, compared to only two such events during the earlier period 1998–2010.

In the Morbihan Gulf, no long-term trend in ZSD was identified (Fig. 3d). As outlined above, the strong interannual variability of the signal complicates the detection of persistent changes and may obscure subtle long-term tendencies. Around Mayotte, no significant trend was detected either (Fig. 3e). This result is consistent with the relatively

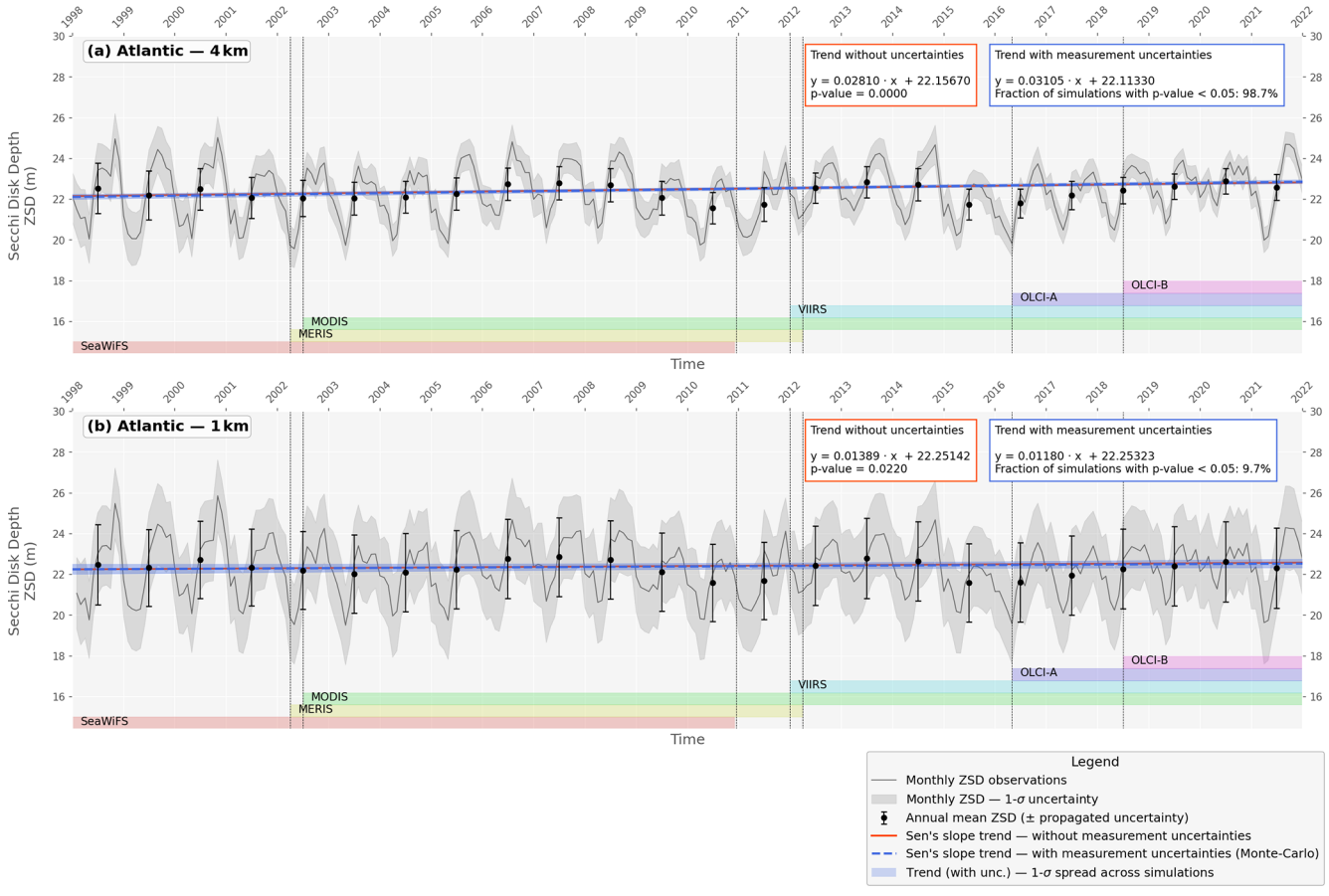


Figure 4. Comparison of Secchi disk depth (ZSD) time series for the North-East Atlantic region over the period 1998–2022, derived from satellite products at 1 and 4 km spatial resolutions. No pixel revisit mask applied.

stable environmental conditions in this region reducing the likelihood of detecting significant long-term variations.

3.3 Spatial comparison and regional implications

A comparative analysis of the Atlantic 1 and 4 km products was conducted to evaluate potential differences in ZSD time series and associated trends. For both products, the study area was restricted to the Northeast Atlantic, excluding the Mediterranean Sea, and no pixel revisit mask was applied to ensure consistency.

The seasonal ZSD signal exhibits a broadly similar pattern at both resolutions, though the 1 km product shows stronger interannual variability, likely reflecting its higher sensitivity to sub-mesoscale heterogeneity and localized dynamics. No systematic offset was observed between the two datasets, as both yield an identical mean ZSD value of 22.4 m. Minor differences in variability may nonetheless be partly related to the finer spatial resolution of the 1 km dataset, which is more sensitive to turbid coastal conditions, whereas the 4 km product tends to smooth these signals.

Trend analyses reveal a consistent long-term increase in transparency across the North-East Atlantic basin. For the 1 km product, the Theil–Sen's slope indicates an average increase of 1.4 cm yr^{-1}, with the SMK test yielding a statistically significant result ($p = 0.022$). In comparison, the 4 km product suggests a stronger increase of 2.8 cm yr^{-1}, with the trend highly significant ($p < 0.0001$). This difference in trend detection is also observed the same way across all other study areas. While the coarser product appears to provide a more statistically robust detection, this does not necessarily imply a more reliable representation of the underlying physical reality. The 1 km dataset, despite its higher sensitivity to small-scale variability and noise, better integrates fine-scale coastal and localized processes that are critical for accurately characterizing the actual evolution of water transparency in these areas. Consequently, both resolutions provide complementary insights: the 4 km product emphasizes the large-scale, smoothed signal, while the 1 km product captures localized dynamics that may ultimately drive the long-term trajectory of transparency.

It is worth noting the marked differences between the ZSD signals derived from the 1 km product and those ob-

tained from the 1 km product restricted to pixels revisited at least 30 % of the time (Figs. 4 and 3a, respectively). In the non-masked case, the signal amplitude is lower, and a much higher interannual variability is observed. When all pixels are included, the signal integrates more heterogeneous observations, particularly in coastal areas or near clouds where data are available more sporadically. This tends to smooth the mean values, reducing the amplitude of the detected variations, but introduces greater interannual variability due to differences in pixel coverage and availability from one year to the next.

4 Conclusions

This study provides a comprehensive assessment of water transparency dynamics across contrasting marine and coastal environments using satellite-derived Secchi depth (ZSD) over the period 1998–2022. By combining multi-decadal time series, robust statistical approaches, and explicit treatment of observational uncertainties, the analysis yields new insights into both the drivers and limitations of satellite-based transparency monitoring.

The results highlight pronounced spatial contrasts in transparency, ranging from highly turbid estuarine systems to oligotrophic tropical and offshore waters. Seasonal variability is strongly site-dependent, with riverine influence and climatic forcing emerging as primary drivers in temperate estuaries of the French metropolitan coast, while tropical systems such as Mayotte show distinct seasonal signatures, likely reflecting the interplay of meteorological and hydrodynamic processes. At interannual scales, extreme river flow events strongly influenced transparency, though their impacts were not uniform across regions.

Long-term trend analysis revealed contrasting outcomes among sites. A robust and significant decrease in transparency was detected in the Gironde estuary, consistent with the rising frequency of high-flow events from the Garonne River. In the Loire estuary, a potential decrease was suggested but its significance weakened when observational uncertainties were considered, underlining the importance of explicitly accounting for product errors. In contrast, no persistent trend was observed in the North-East Atlantic, reflecting the dominance of stable open-ocean waters; in the Gulf of Morbihan, strong interannual variability likely masked any long-term tendencies; and around Mayotte, transparency remained stable due to the relative constancy of its clear, oligotrophic waters.

The comparison of 1 and 4 km products further demonstrated that spatial resolution critically influences both mean transparency values and trend detection. While the coarser dataset yields more stable and statistically robust basin-scale patterns, the finer-resolution product captures essential local variability in estuarine and coastal waters.

Together, these findings confirm the utility of satellite-based indicators for monitoring transparency but also stress the need to integrate uncertainty estimates and resolution effects. Strengthening synergies with in situ observations and biogeochemical models will be essential to improve the reliability of long-term water quality assessments and their application in ecosystem management.

Data availability. All datasets used and described in this study were obtained from the publicly available Copernicus Marine Service and Eau France HydroPortail platforms (Table 1).

Author contributions. AP, MB, PB, and AM contributed to the conception and design of the study. QJ helped with the provision and pretreatment of data. AP and MB drafted the manuscript. PB and AM provided important advice on the scientific analysis and interpretation of the results.

Competing interests. The contact author has declared that none of the authors has any competing interests.

Disclaimer. The Copernicus Marine Service offering is regularly updated to ensure it remains at the forefront of user requirements. In this process, some products may undergo replacement or renaming, leading to the removal of certain product IDs from the catalogue. If readers have any questions or require assistance regarding these modifications, please feel free to reach out to the Copernicus Marine Service user support team for further guidance. They will be able to provide the necessary information to address concerns and find suitable alternatives.

Publisher's note: Copernicus Publications remains neutral with regard to jurisdictional claims made in the text, published maps, institutional affiliations, or any other geographical representation in this paper. The authors bear the ultimate responsibility for providing appropriate place names. Views expressed in the text are those of the authors and do not necessarily reflect the views of the publisher.

Acknowledgements. We gratefully acknowledge the Copernicus Marine Service for providing free and open access to the ocean colour and environmental data used in this study. We also thank the two anonymous reviewers for their insightful and constructive comments, which significantly improved the quality and clarity of the manuscript.

We would also like to thank Pierre Brasseur, the Editor for his support throughout the publication process. We are also grateful to Karina von Schuckmann and the Copernicus Editorial Team for their valuable guidance and constructive feedback during the initial review phase of the manuscript.

Review statement. This paper was edited by Pierre Brasseur and reviewed by two anonymous referees.

References

Bertrand, X., Collobert, M., Besson, D., and Puechberty, R.: Guide pratique Intercomparaisons de mesures de débit en rivière, Eaufrance, https://hydro.eaufrance.fr/documentation/guide-pratique-intercomparaisons-de-mesures-de-debit-en-riviere (last access: 1 September 2025), 2016.

Colella, S., Böhm, E., Cesarini, C., Jutard, Q., and Brando, V. E.: EU Copernicus Marine Service Product User Manual for the North Atlantic Ocean Colour Plankton, Reflectance, Transparency and Optics MY L3 daily observations, OCEANCOLOUR_ATL_BGC_L3_MY_009_113, Issue 5.0, Mercator Ocean International, https://documentation.marine.copernicus.eu/PUM/CMEMS-OC-PUM.pdf (last access: 1 September 2025), 2024a.

Colella, S., Böhm, E., Cesarini, C., Jutard, Q., and Brando, V. E.: EU Copernicus Marine Service Product User Manual for the Global Ocean Colour (Copernicus-GlobColour), Bio-Geo-Chemical, L3 (daily) from Satellite Observations (1997–ongoing), OCEANCOLOUR_GLO_BGC_L3_MY_009_103, Issue 5.0, Mercator Ocean International, https://documentation.marine.copernicus.eu/PUM/CMEMS-OC-PUM.pdf (last access: 1 September 2025), 2024b.

EU Copernicus Marine Service Product: North Atlantic Ocean Colour Plankton, Reflectance, Transparency and Optics MY L3 daily observations, Mercator Ocean International [data set], https://doi.org/10.48670/moi-00286, 2025a.

EU Copernicus Marine Service Product: Global Ocean Colour (Copernicus-GlobColour), Bio-Geo-Chemical, L3 (daily) from Satellite Observations (1997–ongoing), Mercator Ocean International [data set], https://doi.org/10.48670/moi-00280, 2025b.

Franzke, C.: Nonlinear trends, long-range dependence, and climate noise properties of surface temperature, J. Climate, 25, 4172–4183, https://doi.org/10.1175/JCLI-D-11-00293.1, 2012.

Garnesson, P., Mangin, A., Bretagnon, M., and Jutard, Q.: EU Copernicus Marine Service Quality Information Document for the North Atlantic Ocean Colour Plankton, Reflectance, Transparency and Optics MY L3 daily observations, Tech. Rep. OCEANCOLOUR_ATL_BGC_L3_MY_009_113, Issue 5.1, Mercator Ocean International, https://documentation.marine.copernicus.eu/QUID/CMEMS-OC-QUID-009-101to104-111-113-116-118.pdf (last access: 1 September 2025), 2025a.

Garnesson, P., Mangin, A., Bretagnon, M., and Jutard, Q.: EU Copernicus Marine Service Quality Information Document for the Global Ocean Colour (Copernicus-GlobColour), Bio-Geo-Chemical, L3 (daily) from Satellite Observations (1997–ongoing), OCEANCOLOUR_GLO_BGC_L3_MY_009_103, Issue 5.1, Mercator Ocean International, https://documentation.marine.copernicus.eu/QUID/CMEMS-OC-QUID-009-101to104-111-113-116-118.pdf (last access: 1 September 2025), 2025b.

Gomes, A. C., Alcântara, E., Rodrigues, T., and Bernardo, N.: Satellite estimates of euphotic zone and Secchi disk depths in a colored dissolved organic matter-dominated inland water, Ecol. Indic., 110, 105848, https://doi.org/10.1016/j.ecolind.2019.105848, 2020.

Harvey, E. T., Kratzer, S., and Philipson, P.: Satellite-based water quality monitoring for improved spatial and temporal retrieval of chlorophyll-*a* in coastal waters, Remote Sens. Environ., 158, 417–430, https://doi.org/10.1016/j.rse.2014.11.017, 2015.

Hipel, K. W. and McLeod, A. I.: Time series modelling of water resources and environmental systems, vol. 45, Elsevier, https://doi.org/10.1016/s0167-5648%2808%29x7026-1, 1994.

Hirsch, R. M., Slack, J. R., and Smith, R. A.: Techniques of trend analysis for monthly water quality data, Water Resour. Res., 18, 107–121, https://doi.org/10.1029/WR018i001p00107, 1982.

Hughes, C. W. and Williams, S. D. P.: The color of sea level: Importance of spatial variations in spectral shape for assessing the significance of trends, J. Geophys. Res.-Oceans, 115, 148–227, https://doi.org/10.1029/2010JC006102, 2010.

Morel, A., Huot, Y., Gentili, B., Werdell, P. J., Hooker, S. B., and Franz, B. A.: Examining the consistency of products derived from various ocean color sensors in open ocean (Case 1) waters in the perspective of a multi-sensor approach, Remote Sens. Environ., 111, 69–88, https://doi.org/10.1016/j.rse.2007.03.012, 2007.

Son, S., Nezlin, N. P., and Lance, V. P.: Assessing water clarity in the Chesapeake Bay using satellite-derived Secchi disk depth, Int. J. Appl. Earth Obs., 140, 104574, https://doi.org/10.1016/j.jag.2025.104574, 2025.

State Planet, 7-osr10, 11, 2026
https://doi.org/10.5194/sp-7-osr10-11-2026
© Author(s) 2026. This work is distributed under
the Creative Commons Attribution 4.0 License.

Long term trends and variability of the mixed layer depth in the Baltic Sea

Urmas Raudsepp, Ulvi Ahmadov, Ilja Maljutenko, Amirhossein Barzandeh, Mariliis Kõuts, and Priidik Lagemaa

Tallinn University of Technology, Ehitajate tee 5, 19086, Tallinn, Estonia

Correspondence: Ilja Maljutenko (ilja.maljutenko@taltech.ee)

Received: 6 August 2025 – Discussion started: 25 September 2025
Revised: 1 July 2026 – Accepted: 10 August 2026 – Published: 30 September 2026

Abstract. The depth of the upper mixed layer (MLD) in the Baltic Sea is a critical physical parameter that influences heat exchange, nutrient cycling, and oxygenation in this semi-enclosed basin. Variations in MLD have significant ecological consequences: a shallower mixed layer restricts the supply of oxygen and nutrients to deeper waters, potentially exacerbating hypoxia, whereas deeper mixing in previously ice-covered areas can enhance ventilation and nutrient entrainment.

To investigate long-term MLD variability, we analyzed a 30-year (1993–2023) high-resolution ocean reanalysis data set across the Baltic Sea. The results reveal pronounced spatial heterogeneity in MLD trends. In the western and southern Baltic, the MLD has become shallower, driven by surface warming and intensified stratification that stabilizes the upper layer. Conversely, in the eastern and northern Baltic, MLD has deepened, coinciding with reduced winter sea-ice cover and increasing wind speeds that promote wind-driven mixing – despite concurrent warming, increased precipitation, and enhanced stratification.

These region-specific trends highlight the complex interplay among warming, ice loss, and stratification in shaping upper-ocean dynamics. Our findings provide a baseline for understanding mixed-layer variability in the Baltic Sea under climate change and emphasize the need to consider regional differences in future projections.

1 Introduction

The oceanic upper Mixed Layer Depth (MLD) is a fundamental physical parameter governing the exchange of heat, momentum, and gases between the ocean and atmosphere. It plays a central role in modulating climate variability, regulating marine biogeochemical processes, and influencing the structure and productivity of marine ecosystems (Lorbacher et al., 2006; Wang et al., 2022). Variability in MLD is driven by atmospheric forcing (wind stress, air temperature, radiation, and precipitation), surface buoyancy fluxes, and oceanic dynamics, such as eddies and currents, with pronounced seasonal and regional differences (de Boyer Montégut et al., 2004; Treguier et al., 2023).

Globally, the MLD responds to climatic shifts by altering the vertical structure and stratification of the upper ocean (Li et al., 2020; Sallée et al., 2021). In equatorial regions, persistent heating and weak wind stress maintain a shallow MLD, whereas in mid- and high latitudes, stronger winds and surface cooling during winter promote deepening through enhanced vertical mixing and convective processes (Somavilla et al., 2017; Gao et al., 2023; Sallée et al., 2021). The response of the MLD to climate change is not uniform: increasing stratification from surface warming tends to shoal the MLD (Li et al., 2020), whereas intensified wind stress or buoyancy loss can promote deeper mixing (Sallée et al., 2021; Gao et al., 2023; Amaya et al., 2021). These changes have far-reaching implications for heat storage, ocean carbon uptake, and nutrient fluxes, particularly under scenarios of continued global warming (Li et al., 2020; Sallée et al., 2021; Shi et al., 2022).

In semi-enclosed marginal seas like the Baltic Sea, MLD variability reflects a complex interplay of atmospheric forcing (Liblik et al., 2020; Liblik and Lips, 2019; Bulczak et al., 2024), bathymetric constraints (Liblik et al., 2020; Bul-

Table 1. Product table.

Product ref. no.	Product ID & type	Data access	Documentation
1	BALTICSEA_MULTIYEAR_PHY_003_011; Numerical models	EU Copernicus Marine Service Product (2025)	Quality Information Document (QUID): Panteleit et al. (2025); Product User Manual (PUM): Ringgaard et al. (2024)
2	ERA5; Numerical models	Copernicus Climate Change Service (2023)	Product reference: Hersbach et al. (2023) Journal article: Hersbach et al. (2020)

czak et al., 2024), freshwater inflows (Hordoir and Meier, 2012; Väli et al., 2013), and permanent haline stratification (Väli et al., 2013; Liblik and Lips, 2019). The Baltic Sea, with its strong horizontal salinity gradients and seasonal ice cover in the northern basins, presents a unique environment for studying MLD dynamics in a high-latitude coastal setting. Seasonal patterns dominate, with deep wintertime MLDs driven by wind mixing and surface cooling, and shallow summertime MLDs resulting from thermal stratification (Bulczak et al., 2024). Spatial heterogeneity is also prominent: the Baltic Proper often exhibit deeper mixed layers due to enhanced wind exposure and reduced freshwater influence, whereas coastal and ice-covered regions display shallower MLDs (Panteleit et al., 2025).

Recent studies using high-resolution reanalysis datasets and model simulations have begun to reveal long-term trends in MLD across the Baltic Sea (Meier at al., 2022a; Dutheil et al., 2023). These analyses suggest spatially variable responses to climate forcing, with evidence of deepening MLDs in the northern and eastern sub-basins – potentially linked to reduced winter ice cover – and shoaling trends in southern and central areas, possibly related to increased stratification and changes in halocline dynamics.

Given the MLD's pivotal role in modulating biological productivity, carbon cycling, and hypoxia development, understanding its long-term variability is essential for predicting future changes in the Baltic Sea ecosystem. This study aims to assess the spatial and temporal variability of MLD across the Baltic Sea from 1993 to 2023, utilizing state-of-the-art reanalysis products (Table 1, product ref. no. 1). Specifically, we investigate the trends, regional differences, and potential climate forcings of the trends in MLD, with the goal of providing a robust basis for evaluating the ecological and biogeochemical consequences of mixed-layer variability in a warming world.

2 Data and methods

The Baltic Sea physics reanalysis multi-year product (BAL-MYP; product ref. no. 1) is derived from the ocean model NEMO v4.0 (Madec et al., 2019). It assimilates satellite observations of sea surface temperature (SST) (EU Copernicus Marine Service Product, 2025) and in-situ temperature and salinity profiles from the ICES database (ICES Bottle and low-resolution CTD dataset, 2022). The model data is provided on a grid with a horizontal resolution of 1 nmi, including 56 vertical layers, covering the entire Baltic Sea and the transition zone to the North Sea. The dataset covers the period from 1993 to 2023, with the model setup detailed in the Product User Manual (Ringgaard et al., 2024).

The BAL-MYP has been extensively validated, as documented in the Quality Information Document (QuID; Panteleit et al., 2025), focusing on the period from 1 January 1993 to 31 December 2018. Additionally, the BAL-MYP data were evaluated using a clustering method with the K-means algorithm (Raudsepp and Maljutenko, 2022), which provided insights into the reanalysis accuracy by categorising errors (Lindenthal et al., 2024). 57 % of the data are clustered with a bias of $dS = -0.40\,g\,kg^{-1}$ and $dT = -0.02\,°C$, encompassing 57 % of all data points with RMSE $S = 0.92\,g\,kg^{-1}$ and $T = 0.54\,°C$ (Lindenthal et al., 2024). These points are distributed throughout the Baltic Sea. Clusters with high positive and negative temperature biases account for 11 % and 8 % of total points, respectively, with marginal salinity biases and relatively even spatial distributions across the Baltic Sea. 26 % of the points have low temperature but high salinity errors, both negative and positive, predominantly located in the southwestern Baltic Sea, indicating occasional underestimation or overestimation of the inflow/outflow salinity (Lindenthal et al., 2024).

The MLD, also referred to as the Upper Mixed Layer (UML), was included in the analysis using data from a multi-year reanalysis product (product ref. no. 1). The MLD was calculated based on density stratification following the method of de Boyer Montégut et al. (2004), which defines MLD as the depth at which seawater density deviates from the reference density at 10 m depth by a specified threshold. For the Baltic Sea, this threshold was adjusted to $0.03\,kg\,m^{-3}$ to better represent the characteristics of the regional UML (Panteleit et al., 2025).

Panteleit et al. (2025) has performed validation of the reanalysis product of the MLD (product ref. no. 1) with comparison to the observations at eight stations. From observations, the MLD is derived from salinity and temperature pro-

files of ICES-HELCOM observations that are located over the open parts of the Baltic Sea. The cRMSD of MLD for the reanalysis product (product ref. no. 1) is 11.34 m and correlation coefficient is 0.69 for the whole reanalysis period 1993–2019 in the bulk comparison of MLD product with observations. On average the reanalysis product underestimates MLD by 7 m.

The annual cycle of the MLD of the products follows the MLD calculated from observations for the whole reanalysis period (Panteleit et al., 2025). It is possible to observe the seasonal variability of the MLD product in summer and winter. During the summer, the MLD is lower, and during the winter, the MLD is deeper. In the Baltic Proper the MLD is small from late spring until end of summer reaching values of 10–20 m during the period 1 January 1993–30 December 2019. In autumn and winter, MLD increases considerably with a maximum MLD of 70 m. In the Gulf of Bothnia, the MLD varies from 10 to 80 m deep during the reanalysis period. The MLD is small from late spring until the end of summer reaching values of 10–15 m, and in autumn and winter, MLD increases considerably with a maximum MLD of 80 m.

Atmospheric data were sourced from the ERA5 hourly dataset on single levels, available from 1940 to the present (product ref. no. 2), and accessed via the Copernicus Climate Data Store. For this study, based on the availability of MLD data, the analysis focuses on the period 1993–2023. Daily means were calculated for the following parameters: 2 m air temperature, total precipitation, and the wind speed, estimated from the daily averaged zonal (u) and meridional (v) components of 10 m wind.

Higher potential energy anomaly (PEA) corresponds to a more stratified water column, i.e. more energy is required to mix the water column uniformly. The PEA below the MLD was computed to quantify stratification in the Baltic Sea. Daily temperature and salinity profiles obtained from the CMEMS dataset were initially subsetted within a defined geographic region and vertical extent (0.5–250 m). Absolute Salinity and Conservative Temperature were calculated from Practical Salinity and potential temperature using the Gibbs SeaWater (GSW) Oceanographic Toolbox. These derived quantities were subsequently used to compute seawater density (ρ) across pressure levels determined from depth and latitude. To isolate stratification effects, density profiles were masked above the daily MLD, with layers below this depth considered for PEA calculation. The calculation of PEA follows the formula:

$$\mathrm{PEA} = \frac{1}{H-h}\int_{h}^{H} g\,(\rho(z)-\overline{\rho})(z-h)\mathrm{d}z \qquad (1)$$

where g is gravitational acceleration, $\rho(z)$ is the density at depth z, $\overline{\rho}$ is the mean density below the MLD (from depth h to bottom depth H) and z is the depth. The integral of density deviations from the layer-wise mean density, weighted by gravitational acceleration and depth increments, was performed to yield daily PEA fields. These fields were normalized by local bathymetric depth, thus enabling robust spatial comparison. Subsequently, a linear trend analysis was executed on normalized daily PEA over the 1993–2023 period.

3 Results and Discussion

The climatological mean MLD exhibits pronounced regional differences across the Baltic Sea (Fig. 1a). The presented fields (Fig. 1) were computed from monthly averaged data derived from the high-resolution oceanographic reanalysis. Deeper mixed layers occur in the central and southern Baltic basins (e.g., Gotland Basin), while shallower layers dominate in coastal areas and the northern basins, such as the Gulf of Finland and Bothnian Bay. These differences reflect the influence of bathymetry, wind exposure, and surface buoyancy forcing (Lass and Matthäus, 1996; Liblik and Lips, 2012; Liblik et al., 2020).

Figure 1b shows the spatial distribution of the standard deviation of MLD across the Baltic Sea, based on daily-averaged data over the period 1993–2023. This metric represents the statistical dispersion of MLD values at each location – that is, how far individual daily MLD values deviate from the long-term average at that point. Since the standard deviation is derived from daily MLD values over multiple years, it represents how strongly MLD values tend to deviate from their long-term average on a daily basis. The resulting spatial pattern shows clearly defined gradients in standard deviation across the basin. Higher values, ranging from approximately 5 to 15 m, are observed in deeper areas such as eastern parts of BOS, NBP, and SBP. In contrast, much lower standard deviations – typically below 5 m – are found in shallower and more enclosed regions such as the BOB, GOF.

The spatially averaged time series of MLD from 1993 to 2023 (Fig. 2a) shows strong seasonal fluctuations superimposed on a non-significant long-term trend. While individual years exhibit pronounced peaks and troughs, there is an overall shoaling tendency, particularly in winter months, which is consistent with previous studies in the southern Baltic Sea (Bulczak et al., 2024). Such reductions are attributed to increasing thermal stratification and warmer surface waters, both of which inhibit vertical mixing (Bulczak et al., 2024).

The MLD follows a clear seasonal cycle, as illustrated by the monthly climatology (Fig. 2b). Maximum depths are typically observed during winter (October–March), driven by convective mixing under cold air temperatures. Minimum MLDs occur in summer (June–August), when surface heating leads to strong stratification and shallow mixing layers. The transitional periods in spring and autumn are characterized by rapid changes in MLD, reflecting the formation and erosion of seasonal thermoclines. These patterns are consistent with prior studies (e.g., Fu et al., 2012; Bulczak et al.,

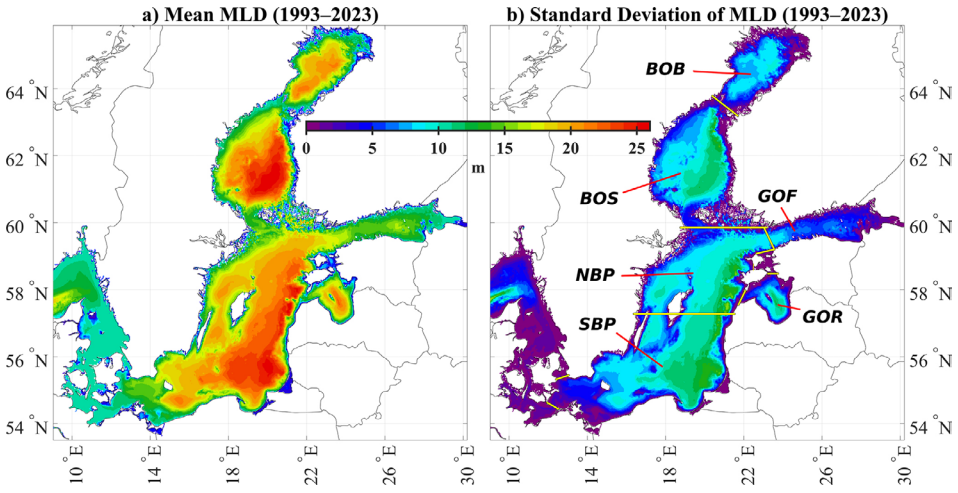


Figure 1. Spatial distribution of the long-term mean **(a)** and standard deviation **(b)** of MLD in the Baltic Sea over the period 1993–2023 (Table 1, product ref. no. 1). Boundaries of major Baltic Sea sub-basins are shown with yellow lines (IHO 2012): the Bothnian Bay (BOB), Bothnian Sea (BOS), Gulf of Finland (GOF), Northern Baltic Proper (NBP), Gulf of Riga (GOR), and Southern Baltic Proper (SBP).

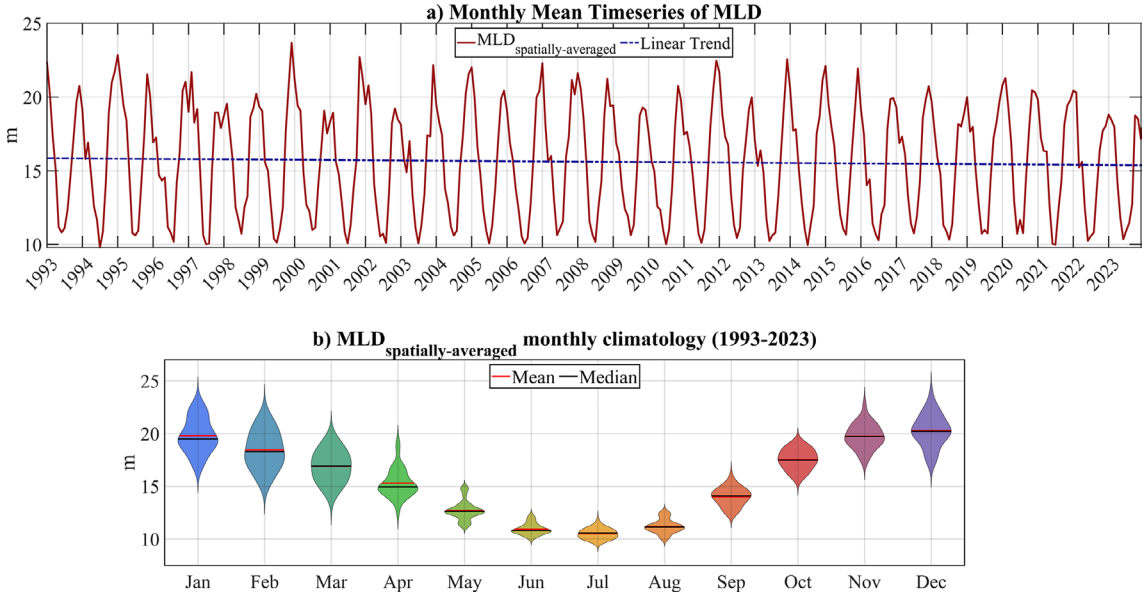


Figure 2. Monthly mean MLD variability in the Baltic Sea over the 29-year period from 1993 to 2023 (Table 1, product ref. no. 1). **(a)** Monthly mean MLD time series alongside a linear trend (red dashed line), highlighting pronounced seasonal variability but minimal overall long-term trend. **(b)** Violin plots illustrating statistical distributions of monthly MLD values, clearly distinguishing deeper, more variable winter mixed layers (December–February), caused by enhanced vertical mixing and cooling events, from shallower, stable summer conditions (June–August) associated with surface warming and increased stratification.

2024) documenting deep winter mixing and shallow summer layers across the Baltic.

The spatial pattern of MLD linear trends (Fig. 3a) reveals a striking west–east dipole: MLD has shoaled in the western Baltic (e.g., western Baltic Proper, Bothnian Sea), while deepening trends are observed in the eastern basins (e.g., eastern coasts of the Baltic Sea, Gulf of Finland, Gulf of Riga, and Eastern Bothnian Bay). This feature is repeated on seasonal trends except for summer (Fig. 4). The spatial contrast suggests region-specific responses to environmental changes. Sea ice volume trends (Fig. 3b), computed for the ice season (November–May), show significant declines. Reduced ice cover extends the open-water period and permits more wind-driven mixing, which likely contributes to the observed deepening of MLD in the eastern/northern regions (Raudsepp et al., 2020). This interpretation is consistent with Singh et al. (2025), who found significant reductions in ice thickness and extent throughout the Baltic.

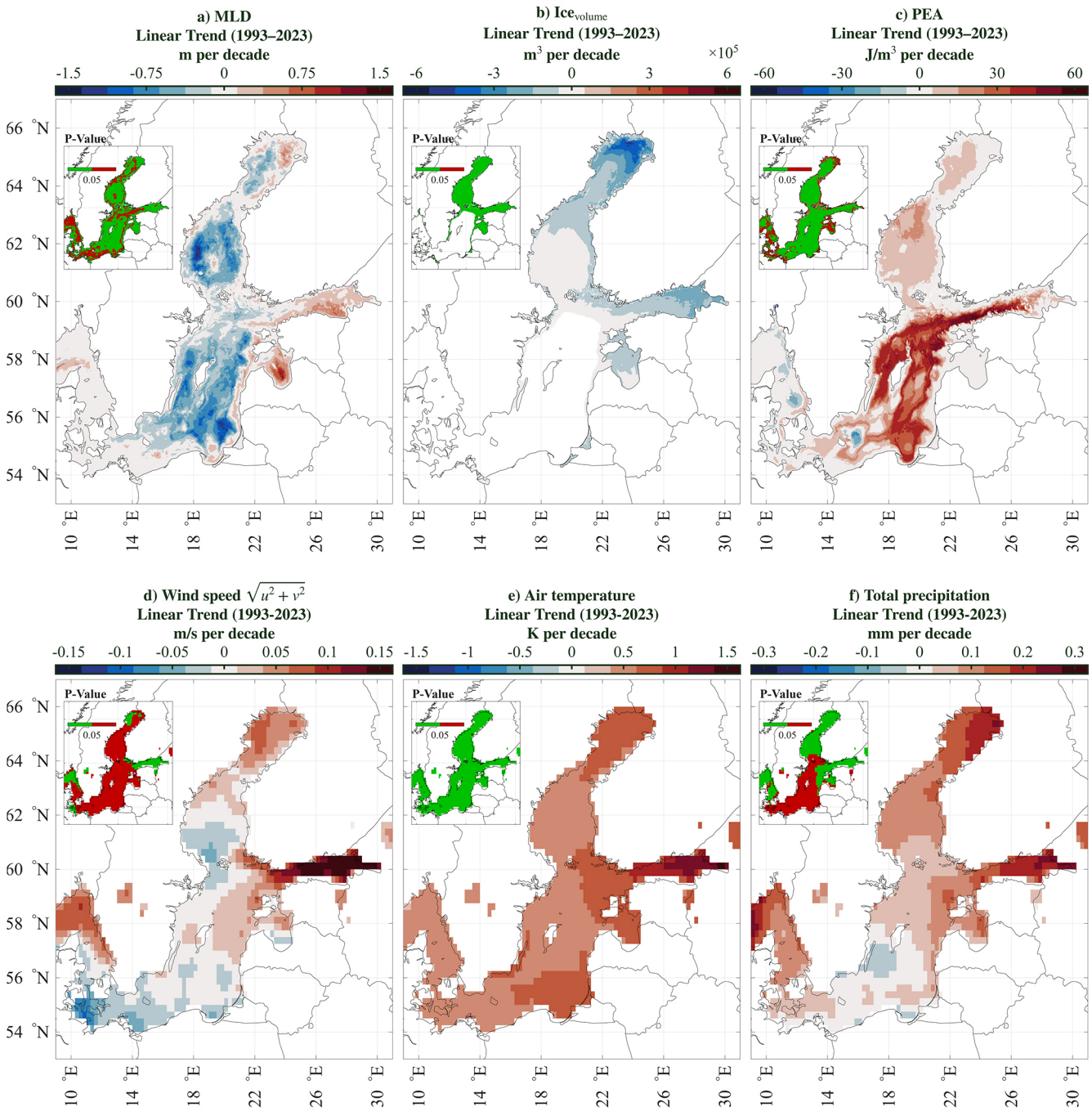


Figure 3. Linear trends (1993–2023) of oceanic and atmospheric parameters in the Baltic Sea region. **(a)** Mixed layer depth (MLD) Eq. (1), **(b)** sea ice volume trend during the ice season (November–May), **(c)** potential energy anomaly (PEA), **(d)** wind speed, **(e)** air temperature, and **(f)** total precipitation (panels **a–c** from product ref. no. 1; panels **d–f** from product ref. no. 2). Inset maps in each panel display p-values associated with the linear trends at each grid point. Areas with $p < 0.05$ (shaded in green) indicate statistically significant trends at the 95 % confidence level, while red areas denote non-significant trends. These p-value maps provide an *uncertainty* metric for the estimated trends and help to distinguish robust regional changes from areas of high variability or low confidence.

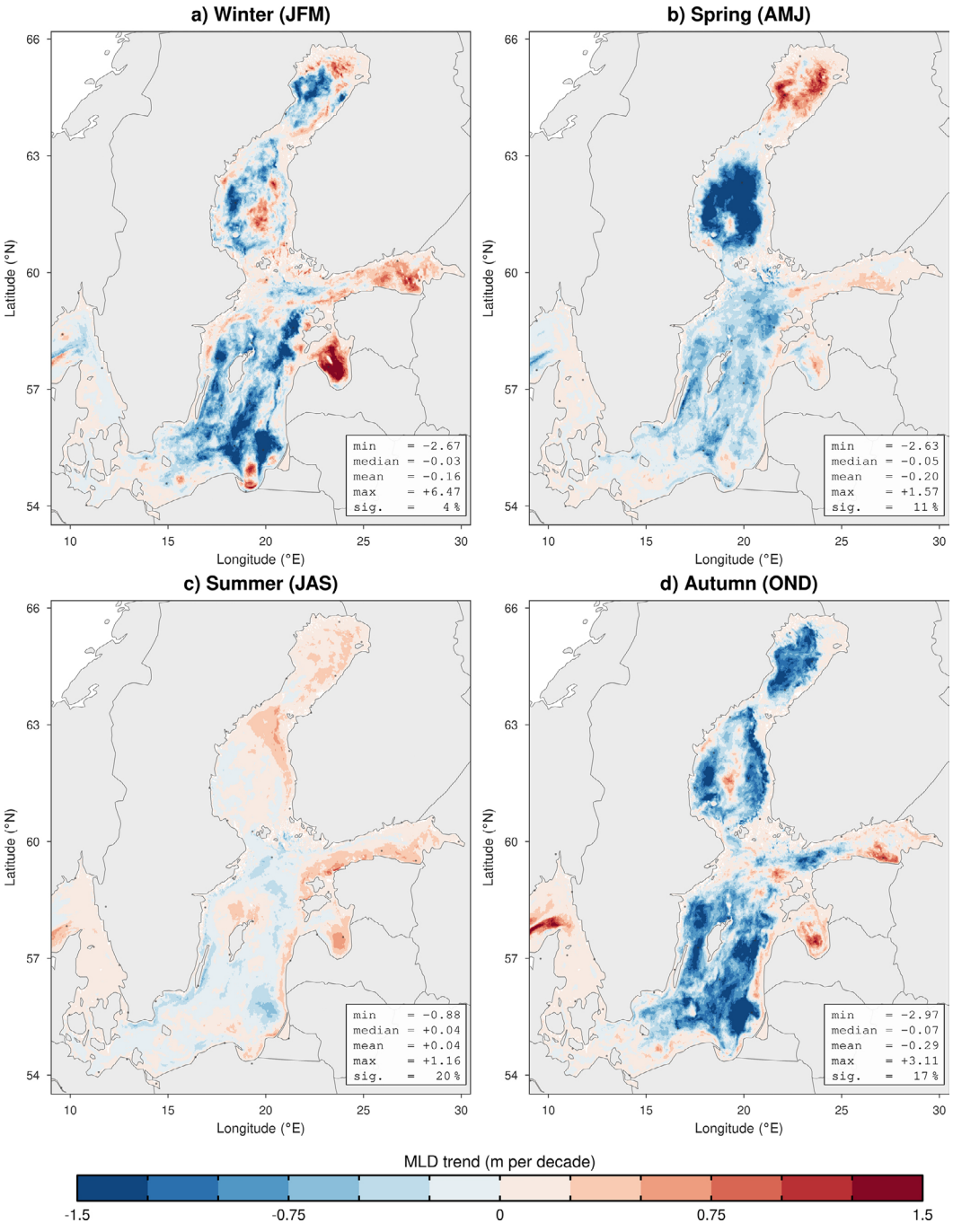


Figure 4. Seasonal linear trends (1993–2023) of mixed layer depth (MLD) in the Baltic Sea region. **(a)** Winter (JFM), **(b)** Spring (AMJ), **(c)** Summer (JAS), and **(d)** Autumn (OND) trends derived from product ref. no. 1. The summary box in the lower-right of each panel reports basin-wide statistics of the underlying slope field – minimum, median, mean, and maximum values (m per decade) – together with the fraction of grid cells (sig.) where the trend is statistically significant. The colorbar is saturated at ±1.5 m per decade; reported minimum and maximum values may therefore exceed the displayed range.

The PEA trends shown in Fig. 3c provide a diagnostic of the stratification barrier relevant to mixed-layer evolution. Positive trends indicate that the water column has become more resistant to further vertical mixing, which favors shallower MLDs where atmospheric forcing is not sufficient to overcome this barrier. Areas with positive PEA trends correspond broadly to regions of MLD shoaling. Conversely, weaker or negative PEA trends indicate a reduced stratification barrier and are consistent with deeper mixing in parts of the eastern and northern Baltic, where reduced sea ice cover

increases the exposure of the water column to wind-driven mixing. As defined in the Methods, the PEA diagnostic used here is evaluated beneath the diagnosed MLD. This formulation is used because the mixed layer itself is already approximately homogeneous, while the density structure below the MLD controls the resistance to further deepening. The diagnostic therefore does not represent the external energy available for mixing, but rather the internal oceanic stratification barrier that must be overcome by mixing processes such as wind-driven turbulence and convective cooling. The MLD trend should therefore be interpreted as the outcome of a balance between stabilizing stratification and mixing supplied by other drivers.

Wind speed trends (Fig. 3d) are spatially heterogeneous and generally weak. Although some localized increases are evident, there is no basin-wide pattern suggesting wind changes as the primary driver of MLD trends. This aligns with previous assessments indicating no clear overall trend in regional wind speed over recent decades (Meier et al., 2022b). In contrast, air temperature trends (Fig. 3e) are uniformly positive, with strongest warming observed in the western Baltic. Warmer air temperatures reduce wintertime surface heat loss, weakening convective mixing and enhancing stratification. This likely contributes to the observed shoaling of MLD in the southwestern basins. Meanwhile, in the eastern Baltic, the concurrent retreat of ice cover may counteract some warming effects, allowing for deeper winter mixing. Precipitation trends (Fig. 3f) are also positive across most of the basin, particularly in the northeastern catchments. Increased rainfall enhances surface freshwater input, which strengthens stratification and supports MLD shoaling. The alignment of increasing precipitation and positive PEA trends in the western Baltic reinforces the role of freshwater in inhibiting mixing.

The pronounced spatial heterogeneity in mean MLD, with deeper layers in the central/southern basins (e.g., Gotland Basin) and shallower layers in coastal zones and northern basins (e.g., Gulf of Finland, Bothnian Bay), aligns well with established knowledge. Bathymetry sets fundamental limits (Omstedt et al., 2004; Leppäranta and Myrberg, 2009), while greater wind exposure over the open central basins promotes deeper mixing compared to the more sheltered coastal and archipelago regions (Kõuts and Omstedt, 1993; Miettunen et al., 2024). Surface buoyancy forcing, particularly the strong haline stratification prevalent in the Baltic (Reissmann et al., 2009; Liblik et al., 2017), is a dominant factor suppressing MLD, especially in areas with significant freshwater inflow like the northern gulfs and nearshore zones. The higher temporal variability (standard deviation) observed in deeper basins (Fig. 1b) reflects their greater responsiveness to synoptic-scale wind events and seasonal buoyancy changes compared to the persistently stratified and shallow regions (Umlauf et al., 2018).

In the western subbasins, the overall shoaling is mechanistically linked to increasing thermal stratification driven by rising air temperatures (Lehmann et al., 2022; Meier et al., 2022a, b) and enhanced precipitation (Rutgersson et al., 2002), both contributing to increased PEA, which stabilizes the water column and impedes vertical mixing.

For the eastern subbasins, the observed deepening trends in the Gulf of Finland, Eastern Gotland Basin, and Eastern Bothnian Bay appear counterintuitive in a warming climate. However, the dramatic decline in sea ice volume (Singh et al., 2025) offers a key mechanistic explanation. Reduced ice cover extends the open-water season – especially during autumn to spring when wind energy is highest – allowing significantly more wind-driven mixing (Vihma and Haapala, 2009; Uotila et al., 2015). This region also exhibits weaker positive or slightly negative PEA trends (Fig. 3c), indicating reduced stratification. The retreat of ice likely counteracts expected thermal stratification from warming by enhancing wind mixing and reducing the freshwater lens effect from melting ice (Hordoir et al., 2019).

Enhanced ageostrophic currents (Barzandeh et al., 2024), driven by increased wind stress over newly ice-free areas (Fig. 3b), may further contribute to deeper mixing due to the loss of the ice damping effect. Our observed MLD deepening (Fig. 3a) aligns with these dynamics (Fig. 3d) and is supported by reduced ice cover (Fig. 3b), which increases wind stress impact and vertical shear at density interfaces. This weakens stratification via Ekman pumping, submeso/mesoscale instabilities, and inertial oscillations (Umlauf et al., 2018; Chrysagi et al., 2021), contributing to deeper mixed layers.

The accompanying weak or negative PEA trends (Fig. 3c) further reflect this stratification reduction. Additionally, Bashiri et al. (2024) report intensified marine heatwaves (MHWs) in the eastern Baltic: atmospheric blocking in summer leads to surface-intensified warming and temporary MLD shoaling, while wintertime advection promotes subsurface warming and suppressed convection. Although both western and eastern Baltic regions exhibit air temperature increases, the influence of atmospheric warming on MLD deepening appears less significant in the east, where oceanic and dynamic atmospheric processes likely dominate stratification and MLD variability.

The observed changes in MLD have significant implications for the Baltic Sea's physical and ecological state. A deeper winter mixed layer in previously ice-covered regions (e.g. northern gulfs) can lead to greater ventilation of the water column (Meier et al., 2019; Droste et al., 2025). This may be a positive outcome in terms of oxygen distribution: deeper mixing in winter helps transport oxygen from the surface to intermediate depths, which can alleviate oxygen depletion that often develops below the halocline (Kõuts et al., 2021a). However, the flip side is that shallower mixing in the central and southern Baltic can exacerbate oxygen stress in those areas. These processes, combined with episodic inflows of warm saline water that strengthen stratification, have been shown to exacerbate oxygen depletion in the western

Baltic (Barghorn et al., 2025). When the mixed layer no longer reaches as deep into the halocline, less oxygen is injected into the deep layer each winter. Over time, this contributes to more severe or persistent hypoxia in the deeper basins (Krapf et al., 2022). The Baltic Sea is already well known for its extensive oxygen-depleted bottom areas, often referred to as "dead zones" (Carstensen et al., 2014; Kõuts et al., 2021a), and stronger stratification only worsens this issue by further isolating the deep water. Recent studies have indeed reported an increasing frequency of hypoxic events in the Baltic Proper, correlating with intensifying stratification and warming (Rolff et al., 2022; Hepach et al., 2024; Liblik et al., 2025; Stockmayer and Lehmann, 2023). Our findings of MLD shoaling in the main basins are thus a warning sign of potentially deteriorating deep-water oxygen conditions if these trends persist.

Another important consideration is the impact on nutrient cycling and biological productivity. The MLD forms the interface between the deep layer and the euphotic zone, thereby controlling growing conditions and nutrient availability for phytoplankton (Wasmund et al., 1998; Hieronymus et al., 2018). A shallower winter mixed layer in the central Baltic means that come spring, a smaller reservoir of deep nutrient-rich water has been entrained to the surface layer (Kõuts et al., 2021b). This could limit the amount of nutrients (like nitrate and phosphate) available for the spring phytoplankton bloom, possibly reducing the magnitude and duration of the bloom (Reissmann et al., 2009). Areas with deepening MLD (e.g. the northern and eastern Baltic) might see enhanced nutrient entrainment, potentially hampering the effect of nutrient input reductions in coastal areas. It should be noted, however, that oxygen conditions strongly influence nutrient fluxes from sediments. Improved bottom-water oxygenation in coastal areas promotes nutrient retention within sediments, whereas increasing oxygen deficiency enhances the release of nutrients, particularly phosphorus, into the water column (Viktorsson et al., 2013; Bonaglia et al., 2014). Consequently, these opposing processes may partially offset the effects of changing stratification and could help explain why corresponding long-term ecosystem trends have not been consistently reported in recent Baltic Sea observations (Olofsson et al., 2020; Stoń-Egiert and Ostrowska, 2022).

Additionally, as shallow summer mixed layer (driven by increased stratification) prolongs periods of nutrient depletion in surface waters, organisms that can utilize alternate nutrient sources or fix nitrogen (e.g. cyanobacteria in summer) have an advantage (Munkes et al., 2021). Cyanobacteria can fix N_2 and thus dominate when nitrate is low and the water is stably stratified (Munkes et al., 2021; Spilling et al., 2025). A trend toward stronger stratification (Fig. 3c) could facilitate cyanobacteria blooms in the long term, since vertical mixing is less available to disrupt their suitable living conditions or to bring up nitrate. This is relevant because the Baltic Sea already experiences extensive cyanobacterial blooms in summer when stratification is strong (Kahru and Elmgren, 2014). We emphasize that MLD represents only one of several interacting factors influencing phytoplankton and cyanobacterial bloom dynamics in the Baltic Sea, alongside variables such as irradiance, and interspecific competition (Olofsson et al., 2020; Degerholm et al., 2006; Mohlin et al., 2012; Kahru et al., 2025). Consequently, the relationship between MLD and bloom development is unlikely to be linear, but can play an important role within the broader set of environmental drivers, especially in a longer time scale.

The physical changes we document are likely to have complex ecosystem effects, from altering the timing and composition of phytoplankton blooms to influencing higher-trophic-level processes that depend on the distribution of nutrients and oxygen. Our results also align with the emerging consensus from Baltic Sea climate assessments, which state that air and water temperatures are rising, and ice extent is decreasing (Meier et al., 2022b). These changes in turn modify physical oceanographic processes such as stratification and vertical mixing. The Baltic Sea is often cited as an amplified case of climate-driven change, reacting faster or more intensely than the global ocean due to its shallowness and restricted exchange (Hepach et al., 2024). The mixed layer trends we observe can thus be seen as part of this larger picture of a system in transition. In particular, the long-term shoaling of the winter mixed layer in the central Baltic is a strong indicator of how increased heat content and salt stratification are altering the fundamental vertical structure of the sea.

The changes in MLD carry important implications for the Baltic Sea ecosystem and biogeochemistry (Fig. 5). In areas where the winter mixed layer has shoaled, likely less oxygen is being delivered to the deep waters each year, which could exacerbate hypoxia and alter nutrient availability. Conversely, deeper winter mixing in the northern and eastern Baltic could improve water column ventilation, nutrient retention in the sediments and nutrient redistribution in those regions. Additionally, a trend toward stronger stratification and shallower summer mixed layers could benefit, in favourable combination with other factors, cyanobacterial blooms by prolonging surface nutrient depletion and stable conditions. These potential changes are obscured by the counteracting influence of oxygen conditions on nutrient dynamics and the complex set of additional factors influencing phytoplankton and cyanobacteria blooms in general.

Overall, the contrasting MLD trends suggest that different parts of the Baltic Sea will face distinct ecological challenges and feedback under continued climate change. Looking ahead, sustained observations and high-resolution modeling will be critical to track and predict how the Baltic Sea's mixed layer evolves under future warming scenarios – especially as winters with little or no ice and more intense summer stratification become increasingly common. By recognizing the region-specific nature of MLD responses, future

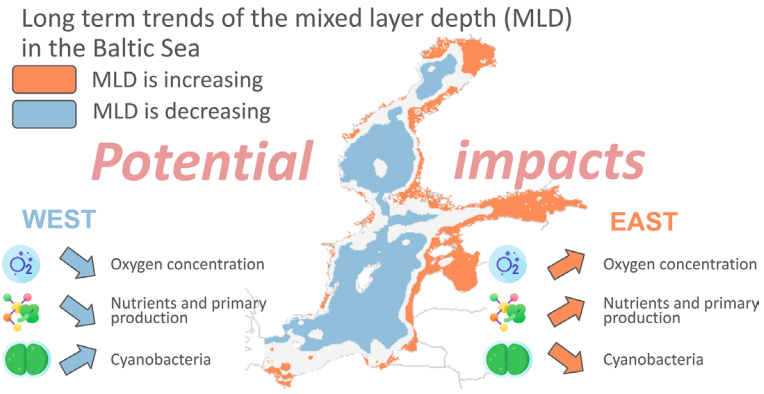


Figure 5. Infographic illustrating the potential relationship between mixed layer depth (MLD) trends and changes in the ecological state of the Baltic Sea, including various eutrophication indicators.

efforts can better anticipate the impacts of climate change on Baltic Sea conditions and ecosystem services.

4 Conclusions

Our study demonstrates that climate-driven changes in the Baltic Sea have led to divergent trends in MLD across different regions. Climate warming emerges as a fundamental driver: higher air and water temperatures, together with feedbacks like reduced ice cover and altered freshwater input, have created conditions for the mixed layer to shoal in some areas and deepen in others. The Baltic Sea's response to this global forcing is highly nuanced – regional differences (such as whether an area is seasonally ice-covered or influenced by strong haline stratification) modulate how the mixed layer responds. We found that from 1993 to 2023, Baltic Sea MLDs exhibit significant spatial and temporal variability, with clear trends linked to atmospheric warming, declining ice extent, and changing stratification patterns. The southern parts of the Baltic are shifting toward a more stratified state with generally shallower winter mixed layers, while the northern subbasins are experiencing enhanced winter mixing due to the loss of ice cover.

Data availability. The model products used in this study from both the Copernicus Marine Service and other sources are listed in Table 1.

Author contributions. UR designed the concept of this study, interpreted the results, and wrote the initial manuscript. UA performed the calculations and prepared the figures. AB and IM contributed to the manuscript development. MK contributed to the study of the variations of MLD on the biogeochemistry and ecology of the Baltic Sea. PL was responsible for the funding. All authors contributed to writing and revising the manuscript.

Competing interests. The contact author has declared that none of the authors has any competing interests.

Disclaimer. The Copernicus Marine Service offering is regularly updated to ensure it remains at the forefront of user requirements. In this process, some products may undergo replacement or renaming, leading to the removal of certain product IDs from the catalogue. If readers have any questions or require assistance regarding these modifications, please feel free to reach out to the Copernicus Marine Service user support team for further guidance. They will be able to provide the necessary information to address concerns and find suitable alternatives.

Publisher's note: Copernicus Publications remains neutral with regard to jurisdictional claims made in the text, published maps, institutional affiliations, or any other geographical representation in this paper. The authors bear the ultimate responsibility for providing appropriate place names. Views expressed in the text are those of the authors and do not necessarily reflect the views of the publisher.

Acknowledgements. OpenAI's GPT-5.x model was used to assist with drafting sections of the manuscript. All content was reviewed, verified, and approved by the authors.

Review statement. This paper was edited by Joanna Staneva and reviewed by two anonymous referees.

References

Amaya, D. J., Alexander, M. A., Capotondi, A., Deser, C., Karnauskas, K. B., Miller, A. J., and Mantua, N. J.: Are long-term changes in mixed layer depth influencing North Pacific marine heatwaves?, B. Am. Meteorol. Soc., 102, S59–S66, https://doi.org/10.1175/BAMS-D-20-0144.1, 2021.

Barghorn, L., Meier, H. E. M., Radtke, H., Neumann, T., and Naumov, L.: Warm saltwater inflows strengthen oxygen

depletion in the western Baltic Sea, Clim. Dyn., 63, 29, https://doi.org/10.1007/s00382-024-07501-x, 2025.

Barzandeh, A., Maljutenko, I., Rikka, S., Lagemaa, P., Männik, A., Uiboupin, R., and Raudsepp, U.: Sea surface circulation in the Baltic Sea: decomposed components and pattern recognition, Sci. Rep., 14, 18649, https://doi.org/10.1038/s41598-024-69463-8, 2024.

Bashiri, B., Barzandeh, A., Männik, A., and Raudsepp, U.: Variability of marine heatwaves' characteristics and assessment of their potential drivers in the Baltic Sea over the last 42 years, Sci. Rep., 14, 22419, https://doi.org/10.1038/s41598-024-74173-2, 2024.

Bonaglia, S., Deutsch, B., Bartoli, M., Marchant, H. K., and Brüchert, V.: Seasonal oxygen, nitrogen and phosphorus benthic cycling along an impacted Baltic Sea estuary: regulation and spatial patterns, Biogeochemistry, 119, 139–160, https://doi.org/10.1007/s10533-014-9953-6, 2014.

Bulczak, A. I., Nowak, K., Jakacki, J., Muzyka, M., Rak, D., and Walczowski, W.: Seasonal variability and long-term winter shoaling of the upper mixed layer in the southern Baltic Sea, Cont. Shelf Res., 276, 105232, https://doi.org/10.1016/j.csr.2024.105232, 2024.

Carstensen, J., Andersen, J. H., Gustafsson, B. G., and Conley, D. J.: Deoxygenation of the Baltic Sea during the last century, P. Natl. Acad. Sci. USA, 111, 5628–5633, 2014.

Chrysagi, E., Umlauf, L., Holtermann, P., Klingbeil, K., and Burchard, H.: High-resolution simulations of submesoscale processes in the Baltic Sea: The role of storm events, J. Geophys. Res.-Oceans, 126, e2020JC016411, https://doi.org/10.1029/2020JC016411, 2021.

Copernicus Climate Change Service, Climate Data Store: ERA5 hourly data on single levels from 1940 to present, Copernicus Climate Change Service (C3S) Climate Data Store (CDS) [data set], https://doi.org/10.24381/cds.adbb2d47, 2023.

de Boyer Montégut, C., Madec, G., Fischer, A. S., Lazar, A., and Iudicone, D.: Mixed layer depth over the global ocean: An examination of profile data and a profile-based climatology, J. Geophys. Res.-Oceans, 109, https://doi.org/10.1029/2004JC002378, 2004.

Degerholm, J., Gundersen, K., Bergman, B., and Söderbäck, E.: Phosphorus-limited growth dynamics in two Baltic Sea cyanobacteria, Nodularia sp. and Aphanizomenon sp., FEMS Microbiol. Ecol., 58, 323–332, https://doi.org/10.1111/j.1574-6941.2006.00180.x, 2006.

Droste, E. S., Bakker, D. C. E., Venables, H. J., Jones, E. M., Meredith, M. P., Dall'Olmo, G., Hoppema, M., Legge, O. J., Lee, G. A., and Queste, B. Y.: Sea ice controls net ocean uptake of carbon dioxide by regulating wintertime stratification, Commun. Earth Environ., 6, 457, https://doi.org/10.1038/s43247-025-02395-x, 2025.

Dutheil, C., Meier, H. E. M., Gröger, M., and Börgel, F.: Warming of Baltic Sea water masses since 1850, Clim. Dynam., 61, 1311–1331, https://doi.org/10.1007/s00382-022-06628-z, 2023.

EU Copernicus Marine Service Product: Baltic Sea Physics Reanalysis, Mercator Ocean international [data set], https://doi.org/10.48670/moi-00013, 2025.

Fu, W., She, J., and Dobrynin, M.: A 20-year reanalysis experiment in the Baltic Sea using three-dimensional variational (3DVAR) method, Ocean Sci., 8, 827–844, https://doi.org/10.5194/os-8-827-2012, 2012.

Gao, Z., Long, S.-M., Shi, J.-R., Cheng, L., Li, G., and Ying, J.: Indian Ocean mixed layer depth changes under global warming, Front. Clim., 5, 1112713, https://doi.org/10.3389/fclim.2023.1112713, 2023.

Madec, G., Bourdallé-Badie, R., Chanut, J., Clementi, E., Coward, A., Ethé, C., Iovino, D., Lea, D., Lévy, C., Lovato, T., Martin, N., Masson, S., Mocavero, S., Rousset, C., Storkey, D., Vancoppenolle, M., Müller, S., Nurser, G., Bell, M., and Samson, G.: NEMO ocean engine. Notes du Pôle de modélisation de l'Institut Pierre-Simon Laplace (IPSL), v4.0, Number 27, Zenodo, https://doi.org/10.5281/zenodo.3878122, 2019.

Hepach, H., Piontek, J., Bange, H. W., Barthelmeß, T., von Jackowski, A., and Engel, A.: Enhanced warming and bacterial biomass production as key factors for coastal hypoxia in the southwestern Baltic Sea, Sci. Rep., 14, 29442, https://doi.org/10.1038/s41598-024-80451-w, 2024.

Hersbach, H., Bell, B., Berrisford, P., Hirahara, S., Horányi, A., Muñoz-Sabater, J., Nicolas, J., Peubey, C., Radu, R., Schepers, D., Simmons, A., Soci, C., Abdalla, S., Abellan, X., Balsamo, G., Bechtold, P., Biavati, G., Bidlot, J., Bonavita, M., De Chiara, G., Dahlgren, P., Dee, D., Diamantakis, M., Dragani, R., Flemming, J., Forbes, R., Fuentes, M., Geer, A., Haimberger, L., Healy, S., Hogan, R.J., Hólm, E., Janisková, M., Keeley, S., Laloyaux, P., Lopez, P., Lupu, C., Radnoti, G., de Rosnay, P., Rozum, I., Vamborg, F., Villaume S., and Thépaut, J.-N.: The ERA5 global reanalysis, Q. J. Roy. Meteor. Soc., 146, 1999–2049, https://doi.org/10.1002/qj.3803, 2020.

Hersbach, H., Bell, B., Berrisford, P., Biavati, G., Horányi, A., Muñoz Sabater, J., Nicolas, J., Peubey, C., Radu, R., Rozum, I., Schepers, D., Simmons, A., Soci, C., Dee, D., and Thépaut, J.-N.: ERA5 hourly data on single levels from 1940 to present, Copernicus Climate Change Service (C3S) Climate Data Store (CDS) [data set], https://doi.org/10.24381/cds.adbb2d47, 2023.

Hieronymus, J., Eilola, K., Hieronymus, M., Meier, H. E. M., Saraiva, S., and Karlson, B.: Causes of simulated long-term changes in phytoplankton biomass in the Baltic proper: a wavelet analysis, Biogeosciences, 15, 5113–5129, https://doi.org/10.5194/bg-15-5113-2018, 2018.

Hordoir, R. and Meier, H. E. M.: Effect of climate change on the thermal stratification of the Baltic Sea: A sensitivity experiment, Clim. Dynam., 38, 1703–1713, https://doi.org/10.1007/s00382-011-1036-y, 2012.

Hordoir, R., Axell, L., Höglund, A., Dieterich, C., Fransner, F., Gröger, M., Liu, Y., Pemberton, P., Schimanke, S., Andersson, H., Ljungemyr, P., Nygren, P., Falahat, S., Nord, A., Jönsson, A., Lake, I., Döös, K., Hieronymus, M., Dietze, H., Löptien, U., Kuznetsov, I., Westerlund, A., Tuomi, L., and Haapala, J.: Nemo-Nordic 1.0: a NEMO-based ocean model for the Baltic and North seas – research and operational applications, Geosci. Model Dev., 12, 363–386, https://doi.org/10.5194/gmd-12-363-2019, 2019.

Kahru, M. and Elmgren, R.: Multidecadal time series of satellite-detected accumulations of cyanobacteria in the Baltic Sea, Biogeosciences, 11, 3619–3633, https://doi.org/10.5194/bg-11-3619-2014, 2014.

Kahru, M., Cahill, B., Elmgren, R., and Rehder, G.: What initiates cyanobacterial blooms in the Baltic Sea?, Harmful Algae, 148, 102924, https://doi.org/10.1016/j.hal.2025.102924, 2025.

Kõuts, T. and Omstedt, A.: Deep water exchange in the Baltic Proper, Tellus A, 45, 311–324, 1993.

Kõuts, M., Maljutenko, I., Elken, J., Liu, Y., Hansson, M., Viktorsson, L., and Raudsepp, U.: Recent regime of persistent hypoxia in the Baltic Sea, Environ. Res. Commun., 3, 075004, https://doi.org/10.1088/2515-7620/ac0cc4, 2021a.

Kõuts, M., Maljutenko, I., Liu, Y., and Raudsepp, U.: Nitrate, ammonium and phosphate pools in the Baltic Sea, in: Copernicus Marine Service Ocean State Report, Issue 5, J. Oper. Oceanogr., 14, s37–s48, https://doi.org/10.1080/1755876X.2021.1946240, 2021b.

Krapf, K., Naumann, M., Dutheil, C., and Meier, H. E. M.: Investigating hypoxic and euxinic area changes based on various datasets from the Baltic Sea, Front. Mar. Sci., 9, 823476, https://doi.org/10.3389/fmars.2022.823476, 2022.

Lass, H. U. and Matthäus, W.: On temporal wind variations forcing salt water inflows into the Baltic Sea, Tellus A, 48, 663–671, https://doi.org/10.1034/j.1600-0870.1996.t01-4-00005.x, 1996.

Lehmann, A., Myrberg, K., Post, P., Chubarenko, I., Dailidiene, I., Hinrichsen, H.-H., Hüssy, K., Liblik, T., Meier, H. E. M., Lips, U., and Bukanova, T.: Salinity dynamics of the Baltic Sea, Earth Syst. Dynam., 13, 373–392, https://doi.org/10.5194/esd-13-373-2022, 2022.

Leppäranta, M. and Myrberg, K.: Physical oceanography of the Baltic Sea, Springer Science & Business Media, https://doi.org/10.1007/978-3-540-79703-6, 2009.

Li, G., Cheng, L., Zhu, J., Trenberth, K. E., Mann, M. E., and Abraham, J. P.: Increasing ocean stratification over the past half-century, Nat. Clim. Chang., 10, 1116–1123, https://doi.org/10.1038/s41558-020-00918-2, 2020.

Liblik, T. and Lips, U.: Variability of synoptic-scale quasi-stationary thermohaline stratification patterns in the Gulf of Finland in summer 2009, Ocean Sci., 8, 603–614, https://doi.org/10.5194/os-8-603-2012, 2012.

Liblik, T. and Lips, U.: Stratification Has Strengthened in the Baltic Sea – An Analysis of 35 Years of Observational Data, Front. Earth Sci., 7, 174, https://doi.org/10.3389/feart.2019.00174, 2019.

Liblik, T., Skudra, M., and Lips, U.: On the buoyant sub-surface salinity maxima in the Gulf of Riga, Oceanologia, 59, 113–128, https://doi.org/10.1016/j.oceano.2016.10.001, 2017.

Liblik, T., Väli, G., Lips, I., Lilover, M.-J., Kikas, V., and Laanemets, J.: The winter stratification phenomenon and its consequences in the Gulf of Finland, Baltic Sea, Ocean Sci., 16, 1475–1490, https://doi.org/10.5194/os-16-1475-2020, 2020.

Liblik, T., Siht, E., Buschmann, F., Kaljumäe, M., Kikas, V., Lips, U., Luik, S. T., Maslova, D., Pärt, K., Salm, K., and Samlas, O.: Recent stagnation period and unprecedented deoxygenation in the Baltic Sea: causes and consequences, Front. Earth Sci., 13, 1638978, https://doi.org/10.3389/feart.2025.1638978, 2025.

Lindenthal, A., Hinrichs, C., Jandt-Scheelke, S., Kruschke, T., Lagemaa, P., van der Lee, E. M., Maljutenko, I., Morrison, H. E., Panteleit, T. R., and Raudsepp, U.: Baltic Sea surface temperature analysis 2022: a study of marine heatwaves and overall high seasonal temperatures, in: 8th edition of the Copernicus Ocean State Report (OSR8), edited by: von Schuckmann, K., Moreira, L., Grégoire, M., Marcos, M., Staneva, J., Brasseur, P., Garric, G., Lionello, P., Karstensen, J., and Neukermans, G., Copernicus Publications, State Planet, 4-osr8, 16, https://doi.org/10.5194/sp-4-osr8-16-2024, 2024.

Lorbacher, K., Dommenget, D., Niiler, P. P., and Köhl, A.: Ocean mixed layer depth: A subsurface proxy of ocean-atmosphere variability, J. Geophys. Res.-Oceans, 111, https://doi.org/10.1029/2003JC002157, 2006.

Meier, H. E. M., Edman, M., Eilola, K., Placke, M., Neumann, T., Andersson, H. C., Brunnabend, S.-E., Dieterich, C., Frauen, C., Friedland, R., Gröger, M., Gustafsson, B. G., Gustafsson, E., Isaev, A., Kniebusch, M., Kuznetsov, I., Müller-Karulis, B., Naumann, M., Omstedt, A., Ryabchenko, V., Saraiva, S., and Savchuk, O. P.: Assessment of uncertainties in scenario simulations of biogeochemical cycles in the Baltic Sea, Front. Mar. Sci., 6, 46, https://doi.org/10.3389/fmars.2019.00046, 2019.

Meier, H. E. M., Dieterich, C., Gröger, M., Dutheil, C., Börgel, F., Safonova, K., Christensen, O. B., and Kjellström, E.: Oceanographic regional climate projections for the Baltic Sea until 2100, Earth Syst. Dynam., 13, 159–199, https://doi.org/10.5194/esd-13-159-2022, 2022a.

Meier, H. E. M., Kniebusch, M., Dieterich, C., Gröger, M., Zorita, E., Elmgren, R., Myrberg, K., Ahola, M. P., Bartosova, A., Bonsdorff, E., Börgel, F., Capell, R., Carlén, I., Carlund, T., Carstensen, J., Christensen, O. B., Dierschke, V., Frauen, C., Frederiksen, M., Gaget, E., Galatius, A., Haapala, J. J., Halkka, A., Hugelius, G., Hünicke, B., Jaagus, J., Jüssi, M., Käyhkö, J., Kirchner, N., Kjellström, E., Kulinski, K., Lehmann, A., Lindström, G., May, W., Miller, P. A., Mohrholz, V., Müller-Karulis, B., Pavón-Jordán, D., Quante, M., Reckermann, M., Rutgersson, A., Savchuk, O. P., Stendel, M., Tuomi, L., Viitasalo, M., Weisse, R., and Zhang, W.: Climate change in the Baltic Sea region: a summary, Earth Syst. Dynam., 13, 457–593, https://doi.org/10.5194/esd-13-457-2022, 2022b.

Miettunen, E., Tuomi, L., Westerlund, A., Kanarik, H., and Myrberg, K.: Transport dynamics in a complex coastal archipelago, Ocean Sci., 20, 69–83, https://doi.org/10.5194/os-20-69-2024, 2024.

Mohlin, M., Roleda, M. Y., Pattanaik, B., Tenne, S. J., and Wulff, A.: Interspecific resource competition – combined effects of radiation and nutrient limitation on two diazotrophic filamentous cyanobacteria, Microb. Ecol., 63, 736–750, https://doi.org/10.1007/s00248-011-9964-y, 2012.

Munkes, B., Löptien, U., and Dietze, H.: Cyanobacteria blooms in the Baltic Sea: a review of models and facts, Biogeosciences, 18, 2347–2378, https://doi.org/10.5194/bg-18-2347-2021, 2021.

Olofsson, M., Suikkanen, S., Kobos, J., Wasmund, N., and Karlson, B.: Basin-specific changes in filamentous cyanobacteria community composition across four decades in the Baltic Sea, Harmful Algae, 91, 101685, https://doi.org/10.1016/j.hal.2019.101685, 2020.

Omstedt, A., Elken, J., Lehmann, A., and Piechura, J.: Knowledge of the Baltic Sea physics gained during the BALTEX and related programmes, Prog. Oceanogr., 63, 1–28, https://doi.org/10.1016/j.pocean.2004.09.001, 2004.

Panteleit, T., Verjovkina, S., Jandt-Scheelke, S., Spruch, L., and Huess, V.: EU Copernicus Marine Service Quality Information Document for the Baltic Sea Physics Reanalysis Product, BALTICSEA_MULTIYEAR_PHY_003_011, Issue 4.1, Mercator Ocean International, https://documentation.marine.copernicus.eu/QUID/CMEMS-BAL-QUID-003-011.pdf (last access: 11 June 2025), 2025.

Raudsepp, U. and Maljutenko, I.: A method for assessment of the general circulation model quality using the K-means clustering algorithm: a case study with GETM v2.5, Geosci. Model Dev., 15, 535–551, https://doi.org/10.5194/gmd-15-535-2022, 2022.

Raudsepp, U., Uiboupin, R., Laanemäe, K., and Maljutenko, I.: Geographical and seasonal coverage of sea ice in the Baltic Sea, J. Oper. Oceanogr., 13, S1–S172, https://doi.org/10.1080/1755876X.2020.1785097, 2020.

Reissmann, J. H., Burchard, H., Feistel, R., Hagen, E., Lass, H. U., Mohrholz, V., Nausch, G., Umlauf, L., and Wieczorek, G.: Vertical mixing in the Baltic Sea and consequences for eutrophication – A review, Prog. Oceanogr., 82, 47–80, 2009.

Ringgaard, I., Korabel, V., Spruch, L., Lindenthal, A., and Huess, V.: EU Copernicus Marine Service Product User Manual for the Baltic Sea Physics Reanalysis Product, BALTICSEA_MULTIYEAR_PHY_003_011, Issue 1.0, Mercator Ocean International, https://documentation.marine.copernicus.eu/PUM/CMEMS-BAL-PUM-003-011-012.pdf (last access: 11 June 2025), 2024.

Rolff, C., Walve, J., Larsson, U., and Elmgren, R.: How oxygen deficiency in the Baltic Sea proper has spread and worsened: The role of ammonium and hydrogen sulphide, Ambio, 51, 2308–2324, https://doi.org/10.1007/s13280-022-01738-8, 2022.

Rutgersson, A., Omstedt, A., and Räisänen, J.: Net precipitation over the Baltic Sea during present and future climate conditions, Clim. Res., 22, 27–39, https://doi.org/10.3354/cr022027, 2002.

Sallée, J.-B., Pellichero, V., Akhoudas, C., Pauthenet, E., Vignes, L., Schmidtko, S., Naveira Garabato, A., Sutherland, P., and Kuusela, M.: Summertime increases in upper-ocean stratification and mixed-layer depth, Nature, 591, 592–598, https://doi.org/10.1038/s41586-021-03303-x, 2021.

Shi, J., Tang, C., Liu, Q., Zhang, Y., Yang, H., and Li, C.: Role of mixed layer depth in the location and development of the Northeast Pacific warm blobs, Geophys. Res. Lett., https://doi.org/10.1029/2022GL098849, 2022.

Singh, S., Maljutenko, I., and Uiboupin, R.: Sea ice in the Baltic Sea during 1993/94–2020/21 ice seasons from satellite observations and model reanalysis, The Cryosphere, 19, 4741–4758, https://doi.org/10.5194/tc-19-4741-2025, 2025.

Somavilla, R., González-Pola, C., and Fernández-Diaz, J.: The warmer the ocean surface, the shallower the mixed layer. How much of this is true? J. Geophys. Res.-Oceans, 122, 7698–7716, https://doi.org/10.1002/2017JC013125, 2017.

Spilling, K., Vanharanta, M., Santoro, M., Villena-Alemany, C., Labrenz, M., Grossart, H. P., and Piwosz, K.: Picophytoplankton act as the primary consumers of excess phosphorus after the spring bloom in the eutrophic Baltic Sea, Limnol. Oceanogr., https://doi.org/10.1002/lno.70027, 2025.

Stockmayer, V. and Lehmann, A:. Variations of temperature, salinity and oxygen of the Baltic Sea for the period 1950 to 2020, Oceanologia, 65, 466–483, https://doi.org/10.1016/j.oceano.2023.02.002, 2023.

Stoń-Egiert, J. and Ostrowska, M.: Long-term changes in phytoplankton pigment contents in the Baltic Sea: Trends and spatial variability during 20 years of investigations, Cont. Shelf Res., 236, 104666, https://doi.org/10.1016/j.csr.2022.104666, 2022.

Treguier, A. M., de Boyer Montégut, C., Bozec, A., Chassignet, E. P., Fox-Kemper, B., McC. Hogg, A., Iovino, D., Kiss, A. E., Le Sommer, J., Li, Y., Lin, P., Lique, C., Liu, H., Serazin, G., Sidorenko, D., Wang, Q., Xu, X., and Yeager, S.: The mixed-layer depth in the Ocean Model Intercomparison Project (OMIP): impact of resolving mesoscale eddies, Geosci. Model Dev., 16, 3849–3872, https://doi.org/10.5194/gmd-16-3849-2023, 2023.

Umlauf, L., Holtermann, P. L., Gillner, C. A., Prien, R. D., Merckelbach, L., and Carpenter, J. R.: Diffusive convection under rapidly varying conditions, J. Phys. Oceanogr., 48, 1731–1747, https://doi.org/10.1175/JPO-D-18-0018.1, 2018.

Uotila, P., Vihma, T., and Haapala, J.: Atmospheric and oceanic conditions and the extremely low Bothnian Bay sea ice extent in 2014/2015, Geophys. Res. Lett., 42, 7740–7749, https://doi.org/10.1002/2015GL064901, 2015.

Väli, G., Meier, H. E. M., and Elken, J.: Simulated halocline variability in the Baltic Sea and its impact on hypoxia during 1961–2007, J. Geophys. Res.-Oceans, 118, 6982–7000, https://doi.org/10.1002/2013JC009192, 2013.

Vihma, T. and Haapala, J.: Geophysics of sea ice in the Baltic Sea: A review, Prog. Oceanogr., 80, 129–148, 2009.

Viktorsson, L., Ekeroth, N., Nilsson, M., Kononets, M., and Hall, P. O. J.: Phosphorus recycling in sediments of the central Baltic Sea, Biogeosciences, 10, 3901–3916, https://doi.org/10.5194/bg-10-3901-2013, 2013.

Wang, Z., Garcia, H. E., Boyer, T. P., Reagan, J., and Cebrian, J.: Controlling factors of the climatological annual cycle of the surface mixed layer oxygen content: A global view, Front. Mar. Sci., 9, 1001095, https://doi.org/10.3389/fmars.2022.1001095, 2022.

Wasmund, N., Nausch, G., and Matthäus, W.: Phytoplankton Spring Blooms in the Southern Baltic Sea – Spatio-Temporal Development and Long-Term Trends, J. Plankton Res., 20, 1099–1117, https://doi.org/10.1093/plankt/20.6.1099, 1998.

State Planet, 7-osr10, 12, 2026
https://doi.org/10.5194/sp-7-osr10-12-2026
© Author(s) 2026. This work is distributed under
the Creative Commons Attribution 4.0 License.

15 years of satellite, in-situ and reanalyzed salinity data: insights into sea surface salinity trends, variability, and water cycle links

Ana Claudia Parracho[1], Patricia Zunino[2], Michela Sammartino[3], Jacqueline Boutin[1], Eric Greiner[2], Bruno Buongiorno Nardelli[3], and Nicolas Kolodziejczyk[4]

[1]LOCEAN, Sorbonne Université, Paris, 75005, France
[2]Collecte Localisation Satellites (CLS), Ramonville-Saint-Agne, 31520, France
[3]National Research Council (CNR), Naples, 80133, Italy
[4]LOPS, Université de Bretagne Occidentale, Brest, 29280, France

Correspondence: Ana Claudia Parracho (ana-claudia.parracho@locean.ipsl.fr)

Received: 30 July 2025 – Discussion started: 6 October 2025
Revised: 27 May 2026 – Accepted: 14 June 2026 – Published: 30 September 2026

Abstract. Sea Surface Salinity (SSS) trends and variability have been studied for long periods of time, using historical archives and Argo float data. Studies in the past have shown that the long-term (50+ years) salinity trend patterns reveal freshening in the climatological fresh region and an increase in salinity in the already salty region, indicating an intensification of the hydrological cycle. However, especially before the Argo period, the spatial and temporal distributions of SSS were sparse and uneven. As of 2025, 15 years of satellite-derived sea surface salinity data are available with unprecedented temporal and global coverage. This is an opportunity to revisit trends and variability in SSS and its link to the intensification of the ocean water cycle. This study looks at linear trends and variability from different SSS datasets for the period between 2011 and 2024 (satellite era). An intercomparison of the trends estimated from the different datasets found a general good agreement between statistically significant trends in all datasets, both in terms of sign of the trends and intensity. Significantly positive trends were found for the North and South Atlantic, the tropical Pacific, and west of Australia; while negative trends were found in the North Pacific, Eastern Indian Ocean and the South Pacific convergence zone, as well as in the regions of the Congo and Amazon River plumes. In general, the saltier regions were found to be trending positively, except for the South Pacific Convergence Zone and East of Australia; while the fresher regions are becoming fresher, except for the Western Pacific. These trends were compared with longer term trends from 1960 to the present. While the relatively short time span limits the detection of climatic signals, some of the trends found in the satellite era were consistent with the long-term trends, most notably an intensification of the interbasin contrasts, with a salting in the Atlantic and a freshening in the northern Pacific. A comparison with the long-term trends also helped to distinguish between interannual to decadal variability and anthropogenic trends, with some of the shorter-term trends in the tropical Pacific for instance being a consequence of the multiple multi-year La Niña events during the satellite period.

Published by Copernicus Publications.

1 Introduction

Anthropogenic climate warming has been shown to intensify the global water cycle (e.g. Held and Soden, 2006; Douville et al., 2021). A warming climate increases the water-holding ability of the atmosphere, as per the Clausius-Clapeyron relation (Borger et al., 2022; Wan et al., 2024), which in turn enables more evaporation and potentially more precipitation. These variables are crucial to assess the intensification of the Earth water cycle, and possible increase in frequency and intensity of extreme events such as floods, droughts, and storms (e.g. O'Gorman, 2015; Gu et al., 2022). Yet, freshwater fluxes are challenging to measure reliably over the oceans and across long term time scales (Gulev et al., 2021). Hence, sea surface salinity (SSS) has been used as an indirect tracer of possible trends in freshwater cycle (Yu et al., 2020). The analysis of the SSS trends reveals the so-called "rich get richer" paradigm, i.e. dryer regions get dryer and wetter regions get wetter, that manifests at the ocean surface by saltier regions getting saltier in historical dataset and future projection (IPCC, 2021). This underlines the importance of using SSS as a source of insight into long-term variations of the water cycle and the effects of climate change (Yu et al., 2020).

Salinity trends have been studied in the past, using in situ data consisting of different combinations of Argo and historical archives. Durack and Wijffels (2010) looked at trends in global ocean salinity for the period between 1950 and 2000. They found that the 50-year linear surface salinity trend patterns follow the climatology patterns closely, highlighting a strengthening of the mean salinity pattern and an intensification of the hydrological cycle in a warmer world as expected by Solomon et al. (2007) and Held and Soden (2006). Terray et al. (2012) presented the linear SSS trends for 1970–2002 from in situ observations and projected trends in climate models (2011–2060). They found a significant freshening in the Pacific and a significant salting in the Atlantic, leading to an increase of the interbasin contrast. This result is consistent across papers that investigate salinity trends (e.g. Durack and Wijffels, 2010). Terray et al. (2012) also showed that these Pacific trends and the increasing interbasin contrast cannot be explained by internal variability alone, indicating an emerging anthropogenic signal. Cheng et al. (2020) analyzed salinity changes from 1960 to 2017 using a new dataset, at both the surface and over the upper 2000 m. They found that contrasts in the subsurface salinity have also increased, with an amplification of existing salinity patterns. They also highlighted that, because subsurface salinity is less affected by interannual variability and sampling error, this amplification signal is probably of anthropogenic origin, rather than due to natural variability. Gould and Cunningham (2021) extended the analysis of changes in surface salinity to almost 150 years, using data from the voyages of HMS Challenger and the HMS Gazelle in the 1870s. They found that the salinity pattern amplification seen for the period between the 1870s and 1950s was 54 ± 10 % lower than for the post-1950s period, which implies an acceleration of the amplification (and, consequently, of the hydrological cycle) for the post-1950s period.

Quite recently, SSS data based on a multivariate interpolation of in situ and satellite measurements – combining both sea surface salinity and temperature (SST) (discussed further here) – were included in a linear inverse model to assess the global ocean empirical dynamical modes over the 1993–2018 period (Buongiorno Nardelli and Iudicone, 2025). The analysis has allowed to filter out the contributions associated with Pacific Decadal Oscillation (PDO) as well as to El Niño/La Niña interannual signals, revealing the ocean response to long-term external forcing as the least-damped non-oscillating mode (Frankignoul et al., 2017). The strongest salinity changes indicate a reduced flow from major rivers, recently linked to human activity (Gudmundsson et al., 2021), and a salinity decrease in the Intertropical Convergence Zone and Antarctic Circumpolar Current. Buongiorno Nardelli and Iudicone (2025) showed that notable salinification occurs in the tropical southern Atlantic, western Indian Oceans, extending to the South Atlantic Current and Agulhas Retroflection. Compared to other studies, salinity trends along the US west coast (midlatitudes) and the subpolar North Atlantic show more complex dynamics than simple water cycle amplification.

Prior to the development of the Argo autonomous profiling floats network in the early 2000s, in situ SSS data were sparsely collected in space and time. Bingham et al. (2002) looked at the distribution of SSS observations in a dataset combining the World Ocean Database 1998 (WOD98) and a thermosalinograph and bucket salinity database. They found that, for the period between 1874 and 1998, 27 % of 1° squares in the world ocean had no observations, while 70 % had only 10 or fewer observations. At this time, the global large-scale time mean SSS field was known, but with almost unexplored interannual and decadal variations.

Since the early 2000s, there has been a large increase in near-surface and subsurface salinity data sampling at a global scale, with the deployment of around 20 000 Argo floats in the global ocean. Over 4000 Argo floats are currently in operation, each providing at least one salinity cast every 10 d in a 3° cell in the top 2 km of the water column (Thierry et al., 2025).

Satellite measurements of sea surface salinity started only in 2010, with the launch of the Soil Moisture and Ocean Salinity (SMOS) satellite mission (Kerr et al., 2010). For the first time, global SSS measurements were obtained continuously every 3 d with about 43 km resolution with a synthetic aperture radiometer operating in L-Band frequency (Font et al., 2010). Another satellite L-Band radiometer, Aquarius, operated from mid-2011 to mid-2015 with an 80–150 km resolution and a 7 d global coverage (Lagerloef et al., 2008). Finally, the Soil Moisture Active Passive (SMAP) radiometer was launched in 2015 and has been providing SSS measure-

Table 1. Products used in the study.

Product ref. no.	Product ID and type	Data access	Documentation
1	CATDS-PDC L3OS 3G, satellite SSS observations only	CATDS (2022)	Boutin et al. (2018) Vergely et al. (2022)
2	ISAS17, in situ data	Kolodziejczyk et al. (2023)	Gaillard et al. (2016) Kolodziejczyk et al. (2023)
3	GLOBAL_MULTIYEAR_PHY_001_030, in situ data and numerical models	EU Copernicus Marine Service Product (2023b)	QUID: Drévillon et al. (2023) PUM: Drévillon et al. (2024)
4	MULTIOBS_GLO_PHY_SSS_L4_MY_015_015, in situ and satellite observations	EU Copernicus Marine Service Product (2024a)	QUID: Kolodziejczyk (2024) PUM: Tarot (2024)
5	MULTIOBS_GLO_PHY_S_SURFACE_MYNRT_015_013, in situ and satellite observations, includes SST	EU Copernicus Marine Service Product (2024b)	QUID: Buongiorno Nardelli et al. (2024) PUM: Buongiorno Nardelli and Sammartino (2023)
6	MULTIOBS_GLO_PHY_TSUV_3D_MYNRT_015_012, in situ and satellite observations	EU Copernicus Marine Service Product (2023a)	QUID: Greiner et al. (2023) PUM: Verbrugge (2023)
7	IAPs-v2, bias-corrected in situ observations	Cheng et al. (2020)	Cheng et al. (2020) Cheng and Zhu (2016)

ments with around 40 km resolution and 3 d global coverage (Entekhabi et al., 2010). Both SMOS and SMAP are still functioning, providing respectively more than 15 years and 10 years of SSS data, which opens the door to deepen the study of trends over recent years.

The novelty of the present study is that it focuses on the satellite era, a period when unprecedented temporal and spatial resolutions of observations allow for better monitoring of SSS variability and trends. Previously, only the paper of Olmedo et al. (2022) has focused on satellite SSS data for global trend analysis. However, this paper was published at a time when less than 10 years of satellite data was available and uses only 8 years of SMOS SSS data, retrieved using a different algorithm than the one used in this study. They found limited regions of statistically significant trends, which were not in good agreement with trends derived from in situ Argo data.

This raises two questions: whether satellite data can reproduce SSS trends seen in in situ data, and what new insights they provide. We aim to answer these questions in this paper. For this, we look at the trends in SSS from seven different SSS datasets (mostly) available in the Copernicus Marine database, for the last 15 years. They include satellite-only SSS datasets, an optimal interpolation dataset that includes only in situ SSS, a model reanalysis that does not assimilate satellite SSS, and products based on combinations of satellite and in situ SSS and SST observations. These datasets are detailed in the next section; the methods for computing the trends and their statistical significance are described in Sect. 3; the results are presented in Sect. 4. Because 15 years is a short period of time for the computation of trends, in Sect. 4 we complement the results with the long-term trends derived from a longer in situ derived product, the Institute of Atmospheric Physics (IAP) global ocean salinity gridded product. Finally, the conclusions are presented in Sect. 5.

2 Data

The number of SSS products is increasing thanks to the advances in satellite remote sensing of SSS. In this paper, we used SSS products yielded from different technologies: satellite-only, in situ-only, and a combination of both satellite and in situ data (also exploiting multivariate approaches). Table 1 summarizes the seven SSS products analyzed in this work, while Table 2 summarizes their input data, resolution and temporal coverage. Products 1–6 provide the core information used to derive trends over the last 15 years. It is important to note that among the included SSS products, some of them provide independent information about SSS temporal variability; for example, the interannual variability in SMOS SSS (product 1) is independent from any product using only in situ SSS measurements, such as ISAS (product 2) or GLORYS (product 3). At the same time, other products are not independent as they use some of the same data. For instance, the SMOS/SMAP OI (product 4) uses SMOS and ISAS data in their optimal interpolation, while the ARMOR3D (product 6) uses the CNR SSS dataset (product 5) in their upstream. In this context, "independent" is used in a relative sense, referring to differences in the underlying salinity data sources rather than to all auxiliary variables used in the processing chains.

Table 2. Input data, resolution and temporal coverage of the products used in the study.

Product ref. no. and abbreviation	Input data	Resolution	Temporal coverage
1 – SMOS	SMOS SSS (CATDS L2Q Copernicus Marine Service datasets, Parracho et al., 2024)	1/4°	2010–present
2 – ISAS	In situ salinity profiles from Argo and Deep Argo floats and other in situ measurements, particularly where Argo sampling is sparse	1/2°	2002–present
3 – GLORYS	In situ salinity profiles (from EN4)	1/12°	1993–present
4 – SMOS/SMAP OI	Optimal interpolation of in situ observations (ISAS) and satellite (SMOS and SMAP) observation	1/4°	2010–present
5 – CNR	Multivariate optimal interpolation combining satellite salinity observations from SMOS and SMAP with in situ salinity measurements (Cora/Easycora Copernicus Marine Service datasets) and satellite OSTIA SST information	1/8°	1993–present
6 – ARMOR3D	In situ observations (Argo profiling floats, XBT, CTD1 and moorings measurements) and satellite observations (the CNR product)	1/4°	1993–present
7 – IAP	Bias-corrected in situ observations of CTD, Argo, Bottle, Glider, mooring etc. from the World Ocean Database, plus data owned by the research group	1°	1940–present

To assess if the significant trends observed for the last 15 years are consistent with longer term trends, the Institute of Atmospheric Physics (IAP, product 7) global ocean salinity gridded product (Cheng, 2022), available from 1940 to present, was used. The trends and statistical significance were computed for the salinity at the surface, for different time periods: 1960–2024 (the full period of the dataset was not used as data for 1940–1959 reportedly has a large uncertainty), 2005–2024 (the Argo period) and 2011–2024 (the satellite period).

3 Methods

The trends were computed using the Theil-Sen method (Theil, 1950; Sen, 1968) on the monthly mean anomalies of each dataset. These anomalies were computed by removing the monthly climatology in each dataset (for the period 2011–2024) from the monthly mean data. The Theil-Sen method is a non-parametric statistic that computes the median slope of all the pairwise combinations of points. This method has been shown to be less sensitive to outliers in the data than the more commonly used least squares method (Parracho et al., 2018).

The significance of the trends was assessed using a modified Mann–Kendall test (Hamed and Rao, 1998), which is suitable for autocorrelated data. A significant trend is one that differs from zero at 95 % confidence.

4 Results

4.1 Intercomparison of results obtained from different Sea Surface Salinity global products

The global SSS trends are shown for the different products in Fig. 1. The areas where the trends are not statistically significant are masked with stippling. The latitudes are restricted to between 50° S and 50° N because there are well known issues in satellite data related to sea-ice contamination and lower sensitivity of the L-Band radiometric signal to SSS near the polar regions where SST is low (Reul et al., 2020; Xie et al., 2023) and there are fewer in situ data (Gabarró et al., 2023).

In general, large areas of positive and negative statistically significant trends are found, and are consistent across the different analyzed SSS products. The agreement between the trends obtained with various products is particularly remarkable for datasets that are independent, such as SMOS (product 1) and GLORYS (product 3). We find similar results for these two datasets, especially away from the coast, and in regions where trends are statistically significant. Besides, consistent trends between SMOS/SMAP OI (product 4) and ISAS (product 2) are found, which can be partly explained by the fact that ISAS is used to constrain the large-scale variability of SMOS/SMAP OI. Some similarities between CNR (product 5) and ARMOR3D (product 6) trends are also expected, because CNR data is used as an upstream in ARMOR3D. The ARMOR3D and CNR products also include in situ observations (and weight them differently considering characteristic temperature decorrelation scales), therefore their trends are also close to ISAS and SMOS/SMAP

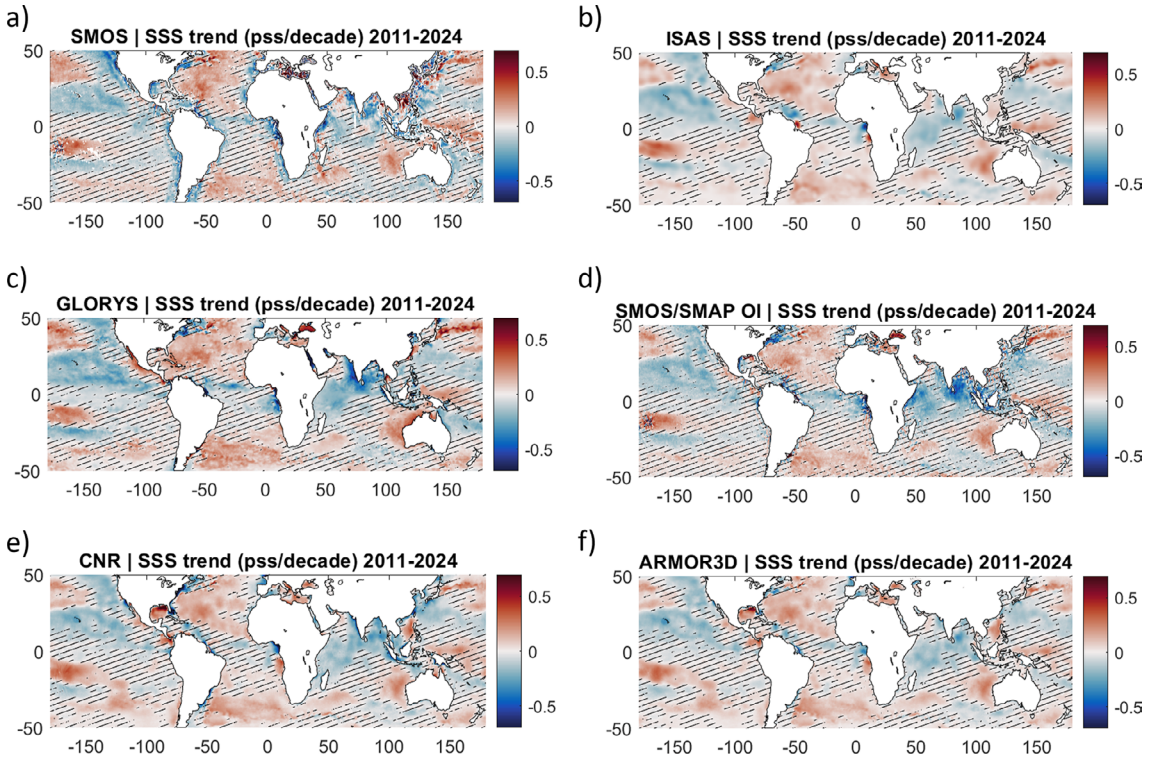


Figure 1. Linear trends (in pss per decade) in SSS computed using the Theil-Sen method for different SSS products: SMOS **(a)**, ISAS **(b)**, GLORYS **(c)**, SMOS/SMAP OI **(d)**, CNR **(e)** and ARMOR3D **(f)**. Regions where the trends are not statistically significant using the Mann-Kendall test are covered by stippling.

OI. Slight differences are observed in the intensity of the trends, with slightly more intense trends found in SMOS and GLORYS data and slightly less intense trends in ISAS (e.g. in the North and South Atlantic). However, there are more regions of statistically significant trends in ISAS than in the other products, likely because the data is smoother. ISAS applies objective analysis with spatial and temporal smoothing to interpolate in-situ data, which reduces short-scale variability and results in a lower standard deviation. There are also differences between the products in smaller regions, such as river plumes (e.g. of the Amazon and Congo rivers),which are areas of higher variability. In the SMOS data, there are negative trends near the coast that are not present in the other datasets(e.g. in the Pacific near the coast of South America and in the Atlantic near the coast of South Africa). Whether this could be related to a temporal evolution of the SMOS land-sea contamination (Kolodziejczyk et al., 2016) remains to be further studied.Nevertheless, these negative trends appear on both ascending and descending SMOS passes (not shown) whereas SMOS land-sea contamination strongly varies between ascending and descending satellite passes. In addition, few in situ measurements are available near land and future studies would be needed to better assess trends there.

In order to quantify the consistency between the trends derived from the different datasets, the mean value and standard deviation (SD) of SSS trends obtained from the 6 products were computed and are presented in Fig. 2a and b, respectively. The standard deviation (Fig. 2b) provides information about the level of uncertainty of the estimated trends, and the grid points where the standard deviation exceeds the trends were overlaid withgrey stippling over the mean trends in Fig. 2a. In general, the SD of the trends are about an order of magnitude smaller than the trends (under 0.05 pss per decade), which means that the trends derived by the different datasets are consistent with each other. However, there are some exceptions. The biggest SD in the trends obtained using the six datasets (Fig. 2b) corresponds to river plumes. For instance, in the Amazon River plume, ISAS shows a small area of positive trends (Fig. 1b) that is not observed in the other datasets, while ISAS, ARMOR3D and CNR show a positive trend in the Congo river plume that is negative in the observations-only datasets, SMOS and GLORYS. These river plumes are also regions of higher standard deviation of the monthly SSS (shown for SMOS in Fig. 2d). Some of the regions of higher SD of the trends also correspond to regions where the radio frequency interferences (RFI) contaminate the L-band radiometric signal, affecting the SMOS data. This

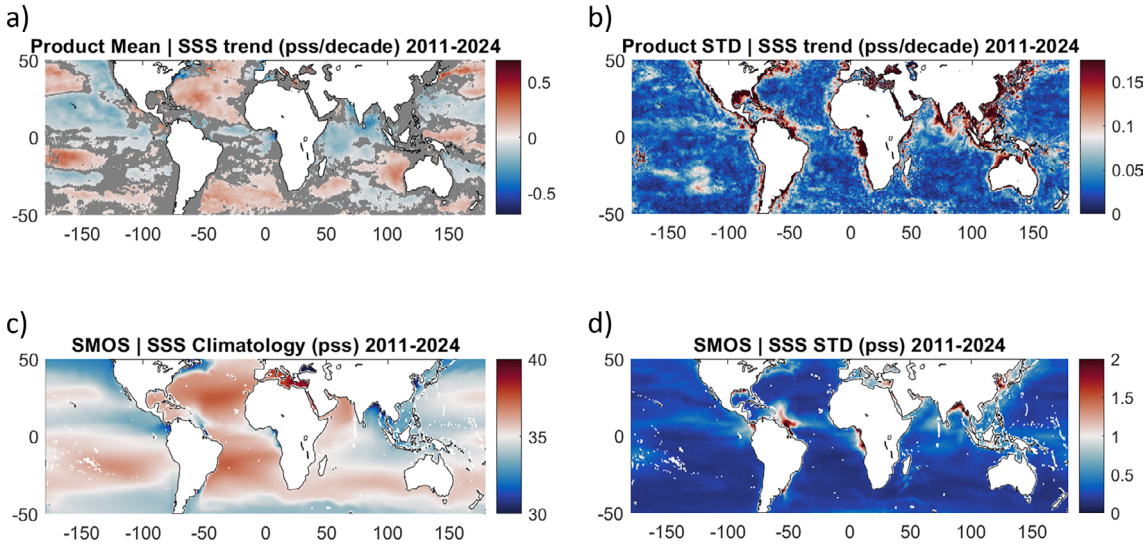


Figure 2. Mean trend **(a)** and standard deviation of the trends **(b)** in the products 1–6. The mean trend is overlaid with grey stippling for the gridpoints where the standard deviation of the trends exceeds the mean of the trends. Climatology **(c)** and standard deviation of SSS **(d)** for the SMOS dataset. The climatology and standard deviation maps for SMOS are consistent with the results obtained from the other datasets in the study (not shown).

is a local effect especially seen around Samoa, Barbados, and the Guinea Gulf (Bonjean et al., 2024).

In order to assess if the observed statistically significant trends correspond to an intensification of salinity patterns, as described in the literature and expected in theory, the trends in Fig. 2a were compared with the SSS climatology (Fig. 2c). We can see that some of the regions of higher salinity (e.g. the North Atlantic) also have positive SSS trends, while regions of lower salinity (e.g. the North Pacific) correspond to regions of negative trends. This reveals an increase in inter-basin contrasts. Other regions where "salty gets saltier and fresh gets fresher" are found in the Indian Ocean east of India (where a fresh region shows a freshening trend) and in the South Atlantic and west of Australia (where already saltier regions have a positive SSS trend).

Some regions, however, do not follow the intensification pattern. In the Southern Pacific Ocean there is a trend-dipole in a region of higher salinity, which closely resembles the patterns of SSS anomalies evolution observed and modelled during La Niña events (Fig. 4 in Hasson et al., 2014). In fact, during the period at study, there were three multi-year La Niña events (2010–2012, 2016–2018 and 2020–2023) which covered most of the investigated period and whose impact can be seen in the trends, with a negative SSS trend in the mid-latitudes in the Pacific and a positive SSS trend slightly south of the equator. Local deviations from simple water cycle amplification patterns are consistent with the results discussed in Buongiorno Nardelli and Iudicone (2025) and the trend dipole identified in the Southwestern Pacific matches the patterns shown in their Fig. S12, associated with the Central Pacific El Niño-Southern Oscillation mode. Both Pacific Decadal Oscillation (PDO) and El Niño Southern Oscillation (ENSO) modes can also explain the differences in the trends estimated for the Amazon plume during the different periods (and applying different techniques, in Buongiorno Nardelli and Iudicone, 2025).

To do an exhaustive analysis of the results obtained from the different products, the SSS variability in regions with statistically significant SSS trends is analyzed further in the next subsection.

4.2 Regions of important changes of Sea Surface Salinity

The regions where the linear trends in most SSS products are significant were delimited by the boxes shown in red in Fig. 3a (see the coordinates of the boxes in Table 3). The monthly time series of average SSS anomalies in each box are shown in Fig. 3b for the six different products and were used to compute the trends presented in Table 4 and Fig. 4, which shows the results for all products and regions. The trends' significance was tested, and non-significant trends are underlined.

The time-series of the SSS anomalies of the 6 datasets in each of the 8 regions show a general good agreement among them, with different products superposing well (Fig. 3b).

In spite of the general good agreement between SSS products, some differences are observed between the time series from the various products (Fig. 3b). On the one hand, some datasets show slightly more variability in certain regions. For example, SMOS and GLORYS show higher variability in the eastern Indian Ocean, where sparse in situ coverage coincides with strong coastal signals linked to river discharge and

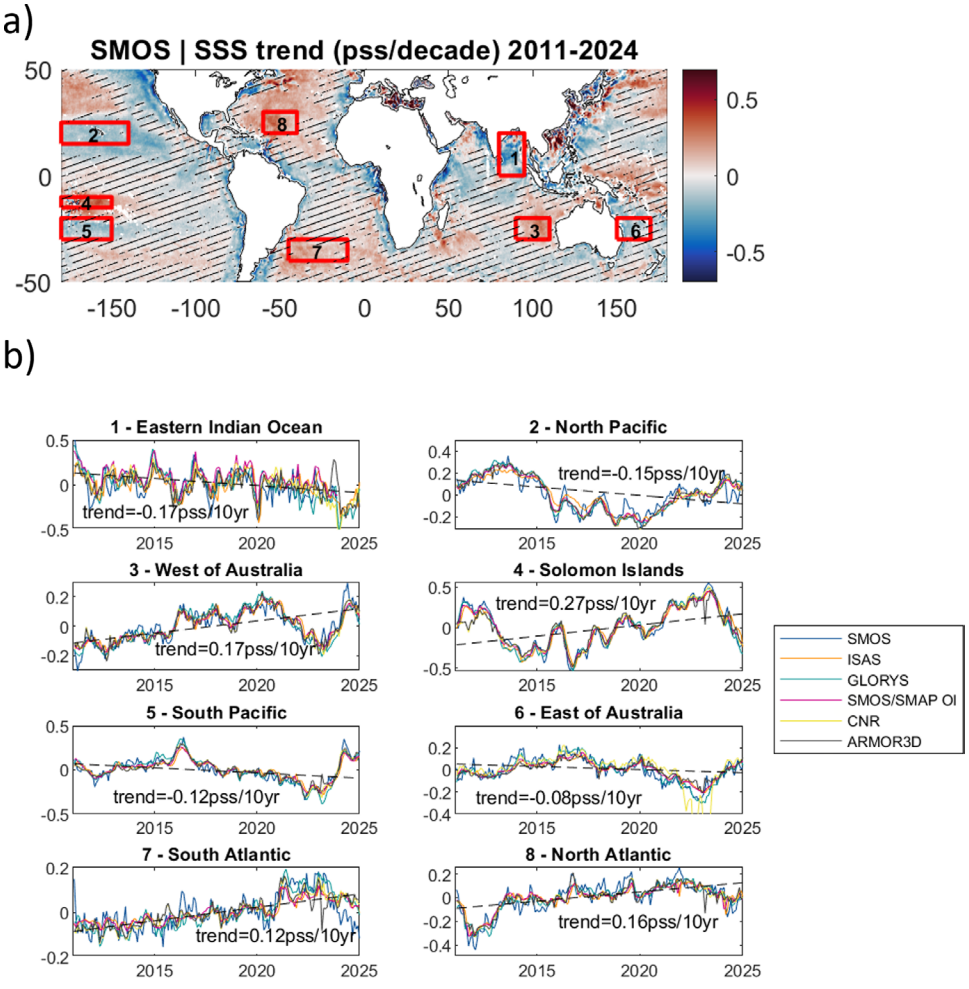


Figure 3. **(a)** Regions selected to depict the mean SSS anomalies time series and their trends are defined by the red rectangles and correspond to the regions where the trends are significant in most of the products. Regions are ordered according to their mean SSS in the regions, from the freshest region (1) to the saltiest region (8). **(b)** Time series of the SSS anomalies averaged over the regions selected in panel **(a)**: 1 is the Eastern Indian Ocean, 2 is the North Pacific, 3 corresponds to West of Australia, 4 to region of the Solomon Islands, 5 to South Pacific, 6 to South Atlantic and 8 to North Atlantic. The mean trend across all products for each region is represented by the dashed line and indicated in each box.

Table 3. Coordinates of the red boxes defined in Fig. 3a.

	Minimum Latitude (° N)	Maximum Latitude (° N)	Minimum Longitude (° E)	Maximum Longitude (° E)
1 – Eastern Indian Ocean	0	20	80	95
2 – North Pacific	15	25	−180	−140
3 – West of Australia	−30	−20	90	110
4 – Solomon Islands	−15	−10	−180	−150
5 – South Pacific	−30	−20	−180	−150
6 – East of Australia	−30	−20	150	170
7 – South Atlantic	−40	−30	−45	−10
8 – North Atlantic	20	30	−60	−40

Table 4. SSS linear trends computed using the Theil-Sen method in the analysed regions (in pss per 10 years). Bold values are NOT significant (p-value > 0.05 in Mann-Kendall test).

	SMOS	ISAS	GLORYS	SMOS/SMAP OI	CNR	ARMOR3D
1 – Eastern Indian Ocean	−0.142	−0.110	−0.262	−0.197	−0.187	−0.127
2 – North Pacific	−0.137	−0.167	−0.164	−0.156	−0.150	−0.155
3 – West of Australia	0.170	0.173	0.168	0.173	0.150	0.161
4 – Solomon Islands	0.233	0.316	0.276	0.258	0.297	0.265
5 – South Pacific	−0.137	−0.106	−0.172	−0.119	−0.087	−0.078
6 – East of Australia	−0.110	**−0.043**	−0.086	−0.051	**−0.028**	**−0.02**
7 – South Atlantic	0.114	0.099	0.150	0.101	0.156	0.124
8 – North Atlantic	0.183	0.136	0.174	0.129	0.156	0.156

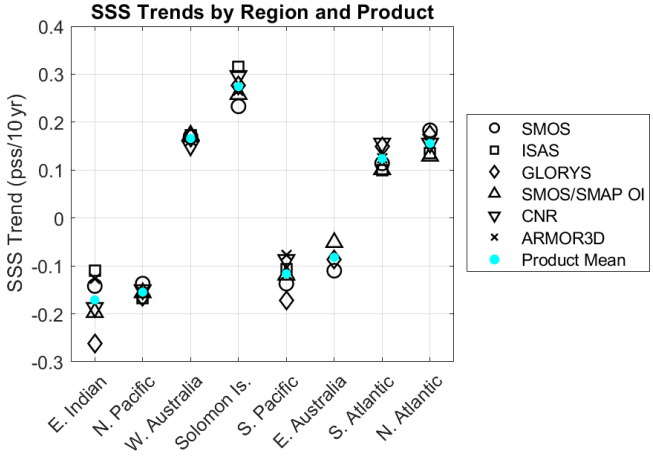


Figure 4. SSS trends computed using the Theil-Sen method in the selected regions, shown in Fig. 3a (in pss per 10 years) for all the data products, excluding the products where the trends are not statistically significant (p-value > 0.05 in Mann-Kendall test). Regions are ordered according to their mean SSS in the regions, from the freshest region on the left to the saltiest region on the right. The light blue dot corresponds to the mean trend across all products.

surface currents that are well captured by SMOS (Akhil et al., 2020). Increased variability in these datasets is also found in stratified regions such as the South Pacific near the South Pacific Convergence Zone (SPCZ), likely reflecting differences in SSS representation. Whereas SMOS samples only the upper centimeter of the ocean and GLORYS represents an average over the top meter (effectively a surface measure), the other datasets are more strongly influenced by deeper in situ observations. In addition, the 1/12° eddy-resolving resolution of GLORYS in the tropics may amplify variability, even at low frequencies, compared to lower-resolution or more strongly filtered products. Conversely, in the Solomon Islands region, the higher SMOS variability may also be related to RFI contamination (Bonjean et al., 2024).

On the other hand, some of the datasets differ from the others at certain periods of time. For instance, the CNR time series separates from the others in the Solomon Islands in 2011. ARMOR3D, based on CNR data, also follows this discrepancy (probably related to the number and treatment of in situ observations, and handling of the background field in their processing chains). In the East of Australia in the 2022–2023 period, the higher weight given to in situ observations in the CNR processing algorithm may enhance the representation of certain regional processes that are less evident in the other datasets. In this context, the stronger negative SSS anomalies observed in CNR SSS in 2022–2023 may be associated with precipitation variability affecting the western New Caledonia region and consequently the East of Australia area in that period (Blunden et al., 2023). ARMOR3D separates from the other time series in February 2023 in the Solomon Islands, the South Atlantic, the North Atlantic, and the Eastern Indian Ocean. This is because of spurious data that should have been flagged and not used in the ARMOR3D near real time (NRT) data that was used to complete the reprocessed time series in the last 2 years of the study. In the Eastern Indian Ocean, there is no SMOS or SMOS/SMAP OI data from December 2023, due to RFI contamination in the satellite data in the region. Finally, SMOS separates from the rest of the time series in the South Atlantic after 2024 for an unclear reason.

For all the datasets, some regions show a clear interannual variability, such as in the North Pacific and the Solomon Islands that can affect the result of the linear trend algorithm. Nevertheless, the statistically significant trends in these regions indicate a robust long-term change despite interannual variability. In general, according to Table 4 and Fig. 4, the trends are statistically significant in these boxes across all datasets, with the exception of East of Australia in the ISAS, CNR and ARMOR3D datasets, with statistically significant trends having the same sign and order of magnitude in most datasets. In the studied regions, the trends obtained for the climatological fresher regions are negative, but not all the trends of the climatological saltier regions are positive, with negative trends obtained in the South Pacific and East of Australia. Finally, the Eastern Indian Ocean is the region where the trends vary the most from one product to another (between −0.110 pss per decade in ISAS and −0.262 pss per decade in GLORYS, Table 4).

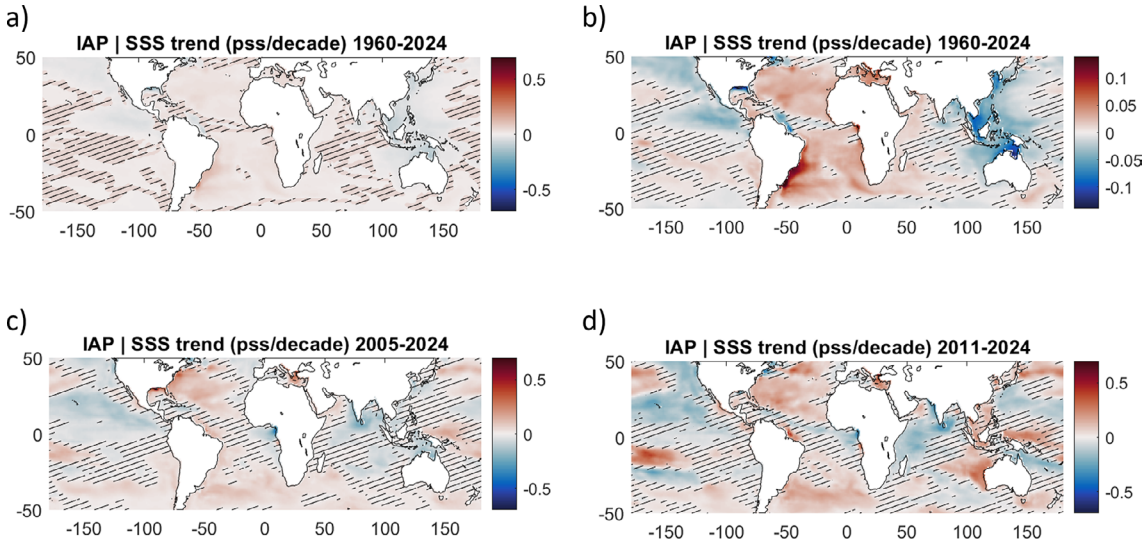


Figure 5. Linear trends in SSS computed using the Theil-Sen method for the IAP product at different periods of time. The regions where the trends are not statistically significant according to the Mann-Kendal test are covered with stippling. The top panels **(a)** and **(b)** correspond to the trends for the 1960–2024 period. They show the same trends with different colorscales. The bottom panel includes the trends for the 2005–2024 **(c)** and 2011–2024 **(d)** periods. The colorscales in panels **(a)**, **(c)** and **(d)** are the same, for easier comparison of the order of magnitude of the trends for different time periods, while the colorscale in panel **(b)** is adjusted to better visualize the less intense trends for 1960–2024.

4.3 Comparison with long term SSS trends

The IAP product was used to assess if the results for the last 15 years are consistent with longer term trends. For the satellite period (2011–2024), the trends obtained in the IAP dataset are consistent with the ones obtained in the other datasets (compare Fig. 2a with Fig. 5d), and the same regions of significant positive and negative trends were found. However, when the period is extended to the Argo period, the trends are less intense (by a factor of 2) and although most regions show a trend of the same sign as the sign of the trends estimated for the satellite period, there are also some differences (e.g. west of Australia). For the longer 1960–2024 period, the trends have an intensity that is even lower than the trends observed for the satellite period by a factor of 5. Moreover, the longer-term trends (Fig. 5a and b) show a pattern very similar to the SSS climatology shown in Fig. 2c (as expected from the literature). These results suggest an intensification of the SSS trends in the last 15 years or could also be due to the scarcity of observations in the pre-Argo period that lead the gridded observations to be too constrained by (and tend more towards) the climatology. In addition, when looking at such a short period as 15 years, interannual and interdecadal variability have a strong influence on the estimation of a linear trend (as seen in the time series of Fig. 3b), and notably, the 2011–2023 period featured the strongest and longest La Niña events since 1980.

In fact, short-term trends can be very affected by internal variability, whereas long-term trends are slowly emerging. By comparing the trends obtained at different time scales we can begin to separate anthropogenic trends from natural variability. In this sense, Fig. 5 highlights that the short-term trends in some regions are consistent with the longer-term trends, most notably the increase in the interbasin contrast, with the increasing salinity trend in the North Atlantic and a decreasing salinity trend in the North Pacific. Short-term trends are also consistent with long-term trends in the increasing salinity of the South Atlantic and freshening Indian ocean off the coast of India. These results agree with an anthropogenic modification of the Hadley cell (Gulev et al., 2021; Pinho et al., 2021) and the long period of negative-phase Pacific Decadal Oscillation (PDO) in the years at study (Sun et al., 2022), as also suggested in Buongiorno Nardelli and Iudicone (2025). Other past studies (e.g. Wills et al., 2018) have also found it difficult to separate global warming from PDO and ENSO.

5 Conclusions

Whereas several papers have already examined long-term salinity trends using in-situ datasets, the novelty of this paper lies in the use of two independent sources of data to compute SSS trends over the past 15 years: up-to-date products derived from satellite data on one hand, and from in situ data on the other hand. Satellite data offer spatial and temporal coverage of SSS that was previously unattainable, and the length of the satellite record is now becoming sufficient for deriving statistically significant trends. In this paper, we analyzed various products from different datasets and found consistent

trends, even when comparing independent datasets such as SMOS (a satellite-only dataset) and GLORYS (a model reanalysis which assimilates only in situ salinity and other in situ and satellite parameters).

Past studies have shown that spatial patterns of salinity change over multiple decades generally resemble the average salinity fields. However, those earlier studies referred to the period from roughly 1950 to 2008 (i.e., the pre-Argo era), when observations were sparse. In contrast, our analysis covers the period from 2011 to the present and identifies several regions where the trends do not follow the pattern of the climatology. This suggests local deviations from simple water cycle amplification patterns. This was also found, for example, by Vinogradova and Ponte (2017) for the period between 1993 and 2010, which they explained by the fact that anthropogenic hydrological signals take longer to emerge in the sea surface salinity compared to the surface freshwater fluxes. Indeed, comparison of our results with a long-term dataset derived from a combination of in situ observations and model outputs reveals consistent trends between the datasets over the past 15 years; however, these patterns differ from the longer-term trends. On the one hand, a comparison with the trends in this dataset for the Argo period (post-2005) showed that the intensity of trends has increased in recent years (although there can also be salinity sensors drift in the Argo data; Wong et al., 2020). While, on the other hand, a comparison with the longer-term trends (1960 to present) allowed us to separate trends that are part of long-term trends (such as the positive trend in the North Atlantic, which is a common feature of all periods and products), from the trends resulting from natural variability (such as the positive and negative trend pattern found in the Tropical Pacific due to the predominance of weak to strong La Niña conditions during the 2011–2024 period).

This study has shown that satellite, in situ and reanalysis SSS trends agree well in most regions (although longer records are still necessary to further minimize the influence of interannual and interdecadal variability), suggesting that these different SSS datasets could be used in the future to derive an SSS Ocean Monitoring Indicator.

Data availability. The datasets used in this study are publicly available at the Copernicus Marine Service (as listed in Table 1). SMOS data is available at SEXTANT: https://doi.org/10.12770/9c97fb5c-d7d5-4bc2-a5c7-57944026cd60 (CATDS, 2022). ISAS data is available at SEANOE: https://doi.org/10.17882/52367 (Kolodziejczyk et al., 2023). IAP data is available at: http://www.ocean.iap.ac.cn/pages/dataService/dataService.html (last access: July 2025).

Author contributions. A.C.P. wrote the manuscript with input from all co-authors and conducted the trend analysis, with assistance from P.Z. and M.S. All co-authors contributed to the conceptualization of the study and the development of the analysis method.

Competing interests. The contact author has declared that none of the authors has any competing interests.

Disclaimer. The Copernicus Marine Service offering is regularly updated to ensure it remains at the forefront of user requirements. In this process, some products may undergo replacement or renaming, leading to the removal of certain product IDs from the catalogue. If readers have any questions or require assistance regarding these modifications, please feel free to reach out to the Copernicus Marine Service user support team for further guidance. They will be able to provide the necessary information to address concerns and find suitable alternatives.

Publisher's note: Copernicus Publications remains neutral with regard to jurisdictional claims made in the text, published maps, institutional affiliations, or any other geographical representation in this paper. The authors bear the ultimate responsibility for providing appropriate place names. Views expressed in the text are those of the authors and do not necessarily reflect the views of the publisher.

Financial support. This research has been supported by the "Copernicus Marine Service – Multi Observation Thematic Center (24251L09-COP-TAC MOB-3200)", by Centre National d"Etudes Spatiales (CNES) project "Centre Aval de Traitement des Données SMOS – Ocean Salinity Expertise Center" (CATDS-CEC 4500084947), and by the European Space Agency (ESA) project "SMOS Expert Support Laboratory (ESL) for Level 2 Ocean Salinity" (4000130567/20/I-BG).

Review statement. This paper was edited by Gilles Garric and reviewed by two anonymous referees.

References

Akhil, V. P., Vialard, J., Lengaigne, M., Keerthi, M. G., Boutin, J., Vergely, J. L., and Papa, F.: Bay of Bengal sea surface salinity variability using a decade of improved SMOS re-processing, Remote Sens. Environ., 248, 111964, https://doi.org/10.1016/j.rse.2020.111964, 2020.

Bingham, F. M., Howden, S. D., and Koblinsky, C. J.: Sea surface salinity measurements in the historical database, J. Geophys. Res.-Oceans, 107, SRF-20, https://doi.org/10.1029/2000JC000767, 2002.

Blunden, J., Boyer, T., and Bartow-Gillies, E. (Eds.): State of the climate in 2022, Bull. Am. Meteorol. Soc., 104, S1–S501, 2023.

Bonjean, F., Boutin, J., Vergely, J. L., Richaume, P., and Sabia, R.: Recovery of SMOS salinity variability in RFI-contaminated regions, IEEE T. Geosci. Remote Sens., https://doi.org/10.1109/TGRS.2024.3408049, 2024.

Borger, C., Beirle, S., and Wagner, T.: Analysis of global trends of total column water vapour from multiple years of OMI observations, Atmos. Chem. Phys., 22, 10603–10621, https://doi.org/10.5194/acp-22-10603-2022, 2022.

Boutin, J., Vergely, J.-L., Marchand, S., D'Amico, F., Hasson, A., Kolodziejczyk, N., Reul, N., Reverdin, G., and Vialard, J.: New SMOS sea surface salinity with reduced systematic errors and improved variability, Remote Sens. Environ., 214, 115–134, https://doi.org/10.1016/j.rse.2018.05.022, 2018.

Buongiorno Nardelli, B. and Iudicone, D.: A dynamical geography of observed trends in the global ocean, Sci. Adv., 11, 3532, https://doi.org/10.1126/sciadv.adq3532, 2025.

Buongiorno Nardelli, B. and Sammartino, M.: EU Copernicus Marine Service Product User Manual for the Multi Observation Global Ocean Sea Surface Salinity and Sea Surface Density, MULTIOBS_GLO_PHY_S_SURFACE_MYNRT_015_013, issue 1.3, Mercator Ocean International, https://documentation.marine.copernicus.eu/PUM/CMEMS-MOB-PUM-015-013.pdf (last access: 16 July 2025), 2023.

Buongiorno Nardelli, B., Pisano, A., and Sammartino, M.: EU Copernicus Marine Service Quality Information Document for the Multi Observation Global Ocean Sea Surface Salinity and Sea Surface Density, MULTIOBS_GLO_PHY_S_SURFACE_MYNRT_015_013, issue 1.4, Mercator Ocean International, https://documentation.marine.copernicus.eu/QUID/CMEMS-MOB-QUID-015-013.pdf (last access: 16 July 2025), 2024.

CATDS: CATDS-PDC L3OS 3G – Debiased Gaussian average daily salinity field product from SMOS satellite, CATDS (CNES, IFREMER, LOCEAN, ACRI) [data set], https://doi.org/10.12770/9c97fb5c-d7d5-4bc2-a5c7-57944026cd60, 2022.

Cheng, L.: IAP observational salinity gridded dataset at 0.25 resolution, Inst. Atmos. Phys., Chin. Acad. Sci., https://doi.org/10.57760/sciencedb.o00122.00001, 2022.

Cheng, L. and Zhu, J.: Benefits of CMIP5 multimodel ensemble in reconstructing historical ocean subsurface temperature variations, J. Climate, 29, 5393–5416, 2016.

Cheng, L., Trenberth, K. E., Gruber, N., Abraham, J. P., Fasullo, J. T., Li, G., Mann, M. E., Zhao, X., and Zhu, J.: Improved estimates of changes in upper ocean salinity and the hydrological cycle, J. Climate, 33, https://doi.org/10.1175/JCLI-D-20-0366.1, 2020.

Douville, H., Raghavan, K., Renwick, J., Allan, R. P., Arias, P. A., Barlow, M., Cerezo-Mota, R., Cherchi, A., Gan, T. Y., Gergis, J., Jiang, D., Khan, A., Pokam Mba, W., Rosenfeld, D., Tierney, J., and Zolina, O.: Water Cycle Changes, in: Climate Change 2021: The Physical Science Basis, Cambridge Univ. Press, 1055–1210, https://doi.org/10.1017/9781009157896.010, 2021.

Drévillon, M., Lellouche, J.-M., Régnier, C., Garric, G., Bricaud, C., Hernandez, O., and Bourdallé-Badie, R.: EU Copernicus Marine Service Quality Information Document for the Global Ocean Physics Reanalysis, GLOBAL_REANALYSIS_PHY_001_030, issue 1.6, Mercator Ocean International, https://documentation.marine.copernicus.eu/QUID/CMEMS-GLO-QUID-001-030.pdf (last access: 16 July 2025), 2023.

Drévillon, M., Fernandez, E., and Lellouche, J.-M.: EU Copernicus Marine Service Product User Manual for the Global Ocean Physics Reanalysis, GLOBAL_REANALYSIS_PHY_001_030, issue 1.6, Mercator Ocean International, https://documentation.marine.copernicus.eu/PUM/CMEMS-GLO-PUM-001-030.pdf (last access: 16 July 2025), 2024.

Durack, P. J. and Wijffels, S. E.: Fifty-year trends in global ocean salinities and their relationship to broad-scale warming, J. Climate, 23, 4342–4362, https://doi.org/10.1175/2010JCLI3377.1, 2010.

Entekhabi, D., Njoku, E. G., O'Neill, P. E., Kellogg, K. H., Crow, W. T., Edelstein, W. N., Entin, J. K., and Yueh, S.: The soil moisture active passive (SMAP) mission, Proc. IEEE, 98, 704–716, https://doi.org/10.1109/JPROC.2010.2043918, 2010.

EU Copernicus Marine Service Product: Multi Observation Global Ocean 3D Temperature Salinity Height Geostrophic Current and MLD, Mercator Ocean International [data set], https://doi.org/10.48670/moi-00052, 2023a.

EU Copernicus Marine Service Product: Global Ocean Physics Reanalysis, Mercator Ocean International [data set], https://doi.org/10.48670/moi-00021, 2023b.

EU Copernicus Marine Service Product: SSS SMOS/SMAP L4 OI – LOPS-v2023, Mercator Ocean International [data set], https://doi.org/10.48670/mds-00369, 2024a.

EU Copernicus Marine Service Product: Multi Observation Global Ocean Sea Surface Salinity and Sea Surface Density, Mercator Ocean International [data set], https://doi.org/10.48670/moi-00051, 2024b.

Font, J., Camps, A., Borges, A., Martin-Neira, M., Boutin, J., Reul, N., Kerr, Y. H., Hahne, A., and Mecklenburg, S.: SMOS: The challenging sea surface salinity measurement from space, Proc. IEEE, 98, 649–665, https://doi.org/10.1109/JPROC.2009.2033096, 2010.

Frankignoul, C., Gastineau, G., and Kwon, Y.-O.: Estimation of the SST response to anthropogenic and external forcing and its impact on the Atlantic multidecadal oscillation and the Pacific decadal oscillation, J. Climate, 30, 9871–9895, 2017.

Gabarró, C., Hughes, N., Wilkinson, J., Bertino, L., Bracher, A., Diehl, T., Dierking, W., Gonzalez-Gambau, V., Lavergne, T., Madurell, T., Malnes, E., and Wagner, P. M.: Improving satellite-based monitoring of the polar regions: Identification of research and capacity gaps, Front. Remote Sens., 4, 952091, https://doi.org/10.3389/frsen.2023.952091, 2023.

Gaillard, F., Reynaud, T., Thierry, V., Kolodziejczyk, N., and von Schuckmann, K.: In-situ based reanalysis of the global ocean temperature and salinity with ISAS: variability of the heat content and steric height, J. Climate, 29, 1305–1323, https://doi.org/10.1175/JCLI-D-15-0028.1, 2016.

Gould, W. J. and Cunningham, S. A.: Global-scale patterns of observed sea surface salinity intensified since the 1870s, Commun. Earth Environ., 2, 76, https://doi.org/10.1038/s43247-021-00161-3, 2021.

Greiner, E., Verbrugge, N., and Mulet, S., and Guinehut, S.: EU Copernicus Marine Service Quality Information Document for the Multi Observation Global Ocean 3D Temperature Salinity Height Geostrophic Current and MLD, MULTIOBS_GLO_PHY_TSUV_3D_MYNRT_015_012, issue 1.2, Mercator Ocean International, https://documentation.marine.copernicus.eu/QUID/CMEMS-MOB-QUID-015-012.pdf (last access: 16 July 2025), 2023.

Gu, L., Yin, J., Slater, L. J., Chen, J., Do, H. X., Wang, H.-M., Lu, C., Jiang, Z., Zhao, T., and Zhang, Y.: Intensification of global hydrological droughts under anthropogenic climate warming, Water Resour. Res., 59, e2022WR032997, https://doi.org/10.1029/2022WR032997, 2022.

Gudmundsson, L., Boulange, J., Do, H. X., Gosling, S. N., Grillakis, M. G., Koutroulis, A. G., and Zhao, F.: Globally observed trends in mean and extreme river flow attributed to climate change, Science, 371, 1159–1162, 2021.

Gulev, S. K., Thorne, P. W., Ahn, J., Dentener, F. J., Domingues, C. M., Gerland, S., and Vose, R. S.: Changing state of the climate system, in: Climate Change 2021: The Physical Science Basis, Contribution of Working Group I to the Sixth Assessment Report of the Intergovernmental Panel on Climate Change, Cambridge Univ. Press, 287–422, https://doi.org/10.1017/9781009157896.004, 2021.

Hamed, K. H. and Rao, A. R.: A modified Mann-Kendall trend test for autocorrelated data, J. Hydrol., 204, 182–196, 1998.

Hasson, A., Delcroix, T., Boutin, J., Dussin, R., and Ballabrera-Poy, J.: Analyzing the 2010–2011 La Niña signature in the tropical Pacific sea surface salinity using in situ data, SMOS observations, and a numerical simulation, J. Geophys. Res.-Oceans, 119, 3855–3867, https://doi.org/10.1002/2014JC009864, 2014.

Held, I. M. and Soden, B. J.: Robust responses of the hydrological cycle to global warming, J. Climate, 19, 5686–5699, https://doi.org/10.1175/JCLI3990.1, 2006.

IPCC: Climate Change 2021: The Physical Science Basis, Contribution of Working Group I to the Sixth Assessment Report of the Intergovernmental Panel on Climate Change, edited by: Masson-Delmotte, V., Zhai, P., Pirani, A., Connors, S. L., Péan, C., Berger, S., Caud, N., Chen, Y., Goldfarb, L., Gomis, M. I., Huang, M., Leitzell, K., Lonnoy, E., Matthews, J. B. R., Maycock, T. K., Waterfield, T., Yelekçi, O., Yu, R., and Zhou, B., Cambridge University Press, Cambridge, United Kingdom and New York, NY, USA, https://doi.org/10.1017/9781009157896, 2021.

Kerr, Y. H., Waldteufel, P., Wigneron, J. P., Delwart, S., Cabot, F., Boutin, J., and Mecklenburg, S.: The SMOS mission: New tool for monitoring key elements of the global water cycle, Proc. IEEE, 98, 666–687, https://doi.org/10.1109/JPROC.2010.2043032, 2010.

Kolodziejczyk, N.: EU Copernicus Marine Service Quality Information Document for the SSS SMOS/SMAP L4 OI - LOPS-v2023, MULTIOBS_GLO_PHY_SSS_L4_MY_015_015, issue 2.0, Mercator Ocean International, https://documentation.marine.copernicus.eu/QUID/CMEMS-MOB-QUID-015-015.pdf (last access: 16 July 2025), 2024.

Kolodziejczyk, N., Boutin, J., Vergely, J. L., Marchand, S., Martin, N., and Reverdin, G.: Mitigation of systematic errors in SMOS sea surface salinity, Remote Sens. Environ., 180, 164–177, 2016.

Kolodziejczyk, N., Prigent-Mazella, A., and Gaillard, F.: ISAS temperature, salinity, dissolved oxygen gridded fields, SEANOE [data set], https://doi.org/10.17882/52367, 2023.

Lagerloef, G., Colomb, F. R., Le Vine, D., Wentz, F., Yueh, S., Ruf, C., Lilly, J., Gunn, J., Chao, Y. I., DeCharon, A., and Feldman, G.: The Aquarius/SAC-D mission: Designed to meet the salinity remote-sensing challenge, Oceanography, 21, 68–81, https://doi.org/10.5670/oceanog.2008.77, 2008.

O'Gorman, P. A.: Precipitation extremes under climate change, Curr. Clim. Change Rep., 1, 49–59, 2015.

Olmedo, E., Turiel, A., González-Gambau, V., González-Haro, C., García-Espriu, A., Gabarró, C., and Scipal, K.: Increasing stratification as observed by satellite sea surface salinity measurements, Sci. Rep., 12, 6279, https://doi.org/10.1038/s41598-022-10265-1, 2022.

Parracho, A., Boutin, J., and Tarot, S.: EU Copernicus Marine Service Quality Information Document for the SMOS CATDS Qualified (L2Q) Sea Surface Salinity product, MULTIOBS_GLO_PHY_SSS_L3_MYNRT_015_014, issue 2.0, Mercator Ocean International, https://documentation.marine.copernicus.eu/QUID/CMEMS-MOB-QUID-015-014.pdf (last access: 14 July 2025), 2024.

Parracho, A. C., Bock, O., and Bastin, S.: Global IWV trends and variability in atmospheric reanalyses and GPS observations, Atmos. Chem. Phys., 18, 16213–16237, https://doi.org/10.5194/acp-18-16213-2018, 2018.

Pinho, T. M. L., Chiessi, C. M., Portilho-Ramos, R. C., Campos, M. C., Crivellari, S., Nascimento, R. A., Albuquerque, A. L. S., Bahr, A., and Mulitza, S.: Meridional changes in the South Atlantic subtropical gyre during Heinrich stadials, Sci. Rep., 11, 9419, https://doi.org/10.1038/s41598-021-88817-0, 2021.

Reul, N., Grodsky, S. A., Arias, M., Boutin, J., Catany, R., Chapron, B., D'Amico, F., Dinnat, E., Donlon, C., Fore, A., Fournier, S., Guimbard, S., Hasson, A., Kolodziejczyk, N., Lagerloef, G., Lee, T., Le Vine, D. M., Lindstrom, E., Maes, C., Mecklenburg, S., Meissner, T., Olmedo, E., Sabia, R., Tenerelli, J., Thouvenin-Masson, C., Turiel, A., Vergely, J.-L., Vinogradova, N., Wentz, F., and Yueh, S.: Sea surface salinity estimates from spaceborne L-band radiometers: an overview of the first decade of observation (2010–2019), Remote Sens. Environ., 242, 111769, https://doi.org/10.1016/j.rse.2020.111769, 2020.

Sen, P. K.: Estimates of the regression coefficient based on Kendall's tau, J. Am. Stat. Assoc., 63, 1379–1389, 1968.

Solomon, S., Qin, D., Manning, M., Alley, R. B., Berntsen, T., Bindoff, N. L., Chen, Z., Marquis, M., Averyt, K. B., Tignor, M., Miller, H. L., and the Core Writing Team: Technical summary, in: Climate Change 2007: The Physical Science Basis. Contribution of Working Group I to the Fourth Assessment Report of the Intergovernmental Panel on Climate Change, edited by: Solomon, S., Qin, D., Manning, M., Chen, Z., Marquis, M., Averyt, K. B., Tignor, M., and Miller, H. L., Cambridge University Press, Cambridge, United Kingdom and New York, NY, USA, ISBN 978-0-521-88009-1, 2007.

Sun, W., Wang, B., Liu, J., and Dai, Y.: Recent changes of Pacific decadal variability shaped by greenhouse forcing and internal variability, J. Geophys. Res.-Atmos., 127, e2021JD035812, https://doi.org/10.1029/2021JD035812, 2022.

Tarot, S.: EU Copernicus Marine Service Product User Manual for the SSS SMOS/SMAP L4 OI – LOPS-v2023, MULTIOBS_GLO_PHY_SSS_L4_MY_015_015, issue 2.0, Mercator Ocean International, https://documentation.marine.copernicus.eu/PUM/CMEMS-MOB-PUM-015-015.pdf (last access: 16 July 2025), 2024.

Terray, L., Corre, L., Cravatte, S., Delcroix, T., Reverdin, G., and Ribes, A.: Near-surface salinity as nature's rain gauge to detect human influence on the tropical water cycle, J. Climate, 25, 958–977, https://doi.org/10.1175/JCLI-D-10-05025.1, 2012.

Theil, H.: A rank-invariant method of linear and polynomial regression analysis, Indag. Math., 12, 173, 1950.

Thierry, V., Claustre, H., Pasqueron de Fommervault, O., Zilberman, N., Johnson, K. S., King, B. A., Wijffels, S. E., Bhaskar, U. T. V. S., Balmaseda, M. A., Belbeoch, M., Bollard, M.,

Boutin, J., Boyd, P., Cancouët, R., Chai, F., Ciavatta, S., Crane, R., Cravatte, S., Dall'Olmo, G., Desbruyères, D., Durack, P. J., Fassbender, A. J., Fennel, K., Fujii, Y., Gasparin, F., González-Santana, A., Gourcuff, C., Gray, A., Hewitt, H. T., Jayne, S. R., Johnson, G. C., Kolodziejczyk, N., Le Boyer, A., Le Traon, P.-Y., Llovel, W., Lozier, M. S., Lyman, J. M., McDonagh, E. L., Martin, A. P., Meyssignac, B., Mogensen, K. S., Morris, T., Oke, P. R., Smith, W. O., Jr., Owens, B., Poffa, N., Post, J., Roemmich, D., Rykaczewski, R. R., Sathyendranath, S., Scanderbeg, M., Scheurle, C., Schofield, O., von Schuckmann, K., Scourse, J., Sprintall, J., Suga, T., Tonani, M., van Wijk, E., Xing, X., and Zuo, H.: Advancing ocean monitoring and knowledge for societal benefit: the urgency to expand Argo to OneArgo by 2030, Front. Mar. Sci., 12, 1593904, https://doi.org/10.3389/fmars.2025.1593904, 2025.

Verbrugge, N.: EU Copernicus Marine Service Product User Manual for the Multi Observation Global Ocean 3D Temperature Salinity Height Geostrophic Current and MLD, MULTIOBS_GLO_PHY_TSUV_3D_MYNRT_015_012, issue 1.2, Mercator Ocean International, https://documentation.marine.copernicus.eu/PUM/CMEMS-MOB-PUM-015-012.pdf (last access: 16 July 2025), 2023.

Vergely, J.-L., Boutin, J., and Kolodziejczyk, N.: SMOS OS Level 3 and Level 4 algorithm theoretical basis document, ACRI-ST, https://doi.org/10.13155/92266, 2022.

Vinogradova, N. T. and Ponte, R. M.: In search of fingerprints of the recent intensification of the ocean water cycle, J. Clim., 30, 5513–5528, 2017.

Wan, N., Lin, X., Pielke Sr., R. A., Zeng, X., and Nelson, A. M.: Global total precipitable water variations and trends over the period 1958–2021, Hydrol. Earth Syst. Sci., 28, 2123–2137, https://doi.org/10.5194/hess-28-2123-2024, 2024.

Wills, R. C., Schneider, T., Wallace, J. M., Battisti, D. S., and Hartmann, D. L.: Disentangling global warming, multidecadal variability, and El Niño in Pacific temperatures, Geophys. Res. Lett., 45, 2487–2496, https://doi.org/10.1002/2017GL076327, 2018.

Wong, A. P. S., Wijffels, S. E., Riser, S. C., Pouliquen, S., Hosoda, S., Roemmich, D., Gilson, J., Johnson, G. C., Martini, K., Murphy, D. J., Scanderbeg, M., Bhaskar, T. V. S. U., Buck, J. J. H., Merceur, F., Carval, T., Maze, G., Cabanes, C., André, X., Poffa, N., Yashayaev, I., Barker, P. M., Guinehut, S., Belbéoch, M., Ignaszewski, M., Baringer, M. O., Schmid, C., Lyman, J. M., McTaggart, K. E., Purkey, S. G., Zilberman, N., Alkire, M. B., Swift, D., Owens, W. B., Jayne, S. R., Hersh, C., Robbins, P., West-Mack, D., Bahr, F., Yoshida, S., Sutton, P. J. H., Cancouët, R., Coatanoan, C., Dobbler, D., Garcia Juan, A., Gourrion, J., Kolodziejczyk, N., Bernard, V., Bourlès, B., Claustre, H., D'Ortenzio, F., Le Reste, S., Le Traon, P.-Y., Rannou, J.-P., Saout-Grit, C., Speich, S., Thierry, V., Verbrugge, N., Angel-Benavides, I. M., Klein, B., Notarstefano, G., Poulain, P.-M., Vélez-Belchí, P., Suga, T., Ando, K., Iwasaska, N., Kobayashi, T., Masuda, S., Oka, E., Sato, K., Nakamura, T., Sato, K., Takatsuki, Y., Yoshida, T., Cowley, R., Lovell, J. L., Oke, P. R., van Wijk, E. M., Carse, F., Donnelly, M., Gould, W. J., Gowers, K., King, B. A., Loch, S. G., Mowat, M., Turton, J., Rama Rao, E. P., Ravichandran, M., Freeland, H. J., Gaboury, I., Gilbert, D., Greenan, B. J. W., Ouellet, M., Ross, T., Tran, A., Dong, M., Liu, Z., Xu, J., Kang, K., Jo, H., Kim, S.-D., and Park, H.-M.: Argo data 1999–2019: Two million temperature-salinity profiles and subsurface velocity observations from a global array of profiling floats, Front. Mar. Sci., 7, 700, https://doi.org/10.3389/fmars.2020.00700, 2020.

Xie, H., Xu, Q., Cheng, Y., Yin, X., and Fan, K.: Reconstructing three-dimensional salinity field of the South China Sea from satellite observations, Front. Mar. Sci., 10, 1168486, https://doi.org/10.3389/fmars.2023.1168486, 2023.

Yu, L., Josey, S. A., Bingham, F. M., and Lee, T.: Intensification of the global water cycle and evidence from ocean salinity: a synthesis review, Ann. N. Y. Acad. Sci., 1472, 76–94, https://doi.org/10.1111/nyas.14354, 2020.

State Planet, 7-osr10, 13, 2026
https://doi.org/10.5194/sp-7-osr10-13-2026
© Author(s) 2026. This work is distributed under
the Creative Commons Attribution 4.0 License.

Decadal variability in the Eastern and Western Mediterranean sea level trends

Federica Borile[1,2], Vladyslav Lyubartsev[2], Begoña Pérez Gómez[3], Jue Lin-Ye[4], Anna Mangilli[5], Emanuela Clementi[2], and Paolo Oddo[1]

[1]Department of Physics and Astronomy, University of Bologna, Bologna, 40127, Italy
[2]CMCC Foundation – Euro-Mediterranean Center on Climate Change, Bologna, 40127, Italy
[3]Climate Change and Prediction Department – Puertos del Estado, Madrid, 28042, Spain
[4]Department of In Situ, Nologin Oceanic Weather Systems, Madrid, 28045, Spain
[5]Collecte Localisation Satellites group, Tolouse, France

Correspondence: Emanuela Clementi (emanuela.clementi@cmcc.it)

Received: 31 July 2025 – Discussion started: 30 September 2025
Revised: 8 May 2026 – Accepted: 16 May 2026 – Published: 30 September 2026

Abstract. The Mediterranean Sea, a semi-enclosed basin highly sensitive to climate change, exhibits complex variability in sea level trends with important environmental and societal implications. This study investigates the sea level rise decadal variability from 1993 to 2024 at sub-basin and coastal scales using satellite altimetry, ocean reanalyses, and tide gauges records. In the Western Mediterranean (WMED) sea level decadal trend has recently accelerated, partly driven by thermal expansion that exceeds halosteric contraction, with the remaining contribution likely associated with sea level mass variability. In the Eastern Mediterranean (EMED) sea level transitioned from a regime dominated by halosteric-induced drop to a recent state where steric contributions offset each other, allowing mass variability to dominate. Local trends generally confirm satellite-derived patterns, though larger differences reported in the EMED highlight the influence of regional processes, including vertical land movement. These results confirm that Mediterranean sea level change is non-linear, with decadal variability superimposed on a long-term positive trend, emphasizing the need to account for such fluctuations in regional adaptation strategies and coastal risk management.

1 Introduction

Sea level rise is a major global concern due to its direct impact on densely populated coastal zones, posing growing challenges for adaptation and risk management (Parmesan et al., 2022). While global mean sea level trends provide an integrated picture, regional sea level change can significantly depart from the global average, especially in semi-enclosed basins, where local processes drive distinct patterns of variability (Calafat et al., 2022; Gräwe et al., 2019; Alothman et al., 2014). The Mediterranean Sea is a prominent example, recognised as a climate change hotspot where environmental and societal risks are closely linked (Tuel and Eltahir, 2020; Cramer et al., 2018; Giorgi, 2006). While regional climate-change driven sea level rise has been already documented (Adloff et al., 2015; Sannino et al., 2022), the goal of this study is to monitor and update, with recent data and products, the decadal variability of Mediterranean sea level changes, which primarily reflects internal climate variability superimposed on the anthropogenic forcing (Calafat et al., 2022).

Decadal sea-level variability in the Mediterranean is mainly controlled by regional atmospheric forcing and steric effects rather than by global mean sea-level signals (Marcos and Tsimplis, 2008): this variability arises from complex interactions between ocean dynamics and external forcing mechanisms that affect the manometric component of sea level (Pinardi et al., 2015; Calafat et al., 2012; Gomis et al., 2008). As a result, the Western and Eastern Mediterranean sub-basins, hereafter referred to as WMED and EMED, exhibit distinct sea-level evolutions (Borile et al., 2025).

Published by Copernicus Publications.

Table 1. Products table.

Product ref. no.	product ID and type	Data access	Documentation
1	SEALEVEL_GLO_PHY_CLIMATE_L4_MY_008_057, (satC3S) (1993–2024) satellite observations	EU Copernicus Marine Service Product (2024a)	QUID: Ballarotta et al. (2024) PUM: Pujol (2024)
2	SEALEVEL_EUR_PHY_L4_MY_008_068, (satCMEMS) (1993–2024) satellite observations	EU Copernicus Marine Service Product (2024b)	QUID: Ballarotta et al. (2025) PUM: Pujol (2025)
3	MEDSEA_MULTIYEAR_PHY_006_004, (MEDREA24) (1987–2025) numerical models	EU Copernicus Marine Service Product (2024c)	QUID: Escudier et al. (2024) PUM: Lecci et al. (2024)
4	GLOBAL_MULTIYEAR_PHY_001_030, (GLORYS12) (1993–2025) numerical models	EU Copernicus Marine Service Product (2023)	QUID: Drévillon et al. (2023) PUM: Drévillon et al. (2024)
5	INSITU_GLO_PHY_SSH_DISCRETE_MY_013_053, (tgCMEMS) (1821–2024) in-situ observations	EU Copernicus Marine Service Product (2024d)	QUID: Pérez Gómez et al. (2024a) PUM: Pérez Gómez et al. (2024b)
6	Tide gauges data, Permanent Service of Mean Sea Level (tgPSMSL) In-situ observations	https://psmsl.org/data/ (last access: 5 July 2025)	Holgate et al. (2013)
7	Vertical land motion at tide gauges, ULR/SONEL group, GLOSS Data Assembly Centre for GNSS at Tide Gauges In Situ observations (GNSS)	URL/SONEL group: https://www.sonel.org/-GPS-.html?lang=en (last access: 27 June 2025)	Gravelle et al. (2023)
8	Dynamic Atmospheric Correction, Centre National d'Etudes Spatiales (DAC) numerical model	AVISO+ alimetry: https://www.aviso.altimetry.fr/en/data/products/auxiliary-products/dynamic-atmospheric-correction.html (last access: 29 December 2025)	Pascual et al. (2008)

The Mediterranean is a concentration basin, with meridional temperature and zonal salinity gradients (Pinardi and Masetti, 2000; Pisano et al., 2020). The interplay between temperature and salinity is thus expected to have an influence on total sea level trends in the region, in contrast to the global ocean where thermal expansion dominates (IPCC, 2023; Milne et al., 2009). Such a process has been analysed at the basin scale, with haline contraction counteracting the effect of ocean warming on sea level (Meli et al., 2023); this work further explores their decadal interplay supporting the interpretation of past sea level variability and the improvement of future projections in the Mediterranean.

Sea level variations at the basin scale also affect coastal areas, where regional ocean processes, human activities, and vertical land movements (Buzzanga et al., 2023) modulate local impacts on coastal communities (Cramer et al., 2018; MedECC, 2024). Building on previous basin-scale assessments, this study investigates Mediterranean decadal sea level trends at both regional and coastal scales, extending the analysis to the coastal domain and supporting decision-making relevant to coastal risk management on decadal timescales.

2 Datasets and methods

Daily sea level anomaly (SLA) data from two satellite altimetry products covering 1993–2024 are analysed to compute decadal trends in the Mediterranean Sea. The satC3S dataset (product ref. no. 1, in Table 1) is a global gridded product at 1/4° spatial resolution designed for climate applications, ensuring long-term stability of mean sea level estimates by relying on a consistent set of two satellite missions (Dibarboure et al., 2011; Pascual et al., 2006). The satCMEMS dataset (product ref. no. 2, in Table 1) includes all available satellite missions and provides higher spatial resolution of 1/16° over European seas. Both datasets are affected by an uncorrected instrumental drift of the TOPEX-A mission until February 1999; since this correction is not yet available in the

current release of either dataset, results involving the 1993–1999 period should be interpreted with caution. Glacial isostatic adjustment (GIA) correction is not applied, as regional estimates report small and time-independent rates that do not affect interdecadal variability within the uncertainty of our decadal trend estimates (Spada and Melini, 2022).

For the sub-basin analysis, SLA data are spatially averaged over the WMED and EMED, bounded at the Sicily Strait along a zonal transect at 37° N. Time series are then analysed following the methodology of Borile et al. (2025), and here summarized: the daily seasonal cycle over the 2000–2023 period is subtracted to obtain de-seasoned SLA, and a low-pass filter is applied to isolate long-term fluctuations. Decadal trends are then computed using 10-year-long sliding windows shifted monthly and fitted with the Theil–Sen estimator (Theil, 1992; Sen, 1968), which is a non-parametric method more robust to outliers than traditional linear regression, but does not allow for the acceleration estimate. Finally, trend uncertainty is assessed using a stationary bootstrap with 1000 resamples to account for temporal autocorrelation (Patton et al., 2009; Politis and Romano, 1994).

The same approach is used to evaluate the decadal trend associated with thermosteric (η_T) and halosteric (η_H) sea level components, whose sum defines the total steric sea level (η_S):

$$\eta_S = \eta_T + \eta_H = \int_{-H}^{0} \alpha \left(T - T_f\right) \mathrm{d}z - \int_{-H}^{0} \beta \left(S - S_f\right) \mathrm{d}z \quad (1)$$

where T_f and S_f are reference temperature and salinity values, α and β are constant linear coefficients of thermal expansion and haline contraction, and H is the spatially varying ocean depth. Both reference values and steric coefficients are taken as spatially constant basin-mean values, consistent with previous studies and suitable for a basin-averaged steric sea level analysis (Borile et al., 2025; Pinardi et al., 2014). The proposed formulation (1) is based on a simplification of the non-linear equation of state, enabling the separation of thermosteric and halosteric sea level contributions. Although this linear approximation introduces region-dependent differences, these are consistent with uncertainties in model temperature and salinity fields, supporting its use for the present analysis.

The steric sea level is estimated using daily temperature and salinity data from the regional MEDREA24 and the global GLORYS12 ocean reanalyses (products ref. no. 3 and 4, in Table 1), with horizontal resolutions of 1/24 and 1/12° respectively (Escudier et al., 2021; Lellouche et al., 2021).

To assess the reliability of satellite-derived sea level trends at the local scale, we analyse mean sea level records from tide gauges of the tgCMEMS and tgPSMSL datasets (products ref. no. 5 and 6, in Table 1). Data from tgPSMSL refer to a common Revised Local Reference (RLR) datum, as recommended for long-term analysis. Similarly, tgCMEMS data are selected based on good quality checks to detect significant datum changes. The tgPSMSL serves as the Global Sea Level Observing System (GLOSS) Data Assembly Center for monthly mean sea level records from tide gauges (Holgate et al., 2013): relying mostly on national providers for quality control, this dataset has been central to IPCC assessments of sea level rise based on in-situ observations (Oppenheimer et al., 2019). On the contrary, tgCMEMS provides centrally validated, delayed-mode sea level data derived from near-real-time observations at hourly resolution (Lin-Ye et al., 2023). Both the tgPSMSL and tgCMEMS datasets were considered, as they may include different sets of stations. In both cases, stations are selected based on record length and data completeness; short data gaps are linearly interpolated, and hourly records are averaged to daily values to match the temporal resolution of SLA data.

Where available, preference is given to stations located nearby GNSS (Global Navigation Satellite System) sensors to allow vertical land movement (VLM) correction, using trend values provided by URL/SONEL data server, ULR7 solution (product ref. no. 7, in Table 1). The ULR7 solution provides vertical velocity estimates in the ITRF2014 (International Terrestrial Reference System) frame (Gravelle et al., 2023). Accordingly, absolute sea level trends at tide gauge locations are computed by adding the VLM rate to the relative sea level trend derived from tide gauge records (Santamaría-Gómez et al., 2012).

Finally, for direct comparison between satellite and in-situ observations, satC3S SLA values are extracted at the grid point closest to each tide gauge. Differences in reference frame and high-frequency signal treatment are minimized by reintroducing the dynamic atmospheric correction (DAC) into altimetry data and applying VLM corrections to tide gauge records. The DAC is taken from the CLS product, based on the Mog2D model and distributed by Aviso+ with support from CNES (product ref. no. 8, in Table 1; Pascual et al., 2008). Overall, these processing choices aim to reduce methodological inconsistencies while acknowledging that satellite altimetry and tide gauges sample sea level variability at different spatial and temporal scales, and therefore provide complementary, rather than strictly equivalent, information.

3 Results

3.1 Decadal trend at the sub-basin scale

The evolution of the sea level decadal trend over the WMED and EMED regions is presented in Fig. 1, based on satC3S and satCMEMS. Each point represents the trend over the decade centered on that date (e.g., the value reported for January 2005 corresponds to the period January 2000–December 2009). Both sub-basins exhibit a decadal variability, with positive sea level trends ranging from negligible values up to $6.4 \pm 1.0\,\mathrm{mm\,yr^{-1}}$, and two periods of relative

slowdown (around 2001 and 2011 in WMED, and 2002 and 2014 in EMED). It is worth noting that satCMEMS generally agrees with satC3S within the associated uncertainty, though the latter is preferred for long-term consistency (Dibarboure et al., 2011). At basin scale, variability is strongly influenced by the sea level mass component, which reflects the large-scale balance between surface freshwater fluxes and boundary volume transports. Recent studies quantify this contribution over the Mediterranean basin as the residual of large but compensating terms, resulting in a basin-mean sea level contribution of about $+8\,\mathrm{mm\,yr^{-1}}$ over 1993–2022, similar to the observed sea level trend from altimetry data (Borile et al., 2025; García-García et al., 2022). Because mass contribution may be highly localized in time and space, its effect on sea level emerges primarily through integration over large domains, shaping the basin-averaged signal rather than local sea level variations.

Focusing on the steric contribution to sea level change, Fig. 2 shows the thermosteric and halosteric components of the mean sea level decadal trend. The concept of steric compensation in the Mediterranean Sea arises from the opposing behaviour of these two components: the thermosteric trend is positive and driven by seawater thermal expansion, while the halosteric contribution is negative and associated with the observed salinity increase. Observational evidence of these processes has been reported at local and basin scales, affecting coastal and deep regions. Recent studies document a general warming and salinification of the Mediterranean (Aydogdu et al., 2023; Kubin et al., 2023; Borghini et al., 2014), alongside regional contrasts in the EMED, such as Ionian freshening and Levantine salinification (Grodsky et al., 2019). Together, these observations highlight the direct link between steric sea level components and changes in underlying thermohaline properties.

Although the steric components play a relatively minor role in the long-term mean sea level budget of the Mediterranean compared to mass-driven contributions (Pinardi et al., 2014), their decadal variability can reach amplitudes comparable to the observed sea level trends. This highlights the importance of accounting for steric processes, together with surface fluxes and boundary transports, to better understand the mechanisms governing the mean sea level change (Borile et al., 2025; Cazenave et al., 2014).

In the WMED (Fig. 1a), neglecting the 1993-1999 period due to the uncorrected TOPEX-A drift, the measured decadal trend increased from 3.0 ± 0.7 to $6.4 \pm 1.0\,\mathrm{mm\,yr^{-1}}$. A temporary slowdown is observed in the decades around 2011, coinciding with a phase during which the combined effect of thermosteric and halosteric components shifts from significantly contributing to sea level trend to becoming nearly neutral (Fig. 2a). Indeed, in both MEDREA24 and GLORYS12, this period marks a transition between two different regimes: before the decade centered in 2009, the steric contribution dampens the total sea level rise, afterward it contributes positively. Accordingly, the increasing decadal trend reported by satC3S is supported by thermal expansion that exceeds haline contraction, consistent with reported sea surface temperature increases and long-term warming trends in the region (Pastor et al., 2018; Pisano et al., 2020).

On the other side of the Sicily Strait, the EMED trend (Fig. 1b) exhibits greater temporal variability compared to the WMED, without a clear increasing value over the entire analysed period. Two periods of negligible trends are observed around the decades centered in 2002 and 2014, separated by a rapid trend increase followed by a smoother slowdown. After the decade centered in 2015 the trend value increases again, showing an almost constant acceleration after 2018 and reaching a peak of $6.4 \pm 1.1\,\mathrm{mm\,yr^{-1}}$ in the latest decade. Notably, while WMED and EMED currently experience similar rates of sea level rise, the EMED exhibits a much sharper acceleration.

The steric components in the EMED (Fig. 2b) help explain this behaviour: halosteric contraction persisted throughout the period, with a strengthening negative trend observed from the decade centered in 2014 onward, while thermal expansion has remained relatively stable since 2007, after a period of minimal contribution centered around 2004. The combined effect of these two components caused the total steric contribution to alternate between negative and positive trend values. In the most recent decadal windows (centered from 2015 onward), the observed EMED sea level trend increases as the total steric component's negative contribution weakens approaching negligible values, as shown in both MEDREA24 and GLORYS12. These features are consistent with documented changes in thermohaline properties of deep waters in the Adriatic–Ionian system, including recent variations in both thermosteric and halosteric contributions and associated salinization signals (Terzić et al., 2025), as well as with broader EMED variability patterns (Mohamed and Skliris, 2022).

Therefore, while WMED shows an increasing mean sea level trend over the long period, the EMED is characterized by a pronounced quasi-decadal variability that tends to mask any linear acceleration (mean trend values are reported in Table 2). The different variability is connected to large-scale circulation changes occurred in the two sub-basins, with a key contribution related to the Adriatic-Ionian Bimodal Oscillating System (BiOS, Civitarese et al., 2023; Gačić et al., 2010). Although originating in a relatively confined region, the BiOS appears sufficiently strong to influence steric sea level variability across the entire EMED (substantial correlation between decadal trend and BiOS variability, $r = 0.61$), consistent with previous findings (e.g. Meli et al., 2023; Civitarese et al., 2023; Meli, 2024), but not to impact the WMED behaviour (with no correlation between decadal trend and BiOS variability, $r = -0.06$).

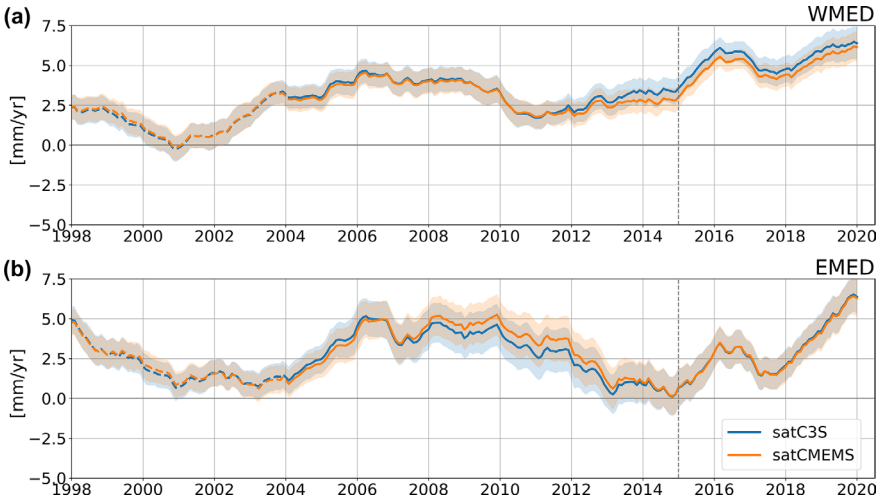


Figure 1. Time series of de-seasoned SLA decadal trend values computed over sliding windows shifted by one month across the period 1993–2024 in the WMED **(a)** and EMED **(b)**. Dashed lines indicate trends computed over windows that partially include the period affected by the uncorrected TOPEX-A drift, when data should be interpreted with caution. Shaded areas represent the trend uncertainty, defined as the standard deviation of the residuals from the bootstrap procedure. The vertical dashed line at January 2015 marks the starting point of tide gauges analysis shown in Fig. 4.

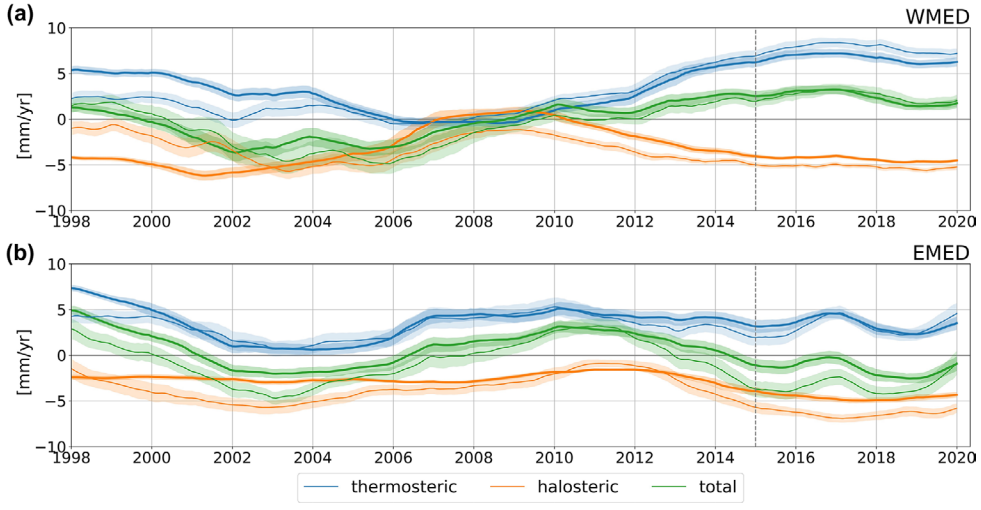


Figure 2. Time series of decadal trend associated to the de-seasoned total steric sea level (η_S), and its thermosteric (η_T) and halosteric (η_H) components, computed over sliding windows shifted by one month across the period 1993–2024 in the WMED **(a)** and EMED **(b)**. Different datasets are shown: MEDREA24 (thick lines) and GLORYS12 (thin lines). Shaded areas represent the trend uncertainty, defined as the standard deviation of the residuals from the bootstrap procedure. The vertical dashed line at January 2015 marks the starting point of tide gauges analysis shown in Fig. 4.

3.2 Decadal trend on coastal areas

To identify the regions where sea level rise has the greatest impact on human activities, we analyse sea level data close to the coast. The accuracy of altimetry data in coastal zones is a known challenge due to land contamination on satellite measurements and small-scale dynamical processes that affect the sea level variability (Vignudelli et al., 2019; Cipollini et al., 2017). Therefore, in-situ data are crucial to validate the altimetry performance.

Figure 3 presents the coastal decadal trend from satC3S, computed over the period 2015–2024 to enable direct comparison with the most recent tide gauge observations from tgCMEMS and tgPSMSL. A general lack of in-situ measurements characterizes the EMED compared to the WMED, with most tide gauges located along the Spanish and French coasts (Pérez Gómez et al., 2022). Nevertheless, despite the coarse resolution of satC3S (grid cell area is $\sim 600\,km^2$), a good agreement is observed between altimetry and tide

Table 2. Summary of the mean decadal sea level trend values derived from Figs. 1 and 2 and computed for decades centered between 2004 and 2020, thus excluding the period affected by the uncorrected TOPEX-A drift. All values are reported in mm yr^{-1}.

	SLA trend		Total steric sea level trend		Thermosteric sea level trend		Halosteric sea level trend	
	satCMEMS	satC3S	MEDREA24	GLORYS12	MEDREA24	GLORYS12	MEDREA24	GLORYS12
WMED	3.69 ± 0.77	3.95 ± 0.79	0.78 ± 0.68	0.10 ± 0.83	3.36 ± 0.55	3.95 ± 0.64	-2.52 ± 0.45	-3.91 ± 0.48
EMED	3.12 ± 1.17	2.95 ± 1.16	0.23 ± 0.67	-1.07 ± 0.92	3.53 ± 0.66	3.30 ± 0.91	-3.15 ± 0.26	-4.15 ± 0.59

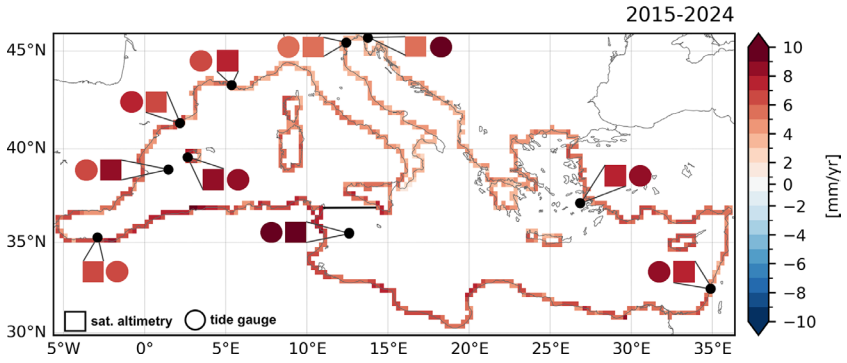


Figure 3. Map of decadal sea level trends computed at coastal points from the satC3S dataset for the 2015–2024 period. This decade is the most recent available for comparing decadal trends from satC3S altimetry (where DAC has been reintroduced), with in-situ observations from tgCMEMS and tgPSMSL, adjusted for VLM. Each black dot indicates the location of a tide gauge discussed in the text. Satellite and tide gauge-derived trends at the same sites are shown as squares and circles, respectively, and are coloured according to the colorbar (values reported in Table 3). The thin black line corresponds to the zonal transect used to define the boundary between WMED and EMED at 37° N.

gauges trends within the estimated uncertainties (Table 3). Larger discrepancies are mainly observed in Trieste, where the in-situ trend from tgCMEMS is double that of the altimetry-based estimate, highlighting the influence of local processes on sea level variability that may not be captured by satellite observations.

At the basin scale, the spatial distribution of trends from satC3S is quite homogeneous, with positive values across most of the Mediterranean coastal areas. Trends exceeding 8 mm yr^{-1} are reported in the WMED, particularly along the Algerian coast, the Balearic Islands, and the western coasts of Sardinia and Corsica. Weaker trends are observed in the Adriatic and Aegean Seas, with the Adriatic showing values below 3 mm yr^{-1}. Notably, marginal seas display a rapid shift of regime compared to the trend computed for the period 2013–2022 in Borile et al. (2025), where negative values were previously reported. This behaviour aligns with the sharp trend increase recently observed at the EMED basin scale.

Figure 4 compares decadal trend time series of absolute sea level from altimetry and tide gauges, focusing on the period from 2010 onward to reduce data gaps and ensure overlap with GNSS-based VLM correction. It is worth noting that the correspondence between coastal sea level trends and steric sea level changes is not persistent everywhere and over time, and may become significant only during specific periods, depending on the dominant local forcing mechanisms (Tsimplis and Rixen, 2002).

In the WMED, data from Melilla, Barcelona, Ibiza, Palma de Mallorca and Marseille all show a gradually increasing decadal trend consistent with the basin-scale evolution. Notably, the time series derived from tgCMEMS and tgPSMSL largely overlap, with only minor differences likely attributed to the distinct preprocessing filters applied in each dataset.

In Barcelona and Melilla, the trend increased steadily from ~ 1 to over 5 mm yr^{-1}. In contrast, Marseille experienced a slightly negative trend until the decade centered in 2019, after which it became positive and aligned with the altimetry trend.

Ibiza and Palma de Mallorca show trends persistently above 5 mm yr^{-1}, though with less pronounced increase over time.

Particularly in Palma de Mallorca, a shift of only two years in the decadal analysis window leads to a doubling of the estimated trend and remained nearly stable afterward. In this case, it is worth noting that the perceived sea level rise is partially dampened by local positive VLM (Table 3).

All WMED stations show a relative maximum trend around the decades centered between 2016 and 2017, consistent with the basin-scale signal. This feature is even more pronounced at tide gauges stations located in the EMED, such as Lampedusa, Leros, Hadera, Venezia and Trieste,

Table 3. Sea level trends near selected coastal cities for the most recent available decade (2015–2024) derived from different datasets: satC3S (with DAC reintroduced), tgCMEMS and tgPSMSL. The VLM trend, with the distance between each tide gauge and its associated GNSS station indicated in brackets, should be added to the in-situ relative sea level trend to allow comparison with the satC3S absolute sea level trend (see Fig. 3). The resulting trend difference is reported in the last column. When both tide gauge datasets are available, tgCMEMS data are used. All trend values are reported in mm yr^{-1}.

	Tide gauge coordinates	Relative sea level trend [tgCMEMS]	Relative sea level trend [tgPSMSL]	Absolute sea level trend [satC3S]	VLM trend [ULR/SONEL]	Sea level trend DIFF [satC3S – tg]
Marseille	43.28° N/5.35° E	–	7.4 ± 1.7	7.5 ± 1.0	-0.49 ± 0.27 (5 m)	0.5 ± 2.2
Barcelona	41.34° N/2.16° E	7.9 ± 1.3	8.1 ± 1.2	6.6 ± 1.7	-0.86 ± 0.23 (0 m)	-0.4 ± 2.3
Melilla	35.29° N/2.92° W	6.3 ± 0.9	6.1 ± 1.1	6.6 ± 1.2	–	0.3 ± 1.5
Mallorca	39.56° N/2.64° E	6.9 ± 1.9	7.0 ± 1.6	8.8 ± 2.1	1.68 ± 0.83 (0 m)	0.2 ± 3.4
Ibiza	38.91° N/1.45° E	7.9 ± 1.8	7.9 ± 1.7	8.1 ± 1.7	-1.28 ± 0.26 (78 m)	1.5 ± 2.7
Lampedusa	35.50° N/12.60° E	11.8 ± 1.4	–	10.0 ± 1.5	-0.36 ± 0.37 (130 m)	-1.5 ± 2.4
Venezia	45.42° N/12.43° E	6.9 ± 3.1	–	5.8 ± 2.0	-1.51 ± 1.56 (741 m)	0.4 ± 5.1
Trieste	45.65° N/13.76° E	13.2 ± 3.5	–	5.6 ± 2.1	0.01 ± 0.14 (6707 m)	-7.6 ± 4.2
Hadera	32.47° N/34.88° E	–	7.7 ± 2.3	7.2 ± 1.7	0.46 ± 0.21 (3145 m)	-0.9 ± 3.0
Leros	37.13° N/26.85° E	–	8.6 ± 1.6	7.7 ± 1.6	–	-0.9 ± 2.2

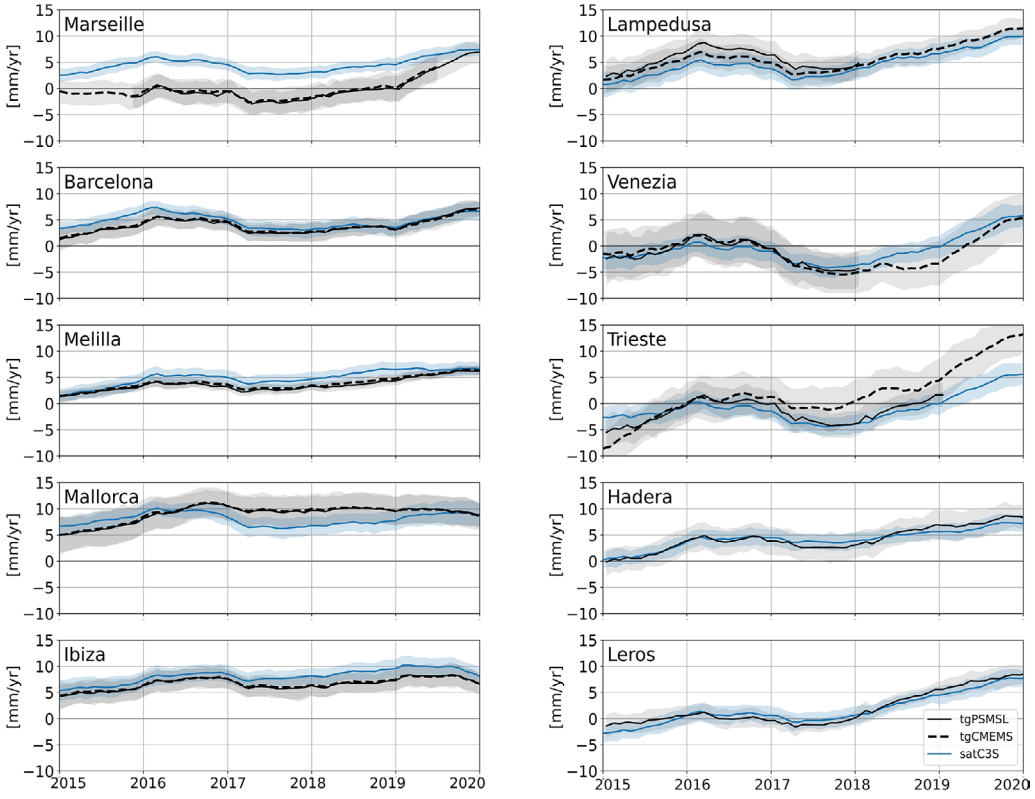


Figure 4. Time series of decadal sea level trends computed nearby coastal cities, using tide gauges data from tgCMEMS, tgPSMSL, and satellite data from satC3S. For a direct comparison between satellite and in-situ data, the VLM trend is added to the relative sea level trend derived from tide gauge records, while DAC is reintroduced to satC3S altimetry. Trends are computed over sliding windows shifted monthly across the period 2010–2024; where tgCMEMS data are not available (Hadera and Leros), only tgPSMSL data are analysed. Shaded areas represent the associated uncertainty, defined as the standard deviation of the residuals from the bootstrap procedure.

where a marked slowdown follows the observed peak. However, the limited availability of data in this region often limits the possibility of a comparison between tgCMEMS and tgPSMSL.

Trieste is the only station where satC3S and tgCMEMS provide decadal trend estimates that differ beyond the uncertainty bounds, likely due to local effects not captured by altimetry. Nevertheless, both datasets capture a transition from negative to positive trends in the most recent period. The case of Venezia is similar, though more complex due to the city's geographical setting and the socio-economic implications of sea level changes (Zanchettin et al., 2021). Here, a minimum trend of $-5.3 \pm 3.7\,\mathrm{mm\,yr^{-1}}$ is reported for the decade centered around 2018, which has recently turned positive according to tgCMEMS. A similar pattern is also observed in Leros, in the Aegean Sea, where the trend remains negligible until the decade centered in 2018, followed by a sharp acceleration in the most recent period.

By contrast, tide gauges outside the marginal seas show consistently positive trends exceeding the uncertainty bounds. At Lampedusa, in the Sicily Strait, the local trend increased sharply after the slowdown, rising from 2.6 ± 2.3 to nearly $10\,\mathrm{mm\,yr^{-1}}$. In Hadera, along the Israeli coast, the trend shows a more gradual acceleration persisting throughout the entire analysed period.

4 Summary and conclusions

This study provides an assessment of decadal sea level trends in the Mediterranean Sea, emphasizing both regional-scale and coastal-scale variability. The results confirm that sea level rise in the basin is not a linear process but exhibits significant decadal fluctuations due to a complex interplay between mass and steric sea level components (Pinardi et al., 2015; García-García et al., 2022; Meli et al., 2023) connected to large-scale circulation changes (Gačić et al., 2010), which reflect internal climate variability.

In the Western Mediterranean (WMED), a sea level acceleration has been observed since the early 2000s, partially sustained by thermal expansion that exceeds haline contraction (Pisano et al., 2020). In contrast, the Eastern Mediterranean (EMED) displays stronger temporal variability, with halosteric contraction playing a major counterbalancing role (Meli et al., 2023; Borghini et al., 2014) correlated to the Adriatic-Ionian Bimodal Oscillating System mechanism (Civitarese et al., 2023). This regional modulation is conceptually analogous to the influence of the El Niño-Southern Oscillation (ENSO) on global mean sea level variability (Nerem et al., 2010), though ENSO is more strongly linked to mass-driven fluctuations (Cazenave et al., 2012).

Only in recent years the EMED reached a comparable rate of sea level rise to the WMED, largely due to a weakening of the overall steric contribution. While this study has focused on the steric component, also the mass component, associated with surface water budget variations and exchanges through the Straits, remains a key factor influencing Mediterranean sea level changes on decadal timescales (Borile et al., 2025). A full interpretation of decadal variability requires a comprehensive perspective that accounts for both contributions, therefore future efforts integrating these components will be essential to achieve a complete understanding of basin sea level evolution.

At the coastal level, altimetry trends are generally consistent with tide gauge observations in the WMED, while larger uncertainties persist in the EMED, underscoring the need for improved in-situ monitoring networks and data sharing, including vertical land movement estimations as a relevant contribution to local effects (Buzzanga et al., 2023; Cramer et al., 2018). The observed reversal of trends in marginal seas such as the Adriatic and Aegean suggests that localized processes, including vertical land motion and regional circulation anomalies, can rapidly alter coastal sea level evolution.

Our findings highlight the decadal variability range of coastal sea level trends in the Mediterranean, indicating that local sea level evolution may temporarily depart from long-term mean trajectories due to regional processes. Such variability, however, should be interpreted as a component of Mediterranean sea level dynamics, superimposed on the long-term mean sea level rise that ultimately drives adaptation needs.

Code and data availability. The publicly available datasets analyzed in this study are referenced in Table 1. Codes used to perform the analysis are available on the Zenodo Repository at: https://doi.org/10.5281/zenodo.20284500 (Borile, 2026).

Author contributions. FB, EC, and PO contributed to the conceptualization, methodology, and analysis. FB, VL, BGP, and JLY were responsible for data curation and organization, with AM contributing to data resources. FB and VL performed software development, formal analysis, investigation, and visualization, while AM, BGP and JLY contributed to data investigation. EC was responsible for funding acquisition, and PO supervised the study. FB prepared the original draft of the manuscript, with contributions from all coauthors in the editing and reviewing.

Competing interests. The contact author has declared that none of the authors has any competing interests.

Disclaimer. The Copernicus Marine Service offering is regularly updated to ensure it remains at the forefront of user requirements. In this process, some products may undergo replacement or renaming, leading to the removal of certain product IDs from the catalogue. If readers have any questions or require assistance regarding these modifications, please feel free to reach out to the

Copernicus Marine Service user support team for further guidance. They will be able to provide the necessary information to address concerns and find suitable alternatives.

Publisher's note: Copernicus Publications remains neutral with regard to jurisdictional claims made in the text, published maps, institutional affiliations, or any other geographical representation in this paper. The authors bear the ultimate responsibility for providing appropriate place names. Views expressed in the text are those of the authors and do not necessarily reflect the views of the publisher.

Acknowledgements. The authors gratefully acknowledge Nadia Pinardi for her insightful interpretation of the various factors driving decadal variability in the Mediterranean Sea. They thank the Copernicus Sea Level TAC and In Situ TAC teams for the valuable discussions that supported the interpretation of data during the preparation of this manuscript. They also acknowledge the constructive comments and suggestions provided by reviewers, which significantly helped to improve the clarity and quality of the manuscript.

Financial support. This research was funded by the Copernicus Marine Service for the Mediterranean Sea Monitoring and Forecasting Centre (contract no. 2425L05-COP-MFC MED-5500). The study was also carried out within the RETURN Extended Partnership and received funding from the European Union Next-Generation EU (National Recovery and Resilience Plan – NRRP, Mission 4, Component 2, Investment 1.3 – D.D. 1243 2/8/2022, PE0000005).

Review statement. This paper was edited by Pierre-Marie Poulain and reviewed by Francisco Mir Calafat and two anonymous referees.

References

Adloff, F., Somot, S., Sevault, F., Jordà, G., Aznar, R., Déqué, M., Herrmann, M., Marcos, M., Dubois, C., Padorno, E., Alvarez-Fanjul, E., and Gomis, D.: Mediterranean Sea response to climate change in an ensemble of twenty first century scenarios, Clim. Dyn., 45, 2775–2802, https://doi.org/10.1007/s00382-015-2507-3, 2015.

Alothman, A. O., Bos, M. S., Fernandes, R. M. S., and Ayhan, M. E.: Sea level rise in the north-western part of the Arabian Gulf, J. Geodyn., 81, 105–110, https://doi.org/10.1016/j.jog.2014.09.002, 2014.

Aydogdu, A., Miraglio, P., Escudier, R., Clementi, E., and Masina, S.: The dynamical role of upper layer salinity in the Mediterranean Sea, in: 7th edition of the Copernicus Ocean State Report (OSR7), edited by: von Schuckmann, K., Moreira, L., Le Traon, P.-Y., Grégoire, M., Marcos, M., Staneva, J., Brasseur, P., Garric, G., Lionello, P., Karstensen, J., and Neukermans, G., Copernicus Publications, State Planet, 1-osr7, 6, https://doi.org/10.5194/sp-1-osr7-6-2023, 2023.

Ballarotta, M., Pujol, M. I., and SL-TAC team: EU Copernicus Marine Service Quality Information Document for the Global Ocean Gridded L 4 Sea Surface Heights And Derived Variables Reprocessed Copernicus Climate Service, SEALEVEL_GLO_PHY_CLIMATE_L4_MY_008_057, issue 3.0, Mercator Ocean International, https://documentation.marine.copernicus.eu/QUID/CMEMS-SL-QUID-008-057.pdf (last access: 30 October 2025), 2024.

Ballarotta, M., Pujol, M. I., and SL-TAC team: EU Copernicus Marine Service Quality Information Document for the European Seas Gridded L 4 Sea Surface Heights And Derived Variables Reprocessed 1993 Ongoing, SEALEVEL_EUR_PHY_L4_MY_008_068, issue 13.0, Mercator Ocean International, https://documentation.marine.copernicus.eu/QUID/CMEMS-SL-QUID-008-032-068.pdf (last access: 30 October 2025), 2025.

Borghini, M., Bryden, H., Schroeder, K., Sparnocchia, S., and Vetrano, A.: The Mediterranean is becoming saltier, Ocean Sci., 10, 693–700, https://doi.org/10.5194/os-10-693-2014, 2014.

Borile, F.: Codes used in the Ocean State Report #10 contribution titled "Decadal variability in the Eastern and Western Mediterranean sea level trends", in: State of the Planet (v0.0), Zenodo [code], https://doi.org/10.5281/zenodo.20284500, 2026.

Borile, F., Pinardi, N., Lyubartsev, V., Ghani, M. H., Navarra, A., Alessandri, J., Clementi, E., Coppini, G., Mentaschi, L., Verri, G., da Costa, V. S., Scoccimarro, E., Misurale, F., Novellino, A., and Oddo, P.: The Eastern Mediterranean Sea mean sea level decadal slowdown: the effects of the water budget, Front. Clim., 7, https://doi.org/10.3389/fclim.2025.1472731, 2025.

Buzzanga, B., Bekaert, D. P. S., Hamlington, B. D., Kopp, R. E., Govorcin, M., and Miller, K. G.: Localized uplift, widespread subsidence, and implications for sea level rise in the New York City metropolitan area, Sci. Adv., 9, eadi8259, https://doi.org/10.1126/sciadv.adi8259, 2023.

Calafat, F. M., Chambers, D. P., and Tsimplis, M. N.: Mechanisms of decadal sea level variability in the eastern North Atlantic and the Mediterranean Sea, J. Geophys. Res.-Oceans, 117, https://doi.org/10.1029/2012JC008285, 2012.

Calafat, F. M., Frederikse, T., and Horsburgh, K.: The Sources of Sea-Level Changes in the Mediterranean Sea Since 1960, J. Geophys. Res.-Oceans, 127, e2022JC019061, https://doi.org/10.1029/2022JC019061, 2022.

Cazenave, A., Henry, O., Munier, S., Delcroix, T., Gordon, A. L., Meyssignac, B., Llovel, H., Palanisamy, H., and Becker, M.: Estimating ENSO Influence on the Global Mean Sea Level, 1993–2010, Mar. Geod., 35, 82–97 https://doi.org/10.1080/01490419.2012.718209, 2012.

Cazenave, A., Dieng, H.-B., Meyssignac, B., von Schuckmann, K., Decharme, B., and Berthier, E.: The rate of sea-level rise, Nat. Clim. Change, 4, 358–361, https://doi.org/10.1038/nclimate2159, 2014.

Cipollini, P., Calafat, F. M., Jevrejeva, S., Melet, A., and Prandi, P.: Monitoring Sea Level in the Coastal Zone with Satellite Altimetry and Tide Gauges, in: Integrative Study of the Mean Sea Level and Its Components, edited by: Cazenave, A., Champollion, N., Paul, F., and Benveniste, J., Springer International Publishing, Cham, 35–59, https://doi.org/10.1007/978-3-319-56490-6_3, 2017.

Civitarese, G., Gačić, M., Batistić, M., Bensi, M., Cardin, V., Dulčić, J., Garić, R., and Menna, M.: The BiOS mechanism: History, theory, implications, Prog. Oceanogr., 216, 103056, https://doi.org/10.1016/j.pocean.2023.103056, 2023.

Cramer, W., Guiot, J., Fader, M., Garrabou, J., Gattuso, J.-P., Iglesias, A., Lange, M. A., Lionello, P., Llasat, M. C., Paz, S., Peñuelas, J., Snoussi, M., Toreti, A., Tsimplis, M. N., and Xoplaki, E.: Climate change and interconnected risks to sustainable development in the Mediterranean, Nat. Clim. Change, 8, 972–980, https://doi.org/10.1038/s41558-018-0299-2, 2018.

Dibarboure, G., Pujol, M.-I., Briol, F., Traon, P. Y. L., Larnicol, G., Picot, N., Mertz, F., and Ablain, M.: Jason-2 in DUACS: Updated System Description, First Tandem Results and Impact on Processing and Products, Mar. Geod., 34, 214–241, https://doi.org/10.1080/01490419.2011.584826, 2011.

Drévillon, M., Lellouche, J. M., Régnier, C., Garric, G., Bricaud, C., Hernandez, O., and Bourdallé-Badie, R.: EU Copernicus Marine Service Quality Information Document for the Global Ocean Physics Reanalysis, GLOBAL_MULTIYEAR_PHY_001_030, issue 1.6, Mercator Ocean International, https://documentation.marine.copernicus.eu/QUID/CMEMS-GLO-QUID-001-030.pdf (last access: 5 July 2025), 2023.

Drévillon, M., Fernandez, E., and Lellouche, J. M.: EU Copernicus Marine Service Product User Manual for the Global Ocean Physics Reanalysis, GLOBAL_MULTIYEAR_PHY_001_030, issue 1.6, Mercator Ocean International, https://documentation.marine.copernicus.eu/PUM/CMEMS-GLO-PUM-001-030.pdf (last access: 5 July 2025), 2024.

Escudier, R., Clementi, E., Cipollone, A., Pistoia, J., Drudi, M., Grandi, A., Lyubartsev, V., Lecci, R., Aydogdu, A., Delrosso, D., Omar, M., Masina, S., Coppini, G., and Pinardi, N.: A High Resolution Reanalysis for the Mediterranean Sea, Front. Earth Sci., 9, https://doi.org/10.3389/feart.2021.702285, 2021.

Escudier, R., Clementi, E., Nigam, T., Aydogdu, A., Fini, E., Pistoia, J., Grandi, A., and Miraglio, P.: EU Copernicus Marine Service Quality Information Document for the Mediterranean Sea Physics Reanalysis, MEDSEA_MULTIYEAR_PHY_006_004, issue 2.4, Mercator Ocean International, https://documentation.marine.copernicus.eu/QUID/CMEMS-MED-QUID-006-004.pdf (last access: 5 July 2025), 2024.

EU Copernicus Marine Service Product: Global Ocean Physics Reanalysis, Mercator Ocean International [data set], https://doi.org/10.48670/moi-00021, 2023.

EU Copernicus Marine Service Product: Global Ocean Gridded L 4 Sea Surface Heights And Derived Variables Reprocessed Copernicus Climate Service, Mercator Ocean International [data set], https://doi.org/10.48670/moi-00145, 2024a.

EU Copernicus Marine Service Product: European Seas Gridded L 4 Sea Surface Heights And Derived Variables Reprocessed 1993 Ongoing, Mercator Ocean International [data set], https://doi.org/10.48670/moi-00141, 2024b.

EU Copernicus Marine Service Product: Mediterranean Sea Physics Reanalysis, Mercator Ocean International [data set], https://doi.org/10.25423/CMCC/MEDSEA_MULTIYEAR_PHY_006_004_E3R1, 2024c.

EU Copernicus Marine Service Product: Global Ocean - Delayed Mode Sea level product, Mercator Ocean International [data set], https://doi.org/10.17882/93670, 2024d.

Gačić, M., Borzelli, G. L. E., Civitarese, G., Cardin, V., and Yari, S.: Can internal processes sustain reversals of the ocean upper circulation? The Ionian Sea example, Geophys. Res. Lett., 37, https://doi.org/10.1029/2010GL043216, 2010.

García-García, D., Vigo, M. I., Trottini, M., Vargas-Alemañy, J. A., and Sayol, J.-M.: Hydrological cycle of the Mediterranean-Black Sea system, Clim. Dyn., 59, 1919–1938, https://doi.org/10.1007/s00382-022-06188-2, 2022.

Giorgi, F.: Climate change hot-spots, Geophys. Res. Lett., 33, https://doi.org/10.1029/2006GL025734, 2006.

Gomis, D., Ruiz, S., Sotillo, M. G., Álvarez-Fanjul, E., and Terradas, J.: Low frequency Mediterranean sea level variability: The contribution of atmospheric pressure and wind, Glob. Planet. Change, 63, 215–229, https://doi.org/10.1016/j.gloplacha.2008.06.005, 2008.

Gravelle, M., Wöppelmann, G., Gobron, K., Altamimi, Z., Guichard, M., Herring, T., and Rebischung, P.: The ULR-repro3 GPS data reanalysis and its estimates of vertical land motion at tide gauges for sea level science, Earth Syst. Sci. Data, 15, 497–509, https://doi.org/10.5194/essd-15-497-2023, 2023.

Gräwe, U., Klingbeil, K., Kelln, J., and Dangendorf, S.: Decomposing Mean Sea Level Rise in a Semi-Enclosed Basin, the Baltic Sea, J. Climate, 32, 3089–3108, https://doi.org/10.1175/JCLI-D-18-0174.1, 2019.

Grodsky, S. A., Reul, N., Bentamy, A., Vandemark, D., and Guimbard, S.: Eastern Mediterranean salinification observed in satellite salinity from SMAP mission, J. Mar. Sys., 198, 103190, https://doi.org/10.1016/j.jmarsys.2019.103190, 2019.

Holgate, S. J., Matthews, A., Woodworth, P. L., Rickards, L. J., Tamisiea, M. E., Bradshaw, E., Foden, P. R., Gordon, K. M., Jevrejeva, S., and Pugh, J.: New Data Systems and Products at the Permanent Service for Mean Sea Level, J. Coast. Res., 29, 493–504, https://doi.org/10.2112/JCOASTRES-D-12-00175.1, 2013.

Intergovernmental Panel on Climate Change (IPCC): Ocean, Cryosphere and Sea Level Change, in: Climate Change 2021 – The Physical Science Basis: Working Group I Contribution to the Sixth Assessment Report of the Intergovernmental Panel on Climate Change, Cambridge University Press, Cambridge, 1211–1362, https://doi.org/10.1017/9781009157896.011, 2023.

Kubin, E., Menna, M., Mauri, E., Notarstefano, G., Mieruch, S., and Poulain, P. M.: Heat content and temperature trends in the Mediterranean Sea as derived from Argo float data, Front. Mar. Sci., 10, 1271638, https://doi.org/10.3389/fmars.2023.1271638, 2023.

Lecci, R., Drudi, M., Grandi, A., and Clementi, E.: EU Copernicus Marine Service Product User Manual for the Mediterranean Sea Physics Reanalysis, MEDSEA_MULTIYEAR_PHY_006_004, issue 2.4, Mercator Ocean International, https://documentation.marine.copernicus.eu/PUM/CMEMS-MED-PUM-006-004.pdf (last access: 5 July 2025), 2024.

Lellouche, J.-M., Greiner, E., Bourdallé-Badie, R., Gilles, G., Melet, A., Drévillon, M., Bricaud, C., Hamon, M., Le Galloudec, O., Regnier, C., Candela, T., Testut, C.-E., Gasparin, F., Ruggiero, G., Mounir, B., Yann, D., and Pierre-Yves, L. T.: The Copernicus Global 1/12° Oceanic

and Sea Ice GLORYS12 Reanalysis, Front. Earth Sci., 9, https://doi.org/10.3389/feart.2021.698876, 2021.

Lin-Ye, J., Pérez Gómez, B., Gallardo, A., Manzano, F., de Alfonso, M., Bradshaw, E., and Hibbert, A.: Delayed-mode reprocessing of in situ sea level data for the Copernicus Marine Service, Ocean Sci., 19, 1743–1751, https://doi.org/10.5194/os-19-1743-2023, 2023.

Marcos, M. and Tsimplis, M. N.: Coastal sea level trends in Southern Europe, Geophys. J. Int., 175, 70–82, https://doi.org/10.1111/j.1365-246X.2008.03892.x, 2008.

MedECC: Summary for Policymakers, in: Climate and Environmental Coastal Risks in the Mediterranean, edited by: Djoundourian, S., Lionello, P., Llasat, M. C., Guiot, J., Cramer, W., Driouech, F., Gattacceca, J. C., and Marini, K., MedECC Reports, MedECC Secretariat, Marseille, France, p. 28, ISBN 978-2-493662-03-3, 2024.

Meli, M.: The potential recording of North Ionian Gyre's reversals as a decadal signal in sea level during the instrumental period, Sci. Rep., 14, 4907, https://doi.org/10.1038/s41598-024-55579-4, 2024.

Meli, M., Camargo, C. M. L., Olivieri, M., Slangen, A. B. A., and Romagnoli, C.: Sea-level trend variability in the Mediterranean during the 1993–2019 period, Front. Mar. Sci., 10, https://doi.org/10.3389/fmars.2023.1150488, 2023.

Milne, G. A., Gehrels, W. R., Hughes, C. W., and Tamisiea, M. E.: Identifying the causes of sea-level change, Nat. Geosci., 2, 471–478, https://doi.org/10.1038/ngeo544, 2009.

Mohamed, B. and Skliris, N.: Steric and atmospheric contributions to interannual sea level variability in the eastern mediterranean sea over 1993–2019, Oceanologia, 64, 50–62, https://doi.org/10.1016/j.oceano.2021.09.001, 2022.

Nerem, R. S., Chambers, D. P., Choe, C., and Mitchum, G. T.: Estimating Mean Sea Level Change from the TOPEX and Jason Altimeter Missions, Mar. Geod., 33, 435–446, https://doi.org/10.1080/01490419.2010.491031, 2010.

Oppenheimer, M., Glavovic, B., Hinkel, J., van deWal, R., Magnan, A. K., Abd-Elgawad, A., Cai, R., Cifuentes-Jara, M., Deconto, R. M., Ghosh, T., Hay, J., Isla, F., Marzeion, B., Meyssignac, B., and Sebesvari, Z.: Sea Level Rise and Implications for Low Lying Islands, Coasts and Communities, in: IPCC Special Report on the Ocean and Cryosphere in a Changing Climate (SROCC), Cambridge University Press, Cambridge, UK and New York, NY, USA, 321–445, https://doi.org/10.1017/9781009157964.006, 2019.

Parmesan, C., Morecroft, M. D., Trisurat, Y., and Mezzi, D.: Climate Change 2022: Impacts, Adaptation and Vulnerability, GIEC, IPCC, hal-03774939, https://hal.science/hal-03774939v1 (last access: 23 April 2026), 2022.

Pascual, A., Faugère, Y., Larnicol, G., and Le Traon, P.-Y.: Improved description of the ocean mesoscale variability by combining four satellite altimeters, Geophys. Res. Lett., 33, https://doi.org/10.1029/2005GL024633, 2006.

Pascual, A., Marcos, M., and Gomis, D.: Comparing the sea level response to pressure and wind forcing of two barotropic models: Validation with tide gauge and altimetry data, J. Geophys. Res.-Oceans, 113, https://doi.org/10.1029/2007JC004459, 2008.

Pastor, F., Valiente, J. A., and Palau, J. L: Sea Surface Temperature in the Mediterranean: Trends and Spatial Patterns (1982–2016), Pure Appl. Geophys., 175, 4017–4029, https://doi.org/10.1007/s00024-017-1739-z, 2018.

Patton, A., Politis, D. N., and White, H.: Correction to "Automatic Block-Length Selection for the Dependent Bootstrap" by D. Politis and H. White, Econom. Rev., https://doi.org/10.1080/07474930802459016, 2009.

Pérez Gómez, B., Vilibić, I., Šepić, J., Međugorac, I., Ličer, M., Testut, L., Fraboul, C., Marcos, M., Abdellaoui, H., Álvarez Fanjul, E., Barbalić, D., Casas, B., Castaño-Tierno, A., Čupić, S., Drago, A., Fraile, M. A., Galliano, D. A., Gauci, A., Gloginja, B., Martín Guijarro, V., Jeromel, M., Larrad Revuelto, M., Lazar, A., Keskin, I. H., Medvedev, I., Menassri, A., Meslem, M. A., Mihanović, H., Morucci, S., Niculescu, D., Quijano de Benito, J. M., Pascual, J., Palazov, A., Picone, M., Raicich, F., Said, M., Salat, J., Sezen, E., Simav, M., Sylaios, G., Tel, E., Tintoré, J., Zaimi, K., and Zodiatis, G.: Coastal sea level monitoring in the Mediterranean and Black seas, Ocean Sci., 18, 997–1053, https://doi.org/10.5194/os-18-997-2022, 2022.

Pérez Gómez, B., Lin-Ye, J., Hibbert, A., and Bradshaw, E.: EU Copernicus Marine Service Quality Information Document for the Global Ocean – Delayed Mode Sea level product, INSITU_GLO_PHY_SSH_DISCRETE_MY_013_053, issue 1.6, Mercator Ocean International, https://documentation.marine.copernicus.eu/QUID/CMEMS-INS-QUID-013-053.pdf (last access: 30 October 2025), 2024a.

Pérez Gómez, B., Lin-Ye, J., Gallardo, A., Bradshaw, E., Hibbert, A., Manzano F., and In Situ TAC partners: EU Copernicus Marine Service Product User Manual for the Global Ocean – Delayed Mode Sea level product, INSITU_GLO_PHY_SSH_DISCRETE_MY_013_053, issue 1.6, Mercator Ocean International, https://documentation.marine.copernicus.eu/PUM/CMEMS-INS-PUM-013-053.pdf (last access: 30 October 2025), 2024b.

Pinardi, N. and Masetti, E.: Variability of the large scale general circulation of the Mediterranean Sea from observations and modelling: a review, Palaeogeogr. Palaeoclimatol. Palaeoecol., 158, 153–173, https://doi.org/10.1016/S0031-0182(00)00048-1, 2000.

Pinardi, N., Bonaduce, A., Navarra, A., Dobricic, S., and Oddo, P.: The Mean Sea Level Equation and Its Application to the Mediterranean Sea, J. Climate, 27, 442–447, https://doi.org/10.1175/JCLI-D-13-00139.1, 2014.

Pinardi, N., Zavatarelli, M., Adani, M., Coppini, G., Fratianni, C., Oddo, P., Simoncelli, S., Tonani, M., Lyubartsev, V., Dobricic, S., and Bonaduce, A.: Mediterranean Sea large-scale low-frequency ocean variability and water mass formation rates from 1987 to 2007: A retrospective analysis, Prog. Oceanogr., 132, 318–332, https://doi.org/10.1016/j.pocean.2013.11.003, 2015.

Pisano, A., Marullo, S., Artale, V., Falcini, F., Yang, C., Leonelli, F. E., Santoleri, R., and Buongiorno Nardelli, B.: New Evidence of Mediterranean Climate Change and Variability from Sea Surface Temperature Observations, Remote Sens., 12, 132, https://doi.org/10.3390/rs12010132, 2020.

Politis, D. N. and Romano, J. P.: The Stationary Bootstrap, J. Am. Stat. Assoc., 89, 1303–1313, https://doi.org/10.1080/01621459.1994.10476870, 1994.

Pujol, M. I.: EU Copernicus Marine Service Product User Manual for the Global Ocean Gridded L 4 Sea Surface Heights And Derived Variables Reprocessed Copernicus Climate Service,

SEALEVEL_GLO_PHY_CLIMATE_L4_MY_008_057, issue 4.0, Mercator Ocean International, https://documentation.marine.copernicus.eu/PUM/CMEMS-SL-PUM-008-057.pdf (last access: 30 October 2025), 2024.

Pujol, M. I.: EU Copernicus Marine Service Product User Manual for the European Seas Gridded L 4 Sea Surface Heights And Derived Variables Reprocessed 1993 Ongoing, SEALEVEL_EUR_PHY_L4_MY_008_068, issue 10.0, Mercator Ocean International, https://documentation.marine.copernicus.eu/PUM/CMEMS-SL-PUM-008-032-068.pdf (last access: 30 October 2025), 2025.

Sannino, G., Carillo, A., Iacono, R., Napolitano, E., Palma, M., Pisacane, G., and Struglia, M.: Modelling present and future climate in the Mediterranean Sea: a focus on sea-level change, Clim. Dyn., 59, 357–391, https://doi.org/10.1007/s00382-021-06132-w, 2022.

Santamaría-Gómez, A., Gravelle, M., Collilieux, X., Guichard, M., Míguez, B. M., Tiphaneau, P., and Wöppelmann, G.: Mitigating the effects of vertical land motion in tide gauge records using a state-of-the-art GPS velocity field, Glob. Planet. Change, 98–99, 6–17, https://doi.org/10.1016/j.gloplacha.2012.07.007, 2012.

Sen, P. K.: Estimates of the Regression Coefficient Based on Kendall's Tau, J. Am. Stat. Assoc., 63, 1379–1389, https://doi.org/10.1080/01621459.1968.10480934, 1968.

Spada, G. and Melini, D.: New estimates of ongoing sea level change and land movements caused by Glacial Isostatic Adjustment in the Mediterranean region, Geophys. J. Int., 229, 984–998, https://doi.org/10.1093/gji/ggab508, 2022.

Terzić, E., Cardin, V., Le Meur, J., Dunić, N., Vodopivec, M., and Vilibić, I.: Unprecedented warming and salinization observed in the deep Adriatic, Limnol. Oceanogr. Lett., 10, 888–898, https://doi.org/10.1002/lol2.70051, 2025.

Theil, H.: A Rank-Invariant Method of Linear and Polynomial Regression Analysis, in: Henri Theil's Contributions to Economics and Econometrics: Econometric Theory and Methodology, edited by: Raj, B. and Koerts, J., Springer Netherlands, Dordrecht, 345–381, https://doi.org/10.1007/978-94-011-2546-8_20, 1992.

Tsimplis, M. N. and Rixen, M.: Sea level in the Mediterranean Sea: The contribution of temperature and salinity changes, Geophys. Res. Lett., 29, 51-1–51-4, https://doi.org/10.1029/2002GL015870, 2002.

Tuel, A. and Eltahir, E. A. B.: Why Is the Mediterranean a Climate Change Hot Spot?, J. Climate, 33, 5829–5843, https://doi.org/10.1175/JCLI-D-19-0910.1, 2020.

Vignudelli, S., Birol, F., Benveniste, J., Fu, L.-L., Picot, N., Raynal, M., and Roinard, H.: Satellite Altimetry Measurements of Sea Level in the Coastal Zone, Surv. Geophys., 40, 1319–1349, https://doi.org/10.1007/s10712-019-09569-1, 2019.

Zanchettin, D., Bruni, S., Raicich, F., Lionello, P., Adloff, F., Androsov, A., Antonioli, F., Artale, V., Carminati, E., Ferrarin, C., Fofonova, V., Nicholls, R. J., Rubinetti, S., Rubino, A., Sannino, G., Spada, G., Thiéblemont, R., Tsimplis, M., Umgiesser, G., Vignudelli, S., Wöppelmann, G., and Zerbini, S.: Sea-level rise in Venice: historic and future trends (review article), Nat. Hazards Earth Syst. Sci., 21, 2643–2678, https://doi.org/10.5194/nhess-21-2643-2021, 2021.

State Planet, 7-osr10, 14, 2026
https://doi.org/10.5194/sp-7-osr10-14-2026
© Author(s) 2026. This work is distributed under
the Creative Commons Attribution 4.0 License.

Metocean study for the planning of the FSRU terminal: a case study at the Estonian coast of the Gulf of Finland

Urmas Raudsepp[1], Ilja Maljutenko[1], Jan-Victor Björkqvist[2], Amirhossein Barzandeh[1], Sander Rikka[1], Aarne Männik[1], Siim Pärt[1], Priidik Lagemaa[1], Victor Alari[1], Kaimo Vahter[1], and Rivo Uiboupin[1]

[1]Tallinn University of Technology, Ehitajate tee 5, 19086, Tallinn, Estonia
[2]Norwegian Meteorological Institute, Allégaten 70, 5007, Bergen, Norway

Correspondence: Ilja Maljutenko (ilja.maljutenko@taltech.ee)

Received: 6 August 2025 – Discussion started: 25 September 2025
Revised: 16 September 2026 – Accepted: 17 September 2026 – Published: 30 September 2026

Abstract. Metocean extreme-value assessment is a necessary input for the planning of coastal and offshore energy infrastructure, particularly in semi-enclosed basins where wind, waves, sea level, and currents vary strongly over short spatial scales. This study provides a site-specific metocean characterization for the planned Floating Storage and Regasification Unit terminal at Pakrineeme/Paldiski on the southern coast of the Gulf of Finland and places the local results in a Baltic Sea-wide context. Long-term observational, satellite, reanalysis, and numerical model datasets were combined, including Copernicus Marine Service products, ERA5 winds, local sea-level and wind observations, satellite wind and sea-level products, and high-resolution NEMO and SWAN simulations. Extreme values of wind speed, sea level, significant wave height, wave period, and surface current speed were estimated using established extreme-value methods, including block maxima and peaks-over-threshold approaches with Generalized Extreme Value and Generalized Pareto distributions.

For the Pakrineeme/Paldiski site, the estimated 50-year marginal return levels are approximately 23 m s^{-1} for 10 m wind speed, +1.5 and −0.7 m for sea-level maxima and minima, 4.1 m for significant wave height, and 0.37 m s^{-1} for surface current speed. These values provide metocean design-basis information for subsequent engineering assessment, but they do not represent direct estimates of vessel motions, mooring loads, fender loads, structural response, or operational downtime. The Baltic-wide analysis shows strong spatial contrasts in 50-year return levels: the largest wave extremes occur in exposed parts of the Baltic Proper, while the largest positive sea-level anomalies occur in constrained sub-basins such as the Gulf of Finland and the Gulf of Riga. The associated uncertainty fields indicate that regional-scale return levels should be interpreted as screening information rather than locally validated design values. The study demonstrates how harmonized multi-source metocean datasets can support site-specific hazard characterization and regional comparison of infrastructure-relevant extremes in the Baltic Sea.

1 Introduction

Meteorological and oceanographic ("metocean") conditions critically influence the design, construction, and operation of offshore energy infrastructure (Bitner-Gregersen, 2015; Robertson et al., 2021; Bailey and Freedman, 2024). A comprehensive metocean study is thus an essential prerequisite for any new offshore installation to ensure it can be built and operated safely, efficiently, and with minimal environmental risk (Valamanesh et al., 2015; Ross et al., 2020; Cheynet et al., 2024). In the case of a Floating Storage and Regasification Unit (FSRU) terminal – a floating liquefied natural gas import facility – the stakes are especially high (Ho, 2008). FSRUs are moored vessels that are directly exposed to wind, wave, current, and sea level extremes, so understanding the full spectrum of these conditions at a proposed site is fundamental to make informed decisions on subsequent engineering assessment and operational planning (Voogt et al., 2014; Mrozowski, 2024), such as safe cargo transfer windows (Allen et al., 2022). Omitting the metocean assessment,

Published by Copernicus Publications.

Table 1. Product Table.

Product ref. no.	Product ID & type	Data access	Documentation
1	BALTICSEA_MULTIYEAR_PHY_003_011; Numerical models	EU Copernicus Marine Service Product (2025a);	Quality Information Document (QUID): Panteleit et al. (2025); Product User Manual (PUM): Ringgaard et al. (2024)
2	BALTICSEA_REANALYSIS_WAV_003_015; Numerical models	EU Copernicus Marine Service Product (2024a)	QUID: Kanarik et al. (2024) PUM: Lindgren et al. (2024)
3	ERA5; Numerical models	Copernicus Climate Change Service (2023)	Product reference: Copernicus Climate Change Service (2023) Journal article: Hersbach et al. (2020)
4	WIND_GLO_PHY_L3_MY_012_005; Satellite observations	EU Copernicus Marine Service Product (2024b)	QUID: Driesenaar et al. (2024a) PUM: Driesenaar et al. (2024b)
5	WIND_BAL_PHY_HR_L3_MY_012_107; Satellite observations	EU Copernicus Marine Service Product (2025b)	QUID: Husson et al. (2025) PUM: CLS et al. (2025)
6	Paldiski North Port (sea level)	Raudsepp et al. (2026b)	
7	SEALEVEL_EUR_PHY_L4_MY_008_068; Satellite observations	EU Copernicus Marine Service Product (2025c)	QUID: Ballarotta et al. (2025a) PUM: Pujol (2025a)
8	SEALEVEL_EUR_PHY_L3_MY_008_061; Satellite observations	EU Copernicus Marine Service Product (2025d)	QUID: Ballarotta et al. (2025b) PUM: Pujol (2025b)
9	NEMO-EST05	Raudsepp et al. (2026b)	Pärt et al. (2023); Barzandeh et al (2025)
10	GETM	MSI*	Maljutenko and Raudsepp (2019)
11	LainePoiss	MSI*	Alari et al. (2022)
12	SWAN-EST05	Raudsepp et al. (2026b)	Pärt et al. (2023)
13	Pakri coastal weather station (wind)	Raudsepp et al. (2026b)	Keevallik and Soomere (2009)
14	WAVE_GLO_PHY_SWH_L3_MY_014_005; Satellite observations	EU Copernicus Marine Service Product (2025e)	QUID: Charles and Ollivier (2026) PUM: Nigou and Ollivier (2026)

* MSI – data access upon request.

or underestimating its importance, can compromise the environmental information available for subsequent engineering decisions.

Beyond site-specific engineering concerns, the regional context of this study underscores the importance of robust metocean data. Across Europe, recent geopolitical shifts have prompted urgent efforts to diversify natural gas supply and bolster energy security – since early 2022, the EU has fast-tracked on the order of 30 new liquefied natural gas (LNG) import terminal projects (Ostrowski, 2022; Rymut and Mihaylov, 2025). In the Baltic region, countries are rapidly developing LNG infrastructure (including FSRU-based terminals) to reduce reliance on single pipeline routes and ensure reliable energy supply (Slakaityte et al., 2022). Estonia's planned LNG terminal near Paldiski, on the coast of the Gulf of Finland (Fig. 1), is such a case: the project was fast-tracked in 2022 as part of a broader strategy to improve the Baltic's energy resilience. Reliable metocean information is needed to assess structural safety and define permissible operating conditions. This high strategic importance places additional emphasis on getting the environmental design criteria right from the outset.

The Baltic Sea – and the Gulf of Finland in particular – presents unique metocean challenges that must be factored into design. This shallow, semi-enclosed sea has an irregular, fragmented coastline and complex bathymetry that produce highly localized wind, wave, and current patterns often harder to predict than those in the open ocean (Alenius et al., 1998; Soomere, 2005; Westerlund et al., 2019; Pellikka et al., 2023). The Gulf of Finland is a long, narrow sub-basin with complex coastal geometry. Its geometry and wind forcing can produce substantial non-tidal water-level variability, including storm-driven setup and the seiches (Medvedev and Kulikov, 2021; Barzandeh et al., 2025; Lorenz et al., 2025). The gulf's geometry limits the development of long-period swells; storms instead generate short-period, steep wind seas that – while lower in height than ocean swells – (Björkqvist et al., 2017; Kanarik et al., 2021; Björkqvist et al., 2021) can in-

duce vigorous motions and cyclic loads on a moored FSRU. In winter, parts of the Gulf freeze over with seasonal sea ice, which dampens waves but introduces ice loading and operational constraints (Lu et al., 2024). These combined factors – non-tidal water level extremes, steep short waves, complex coastal currents, and periodic ice cover – create a demanding environment where high-resolution, site-specific metocean data and modeling are required to capture the full range of conditions for design and operations.

To meet these challenges, the present study leverages state-of-the-art long-term datasets and numerical modeling tools to characterize the metocean climate of the Paldiski site (Fig. 1). The Pakrineeme/Paldiski study site lies on the Pakri Peninsula, on Estonia's southern Gulf of Finland coast (Fig. 1), in a predominantly bedrock-controlled coastal setting. The FSRU berth has a representative water depth of approximately 16 m. Compared with the open Baltic Proper, the site is relatively sheltered from waves but remains susceptible to sea-level extremes and episodic wind-driven events. Modern metocean analyses increasingly rely on multi-decadal hindcasts and reanalyses to provide continuous, high-quality records of environmental parameters (Penalba et al., 2022; D'Agostini et al., 2024). Here we utilize roughly 30 years of data (spanning from the early 1990s to the 2020s) from open-access sources such as the Copernicus Marine Environment Monitoring Service (CMEMS) and ECMWF ERA5 Reanalysis, which offers specialized hindcast/reanalysis products for European regional seas. These include modeled time series of Baltic Sea wind speeds, wave heights, sea level variations, and currents that have been consistently processed and quality-controlled. Drawing on such extensive datasets ensures that both typical conditions and rare extremes are accounted for, providing a robust statistical basis for estimating the design environmental criteria.

In addition to analyzing historical data, we apply high-resolution numerical models to downscale and resolve local metocean conditions at the terminal site. A nested modeling approach is adopted: the regional Baltic wave model WAM (The Wamdi Group, 1988) provides boundary conditions to a fine-resolution nearshore wave model SWAN (Simulating WAves Nearshore; Booij et al., 1999) configured with detailed coastal bathymetry, thereby simulating how offshore waves transform as they propagate into the shallow gulf and around complex shoreline features. For hydrodynamics, we employ the NEMO (Nucleus for European Modelling of the Ocean; Madec et al., 2017) framework, NEMO-EST05 in particular, and the GETM (General Estuarine Transport Model; Burchard and Bolding, 2002) to reproduce local current patterns and sea level responses under various wind and pressure scenarios. NEMO-EST05 and GETM are independent downscaling simulations that both use boundary conditions from the CMEMS reanalysis. All these models have been calibrated for Baltic Sea conditions – accounting for factors like bottom friction and seasonal ice coverage – and their performance tested in past Baltic applications (Björkqvist et al., 2018; Kärnä et al., 2021; Raudsepp and Maljutenko, 2022; Björkqvist et al., 2024). By combining broad-scale reanalysis data with targeted local modeling, our study captures both large-scale climatic influences and fine-scale site effects in the metocean conditions.

To quantify the design extremes, we perform statistical extreme value analysis on the assembled data. Both block-maxima and peaks-over-threshold techniques are employed, fitting Generalized Extreme Value (GEV) distributions and Generalized Pareto Distributions (GPD) respectively to the long-term time series. This yields estimated return levels for various return periods (e.g. 10-year, 50-year, 100-year events) for each key parameter: wind speed, significant wave height, extreme high and low sea levels, and surface current speed. For the 50-year return period, for instance, our analysis indicates roughly a $23\,\mathrm{m\,s^{-1}}$ extreme wind, a 4.1 m significant wave height, a $+1.5$ m storm surge high water (and -0.7 m extreme low water), and about a $0.37\,\mathrm{m\,s^{-1}}$ surface current. The results provide marginal metocean return levels and uncertainty estimates that can be used as environmental input parameters for later design-load calculations.

A crucial aspect of our approach is the integration and distribution-based evaluation of multiple data sources, aligning with best practices in modern metocean studies. We compare model outputs and hindcast data against available observations – including satellite measurements (for example, altimeter-derived sea levels and scatterometer winds) and in situ records from local buoys and tide gauges – to assess consistency with the available observations. This multi-source comparison helps to quantify uncertainties and biases in the datasets, allowing us to correct the model predictions where necessary and improve confidence in the results. By fusing information from global reanalyses, regional models, remote sensing, and on-site measurements, the study minimizes the risk of relying on any single source. This data-driven, ensemble approach provides a multi-source characterization and identifies differences among the available estimates that can be trusted for engineering design and risk assessment in a high-stakes project.

The study addresses two linked questions. First, how can long-term observational, satellite, reanalysis, and high-resolution model datasets be combined to characterize metocean extremes at a specific coastal infrastructure site? Second, how do the resulting site-specific estimates relate to the spatial variability of extreme conditions across the Baltic Sea? We address these questions through a detailed assessment of the Pakrineeme/Paldiski FSRU site followed by a Baltic Sea-wide analysis of 50-year return levels. The purpose is not to introduce a new extreme-value method, but to demonstrate a transferable workflow in which regional datasets are evaluated and, where justified, locally adjusted for site-specific assessment, while spatially consistent regional products are used to provide the broader basin-scale context. The Baltic-wide results are therefore intended for regional comparison and screening; site-specific applications

elsewhere require local observations, representativeness assessment, and, where necessary, local bias treatment.

2 Data and methods

To support the metocean design basis for the proposed FSRU terminal near Paldiski, we employed a multi-source, multi-model approach combining observational datasets, global and regional reanalyses, and high-resolution numerical modeling. This section outlines the sources of environmental data and the methods used to derive local wind, sea level, wave, and current statistics, with particular focus on extreme value analysis. Where independent observations were available, model and reanalysis products were evaluated through comparisons with satellite and in situ measurements. This multi-source approach supports evaluation of dataset consistency and selection for the site-specific extreme-value assessment. For the site-specific assessment, data harmonization included aligning sea-level datasets to a common vertical datum, matching temporal resolution where direct model comparisons were required, and applying the observation-based wind and wave adjustments described below and in the Supplement. For the Baltic-wide assessment, the original gridded datasets were retained to preserve spatial consistency. The dataset-specific preprocessing is summarized in Table A1.

2.1 Wind Data and Modeling

Surface wind conditions were assessed using a combination of in situ measurements, satellite observations, and reanalysis products. Long-term wind observations from the Paldiski meteorological station (59.39° N, 24.04° E) were used as a reference (product ref. no. 13). This record spans from 1993 to 2021, with 3-hourly resolution until 2003 and hourly resolution thereafter.

ERA5 reanalysis (Hersbach et al., 2020; product ref. no. 3), with 10 m wind data at 0.25° resolution, served as the primary dataset for wind climatology and was used to drive wave and hydrodynamic models. Alternative regional reanalyses – COSMO-REA6 (Bollmeyer et al., 2015), BaltAn65+ (Luhamaa et al., 2011), and NORA3 (Solbrekke et al., 2021) – were evaluated but ultimately excluded due to systematic biases and inconsistencies when compared with coastal wind observations. COSMO-REA6 and BaltAn65+ consistently overestimated wind speeds during high wind events, with COSMO-REA6 also exhibiting unrealistic wind spikes. NORA3, despite its higher resolution, substantially underestimated high wind speeds. In contrast, ERA5 showed better agreement with in situ measurements throughout the year, justifying its selection as the primary wind dataset. Remote sensing data included ASCAT Level-3 scatterometer wind fields (MetOp A/B/C; 12.5 km resolution, 2007–present) (product ref. no. 4) and Sentinel-1 SAR Level-2 surface wind vectors (1 km resolution, 2017–present) (product ref. no. 5). Satellite wind data were extracted from open-sea locations approximately 15–20 km from the terminal site.

Using ASCAT wind speed measurements and ERA5 wind speed values a corrective function based on sigmoid was developed and applied for ERA5 wind speeds to reflect better measured open sea values in the region (Supplement, S1 Wind correction).

2.2 Sea Level Data and Modeling

Tide gauge measurements from the Paldiski North Port (59.34972° N, 24.0475° E) (product ref. no. 6) were used to evaluate sea level variability. Visual readings were available for 1993–2009, and hourly automated records for 2016–2021. Data gaps between 2010 and 2016 were filled using the CMEMS Baltic Sea Physics Reanalysis sea surface height time series (product ref. no. 1) at the nearest grid cell, after aligning the model series to the gauge datum and mean level over the overlapping period.

Satellite-derived sea surface height data included Level-3 along-track altimetry and gridded Level-4 products from multiple altimeter missions (Jason, Sentinel-3A, CryoSat-2, ENVISAT, etc.), obtained from the CMEMS database (product ref. no. 8 and 7).

Three model sources provided high-resolution sea level time series: (1) CMEMS Baltic Sea Physical Reanalysis (1 nmi resolution, 1993–2017) (product ref. no. 1), based on the NEMO-Nordic model; and two independent model simulations dynamically downscaled from the CMEMS reanalysis onto 0.5 nmi grids: (2) NEMO-EST05 hindcast (product ref. no. 9); (3) GETM barotropic surge model (Maljutenko and Raudsepp, 2019; product ref. no. 10). All sea level heights were converted to the same vertical datum as the Paldiski gauge (normalized to its 1993–2009 mean water level of +0.21 m) so that model and observed datasets could be consistently compared.

2.3 Wave Data and Modeling

Wave statistics were derived from two primary hindcast sources: (1) CMEMS Wave Reanalysis (WAM Cycle 4.6.2; 1 nmi grid, 1993–2020) (product ref. no. 2); (2) SWAN-EST05 high-resolution model (0.5 nmi grid, 2000–2009) (product ref. no. 12). The CMEMS hindcast was calibrated using short-term wave buoy observations (LainePoiss buoy (Alari et al., 2022), May–June 2022) collected near the terminal site (59.399° N, 24.103° E) (product ref. no. 11). A comparison of the CMEMS hindcast (product ref. no. 2) to the short-term in situ measurements (product ref. no. 11) revealed that the model had a slight high bias in wave heights. The summer 2022 buoy data, although limited, indicated that CMEMS over-predicted significant wave height by roughly 15 % during the comparison period. For the local analysis, significant wave heights were therefore reduced by 15 % and wave periods by 5 % using multiplicative scaling based on

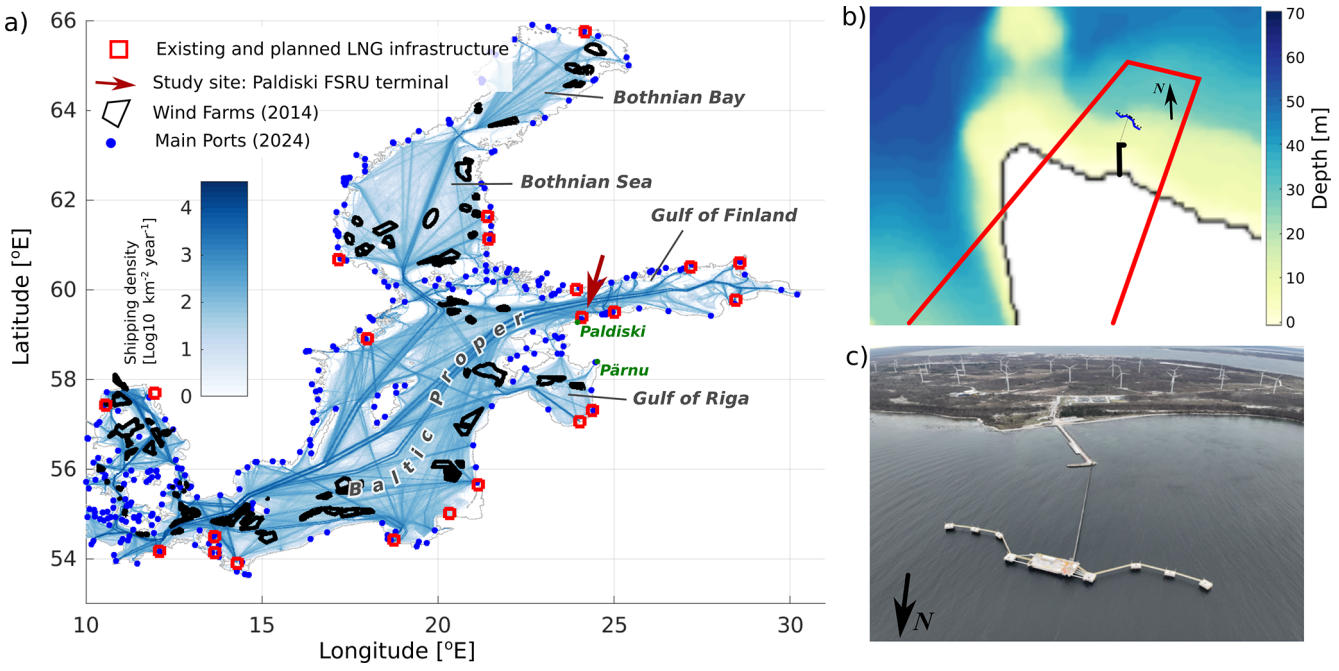


Figure 1. Map of the Baltic Sea showing locations of various human activities **(a)**. Existing and planned LNG infrastructure is redrawn from Gas Infrastructure Europe (2019), Global Energy Monitor (2024); offshore wind farms from European Marine Observation and Data Network (EMODnet; 2024a); main ports from EMODnet (2024b); and vessel traffic density from EMODnet (2024c). Panels **(b)** and **(c)** highlight LNG terminals and the location of the FSRU mooring quay. Panel **(c)** presents a drone photograph taken after construction. © Pärt (2026) Distributed under the Creative Commons Attribution 4.0 License. The red rectangle in panel **(b)** indicates the drone's field of view and the extent of the photograph shown in panel **(c)**. GIE (2019) LNG infrastructure data reproduced under the Gas Infrastructure Europe usage terms (https://www.gie.eu, last access: 15 July 2025). GEM (2024) LNG infrastructure data courtesy of the Global Energy Monitor (https://globalenergymonitor.org, last access: 15 July 2025). EMODnet (2024a, b, c) offshore wind farms, ports, and vessel traffic density data provided by the European Marine Observation and Data Network (https://emodnet.ec.europa.eu, last access: 15 July 2025).

the near-site comparison (Supplement, Sect. S2 Wave correction). Because this adjustment is proportional to the original value, its absolute magnitude increases with wave height or period and it should not be interpreted as removal of a constant additive mean bias. Satellite altimeter data (Level-3, 2002–2020) (product ref. no. 14) were also used to assess significant wave height distributions.

2.4 Current Data and Modeling

Surface current were obtained from the CMEMS Baltic Sea Reanalysis (product ref. no. 1), available as daily means, and from the NEMO-EST05 high-resolution hindcast (product ref. no. 9), available at 1 h temporal resolution. For the distribution-based comparison in Fig. 2, the hourly NEMO-EST05 currents were averaged to daily means to match the temporal resolution of the CMEMS product. This averaging was used only for the direct comparison between the two datasets; the site-specific extreme-value analysis was based on the native hourly NEMO-EST05 current series.

2.5 Extreme value analysis framework

2.5.1 Site-specific Extreme Value Analysis (EVA)

To characterize metocean extremes, we applied statistical extreme value theory to the long-term time series. Two complementary methods were used: (1) Block Maxima Method, fitting Generalized Extreme Value (GEV) distributions to annual maxima (yearly values); (2) Peaks Over Threshold (POT), fitting Generalized Pareto Distributions (GPD) to exceedances over a high threshold. The main strengths of the Block Maxima Method are straightforward implementation and the absence of a threshold-selection requirement, making it convenient for consistent comparisons across variables and locations. However, retaining only one value per year discards other potentially informative storm events, while including maxima from relatively calm years. By retaining several independent extreme events per year, POT can use the available record more efficiently and potentially improve the precision of return-level estimates. Its main limitations are sensitivity to threshold selection and the need to separate dependent observations associated with the same storm (Jonathan and Ewans, 2013; Caruso and Marani, 2022). For the POT data a censoring time of 24 h was used to

reduce dependence between exceedances associated with the same event . Model fits were performed via Maximum Likelihood Estimation (MLE). Special cases, including the Gumbel (GEV with shape = 0) and Exponential (GPD with shape = 0) distributions, were used where justified by the data. In practice, the GEV distribution provides additional flexibility by estimating the shape parameter from the annual maxima, allowing different tail behaviours to be represented. However, for records spanning only a few decades, the shape parameter may itself be weakly constrained and sensitive to individual extreme years. Consequently, the GEV was not assumed a priori to be superior to the simpler Gumbel distribution; the fitted distributions were evaluated together with their physical plausibility, and long-return-period estimates were interpreted cautiously (Jonathan and Ewans, 2013; Jonathan et al., 2021).

The return levels for 10, 20, 50, and 100-year periods were estimated for wind speed (product ref. no. 3, 13), significant wave height (product ref. no. 2, 12), sea level extremes (both high and low) (product ref. no. 1, 6, 9), and surface current speed (product ref. no. 9) at the LNG site (Fig. 1). A 100-year return level is a fitted probability statement, not an observed event that requires a 100-year record by definition. Nevertheless, estimating return levels beyond the length of the available record involves extrapolation of the fitted tail, and the associated uncertainty increases when only a few decades of extremes are available (Jonathan and Ewans, 2013; Jonathan et al., 2021). Therefore, we mainly focus on the 50-year estimates for local-regional comparison, and retain 100-year estimates only as explicitly qualified longer-return-period extrapolations. Selection of the final model and dataset for each parameter was based on best fit, physical plausibility, and consistency across data sources. The complete time series used for the site-specific assessment, together with the associated analysis scripts, are available in the data repository of Raudsepp et al. (2026b). Given the length and temporal resolution of these records, the manuscript presents their statistical distributions and extreme-value diagnostics rather than compressed plots of the complete time series.

2.5.2 Regional extreme value analysis

The regional extension of the EVA was designed to place the local FSRU site results within a broader Baltic Sea context while recognizing the different roles of the two analyses. At Paldiski, local observations and high-resolution modelling are used to evaluate the representativeness of the long-term datasets and support site-specific preprocessing. For the Baltic-wide analysis, the original gridded long-term datasets are retained so that a spatially consistent methodology can be applied across the basin. The correction factors derived at Paldiski are therefore not transferred to other locations, because their magnitude is expected to depend on local exposure, bathymetry, coastal geometry, and observation-to-grid representativeness While the EVA methods used here are standard, their consistent application across basin-wide, long-term metocean datasets allows the spatial distribution of return levels and associated uncertainty to be compared among different coastal and offshore infrastructure regions. This distinction is important because metocean extremes in the Baltic Sea are strongly controlled by basin geometry, fetch limitation, bathymetry, and sub-basin-scale circulation, and therefore local design values cannot be reliably generalized from one site to another. The regional estimates support preliminary comparison of rare-event exposure, while the local analysis addresses site-specific representativeness and preprocessing. However, return-level maps alone do not quantify the frequency or duration of calm conditions, operational weather windows or optimal siting. Those questions require additional time-series, directional, persistence and engineering analyses.

To extend the EVA regionally, we leverage comprehensive long-term datasets from the Copernicus Marine Service. The hindcast data underpinning our analysis include the Baltic Sea Multi-Year Physics Reanalysis for sea levels and currents (product ref. no. 1), and the Baltic Sea wave hindcast/reanalysis for wave heights (product ref. no. 2). These products provide a 31-year (1993–2024) homogeneous time series with daily temporal resolution (sea level and currents) and hourly (bulk wave parameters) at spatial resolution of 1 nautical mile, which are crucial for stable extreme statistics. Accordingly, the Baltic-wide current EVA is based on daily-mean surface currents and should be interpreted as a regional screening estimate rather than an estimate of sub-daily peak currents. Wind forcing is taken from the ERA5 global atmospheric reanalysis (hourly, ~ 31 km grid) (product ref. no. 3), whose 10 m wind speeds have been rigorously validated and widely used for wave modeling in European seas (Hersbach et al., 2020). Recent evaluations indicate that using ERA5 winds can improve the representation of Baltic wave extremes, even if some regional reanalyses better capture the mean wave climate (Giudici et al., 2023).

The Baltic-wide EVA was performed using the original gridded long-term datasets in order to preserve spatial consistency. Block Maxima Method, fitting Generalized Extreme Value (GEV) distributions to annual maxima was used for the EVA. Annual-maxima GEV fitting provides a uniform framework for regional comparison. It avoids the location- and variable-specific threshold selection and storm-declustering diagnostics required by POT, simplifying regional implementation. This is a practical methodological choice – not evidence that POT is unsuitable – with the trade-off that additional extreme events within each year are discarded. To estimate the uncertainties in EVA of wind speed, wave height, sea level, and currents – a bootstrap resampling method was used. It is a non-parametric approach that involves resampling the original dataset (with replacement) many times and refitting the extreme value model each time. The method provides empirical distributions of return levels, from which confidence intervals can be derived. This is

particularly useful when the sample size is small or when the distribution is skewed. We used this method to estimate the ranges of return values. We used 180 iterations, with the 2.5th and 97.5th percentiles as the lower and upper bounds of the results. Thus, the 95 % between them gives a full "confidence" interval.

The resulting maps should be interpreted as regional-scale estimates of metocean exposure rather than as locally bias-corrected design values. For site-specific applications elsewhere in the Baltic Sea, especially in nearshore or morphodynamically active areas, local validation against observations and local bias correction are required.

3 Results and Discussion

3.1 Wind Speed

A comparison of reanalysis and observed wind data (wind gusts excluded) indicated that the ERA5 10 m wind speeds (product ref. no. 3) underestimated the highest winds recorded at the Pakri coastal weather station (product ref. no. 13). After applying the correction function (see Supplement, Sect. S1 Wind correction), the distribution of ERA5 winds closely resembled open-sea conditions and aligned well with satellite scatterometer (ASCAT) measurements (product ref. no. 4) over the overlapping period 2012–2021, while still matching the high-end values recorded at Pakri (Fig. 2a, b). The Pakri station data, as expected for a land-based site, show a higher frequency of low wind speeds due to sheltering when winds blow from land, but they also captured a few extreme gusts that the coarser ASCAT sampling likely missed. Overall, the adjusted ERA5 dataset provides a representative wind climate for the offshore terminal location, capturing both the predominance of moderate maritime winds and the magnitude of rare storm peaks (Fig. 2a, b).

The fitted models describe the wind extremes well, including the highest recorded storm winds (Fig. 3a, b). The resulting 100-year return period wind speed – meaning the wind speed with a 1 % annual probability of exceedance – is approximately 24 m s^{-1} at 10 m elevation. Lower return period estimates follow accordingly (e.g. about 23 m s^{-1} for a 50-year return period; see Table 2). This $\sim$24 m s^{-1} extreme wind represents a critical design value for the FSRU terminal, defining the upper limit of wind loading that the mooring system and vessel must withstand.

3.2 Sea Level

Five different sea level datasets were evaluated to characterize water level variability at the site. These include the CMEMS Baltic Sea reanalysis (product ref. no. 1; 1 nmi resolution), the subregional NEMO-EST05 model (product ref. no. 9; 0.5 nmi resolution), the regional GETM model (product ref. no. 10; 0.5 nmi resolution), along with satellite altimetry (instantaneous along-track Level 3 and daily-averaged gridded Level 4 products) (product ref. no. 8 and 7), and the tide gauge observations at Paldiski (product ref. no. 6). Figure 2c, d illustrates the probability distributions of sea level from these sources over their common period. The three continuous hindcasts (CMEMS, NEMO-EST05, and GETM), which provide hourly sea level time series for 1993–2017, show very similar distributions and are broadly in agreement with the statistical behavior of the Paldiski gauge record (which spans 1993–2009 with gaps). In contrast, the satellite-based records are either smoothed or sparse: the Level 4 product, with its daily averaging, smooths out short-lived peaks and thus underrepresents extreme high or low water events, whereas the instantaneous Level 3 altimeter data capture the full range of variability but contain relatively few data points near the study area. These differences in sampling density are reflected in the lengths of the distribution curves in Fig. 2c, d. When examining the upper and lower tails of the sea level distributions on a logarithmic scale (Fig. 2d), we find generally good agreement, but with some differences in extreme values across datasets. In the high-water (positive) tail, the CMEMS hindcast (product ref. no. 1) tends to predict slightly more frequent very high water levels than the NEMO-EST05 (product ref. no. 9) and GETM (product ref. no. 10) models. For instance, near the observed maximum sea levels, the CMEMS curve extends a bit further, suggesting a higher likelihood of extreme surge events in that dataset. The GETM and NEMO hindcasts yield somewhat lower extreme probabilities, but all three model-based datasets exhibit a similarly steep drop-off in the tail (Fig. 2c, d), indicating they capture the rarity of extreme surges in the Gulf of Finland. In summary, while the lower-to-moderate sea level range is consistently represented across all sources, the CMEMS data provide a somewhat more conservative estimate of the highest water levels, making it a useful dataset for extreme analysis.

For extreme high sea levels, we focused on the model hindcasts and reanalysis for return period estimation, while using the Paldiski tide gauge data (product ref. no. 6) for context and validation. The annual maximum sea level in each year of the CMEMS (product ref. no. 1) and NEMO-EST05 (product ref. no. 9) series was extracted and fitted to GEV distributions. Both models yielded consistent results, with Gumbel-type fits adequately describing the upper tail (Fig. 3c–e). The CMEMS hindcast produced slightly higher estimates for a given return period, and we adopted those as a conservative choice for design criteria. Notably, the largest storm surge on record in these series corresponds to the January 2005 cyclone "Gudrun," which produced a water level of roughly +1.5 m at the site (Suursaar and Sooäär, 2007). In the CMEMS data, this event falls around the 100-year return level on the fitted curve, whereas in the NEMO-EST05 data it appears closer to a 50-year event based on extrapolation. The extreme value analysis yields a 100-year return high water level of about +1.6 m relative to the local mean sea level

(Fig. 3c). This value is taken as the extreme storm surge level for design purposes.

The annual minimum sea level from each year was used for the block-maxima analysis (since the lowest water level of each year represents the most extreme drop). This approach was chosen over a POT method because the very lowest value on record was a clear outlier that made threshold-based fitting unstable. The GEV fits to the annual minima from both the CMEMS (product ref. no. 1) and NEMO hindcasts (product ref. no. 9) suggest nearly identical low-water extremes. The estimated 100-year return period minimum sea level is approximately −0.8 m (i.e. 0.8 m below the mean sea level baseline). In practical terms, such an extreme low sea level, while infrequent, must be considered in FSRU design to ensure sufficient draught and flexible connections during extreme low-water events. The symmetry between the +1.6 m high and −0.8 m low centennial levels highlights the Gulf's propensity for greater positive storm surges than negative seiches (since the basin's geometry and prevailing winds favor high-water extremes (Medvedev and Kulikov, 2021).

3.3 Waves

To characterize the wave climate, we compared significant wave height data from multiple sources, emphasizing long-term model hindcasts as the basis for statistics. The primary datasets were the CMEMS Baltic Sea wave reanalysis (product ref. no. 2) and a high-resolution SWAN hindcast (product ref. no. 12). Available observations were limited to a short-term wave buoy deployment near the site in summer 2022 (product ref. no. 11) and a sparse set of satellite altimeter passes (Level-3 data, product ref. no. 8), which are insufficient to capture extreme wave conditions. As shown in Fig. 2e, f, the two models exhibit generally consistent wave-height distributions after the correction factor was applied to the CMEMS Baltic Sea wave reanalysis (Supplement, Sect. S2 Wave correction). Both suggest that most of the time the significant wave height is relatively modest (< 2 m) consistent with the fetch-limited nature of the gulf. For significant wave heights above approximately 0.4 m, however, the SWAN-EST05 distribution is generally higher than that of the CMEMS wave reanalysis. Because the datasets differ in model configuration, spatial resolution, and forcing, the comparison does not allow this difference to be attributed to a single cause (Najafzadeh et al., 2021, 2024). Overall, both model datasets identify a similar wave-climate regime dominated by short-period wind seas, and provide complementary estimates for the extreme-wave analysis.

Despite the different spatial resolution and time span of the two wave models, their extreme value statistics turned out to be in strong agreement. GEV fits to the annual maxima from CMEMS (product ref. no. 2) and SWAN-EST05 (product ref. no. 12) provided a better fit than the Gumbel distribution. For the POT analysis, the GPD fits with an exponential tail, adequately captured the upper-end behaviour of both datasets (Figs. 3j, k; A1j, k). For example, the statistically estimated 100-year return significant wave height is on the order of 3.6 m based on these fits.

3.4 Currents

Observations of surface currents in the Gulf of Finland are sparse, so we relied on hydrodynamic model data to assess current speed statistics. Two model sources were considered: the NEMO-EST05 high-resolution Baltic Sea circulation hindcast (1993–2017) (product ref. no. 9) and the surface current product from the CMEMS reanalysis (daily outputs over a similar period) (product ref. no. 1). To enable a direct comparison, the NEMO-EST05 1 h data (nemoh) were averaged into daily means (nemod) to match the temporal resolution of CMEMS. The resulting distributions of surface current speed from the two models are plotted in Fig. 2g, h on a logarithmic scale. Both datasets indicate that currents at the proposed terminal location are generally weak. Typical surface flow speeds are on the order of a few centimeters per second, and even the upper quantiles remain modest (on the order of 0.25–0.35 m s^{-1}). The two hindcasts agree well on this overall magnitude: their probability density curves overlap closely through most of the range. Both models paint a consistent picture of a low-energy surface circulation regime at the site, driven primarily by wind and seiche events in the semi-enclosed gulf. More generally, Baltic Sea surface circulation reflects the combined contributions of geostrophic and ageostrophic currents, with wind and sea-level variability contributing to the spatial circulation patterns (Barzandeh et al., 2024). Recent data-driven analyses of daily surface-current fields further indicate strong spatial heterogeneity, with wind providing important basin-scale predictive information while coastal, strait, and boundary regions exhibit stronger local constraints and day-to-day complexity (Barzandeh et al., 2026a, b).

For the site-specific extreme-current analysis, annual maximum surface current speeds were extracted from the the native 1 h NEMO-EST05 hindcast (considering the top 1 m layer average) (product ref. no. 9) rather than from the daily-averaged series used for the inter-model comparison in Fig. 2. The NEMO-based extreme value curves suggest that 100-year return period surface currents are on the order of 0.4 m s^{-1}. The GEV fit for the annual maxima had a positive shape parameter (indicating an upward-curving tail in Fig. 3k), while the exponential-tail POT fit captured the few highest current events well (Fig. A1k); both methods yielded similar 100-year estimates around 0.39–0.43 m s^{-1}. It should be noted that these values come with larger uncertainty bands compared to the other parameters, mainly due to the lack of long-term current measurements for validation and the inherent variability in modeling coastal currents. We interpret ~ 0.4 m s^{-1} as a reasonable upper-bound estimate for the site's surface current under present climate conditions. Although this extreme current speed is relatively low

in comparison to open-ocean currents, in combination with high winds and waves it could still contribute to the total environmental force on the moored FSRU.

3.5 Extension of the Extreme value analysis to the whole Baltic Sea

Having used the Paldiski case to assess how regional products represent local extremes relative to observations and higher-resolution datasets, we extend the same EVA framework across the Baltic Sea to examine the spatial variability of 50-year return levels and their uncertainties (Fig. 4).

The wind speed values are higher over the sea area than over the land (Fig. 4a). This is because of the absence of orographic restrictions over the sea area. Over the sea, extreme wind speeds show a north-south and coastal-offshore variability. In the south-western Baltic Sea, the ERA5-based 50-year return level reaches approximately 28 m s^{-1}. The corresponding 95 % confidence interval is wide, with an uncertainty range of up to about 10 m s^{-1} in some grid cells, indicating substantial uncertainty in the fitted tail distribution. The most severe Baltic windstorms, often following a track across the open sea, have produced 10 min mean wind speeds above 30 m s^{-1} over water (Björkqvist et al., 2020). For example, the January 2019 storm's peak winds reached 32.5 m s^{-1} over the Baltic Proper, driving the extreme waves (Björkqvist et al., 2020).

Our analysis shows high extreme values of the wave height and wave period over the eastern Baltic Proper (Fig. 4c–f). The 50-year significant-wave-height return level reaches approximately 10 m in the most exposed parts of the Baltic Proper. The 95 % confidence-interval width locally exceeds 5 m, so these values should be interpreted as regional screening estimates rather than site-specific design values. A significant wave height of 8.1 m was measured in the northern Baltic – the highest on record – with hindcasts suggesting waves up to 9 m in the Bothnian Sea (Björkqvist et al., 2020).

The Baltic-wide wind-speed return levels are based on ERA5 10 m hourly wind fields. They therefore represent gridded hourly 10 m wind-speed return levels, not gusts, 10 min station wind maxima, or wind speeds adjusted to turbine-hub height or vessel-superstructure height. This distinction is important because temporal averaging, vertical level, and spatial resolution all affect the magnitude of estimated extremes. The mapped values may therefore appear low when compared with observed gusts or short-duration storm maxima.

The large confidence intervals in parts of the south-western Baltic Sea are caused mainly by the limited number of years that are covered by the data set, strong inter-annual variability, and sensitivity of the unconstrained GEV shape parameter. The uncertainty is therefore partly statistical and partly structural. In addition, ERA5 is known to smooth small-scale wind maxima and may underestimate high-wind events in the Baltic Sea. Consequently, the ERA5-based wind map should be interpreted as an internally consistent regional screening product. Local design applications require validation against local observations and, where appropriate, local bias correction.

Sea surface current speeds are high at the coastal sea, where locally, the extreme values could reach 1 m s^{-1} (Fig. 4g). Simultaneously, the uncertainties of these extreme values are almost 2 m s^{-1} (Fig. 4h).

Storm surge (sea level) extremes display particularly strong spatial variability due to the Baltic's complex geometry and bathymetry. We should note that long-term mean sea level was not removed from the analysed data. Extreme sea levels in the Baltic Sea are driven by wind-driven surge, atmospheric pressure, and seiche oscillations. The highest surges occur when strong winds align with the basin's long axis and push water into narrow bays or gulfs. Maximum sea level anomalies are expected in the eastern Gulf of Finland and the Gulf of Riga (Fig. 4i). There, the extreme sea level corresponding to the 50-year return period could be as high as 1.3 m. At the end of the Gulf of Finland, uncertainties of the extreme value estimate are also high, reaching up to 1.3 m (Fig. 4j). In the Gulf of Riga the uncertainties remain below 0.8 m (Fig. 4j). In the Gulf of Riga, the town of Pärnu has suffered two record surges: 2.53 m in 1967 and 2.75 m in January 2005 (Lorenz et al., 2025; Suursaar and Sooäär, 2007) – the latter being one of the highest reliably measured sea levels in the entire Baltic during the last century.

The uncertainties in the maximum sea-level anomaly map should be interpreted with caution. The Baltic wide sea level EVA is based on daily gridded CMEMS physical reanalysis output, whereas local tide gauges and site-specific studies may use hourly or higher-frequency records. Daily fields can smooth short-lived storm-surge peaks and may underestimate the highest instantaneous water levels. In narrow sub-basins such as the eastern Gulf of Finland and the Gulf of Riga, annual maxima are also strongly influenced by a small number of major storm-surge events, which makes the fitted GEV tail sensitive to individual years. The confidence intervals shown in the map therefore represent statistical uncertainty of the gridded daily-field EVA, but not the full uncertainty associated with temporal resolution, vertical datum, local bathymetry, or gauge-to-grid representativeness.

Correspondingly, minimum sea levels were found to be around −0.7 m for a 50-year return period at the site of the LNG terminal (Table 2). The Baltic Sea wide estimates provide minimum sea levels down to −0.4 m (Fig. 4k) with maximum uncertainty of up to 0.3 m (Fig. 4l) corresponding to a return period of 50-years. The discrepancy could be related to the fact that hourly sea level values were used at the LNG while daily values for the whole Baltic Sea. We note that uncertainty in these return level estimates is considerable, owing to the relatively short observational records (30 years) and natural variability. We like to note that extreme values of high sea level are significantly higher than low sea levels relative to zero sea level.

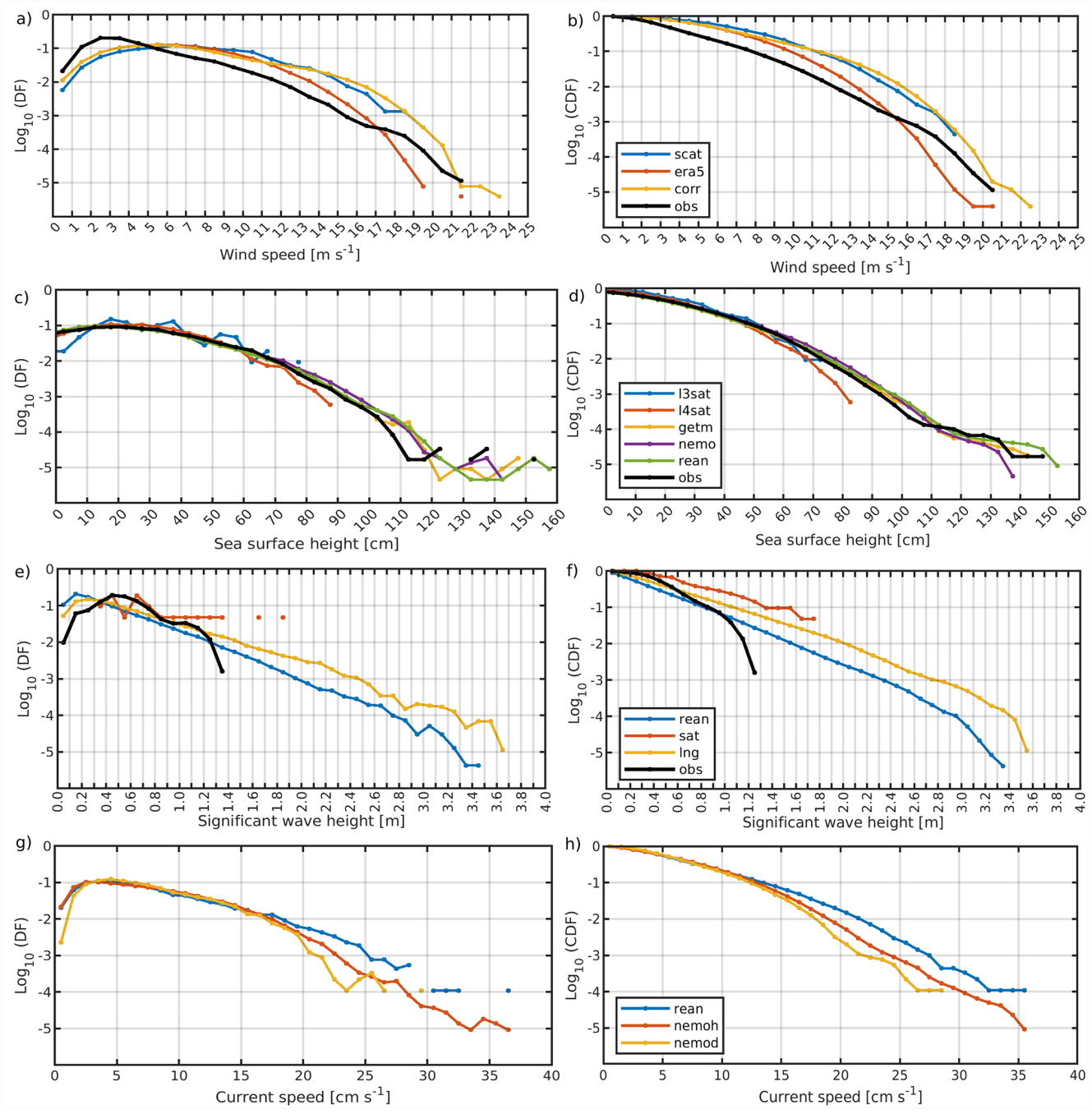


Figure 2. Log scale density distribution functions (DF) (left column) and cumulative distribution function (CDF) (right column) of wind speed (**a**, **b**; product ref. nos. 3, 4, 13; product 3 is also shown after the site-specific wind adjustment), sea surface height (**c**, **d**; product ref. nos. 1, 6, 7, 8, 9, 10), and significant wave height (**e**, **f**; product ref. nos. 2, 14, 12, 11) sea surface current speed (**g**, **h**; product ref. nos. 1, 9) of various data sources at the terminal location. Temporal coverage differs among the data sources and is reported in Sect. 2.1–2.4 and in Table A1.

Metocean criteria derived from local and Baltic-wide EVA provide environmental inputs for subsequent, separate engineering analyses for the engineering specifications for mooring systems, platform freeboards, breakwater heights, and operational limits. For example, the calculated extreme significant wave height guides the required height of mooring dolphins and fenders to avoid collision or overtopping in a storm. The extreme wind speed and currents inform the loads on the FSRU's mooring lines and the tension capacity needed to keep it in place during a gale. Even extreme low water lev-

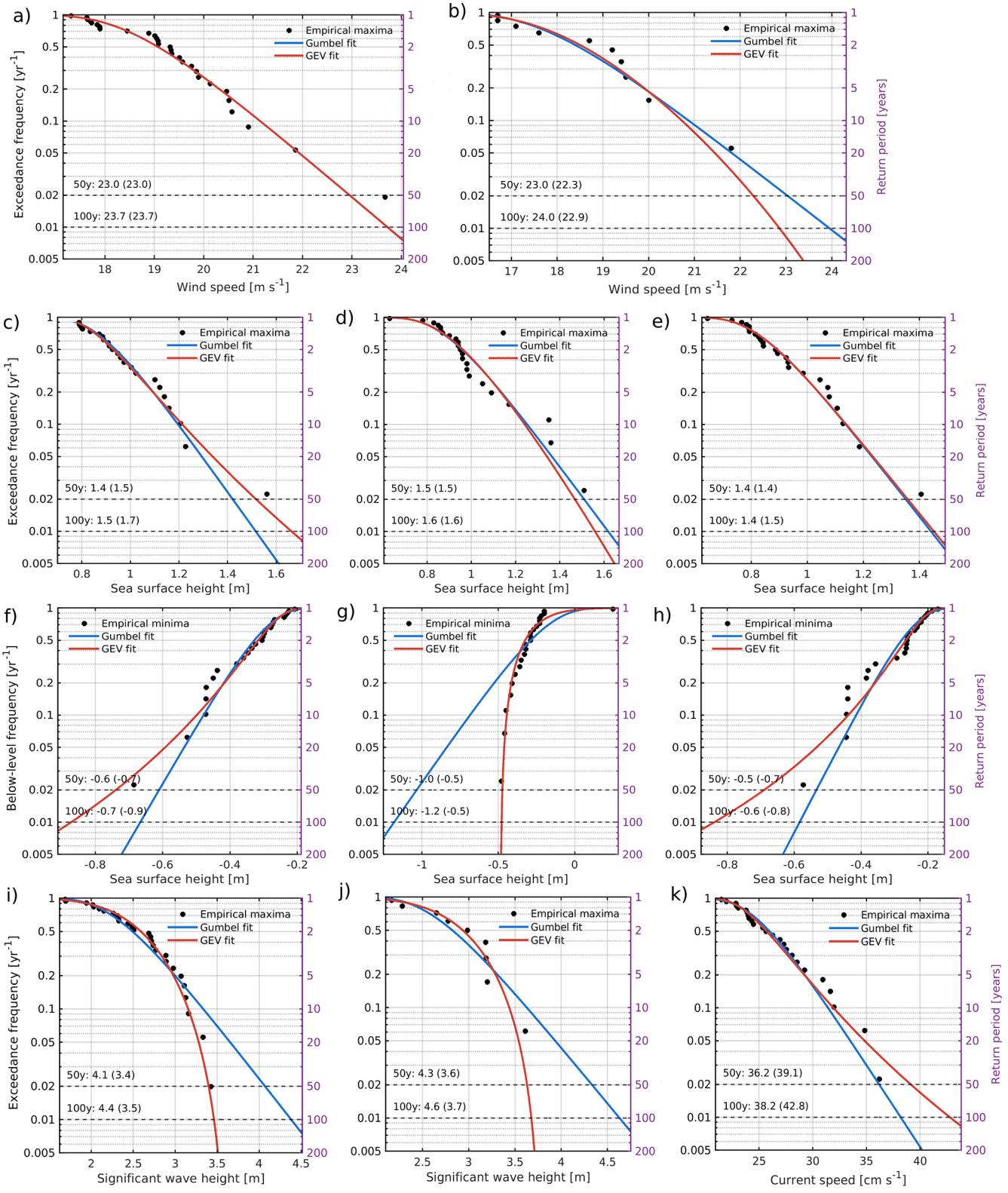


Figure 3. Generalized Extreme Value (GEV) and Gumbel distributions fitted to annual maxima and minima of key oceanographic variables: wind speed **(a–b)** (product ref. no. 3 – **a**, 13 – **b**), sea surface height maxima **(c–e)** (product ref. no. 1 – **c**, 6 – **d**, 9 – **e**), sea surface height minima **(f–h)** (product ref. no. 1 – **f**, 6 – **g**, 9 – **h**), significant wave height maxima (panels **i–j**) (product ref. no. 2 – **i**, 12 – **j**), and surface current speed maxima **(k)** (product ref. no. 9 – **k**). Horizontal dashed lines denote the 50- and 100-year return periods, with corresponding return levels for Gumbel fits shown (GEV estimates indicated in brackets).

Table 2. An overview of the return levels for the environmental variables for return periods of 10, 20, 50 and 100 years at LNG site. One asterisk corresponds to Gumbel and two asterisks to GEV fit.

	10 years	20 years	50 years	100 years
Wind speed ($m\,s^{-1}$)*	21	22	23	24
Sea surface height (m)*	+1.3	+1.4	+1.5	+1.6
Sea surface minima (m)*	−0.5	−0.5	−0.6	−0.7
Significant wave height (m)**	3.4	3.5	3.6	3.7
Surface current ($cm\,s^{-1}$)*	31	33	36	38

els (e.g. −0.7 m in our 50-year estimate) are important, as they determine the minimum under-keel clearance and the design of intake/outlet systems for the FSRU.

3.6 Synthesis of site-specific and Baltic Sea-wide assessments

Comparison of the site-specific and Baltic Sea-wide results demonstrates the importance of local exposure and temporal resolution when translating regional extreme-value estimates to infrastructure applications. At the Paldiski FSRU site, the 50-year return levels are approximately $23\,m\,s^{-1}$ for wind speed, 4.1 m for significant wave height, $0.37\,m\,s^{-1}$ for surface current speed, and +1.5 m and −0.7 m for maximum and minimum sea level, respectively. The regional assessment shows considerably larger wind, wave, and current extremes in more exposed parts of the Baltic Sea, with wind-speed return levels reaching approximately $28\,m\,s^{-1}$, significant wave heights approaching 10 m in the Baltic Proper, and surface currents locally approaching $1\,m\,s^{-1}$. This confirms that the Paldiski site is relatively sheltered with respect to waves and currents compared with the most exposed Baltic regions.

Sea level shows a different spatial behaviour. The largest positive regional anomalies occur in geometrically constrained sub-basins such as the Gulf of Finland and Gulf of Riga. The site-specific sea-level extremes are also larger than those obtained from the Baltic-wide daily fields at the corresponding regional scale, particularly for low water. This difference is partly attributable to temporal resolution, because the site-specific analysis uses hourly data whereas the regional assessment uses daily fields that can smooth short-lived extrema. The comparison therefore demonstrates that the Baltic-wide maps provide a consistent regional screening framework, whereas infrastructure design requires site-specific data and evaluation at an appropriate temporal and spatial resolution.

3.7 Model and data limitations

Beyond the statistical uncertainty of the fitted return levels shown in Fig. 4, the assessment is affected by limitations in model formulation and input data. We consider three main sources: the absence of two-way wave–circulation coupling, the use of fixed bathymetry without morphodynamic changes, and the choice and spatial resolution of atmospheric forcing.

The wave and hydrodynamic datasets used in this study are not fully two-way coupled. The CMEMS multi-year Baltic Sea wave product is based on WAM, while the corresponding physical reanalysis is based on NEMO; these long-term production systems are run independently without exchange of wave, current, or waterlevel parameters. Similarly, the high resolution SWAN-EST05 and NEMO-EST05 datasets were used here as separate wave and hydrodynamic products. This means that current-induced wave refraction, water-level-dependent wave transformation, wave-induced set-up, radiation stress effects, and Stokes drift feedback on currents are not fully represented in the long-term extreme value analysis. Explicit wave forcing can also modify ocean-side stress, Stokes–Coriolis forcing, turbulence, and upper-ocean mixing, demonstrating that the absence of wave feedbacks can affect the simulated hydrodynamic state (Haapaniemi et al., 2026).

The possible effect of this decoupling was assessed qualitatively and by scale analysis. At the FSRU site, currents are generally weak, and the estimated 50-year return surface current is approximately $0.37\,m\,s^{-1}$. Previous Baltic Sea sensitivity experiments have shown that including modelled currents usually produces small changes in significant wave height, although local changes can become larger during strong-current events, especially in coastal areas and in the Gulf of Finland (Kanarik et al., 2021). The berth is also relatively deep compared with the estimated design wave height: using a representative berth depth of about 16 m and a 50-year significant wave height of 4.1 m gives $Hs/h \approx 0.25$, where h is local water depth, indicating that the local wave extreme is not expected to be primarily depth limited. Water-level variations therefore influence local wave transformation but are unlikely to dominate the significant wave height return level at the berth.

The uncertainty introduced by missing coupling is considered a structural model uncertainty. For significant wave height, we estimate that the effect is likely small for the marginal return levels, but individual storm events with strong opposing currents may produce deviations of order 0.1–0.3 m and, in rare local cases, up to approximately

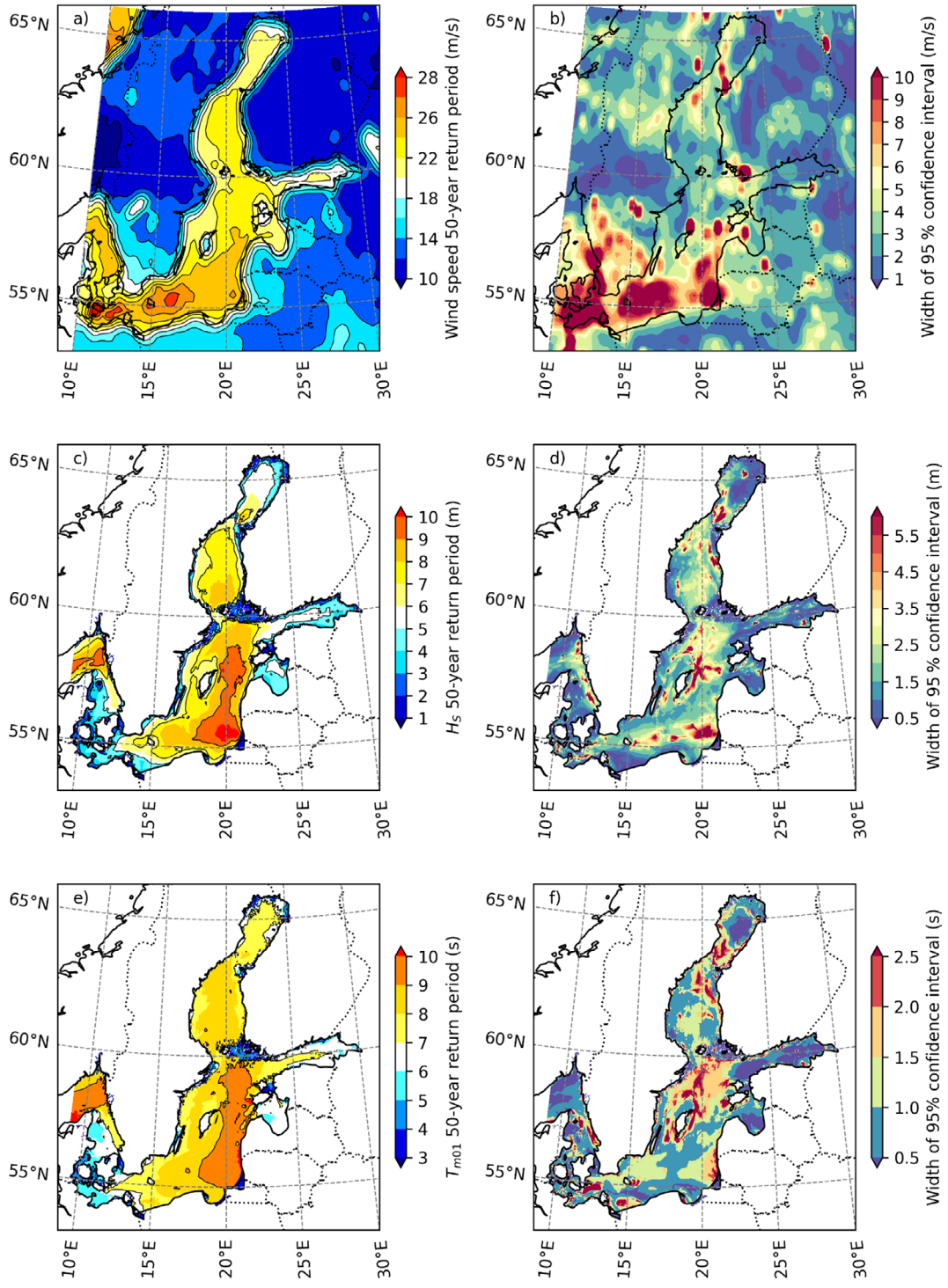

a)
b)
c)
d)
e)
f)
65°N
60°N
55°N
10°E
15°E
20°E
25°E
30°E
Wind speed 50-year return period (m/s)
Width of 95 % confidence interval (m/s)
H_S 50-year return period (m)
Width of 95 % confidence interval (m)
T_{m01} 50-year return period (s)
Width of 95% confidence interval (s)

Figure 4.

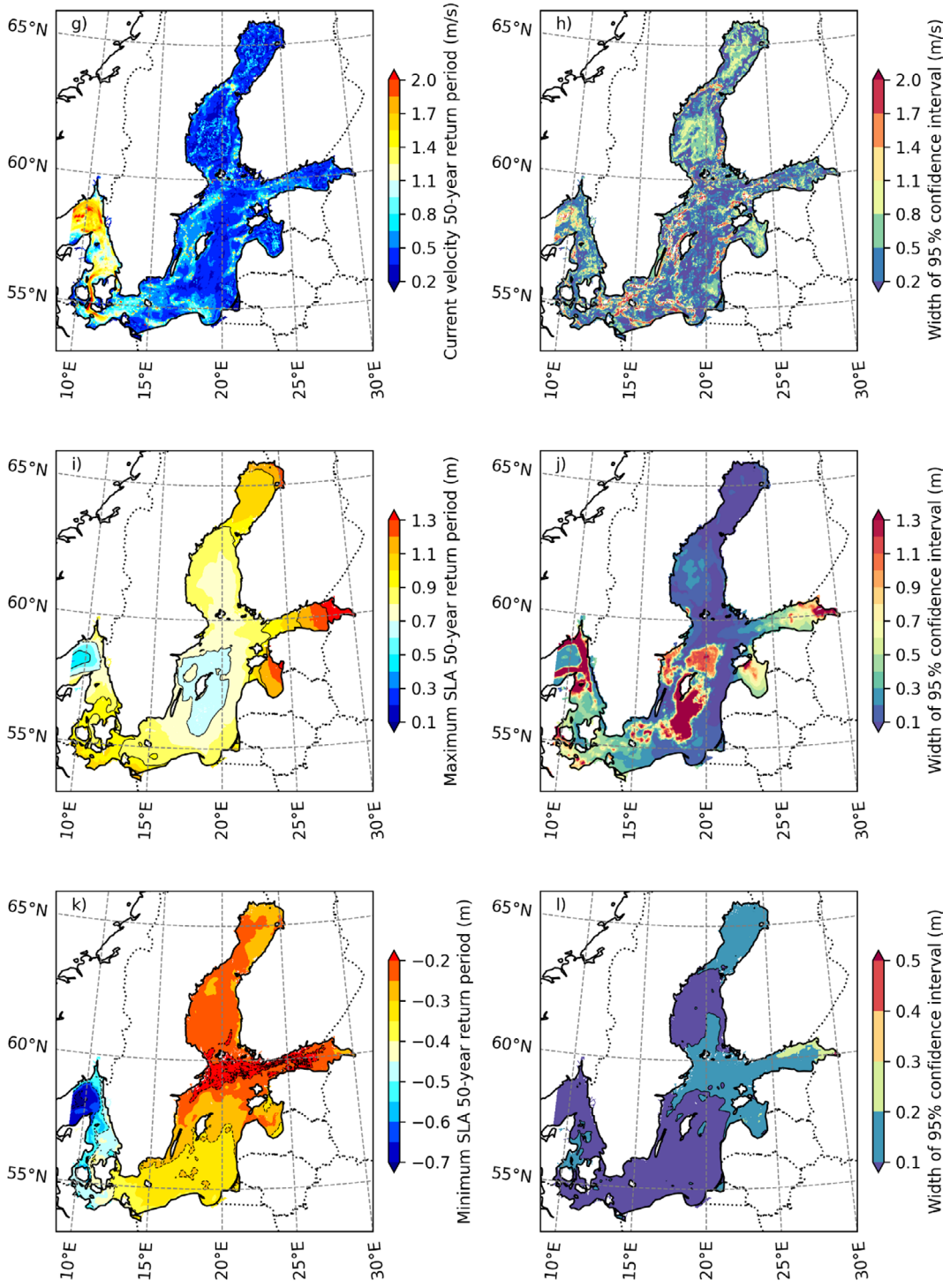


Figure 4. Extreme values corresponding to the return period of 50-years (left panels) and the uncertainties of their estimates (right panels). Wind speed **(a, b)** from product ref. no. 3, significant wave height **(c, d)** and peak period **(e, f)** from product ref. no. 2, current velocity **(g, h)** from product ref. no. 1, and maximum **(i, j)** and minimum **(k, l)** sea level anomaly from product ref. no. 1.

0.5–0.6 m. This uncertainty is comparable in magnitude to the site-specific multiplicative wave-height adjustment and the spread between the independent wave datasets. Previous Baltic Sea sensitivity experiments with WAM forced by NEMO surface currents showed that current effects on the wave field are generally small: changes exceeding 0.10 m in significant wave height or 1 s in peak period occurred only in limited areas and typically less than 3 % of the time, although event-scale changes up to about 0.6 m in maximum significant wave height can occur locally, especially near coasts and in the Gulf of Finland (Kanarik et al., 2021). The decoupled approach is therefore considered adequate for estimating marginal long-term return levels, but fully coupled event based simulations are recommended for final engineering design and operational limit assessment.

The present study focuses on long-term metocean extremes derived from observational, reanalysis, and numerical model datasets. Sediment transport and morphological change were not explicitly simulated. The wave and hydrodynamic products used in the EVA are based on fixed bathymetry and therefore do not include feedbacks from erosion, deposition, nearshore bar migration, dredging, or seabed recovery after storms. This limitation is particularly relevant in very shallow sandy nearshore areas, where changes in seabed morphology can modify wave breaking, wave refraction, current patterns, under-keel clearance, and local water-level impacts.

For the Pakrineeme FSRU site, this source of uncertainty is considered limited for the marginal return levels reported here. The terminal is located at the Pakri Peninsula, a predominantly bedrock-controlled coastal setting associated with the North Estonian limestone klint. The berth is also situated at a relatively deep jetty rather than directly on a sandy surf-zone coast. Existing project documentation indicates that the jetty is mainly pile supported and that no breakwaters were planned, while local dredging was carried out to secure the required berthing depth. These local seabed modifications are relevant for construction, maintenance dredging, and detailed engineering design, but they are not expected to dominate the long-term wind, wave, current, and sea level return levels estimated in this study.

For the Baltic-wide assessment, the uncertainty is larger. The regional EVA maps are based on gridded metocean products and should not be interpreted as resolving site-specific morphodynamics in the first nearshore grid cells. Along sandy and morphodynamically active coasts, especially in the southern and south-eastern Baltic Sea, erosion, deposition, nearshore bar migration, and harbour-related sediment interruption can substantially alter local bathymetry and therefore local metocean conditions. Baltic Sea coastal change studies show that erosion and accretion depend strongly on hydrodynamic conditions, wave climate, wave approach angle, sediment availability, and sediment compartments; sedimentary shores can be sensitive to relatively small variations in these drivers (Weisse et al., 2021). In the south-eastern Baltic, studies of the Curonian Spit show active nearshore sandbar switching and beach foredune response on storm, interannual, and decadal timescales, demonstrating that sandy nearshore morphology can change substantially over periods relevant to infrastructure planning (Janušaitė et al., 2023). The confidence intervals shown in the Baltic-wide maps (Fig. 4) represent statistical uncertainty of the extreme-value estimates, but they do not include morphological uncertainty. Consequently, the Baltic-wide results should be used as regional screening information, while detailed design at sandy nearshore sites requires local bathymetric surveys and sediment-transport or morphodynamic modelling.

The Baltic-wide results show that metocean design conditions are not spatially uniform and that the dominant hazard type differs between sub-basins (Fig. 4). Exposed areas of the Baltic Proper are characterized by the largest wave-height and wave-period extremes, whereas the highest positive sea-level anomalies occur in geometrically constrained regions such as the eastern Gulf of Finland and the Gulf of Riga. In contrast, the Paldiski FSRU site is relatively sheltered with respect to wave exposure compared with the Baltic Proper, but remains sensitive to sea level extremes and episodic wind driven events. This contrast demonstrates why a single regional design criterion is insufficient for Baltic Sea infrastructure planning. The uncertainty maps further show that some areas with high return levels also have broad confidence intervals, indicating where additional observations or higher-resolution modelling would most improve future risk assessments.

The Baltic-wide EVA results should be interpreted as regional-scale return levels of the uncorrected datasets. The confidence intervals shown in Fig. 4 describe statistical uncertainty from the EVA procedure, but they do not include uncertainty associated with spatially varying model bias. At the Paldiski site, the observation-based adjustments applied to the local analysis were approximately 5 %–10 % for wind speed, 15 % for significant wave height, and 5 % for wave period. These values are provided only as an example of the magnitude of model − observation differences at one coastal location. They were not applied to the Baltic-wide analysis and should not be interpreted as basin-wide uncertainty estimates, because the magnitude and potentially the sign of model bias may vary with local exposure, bathymetry, coastal geometry, and observation-to-grid representativeness. Site-specific applications therefore require evaluation and, where justified, local adjustment.

The choice of atmospheric forcing is an additional source of structural uncertainty in the Baltic-wide EVA. Although CERRA (Ridal et al., 2024) provides a substantially higher horizontal resolution than ERA5, it was not used in the present analysis because the marine products used here are ERA5-forced. A CERRA based wind map alone would not reduce uncertainty in the coupled interpretation of metocean extremes unless the corresponding wave and hydrodynamic fields were also generated using the same atmospheric

forcing. This is particularly important because the CMEMS Baltic wave hindcast has been tuned for ERA5 wind forcing. Therefore, the Baltic-wide maps presented here should be interpreted as internally consistent ERA5-forced regional screening products.

Future work should assess the sensitivity of Baltic Sea metocean extremes to atmospheric forcing by comparing ERA5, CERRA, and possibly other regional reanalysis forced wave and hydrodynamic hindcasts. Such a study would require basin-wide validation against wind stations, satellite winds, wave buoys, tide gauges, and current observations. The present study does not perform this full forcing sensitivity experiment, and the resulting uncertainty is now explicitly acknowledged.

Finally, the broader strategic relevance of extreme value studies in the Baltic Sea must be underscored. The Baltic region is characterized by sensitive environmental conditions and heavily used sea routes (Fig. 1a) (for commerce and increasingly for energy transport). Geopolitical factors – such as shifting trade patterns, military considerations, and transnational energy projects – mean that infrastructure robustness is part of national resilience. For example, the disruption of one LNG terminal by an extreme storm could have ripple effects on multiple countries' energy supply. Therefore, the Baltic-wide EVA provides a regional screening framework for comparing the relative exposure of existing and prospective infrastructure areas to metocean extremes. It is not intended to identify operational refuge locations, towing destinations, or optimal terminal sites, which would require additional analyses of persistence, directionality, accessibility, navigation constraints, and engineering requirements.

4 Conclusions

This study provides an integrated assessment of metocean extremes for the planned FSRU terminal on the Estonian coast of the Gulf of Finland and places the local results in a Baltic Sea-wide context. The statistical methods used are established EVA approaches; the scientific contribution lies in the harmonized integration of multiple long-term observational, satellite, reanalysis, and high-resolution model datasets, together with distribution-based evaluation against available observations and independent model products, to derive consistent extreme-value estimates for wind, sea level, waves, and currents. For the FSRU site, the resulting 50-year return levels are approximately 23 m s^{-1} for wind speed, +1.5 and −0.7 m for sea-surface-height maxima and minima, 4.1 m for significant wave height, and 0.37 m s^{-1} for surface current speed. These values provide a site-specific metocean characterization for a sheltered but strategically important coastal location.

Extending the analysis to the entire Baltic Sea reveals strong spatial contrasts in 50-year return levels and their uncertainties. The largest wave extremes occur in exposed parts of the Baltic Proper, whereas the largest positive sea-level anomalies occur in constrained sub-basins such as the Gulf of Finland and the Gulf of Riga. These results show that metocean risk cannot be inferred from a single location or parameter, but requires a spatially resolved, multi-variable assessment. The basin-wide uncertainty estimates further identify areas where present datasets are less robust and where additional observations or higher-resolution modelling would be most valuable. The study therefore contributes not by proposing a new EVA method, but by providing a transparent, transferable framework for linking evaluated multi-source metocean datasets, local infrastructure needs, and regional-scale hazard assessment in the Baltic Sea. The Baltic-wide maps should therefore be used as regional screening products, while detailed design at other Baltic Sea sites requires local validation and site-specific bias assessment.

Appendix A

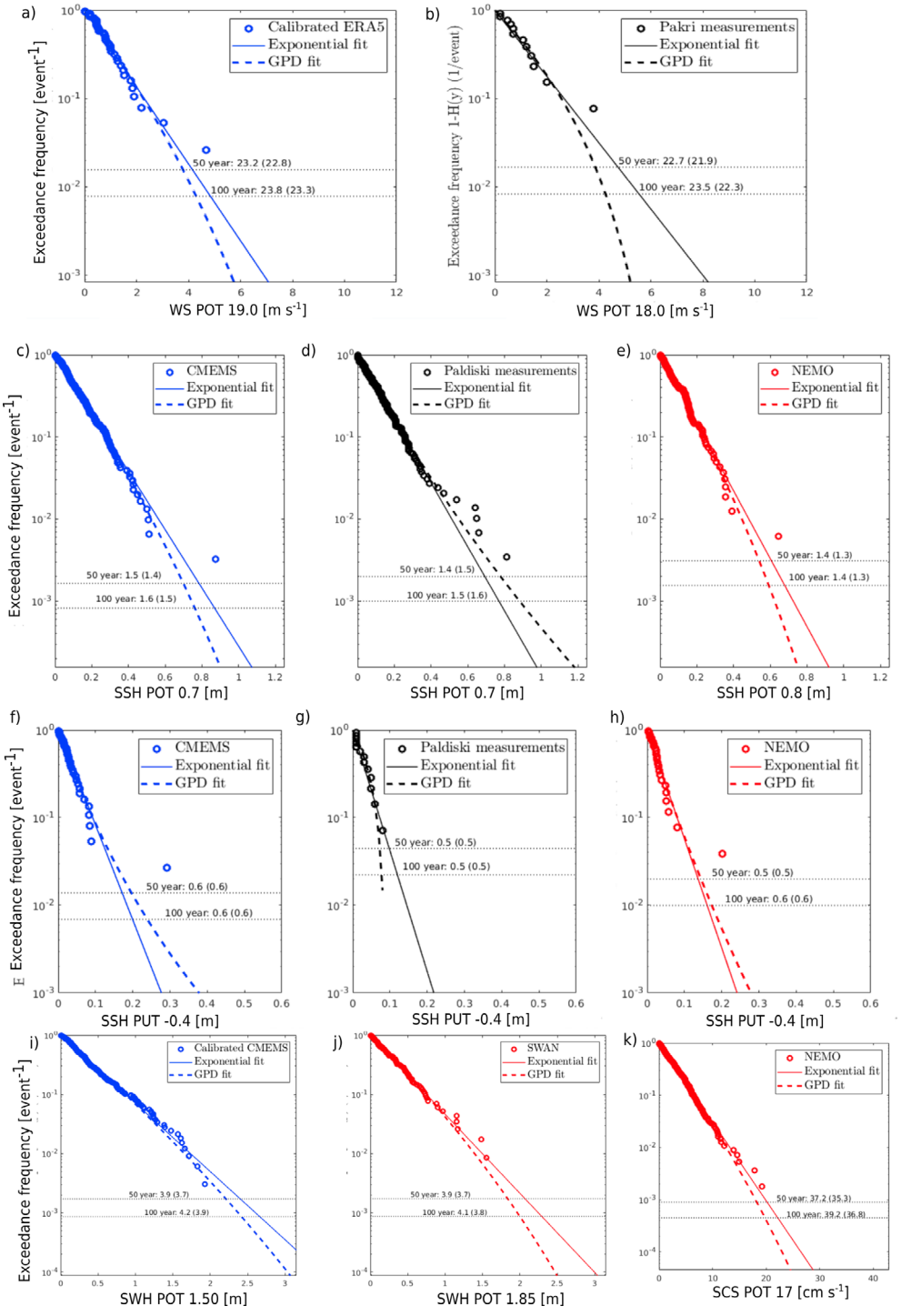


Figure A1. Generalized Pareto Distribution (GPD) and Exponential distribution fits to peaks over/under thresholds (POT/PUT) for selected oceanographic variables: wind speed (WS ymax, panels **a**–**b**) (product ref. no. 3 – **a**, 13 – **b**), sea surface height maxima (SSH ymax, panels **c**–**e**) (product ref. no. 1 – **c**, 6 – **d**, 9 – **e**), sea surface height minima (SSH ymin, panels **f**–**h**) (product ref. no. 1 – **f**, 6 – **g**, 9 – **h**), significant wave height maxima (SWH ymax, panels **i**–**j**) (product ref. no. 2 – **i**, 12 – **j**), and surface current speed maxima (SCS ymax, panel **k**) (product ref. no. 9 – **k**). For SSH minima, positive values represent depressions below the threshold (i.e., negative sea level excursions). Horizontal lines indicate the 50- and 100-year return periods, with corresponding return levels shown (GPD estimates indicated in brackets).

Table A1. Datasets used in the study, their temporal and spatial resolution, and study-specific pre-processing.

Product ref. no.	Dataset/product	Variable(s) used	Period used in this study	Temporal resolution	Spatial resolution/extraction	Pre-processing applied in this study
1	BALTICSEA_MULTIYEAR_PHY_003_011	Sea level; Surface current speed	Local analysis: 1993–2017 Regional EVA: 1993–2024	SSH: hourly Surface currents: daily mean Regional EVA: daily	1 nmi; nearest grid points at terminal and open-sea reference locations for local analysis	Local sea level converted to the common Paldiski vertical datum, normalized to the 1993–2009 mean water level (+0.21 m). Regional EVA used the original gridded data.
2	BALTICSEA_REANALYSIS_WAV_003_015	Significant wave height (Hs); Wave period	Local analysis: 1993–2020 Regional EVA: 1993–2024	Hourly	1 nmi; nearest grid points at terminal and open-sea reference locations for local analysis	For the local analysis, Hs and wave period were adjusted by 15 % and 5 %, respectively, based on near-site observations. No site-specific adjustments were applied to the regional EVA.
3	ERA5	Wind speed	Local analysis/EVA: 1993–2021 Correction/evaluation: 2012–2021 Regional EVA: 1993–2024	Hourly	0.25° (∼ 31 km); closest sea-covered grid cell for local analysis	Local wind speed corrected using an ASCAT-derived sigmoid function. The local correction was not applied to the regional EVA.
4	WIND_GLO_PHY_L3_MY_012_005 (ASCAT)	Wind speed	2012–2021	Daily files; instantaneous measurements	12.5 km (0.125°); open-sea data extracted approximately 15–20 km from the terminal	ASCAT sampling times used as reference; ERA5 and Pakri matched using nearest-time samples; records with missing values removed.
5	WIND_BAL_PHY_HR_L3_MY_012_107 (Sentinel-1 SAR)	Wind speed	2017–2021	Daily files; instantaneous measurements	0.012° grid; open-sea data extracted approximately 15–20 km from the terminal	ASCAT sampling times used as reference; ERA5 and Pakri matched using nearest-time samples; records with missing values removed.
6	Paldiski North Port (sea level)	Sea level	1993–2021	1993–2009: three observations per day 2016–2021: hourly	Point observation: 59.34972° N, 24.0475° E	The 2010–2016 gap was filled using nearest-grid-cell CMEMS Physics SSH after alignment to the gauge datum and mean level over the overlapping period.
7	SEALEVEL_EUR_PHY_L4_MY_008_068	Sea level	2012–2021 (comparison)	Daily	1/16° × 1/16° (0.0625°); nearest grid point at 59.4375° N, 24.0625° E	Sea level converted to the common Paldiski vertical datum.
8	SEALEVEL_EUR_PHY_L3_MY_008_061	Sea level anomaly (SLA)	2012–2021 (comparison)	Daily files; instantaneous along-track measurements	∼ 7 km (1 Hz) along-track; observations selected within 7 km of the terminal and open-sea reference locations	Sea level converted to the common Paldiski vertical datum.
9	NEMO-EST05	Sea level; Surface current speed	1993–2017	SSH: hourly Currents: hourly; averaged to daily means for CMEMS comparison	0.5 nmi; nearest grid points at terminal and open-sea reference locations	Sea level converted to the common Paldiski vertical datum. Surface currents averaged over the upper 1 m for local EVA.
10	GETM	Sea level	1993–2017	Hourly	0.5 nmi; same local extraction locations as NEMO-EST05	Sea level converted to the common Paldiski vertical datum.
11	LainePoiss	Significant wave height (Hs); Wave period	May–June 2022	Processed wave-parameter output: default 21 min 51 s	Point observation: approximately 59.399° N, 24.103° E	No additional preprocessing was applied before comparison with CMEMS. The raw 50 Hz inertial data were processed into 21 min displacement records to derive wave spectra and bulk wave parameters.
12	SWAN-EST05	Significant wave height (Hs); Wave period	2000–2009	Hourly	0.5 nmi; local output extracted at terminal and reference locations	Adjusted local bathymetry consistent with the NEMO-EST05 setup was used; hourly wave parameters were extracted at the terminal and reference locations
13	Pakri coastal weather station (wind)	Wind speed	1993–2021 ASCAT comparison: 2012–2021	3-hourly until 2003; hourly thereafter	Point station: 59.355° N, 24.051° E until Jan 2002; 59.389° N, 24.040° E thereafter	Matched to ASCAT sampling times using nearest-time samples; records with missing values removed.
14	WAVE_GLO_PHY_SWH_L3_MY_014_005	Significant wave height	2002–2020	Along-track satellite observations	Along-track observations; no regular grid	Used for comparison of significant-wave-height distributions;

https://doi.org/10.5194/sp-7-osr10-14-2026

Data availability. This study is based on public databases and the references are listed in Table 1. The datasets and software codebases are published in Zenodo data repositories (https://doi.org/10.5281/zenodo.20378599, Raudsepp et al., 2026a and https://doi.org/10.5281/zenodo.20356006, Raudsepp et al., 2026b).

Supplement. The supplement related to this article is available online at https://doi.org/10.5194/sp-7-osr10-14-2026-supplement.

Author contributions. UR led the research, drafted the original manuscript, and contributed to manuscript review and editing. IM, JVB, AB, SR, AM, and SP curated the data and conducted the analysis. SP and KV conducted the wave observations. PL, VA, and RU contributed to the conceptualization and design of the study. All authors participated in scientific discussions and reviewed the manuscript.

Competing interests. The contact author has declared that neither of the authors has any competing interests.

Disclaimer. The Copernicus Marine Service offering is regularly updated to ensure it remains at the forefront of user requirements. In this process, some products may undergo replacement or renaming, leading to the removal of certain product IDs from the catalogue. If readers have any questions or require assistance regarding these modifications, please feel free to reach out to the Copernicus Marine Service user support team for further guidance. They will be able to provide the necessary information to address concerns and find suitable alternatives.

Publisher's note: Copernicus Publications remains neutral with regard to jurisdictional claims made in the text, published maps, institutional affiliations, or any other geographical representation in this paper. The authors bear the ultimate responsibility for providing appropriate place names. Views expressed in the text are those of the authors and do not necessarily reflect the views of the publisher.

Acknowledgements. OpenAI's GPT-4o model was used to assist with initial drafting sections of the manuscript. All content was reviewed, verified, and approved by the authors.

Review statement. This paper was edited by Joanna Staneva and reviewed by three anonymous referees.

References

Alari, V., Björkqvist, J.-V., Kaldvee, V., Mölder, K., Rikka, S., Kask-Korb, A., Vahter, K., Pärt, S., Vidjajev, N., and Tõnisson, H.: LainePoiss® – A Lightweight and Ice-Resistant Wave Buoy, J. Atmos. Ocean. Tech., 39, 573–594, https://doi.org/10.1175/JTECH-D-21-0091.1, 2022.

Alenius, P., Myrberg, K., and Nekrasov, A.: The physical oceanography of the Gulf of Finland: a review, Boreal Environ. Res, 3, 97–125, 1998.

Allen, T. R., McLeod, G., and Hutt, S.: Sea level rise exposure assessment of US East Coast cargo container terminals, Marit. Policy Manag., 49, 577–599, https://doi.org/10.1080/03088839.2021.1903597, 2022.

Bailey, B. H. and Freedman, J. M.: Developments in metocean information in support of US offshore wind energy and the ocean sciences, Oceanography, 37, 30–41, https://doi.org/10.5670/oceanog.2024.503, 2024.

Ballarotta, M., Pujol, M.-I., and SL-TAC team: EU Copernicus Marine Service Quality Information Document for European Seas Gridded L4 Sea Surface Heights and Derived Variables Reprocessed (1993–ongoing), SEALEVEL_EUR_PHY_L4_MY_008_068, Issue 13.0, Mercator Ocean International, https://documentation.marine.copernicus.eu/QUID/CMEMS-SL-QUID-008-032-068.pdf (last access: 15 July 2025), 2025a.

Ballarotta, M., Pujol, M.-I., and SL-TAC team: EU Copernicus Marine Service Quality Information Document for European Seas Along Track L 3 Sea Surface Heights Reprocessed 1993 Ongoing Tailored For Data Assimilation, SEALEVEL_EUR_PHY_L3_MY_008_061, Issue 13.0, Mercator Ocean International, https://documentation.marine.copernicus.eu/QUID/CMEMS-SL-QUID-008-032-068.pdf (last access: 15 July 2025), 2025b

Barzandeh, A., Maljutenko, I., Rikka, S., Lagemaa, P., Männik, A., Uiboupin, R., and Raudsepp, U.: Sea surface circulation in the Baltic Sea: decomposed components and pattern recognition, Scientific Reports, 14, 18649, https://doi.org/10.1038/s41598-024-69463-8, 2024.

Barzandeh, A., Maljutenko, I., Rikka, S., and Raudsepp, U.: sciCUN: A deep learning model for daily sea surface current fields inference – A case study of the Gulf of Riga, Ocean Model., 201, 102693, https://doi.org/10.1016/j.ocemod.2026.102693, 2026a.

Barzandeh, A., Manss, C., Stahl, F., Maljutenko, I., Rikka, S., and Raudsepp, U.: Data-Driven Emulation of Numerically Simulated Baltic Sea Surface Currents With a Deep Convolutional U-Net: Explainability and Potential Forecast Skill, J. Geophys. Res. Mach. Learn. Comput., 3, e2026JH001321, https://doi.org/10.1029/2026JH001321, 2026b.

Barzandeh, A., Ličer, M., Rus, M., Kristan, M., Maljutenko, I., Elken, J., Lagemaa, P., and Uiboupin, R.: Application of the HIDRA2 deep-learning model for sea level forecasting along the Estonian coast of the Baltic Sea, Ocean Sci., 21, 1315–1327, https://doi.org/10.5194/os-21-1315-2025, 2025.

Bitner-Gregersen, E. M.: Joint met-ocean description for design and operations of marine structures, Appl. Ocean Res., 51, 279–292, https://doi.org/10.1016/j.apor.2015.01.007, 2015.

Björkqvist, J.-V., Tuomi, L., Fortelius, C., Pettersson, H., Tikka, K., and Kahma, K. K.: Improved estimates of nearshore wave conditions in the Gulf of Finland, J. Mar. Syst., 171, 43–53, https://doi.org/10.1016/j.jmarsys.2016.07.005, 2017.

Björkqvist, J.-V., Lukas, I., Alari, V., van Vledder, G. Ph., Hulst, S., Pettersson, H., Behrens, A., and Männik, A.: Comparing a 41-year model hindcast with decades of wave mea-

surements from the Baltic Sea, Ocean Eng., 152, 57-71, https://doi.org/10.1016/j.oceaneng.2018.01.048, 2018.

Björkqvist, J.-V., Rikka, S., Alari, V., Männik, A., Tuomi, L., and Pettersson, H.: Wave height return periods from combined measurement–model data: a Baltic Sea case study, Nat. Hazards Earth Syst. Sci., 20, 3593–3609, https://doi.org/10.5194/nhess-20-3593-2020, 2020.

Björkqvist, J.-V., Pärt, S., Alari, V., Rikka, S., Lindgren, E., and Tuomi, L.: Swell hindcast statistics for the Baltic Sea, Ocean Sci., 17, 1815–1829, https://doi.org/10.5194/os-17-1815-2021, 2021.

Björkqvist, J.-V., Kanarik, H., Tuomi, L., Niskanen, L., and Kankainen, M.: Event-based wave statistics for the Baltic Sea, in: 8th edition of the Copernicus Ocean State Report (OSR8), edited by: von Schuckmann, K., Moreira, L., Grégoire, M., Marcos, M., Staneva, J., Brasseur, P., Garric, G., Lionello, P., Karstensen, J., and Neukermans, G., Copernicus Publications, State Planet, 4-osr8, 10, https://doi.org/10.5194/sp-4-osr8-10-2024, 2024.

Bollmeyer, C., Keller, J. D., Ohlwein, C., Wahl, S., Crewell, S., Friederichs, P., Hense, A., Keune, J., Kneifel, S., Pscheidt, I., Redl, S., and Steinke, S.: Towards a high-resolution regional reanalysis for the European CORDEX domain, Q. J. Roy. Meteor. Soc., 141, 1–15, https://doi.org/10.1002/qj.2486, 2015.

Booij, N., Ris, R. C., and Holthuijsen, L. H.: A third-generation wave model for coastal regions: 1. Model description and validation, J. Geophys. Res.-Oceans, 104, 7649–7666; https://doi.org/10.1029/98JC02622, 1999.

Burchard, H. and Bolding, K. K.: GETM, a General Estuarine Transport Model, Technical Report, European Commission, Joint Research Centre, Institute for Environment and Sustainability, https://publications.jrc.ec.europa.eu/repository/handle/JRC23237 (last access: 22 September 2026), 2002.

Caruso, M. F. and Marani, M.: Extreme-coastal-water-level estimation and projection: a comparison of statistical methods, Nat. Hazards Earth Syst. Sci., 22, 1109–1128, https://doi.org/10.5194/nhess-22-1109-2022, 2022.

Charles, E. and Ollivier, A.: EU Copernicus Marine Service Quality Information Document for the Global Ocean L3 Significant Wave Height From Reprocessed Satellite Measurements, WAVE_GLO_PHY_SWH_L3_MY_014_005, Issue 2.0, Mercator Ocean International, https://documentation.marine.copernicus.eu/QUID/CMEMS-WAVE-QUID-014-005.pdf (last access: 15 September 2026), 2026.

Cheynet, E., Li, L., and Jiang, Z.: Metocean conditions at two Norwegian sites for development of offshore wind farms, Renew. Energy, 224, 120184, https://doi.org/10.1016/j.renene.2024.120184, 2024.

CLS, IFREMER, OCEANSCOPE, De Carlo, M., Piollé, J.-F., and Husson, R.: EU Copernicus Marine Service Product User Manual for the High-resolution L3 Sea Surface Wind from MY Satellite Measurements over the Baltic Sea, WIND_BAL_PHY_HR_L3_MY_012_107, Issue 1.2, Mercator Ocean International, https://documentation.marine.copernicus.eu/PUM/CMEMS-WIND-PUM-012-100to109.pdf (last access: 15 July 2025), 2025.

Copernicus Climate Change Service: Complete ERA5 global atmospheric reanalysis, Copernicus Climate Change Service (C3S) Climate Data Store (CDS) [data set], https://doi.org/10.24381/cds.143582cf, 2023.

D'Agostini, A., Campos, R. M., and Soares, C. G.: Assessments of multiple metocean forecasts in the North Atlantic Ocean, Ocean Eng., 312, 119199, https://doi.org/10.1016/j.oceaneng.2024.119199, 2024.

Driesenaar, T., de Kloe, J., Belmonte Rivas, M., Giesen, R., Stoffelen, A., Bentamy, A., Hackett, B., and Garcia Hermosa, I.: EU Copernicus Marine Service Quality Information Document for Global Ocean Daily Gridded Reprocessed L3 Sea Surface Winds from Scatterometer, WIND_GLO_PHY_L3_MY_012_005, Issue 1.19, Mercator Ocean International, https://documentation.marine.copernicus.eu/QUID/CMEMS-WIND-QUID-012-002-005.pdf (last access: 15 July 2025), 2024a.

Driesenaar, T., de Kloe, J., Belmonte Rivas, M., Stoffelen, A., Forneris, V., van Zadelhoff, G.-J., and Giesen, R.: EU Copernicus Marine Service Product User Manual for the Global Ocean Daily Gridded Reprocessed L3 Sea Surface Winds from Scatterometer, WIND_GLO_PHY_L3_MY_012_005, Issue 2.26, Mercator Ocean International, https://documentation.marine.copernicus.eu/PUM/CMEMS-WIND-PUM-012-002-005.pdf (last access: 15 July 2025), 2024b.

EMODnet: Centro Tecnológico del Mar – Fundación CETMAR: EMODnet Human Activities – Energy – Offshore Wind Farms, EMODNET_HA_ENERGY_WINDFARMS, Version 2024, European Marine Observation and Data Network, https://emodnet.ec.europa.eu/geonetwork/srv/eng/catalog.search#/metadata/8201070b-4b0b-4d54-8910-abcea5dce57f (last access: 15 July 2025), 2024a.

EMODnet: Eurofish International Organisation and Cogea Srl: EMODnet Human Activities – Main Ports, Goods-Passengers-Vessels Traffic (annual aggregation, 1997–2024), EMODNET_HA_MainPorts_Traffic_20241112, Version 2024, European Marine Observation and Data Network, https://emodnet.ec.europa.eu/geonetwork/srv/eng/catalog.search#/metadata/379d0425-8924-4a41-a088-1a002d2ea748 (last access: 15 July 2025), 2024b.

EMODnet: Falco, L. and Adnams, W.: EMODnet Human Activities – Vessel Density Map (EU waters, 2017–2023), EMODNET_HA_Vessel_Density_Map_20240304, Version 2024, European Marine Observation and Data Network, https://emodnet.ec.europa.eu/geonetwork/srv/eng/catalog.search#/metadata/0f2f3ff1-30ef-49e1-96e7-8ca78d58a07c (last access: 15 July 2025), 2024c.

EU Copernicus Marine Service Product: Baltic Sea Wave Hindcast, Marine Data Store (MDS) [data set], https://doi.org/10.48670/moi-00014, 2024a.

EU Copernicus Marine Service Product: Global Ocean Daily Gridded Reprocessed L3 Sea Surface Winds from Scatterometer, Marine Data Store (MDS) [data set], https://doi.org/10.48670/moi-00183, 2024b.

EU Copernicus Marine Service Product: Baltic Sea Physics Reanalysis, Marine Data Store (MDS) [data set], https://doi.org/10.48670/moi-00013, 2025a.

EU Copernicus Marine Service Product: High-resolution L3 Sea Surface Wind from MY Satellite Measurements over the Baltic Sea, Marine Data Store (MDS) [data set], https://doi.org/10.48670/mds-00340, 2025b.

EU Copernicus Marine Service Product: European Seas Gridded L 4 Sea Surface Heights And Derived Variables Repro-

cessed 1993 Ongoing, Marine Data Store (MDS) [data set], https://doi.org/10.48670/moi-00141, 2025c.

EU Copernicus Marine Service Product: European Seas Along Track L3 Sea Surface Heights Reprocessed 1993 Ongoing Tailored For Data Assimilation, Marine Data Store (MDS) [data set], https://doi.org/10.48670/moi-00139, 2025d.

EU Copernicus Marine Service Product: Global Ocean L3 Significant Wave Height from Reprocessed Satellite Measurements, Marine Data Store (MDS) [data set], https://doi.org/10.48670/moi-00176, 2025e.

Global Energy Monitor (GEM): Global Gas Infrastructure Tracker – Pipelines (Release: December 2024) and LNG Terminals (Release: September 2024), https://globalenergymonitor.org/projects/global-gas-infrastructure-tracker (last access: 15 July 2025), 2024.

Gas Infrastructure Europe (GIE): GIE LNG Map 2019 existing, under construction, planned, and proposed LNG terminals across Europe, Version: May 2019, https://www.gie.eu/download/maps/2019/GIE_LNG_2019_A0_1189x841_FULL_Final3.pdf (last access: 15 July 2025), 2019.

Giudici, A., Jankowski, M. Z., Männikus, R., Najafzadeh, F., Suursaar, Ü., and Soomere, T.: A comparison of Baltic Sea wave properties simulated using two modelled wind data sets, Estuar. Coast. Shelf Sci., 290, 108401, https://doi.org/10.1016/j.ecss.2023.108401, 2023

Haapaniemi, V., Tuomi, L., Björkqvist, J.-V., Twelves, A., Murawski, J., Kanarik, H., Falahat, S., Westerlund, A., and Nummelin, A.: Surface wave impacts on turbulent roughness length parameterization, Ocean Model., 202, 102742, https://doi.org/10.1016/j.ocemod.2026.102742, 2026.

Hersbach, H., Bell, B., Berrisford, P., Hirahara, S., Horányi, A., Muñoz-Sabater, J., Nicolas, J., Peubey, C., Radu, R., Schepers, D., Simmons, A., Soci, C., Abdalla, S., Abellan, X., Balsamo, G., Bechtold, P., Biavati, G., Bidlot, J., Bonavita, M., De Chiara, G., Dahlgren, P., Dee, D., Diamantakis, M., Dragani, R., Flemming, J., Forbes, R., Fuentes, M., Geer, A., Haimberger, L., Healy, S., Hogan, R.J., Hólm, E., Janisková, M., Keeley, S., Laloyaux, P., Lopez, P., Lupu, C., Radnoti, G., de Rosnay, P., Rozum, I., Vamborg, F., Villaume S., and Thépaut, J.-N.: The ERA5 global reanalysis, Q. J. Roy. Meteor. Soc., 146, 1999–2049, https://doi.org/10.1002/qj.3803, 2020.

Ho, R.-T.: Engineering Considerations for Offshore FSRU LNG Receiving Terminals, in: Offshore Technology Conference, Houston, Texas, USA, May 2008, https://doi.org/10.4043/19439-MS, 2008.

Husson, R., De Carlo, M., Colin, A., Peureux, C., Singhoff, H., Nedellec, M., Mouche, A., Piolle, J.-F., and Cevaer, T.: EU Copernicus Marine Service Quality Information Document for High-resolution L3 Sea Surface Wind from MY Satellite Measurements over the Baltic Sea, WIND_BAL_PHY_HR_L3_MY_012_107, Issue 1.2, Mercator Ocean International, https://documentation.marine.copernicus.eu/QUID/CMEMS-WIND-QUID-012-100to109.pdf (last access: 15 July 2025), 2025.

Janušaitė, R., Jarmalavičius, D., Pupienis, D., Žilinskas, G., and Jukna, L.: Nearshore sandbar switching episodes and their relationship with coastal erosion at the Curonian Spit, Baltic Sea, Oceanologia, 65, 71–85, https://doi.org/10.1016/j.oceano.2021.11.004, 2023.

Jonathan, P. and Ewans, K.: Statistical modelling of extreme ocean environments for marine design: A review, Ocean Eng., 62, 91–109, https://doi.org/10.1016/j.oceaneng.2013.01.004, 2013.

Jonathan, P., Randell, D., Wadsworth, J., and Tawn, J.: Uncertainties in return values from extreme value analysis of peaks over threshold using the generalised Pareto distribution, Ocean Eng., 220, 107725, https://doi.org/10.1016/j.oceaneng.2020.107725, 2021.

Kanarik, H., Tuomi, L., Björkqvist, J.-V., and Kärnä, T.: Improving Baltic Sea wave forecasts using modelled surface currents, Ocean Dynam., 71, 635–653, https://doi.org/10.1007/s10236-021-01455-y, 2021.

Kanarik, H., Tuomi, L., and Lindgren, E..: EU Copernicus Marine Service Quality Information Document for the Baltic Sea Wave Hindcast Product, BALTICSEA_REANALYSIS_WAV_003_015, Issue 2.0, Mercator Ocean International, https://documentation.marine.copernicus.eu/QUID/CMEMS-BAL-QUID-003-015.pdf (last access: 11 June 2025), 2024.

Kärnä, T., Ljungemyr, P., Falahat, S., Ringgaard, I., Axell, L., Korabel, V., Murawski, J., Maljutenko, I., Lindenthal, A., Jandt-Scheelke, S., Verjovkina, S., Lorkowski, I., Lagemaa, P., She, J., Tuomi, L., Nord, A., and Huess, V.: Nemo-Nordic 2.0: operational marine forecast model for the Baltic Sea, Geosci. Model Dev., 14, 5731–5749, https://doi.org/10.5194/gmd-14-5731-2021, 2021.

Keevallik, S. and Soomere, T.: Seasonal and diurnal variations of wind parameters at Pakri, Estonian J. Eng., 15, 227–239, https://doi.org/10.3176/eng.2009.3.06, 2009.

Lindgren, E., Tuomi, L., Kanarik, H., and Huess, V.: EU Copernicus Marine Service Product User for the Baltic Sea Wave Hindcast Product, BALTICSEA_REANALYSIS_WAV_003_015, Issue 2.0, Mercator Ocean International, https://documentation.marine.copernicus.eu/PUM/CMEMS-BAL-PUM-003-015.pdf (last access: 11 June 2025), 2024.

Lorenz, M., Viigand, K., and Gräwe, U.: Untangling the waves: decomposing extreme sea levels in a non-tidal basin, the Baltic Sea, Nat. Hazards Earth Syst. Sci., 25, 1439–1458, https://doi.org/10.5194/nhess-25-1439-2025, 2025.

Lu, L., Kondratenko, A., Kulkarni, K., Li, F., Kujala, P., and Musharraf, M.: An Investigation of Winter Navigation and Icebreaker Needs in the Ice-Infested Water: The Gulf of Finland and the Gulf of Riga, in: International Conference on Offshore Mechanics and Arctic Engineering, V006T07A006, https://doi.org/10.1115/OMAE2024-127955, 2024.

Luhamaa, A., Kimmel, K., Männik, A., and Rõõm, R.: High resolution re-analysis for the Baltic Sea region during 1965–2005 period, Clim. Dynam., 36, 727–738, https://doi.org/10.1007/s00382-010-0842-y, 2011.

Madec, G., Bourdallé-Badie, R., Bouttier, P.-A., Bricaud, C., Bruciaferri, D., Calvert, D., Chanut, J., Clementi, E., Coward, A., and Delrosso, D.: NEMO ocean engine, Zenodo, https://doi.org/10.5281/zenodo.3248739, 2017.

Maljutenko, I. and Raudsepp, U: Long-term mean, interannual and seasonal circulation in the Gulf of Finland – the wide salt wedge estuary or gulf type ROFI, J. Mar. Syst., 195, 1–19, https://doi.org/10.1016/j.jmarsys.2019.03.004, 2019.

Medvedev, I. P. and Kulikov, E. A.: Extreme Storm Surges in the Gulf of Finland: Frequency-Spectral Properties and the Influence

of Low-Frequency Sea Level Oscillations, Oceanology, 61, 459–468, https://doi.org/10.1134/S0001437021040111, 2021.

Mrozowski, P.: Method for determining location of FSRU terminal, TransNav Int. J. Mar. Navig. Saf. Sea Transp., 18, https://doi.org/10.12716/1001.18.01.05, 2024.

Najafzadeh, F., Jankowski, M. Z., Giudici, A., Männikus, R., Suursaar, Ü., Viška, M., and Soomere, T.: Spatiotemporal variability of wave climate in the Gulf of Riga, Oceanologia, 66, 56–77, https://doi.org/10.1016/j.oceano.2023.11.001, 2024.

Najafzadeh, F., Kudryavtseva, N., and Soomere, T.: Effects of large-scale atmospheric circulation on the Baltic Sea wave climate: application of the EOF method on multi-mission satellite altimetry data, Clim. Dynam., 57, 3465–3478, https://doi.org/10.1007/s00382-021-05874-x, 2021.

Nigou, A. and Ollivier, A.: EU Copernicus Marine Service Product User Manual for the Global Ocean L3 Significant Wave Height From Reprocessed Satellite Measurements, WAVE_GLO_PHY_SWH_L3_MY_014_005, Issue 1.0, Mercator Ocean International, https://documentation.marine.copernicus.eu/PUM/CMEMS-WAVE-PUM-014-005.pdf (last access: 15 September 2026), 2026.

Ostrowski, W.: The twenty years' crisis of European energy security: Central and Eastern Europe and the US, Geopolitics, 27, 875–897, https://doi.org/10.1080/14650045.2020.1835863, 2022.

Panteleit, T., Verjovkina, S., Jandt-Scheelke, S., Spruch, L., and Huess, V.: EU Copernicus Marine Service Quality Information Document for the Baltic Sea Physics Reanalysis Product, BALTICSEA_MULTIYEAR_PHY_003_011, Issue 4.1, Mercator Ocean International, https://documentation.marine.copernicus.eu/QUID/CMEMS-BAL-QUID-003-011.pdf (last access: 11 June 2025), 2025.

Pärt, S., Björkqvist, J. V., Alari, V., Maljutenko, I., and Uiboupin, R.: An ocean–wave–trajectory forecasting system for the eastern Baltic Sea: Validation against drifting buoys and implementation for oil spill modeling, Mar. Pollut. Bull., 195, 115497, https://doi.org/10.1016/j.marpolbul.2023.115497, 2023.

Pellikka, H., Johansson, M. M., Nordman, M., and Ruosteenoja, K.: Probabilistic projections and past trends of sea level rise in Finland, Nat. Hazards Earth Syst. Sci., 23, 1613–1630, https://doi.org/10.5194/nhess-23-1613-2023, 2023.

Penalba, M., Aizpurua, J. I., Martinez-Perurena, A., and Iglesias, G.: A data-driven long-term metocean data forecasting approach for the design of marine renewable energy systems, Renew. Sustain. Energy Rev., 167, 112751, https://doi.org/10.1016/j.rser.2022.112751, 2022.

Pujol, M.-I.: EU Copernicus Marine Service Product User Manual for European Seas Gridded L4 Sea Surface Heights and Derived Variables Reprocessed (1993–ongoing), SEALEVEL_EUR_PHY_L4_MY_008_068, Issue 10.0, Mercator Ocean International, https://documentation.marine.copernicus.eu/PUM/CMEMS-SL-PUM-008-032-068.pdf (last access: 15 July 2025), 2025a.

Pujol, M.-I.: EU Copernicus Marine Service Product User Manual for European Seas Along-Track L3 Sea Surface Heights Reprocessed (1993–ongoing) Tailored For Data Assimilation, SEALEVEL_EUR_PHY_L3_MY_008_061, Issue 10.0, Mercator Ocean International, https://documentation.marine.copernicus.eu/PUM/CMEMS-SL-PUM-008-032-068.pdf (last access: 15 July 2025), 2025b

Raudsepp, U. and Maljutenko, I.: A method for assessment of the general circulation model quality using the K-means clustering algorithm: a case study with GETM v2.5, Geosci. Model Dev., 15, 535–551, https://doi.org/10.5194/gmd-15-535-2022, 2022.

Raudsepp, U., Maljutenko, I., Björkqvist, J.-V., Barzandeh, A., Rikka, S., Männik, A., Pärt, S., Alari, V., Vahter, K., and Uiboupin, R.: 50-Year return level datasets for the Baltic Sea, Version v1, Zenodo [data set], https://doi.org/10.5281/zenodo.20378599, 2026a

Raudsepp, U., Maljutenko, I., Björkqvist, J.-V., Barzandeh, A., Rikka, S., Männik, A., Pärt, S., Lagemaa, P., Alari, V., Vahter, K., and Uiboupin, R.: Metocean Data and Analysis Scripts for FSRU Terminal Planning on the Estonian Coast of the Gulf of Finland, Zenodo [data set], https://doi.org/10.5281/zenodo.20356006, 2026b

Ridal, M., Bazile, E., Le Moigne, P., Randriamampianina, R., Schimanke, S., Andrae, U., Berggren, L., Brousseau, P., Dahlgren, P., Edvinsson, L., El-Said, A., Glinton, M., Hagelin, S., Hopsch, S., Isaksson, L., Medeiros, P., Olsson, E., Unden, P., and Wang, Z. Q.: CERRA, the CopernicusEuropean Regional Reanalysis system, Q. J. Roy. Meteor. Soc., 150, 3385–3411, https://doi.org/10.1002/qj.4764, 2024.

Ringgaard, I., Korabel, V., Spruch, L., Lindenthal, A., and Huess, V.: EU Copernicus Marine Service Product User Manual for the Baltic Sea Physics Reanalysis Product, BALTICSEA_MULTIYEAR_PHY_003_011, Issue 1.0, Mercator Ocean International, https://documentation.marine.copernicus.eu/PUM/CMEMS-BAL-PUM-003-011-012.pdf (last access: 11 June 2025), 2024.

Robertson, B., Dunkle, G., Gadasi, J., Garcia-Medina, G., and Yang, Z.: Holistic marine energy resource assessments: A wave and offshore wind perspective of metocean conditions, Renew. Energy, 170, 286–301, https://doi.org/10.1016/j.renene.2021.01.136, 2021.

Ross, E., Astrup, O. C., Bitner-Gregersen, E., Bunn, N., Feld, G., Gouldby, B., Huseby, A., Liu, Y., Randell, D., Vanem, E., and Jonathan, P.: On environmental contours for marine and coastal design, Ocean Eng., 195, 106194, https://doi.org/10.1016/j.oceaneng.2019.106194, 2020.

Rymut, K. and Mihaylov, V.: Spatial aspects of natural gas supply diversification in the context of energy security in the countries of the European Union, Environ. Socio-Economic Stud., 13, 28–40, https://doi.org/10.2478/environ-2025-0003, 2025.

Slakaityte, V., Surwillo, I., and Berling, T. V.: Energy Security in the Baltic Sea Region, Danish Inst. Int. Stud., no. 8, Copenhagen, Denmark, ISBN 9788772360966, 2022.

Solbrekke, I. M., Sorteberg, A., and Haakenstad, H.: The 3 km Norwegian reanalysis (NORA3) – a validation of offshore wind resources in the North Sea and the Norwegian Sea, Wind Energ. Sci., 6, 1501–1519, https://doi.org/10.5194/wes-6-1501-2021, 2021.

Soomere, T.: Wind wave statistics in Tallinn Bay, Boreal Environ. Res., 10, 103–118, 2005.

Suursaar, Ü. and Sooäär, J.: Decadal variations in mean and extreme sea level values along the Estonian coast of the Baltic Sea, Tellus A, 59, 249–260, https://doi.org/10.1111/j.1600-0870.2006.00220.x, 2007.

The Wamdi Group: The WAM model – A third generation ocean wave prediction model, J. Phys. Oceanogr., 18, 1775–1810, 1988.

Valamanesh, V., Myers, A. T., and Arwade, S. R.: Multivariate analysis of extreme metocean conditions for offshore wind turbines, Struct. Saf., 55, 60–69, https://doi.org/10.1016/j.strusafe.2015.03.002, 2015.

Voogt, A., Wilde, J. de, and Dekker, J.: Integrating hydrodynamic and nautical studies for offshore LNG operations, in: Offshore Technology Conference, Houston, Texas, May 2014, https://doi.org/10.4043/25383-MS, 5 May 2014.

Weisse, R., Dailidienė, I., Hünicke, B., Kahma, K., Madsen, K., Omstedt, A., Parnell, K., Schöne, T., Soomere, T., Zhang, W., and Zorita, E.: Sea level dynamics and coastal erosion in the Baltic Sea region, Earth Syst. Dynam., 12, 871–898, https://doi.org/10.5194/esd-12-871-2021, 2021.

Westerlund, A., Tuomi, L., Alenius, P., Myrberg, K., Miettunen, E., Vankevich, R. E., and Hordoir, R.: Circulation patterns in the Gulf of Finland from daily to seasonal timescales, Tellus A, 71, 1627149, https://doi.org/10.1080/16000870.2019.1627149, 2019.

State Planet, 7-osr10, 15, 2026
https://doi.org/10.5194/sp-7-osr10-15-2026
© Author(s) 2026. This work is distributed under
the Creative Commons Attribution 4.0 License.

Impact of Storm Louis on two Spanish harbours: a multi-platform approach

Pablo Lorente[1], Garbiñe Ayensa[2], Marta De Alfonso[1], Samuel Galán[1], Pilar Gil[1], Fernando Manzano[1], Anna Magdalena Matulka[1], Pedro Montero[2], Verónica Morales-Márquez[1], Begoña Pérez-Gómez[1], Cristina Pérez-Íñigo[1], Susana Pérez-Rubio[1], and M. Isabel Ruiz[1]

[1]Puertos del Estado, Madrid, 28042, Spain
[2]INTECMAR (Instituto Tecnolóxico para o Control do Medio Mariño de Galicia), Vilagarcia de Arousa, 36611, Spain

Correspondence: Pablo Lorente (plorente@puertos.es)

Received: 30 July 2025 – Discussion started: 22 September 2025
Revised: 15 January 2026 – Accepted: 28 January 2026 – Published: 30 September 2026

Abstract. Storm Louis struck southwestern Europe between 22 and 26 February 2024, producing severe metocean conditions that led to significant disruptions in transportation networks, widespread power outages, and one confirmed fatality. This high-impact event exemplified the growing threat that deep extratropical cyclones pose to European coastal infrastructure. The synoptic-scale characteristics of Storm Louis were examined using ERA5 reanalysis data, revealing a marked Azores High–Iceland Low pressure dipole configuration, indicative of the canonical manifestation of the positive phase of the North Atlantic Oscillation. A strong SW–NE pressure gradient gave rise to persistent and anomalously intense northwesterly maritime-polar winds over the northeastern Atlantic Ocean and the Iberian Peninsula that induced significant wave heights above 8 m. The concurrent impact on two geographically distant Spanish ports – Langosteira in the northwestern Iberian (NWI) region and Tarragona in the northeastern Iberian (NEI) region – was evaluated using a multi-platform observational framework that integrates in situ measurements from four moored buoys and two tide gauges with remotely sensed data provided by two high-frequency radar (HFR) systems. In the NWI (NEI) area, multiple observed wind and wave parameters associated with Storm Louis exceeded the 99.9th (99th) historical percentiles, based on the available 11-year observational record period spanning 2014–2024. Analysis of high-frequency sea level oscillations, recorded by tide gauges at both ports during Storm Louis, revealed contrasting wave-induced agitation responses between the Langosteira and Tarragona harbours, despite exceedance of their respective historical 99th percentile threshold. The former experienced a moderate but prolonged (33 h long) event peaking at 0.68 m with minimal storm surge influence, while the latter underwent a shorter (16 h long), more intense peak of 1.77 m, also decoupled from storm surge. Over the 2014–2024 period, the relationship between offshore wave parameters and inner-harbour agitation was explored to isolate the open-ocean conditions most strongly associated with critical in-port sea states likely to compromise maritime operations. Results revealed significantly high linear correlations between offshore wave height conditions and harbour agitation ($R = 0.88$ for Langosteira, $R = 0.75$ for Tarragona). However, Tarragona harbour exhibited a more complex, bimodal directional response: peak agitation events were predominantly associated with moderate offshore wave heights (< 3 m) propagating from the southernmost sector, underscoring the harbour's marked sensitivity to wave incidence angle and its role in amplifying internal hydrodynamic response. Finally, HFR wave data, validated against buoy observations, reliably captured storm-induced waves, highlighting their value for real-time extreme-hazard assessment and climate-resilient port infrastructure.

Published by Copernicus Publications.

1 Introduction

The genesis of deep extratropical cyclones over central Europe is governed by a complex interplay of synoptic-scale atmospheric and oceanic factors (Mohr et al., 2020). These systems commonly emerge when warm, moisture-laden air advected from the Mediterranean or North Atlantic converges with cold and dry continental air masses of Arctic or Siberian origin. The resulting sharp thermal and moisture gradients create atmospheric instability: as the warm air ascends and the colder air descends, a low-pressure centre forms, making the region susceptible to highly dynamic and rapidly evolving weather conditions. Such systems are often associated with intense windstorms; heavy precipitation; and, in some cases, catastrophic flooding, particularly during the winter season (Álvarez-Fanjul et al., 2022; Owen et al., 2021; Jacobeit et al., 2006; Wanner et al., 2004).

The socio-economic relevance of extreme extratropical cyclones has become increasingly prominent in recent decades, particularly in the context of anthropogenic climate change altering their frequency, intensity, and spatial distribution (Khodayar et al., 2025; Cao and Su, 2025; Kleespies et al., 2024; Konisky et al., 2015). These high-impact events have exposed the structural vulnerabilities of western Europe, highlighting the substantial risk posed to critical infrastructure, human assets, and regional economies (Leal Filho et al., 2024; Mateos et al., 2023; Forzieri et al., 2018). For instance, Storm Kyrill (17–19 January 2007) produced hurricane-force winds across large areas of Europe, resulting in 47 fatalities and generating the highest insured storm losses recorded in Europe to date (Kettle, 2023; Fink et al., 2009). Similarly, Storm Klaus (23–24 January 2009) caused 26 direct fatalities while impacting northern Iberia and southern France, with more than 715 000 insurance claims filed and total losses exceeding USD 6.0 billion, ranking it the costliest weather-related disaster globally that year (Liberato et al., 2011; Aon-Benfield, 2010). Storm Gloria (19–24 January 2020) caused several casualties and multi-million USD worth of damages in susceptible coastal areas of eastern Spain (Álvarez-Fanjul et al., 2022). These events illustrate the mounting economic burden of windstorms under current climatic conditions and underscore the urgency of improved risk assessment, adaptation strategies, and early warning systems.

Severe sea states associated with extreme storm events can significantly disrupt port operations and damage coastal infrastructure, particularly in vulnerable locations such as deltas, low-lying areas, and erosion-prone shorelines (Lucio et al., 2024). Given their strategic role as logistic hubs within maritime transport networks, international supply chains, and global trade, ports are critical economic assets (Verschuur et al., 2022). Consequently, storm-induced disruptions can result in substantial financial losses, not only from direct damages and operational delays but also from reputational impacts in an increasingly competitive global marketplace (Verschuur et al., 2023).

In recent years, extensive research has focused on assessing the vulnerability of port infrastructure to extreme weather, advancing climate risk analyses and formulating adaptation strategies within the Spanish port system (Fernández-Pérez et al., 2024; Portillo Juan et al., 2022; Izaguirre et al., 2021; Camus et al., 2019; Sánchez-Arcilla et al., 2016). At the global scale, a comprehensive survey by Asariotis et al. (2017), encompassing port authorities in 29 countries across all world regions, reported that approximately 70 % of respondents had experienced weather-related disruptions. These included impacts on operations (76 %), delays (60 %), and physical damage (45 %). The most frequently cited climatic stressors – ranked in decreasing order – were strong winds, heavy precipitation, storm surges, fog, and wave penetration.

While high wind speeds can severely hinder crane operations and cargo handling efficiency within port terminals (Piñeres-Castillo and Mojica-Herazo, 2024), the operability of vessels is predominantly governed by the energy and directionality of incident offshore waves penetrating into the port basin, where they interact with complex bathymetry, harbour geometries, and structural elements (Romano-Moreno et al., 2022; Sierra et al., 2015, 2023). The resulting intra-harbour wave dynamics – commonly referred to as *wave agitation* – can significantly degrade operational efficiency and compromise safety margins. Excessive wave agitation amplifies vessel motions at berth, increasing the risk of mooring line failures and vessel–structure collisions, with potential damage to both ships and port infrastructure (Díaz-Hernández et al., 2021).

In this context, the precise monitoring and comprehensive understanding of extreme-weather-related hazards are essential not only for the implementation of effective prevention strategies and the informed management of port operations, but also for strengthening the socio-ecological resilience of coastal communities (Linnenluecke et al., 2012). The present study focuses on the characterization of Storm Louis, which was associated with a deep low-pressure system (Fig. 1a) that traversed the North Atlantic, delivering severe weather conditions across large areas of western Europe between 22 and 26 February 2024. The storm was marked by intense rainfall and powerful winds (Fig. 1b), with sustained gusts exceeding $20\,\mathrm{m\,s^{-1}}$ that caused widespread disruptions, including transportation delays, power outages, and one fatality reported in France. In Spain, the event was officially classified by the State Meteorological Agency (AEMET) as a high-impact storm, reflecting wind gusts locally exceeding $140\,\mathrm{km\,h^{-1}}$ and the generation of extreme sea states (AEMET, 2025). From an oceanographic standpoint, the northwesterly winds accompanying the storm generated pronounced swell, with significant wave heights in the range of 6–8 m and local maxima exceeding 8 m (Fig. 1c), which severely impacted the Galician and Cantabrian coastlines (NW Iberia region) and, more specifically, Langosteira harbour (Figs. 1d and A1a). Additionally, harsh metocean

Table 1. Products from the Copernicus Marine Service and other complementary datasets used in this study, including the Product User Manual (PUM) and QUality Information Document (QUID). For complementary datasets, the link to the product description, data access, and scientific references are provided. Last access for all web pages cited in this table: 21 July 2025.

Product ref. no.	Product ID and type	Data access	Documentation
1	ERA5 global reanalysis, numerical models	Hersbach et al. (2023)	Copernicus Climate Change Service, Climate Data Store (2023)
2	INSITU_IBI_PHYBGCWAV_DISCRETE_MYNRT_013_033, in situ observations	EU Copernicus Marine Service Product (2024)	PUM: in situ TAC partners (2024) QUID: Wehde et al. (2024)
3	2 Hz data, high-frequency sea level oscillations, and agitation parameters from tide gauges and in situ observations	Puertos del Estado website: https://portus.puertos.es Puertos del Estado website: https://portuscopia.puertos.es	García-Valdecasas et al. (2021) Product description: https://bancodatos.puertos.es/BD/informes/INT_3.pdf
4	30 min wave estimations provided by high-frequency radars and remote observations	Puertos del Estado website: https://portus.puertos.es. Puertos del Estado website: https://portuscopia.puertos.es	Product description: https://bancodatos.puertos.es/BD/informes/INT_6.pdf

conditions were also observed in NE Iberia: strong southeasterly winds (above 12 m s^{-1}, Fig. 1b) induced high waves that easily penetrated into Tarragona harbour due to its mouth orientation (Figs. 1e and A1b). While these conditions may have challenged port operations at the entrance, no operational disruptions were officially reported along the piers.

The signature of Storm Louis was investigated through a multi-platform observational framework, integrating both in situ instruments (four directional wave moored buoys and two tide gauges) and remote sensing technology (two high-frequency radar networks, hereinafter HFR) – to capture the storm's concurrent impact on two geographically distant Spanish harbours, located in the northwestern and northeastern Iberian areas, respectively (NWI and NEI, in Fig. 1a). A key novelty of this work lies in the integrated use of these complementary observational platforms, which allows for a comprehensive, cross-scale characterization of storm-driven harbour impacts (Davidson et al., 2019; Tintoré et al., 2019). This approach enabled a detailed assessment of the relationship between offshore wave characteristics and the resulting sea state within each harbour domain. The analysis aimed to identify which open-ocean conditions are most likely to trigger hazardous port conditions, potentially disrupting maritime operations and compromising the cost–time efficiency of port logistics (Lorente et al., 2024; Romano-Moreno et al., 2022; Díaz-Hernández et al., 2021; Sierra et al., 2015, 2023).

As a secondary objective, the performance of both HFR networks in accurately monitoring extreme offshore wave conditions during Storm Louis was quantitatively assessed. While this land-based remote sensing technology has achieved global recognition for its capability to deliver reliable, near-real-time, two-dimensional surface current maps (Roarty et al., 2019; Rubio et al., 2017), its application to wave field characterization remains relatively limited within operational oceanography, with most studies confined to academic research settings (Morales-Márquez et al., 2024; Saviano et al, 2022; Lorente et al., 2022; López and Conley, 2019; Wyatt et al., 2005; Wyatt, 1986). To address this gap, a skill assessment was conducted by comparing HFR-derived wave parameters against in situ wave measurements from moored buoys located within the HFR coverage area. This evaluation aimed to enhance confidence in the use of HFR networks for monitoring extreme wave events, thereby supporting their integration into operational coastal hazard forecasting and maritime risk management frameworks (Basañez et al., 2019; Atan et al., 2015, 2016).

This work is structured as follows. Section 2 outlines the observational and modelled data sources. Section 3 describes the methodology adopted. Results are presented and discussed in Sect. 4. Finally, principal conclusions are drawn in Sect. 5.

2 Data

All modelled and observational datasets employed in this study are summarized in Tables 1 and 2 and are briefly described below. While some in situ instruments were deployed prior to 2014, the observational time series were standardized to the 2014–2024 period for consistency reasons, as the collection of directional wave data by the Langosteira coastal buoy started on June 2013 (Table 3).

2.1 ERA5 reanalysis

ERA5, the fifth-generation reanalysis for the global climate and weather produced by the European Centre for Medium-Range Weather Forecasts (ECMWF), provides high-resolution, consistent, and quality-controlled datasets

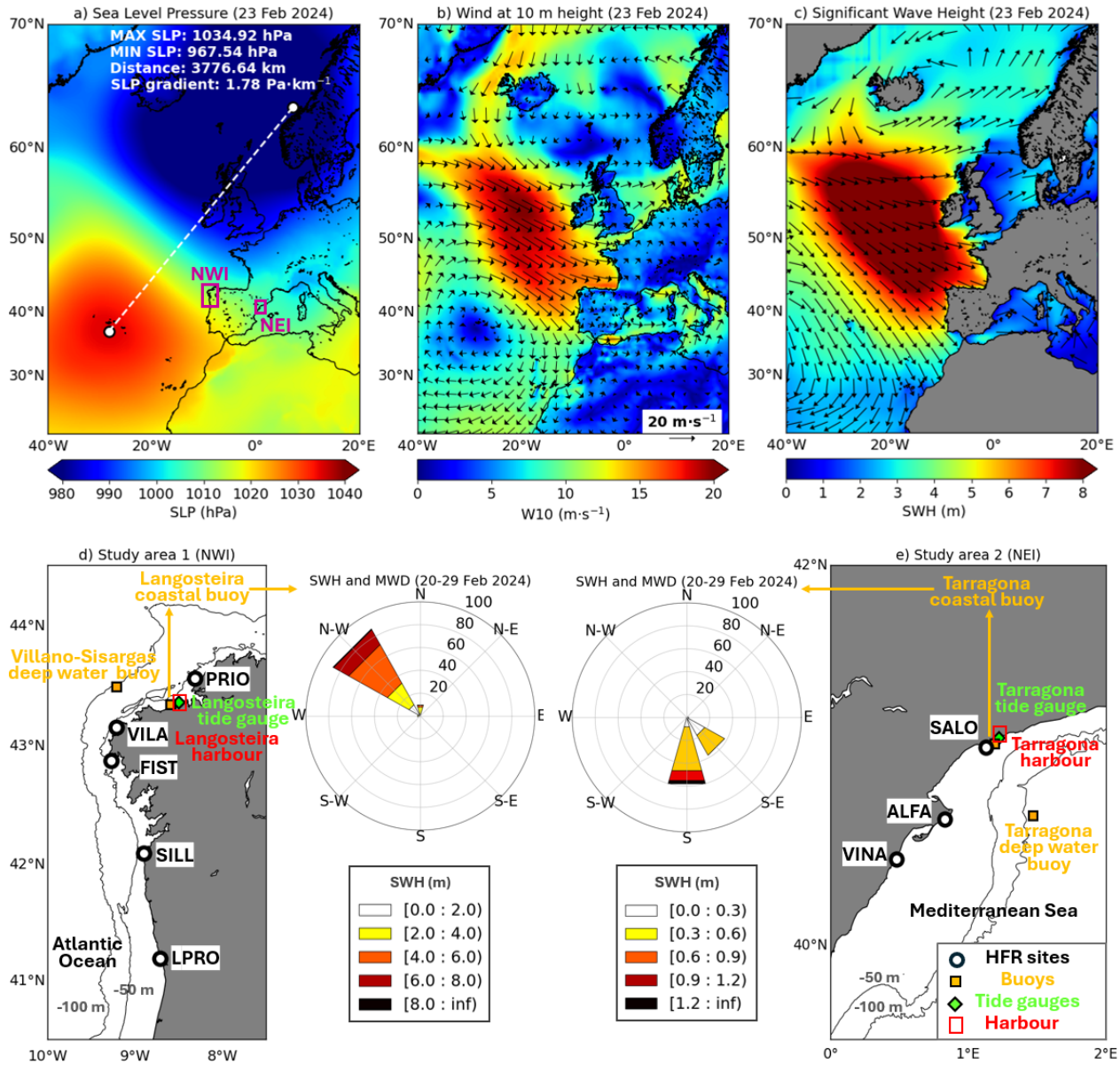


Figure 1. **(a–c)** Synoptic-scale metocean conditions during Storm Louis as derived from ERA5 (product ref. no. 1, Table 1): daily maps of sea level pressure (SLP), wind at 10 m height (W10), and significant wave height (SWH) for 23 February 2024 (peak intensity of Storm Louis). **(d–e)** Study areas: northwestern Iberia (NWI) and northeastern Iberia (NEI) regions, respectively. The location of each ocean sensor – product ref. nos. 2, 3, and 4 (Table 1) – employed in this work is depicted. The orange squares, green diamonds, and white dots denote the location of moored buoys, tide gauges, and high-frequency radar (HFR) sites, respectively. The red boxes denote the harbour's location. Isobath depths are labelled every 50 m. Wave roses illustrate the mean incoming wave direction (MWD) and SWH during a 10 d period (20–29 February 2024) – product ref. no. 2 (Table 1).

extending back to 1940 (product ref. no. 1 in Table 1). ERA5 offers hourly estimates of a wide range of atmospheric and oceanic variables, which are regridded, respectively, to a regular 0.25° and 0.5° horizontal grid. Synoptic-scale analyses of daily-averaged fields of sea level pressure (SLP), 10 m wind speed (W10), significant wave height (SWH), and mean wave direction (MWD) were conducted over the North Atlantic domain (40° W–20° E, 20–70° N) to characterize the dominant metocean features during the peak phase of Storm Louis (Table 2, no. 1).

2.2 In situ moored buoys

Two deep-water and two coastal moored buoys, operated by Puertos del Estado, were utilized in this study (Figs. 1d–e and A1). These in situ observational platforms provide

Table 2. Complementary information about the data sources used in this study. The temporal resolution column corresponds to the processed datasets employed in the analysis and do not reflect the native resolution of the original, raw data. SLP, W10, SWH, MWP, PWP, CWP, and MWD stand for sea level pressure, wind at 10 m height, significant wave height, mean wave period, peak wave period, centroid wave period, and incoming mean wave direction, respectively.

Source (product ref. no.)	Type	Location (coverage)	Variable (unit)	Temporal resolution	Time span used	Spatial resolution
Numerical model (1)	ERA5 reanalysis	Regional domain (40° W–20° E, 20–70° N)	SLP (Pa) W10 ($m\,s^{-1}$) SWH (m) MWD (°)	Daily	February 2024	0.25° 0.25° 0.5° 0.5°
In situ sensor (2)	Buoy	Coastal locations	SWH (m) MWP (s) PWP (s) MWD (°)	Hourly	2014–2024	Pointwise location
In situ sensor (3)	Buoy	Deep-water locations	SWH (m) MWP (s) PWP (s) MWD (°) SLP (Pa) W10 ($m\,s^{-1}$)	Hourly	2014–2024	Pointwise location
In situ sensor (4)	Tide gauge	Port location	Sea level (m) Agitation (m)	Hourly	2014–2024	Pointwise location
Remote sensor (5)	HFR	Coastal and deep-water locations	SWH (m) CWP (s) MWD (°)	Hourly	2014–2024	Concentric arcs: 5.1 km wide for HFR-Galicia, 1.66 km wide for HFR-DeltaEbro

Table 3. Technical description of the four in situ moored buoys used in the present study.

Buoy	Villano-Sisargas	Langosteira	Tarragona	Tarragona
Study area	1 (NWI)	1 (NWI)	2 (NEI)	2 (NEI)
Type of buoy	Deep water	Coastal	Deep water	Coastal
Type of sensor	SeaWatch	WatchMate	SeaWatch	Triaxys
Longitude	9.21° W	8.56° W	1.47° E	1.19° E
Latitude	43.50° N	43.35° N	40.69° N	41.07° N
Depth	386 m	60 m	688 m	15 m
First deployment	May 1998	June 2013	August 2004	November 1992

quality-controlled, hourly-averaged measurements of a range of oceanographic parameters (product ref. no. 2 in Table 1), including SWH, MWD, wave period at spectral peak (or peak wave period, PWP), and mean wave period (MWP) (Table 2, no. 2 and no. 3). Additionally, deep-water moored buoys also provide hourly-averaged estimations of atmospheric parameters (SLP and wind). Comprehensive technical specifications for each buoy are detailed in Table 3.

The quality control, defined by the Copernicus Marine Service in situ team (Copernicus Marine In situ Team, 2020), was based on a battery of automatic checks performed in real time to flag and subsequently filter inconsistent values: the spike test, stuck value check, and rate of change over time, among others.

2.3 Tide gauges

Two radar tide gauges, manufactured by Miros and operated by Puertos del Estado as part of the REDMAR network (Pérez et al., 2014), have been deployed at the mouth of Langosteira (Figs. 1d and A1a) and Tarragona (Figs. 1e and A1b) harbours since November 2012 and May 2011, respectively (Table 4). These sensors deliver quality-controlled sea level measurements at a sampling rate of 2 Hz (product ref. no. 3, Table 1), facilitating the analysis of high-frequency oscillations such as meteotsunamis and infragravity waves (García-Valdecasas et al., 2021). Complementarily, 20 min averaged estimates of port agitation – defined as port-scale oscillations induced by incoming wind waves with periods shorter than 30 s – were derived using an eighth-order Butterworth high-

pass digital filter with a cut-off frequency of 1/30 Hz. The resulting agitation time series were subsampled to hourly intervals (Table 2, no. 3) for subsequent analysis:

i. The agitation time series were analysed over the period of 20–29 February 2024 to evaluate harbour response under extreme weather conditions. Complementarily, hourly storm surge estimates (i.e. meteorological residuals) were examined to assess their potential contribution to wave-induced agitation during Storm Louis.

ii. The agitation time series were analysed over the 11-year observational record period spanning 2014–2024 to investigate the relationship between offshore energetic wave conditions and the sea state within both harbours, with a focus on the directional dependencies influencing wave penetration and the resulting agitation response.

2.4 High-frequency radars (HFRs)

Two "direction-finding" SeaSonde HFR networks (Barrick et al., 1977), manufactured by CODAR Ocean Sensors, were employed in this study (Table 5). While the first one (composed of five sites) was deployed along the northwestern Iberian Peninsula (HFR-Galicia) in July 2010, the second one (formed by three sites) was installed in the northeastern Iberian Peninsula (HFR-DeltaEbro) in December 2013. The geographical distribution of the radar stations is shown in Fig. 1d and e, respectively.

In both study regions, the HFR installations provide wide and unobstructed coverage, ensuring stable and reliable directional solutions. In the case of the HFR-Galicia network, all HFR sites are installed at lighthouse locations, which offer elevated, exposed positions with a clear line of sight over the ocean and minimal physical obstructions. In the HFR-DeltaEbro network, the HFR sites are deployed within a protected natural area, where infrastructure is limited and the surrounding environment is well preserved, resulting in minimal electromagnetic or physical interference. These site characteristics ensure favourable geometric configurations and stable directional performance for wave retrieval in both regions.

Each network provides half-hourly wave observations (product ref. no. 4, Table 1) – including SWH, centroid wave period (CWP), and MWD – retrieved in near real time across multiple annular rings (circular concentric range arcs) extending radially from each onshore radar site (Fig. A2). For this study, HFR-derived wave measurements were subsampled to 60 min intervals (Table 2, no. 4) to ensure temporal consistency across datasets, enabling not only the investigation of wave conditions during Storm Louis but also a robust long-term skill assessment over the 2014–2024 period.

3 Methodology

3.1 Characterization of Storm Louis

To elucidate the driving mechanisms underlying the development of Storm Louis, the prevailing atmospheric conditions were briefly examined at the synoptic scale, with particular emphasis on daily mean fields of SLP and W10. This analysis aimed to identify the large-scale barometric patterns, pressure gradients, and wind structures that contributed to the storm's intensification, thereby enabling a better understanding of the meteorological forcing responsible for the observed oceanographic impacts, especially within the affected harbour environments.

Recognizing the interconnected nature of hydrodynamic variables, an isolated analysis of individual extremes was deemed inadequate to capture the full spatial and temporal footprint of Storm Louis. Instead, a percentile-based statistical framework was employed to characterize the tail behaviour of key environmental variables, including W10, SWH, and MWP, among others. The 1st, 5th, 25th, 50th, 75th, 90th, 95th, 99th, and P99.9th historical percentiles (P1, P5, P25, P50, P75, P90, P95, P99, and P99.9, hereinafter) were derived from an 11-year (2014–2024) observational dataset to contextualize storm Louis within its broader climatological distribution (Coles, 2001). These high-impact thresholds may serve as operational benchmarks for impact-based analysis, facilitating the identification of critical exceedance frequencies relevant to risk assessment and port operational management. Notably, similar percentile-based thresholds have previously been proposed in the context of coastal storm characterization by Harley (2017), Morales-Márquez et al. (2020), and Fanti et al. (2023). In the specific case of port agitation, historical percentiles were intended as purely statistical indicators of anomalous harbour response rather than direct representations of formal operational limits applied by port authorities. Hourly estimations of storm surge components (meteorological residuals) were analysed to assess their potential contribution to the pronounced increase in harbour agitation observed during Storm Louis. This evaluation aimed to determine whether elevated water levels played a significant role in amplifying the port response under storm conditions. In this context, connected extremes are of particular concern for harbour operability. Their combined impacts can interact nonlinearly, resulting in synergistic effects that pose a greater threat to port infrastructure than isolated extreme events (Velpuri et al., 2023).

The long-term relationship between energetic offshore wave conditions (SWH, MWP, and MWD) and port agitation was analysed to assess directional dependencies and harbour response under extreme-forcing scenarios, as the direction of the most energetic incoming waves may be critical to harbour impacts. Scatter plots were thereby computed to infer the dependence between port agitation and offshore SWH data.

Table 4. Technical description of the two tide gauges used in the present study.

Tide gauge	Langosteira	Tarragona
Type (manufacturer)	Radar (MIROS)	Radar (MIROS)
First deployment	November 2012	May 2011
Owned by	A Coruña port authority	Tarragona port authority
Operated and maintained by	Puertos del Estado	Puertos del Estado
Longitude	8.53° W	1.21° W
Latitude	43.35° N	41.08° N
Location	At the end of the breakwater, protected by an inner breakwater	At the end of the breakwater, not protected by an inner breakwater

Table 5. Technical description of the two high-frequency radar (HFR) systems used in the present study. Official names registered in the European HFR Node are shown.

HFR networks	HFR-Galicia	HFR-DeltaEbro
Type of radar	CODAR SeaSonde	CODAR SeaSonde
"Direction of arrival" method	Direction finding	Direction finding
Number of sites (name: from north to south)	Five (PRIO, VILA, FIST, SILL, and LPRO)	Three (SALO, ALFA, and VINA)
First deployment	July 2010	December 2013
Operated by	Puertos del Estado Intecmar Portuguese Hydrographic Institute	Puertos del Estado Magrama Acuamed
Frequency (MHz)	4.46 (and 13.5 MHz for Leça de Palmeira)	13.5
Bandwidth (KHz)	29.41	90.67
Time resolution of wave data	30 min	30 min
Site selected in this work	VILA	ALFA
Number of range cells	5	7
Range cell selected	4	3
Saturation (upper) limit (m)	21.41	7.07

In addition, the monthly distribution of extreme hourly agitation events – defined as values exceeding the P90, P95, and P99 thresholds – was derived from the 11-year observational time series provided by the Langosteira (NWI) and Tarragona (NEI) tide gauges. This analysis aimed to identify potential seasonal patterns or preferential timing in the occurrence of high-agitation conditions, thereby providing insight into whether certain phases of the annual cycle are more prone to operational disruptions due to extreme metocean forcing.

3.2 HFR: fundamentals and data treatment

The HFR land-based remote sensing technology is based on measurements of the radio-wave-backscattered signal from ocean surface gravity waves in the 3–30 MHz range of the electromagnetic spectrum (Crombie, 1955). CODAR SeaSonde "direction-finding" HFR networks measure the return signal continuously over all angles, exploiting the directional properties of a collocated three-element receive antenna system to infer the direction of the incoming signals (Barrick et al., 1977).

While fine-resolution maps of the surface circulation are obtained from the Doppler shift of the predominant first-order peaks in the sea-echo Doppler spectrum, wave parameters are deduced from the weaker and noisier second-order peaks. The second-order scattering-based methods rely significantly on echo quality, which varies with sea state and radar frequency (Wyatt et al., 2005). The relative contribution of the second-order spectrum increases with both the radar frequency and the wave height since wave data are dependent upon the occurrence of both Bragg and larger sur-

face gravity waves. There is a minimum threshold for sea states at a given radar frequency in which reliable wave parameters can be determined. Below such a sensitivity threshold, the lower-energy second-order spectrum is closer to the noise floor and more likely to be contaminated with spurious contributions that might result in wave height overestimation or limited temporal continuity in wave measurements (Tian et al., 2017; Lipa et al., 2022; Lipa and Nyden, 2005). During extreme weather events, there is also a limiting factor for HFR accuracy as the wave height increases and exceeds the saturation limit defined (on an inverse proportion) by the radar transmit frequency. If the radar spectrum saturates, the first- and second-order peaks merge, and interpretation of the spectra becomes impossible with existing methods (Forney et al., 2015). It is worth mentioning that theoretical upper performance thresholds for each HFR system (Table 5) were not exceeded during Storm Louis.

The HFR directional wave spectrum and derived parameters (SWH, CWP, and MWD) can be determined from the weaker second-order sea-echo Doppler spectrum by adopting two main approaches: full integral inversion or fitting with a model of ocean wave spectrum (Lipa and Nyden, 2005). A variety of inverse techniques have been developed over the last few decades (Barrick et al., 1977; Wyatt, 1990; Hisaki, 1996). The wave parameters used in this study, based on 30 min averaged backscatter data, were obtained directly by CODAR radar proprietary software: SeaSonde Radial Suite Software Release 7 (R7). This wave-processing tool performs a least squares fitting technique between the second-order radar spectrum and a Pierson–Moskowitz with cardioid directional function model. Specifically, SeaSonde HFR networks measure a wave period that represents the centroid of the model being fitted to the second-order Doppler spectrum (Lipa and Nyden, 2005), hence hereafter referred to as the centroid wave period (CWP).

HFR wave data were collected in near real time, assuming homogeneity over the entirety of each range cell (RC). Specifically, each site including the HFR-Galicia system has five individual RCs (5.1 km wide), which extend radially from an origin at the onshore radar site to a distance 25.5 km offshore (Fig. A2a). Each site from HFR-DeltaEbro presents seven RCs (1.66 km wide), which extend radially from an origin at the onshore radar site to a distance 11.62 km offshore (Fig. A2b). While the returned signal might be too weak for the outermost RCs, shallow-water effects can become significant for innermost RCs, also impacting on radar sea echo (Lipa et al., 2008). Therefore, we selected the intermediate RC that recorded the highest percentage of valid data, based on the same quality control procedures previously applied to the in situ wave observations. Accordingly, RC3 from the VILA site (HFR-Galicia) and RC4 from the ALFA site (HFR-DeltaEbro) were selected for comparison with in situ wave observations from Villano-Sisargas and Tarragona moored buoys, respectively, in order to evaluate the HFRs' accuracy in capturing extreme offshore wave conditions (Fig. A2). The selected sites were those closest to their corresponding deep-water moored buoys and/or those that exhibited the highest wave data availability throughout the lifecycle of Storm Louis.

Finally, the statistical metrics used in the present study to compare two datasets included the mean, the standard deviation (σ), the root mean squared error (RMSE), and the Pearson correlation coefficient (R) (Emery and Thompson, 2001).

4 Results

4.1 Analysis of Storm Louis

The large-scale synoptic conditions associated with Storm Louis were characterized using daily-averaged ERA5 reanalysis data for SLP, W10, and SWH (Fig. 1a–c). The prevailing SLP pattern featured a classic dipole structure, consisting of a persistent subtropical high ($\sim$ 1035 hPa) over the southwestern North Atlantic and a deep low ($\sim$ 968 hPa) centred over northeastern Europe (Fig. 1a). This configuration, commonly referred to as the Azores High–Icelandic Low dipole, is a key expression of the North Atlantic Oscillation, a dominant mode of atmospheric variability modulating storm tracks and weather extremes across the North Atlantic sector (Hurrell and Deser, 2009). During the peak phase of the storm (23 February 2024), the pressure gradient exceeded 1.7 Pa km^{-1} and was oriented along a southwest–northeast axis, promoting sustained northwesterly winds with velocities surpassing 18 m s^{-1} over the northeastern Atlantic (Fig. 1b). These intense winds generated high-energy swell systems with SWH exceeding 8 m (Fig. 1c).

To place the magnitude of Storm Louis in context, these values can be compared with those reported for the exceptional Storm Gloria in January 2020 (Álvarez-Fanjul et al., 2022). During Gloria, wind speeds also exceeded 18 m s^{-1}, while SWH and MWP ranged between 4.5–7.6 m and 7–9 s, respectively (Lorente et al., 2021). The similarity in wind forcing and SWH values suggests that Storm Louis may be considered an event of comparable meteo-oceanic impact.

In particular, the NWI study area (Fig. 1d) and Langosteira harbour (Fig. A1a) experienced substantial wave impact and atmospheric pressure anomalies. The Villano-Sisargas deep-water buoy recorded a cumulative SLP drop of 33 hPa between 20–25 February, reaching a minimum of 1000 hPa (Fig. 2a), a value slightly below the P5 threshold derived from the 2014–2024 reference period (Fig. 2b). Concurrently, peak offshore wind speeds reached 17.57 m s^{-1}, exceeding the local P99.9 percentile (Fig. 2c). The Langosteira coastal buoy detected extremely energetic sea states from the northwest (Fig. 1d), with a peak SWH of 8.44 m and a peak MWP of 13.7 s recorded on 24 February (Fig. 2a). Notably, the P99.9 threshold of SWH (8.04 m) was occasionally exceeded during 2 non-consecutive hours, while the observed MWP moderately surpassed the P99.9 level (12.0 s), nearly

CHAPTER 4.1

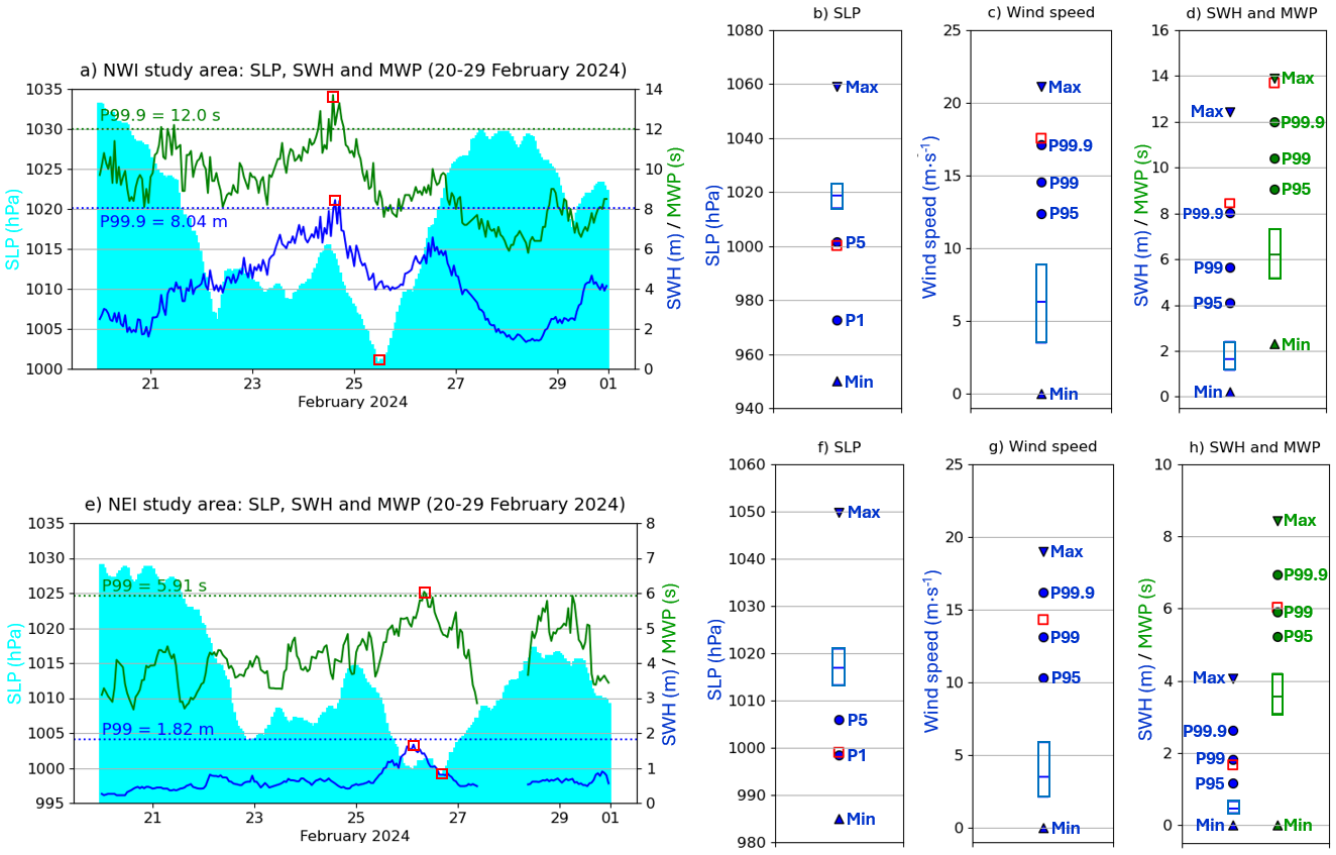


Figure 2. **(a)** Hourly time series of SLP (from Villano-Sisargas buoy: cyan bars), SWH (from Langosteira buoy: blue line), and MWP (from Langosteira buoy: green line) – product ref. no. 2 in Table 1 – during Storm Louis in the NWI area. The P99.9 thresholds are indicated by the dotted blue and green lines, respectively. The red squares represent peaks of SWH and MWP and the minimum value of SLP. **(b–d)** Retrospective analysis for the 2014–2024 period: the minimum value of SLP and peaks of wind speed (from Villano-Sisargas buoy) during Storm Louis, along with peaks of SWH and MWP (from Langosteira buoy), are indicated with the red squares. In each box, the central mark is P50, and the edges of the box are the P25 and P75 thresholds. **(e)** Hourly time series of SLP (from Tarragona deep-water buoy), SWH (from Tarragona coastal buoy), and MWP (from Tarragona coastal buoy) – product ref. no. 2 in Table 1 – during Storm Louis in the NEI area. **(f–h)** Retrospective analysis for the 2014–2024 period: the minimum value of SLP and peaks of wind speed (from Tarragona deep-water buoy) during Storm Louis, along with peaks of SWH and MWP (from Tarragona coastal buoy), are indicated with the red squares.

matching the all-time maximum value of 13.9 s recorded during the 2014–2024 reference period (Fig. 2d).

Severe oceanographic conditions were also observed in the NEI study area (Fig. 1e). Near Tarragona harbour (Fig. A1b), the deep-water buoy recorded an SLP minimum of 999 hPa (Fig. 2e), approaching the P1 threshold for the region (Fig. 2f). Offshore wind speeds peaked at 14.29 m s^{-1}, exceeding the local P99 (Fig. 2g). The Tarragona coastal buoy recorded high waves coming from the southernmost sector (Fig. 1e), with SWH and MWP peaking at 1.67 m and 6.04 s, respectively, during the early hours of 26 February (Fig. 2e). These values were close to or marginally above the P99 thresholds for the corresponding wave parameters (Fig. 2h).

4.2 Sea state within two harbours

Hourly time series of the storm surge component (meteorological residuals) and port wave agitation, measured during the full lifecycle of Storm Louis at the Langosteira (NWI area) and Tarragona (NEI area) tide gauges, are presented in Fig. 3a and b, respectively. While both sites experienced high wave agitation above historical P99 thresholds, the intensity and temporal structure of these events differed substantially. The Langosteira tide gauge displayed a moderate but prolonged agitation episode, reaching a peak of 0.68 m on the afternoon of 24 February (Fig. 3a). The P99 threshold for the 2014–2024 period (set to 0.52 m) was surpassed slightly for 33 non-consecutive hours. The storm surge component remained relatively subdued throughout the event, with fluctuations mostly below 0.50 m and no clear peak coinciding with the maximum agitation. By contrast, the Tarragona tide

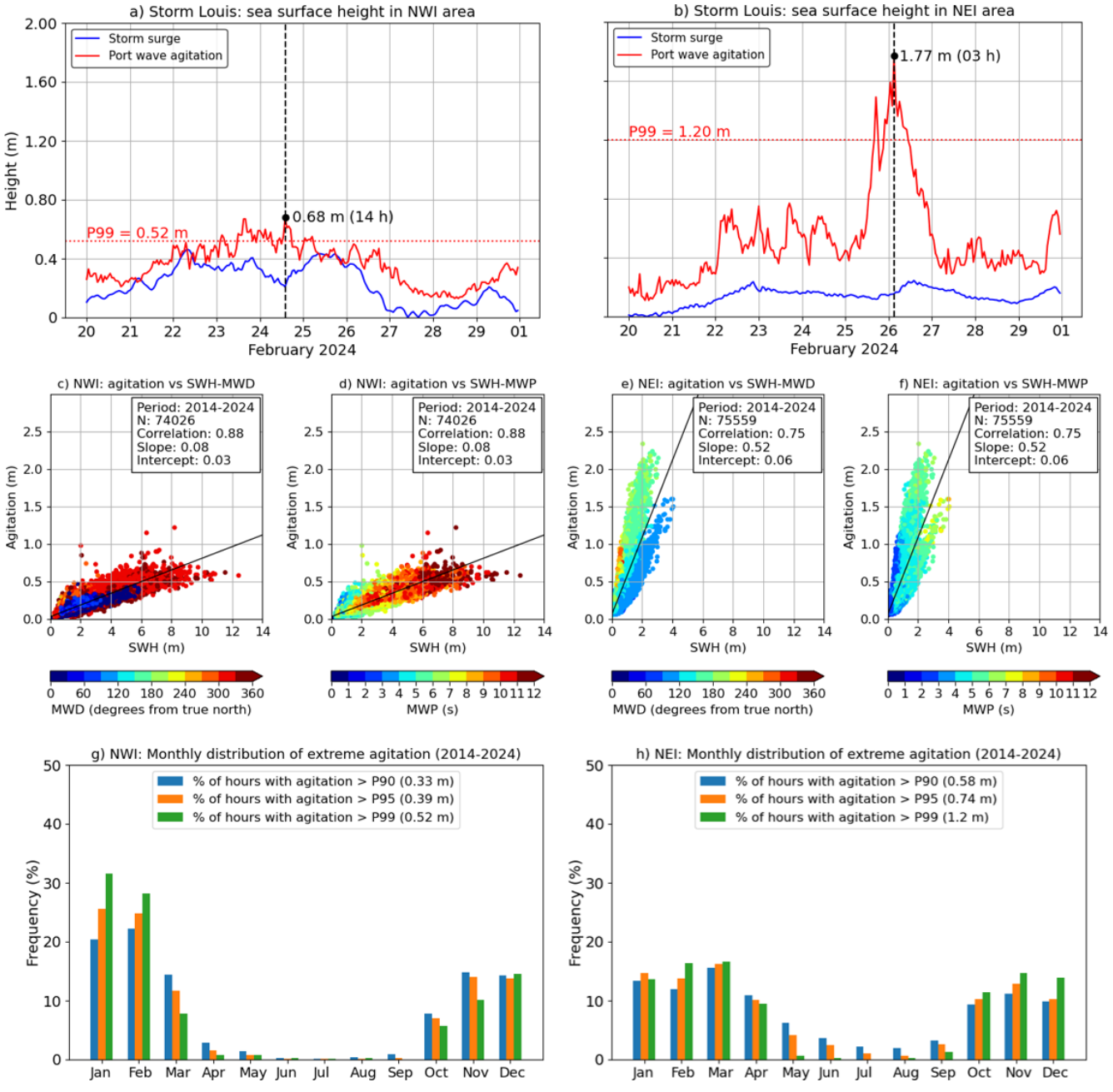


Figure 3. Hourly time series of storm surge (meteorological residual) and port wave agitation (product ref. no. 3 in Table 1) recorded during Storm Louis (20–29 February 2024) by the **(a)** Langosteira and **(b)** Tarragona tide gauges (Fig. 1a). The 99th percentile (P99) thresholds for agitation are indicated by the dashed red lines. Scatter plots relating port agitation (product ref. no. 3 in Table 1) to coastal wave conditions (product ref. no. 2 in Table 1) during the 2014–2024 period for Langosteira **(c–d)** and **(b)** Tarragona harbours **(e–f)**. Hourly data from the Langosteira coastal buoy and Langosteira tide gauge were used for Langosteira harbour (NWI area), while hourly observations from the Tarragona coastal buoy and Tarragona tide gauge were employed for Tarragona harbour (NEI area). Statistical metrics are marked in the white boxes. Monthly distribution of extreme port agitation (product ref. no. 3 in Table 1) events from 2014 to 2024, expressed as the percentage of hours exceeding the 90th (P90), 95th (P95), and 99th (P99) percentiles at **(g)** Langosteira and **(h)** Tarragona harbours.

gauge captured an intense and short-lived event, peaking at 1.77 m early on 26 February 2024 (Fig. 3b). The local P99 threshold for the 2014–2024 period (set to 1.20 m) was far exceeded for 16 consecutive hours. The storm surge signal at the Tarragona tide gauge remained modest, with magnitudes generally under 0.3 m, exhibiting minimal correlation with the agitation peak, consistent with a wave-driven dynamic.

These contrasting behaviours can be interpreted within a multi-scale framework linking large-scale wave generation to local harbour response. Wave energy generated in the North Atlantic required a finite amount of time to propagate toward the regional offshore domains and underwent directional evolution before interacting with each harbour. At the local scale, harbour agitation did not respond instantaneously to offshore wave forcing; rather, it was strongly modulated by site-specific factors, including directional sensitivity, wave transformation processes at the harbour entrance, and intrinsic response times associated with wave–structure interactions. Processes such as diffraction and reflection within the harbour basins played a key role in shaping both the magnitude and the temporal persistence of the observed agitation, thereby explaining the pronounced differences between the two sites despite their exposure to the same synoptic-scale storm event.

Hourly scatter plot analyses conducted over the 11-year study period (2014–2024) revealed a strong statistical correlation between offshore wave conditions and internal harbour agitation across both study sites (Fig. 3c–f). Linear regression analysis of the SWH against harbour agitation yielded significantly high correlation coefficients, specifically $R = 0.88$ for Langosteira harbour and $R = 0.75$ for Tarragona harbour. In the case of Langosteira harbour (Fig. 3c–d), a total of 743 hourly records exceeded the P99 agitation threshold (0.52 m). Of these, 100 % were associated with MWP above 6 s and incident wave directions within the prevailing sector of 295–360° (clockwise from true north). By contrast, the scatter plot for Tarragona harbour exhibited a more complex, bimodal directional response (Fig. 3e–f). Despite the highest offshore SWH (> 3 m) and MWP (> 7 s) values being observed from wave directions between 90 and 120°, these did not correspond to peak agitation events within the port basin. Instead, agitation events exceeding 2 m were predominantly driven by moderate offshore wave heights ($\sim$ 2–3 m), associated with MWP values in the range 5–7 s, penetrating from the southernmost sector (150–210°). This indicates a pronounced sensitivity of the harbour's internal hydrodynamics to wave approach angles, likely modulated by local bathymetric features and structural configurations at the port entrance (Fig. 3c and e, respectively).

In addition, the monthly distribution of extreme-wave-induced agitation was assessed over an 11-year period (2014–2024), as shown in Fig. 3g–h. A pronounced seasonal signal was evident in Langosteira harbour, with peak exceedance frequencies occurring during the boreal winter months (Fig. 3g). Specifically, January through March exhibit the most severe agitation conditions: cumulative exceedance percentages over the 3-month period reached approximately 57 %, 61 %, and 68 % of total hours above the P90, P95, and P99 thresholds, respectively. As the annual cycle advances, a marked decline in exceedance frequency is observed, reaching near-negligible levels between June and August. This attenuation coincides with the seasonal minimum in offshore wave energy flux. From September onwards, there is a gradual resurgence in the frequency of agitation exceedance, with a secondary peak observed in October through December. This bimodal distribution suggests that, in addition to the primary forcing by winter storm activity, transitional swell events and associated synoptic-scale disturbances during the late autumn months contribute substantially to Langosteira harbour agitation.

By contrast, the monthly distribution at Tarragona harbour revealed a more evenly spread regime for extreme agitation (Fig. 3h). High exceedance percentages were evident during the first 4 months of the year, particularly in March, where the percentages across all thresholds approached 16 %–17 %. Unlike Langosteira harbour, where agitation was heavily concentrated in January and February, Tarragona harbour exhibited a more gradual onset and decay of agitation activity during the winter-to-spring transition. From June to September, the proportion of hourly agitation exceeding any threshold fell below 5 %, marking a seasonal minimum consistent with the calm summer wave climate typical of the western Mediterranean Sea. A second rise in extreme agitation was observed in the final quarter of the year. November and December, in particular, exhibited a high proportion of hours exceeding the P99 threshold, reaching nearly 15 %. These outcomes underscore Tarragona harbour's sensitivity to storm events, particularly those originating from southern or southeastern sectors, which are known to be energetically effective in exciting agitation in this specific port geometry.

4.3 Remote wave monitoring with two HFR networks

A quantitative skill assessment of HFR-derived wave estimates during Storm Louis was performed. In the NWI region, time series from the VILA site and the Villano-Sisargas deep-water buoy exhibited strong visual agreement throughout the extreme event (Fig. 4a). The correlation coefficient for SWH is high ($R = 0.92$), with an RMSE of 0.96 m, indicating a high degree of coherence. Both sensors captured the initial wave growth from 21 February, the primary energy peak between 24–25 February, and a secondary crest around 26–27 February. The VILA site slightly overestimated SWH maxima relative to the buoy, particularly during the storm's mature phase, although both records converge during the storm's decay stage. The concurrent wave period time series in the NWI area showed moderate agreement ($R = 0.66$, Fig. 4b), with the HFR-derived CWP and buoy PWP estimates both resolving the rise to values above 14 s during the 21–22 February surge, a brief drop around 23 February, and

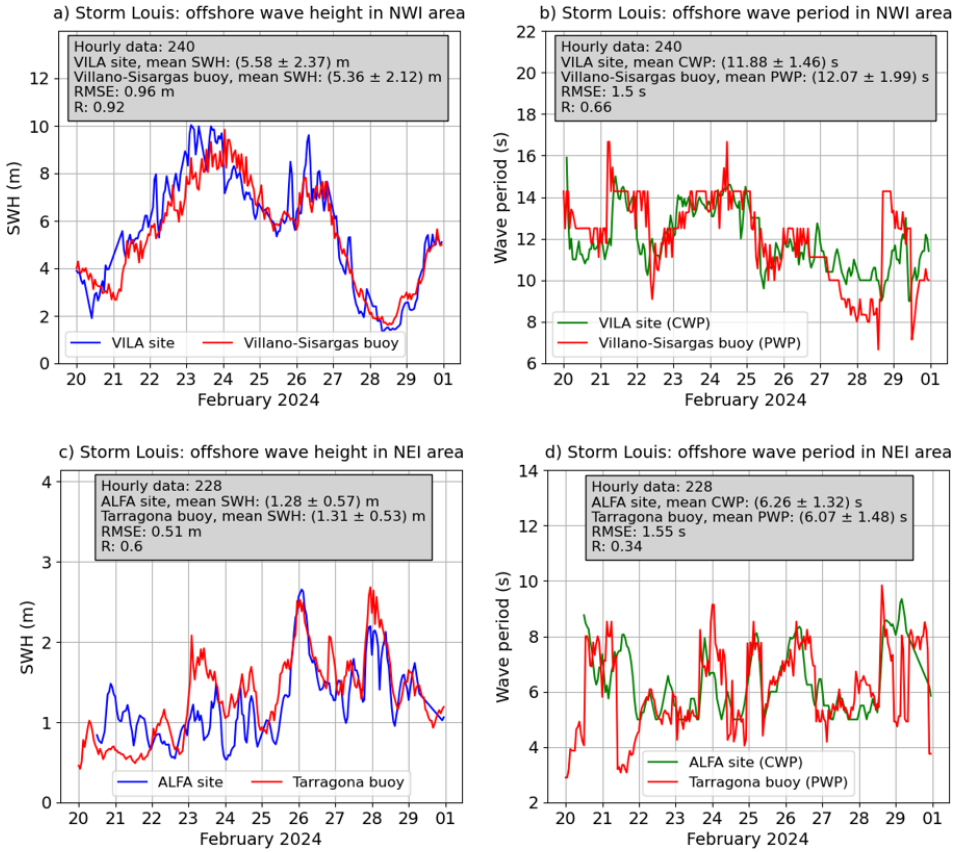


Figure 4. Comparison of hourly estimations of offshore significant wave height (SWH; **a, c**) and centroid/peak wave period (CWP/PWP; **b, d**) provided by high-frequency radar (HFR) sites (product ref. no. 4 in Table 1) against in situ buoy observations (product ref. no. 2 in Table 1) during Storm Louis in the northwestern Iberia (NWI; **a, b**) and northeastern Iberia (NEI; **c, d**) areas. Hourly data from the Villano-Sisargas deep-water buoy and VILA site were used for the NWI area, while hourly observations from the Tarragona deep-water buoy and ALFA site were employed for the NEI area. Statistical metrics are indicated in the grey boxes. For the sake of proper interpretation and comparison, the reader should note that the *y*-axis scales differ between the NWI area and NEI area.

a sustained 13–15 s regime during the storm's main phase. The HFR data tend to smooth out high-frequency fluctuations, leading to an underestimation (~ 1 s) of the maximum buoy-reported wave periods (16–17 s) and an overestimation during the waning stage of the storm. It is worth mentioning that SeaSonde HFR networks measure a wave period (CWP) that represents the centroid of the model being fitted to the second-order Doppler spectrum (Lipa and Nyden, 2005). Thus, HFR centroid periods always dropped between PWP and MWP collected at the Villano-Sisargas buoy. This fact is relevant to properly interpret the skill metrics obtained from comparison, which was conducted against PWP.

By contrast, wave field dynamics in the NEI sector exhibited lower overall energy levels. Both the ALFA site and the Tarragona deep-water buoy recorded relatively calm conditions until 23 February, followed by a marked intensification and a first peak on 26 February. After a rapid decline, a new peak reaching 2.6 m was observed on 28 February (Fig. 4c). Agreement is weaker in this region, with a correlation coefficient of 0.60 and an RMSE of 0.51 m. Wave period estimates in the NEI region (Fig. 4d) demonstrated poorer agreement ($R = 0.34$ and RMSE $= 1.55$ s). The buoy data exhibited pronounced high-frequency variability, with wave periods ranging from 3 to 10 s. However, the HFR-derived CWP was smoother, capturing the dominant 5–8 s wave band during 24–26 February but underrepresenting both short-period (< 4 s) and long-period (> 9 s) oscillations by up to 2 s.

Overall, the results confirm that HFR networks effectively captured the general evolution and magnitude of extreme-storm-induced wave fields, exhibiting consistently higher skill in the estimation of SWH compared to wave period. Performance was notably better in the NWI region, likely reflecting the combination of higher incident wave energy and more comprehensive radar coverage. This spatially dependent variability in performance is consistent with the results reported by Saviano et al. (2022), who documented similar HFR–buoy skill contrasts under differing wave energy regimes and bathymetric conditions. These findings underscore both the potential and the limitations of HFR technol-

ogy for real-time wave monitoring under severe weather conditions, particularly in high-energy offshore environments.

Additionally, a comprehensive long-term validation of HFR-derived wave parameters provided by the VILA site was conducted using in situ measurements from the Villano-Sisargas deep-water buoy over an 11-year concurrent period (2014–2024). The scatter analysis of SWH (Fig. A3a) demonstrated strong agreement between the two sensors, with a significantly high correlation coefficient ($R = 0.87$), a moderately low RMSE of 0.82 m, and a best-fit regression slope near unity (1.02). The negligible intercept (−0.01 m) and close clustering along the 1 : 1 reference line further confirm the HFR system's ability to capture both the magnitude and the variability of SWH over extended timescales. By contrast, the comparison of wave periods (Fig. A3b) yielded a moderate yet statistically significant correlation coefficient ($R = 0.71$) accompanied by a higher RMSE of 1.61 s. The best-fit slope of 0.61 and intercept of 4.25 s indicate a systematic divergence between the HFR-derived CWP and the buoy-derived PWP. Specifically, the HFR tends to underestimate high-period events, while overestimating lower-period regimes, reflecting inherent methodological differences in how each system resolves wave spectral characteristics. For MWD (Fig. A3c), the scatter distribution is more dispersed, with a reduced slope (0.52), an intercept of 135.28°, and an RMSE of 33.97°. Despite a moderate correlation ($R = 0.66$), the observed bias and compression of the directional range suggest limitations in the angular resolution of the HFR system, particularly at longer ranges where reduced Bragg scattering coherence may degrade directional accuracy.

These outcomes, which are in accordance with previous statistical results reported in the literature (Atan et al., 2015; Long et al., 2011), collectively demonstrate that the VILA site provided robust long-term estimates of SWH, moderately reliable wave period data, and qualitatively accurate but less precise wave direction estimates. The performance differences across parameters reflect known limitations of HFR networks in estimating wave direction and longer-period waves, especially under complex sea states or reduced HFR return conditions. Although the unimodal Pierson–Moskowitz spectral model has proven suitable for wind- and swell-dominated conditions, its applicability may be limited in complex metocean environments characterized by multimodal sea states (Lipa et al., 2022). It is also important to note that the substantial separation between the deep-water buoy locations and the selected RCs – 22.52 km for HFR-Galicia (Fig. A2a) and 47.39 km for HFR-DeltaEbro (Fig. A2b) – constitutes a potential source of discrepancy that may affect the derived skill metrics and partially accounts for the observed differences in performance between the two study areas. Moreover, the assumption of spatial homogeneity within each circular RC in CODAR SeaSonde HFR systems may further contribute to the observed discrepancies, particularly in intricate coastal environments where pronounced bathymetric variability and wave transformation processes – such as refraction, dissipation, and breaking – play a dominant role (Wyatt et al., 2005).

5 Conclusions

The projected rise in both the frequency and the intensity of extreme extratropical cyclones presents a growing threat to the resilience of European coastal infrastructure (Little et al., 2023). These powerful storm systems can generate severe metocean conditions, including high winds, heavy precipitation, and dynamic sea level fluctuations. Among the most vulnerable components of coastal infrastructure are ports, which serve as critical hubs in the global maritime transport network and are essential to international trade and economic stability (Verschuur et al., 2022). As mean sea levels continue to rise due to climate change, the impact of storm surges and extreme wave events is expected to intensify. In particular, wave-induced port agitation poses a significant operational hazard, as energetic wave conditions can severely disrupt internal basin dynamics, impair docking manoeuvers, and reduce overall port efficiency even in the absence of structural damage. Such phenomena can lead to both temporary and, in some cases, permanent inundation of port facilities, disrupting operations, damaging equipment and structures, and incurring significant economic costs (Verschuur et al., 2023). The combined effect of these hazards underscores the urgent need for adaptive measures and resilient design in coastal and port infrastructure planning.

This study investigates the meteorological and oceanographic features of Storm Louis, a high-impact deep low-pressure system that affected large areas of western Europe during 22–26 February 2024. This extreme metocean event was characterized by a pronounced Azores High–Icelandic Low dipole pattern, a canonical manifestation of the positive phase of the North Atlantic Oscillation, which imposed an intensified southwest–northeast pressure gradient exceeding 1.7 Pa km^{-1}. This synoptic configuration facilitated persistent and anomalously strong northwesterly wind over the northeastern Atlantic Ocean (with peaks above 17.57 m s^{-1}), generating high-energy wave systems (with SWH and MWP values exceeding 8 m and 13 s, respectively) that significantly impacted the western European coastline.

Two Spanish harbours – Langosteira in the NWI region and Tarragona in the NEI region – were used as case studies to examine the storm's impact. A multi-platform observational analysis, combining in situ observations from four moored buoys and two tide gauges with remotely sensed data from two HFR networks, was performed to evaluate the relationship between open-ocean wave parameters and the wave-induced agitation within the harbour domain. In the NWI (NEI) area, multiple observed wind and wave parameters associated with Storm Louis exceeded the 99.9th (99th) historical percentiles, based on the available 11-year observational record period spanning 2014–2024.

The analysis of high-frequency sea level oscillations during Storm Louis revealed differences in harbour agitation between the Langosteira and Tarragona tide gauges, despite both exceeding their respective historical P99 thresholds. Langosteira experienced a moderate but prolonged event peaking at 0.68 m, with minimal storm surge influence, while Tarragona underwent a shorter, more intense peak of 1.77 m, also decoupled from storm surge. This heterogeneity in storm response between both harbours may be attributable to (i) differences in mouth orientation relative to the predominant incident wave direction and (ii) the contrasting exposure levels of the tide gauge locations. Specifically, the Tarragona tide gauge is situated in an exposed position at the harbour entrance, at the seaward terminus of the main breakwater (Fig. A1b), which makes it more susceptible to incoming wave energy. By contrast, the Langosteira tide gauge is located in a more protected position, behind a secondary breakwater (Fig. A1a), resulting in significantly lower agitation levels during the same storm event. This outcome highlights the critical functional role of secondary defensive structures – such as inner or secondary breakwaters – in mitigating wave-induced agitation. Long-term data (2014–2024) showed strong correlations between offshore wave height conditions and harbour agitation ($R = 0.88$ for Langosteira, $R = 0.75$ for Tarragona), though Tarragona port exhibited a more complex, directionally sensitive response. Peak agitation events were predominantly associated with moderate offshore wave heights (below 3 m) propagating from the southernmost sector, underscoring the harbour's marked sensitivity to wave incidence angle and its role in amplifying internal hydrodynamic response. In addition to directional sensitivity – largely controlled by the configuration of the breakwaters and the harbour entrance – other structural features not analysed in this study, such as the basin layout (including basin shape, dimensions, and depth), have also been shown to influence how incoming waves from different directions are transmitted and amplified within a port (Casas-Prat and Sierra, 2012). Seasonally, agitation in Langosteira harbour was sharply concentrated in winter, especially January–March, with negligible summer activity, whereas Tarragona port displayed a more evenly distributed pattern with notable secondary peaks in late autumn, particularly December. Furthermore, the threshold values defining P90, P95, and especially P99 are significantly higher in Tarragona, indicating that Tarragona port experiences generally higher agitation magnitudes than Langosteira port. This analysis of agitation exceedance over time emphasizes the importance of integrating seasonal variability into port management practices and engineering design frameworks, ensuring that they reflect the fluctuating intensity of metocean forcing throughout the year.

Beyond the event-scale analysis, this study contributes to the broader framework of climate-resilient port management by illustrating how compound metocean hazards and associated wave agitation may compromise critical harbour operations. The impacts observed at Langosteira and Tarragona harbours underscore the need for integrated multi-hazard early warning systems to support anticipatory decision-making and robust, evidence-based assessments of harbour operability. Such approaches align with the objectives of the EU Mission "Ocean and Waters", which promotes the enhancement of long-term infrastructure resilience and the translation of scientific knowledge into operational tools for sustainable ocean governance under a changing climate (EU Mission Ocean and Waters, 2025).

In addition, the capacity of HFR technology to capture extreme wave conditions was evaluated through direct comparison with in situ buoy measurements. Results suggest that HFR networks are capable of reliably characterizing storm-induced offshore wave fields, supporting their broader adoption in operational monitoring frameworks. Complementarily, a long-term (2014–2024) validation of HFR-derived wave parameters from the VILA site against in situ data from the Villano-Sisargas deep-water buoy revealed strong agreement for SWH ($R = 0.87$) and moderate concordance for CWP ($R = 0.71$) but systematic biases due to methodological differences. MWD showed greater dispersion and reduced accuracy ($R = 0.66$), reflecting well-known HFR limitations, such as radio frequency interference under low-wave conditions. The considerable distance between the deep-water buoy locations and the selected RCs (shown in Fig. 2a) should also be acknowledged, as it may influence the accuracy and interpretation of the derived skill metrics. The sensitivity of wave parameter estimates to the aforementioned low-frequency noise could be mitigated through the implementation of a multi-frequency HFR system. By alternating the transmit frequency from 5 to 13 MHz during low to moderate sea states – typically occurring in NWI during late spring and summer – measurement performance across a broad range of SWH may be substantially improved (Wyatt and Green, 2009).

In summary, the present study underscores the importance of integrated observational platforms for real-time extreme-hazard assessment and highlights the critical need to develop climate-resilient port infrastructure capable of withstanding intensifying ocean–atmosphere extremes.

CHAPTER 4.1

Appendix A

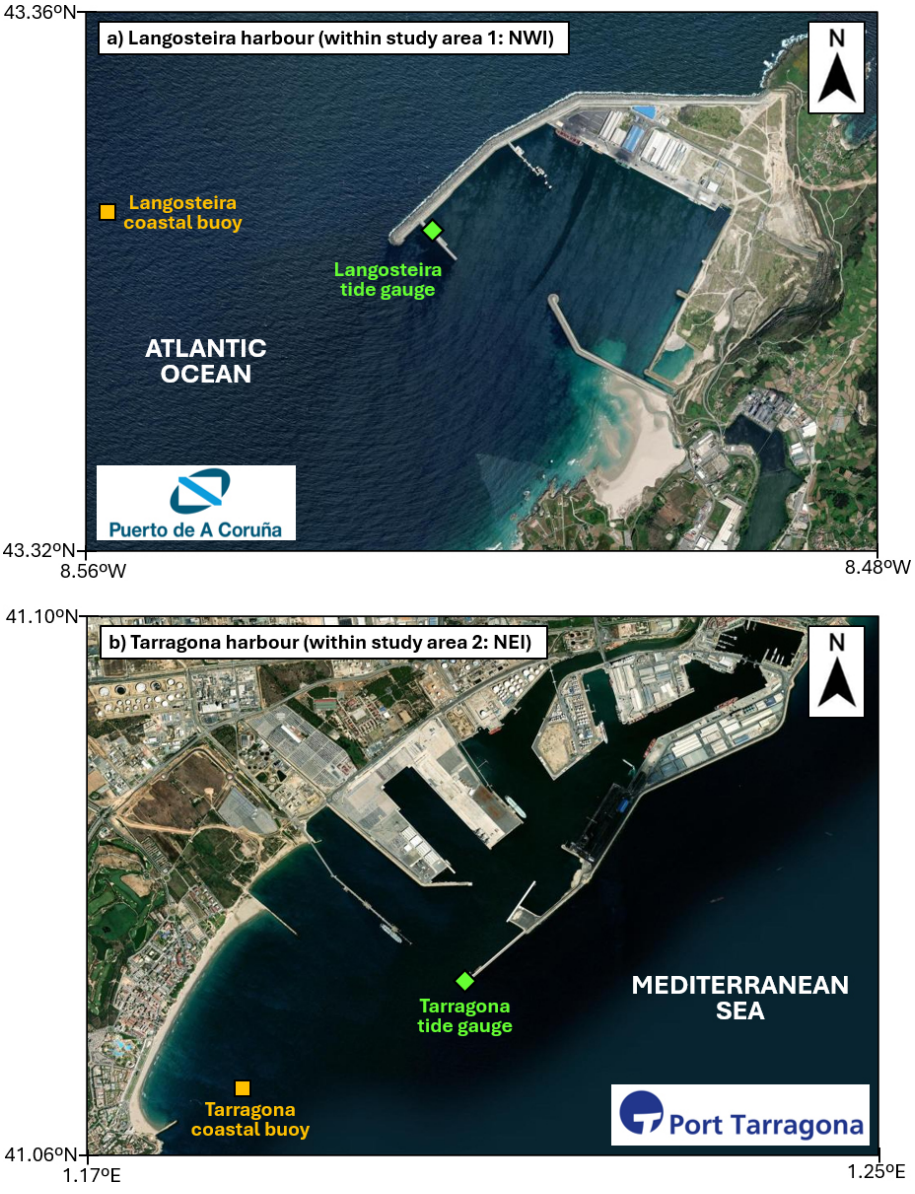


Figure A1. Aerial snapshot showing the geometry of two Spanish harbours: **(a)** Langosteira harbour (which belongs to the A Coruña port authority), located in the northwestern Iberia (NWI) area, and **(b)** Tarragona harbour, situated in the northeastern Iberia (NEI) area. The orange squares and green diamonds denote the location of coastal moored buoys and tide gauges, respectively. Map by © ArcgGis.

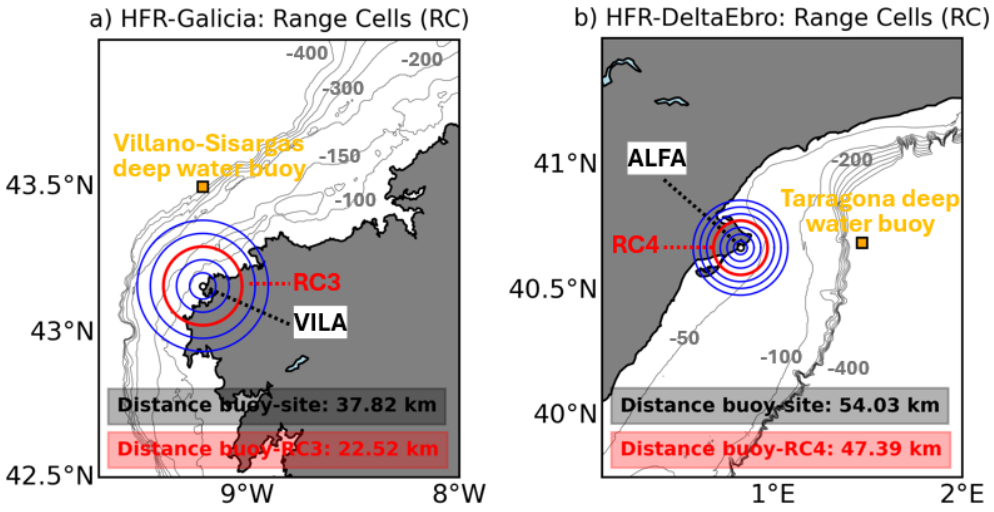


Figure A2. Spatial distribution of the concentric range cells (RCs) extending radially from the onshore origin at **(a)** the VILA site (HFR-Galicia system) and **(b)** the ALFA site (HFR-DeltaEbro system). Wave data derived from HFR (product ref. no. 4 in Table 1) for the selected RC (highlighted in red) were compared with in situ measurements (product ref. no. 2 in Table 1) from moored buoys (indicated by orange squares). Isobath depths are labelled every 100 m. Distances between moored buoys, their respective sites, and selected RCs are shown in the lower boxes.

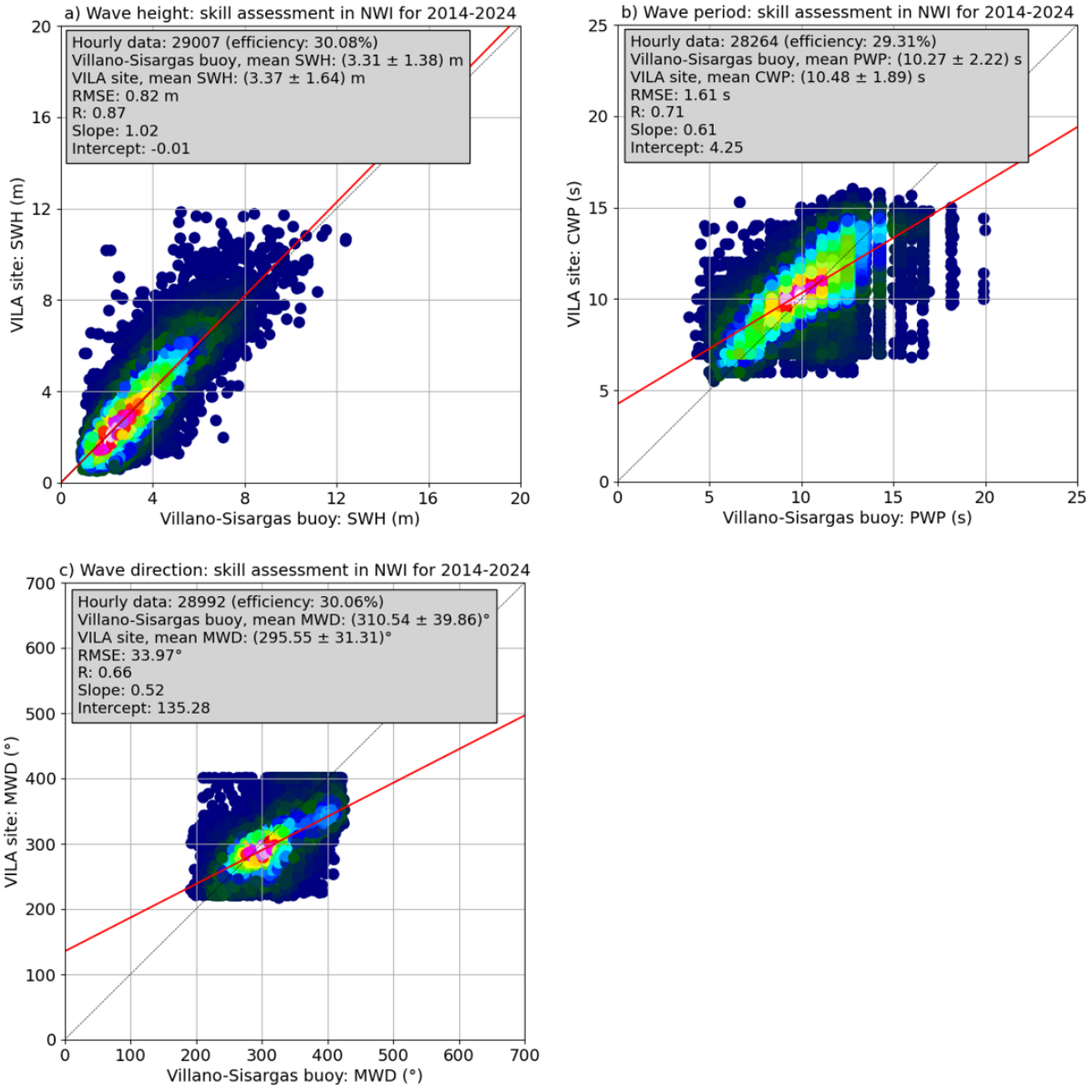


Figure A3. Long-term skill assessment of VILA site wave data at range cell 3 (RC3) (product ref. no. 4 in Table 1) compared with in situ observations provided by the Villano-Sisargas deep-water buoy (product ref. no. 2 in Table 1) for the concurrent 11-year period (2014–2024): best linear fit (solid red line) of scatter plot between hourly observations of **(a)** significant wave height (SWH), **(b)** period (centroid and peak wave period – CWP and PWP, respectively), and **(c)** mean wave direction (MWD), where angles less than 60° were adjusted by adding 360° to improve visibility and facilitate linear regression. The dotted black line represents the result of perfect agreement with a slope of 1.0 and an intercept of 0. Statistical metrics are presented in the grey box.

Data availability. The model and observation products used in this study from both the Copernicus Marine Service and other sources are listed in Table 1.

Author contributions. PL, GA, PM, SG, CPI, MA, VMM, PG, FM, AMM, BPG, SPR, and MIR conducted the pilot study through fruitful discussions in the framework of working team meetings. PL designed the experiment, analysed the data, created the figures, and prepared a first version of the draft with inputs from all co-authors. MA, SM, and CPI conducted a bibliographic revision of extreme metocean events that had previously occurred in the study areas. PG, AMM, and MIR prepared the ERA5 dataset. FM ex-

tracted time series from the Puertos del Estado internal database and prepared diverse in situ sensor datasets. BPG proposed the agitation study in both ports and analysed the corresponding tide gauge records. SPR analysed the atmospheric driving mechanisms during the event. MIR applied quality control to the historical time series of wave parameters from coastal moored buoys. PM and GA prepared datasets from the VILA site, while VMM did so for the ALFA site. Finally, all authors participated in the drafting and revision of the paper through successive iterations.

Competing interests. The contact author has declared that none of the authors has any competing interests.

Disclaimer. The Copernicus Marine Service offering is regularly updated to ensure it remains at the forefront of user requirements. In this process, some products may undergo replacement or renaming, leading to the removal of certain product IDs from the catalogue. If readers have any questions or require assistance regarding these modifications, please feel free to reach out to the Copernicus Marine Service user support team for further guidance. They will be able to provide the necessary information to address concerns and find suitable alternatives.

Publisher's note: Copernicus Publications remains neutral with regard to jurisdictional claims made in the text, published maps, institutional affiliations, or any other geographical representation in this paper. The authors bear the ultimate responsibility for providing appropriate place names. Views expressed in the text are those of the authors and do not necessarily reflect the views of the publisher.

Acknowledgements. The authors are grateful to the Copernicus Marine Service for providing the data and INTECMAR–Consellería do Mar–Xunta de Galicia and the Hydrographic Institute of Portugal for the strong cooperation in jointly operating the HFR-Galicia network.

Review statement. This paper was edited by Marta Marcos and reviewed by two anonymous referees.

References

AEMET: https://www.aemet.es/es/web/conocermas/borrascas/2023-2024/estudios_e_impactos/louis, last access: 26 December 2025.

Álvarez-Fanjul, E., Pérez Gómez, B., de Alfonso Alonso-Muñoyerro, M., Lorente Jiménez, P., García Sotillo, M., Lin-Ye, J., Aznar Lecocq, R., Ruíz Gil de la Serna, M., Pérez Rubio, S., Clementi, E., Coppini, G., García-León, M., Fernandes, M., García Valdecasas, J., García Valdecasas, J. M., Santos Muñoz, D., Luna Rico, M. Y., Mestres, M., Molina, R., Tintoré, J., Mourre, B., Masina, S., Mosso, C., Reyes, E., and Santana, A.: Western Mediterranean record-breaking storm Gloria: An integrated assessment based on models and observations, in: Copernicus Ocean State Report, issue 6, edited by: von Schuckmann, K., Journal of Operational Oceanography, 1–220, https://doi.org/10.1080/1755876X.2022.2095169, 2022.

Aon-Benfield: Annual global climate and catastrophe report, Impact Forecasting 2009, Chicago, Illinois, http://www.aon.com/attachments/reinsurance/200912_ab_if_impact_forecasting_2009_report.pdf, last access: 26 December 2025.

Asariotis, R., Benamara, H., and Mohos-Naray, V.: Port industry survey on climate change impacts and adaptation, United Nations Conference on Trade and Development (UNCTAD), Research Paper, 18, 1–66, https://doi.org/10.13140/RG.2.2.28176.66569, 2017.

Atan, R., Goggins, J., Hartnett, M., Nash, S., and Agostinho, P.: Assessment of Extreme Wave Height Events in Galway Bay Using High Frequency Radar (CODAR) Data, Renewable Energies Offshore, 49–56, https://doi.org/10.1201/b18973-8, 2015.

Atan, R., Goggins, J., and Nash, S.: A Detailed Assessment of the Wave Energy Resource at the Atlantic Marine Energy Test Site, Energies, 9, 967, https://doi.org/10.3390/en9110967, 2016.

Barrick, D. E., Evans, M. W., and Weber, B. L.: Ocean surface currents mapped by radar, Science, 198, 138–144, https://doi.org/10.1126/science.198.4313.138, 1977.

Basañez, A., Lorente, P., Montero, P., Álvarez-Fanjul, E., and Pérez-Muñuzuri, V.: Quality assessment and practical interpretation of the wave parameters estimated by HF Radars in NW Spain, Remote Sens., 12, 598, https://doi.org/10.3390/rs12040598, 2019.

Camus, P., Tomás, A. Díaz-Hernández, G., Rodríguez, B., Izaguirre, C., and Losada, I.J.: Probabilistic assessment of port operation downtimes under climate change, Coastal Engineering, 147, 12–24, https://doi.org/10.1016/j.coastaleng.2019.01.007, 2019.

Cao, X. and Su, Z.: Do Extreme Weather Events Increase Public Concern, Knowledge, and Attention to Climate Change in China?, British Journal of Political Science, 55, e10, https://doi.org/10.1017/S0007123424000565, 2025.

Casas-Prat, M. and Sierra, J. P.: Trend analysis of wave direction and associated impacts on the Catalan coast, Climatic Change, 115, 667–691, https://doi.org/10.1007/s10584-012-0466-9, 2012.

Coles, S.: An Introduction to Statistical Modelling of Extreme Values, Springer-Verlag, https://doi.org/10.1007/978-1-4471-3675-0, 2001.

Copernicus Climate Change Service, Climate Data Store: ERA5 hourly data on single levels from 1940 to present, Copernicus Climate Change Service (C3S) Climate Data Store (CDS), https://doi.org/10.24381/cds.adbb2d47, 2023.

Copernicus Marine In situ Team: Copernicus in Situ TAC, Real Time Quality Control for WAVES, Copernicus in situ TAC, Toulouse, France, 1–16, https://doi.org/10.13155/46607, 2020.

Crombie, D. D.: Doppler spectrum of sea echo at 13.56 Mc/S, Nature, 175, 681–682, https://doi.org/10.1038/175681a0, 1955.

Davidson, F., Alvera-Azcárate, A., Barth, A., Brassington, G. B., Chassignet, E. P., Clementi, E., De Mey-Frémaux, P., Divakaran, P., Harris, C., Hernandez, F., Hogan, P., Hole, L. R., Holt, J., Liu, G., Lu, Y., Lorente, P., Maksymczuk, J., Martin, M., Mehra, A., Melsom, A., Mo, H., Moore, A., Oddo, P., Pascual, A., Pequignet, A-C, Kourafalou, V., Ryan, A., Siddorn, J., Smith, G., Spindler, D., Spindler, T., Stanev, E. V., Staneva, J., Storto, A., Tanajura, C., Vinayachandran, P. N., Wan, L., Wang, H., Zhang,

Y., Zhu, X., and Zu, Z.: Synergies in Operational Oceanography: The intrinsic need for sustained ocean observations, Front. Mar. Sci., 6, 450, https://doi.org/10.3389/fmars.2019.00450, 2019.

Díaz-Hernández, G., Rodríguez Fernández, B., Romano-Moreno, E., and Lara, J. L.: An improved model for fast and reliable harbour wave agitation assessment, Coastal Engineering, 170, 104011, https://doi.org/10.1016/j.coastaleng.2021.104011, 2021.

Emery, W. J. and Thompson, R. E.: Data Analysis Methods in Physical Oceanography, Elsevier Science, Amsterdam, 654 pp., ISBN 9780080477008, 2001.

EU Copernicus Marine Service Product: Atlantic Iberian Biscay Irish Ocean-In-Situ Near Real Time Observations, Mercator Ocean International [data set], https://doi.org/10.48670/moi-00043, 2025.

EU Mission Ocean and Waters: https://oceans-and-fisheries.ec.europa.eu/news/mission-ocean-and-waters-over-1000-initiatives-protect-and-restore-marine-and-freshwater-ecosystems-2025-06-02_en, last access: 26 December 2025.

Fanti, V., Ferreira, Ó., Kümmerer, V., and Loureiro, C.: Improved estimates of extreme wave conditions in coastal areas from calibrated global reanalyses, Commun. Earth Environ., 4, 151, https://doi.org/10.1038/s43247-023-00819-0, 2023.

Fernández-Pérez, A., Lara, J. L., Lucio, D., and Losada, I. J.: Compound climate change risk analysis for port infrastructures, Coastal Engineering, 193, 104560, https://doi.org/10.1016/j.coastaleng.2024.104560, 2024.

Fink, A. H., Brücher, T., Ermert, V., Krüger, A., and Pinto, J. G.: The European storm Kyrill in January 2007: synoptic evolution, meteorological impacts and some considerations with respect to climate change, Nat. Hazards Earth Syst. Sci., 9, 405–423, https://doi.org/10.5194/nhess-9-405-2009, 2009.

Forney, R., Roarty, H., and Glenn, S.: Measuring waves with a compact HF radar, OCEANS 2015 – MTS/IEEE Washington, Washington, DC, USA, 1–5, https://doi.org/10.23919/OCEANS.2015.7404428, 2015.

Forzieri, G., Bianchi, A., Batista e Silva, F., Marin Herrera, M. A., Leblois, A., Lavalle, C., Aerts, J. C. J. H., and Feyen, L.: Escalating impacts of climate extremes on critical infrastructures in Europe, Global Environmental Change, 48, 97–107, https://doi.org/10.1016/j.gloenvcha.2017.11.007, 2018.

García-Valdecasas, J., Pérez Gómez, B., Molina, R., Rodríguez, A., Rodríguez, D., Pérez, S., Campos, A., Rodríguez-Rubio, P., Gracia, S., Ripollés, L., Terrés Nicoli, J. M., de los Santos, F. J., and Álvarez-Fanjul, E.: Operational tool for characterizing high-frequency sea level oscillations, Nat. Hazards, 106, 1149–1167, https://doi.org/10.1007/s11069-020-04316-x, 2021.

Harley, M.: Coastal storm definition, in: Coastal storms: processes and impacts, edited by: Ciavola, P. and Coco, G., John Wiley and Sons, 1–21, https://doi.org/10.1002/9781118937099.ch1, 2017

Hersbach, H., Bell, B., Berrisford, P., Biavati, G., Horányi, A., Muñoz Sabater, J., Nicolas, J., Peubey, C., Radu, R., Rozum, I., Schepers, D., Simmons, A., Soci, C., Dee, D., and Thépaut, J.-N.: ERA5 hourly data on single levels from 1940 to present, Copernicus Climate Change Service (C3S) Climate Data Store (CDS) [data set], https://doi.org/10.24381/cds.adbb2d47, 2023.

Hisaki, Y.: Nonlinear inversion of the integral equation to estimate ocean wave spectra from HF radar, Radio Sci., 31, 25–39, https://doi.org/10.1029/95RS02439, 1996.

Hurrell, J. W. and Deser, C.: North Atlantic climate variability: The role of the North Atlantic Oscillation, J. Mar. Syst., 78, 28–41, https://doi.org/10.1016/j.jmarsys.2009.11.002, 2009.

In Situ TAC partners: EU Copernicus Marine Service Product User Manual for the Atlantic Iberian Biscay Irish Ocean-In-Situ Near Real Time Observations, INSITU_IBI_PHYBGCWAV_DISCRETE_MYNRT_013_033, Issue: 2.2, Mercator Ocean International, https://documentation.marine.copernicus.eu/PUM/CMEMS-INS-PUM-013-030-036.pdf (last access: 21 July 2025), 2024.

Izaguirre, C., Losada, I. J., Camus, P., Vigh, J. L., and Stenek, V.: Climate change risk to global port operations, Nat. Clim. Chang., 11, 14–20, https://doi.org/10.1038/s41558-020-00937-z, 2021.

Jacobeit, J., Philipp, A., and Nonnenmacher, M.: Atmospheric circulation dynamics linked with prominent discharge events in Central Europe, Hydrological Sciences Journal, 51, 946–965, https://doi.org/10.1623/hysj.51.5.946, 2006.

Kettle, A. J.: Storm Kyrill and the storms of mid-January 2007: Societal and Energy Impacts in Europe, Adv. Geosci., 58, 135–147, https://doi.org/10.5194/adgeo-58-135-2023, 2023.

Kleespies, M. W., Friedrich, T., Marg, O., Völker, C., and Schiwy, S.: Assessing the unseen consequences: influence of an extreme weather event on environmental perceptions and connection to nature, Environ. Sci. Eur., 36, 122, https://doi.org/10.1186/s12302-024-00950-5, 2024.

Khodayar, S., Kushta, J., Catto, J. L., Dafis, S., Davolio, S., Ferrarin, C. Flaounas, E., Groenemeijer, P., Hatzaki, M., Hochman, A., Kotroni, V., Landa, J., Láng-Ritter, I., Lazoglou, G., Liberato, M. L. R., Miglietta, M. M., Papagiannaki, K., Patlakas, P., Stojanov, R., and Zittis, G.: Mediterranean cyclones in a changing climate: A review on their socio-economic impacts, Reviews of Geophysics, 63, e2024RG000853, https://doi.org/10.1029/2024RG000853, 2025.

Konisky, D. M., Hughes, L., and Kaylor, C. H.: Extreme weather events and climate change concern, Clim. Change, 134, 533–547, https://doi.org/10.1007/s10584-015-1555-3, 2015.

Leal Filho, W., Abeldaño Zuñiga, R. A., Sierra, J., Dinis, M. A. P., Corazza, L., Nagy G. J., and Aina, Y. A.: An assessment of priorities in handling climate change impacts on infrastructures, Sci. Rep., 14, 14147, https://doi.org/10.1038/s41598-024-64606-3, 2024.

Liberato, M. L. R., Pinto, J. G., Trigo, I. F., and Trigo, R. M.: Klaus – an exceptional winter storm over northern Iberia and southern France, Weather, 66, 330–334, https://doi.org/10.1002/wea.755, 2011.

Linnenluecke, M. K., Griffiths, A., and Winn, M.: Extreme weather events and the critical importance of anticipatory adaptation and organizational resilience in responding to impacts, Bus. Strat. Environ., 21, 17–32, https://doi.org/10.1002/bse.708, 2012.

Lipa, B. J. and Nyden, B.: Directional wave information from the SeaSonde, IEEE J. Oceanic Eng., 30, 221–231, https://doi.org/10.1109/joe.2004.839929, 2005.

Lipa, B. J., Nyden, B., Barrick, D., and Kohut, J.: HF Radar Sea-Echo from Shallow Water, Sensors, 8, 4611–4635, 2008.

Lipa, B., Daugharty, M., Losekoot, M., and Fernandes, M.: Progress in Compact HF Radar Measurement of Bimodal Ocean Wave Parameters, Remote Sensing, 14, 2631, https://doi.org/10.3390/rs14112631, 2022.

Little, A. S., Priestley, M. D. K., and Catto, J. L.: Future increased risk from extratropical windstorms in northern Europe, Nat. Commun., 14, 4434, doi.10.1038/s41467-023-40102-6, 2023.

Long, R. M., Barrick, D., Largier, J. L., and Garfield, N.: Wave Observations from Central California: SeaSonde Systems and in Situ Wave Measurements, Journal of Sensors, 2011, 1–18, https://doi.org/10.1155/2011/728936, 2011.

Lopez, G. and Conley, D. C.: Comparison of HF Radar Fields of Directional Wave Spectra Against In Situ Measurements at Multiple Locations, Journal of Marine Science and Engineering, 7, 271, https://doi.org/10.3390/jmse7080271, 2019.

Lorente, P., Lin-Ye, J., García-León, M., Reyes, E., Fernandes, M., Sotillo, M. G., Espino, M., Ruiz, M. I., Gracia, V., Pérez, S., Aznar, R., Alonso-Martirena, A., and Álvarez-Fanjul, E.: On the Performance of High Frequency Radar in the Western Mediterranean During the Record-Breaking Storm Gloria, Front. Mar. Sci., 8, 645762, https://doi.org/10.3389/fmars.2021.645762, 2021.

Lorente, P., Aguiar, E., Bendoni, M., Berta, M., Brandini, C., Cáceres-Euse, A., Capodici, F., Cianelli, D., Ciraolo, G., Corgnati, L., Dadić, V., Doronzo, B., Drago, A., Dumas, D., Falco, P., Fattorini, M., Gauci, A., Gómez, R., Griffa, A., Guérin, C.-A., Hernández-Carrasco, I., Hernández-Lasheras, J., Ličer, M., Magaldi, M. G., Mantovani, C., Mihanović, H., Molcard, A., Mourre, B., Orfila, A., Révelard, A., Reyes, E., Sánchez, J., Saviano, S., Sciascia, R., Taddei, S., Tintoré, J., Toledo, Y., Ursella, L., Uttieri, M., Vilibić, I., Zambianchi, E., and Cardin, V.: Coastal high-frequency radars in the Mediterranean – Part 1: Status of operations and a framework for future development, Ocean Sci., 18, 761–795, https://doi.org/10.5194/os-18-761-2022, 2022.

Lorente, P., de Alfonso, M., Gil, P., Manzano, F., Matulka, A. M., Pérez-Gómez, B., Pérez-Rubio, S., and Ruiz, M. I.: Monitoring the record-breaking wave event in Melilla harbour (SW Mediterranean Sea), in: 8th edition of the Copernicus Ocean State Report (OSR8), edited by: von Schuckmann, K., Moreira, L., Grégoire, M., Marcos, M., Staneva, J., Brasseur, P., Garric, G., Lionello, P., Karstensen, J., and Neukermans, G., Copernicus Publications, State Planet, 4-osr8, 19, https://doi.org/10.5194/sp-4-osr8-19-2024, 2024.

Lucio, D., Lara, J. L., Tomás, A., and Losada, I. J.: Probabilistic assessment of climate-related impacts and risks in ports, Reliability Engineering and System Safety, 251, 110333, https://doi.org/10.1016/j.ress.2024.110333, 2024.

Mateos, R. M., Sarro, R., Díez-Herrero, A., Reyes-Carmona, C., López-Vinielles, J., Ezquerro, P., and Monserrat, O.: Assessment of the socio-economic impacts of extreme weather events on the coast of southwest Europe during the period 2009–2020, Applied Sciences, 13, 2640, https://doi.org/10.3390/app13042640, 2023.

Mohr, S., Wilhelm, J., Wandel, J., Kunz, M., Portmann, R., Punge, H. J., Schmidberger, M., Quinting, J. F., and Grams, C. M.: The role of large-scale dynamics in an exceptional sequence of severe thunderstorms in Europe May–June 2018, Weather Clim. Dynam., 1, 325–348, https://doi.org/10.5194/wcd-1-325-2020, 2020.

Morales-Márquez, V., Orfila, A., Simarro, G., and Marcos, M.: Extreme waves and climatic patterns of variability in the eastern North Atlantic and Mediterranean basins, Ocean Sci., 16, 1385–1398, https://doi.org/10.5194/os-16-1385-2020, 2020.

Morales-Márquez, V., Dumas, D., and Guérin, C. A.: HF radar estimation of ocean wave parameters: Second-order Doppler spectrum versus Bragg wave modulation approach, Coastal Engineering, 198, 104719, https://doi.org/10.1016/j.coastaleng.2025.104719, 2024.

Owen, L. E., Catto, J. L., Stephenson, D. B., and Dunstone, N. J.: Compound precipitation and wind extremes over Europe and their relationship to extratropical cyclones, Weather and Climate Extremes, 33, 100342, https://doi.org/10.1016/j.wace.2021.100342, 2021.

Pérez, B., Payo, A., López, D., Woodworth, P. L., and Alvarez Fanjul, E.: Overlapping sea level time series measured using different technologies: an example from the REDMAR Spanish network, Nat. Hazards Earth Syst. Sci., 14, 589–610, https://doi.org/10.5194/nhess-14-589-2014, 2014.

Piñeres-Castillo, A. P. and Mojica-Herazo, J. C.: A Review of Wind Impact on Container Port Operations: Current Technologies, Strategies and Future Perspectives, The 2nd International Symposium on Intelligent Systems and Future Networks (ISFN 2024) 28–30 October 2024, Leuven, Belgium, Procedia Computer Science, 251, 783–788, https://doi.org/10.1016/j.procs.2024.11.185, 2024.

Portillo Juan, N., Negro Valdecantos, V., and del Campo, J. M.: Review of the Impacts of Climate Change on Ports and Harbours and Their Adaptation in Spain, Sustainability, 14, 7507, https://doi.org/10.3390/su14127507, 2022.

Roarty, H., Cook, T., Hazard, L., George, D., Harlan, J., Cosoli, S., Wyatt, L., Álvarez Fanjul, E., Terrill, E., Otero, M., Largier, J., Glenn, S., Ebuchi, N., Whitehouse, B., Bartlett, K., Mader, J., Rubio, A., Corgnati, L., Mantovani, C., Griffa, A., Reyes, E., Lorente, P., Flores-Vidal, X., Saavedra-Matta, K. J., Rogowski, P., Prukpitikul, S., Lee, S.-H., Lai, J.-W., Guerin, C.-A., Sánchez, J., Hansen, B., and Grilli, S.: The Global High Frequency Radar Network, Front. Mar. Sci., 6, 164, https://doi.org/10.3389/fmars.2019.00164, 2019.

Romano-Moreno, E., Diaz-Hernandez, G., Lara, J. L. Tomás, A., and Jaime, F. F.: Wave downscaling strategies for practical wave agitation studies in harbours, Coast. Eng., 175, 104140, https://doi.org/10.1016/j.coastaleng.2022.104140, 2022.

Rubio, A., Mader, J., Corgnati, L., Mantovani, C., Griffa, A., Novellino, A., Quentin, C., Wyatt, L., Schulz-Stellenfleth, J., Horstmann, J., Lorente, P., Zambianchi, E., Hartnett, M., Fernandes, C., Zervakis, V., Gorringe, P., Melet, A., and Puillat, I.: HF radar activity in European coastal seas: next steps towards a panEuropean HF radar network, Front. Mar. Sci., 20, 8, https://doi.org/10.3389/fmars.2017.00008, 2017.

Sánchez-Arcilla, A., Sierra, J.P., Brown, S., Casas-Prat, M., Nicholls, R. J., Lionello, P., and Conte, D.: A review of potential physical impacts on harbours in the Mediterranean Sea under climate change, Reg. Environ. Change, 16, 2471–2484, https://doi.org/10.1007/s10113-016-0972-9, 2016.

Saviano, S., Biancardi, A. A., Uttieri, M., Zambianchi, E., Cusati, L. A., Pedroncini, A., Contento, G., and Cianelli, D.: Sea Storm Analysis: Evaluation of Multiannual Wave Parameters Retrieved from HF Radar and Wave Model, Remote Sens., 14, 1696, https://doi.org/10.3390/rs14071696, 2022.

Sierra, J. P., Casas-Prat, M., Virgili, M., Mösso, C., and Sánchez-Arcilla, A.: Impacts on wave-driven harbour agitation due to cli-

mate change in Catalan ports, Nat. Hazards Earth Syst. Sci., 15, 1695–1709, https://doi.org/10.5194/nhess-15-1695-2015, 2015.

Sierra, J. P., Sánchez-Arcilla, A., Gironella, X., Gracia, V., Altomare, C., Mösso, C., González-Marco, D., Gómez, J., Barceló, M., and Barahona, C.: Impact of climate change on berthing areas in ports of the Balearic Islands: adaptation measures, Front. Mar. Sci., 10, 1124763, https://doi.org/10.3389/fmars.2023.1124763, 2023.

Tian, Z., Wen, B., Jin, L., and Tian, Y.: Radio frequency interference suppression algorithm in spatial domain for compact high-frequency radar, IEEE Geosci. Remote Sens. Lett., 15, 102–106, 2017.

Tintoré, J., Pinardi, N., Álvarez-Fanjul, E., Aguiar, E., Álvarez-Berastegui, D., Bajo, M., Balbin, R., Bozzano, R., Nardelli, B. B., Cardin, V., Casas, B., Charcos-Llorens, M., Chiggiato, J., Clementi, E., Coppini, G., Coppola, L., Cossarini, G., Deidun, A., Deudero, S., D'Ortenzio, F., Drago, A., Drudi, M., El Serafy, G., Escudier, R., Farcy, P., Federico, I., Fernández, J. G., Ferrarin, C., Fossi, C., Frangoulis, C., Galgani, F., Gana, S., García Lafuente, J., Sotillo, M. G., Garreau, P., Gertman, I., Gómez-Pujol, L., Grandi, A., Hayes, D., Hernández-Lasheras, J., Herut, B., Heslop, E., Hilmi, K., Juza, M., Kallos, G., Korres, G., Lecci, R., Lazzari, P., Lorente, P., Liubartseva, S., Louanchi, F., Malacic, V., Mannarini, G., March, D., Marullo, S., Mauri, E., Meszaros, L., Mourre, B., Mortier, L., Muñoz-Mas, C., Novellino, A., Obaton, D., Orfila, A., Pascual, A., Pensieri, S., Pérez Gómez, B., Pérez Rubio, S., Perivoliotis, L., Petihakis, G., de la Villéon, L. P., Pistoia, J., Poulain, P.-M., Pouliquen, S., Prieto, L., Raimbault, P., Reglero, P., Reyes, E., Rotllan, P., Ruiz, S., Ruiz, J., Ruiz, I., Ruiz-Orejón, L. F., Salihoglu, B., Salon, S., Sammartino, S., Sánchez Arcilla, A., Sánchez-Román, A., Sannino, G., Santoleri, R., Sardá, R., Schroeder, K., Simoncelli, S., Sofianos, S., Sylaios, G., Tanhua, T., Teruzzi, A., Testor, P., Tezcan, D., Torner, M., Trotta, F., Umgiesser, G., von Schuckmann, K., Verri, G., Vilibic, I., Yucel, M., Zavatarelli, M., and Zodiatis, G.: Challenges for Sustained Observing and Forecasting Systems in the Mediterranean Sea, Front. Mar. Sci., 6, 568, https://doi.org/10.3389/fmars.2019.00568, 2019.

Velpuri, M., Das, J., and Umamahesh, N. V.: Spatio-temporal compounding of connected extreme events: Projection and hotspot identification, Environmental Research, 235, 116615, https://doi.org/10.1016/j.envres.2023.116615, 2023.

Verschuur, J., Koks, E. E., and Hall, J. W.: Ports' criticality in international trade and global supply-chains, Nat. Commun., 13, 4351, https://doi.org/10.1038/s41467-022-32070-0, 2022.

Verschuur, J., Koks, E. E., Li, S., and Hall, J. W.: Multi-hazard risk to global port infrastructure and resulting trade and logistics losses, Commun. Earth Environ., 4, 5, https://doi.org/10.1038/s43247-022-00656-7, 2023.

Wanner, H., Beck, C., Brázdil, R., Casty, C., Deutsch, M., Glaser, R., Jacobeit, J., Luterbacher, J., Pfister, C., Pohl, S., Sturm, K., Werner, P. C., and Xoplaki, E.: Dynamic and socioeconomic aspects of historical floods in Central Europe, Erdkunde, 58, 1–16, http://www.jstor.org/stable/25647628 (last access: 21 July 2025), 2004.

Wehde, H., Schuckmann, K. V., Pouliquen, S., Grouazel, A., Bartolome, T., Tintoré, J., De Alfonso Alonso-Muñoyerro, M., Carval, T., Racapé, V., and the INSTAC team: EU Copernicus Marine Service Quality Information Document for the Atlantic Iberian Biscay Irish Ocean- In-Situ Near Real Time Observations, INSITU_IBI_PHYBGCWAV_DISCRETE_MYNRT_013_033, Issue 2.4, Mercator Ocean International, https://documentation.marine.copernicus.eu/QUID/CMEMS-INS-QUID-013-030-036.pdf (last access: 17 June 2025), 2024.

Wyatt, L. R.: The Measurement of the Ocean Wave Directional Spectrum from HF Radar Doppler Spectra, Radio Science, 21, 473–485, https://doi.org/10.1029/RS021i003p00473, 1986.

Wyatt, L. R.: A Relaxation Method for Integral Inversion Applied to HF Radar Measurement of the Ocean Wave Directional Spectrum, International Journal of Remote Sensing, 11, 1481–1494, https://doi.org/10.1080/01431169008955106, 1990.

Wyatt, L. R. and Green, J. J.: Measuring High and Low Waves with HF Radar, in: Proceedings of OCEAN_EUROPE, Bremen, Germany, 11–14 May 2009, 1–5, https://doi.org/10.1109/OCEANSE.2009.5278328, 2009.

Wyatt, L. R., Liakhovetski, G., Graber, H. C., and Haus, B. K.: Factors Affecting the Accuracy of SHOWEX HD Radar Wave Measurements, J. Atmos. Ocean. Tech., 22, 847–859, https://doi.org/10.1175/JTECH1728.1, 2005.

State Planet, 7-osr10, 16, 2026
https://doi.org/10.5194/sp-7-osr10-16-2026
© Author(s) 2026. This work is distributed under
the Creative Commons Attribution 4.0 License.

Record low sea levels in the Bothnian Bay in November 2024

Laura Tuomi[1], Milla M. Johansson[1], Andrew Twelves[1], Mika Rantanen[1], Priidik Lagemaa[2], Hedi Kanarik[1], Jani Särkkä[1], Urmas Raudsepp[2], and Antti Westerlund[1]

[1]Finnish Meteorological Institute, Helsinki, Finland
[2]Department of Marine Systems, Tallinn University of Technology, Tallinn, Estonia

Correspondence: Laura Tuomi (laura.tuomi@fmi.fi)

Received: 4 August 2025 – Discussion started: 19 September 2025
Revised: 26 January 2026 – Accepted: 10 February 2026 – Published: 30 September 2026

Abstract. On 21 November 2024, there was an extreme event within the Bothnian Bay, a sub-basin of the Baltic Sea, when a record low sea level of −153 cm was measured at Kemi, at the northern end of the basin. This minimum was 34 cm lower than the previous minimum measured in 2022. We calculate that the estimated return period for this event is several thousands of years, based on the Kemi tide gauge time series from the 1970s to the day preceding the storm. When the new record low is included in the analysis, the estimated return period for this event is reduced to just 151 years. In this study we also investigate the accuracy of the Baltic Sea Monitoring and Forecasting Centre (BAL MFC) Near Real Time (NRT) physical system in predicting the storm event, and show that the accuracy of the forecast was good up to 3–4 d before the event. Longer lead-time forecasts failed to predict the record low sea level at Kemi, although they did indicate a decrease in sea level during the storm. During the 2024 event, north-easterly winds were measured at coastal weather stations with a maximum 10 min average speed of $\sim 28\,\mathrm{m\,s^{-1}}$ (with gusts of $32\,\mathrm{m\,s^{-1}}$). However, we find that the storm intensity alone likely does not explain the magnitude of the sea level extreme, with the exceptionally long duration and unusual track of the storm also playing large roles. This highlights the sensitivity of coastal risk assessment to natural variations in storm tracks, which have the potential to produce rare but high-impact events.

1 Introduction

Extreme sea level events, both high and low, affect coastal areas in several ways. High sea levels may cause flooding, coastal erosion and damage to coastal infrastructure. Low sea levels can make shallow coastal fairways inaccessible for larger vessels, leading to delays in maritime traffic and cargo transport. Sea level variations in the Baltic Sea result from two types of processes: those that change the total water volume in the semi-enclosed basin, and those that redistribute water within it (e.g. Leppäranta and Myrberg, 2009; Weisse et al., 2021). The first category includes factors such as eustatic sea level rise, post-glacial land uplift, and water exchange with the North Sea. The second involves wind forcing, atmospheric pressure variations, seiches (internal oscillations), and tides.

Extreme high and low sea levels in the Baltic Sea occur as a result of several mutually interacting factors occurring at the same time. High sea level events typically have a preconditioning of increased total water volume in the Baltic Sea (e.g. Weisse et al., 2021; Rutgersson et al., 2022). Low sea level events on the other hand are more typical when the total water volume in the Baltic Sea is close to or below the long-term mean. Extremely low sea level events also require strong or storm-force winds pushing water away from the coast, together with an atmospheric pressure gradient resulting in a suitably oriented sea level gradient along the basin. Such extremes can be further amplified by a seiche oscillation or tidal variation occurring in a suitable phase; seiche is the dominant of these two components due to the small amplitude of tidal variation in the Baltic Sea, which is less than 5 cm in the Gulf of Bothnia (Medvedev et al., 2013).

Published by Copernicus Publications.

Table 1. Copernicus Marine Service and other products used in this study, including information on data documentation.

Product ref. no.	Product ID and type	Data access	Documentation
1.	BALTICSEA_ANALYSISFORECAST_PHY_003_006 (BAL MFC NRT); numerical models	EU Copernicus Marine Service Product (2024a)	Quality Information Document (QUID): Jandt-Scheelke et al. (2024) Product User Manual (PUM): Lindenthal et al. (2024)
2.	INSITU_BAL_PHYBGCWAV_DISCRETE_MYNRT_013_032; in-situ observations	EU Copernicus Marine Service Product (2024b)	QUID: Wehde et al. (2024) PUM: In Situ TAC partners (2024)
3.	Finnish tide gauge measurements with 1 min resolution; in-situ observations; data producer: Finnish Meteorological Institute (FMI)	FMI (2026)	List of FMI observation stations: https://en.ilmatieteenlaitos.fi/observation-stations (last access: 9 March 2026) description of the observations: https://en.ilmatieteenlaitos.fi/mareograph (last access: 19 January 2026)
4.	Swedish tide gauge measurements with 1 min resolution; in-situ observations; data producers: Swedish Meteorological and Hydrological Institute (SMHI) and Swedish Maritime Administration	SMHI (2025)	List and description of Swedish sea level observations: https://www.smhi.se/data/hav-och-havsmiljo/havsvattenstand/sealevelrh2000 (last access: 19 January 2026, in Swedish)
5.	BALTICSEA_ANALYSISFORECAST_PHY_003_006 (BAL MFC NRT forecast); numerical models	available upon request	PUM: Lindenthal et al. (2024)
6.	Automatic Weather Station (AWS) data with 10 min averages; in-situ observations; data producer: FMI	FMI (2026)	List of FMI observation station: https://en.ilmatieteenlaitos.fi/observation-stations Description of the observation network: https://en.ilmatieteenlaitos.fi/weather-observations (last access: 19 January 2026)
7.	ERA5 gridded reanalysis (0.25° × 0.25°); numerical models	Hersbach et al. (2023)	Product description: Hersbach et al. (2020) Accuracy of ERA5 surface winds within the Baltic Sea: Laurila et al. (2025)

Accurate prediction of low sea level events is extremely important for ensuring safe and efficient maritime traffic. Short-term forecasts (ranging from a few hours to a few days) support the real-time manoeuvring of vessels entering or leaving harbours, while mid-range forecasts (up to 10 d) can assist in planning cargo loads, allowing ships to access ports safely and on schedule. Sea level forecasts for the Baltic Sea are provided both by the Copernicus Marine Service Baltic Monitoring and Forecasting Centre (BAL MFC) and by national weather and oceanographic centres in the region. The BAL MFC physical Near Real Time (NRT, product ref. no. 1, Table 1) system is based on a setup of the Nucleus for European Modelling of the Ocean (NEMO; Madec and the NEMO System Team, 2023) for the North and Baltic Seas (Kärnä et al., 2021). It is generally able to reproduce sea surface height (SSH) with good accuracy (Jandt-Scheelke et al., 2024).

National sea level forecasting systems vary, from simple 2D systems through to complex 3D model systems. For instance, both the Finnish Meteorological Institute (FMI) and the Swedish Meteorological and Hydrological Institute (SMHI) operate national sea level forecasting systems built on NEMO-based modelling configurations, with many attributes (such as the resolution) resembling the BAL MFC system. However, customisations have been made so that national forecasts better serve the specific needs of their users. For example, FMI has tuned its own system to focus on results for the northern Baltic Sea, and runs its own water level forecast four times a day, in contrast to the twice-daily BAL MFC system. In addition, FMI uses a separate lightweight 2D water level ensemble that is run twice a day to supplement the information provided by the NEMO-based system. These sea level forecasts are used to support national weather warning systems that provide information on potentially dangerous weather phenomena. Cooperation within the Baltic Sea Operational Oceanographic System (BOOS, http://www.boos.org, last access: 9 March 2026) has also lead to a community prod-

uct that combines the existing SSH forecasts to produce a Multi-Model Ensemble (MME, https://www.boos.org/multi-model-ensemble-of-forecast-products/, last access: 9 March 2026), offering a best estimate based on the weighted average of the forecasts, where each weighting is a function of the forecast accuracy over preceding days. A general description of the MME system can be found in Golbeck et al. (2015).

In this paper, we investigate the extremely low sea level event that occurred in the northernmost sub-basin of the Baltic Sea, the Bay of Bothnia, on 21 November 2024. A record low sea level of −153 cm (in relation to the N2000 height reference system) was measured at Kemi (Fig. 1), at the northern end of the bay. This minimum was 34 cm lower than the previous record set in 2022. During the event, northeasterly winds were measured with a maximum 10 min average speed $\sim 28\,\mathrm{m\,s^{-1}}$, with gusts of $32\,\mathrm{m\,s^{-1}}$, at Kalajoki Ulkokalla station. In addition, waves were high in the Bothnian Bay, with a significant wave height of 5 m measured in the central parts of the basin by FMI's operational wave buoy. This low sea level event led to disturbances to maritime traffic in the northern part of the Bothnian Bay. For example, ferry traffic from the mainland to Hailuoto island was halted for 18 h on 21 November. According to media reports, this was only the third time in the 56-year history of the Hailuoto ferry route that the ferry was out of use due to the sea level being too low (https://yle.fi/a/74-20126375, last access: 9 March 2026, in Finnish).

Here we study the meteorological and oceanographic conditions that led to this extreme low sea level event at the northern end of the Bay of Bothnia. We assess how well the present BAL MFC NRT system was able to predict it in advance, and use the extensive sea level time series from Kemi to evaluate the return period of the event.

2 Data

We use tide gauge data from FMI, SMHI and Tallinn University of Technology (Taltech) stations in the Bothnian Bay and Gulf of Finland to study sea level variation during the event (product ref. no. 2, Table 1, locations shown in Fig. 1a). For the time of the storm we use additional data, with higher temporal resolution, from some of the Finnish (product ref. no. 3, Table 1) and Swedish (product ref. no. 4, Table 1) tide gauges. The tide gauge data are given in relation to the height systems N2000, RH2000, and EH2000, which are the national realisations of the common European height system EVRS. Of the FMI stations we consider Kemi (65°40′24″ N, 24°30′54″È), Raahe/Brahestad (64°39′59″ N, 24°24′25″ E), Pietarsaari/Jakobstad (63°42′31″ N, 22°41′22″ E), Helsinki (60°9′13″ N, 24°57′22″ E), and Hamina (60°33′46″ N, 27°10′45″ E). Of the SMHI stations we consider Furuögrund (64°54′57″ N, 21°13′50″ E) and Kalix Storön (65°41′ 49″ N, 23°5′46″ E); of the TalTech stations we consider Narva (59°27′47″ N, 28°2′45″ E) and Tallinn (59°26′58″ N, 24°46′ 32″ E).

To study the accuracy of the BAL MFC sea level forecast in predicting the extreme event, we use model outputs from the NRT physical system (product ref. no. 1 and no. 5, Table 1). This system is built on numerical simulations with the Nucleus for European Modelling of the Ocean (NEMO; Madec and the NEMO System Team, 2023), run on a 1 nautical mile resolution grid covering the North Sea as well as the Baltic Sea, with assimilation from multiple data sources (sea level not included). Extensive description and validation of an earlier version of the Baltic Sea domain (NEMO-Nordic) was provided by Kärnä et al. (2021); the updated version used here includes an upgrade of the NEMO code from version 4.0 to 4.2.1 and is archived at https://doi.org/10.5281/zenodo.14507734 (Swedish Meteorological and Hydrological Institute et al., 2024). In this study we use only the sea surface height from the NRT system, and compare forecasts starting every 12 h, up to a forecast lead-time of 6 d. As meteorological forcing, the model uses forecasts from the Meteorological Cooperation on Operational Numerical Weather Prediction (MetCoOp; Müller et al., 2017) for the first 66 h, and thereafter forecasts from the European Centre for Medium-Range Weather Forecasts (ECMWF, 2024) for the remaining days. The NRT system has been shown to successfully reproduce sea level at Kemi over a validation period from November 2020 to October 2022, with a bias of −1 cm relative to the tide gauge data, and a centred Root Mean Square Deviation (cRMSD) of 7 cm (Jandt-Scheelke et al., 2024).

We use wind data from automatic weather stations (AWS, product ref. no. 6, Table 1) together with ERA5 reanalysis (product ref. no. 7, Table 1) to evaluate the prevailing weather conditions during the storm. We present 10 min average wind speed and direction measured at 1 h intervals at Kalajoki Ulkokalla AWS (64°19′51″ N, 23°26′47″ E) in the Bothnian Bay and at Porvoo Kalbådagrund AWS (59°59′8″ N, 25°35′56″ E) in the Gulf of Finland (locations also in Fig. 1b). At Ulkokalla AWS, wind measurements are made at an elevation of 17 m above sea level on the treeless Ulkokalla islet, with the nearest mainland approximately 18 km to the southeast. At this station, wind measurements are slightly affected to the north by a building approximately 8 m high, located 30 m from the wind sensor (sector 340–20°), and to the north-northwest (330°) by a lighthouse about 12 m high, situated 40 m from the sensor. At Kalbådagrund AWS, wind measurements are made at an elevation of 32 m above the sea level, approximately 30 km south of the mainland. The observation instruments are located in a lighthouse tower, with the wind meter positioned southwest of the lighthouse helipad. ERA5 reanalysis data is used to support the analysis of the synoptic evolution and the track of the windstorm responsible for the sea level event. From ERA5, we use 10 m wind speed, wind gust, and mean sea level pressure at 3 h intervals, and download the data on a

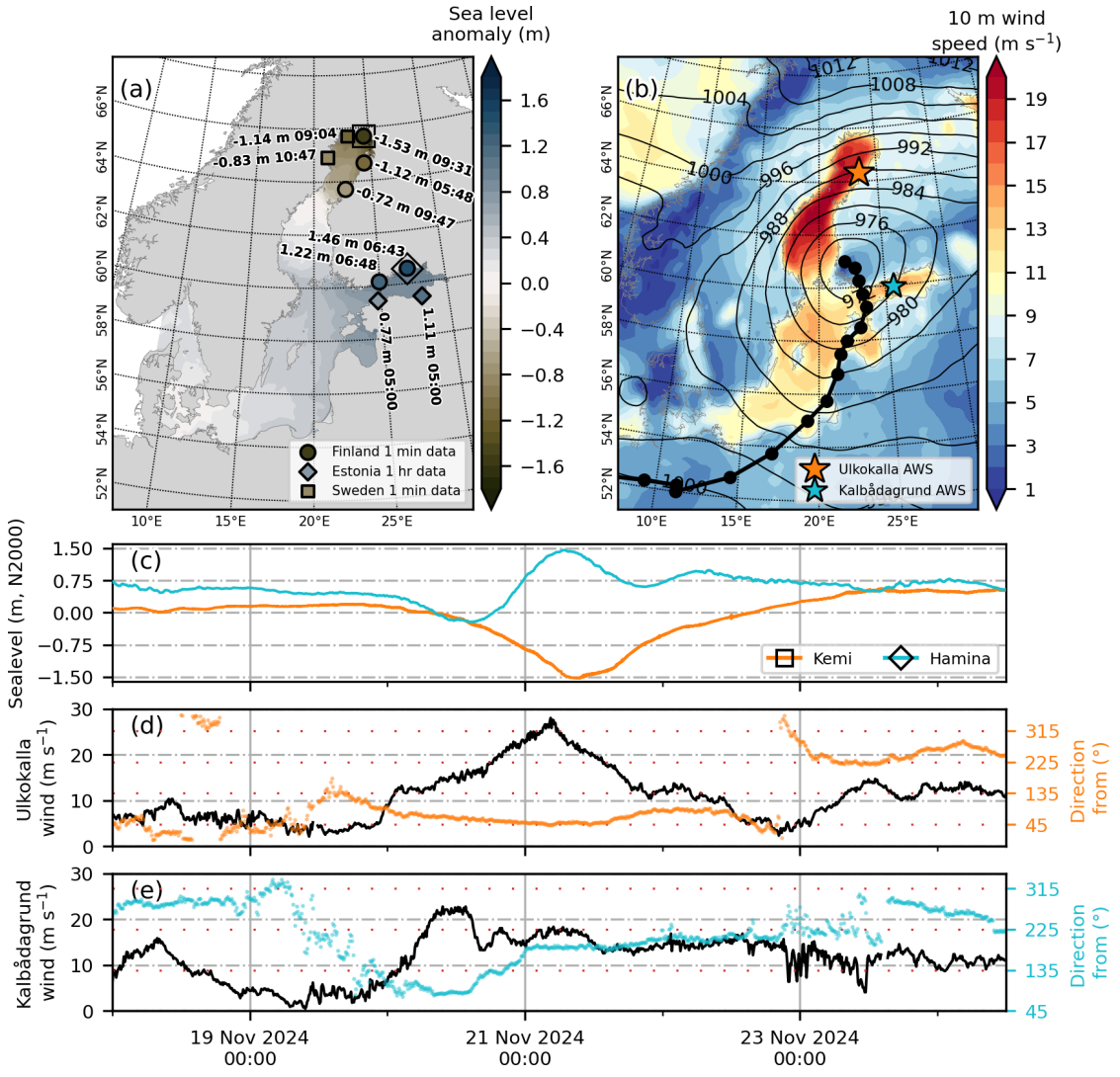


Figure 1. **(a)** NEMO modelled sea level (shading) from the BAL-MFC NRT system, at 09:30 UTC on 21 November 2024, shown relative to the mean dynamic topography; overlaid with tide gauge data (from Finnish, Estonian or Swedish measurements as indicated on legend). Beginning at the westernmost station and following the coastline clockwise, the stations shown are Furuögrund, Kalix, Kemi, Raahe/Brahestad, Pietarsaari/Jakobstad, Helsinki, Hamina, Narva and Tallinn. Minimum measured sea levels on 21 November 2024 are shown in the Bothnian Bay, and maximum sea levels on 21 November 2024 are shown in the Gulf of Finland; in both cases the timing of the minimum/maximum is displayed next to the measured sea level values in the RH2000/N2000/EH2000 reference system. Panel **(b)** shows 10 m wind speed (shading) and mean sea level pressure (contours) from the ERA5 reanalysis at 21 November 2024 06:00 UTC. The track of the storm from 06:00 UTC on 19 November 2024 to 06:00 UTC on 21 November 2024 is shown with the black line, with the location of the centre marked every 3 h by a dot. Panel **(c)** shows a time series of observed sea levels from Kemi and Hamina (corresponding locations are marked with a square outline and a diamond outline respectively in panel **a**). Sea level values are shown in the N2000 height system with simultaneous wind measurements from Ulkokalla **(d)** and Kalbådagrund **(e)** AWS stations, locations marked in panel **(b)**.

$0.25° \times 0.25°$ resolution grid from the Copernicus Climate Data Store (https://cds.climate.copernicus.eu/, last access: 28 April 2025).

3 Results

3.1 Observed sea levels in the Bothnian Bay and the Gulf of Finland

The extreme low sea level event occurred in the northernmost part of the Bothnian Bay on 21 November 2024, when sea ice in the bay was minimal. The primary cause of the event was a deepening low-pressure system that arrived in Finland from

the southwest (SW) a day earlier, on 20 November 2024. While SW is one of the most common arrival directions for windstorms in Finland, such storms typically follow a more zonal (west-to-east) track and pass quickly over the country (Láng-Ritter et al., 2025). In this case, however, the windstorm followed an unusual track. The storm formed early on 19 November 2024 over Northwest Europe. After crossing northern Germany, it started to deepen and turned northward along the eastern coast of the Baltic Sea (Fig. 1b). The windstorm reached its lowest central pressure of 967 hPa (as per ERA5 reanalysis) on the next day, at 21:00 UTC 20 November 2024, when the centre of the storm made landfall on the Finnish coast.

Although the central pressure of the storm began to gradually rise on 21 November 2024, the storm itself remained nearly stationary over SW-Finland (Fig. 1b). Due to the slow movement and the orientation of the track, a prolonged and strong northeasterly wind prevailed over the Gulf of Bothnia. This effectively pushed seawater south-westward, resulting in an extremely low sea level of −153 cm at Kemi (Fig. 1). The measured minimum was 34 cm lower than the previous minimum measured in 2022. Other tide gauge stations in the northern end of the Bothnian Bay also showed low values (Fig. 1a), but Kemi was the only one of the stations with long-term measurements where a record for low sea level was measured. Measured mean sea levels at Föglö tide gauge, located in the Archipelago Sea (60°01′55″ N, 20°23′05″ E), have been shown to reliably represent the water volume of the Baltic Sea (e.g. Johansson and Kahma, 2016). During the week preceding the minimum event at Kemi on 21 November 2024, the mean sea level at Föglö was 24 cm (N2000). In the previous two extremely low sea level events at the Kemi tide gauge, −116 cm on 14 January 2016 and −119 cm on 13 December 2022, the respective weekly mean sea levels at Föglö tide gauge were 0 and −10 cm. This emphasises the strength of the 2024 event.

Concurrent with the low sea level event in the Bothnian Bay, the sea level rose moderately high in the eastern end of the Gulf of Finland. The sea level at Hamina reached +146 cm (still considerably less than the measured maximum of +213 cm). The low sea levels in the Bothnian Bay and the relatively high level in the eastern Gulf of Finland resulted in a record for the largest difference measured between the Kemi and Hamina tide gauges, reaching 294 cm (−152 cm at Kemi and +142 cm at Hamina) at 10:03 UTC on 21 November 2024. The high sea levels in Hamina were preceded by a situation where easterly winds were blowing in the Gulf of Finland, leading to a decreasing sea level, with a minimum value of −22 cm on the preceding day (20 November). This in turn induced a seiche, with a typical period of ∼ 27 h, in the Gulf of Finland. The eastwards return flow associated with this seiche, together with the winds shifting to blow from the SW in the Gulf of Finland after the centre of the storm had passed, induced the high sea level in the eastern part of the Gulf of Finland.

3.2 Forecast

We use sea level from the BAL MFC NRT physical product to assess the NRT system skill in forecasting this event. For the purposes of our analysis we extract the model output at the closest point to the tide gauge. We make the bias correction for the model output by first calculating the mean sea level in the tide gauge observations over the month of November; then calculating the mean sea level in the NRT system by averaging across the first 12 h in each of the November forecasts. We subtract the model mean from the observed mean to obtain the model bias and subtract this from the full time series in each forecast before proceeding with our analysis. Thus we correct each forecast based on the accuracy of forecasts both before and after; in practice, forecasting centres must make corrections based only on the accuracy of preceding forecasts. The exact protocol for this differs between different forecasting centres, and end users of the NRT product may also apply their own bias correction method. For this study, our main interest is in the impact of forecast lead-time on forecast accuracy, not on impacts from the choice of bias correction method.

In Fig. 2 we consider the time series from four of these forecasts in particular: those initialised at 12:00 UTC on 17, 18, 19 and 20 November. These four forecast runs correspond to forecast lead-times of 84–96, 60–72, 36–48, and 12–24 h respectively. We also show the model anomaly difference in forecasting the extreme sea levels on the morning of 21 November, as a function of each forecast lead-time from 0–12 to 132–144 h inclusive.

At Kemi (Fig. 2a–b), the 0–12 h forecast underestimates the sea level minimum, and thus overestimates the magnitude of the extreme, by approximately 19 cm. The forecasts at 12–24 and at 24–36 h also overestimate the peak, but by only 5 and 1 cm respectively. At forecast lead-times beyond 36 h, the model underestimates the peak, though only by 2 cm in the 36–48 h forecast. The forecasts at 48–60 and 60–72 h both underestimate the peak by approximately 19 cm; however the 72–84 h forecast shows a sharp improvement in forecast skill, only underestimating the peak by 2 cm. The accurate prediction of extreme sea level events in the Baltic Sea is very sensitive to the accuracy of the NWP systems in capturing the storm track. More information about the forecast accuracy of these NWP systems can be found in Haiden et al. (2024).

The NRT system generally performs worse in forecasting the maximum at Hamina (Fig. 2c–d) than the minimum at Kemi. The best forecast is that at lead-time 0–12 h, which underestimates the maximum by approximately 19 cm; all forecasts with longer lead-times perform worse. Again, the decrease in model skill is not monotonic, with the 72–84 h forecast substantially outperforming the forecast at 60–72 h. In all cases the forecast error takes the form of an underestimate of peak sea level.

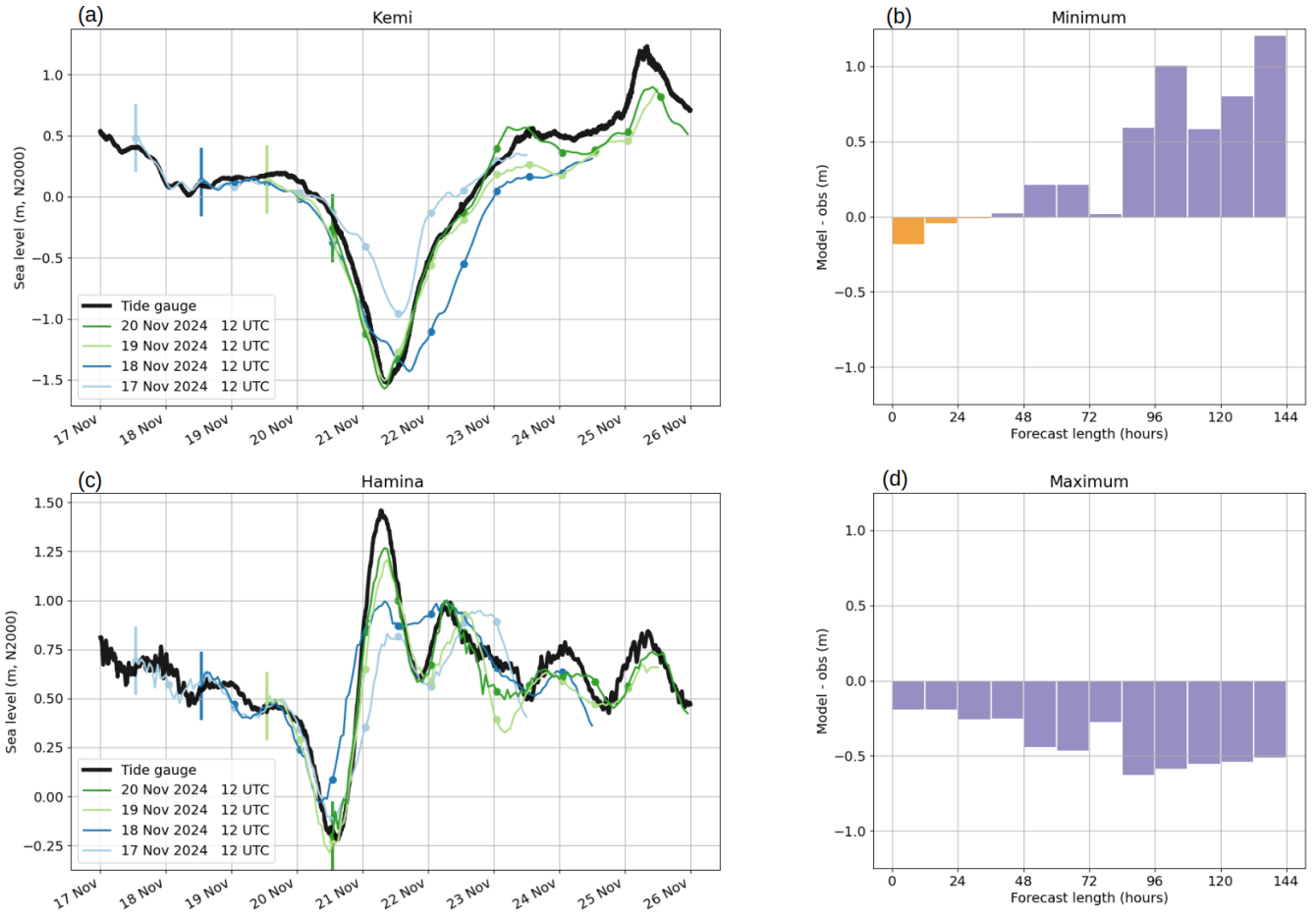


Figure 2. Analysis of BAL MFC NRT forecast skill at Kemi **(a, b)** and at Hamina **(c, d)** during the November 2024 storm. In panels **(a)** and **(c)**, the dark green, pale green, dark blue and pale blue lines show outputs from forecasts starting at noon on 20, 19, 18 and 17 November respectively; these correspond to the 12–24, 36–48, 60–72 and 84–96 h lead-time forecasts assessed at the time of the extreme sea levels. The first value in each forecast is indicated with a vertical line; each of the subsequent dots marks the end of a 12 h period. The thick black lines in panels **(a)** and **(c)** show the time series of observations from each tide gauge. In panels **(b)** and **(d)** we show the difference between each forecast and the tide gauge observations in the sea level minimum (**b**, Kemi) and the sea level maximum (**d**, Hamina) as a function of forecast lead-time, including all forecasts from the shortest (0–12 h) to the longest (132–144 h). Purple shading indicates that the model has underestimated the magnitude of the sea level extreme, orange shading indicates that the model has overestimated the magnitude of the sea level extreme.

3.3 Return periods

Return periods of sea levels are typically used to evaluate the probabilities of extreme events for coastal areas. Such estimates are valuable for coastal planning, for example to account for extreme high sea level events that would cause flooding. On the Finnish coast, return periods for high sea levels have been estimated by e.g. Räty et al. (2023) and Pellikka et al. (2018). Information on return periods for extreme low sea levels is harder to find, though such information would be valuable for planning of fairways, harbours etc. in shallow coastal areas – especially in areas where land uplift still dominates over eustatic sea level rise.

To estimate the return period for this storm-driven event in Kemi, we use observed annual sea level minima from the Kemi tide gauge for the period of 1977–2024. There do exist measurements from a longer period from the Kemi area, but we discount those prior to 1977, when the location of the tide gauge was moved from its original site inside the harbour; due to land uplift (among other reasons), this location was no longer able to properly measure the sea level variation.

To exclude the effect of the long-term mean sea level trend, we detrend the data by removing the 1977–2024 trend of annual mean sea levels from the annual minima measured in the N2000 height system. We fit Generalized Extreme Value (GEV) distributions to the detrended annual minima; first including the 2024 record value on the fit, then excluding it (Fig. 3). We estimate the 95 % confidence intervals using a nonparametric bootstrap approach with 1000 resamples. There is a substantial difference in the estimated re-

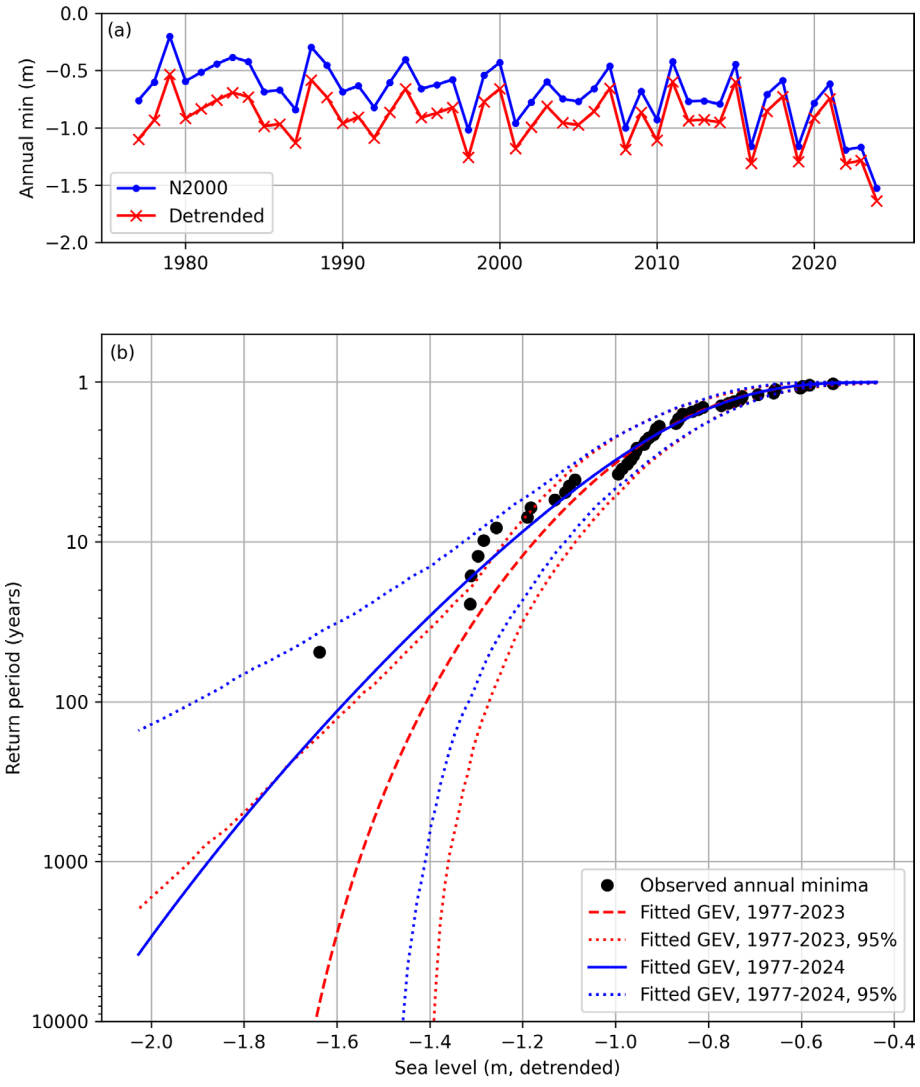


Figure 3. **(a)** Time series of Kemi observed annual minima 1977–2024 in the N2000 height system, and detrended by removing the trend of annual mean sea levels in 1977–2024, to exclude the effect of long-term mean sea level change. In panel **(b)**, cumulative probability distribution of the detrended annual minima is shown. Generalized Extreme Value (GEV) distributions were fitted to the values with the 2024 record value included in the fit (solid blue line), and without the 2024 value (dashed red line). The 95 % confidence intervals (dotted lines) are based on 1000 nonparametric bootstrap samples.

turn period of the record-low Kemi minimum (−164 cm in the detrended data set) depending on whether the record-low value is included in the fit or not. If it is included, the estimated return period is 151 years, with the lower bound of the 95 % confidence interval at 38 years (Fig. 3). However, when the event is excluded, and the analysis is based only on annual minima from 1977–2023, the estimated return period increases to 7700 years, with the lower bound of the 95 % confidence interval at 140 years.

4 Discussion and Summary

The long-term mean sea level in relation to the RH2000/N2000 height systems is decreasing in the Bothnian Bay, since land uplift is stronger than the eustatic mean sea level rise. Thus, extreme lows in sea level tend to get lower with time, even if the short-term variability and weather conditions remain unchanged. When analysing whether a given sea level event is in fact a “record low”, it is thus customary to refer the values to a time-changing long-term mean sea level estimate instead of RH2000/N2000. In Finland and Sweden, slightly different definitions for such mean sea level estimate (MSL) are used.

During the extreme low sea level event that took place on 21 November 2024 within the Bothnian Bay, Kemi tide gauge was the only long-term sea level station in the region that measured a record low value relative to MSL. However several other sea level stations in the Bothnian Bay did measure values close to their earlier record low values. At the Finnish tide gauge Oulu (located at 65°02′25″ N, 25°25′06″ E), between the Kemi and Raahe tide gauges, recording of the sea level stopped at 05:48 UTC, more than 3 h before the lowest value was reached at Kemi (09:31 UTC). This was due to the float in the tide gauge hitting the well bottom. The record value at Oulu is −131 cm with respect to MSL, measured on 19 January 1929. The observed decline in relative mean sea level during the past 100 years at Oulu has been 63 cm (Pellikka et al., 2023), as a result of land uplift after the last glaciation period, partially counteracted by eustatic mean sea level rise. Therefore, the record value of −131 cm in 1929 corresponds to about −70 cm in the present mean sea level at Oulu. This illustrates the fact that the Oulu tide gauge has now become so "elevated" compared to the mean sea level that it is unable to capture the lowest extremes. At Kalix Storön the sea level was 4 cm lower (relative to MSL) during the record low sea level event on 19 January 1998 compared to the value measured during the November 2024 event. There is also a newer tide gauge station, located north of Kalix Storön and operated by the Swedish Maritime Administration (Kalix-Kalrsborg Sjöv, 65°47′21″ N, 23°18′02″ E), where the measured sea level on 21 November 2024 was lower than at Kalix Storön. This lowest measured value was −126 cm in RH2000. However, the time series from this station only extends back to 2009, so here it is not possible to compare the November 2024 event to values measured in 1998. It is important to note that the north-easterly wind direction during the November 2024 event provided more optimal conditions to reach record low values on the Finnish side of the gulf than on the Swedish side.

Two significant factors behind the record value were the unusual track of the windstorm and its intensity. To get preliminary information about the severity of the storm, we analyse maximum daily wind gusts during the extended winter season (October–March, ONDJFM) from 1950/1951 to 2024/2025 using ERA5 reanalysis data. The maximum gust of 34.2 m s^{-1}, occurring on 21 November 2024, was the highest value observed in the Bothnian Bay (marine areas north of 63° N) during this 75-year period. It is important to note, however, that this preliminary analysis does not fully capture the exceptional nature of the windstorm. The extremely low sea levels result not only from peak wind speeds but also from the duration and direction of the wind, in particular the prolonged northeasterly flow in this region. A more comprehensive analysis of the characteristics of the windstorm is beyond the scope of this paper and is left for future work.

At the time of the extreme low sea level event, the ice season had started in the Bothnian Bay, but ice cover was restricted to thin new ice in some coastal areas. Consequently, the event was not substantially influenced by the damping effect of sea ice. More information about the Baltic sea ice season 2024/2025 can be found at https://en.ilmatieteenlaitos.fi/ice-winter-2024-2025 (last access: 22 January 2026).

The accuracy of weather forecasts, and consequently oceanographic forecasts, generally decreases as the forecast lead-time increases. This particularly affects the prediction of extreme sea level events in the Baltic Sea, which are highly dependent on accurate forecasting of low-pressure system tracks over the sea area. The quality of the sea level forecast is assessed daily within the BAL MFC, and daily near-real-time validation is presented in the Product Quality Dashboard (https://pqd.mercator-ocean.fr/, last access: 9 March 2026). This shows that the overall cRMSD of the sea level analysis is generally below 5 cm, while the cRMSD of the sea level forecast increases by approximately 1 cm per forecast day. However forecast errors can be significantly larger than the overall cRMSD during extreme events.

The accuracy of the NEMO-Nordic system in reproducing the observed sea level variations can be estimated from the best-estimate short-range forecasts, in which the weather forecast is assumed to be of the highest reliability. Kärnä et al. (2021) found that the best-estimate SSH from NEMO-Nordic tends to overestimate the magnitude (i.e. give a negative elevation anomaly relative to observations) for extreme low sea levels in the Bothnian Bay and underestimate the magnitude of extreme high sea levels in the Gulf of Finland. Our analysis shows the same pattern in the 12 h forecasts, with the magnitude of the record minimum at Kemi overestimated and the maximum at Hamina underestimated compared to observations. At Kemi this overestimation remains (but is reduced in magnitude) in the 24 and 36 h forecasts, beyond which the minimum is instead underestimated. However, for all forecast lead-times below 84 h, even this underestimated sea level extreme is beyond the previous record.

The worsening of the quality in the forecasts with lead times of 48–60 and 60–72 h compared to both shorter (< 44 h) and longer (> 72 h) forecast lead-times may be due to the shift of meteorological forcing from MetCoOp to ECMWF 66 h into the forecast. The discrepancies between the forecasts at 66 h lead-times have the potential to cause discontinuities in the description of meteorological conditions. Depending on the scale of the differences, it may take several hours for the forecast system to adapt to this change. Similar deterioration of forecast quality around forecast lead-times of 60–72 h has also been reported in the BAL MFC wave forecasts (Aguiar et al., 2024).

The requirements for forecast accuracy may vary depending on the use case. Weather centres typically issue warnings for potentially dangerous weather phenomena based on predefined thresholds. If the forecasting system can provide information with sufficient accuracy for the warning process,

small deviations may not have a significant impact. For example, FMI issues warnings for both high and low sea levels along the Finnish coast. The threshold level for low sea level warning is based on the low sea level that has a return period of one year, calculated from the sea level statistics of the nearest tide gauge. The warning levels change yearly to account for land uplift and mean sea level rise. For Kemi, the low sea level warning level was −72 cm in 2024. Using our bias-correction method, all forecasts with lead times less than 96 h predict a sea level minimum below this threshold on the morning of the 21 November 2024. This suggests that early warnings could be given up to 4 d before the event, though the triggering of such an early warning system is dependent on the method chosen for bias correction.

There is large uncertainty associated with long return periods. Due to the relatively short measurement time series, they can be low-or high-biased depending on whether extreme events have occurred during the measurement period. The corresponding uncertainty in the return period of the November 2024 event at Kemi is large. When the 2024 record-low sea level event is included in our analysis, the estimated return period at Kemi is 151 years (lower bound 38 years). However, when the event is excluded, the return period estimate increases to 7700 years (lower bound 140 years). This emphasises the importance of considering confidence intervals when using the return periods of low probability events to inform coastal or near-shore planning and construction. The estimation of future low extremes is further complicated by the projected decrease of mean sea level in the Bothnian Bay (Pellikka et al., 2023), where the land uplift rate will likely exceed mean sea level rise throughout this century. A decreasing mean sea level implies an increase in the likelihood of low sea level events even more extreme than the one that occurred in November 2024. Pellikka et al. (2018) have studied the probabilities of extremely high sea level events in the future climate by combining mean sea level scenarios and observation-based probabilities of extremes, but corresponding studies for low sea level extremes on the Finnish coast have not been conducted thus far. Such studies may prove valuable, for instance in the planning of fairways and harbours that ensures safety of maritime traffic and smooth transport of goods in this region into the future.

Data availability. Copernicus Marine products (product ref. no. 1 and 2, Table 1) are openly available through https://marine.copernicus.eu/ (last access: 10 February 2025) and the whole forecast length of the BAL MFC NRT forecast (product ref. no. 5) is available upon request from the authors or upon request via the Copernicus Marine website. Finnish wind (product ref. no. 6) and minute sea level data (product ref. no. 3) are publicly available from the FMI open data portal (https://en.ilmatieteenlaitos.fi/open-data, last access: 19 January 2026). Swedish 1 min sea level observations (product ref. no. 4) are available through SMHI's open data portal (https://www.smhi.se/data, last access: 17 February 2025). The ERA5 reanalysis (product ref. no. 6) is openly available through the Climate Data Store (https://cds.climate.copernicus.eu/, last access: 28 April 2025).

Author contributions. The study was initiated and overseen by LT, with support from HK. The analysis and the description of the storm event was performed by MJ, AT, MR and JS, the forecasting capability of the NRT model was analysed by PL and AT, and return periods were calculated and analysed by MJ. The original version of the manuscript was prepared and revised by all authors.

Competing interests. The contact author has declared that none of the authors has any competing interests.

Disclaimer. The Copernicus Marine Service offering is regularly updated to ensure it remains at the forefront of user requirements. In this process, some products may undergo replacement or renaming, leading to the removal of certain product IDs from the catalogue. If readers have any questions or require assistance regarding these modifications, please feel free to reach out to the Copernicus Marine Service user support team for further guidance. They will be able to provide the necessary information to address concerns and find suitable alternatives.

Publisher's note: Copernicus Publications remains neutral with regard to jurisdictional claims made in the text, published maps, institutional affiliations, or any other geographical representation in this paper. The authors bear the ultimate responsibility for providing appropriate place names. Views expressed in the text are those of the authors and do not necessarily reflect the views of the publisher.

Financial support. This research has been supported by the European Union through the Copernicus Marine Service Programme.

Review statement. This paper was edited by Johannes Karstensen and reviewed by two anonymous referees.

References

Aguiar, D., Kanarik, H., Tuomi, L., and Jokiniemi, A.: Evaluating accuracy of Baltic Sea wave forecasts, Geophysica, 59, 3–19, https://www.geophysica.fi/pdf/geophysica_2024_59_1_003_aguiar.pdf (last access: 9 March 2026), 2024.

ECMWF: IFS documentation, CY49R1, Part V: Ensemble Prediction System, IFS Documentation CY49R1, ECMWF, https://doi.org/10.21957/956d60ad81, 2024.

EU Copernicus Marine Service Product: Baltic Sea Physics Analysis and Forecast, Mercator Ocean International [data set], https://doi.org/10.48670/moi-00010, 2024a.

EU Copernicus Marine Service Product: Baltic Sea – In Situ Near Real Time Observations, Mercator Ocean International [data set], https://doi.org/10.48670/moi-00032, 2024b.

FMI: Weather and Sea level Real-time observations, FMI's Open data service [data set], https://en.ilmatieteenlaitos.fi/download-observations (last access: 9 March 2026), 2026.

Golbeck, I., Li, X., Janssen, F., Brüning, T., Nielsen, J. W., Huess, V., Söderkvist, J., Büchmann, B., Siiriä, S. M., Vähä-Piikkiö, O., and Hackett, B.: Uncertainty estimation for operational ocean forecast products – a multi-model ensemble for the North Sea and the Baltic Sea, Ocean Dynam., 65, 1603–1631, https://doi.org/10.1007/s10236-015-0897-8, 2015.

Haiden, T., Janousek, M., Vitart, F., Tanguy, M., Prates, F., and Chevalier, M.: Evaluation of ECMWF forecasts, ECMWF Technical Memoranda, 918, ECMWF, https://doi.org/10.21957/52f2f31351, 2024.

Hersbach, H., Bell, B., Berrisford, P., Hirahara, S., Horányi, A., Muñoz-Sabater, J., Nicolas, J., Peubey, C., Radu, R., Schepers, D., Simmons, A., Soci, C., Abdalla, S., Abellan, X., Balsamo, G., Bechtold, P., Biavati, G., Bidlot, J., Bonavita, M., De Chiara, G., Dahlgren, P., Dee, D.,Diamantakis, M., Dragani, R., Flemming, J., Forbes, R., Fuentes, M., Geer, A., Haimberger, L., Healy, S., Hogan, R. J., Hólm, E., Janisková, M., Keeley, S., Laloyaux, P., Lopez, P., Lupu, C., Radnoti, G., de Rosnay, P., Rozum, I., Vamborg, F., Villaume, S., and Thépaut, J. N.: The ERA5 global reanalysis, Q. J. R. Meteorol. Soc., 146, 1999–2049, https://doi.org/10.1002/qj.3803, 2020.

Hersbach, H., Bell, B., Berrisford, P., Biavati, G., Horányi, A., Muñoz Sabater, J., Nicolas, J., Peubey, C., Radu, R., Rozum, I., Schepers, D., Simmons, A., Soci, C., Dee, D., and Thépaut, J.-N.: ERA5 monthly averaged data on single levels from 1940 to present, Copernicus Climate Change Service (C3S) Climate Data Store (CDS) [data set], https://doi.org/10.24381/cds.f17050d7, 2023.

In Situ TAC partners: EU Copernicus Marine Service Product User Manual for the Baltic Sea- In Situ Near Real Time Observations In situ products, INSITU_BAL_PHYBGCWAV_DISCRETE_MYNRT_013_032, Issue 2.2, Mercator Ocean International, https://documentation.marine.copernicus.eu/PUM/CMEMS-INS-PUM-013-030-036.pdf (last access: 15 May 2025), 2024.

Jandt-Scheelke, S., Panteleit, T., Verjovkina, S., Lagemaa, P., Spruch, L., and Morrison, H.: EU Copernicus Marine Service Quality Information Document for the Baltic Sea Physics Analysis and Forecast, BALTICSEA_ANALYSISFORECAST_PHY_003_006, Issue 8.0, Mercator Ocean International, https://documentation.marine.copernicus.eu/QUID/CMEMS-BAL-QUID-003-006.pdf (last access: 6 February 2025), 2024.

Johansson, M. M. and Kahma, K. K.: On the statistical relationship between the geostrophic wind and sea level variations in the Baltic Sea, Boreal Env. Res., 21, 25–43, 2016.

Kärnä, T., Ljungemyr, P., Falahat, S., Ringgaard, I., Axell, L., Korabel, V., Murawski, J., Maljutenko, I., Lindenthal, A., Jandt-Scheelke, S., Verjovkina, S., Lorkowski, I., Lagemaa, P., She, J., Tuomi, L., Nord, A., and Huess, V.: Nemo-Nordic 2.0: operational marine forecast model for the Baltic Sea, Geosci. Model Dev., 14, 5731–5749, https://doi.org/10.5194/gmd-14-5731-2021, 2021.

Láng-Ritter, I., Laurila, T. K., Mäkelä, A., Gregow, H., and Sinclair, V. A.: Classifying extratropical cyclones and their impact on Finland's electricity grid: insights from 92 damaging windstorms, Nat. Hazards Earth Syst. Sci., 25, 1697–1717, https://doi.org/10.5194/nhess-25-1697-2025, 2025.

Laurila, T. K., Laapas, M., Olsson, T., and Jylhä, K.: Wind speeds and gusts in Finland: a comparison of observations and ERA5 reanalysis, Boreal Env. Res., 30, 181–193, https://doi.org/10.60910/ber2025.q6kf-qp39, 2025.

Leppäranta, M. and Myrberg, K.: Physical oceanography of the Baltic Sea, Springer-Praxis books in geophysical sciences, Springer/Praxis Pub., Berlin, Chichester, UK, ISBN 978-3-540-79702-9, 2009.

Lindenthal, A., Nord, A., Ljungemyr, P., Fyrstedt, S., and Huess, V.: EU Copernicus Marine Service Product User for the Baltic Sea Physics Analysis and Forecast, BALTICSEA_ANALYSISFORECAST_PHY_003_006, Issue 1.2, Mercator Ocean International, https://documentation.marine.copernicus.eu/PUM/CMEMS-BAL-PUM-003-006-007.pdf (last access: 6 February 2025), 2024.

Madec, G. and the NEMO System Team: NEMO Ocean Engine Reference Manual, Zenodo, https://doi.org/10.5281/zenodo.8167700, 2023.

Medvedev, I. P., Rabinovich, A. B., and Kulikov, E. A.: Tidal oscillations in the Baltic Sea, Oceanology, 53, 526–538, https://doi.org/10.1134/S0001437013050123, 2013.

Müller, M., Homleid, M., Ivarsson, K., Køltzow, M. A. Ø., Lindskog, M., Midtbø, K. H., Andrae, U., Aspelien, T., Berggren, L., Bjørge, D., Dahlgren, P., Kristiansen, J., Randriamampianina, R., Ridal, M., and Vignes, O.: AROME-MetCoOp: A Nordic Convective-Scale Operational Weather Prediction Model, Wea. Forecasting, 32, 609–627, https://doi.org/10.1175/WAF-D-16-0099.1, 2017.

Pellikka, H., Leijala, U., Johansson, M. M., Leinonen, K., and Kahma, K. K.: Future probabilities of coastal floods in Finland, Cont. Shelf Res., 157, 32–42, https://doi.org/10.1016/j.csr.2018.02.006, 2018.

Pellikka, H., Johansson, M. M., Nordman, M., and Ruosteenoja, K.: Probabilistic projections and past trends of sea level rise in Finland, Nat. Hazards Earth Syst. Sci., 23, 1613–1630, https://doi.org/10.5194/nhess-23-1613-2023, 2023.

Räty, O., Laine, M., Leijala, U., Särkkä, J., and Johansson, M. M.: Bayesian hierarchical modelling of sea-level extremes in the Finnish coastal region, Nat. Hazards Earth Syst. Sci., 23, 2403–2418, https://doi.org/10.5194/nhess-23-2403-2023, 2023.

Rutgersson, A., Kjellström, E., Haapala, J., Stendel, M., Danilovich, I., Drews, M., Jylhä, K., Kujala, P., Larsén, X. G., Halsnæs, K., Lehtonen, I., Luomaranta, A., Nilsson, E., Olsson, T., Särkkä, J., Tuomi, L., and Wasmund, N.: Natural hazards and extreme events in the Baltic Sea region, Earth Syst. Dynam., 13, 251–301, https://doi.org/10.5194/esd-13-251-2022, 2022.

SMHI: Sea level observations from Swedish Meteorological and Hydrological Institute and Swedish Maritime Administration, SMHI's Open data service [data set], https://www.smhi.se/data/hav-och-havsmiljo/havsvattenstand/ (last access: 9 March 2026), 2025.

Swedish Meteorological and Hydrological Institute, Danish Meteorological Institute, Finnish Meteorological Institute, Federal Maritime and Hydrographic Agency, and TalTech (Tallin University of Technology): NEMO BAL MFC EIS-202411, Zenodo [code], https://doi.org/10.5281/zenodo.14507734, 2024.

Wehde, H., von Schuckmann, K., Pouliquen, S., Grouazel, A., Bartolome, T., Tintore, J., De Alfonso Alonso-Munoyerro, M., Carval, T., Racapé, V., and the INSTAC team: EU Copernicus Marine Service Quality Information Document for the Baltic Sea- In Situ Near Real Time Observations, INSITU_BAL_PHYBGCWAV_DISCRETE_MYNRT_013_032, Issue 2.4, Mercator Ocean International, https://documentation.marine.copernicus.eu/QUID/CMEMS-INS-QUID-013-030-036.pdf (last access: 15 May 2025), 2024.

Weisse, R., Dailidienė, I., Hünicke, B., Kahma, K., Madsen, K., Omstedt, A., Parnell, K., Schöne, T., Soomere, T., Zhang, W., and Zorita, E.: Sea level dynamics and coastal erosion in the Baltic Sea region, Earth Syst. Dynam., 12, 871–898, https://doi.org/10.5194/esd-12-871-2021, 2021.

State Planet, 7-osr10, 17, 2026
https://doi.org/10.5194/sp-7-osr10-17-2026
© Author(s) 2026. This work is distributed under
the Creative Commons Attribution 4.0 License.

Insights into exceptional freshening events in the northern Adriatic Sea throughout 2023–2024

Naomi Krauzig[1,2,3], Alessandro Coluccelli[1], Francesco Memmola[1], Pierluigi Penna[4], Fabrizio Moro[4], Enrico Zambianchi[5,2], and Pierpaolo Falco[1,2]

[1]Dipartimento di Scienze della Vita e dell'Ambiente, Università Politecnica delle Marche, Ancona, Italy
[2]Consorzio Nazionale Interuniversitario per le Scienze del Mare, Roma, Italy
[3]GEOMAR Helmholtz Centre for Ocean Research Kiel, Kiel, Germany
[4]Istituto per le Risorse Biologiche e le Biotecnologie Marine, Consiglio Nazionale delle Ricerche, Ancona, Italy
[5]Dipartimento di Scienze della Terra, Sapienza Università di Roma, Roma, Italy

Correspondence: Naomi Krauzig (nkrauzig@geomar.de)

Received: 11 August 2025 – Discussion started: 5 October 2025
Revised: 3 March 2026 – Accepted: 17 April 2026 – Published: 30 September 2026

Abstract. The northern Adriatic Sea experienced multiple extreme freshening events in 2023 and 2024, underscoring the intensifying influence of heavy precipitation, river discharge, and coastal flooding in the region. This study combines high-frequency in-situ observations from two autonomous meteo-marine monitoring platforms offshore of Fano and Senigallia with river discharge records, satellite imagery, and Copernicus Marine Service products to examine the evolution, drivers, and ecological implications of these events.

The first freshening event in early summer 2023 was linked to consecutive heavy rainfall episodes, including Storm Minerva, which triggered catastrophic flooding across the Emilia-Romagna region in northern Italy. Near-surface salinity declined from $\sim 36\,\mathrm{g\,kg^{-1}}$ to below $24\,\mathrm{g\,kg^{-1}}$ within two weeks, corresponding to an estimated freshwater input of $\sim 42.5\,\mathrm{m^3\,h^{-1}}$ in the vicinity of the buoy. Events in late 2023 and 2024 were even more abrupt and intense, culminating in late October 2024 with salinity values dropping to $\sim 15\,\mathrm{g\,kg^{-1}}$ following Storm Boris. A key distinction between the two years was the marked recovery of Po River discharge in 2024 after a prolonged drought, which significantly amplified freshwater inputs. These events triggered cascading environmental responses, including stratification, turbidity peaks, and phytoplankton blooms including summertime mucilage-forming aggregations, posing risks to aquaculture, water quality, and coastal tourism.

By combining autonomous in-situ measurements, satellite observations, and Copernicus reanalysis products, this study demonstrates a robust and cost-effective approach to tracking extreme hydrological events in coastal zones. The integrated dataset not only captures rapid thermohaline and biogeochemical changes near-real time but also places them in a broader environmental context. These findings underscore the value of sustained and interoperable observing systems in supporting early warning capabilities, scientific research, and climate adaptation in vulnerable marine regions such as the northern Adriatic Sea.

1 Introduction

Coastal regions like the shallow Northern Adriatic are complex and densely-populated socio-ecological systems that provide high-value services (Costanza et al., 2014) which are susceptible to the impacts of climate change and other anthropogenic and natural pressures.

Among these, flooding events, triggered by factors such as high tides, storm surges and precipitation whiplashes can lead to large adverse impacts on human and natural systems (Zscheischler et al., 2018; Wright and Nichols, 2019; Tan et al., 2023). According to the latter, precipitation whiplashes, including abrupt shifts between dry and wet extremes, favor the generation of significant surface runoff and flooding,

Published by Copernicus Publications.

Table 1. Products from the Copernicus Service and other complementary datasets used in this study, including the Product User Manual (PUM) and Quality Information Document (QUID). For complementary datasets, the links to the product description, data access and/or references are provided.

Product Ref. No.	Product ID & type	Data Access	Documentation
1	Fortunae Buoy, in-situ data	Fano Marine Center (2025)	Penna et al. (2025a)
2	Senigallia Meda, in-situ data	IRBIM-CNR (2025)	Penna et al. (2025b)
3	ERA5, numerical models	Hersbach et al. (2023)	Copernicus Climate Change Service (2023)
4	CEMS EFAS, numerical models	Mazzetti et al. (2023)	Copernicus Emergency Management Service (2025)
5	SST_MED_SST_L4_NRT, satellite observations	EU Copernicus Marine Service Product (2024a)	QUID: Pisano et al. (2024a); PUM: Pisano et al. (2024b)
6	OCEANCOLOUR_MED_BGC_L4_NRT_009_142, satellite observations	EU Copernicus Marine Service Product (2025)	QUID: Colella et al. (2025); PUM: Colella et al. (2024)
7	MEDSEA_ANALYSIS_FORECAST_PHY_006_013, numerical models	EU Copernicus Marine Service Product (2024b)	QUID: Gualtieri et al. (2024); PUM: Lecci et al. (2024a)
8	MEDSEA_ANALYSIS_FORECAST_BGC_006_014, numerical models	EU Copernicus Marine Service Product (2024c)	QUID: Feudale et al. (2024); PUM: Lecci et al. (2024b)

concurrent landslides and erosion that can also amplify negative trends in water quality. Overall, river discharge plays a crucial role in coastal ecosystems by providing freshwater and nutrients that impact hydrology, biogeochemistry, and productivity. Along the Northwestern Adriatic coast, several small rivers and the major Po river discharge nutrient-rich freshwater which is mainly transferred southward along the Italian coast by the Western Adriatic Current (Goudeau et al., 2013), while the Po plume is known to remain close to the coast under stratified conditions (Cozzi and Giani, 2011). This, in turn, affects nutrient cycling, species growth and survival rates (Ludwig et al., 2009; Cozzi and Giani, 2011) as well as water mass formation processes (Falcieri et al., 2014).

The coastal impacts of flooding events extend beyond environmental concerns, affecting local communities and economies that depend on infrastructure and marine resources (e.g., IPCC, 2022, 2023). The need for coastal observations and monitoring efforts is therefore increasingly recognized as essential for guiding policy and public safety needs. The Copernicus Marine Service plays a key role in this context by offering a wide range of physical and biogeochemical near-real time data. However, the location, rapidity and complexity of floods and the related coastal events present specific challenges. Accurate detection and monitoring require an integrated methodology that combines local high-resolution in-situ measurements, satellite data and modeling approaches. This study leverages the high-resolution data from a coastal meteo-marine buoy and several Copernicus sources to provide a comprehensive analysis of a series of exceptional freshening events in the northern Adriatic Sea throughout the last 2 years.

2 Methodology

In order to assess the spatio-temporal characteristics, environmental drivers, and ecological impact of extreme freshening events in the northwestern Adriatic Sea during 2023 and 2024, we integrated a set of in-situ, satellite-derived, reanalysis, and model-based datasets.

2.1 Local meteo-marine conditions

High-frequency in-situ measurements of thermohaline, atmospheric and biogeochemical properties were obtained from two autonomous meteo-marine monitoring systems, positioned ~ 3.7 km offshore of Fano (43°53′30.0″ N, 13°00′30.0″ E) and Senigallia (43°45′20.9″ N, 13°12′32.4″ E) on the western coast of the northern Adriatic Sea (product ref. 1 and 2; Table 1).

Raw data from these platforms (mentioned as Buoy Fortunae offshore of Fano and Meda Station offshore of Senigallia henceforth) were first converted with the calibration coefficients in the configuration file provided by Sea-Bird Electronics and processed according to the typical SBE data processing sequences. The necessary calculation and analysis of thermodynamic properties was based on the Gibbs Seawater (GSW) Oceanographic Toolbox (IOC et al., 2010), which contains the TEOS-10 subroutines (http://www.TEOS-10.org, last access: 12 February 2025) for the evaluation of

seawater properties (McDougall and Barker, 2011). Detailed sensor specifications and processing steps are available in Appendix A1.1–A1.3.

2.2 Precipitation and river discharge

Hourly precipitation data were retrieved from the ERA5 reanalysis dataset, produced by the Copernicus Climate Change Service, which provides gridded atmospheric fields at 0.25° spatial and 1 h temporal resolution (product ref. 3; Table 1). In parallel, 6-hourly river discharge estimates were extracted from the European Flood Awareness System (EFAS) model, based on the LISFLOOD hydrological model forced with gridded meteorological observations (product ref. 4; Table 1). Considering the dominant southeastward flow of the Western Adriatic Current, freshwater input from major (Po, Adige, Reno) and minor regional rivers (e.g., Lamone, Savio, Metauro, and 14 others) was assessed at their upstream mouths along the northwestern Adriatic coast (see Fig. 3 for river mouth locations and characteristic circulation patterns).

2.3 Freshwater rate estimation

To estimate the required freshwater inflow necessary to account for the observed decrease in surface seawater salinity over a given time period, a simplified salt mass conservation approach was applied. This method was based on in-situ salinity data from the Fortunae buoy (product ref. 1; Table 1) and the estimated area of the affected region, derived from satellite SST and ocean-colour observations (product refs. 5 and 6; Table 1) capturing the cold and turbid coastal plume. Assuming that salinity and density are conserved during mixing and proportional to the volumes involved, the following salt mass balance equation was applied:

$$\rho_1 S_1 V_1 = \rho_2 S_2 V_2 \quad (1)$$

where ρ_1 and ρ_2 are the initial and final density in $\mathrm{kg\,m^{-3}}$; S_1 and S_2 are the initial and final salinity in $\mathrm{g\,kg^{-1}}$; V_1 is the initial considered volume of seawater in $\mathrm{m^3}$; V_2 is the final volume after mixing with the added freshwater in $\mathrm{m^3}$.

And the freshwater flow (Q) in $\mathrm{m^3\,s^{-1}}$, required to achieve the observed salinity decrease over the time period Δt is calculated as:

$$Q = \frac{\Delta V}{\Delta t} \quad (2)$$

A practical example of this calculation, including measured values from the Fortunae buoy and assumptions on the affected volume based on the buoy's position and local bathymetry, is provided in Appendix A2, along with a schematic diagram illustrating the considered water volume (Fig. A1).

2.4 Complementary satellite and model-based datasets

To complement the in-situ observations and support the freshwater rate estimation (Sect. 2.3), we incorporated satellite-derived and model-based datasets (products 5–8; Table 1) providing full spatial coverage of the northwestern Adriatic Sea. These included daily fields of sea surface temperature (SST; 0.01° × 0.01°), chlorophyll *a* concentration (Chl-a, 1 km × 1 km), light attenuation coefficient at 490 nm (KD490; 1 km × 1 km), surface salinity (SSS; 0.042° × 0.042°), and horizontal current components (u and v).

These datasets served three main purposes:

1. to delineate the surface extent of freshwater-affected waters and define the horizontal area used in freshwater input calculations (see Appendix A2);
2. to fill temporal gaps in the buoy and coastal station records, ensuring continuous environmental context during key periods of data loss; and
3. to extend the analysis beyond the nearshore region, offering insight into the broader evolution of surface thermohaline and biogeochemical properties across the Adriatic Sea.

The satellite products provided gap-free, multi-sensor interpolated surface fields, while model outputs offered physically consistent estimates of key oceanographic variables across space and time.

2.5 Statistical analysis

Basic statistics were computed following Emery and Thomson (1998). Root Mean Square Difference (RMSD), bias, and cross-correlation were applied to evaluate temporal coherence between thermohaline, biogeochemical and environmental conditions. Detailed equations and assumptions are reported in Appendix A3.

3 Results

Over the past two years, the northern Adriatic Sea experienced a series of hydro-meteorological extremes, resulting in rapid and recurrent freshening episodes with cascading environmental and societal implications.

3.1 Surface freshening

Between May 2023 and November 2024, five distinct surface freshening events were identified in the northern Adriatic Sea from high-frequency salinity observations collected by the Fortunae buoy and the Senigallia Meda Station. These events varied in duration (12 to 53 d), intensity (6.7 to 20.1 $\mathrm{g\,kg^{-1}}$ salinity drop), and temporal structure, shaped both by prolonged and abrupt freshwater input dynamics (Tables A4 and A5).

Event I (2 May–24 June 2023) was the longest, spanning 53 d. It was characterized by a multi-phase freshening, including an extended period of anomalously low salinity and a gradual recovery. The most pronounced salinity decrease occurred over 13 d (11–24 May), with salinity dropping by 12.77 g kg^{-1}, from 36.19 to 23.42 g kg^{-1}. This prolonged freshening suggests sustained riverine discharge into the northwestern Adriatic. Event II (29 September–16 October 2023, 17 d) showed a more abrupt signature. Over just 5 d, salinity fell by 6.72 g kg^{-1} (from 37.17 to 30.45 g kg^{-1}), indicating a rapid freshwater input followed by a relatively short recovery. Event III (12 November–2 December 2023, 20 d) included the highest initial salinity observed (37.63 g kg^{-1}), followed by a significant 14 d drop to 26.53 g kg^{-1}, which corresponds to a total decrease of 11.10 g kg^{-1}. Event IV (9–21 April 2024, 12 d) was short but intense, featuring a 6 d salinity decrease of 13.89 g kg^{-1}, from 36.16 to 22.27 g kg^{-1}, representing one of the steepest gradients recorded. Event V (20 October–22 November 2024, 33 d) was the most extreme in terms of salinity reduction. A 10 d drop of 20.12 g kg^{-1} brought surface salinity from 35.09 to 14.97 g kg^{-1}, making this the most intense freshening event of the record.

These events illustrate the basin's dual sensitivity to sustained meteorological forcing and intense short-term hydrological extremes. Cross-event comparisons emphasize differing recovery behaviors and highlight the coupling between catchment saturation and downstream marine responses (Figs. A2–A6).

3.2 Environmental connections

Hydrological analysis revealed that major freshening events coincided with intense precipitation and river discharge anomalies in the Emilia-Romagna region, with events driven by both catchment saturation and localized convective storms.

A sequence of five rainfall episodes culminated in catastrophic flooding from 1–24 May 2023 (Fig. 2b). The first rainstorm (1–3 May) brought over 200 mm of precipitation to central-eastern Emilia-Romagna. Initial flooding affected the Reno and Lamone basins. Two subsequent moderate episodes (9–10 and 12–14 May) further saturated soils. The most severe storm, associated with Storm Minerva (16–18 May), delivered over 300 mm in areas such as Forlì, with cumulative precipitation more than 5 times the monthly climatological average.

During this period, the Po River remained well below the climatological average discharge, with values around 2000 m^3 s^{-1}, as the most intense rainfall did not affect its main basin, whereas local rivers like the Lamone, Savio, and Reno exceeded historical flood levels (Fig. 3c). Cross-correlation analysis between accumulated precipitation and river discharge (Fig. A5) confirmed statistically significant relationships ($p < 0.05$), with time lags ranging from −6 to −120 h. Rapid response was observed in local rivers with short catchments, such as Rubicone ($r = 0.74$, lag = −6 h), while larger basins like the Adige exhibited longer delays ($r = 0.71$, lag = −36 h).

No widespread heavy precipitation was recorded in correspondence with Event II in late September 2023, but localized convective storms likely impacted the Marche region, just south of Emilia-Romagna, between 25–29 September. An increase in the discharge of the Adige and Po was reported and the freshening signal suggests a short-lived but intense localized input (Fig. 1). In accordance, two prolonged rainfall episodes occurred later during 2–5 November and 30 November–2 December (Event III). The latter was the most severe, with up to 383 mm of rainfall recorded inland, in the Parma Apennines. A third, minor event on 4–5 December followed the main storm.

During spring 2024, an unseasonable storm system between 20–24 April brought 70–80 mm of weak but steady rainfall and rivers with short response times reacted quickly to the precipitation input, leading to the abrupt salinity drop during Event IV (Fig. 1).

Autumn 2024 saw the return of exceptional rains. Between 17–20 September, Storm Boris delivered ∼ 300 mm of rainfall in eastern Emilia-Romagna, causing major river discharges in local rivers like the Savio, Fiumi Uniti and Lamone River (Fig. 3c). Less than a month later (18–19 October), another storm triggered river discharge records for all major rivers, especially for the Po River (record value = 7880 m^3 s^{-1}), reflecting a marked hydrological recovery after prolonged drought.

This analysis affirms that both large-scale catchment saturation and localized storm activity contributed significantly to the observed salinity anomalies. Rivers with differing catchment sizes showed distinct response times, with immediate peaks in small rivers and delayed responses in larger ones. Figures 2 and 3, along with Appendix Figs. A2–A6, provide a spatial and temporal context for precipitation and discharge patterns associated with each event.

3.3 Ecological implications

Each freshening event identified in this study (Fig. 1) triggered a marked biogeochemical response in the northern Adriatic Sea, as captured by the high-frequency in-situ measurements of chlorophyll *a*, turbidity, and dissolved oxygen collected by the Fortunae Buoy and the Senigallia Meda Station (Fig. 4). These parameters serve as proxies for primary productivity, sediment transport, and oxygen dynamics, offering direct evidence of ecosystem perturbations following extreme hydro-meteorological events.

Following Event I (May 2023), which was preceded by a sequence of five intense rainfall episodes in the Emilia-Romagna region and culminated in catastrophic flooding (Fig. 2b–e), an extreme turbidity increase (∼ 70 NTU average) was recorded for more than a month, along with

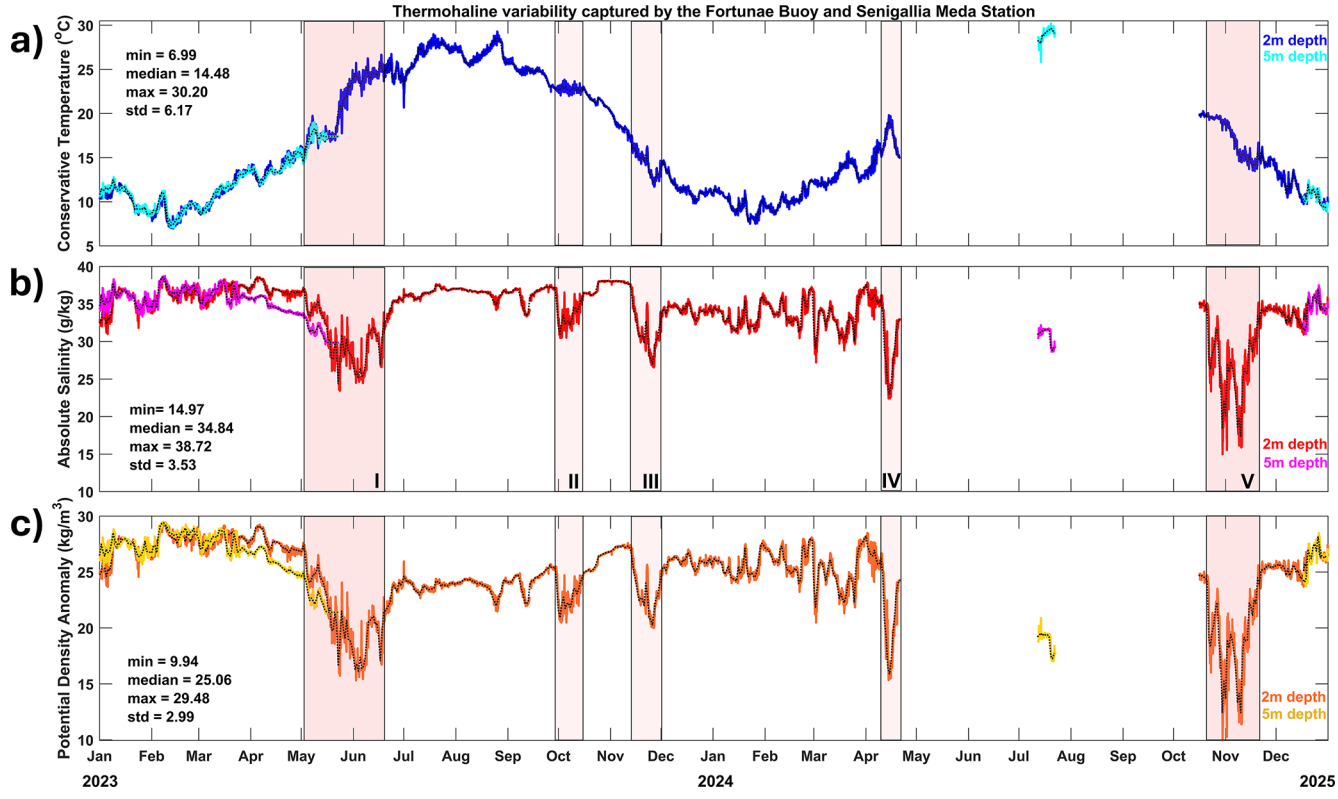


Figure 1. Hourly (colored lines) and daily-averaged (black dotted lines) time series of **(a)** conservative temperature, **(b)** absolute salinity, and **(c)** potential density anomaly recorded at 2 and 5 m depth offshore of Fano and Senigallia, respectively (product ref. 1 and 2; Table 1). Basic statistical descriptors (minimum, maximum, median, standard deviation) for each thermohaline property are reported in the top left corner of each panel. Light red shaded areas (I–V) indicate the timing of the five most significant surface freshening events identified between 2023 and 2024.

chlorophyll *a* concentrations exceeding $10\,\mu g\,L^{-1}$ (Fig. 4). These responses reflect the combined influence of excess sediment transport and nutrient enrichment, especially from local rivers like the Lamone, Reno, and Savio, which exceeded historical discharge levels (Fig. 3c). The sustained rainfall and resulting prolonged runoff seem to have led to a persistent stratified surface layer that confined biological activity and promoted bloom formation.

After the record May flood period, a particularly notable anomaly was observed in June–July 2023, with sustained extreme turbidity (> 200 NTU) and following chlorophyll *a* values ($> 30\,\mu g\,L^{-1}$). Subsequent visual inspections of the buoy infrastructure revealed the presence of mucilage-forming macroaggregates, consistent with recurring gelatinous algal blooms historically observed in the Adriatic under warm, stratified, and nutrient-enriched conditions (Arrighi and Domeneghetti, 2024). These mucilage events have well-documented impacts on marine ecosystems, coastal water quality, and economic sectors such as aquaculture and tourism.

The response to Event II (late September–October 2023) presented a contrasting case. While no widespread heavy precipitation and flooding occurred in Emilia-Romagna, localized convective storms over the Marche region and rising discharges in the Adige and Po rivers triggered a short-lived but intense freshening. While turbidity remained low, the biogeochemical response included a marked increase in chlorophyll *a* concentration and oxygen supersaturation reaching approximately 150 %, indicating a nutrient rich but low sediment freshwater input. Moreover, dissolved oxygen rose near-synchronously with chlorophyll *a* concentrations ($r = 0.77$, lag = 0 h), consistent with well-lit bloom conditions. This event exemplifies how smaller, convective systems can fuel biological productivity without large sediment loads, while favorable light conditions likely allowed rapid phytoplankton growth.

The prolonged rainfall in early and late November 2023 preceded Event III, which produced another strong bloom and variable oxygen patterns. This response suggests that delayed runoff from larger, saturated catchments delivered substantial nutrient loads, with peak phytoplankton activity followed by oxygen variability related to organic matter remineralization and light attenuation during turbid phases.

The corresponding biogeochemical response to event IV followed an unseasonable storm system in April 2024. Rapid response from short catchment rivers like the Rubicone and

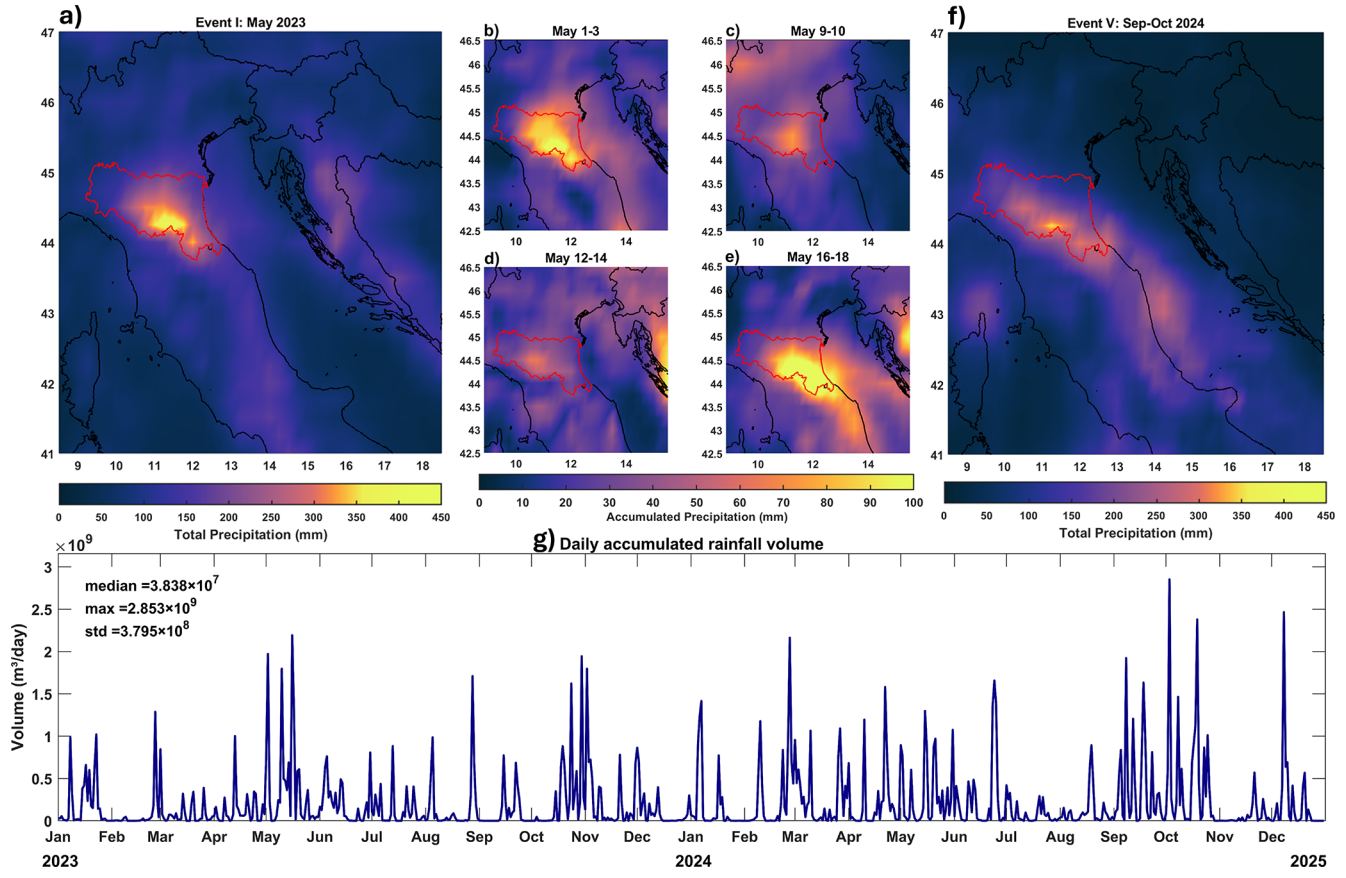


Figure 2. Spatial distribution of accumulated precipitation (product ref. 2; Table 1) over Emilia-Romagna and surrounding areas during key extreme rainfall events associated with surface freshening Event I and Event V (see Fig. 1). **(a)** Total precipitation during the combined May 2023 period (Event I). Accumulated precipitation during individual May 2023 storm episodes: **(b)** 1–3 May, **(c)** 9–10 May, **(d)** 12–14 May, and **(e)** 16–18 May. **(f)** Total precipitation during the two September–October 2024 events (Event V). The Emilia-Romagna region is outlined in red in each panel. **(g)** Time series of daily accumulated rainfall volume ($m^3\,d^{-1}$) over the domain, highlighting the timing and intensity of individual rainfall peaks between January 2023 and December 2024. Basic statistical descriptors (minimum, maximum, median, standard deviation) are reported in the upper left corner.

Uso led to an abrupt salinity drop (Fig. 1) and sharp turbidity and chlorophyll peaks, consistent with the fast land-sea transfer typical of springtime storms over saturated terrain. These dynamics emphasize the system's sensitivity even to moderate precipitation when antecedent soil conditions favor immediate runoff.

Finally, Event V in autumn 2024 was preceded by two major storm systems: Storm Boris (17–20 September) and an intense October storm (18–19 October), the latter driving the Po River to record discharge levels (Fig. 3c). This sequence produced the most intense surface freshening and the highest chlorophyll *a* concentration observed during the study period, exceeding $60\,\mu g\,L^{-1}$. Interestingly, these extremely high chlorophyll *a* levels occurred in conjunction with notably low turbidity, suggesting that sediment-laden runoff from the Po River may have settled or dispersed before reaching the offshore monitoring sites at Fano and Senigallia. This decoupling implies that nutrient transport remained effective despite reduced suspended particulate matter, allowing for favorable light conditions and enhanced primary productivity which is consistent with a multi-day negative turbidity–chlorophyll relationship ($r = -0.32$ at -144 h lag) and near-synchronous, positive chlorophyll–oxygen coupling ($r = 0.86$ at 0 h lag), together indicating strong photosynthetic control under clear conditions.

Across all events, dissolved oxygen dynamics reflected a combination of photosynthetic production during bloom conditions and oxygen depletion during periods of high turbidity and organic matter degradation. Event-scale lead–lag patterns showed a biphasic turbidity–chlorophyll response with a short-lag negative branch when high turbidity limits light, and a positive branch at multi-day delays when nutrient delivery and stratification promote blooms. The chlorophyll–oxygen coupling is typically positive and near-synchronous, with longer-lag negatives appearing during potential bloom decay and post-bloom respiration.

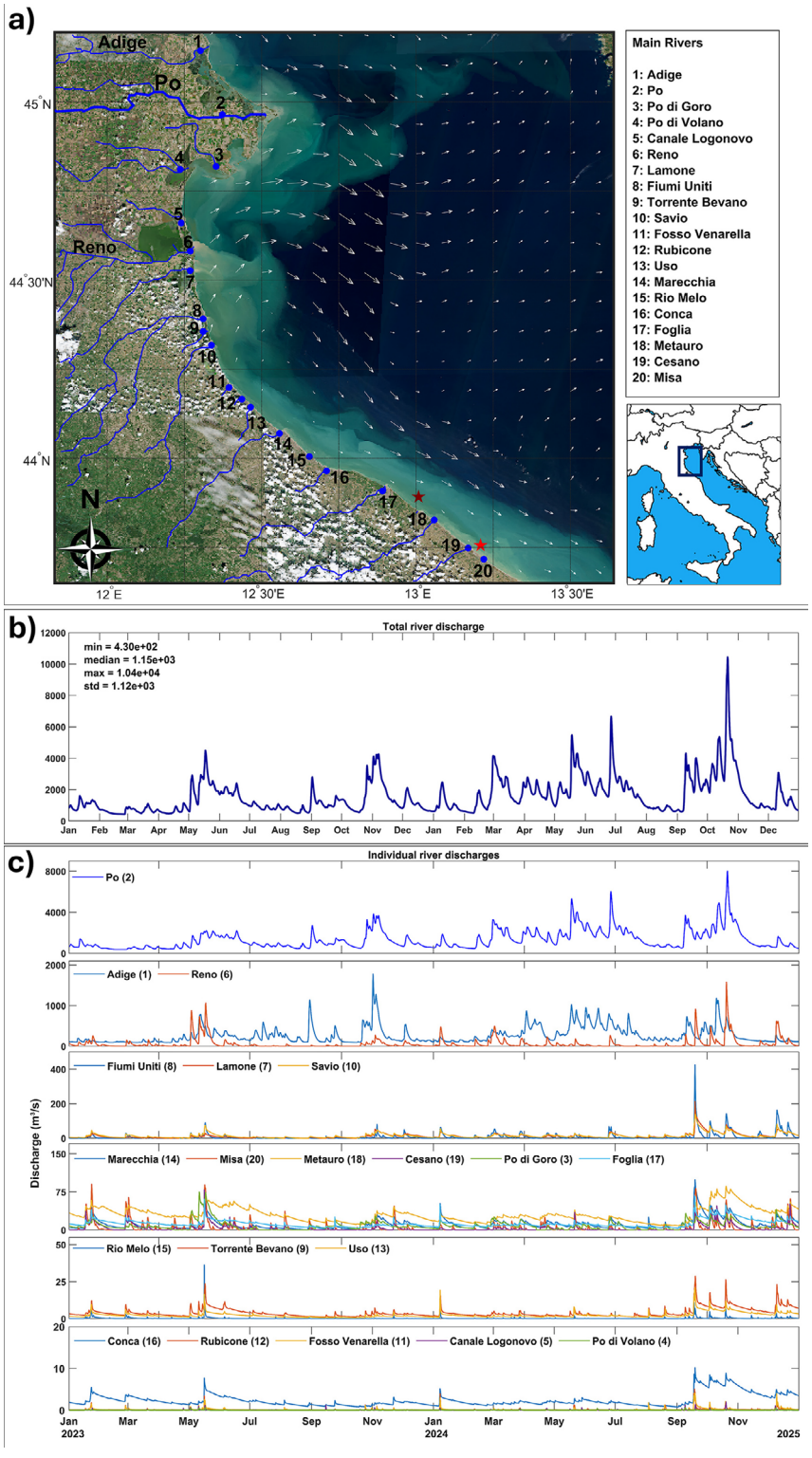


Figure 3. Overview of **(a)** the study area with the location of the 20 assessed river mouths (blue dots) and the positions of the autonomous monitoring platforms offshore of Fano and Senigallia (dark and light red star, respectively). The background corresponds to a Sentinel-2 Level 2A true-color image (https://dataspace.copernicus.eu/browser, last access: 17 August 2025) acquired on 31 October 2024, overlaid with surface current vectors derived from the numerical circulation model (product ref. 8; Table 1) for the same date. **(b)** Daily time series of the total accumulated river discharge ($m^3\ s^{-1}$) from all 20 rivers for the period January 2023–December 2024 (product ref.3; Table 1). Key descriptive statistics (minimum, median, maximum, standard deviation) are indicated. **(c)** Individual river discharge time series, grouped by magnitude, with numeric labels corresponding to the river mouth positions indicated in panel **(a)**.

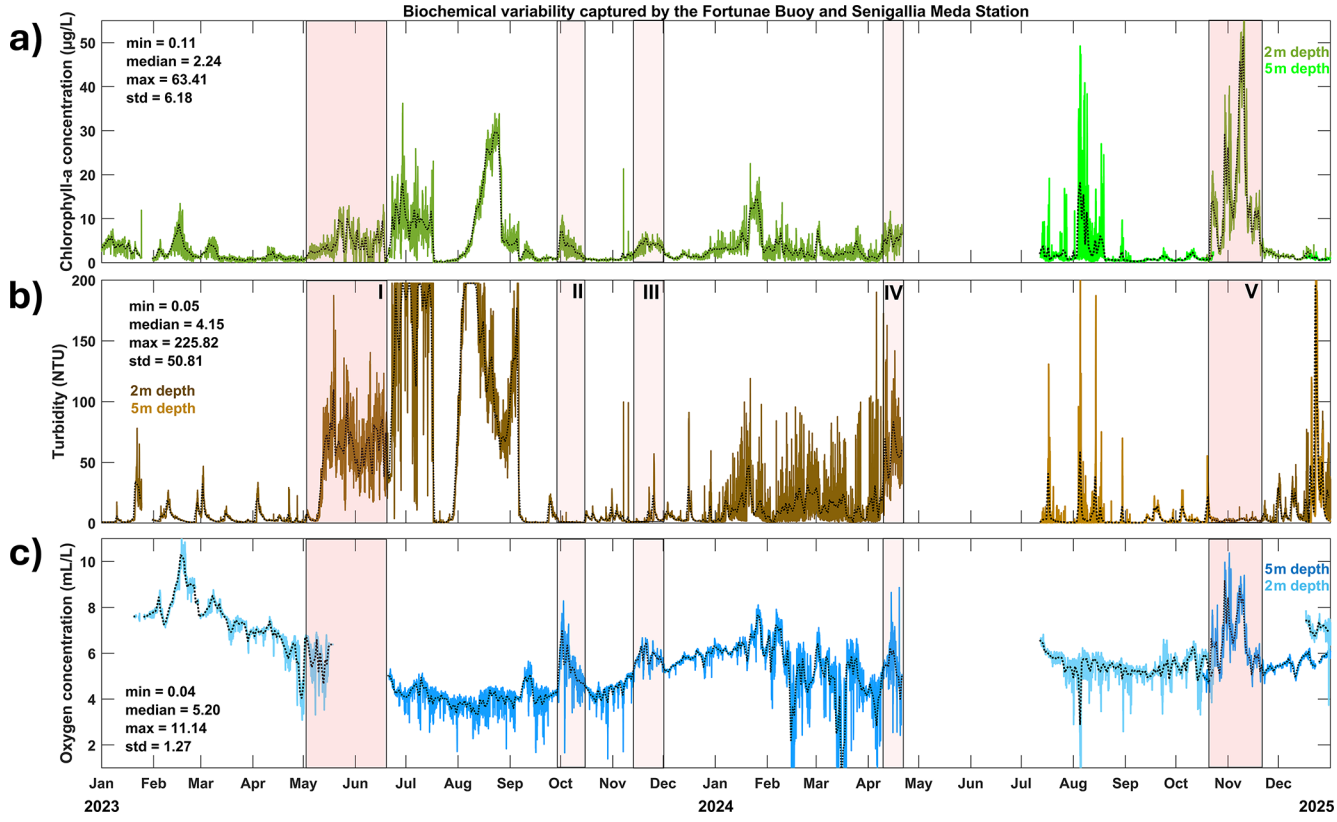


Figure 4. Hourly (colored lines) and daily-averaged (black dotted lines) time series of **(a)** chlorophyll *a* concentration, **(b)** turbidity, and **(c)** dissolved oxygen concentration measured at 2 and 5 m depths by the Fortunae buoy (offshore of Fano) and the Senigallia Meda station, respectively (product ref. 1 and 2; Table 1). Basic statistical descriptors (minimum, maximum, median, standard deviation) are reported in the left corner of each panel. Red shaded areas (I–V) denote the timing of the five most pronounced surface freshening events as identified in Fig. 1. Biogeochemical responses, including sharp increases in turbidity and chlorophyll *a*, coincide with or follow these events, reflecting ecosystem perturbations.

These findings confirm that hydro-meteorological forcing, whether through widespread rainfall, localized storms, or antecedent soil saturation, directly drive ecosystem-level responses in the northern Adriatic Sea. The magnitude and timing of these responses depend not only on precipitation intensity and discharge volume, but also on the sediment load, nutrient delivery, and seasonal conditions governing stratification and light availability.

4 Discussion and conclusions

The northern Adriatic experienced a series of extreme freshening events between 2023 and 2024, underscoring its vulnerability to compound hydro-meteorological extremes. Events such as Storm Minerva and Storm Boris were marked by intense precipitation and widespread flooding, with significant hydrological and ecological repercussions. These cases highlight the increasing role of precipitation whiplash and flood-drought cycles in modulating coastal hydrography.

According to the IPCC's Sixth Assessment Report, heavy rainfall events and the corresponding overflow are projected to increase in frequency and intensity as global temperatures rise beyond 1.5 °C (IPCC, 2023). River floods in central and western Europe are already increasing, and small catchments, like those affected along the northwestern Adriatic coast, are especially vulnerable. Future storms may more frequently exceed their coping capacities, reinforcing the urgency of adaptive monitoring systems.

In the Northern Adriatic, where the Po River and smaller local rivers drive salinity and biogeochemical patterns, such shifts have significant implications. As the shallowest and northernmost basin of the Mediterranean, it is particularly vulnerable to such perturbations due to its limited flushing, strong land-sea coupling, and intensive human pressure (Coll et al., 2010). Its physical and ecological sensitivity to episodic freshwater pulses, such as those examined here, underscores the growing importance of continuous monitoring in the context of climate change.

Surface freshening alters water column structure, promotes stratification, and modulates ecological responses. In summer 2023 and 2024, sea surface temperatures exceeded 30 °C, accompanied by extensive mucilage-forming algal ag-

gregations. These events compromise water quality, threaten aquaculture viability, and negatively impact tourism, posing socio-ecological risks.

High-resolution in-situ observations play a critical role in capturing such rapid and localized phenomena. Coastal meteo-marine platforms, such as the utilized Fortunae buoy and Senigallia Meda station, offer a cost-effective, automated system capable of operating under harsh conditions and at high sampling rates in complex nearshore zones.

We therefore recommend a collective effort that incorporates such observational datasets into Copernicus and broader databases. Such an integration would bridge existing gaps in coastal coverage, complementing the basin-wide scope of satellite and reanalysis products with finer-scale, real-time data. As climate-induced extremes accelerate, safeguarding ecological and societal resilience in shallow semi-enclosed seas, such as the Adriatic Sea, requires sustained, integrated, and transdisciplinary efforts anchored in robust, real-time observations and openly accessible data.

Appendix A

A1 Overview of the meteo-marine buoy Fortunae

The multidisciplinary buoy is equipped with a series of sensors that measure atmospheric parameters at 2 m height; wave parameters at sea level; as well as current, thermohaline and biochemical parameters at $\sim$2 m depth below the sea level.

A1.1 Atmospheric conditions at 2 m height

More precisely, the following atmospheric parameters are systematically sampled every 30 min at 2 m above sea level using a GILL MaxiMet GMX500 Compact Weather Station equipped with GPS (https://gillinstruments.com/, last access: 10 May 2026; Table A1).

Table A1. Overview of the observed atmospheric parameters with the corresponding technical details and characteristics. Additional information are available under the feature specification of the GMX500 Model: https://gillinstruments.com/wp-content/uploads/2022/08/1957-008-Maximet-gmx500-Iss-9.pdf, last access: 10 May 2026.

Measured Parameters				
Parameter	Unit	Range	Resolution	Accuracy
Air pressure (P_{air})	hPa	300 to 1100	0.1	$\pm$0.5 hPa @ 25 °C
Air temperature (T_{air})	°C	-40 to $+70$	0.1	$\pm$0.3 °C @ 20 °C
Dew point (T_{dew})	°C	-40 to $+70$	0.1	$\pm$0.3 °C @ 20 °C
Relative Humidity (RH)	%	0 to 100	1	$\pm$2 % @ 20 °C
Wind direction (D_w)	degree	0 to 359	1	$\pm$3° to 40 m s^{-1}
Wind speed (U_w) and gust (U_G)	m s^{-1}	0.1 to 60	0.01	$\pm$3 % to 40 m s^{-1}

A1.2 Wave conditions at sea level

Note that wave measurements are available from the platform but were not utilized in the present study. The following wave parameters are systematically sampled every 60 min at sea level utilizing a Brizo-X Directional Wave Height Sensor with an integrated Global Navigation Satellite System (GNSS) from Xeos Technologies (https://xeostech.com/brizo-x, last access: 14 May 2026; Table A2).

The Brizo-X Directional Wave Height Sensor utilizes standard spectral analysis techniques and formulas to calculate wave parameters for waves of periods from 1.6 s to 33 s (Earle, 1996). The energy density spectrum of a sea state is generally designated by $E(f)$ and the total energy is given by

$$\overline{E} = \int_0^\infty E(f)\mathrm{d}f \tag{A1}$$

The wave frequency spectrum can, therefore, be determined from a wave record $\eta(t)$ by using a Fourier transform as follows: The wave energy averaged over a period $[-T/2 < (t - t_0) < T/2]$ is given by

$$\overline{E} = \frac{g\rho}{T} \int_{-T/2}^{T/2} (\eta(t - t_0) - \langle\eta\rangle)^2 \mathrm{d}t \tag{A2}$$

where $\langle\eta\rangle$ is the mean value.

Inserting in this expression the Fourier development of $(\eta(t - t_0) - \langle\eta\rangle)$, gives

$$\overline{E} = \sum_{k=1}^{\infty} E(f_k)\,\Delta f, \quad f_k = k\Delta f, \quad \Delta f = \frac{1}{T},$$

$$E(f_k)\,\Delta f = \frac{g\rho}{8}|H_k|^2,$$

$$H_k = \frac{4}{T} \int_{-T/2}^{T/2} (\eta(t - t_0) - \langle\eta\rangle) e^{-2i\pi f_k t} \mathrm{d}t \tag{A3}$$

where g is the gravitational acceleration, ρ is the seawater density.

Table A2. Overview of the observed wave characteristics with the corresponding technical details. Wave height range information stem from Wang et al. (2016). Additional information is available under the feature specification of the Brizo-X Model: https://xeostech.com/sites/default/files/2019-08/BrizoX%20Brochure%20WEB.pdf, last access: 14 May 2026.

Measured Parameters			
Parameter	Unit	Range	Accuracy
Significant wave height (H_s)	m	0.2–20	±1 % @ −40 to +60 °C
Maximum wave height (H_{max})	m	0.2–20	±1 % @ −40 to +60 °C
Waves mean period (T_z)	s	1.56 to 33.33	±1 % @ −40 to +60 °C
Waves maximum period ($T_{H_{max}}$)	s	1.56 to 33.33	±1 % @ −40 to +60 °C
Wave direction (D_P)	degree	0 to 359	±3° @ −40 to +60 °C
Directional spread (B_m)	degree	0 to 359	±3° @ −40 to +60 °C

CHAPTER 4.3

A1.3 Thermohaline and biochemical conditions at 2 m depth

Additionally, the following oceanographic parameters are systematically sampled every 30 min at ∼ 2 m depth below the sea level by a submerged MicroCAT SBE-37 SIP (Serial Interface Pumped) CTD (Conductivity-Temperature-Depth) and a WET Labs ECO-FLNTU fluorescence sensor with Bio-Wiper option from Sea-Bird (https://www.seabird.com/, last access: 14 May 2026; Table A3).

The TEOS-10 GSW Matlab routines (version 3.05.5) were applied to derive Absolute Salinity (S_A) (mass fraction of dissolved material, in g kg^{-1}) and of Conservative Temperature (CT, in °C) from of Practical Salinity (S, unitless) and Potential Temperature (θ, in °C), respectively. According to McDougall and Barker (2011) these properties are calculated as follows:

$$S_A = \left(\frac{35.16504}{35}\right) S + \delta S_A(x, y, p) \quad \text{(A4)}$$

where $\delta S_A = S_A - S_R$ is the difference between the Absolute Salinity and Reference Salinity (S_R) based on the location, with x and y being the longitude and latitude in decimal degrees and p the pressure in dbar.

$$\mathrm{CT} = \frac{h^0}{C_p^0} \quad \text{(A5)}$$

where $C_p^0 = 3991.86795711963\,\mathrm{J\,kg^{-1}\,K^{-1}}$ is a reference value of the specific heat capacity, chosen to be as close as possible to the spatial average of the heat capacity over the ocean surface and h^0 is the potential enthalpy which corresponds to the enthalpy (h, in J kg^{-1}) at a reference pressure:

$$h^0(S, \theta, p_r) = h(S, \theta, p) - \int_{p_r}^{p} \frac{1}{\rho(S, \theta, p)} \mathrm{d}p \quad \text{(A6)}$$

Table A3. Overview of the observed oceanographic parameters* with the corresponding technical details and characteristics. Additional information is available in the SBE feature specifications: https://www.seabird.com/products/sbe-37-microcat (last access: 14 May 2026).

Measured Parameters			
Parameter	Unit	Range	Accuracy/ Sensitivity
Pressure (P)	Pa	to ∼ 6 022 000	±0.1 %
Temperature (T)	°C	−5 to +45	±0.002
Conductivity (Cond)	S m^{-1}	0 to 7	±0.0003
Turbidity (turb)	NTU	0.01 to 25	0.01
Chlorophyll *a* (chl *a*)	µg L^{-1}	0.01 to 50	0.025

* Though not included in this study, additional parameters are available from an SBE optical oxygen sensor and a Nortek Aquadopp current meter from 14 July 2023 onwards.

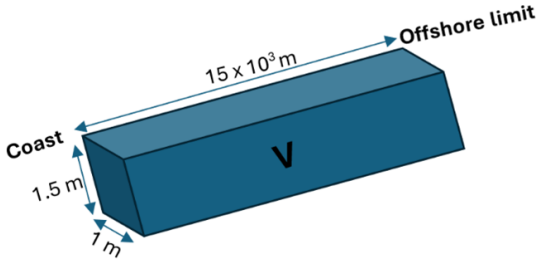


Figure A1. Indication of the considered volume of seawater.

Readers interested in the full observational capabilities of the buoy are referred to Table 1 and Penna et al. (2025a).

A2 Freshwater flow rate calculation

Following the salt mass balance equation (Eq. 1) and based on the in-situ data from the Fortunae buoy (Product Ref. No. 1) and the estimated impacted area from the satellite observations (Product Ref. No. 5 and 6), the freshwater input leading to the first extreme freshening can be calculated as follows.

Taking into account that

- $\rho_1 = 1026.212\,\mathrm{kg\,m^{-3}}$ is the initial seawater density measured by the buoy;
- $\rho_2 = 1015.725\,\mathrm{kg\,m^{-3}}$ is the final seawater density measured by the buoy;
- $S_1 = 36.194\,\mathrm{g\,kg^{-1}}$ is the initial seawater salinity measured by the buoy;
- $S_2 = 23.424\,\mathrm{g\,kg^{-1}}$ is the final seawater salinity measured by the buoy;
- $V_1 = 22.5 \times 10^3\,\mathrm{m^3}$ is the initial volume of seawater confined by the distance from the shore (15×10^3 m), the width (1 m) and depth (1.5 m) considering the position of the buoy sensors;
- V_2 is the final volume.

Note that the control volume is defined by an offshore distance of 15×10^3 m, consistent with the observed plume extent, a depth of 1.5 m corresponding to the buoy sensor level, and an alongshore width of 1 m. This width is intentionally chosen to express the freshwater requirement per meter of coastline. The resulting freshwater rate therefore represents the required freshwater inflow per meter of coastline near the buoy location, rather than the total discharge integrated along the entire coastal segment.

Equation $\rho_1 S_1 V_1 = \rho_2 S_2 V_2$ can be solved for $V_2 = V_1 \rho_1 S_1 / \rho_2 S_2 = 35.762 \times 10^3\,\mathrm{m^3}$ and the corresponding volume change $\Delta V = V_2 - V_1 = 13.262 \times 10^3\,\mathrm{m^3}$ provides the freshwater volume and the flow rate (Q_f) required to achieve the average salinity change of $0.982\,\mathrm{g\,kg^{-1}\,d^{-1}}$ (from 36.194 to 23.424 g kg^{-1}) over the first specified 13 d period as follows: $Q_f = \Delta V / \Delta t = 1020.222\,\mathrm{m^3\,d^{-1}}$ or $42.509\,\mathrm{m^3\,h^{-1}}$.

A3 Statistical analysis

Following Emery and Thomson (1998), the standard deviation (σ) and the corresponding standard error (S_ε) were calculated from the variance (σ^2) as follows:

$$\sigma^2 = \frac{1}{N-1}\sum_{i=1}^{N}(x_i - \overline{x})^2 \tag{A7}$$

$$S_\varepsilon = \frac{\sigma}{\sqrt{N}} \tag{A8}$$

where x_i is the ith data point in the dataset and N is the number of data points.

Correspondingly, the Root Mean Square Difference (RMSD) and bias of the different datasets (x, y) were calculated based on the following equations:

$$\mathrm{RMSD} = \sqrt{\frac{\sum_{i=1}^{N}(y_i - x_i)^2}{N}} \tag{A9}$$

$$\mathrm{bias} = \frac{\sum_{i=1}^{N}(y_i - x_i)}{N} \tag{A10}$$

In addition, the cross-covariance (C_{xy}) and cross-correlation (r_{xy}) function was used to assess the relationship between two time series (Emery and Thomson, 1998). Assuming that x and y are the relative variables, the function was calculated as follows:

$$C_{xy}(\tau) = \frac{1}{N-k}\sum_{i=1}^{N-k}\left[y_i - \overline{y}\right]\left[x_{i+k} - \overline{x}\right] \tag{A11}$$

where $\tau = k\Delta t$ is the lag time for k sampling time increments of duration Δt

$$r_{xy}(\tau) = \frac{C_{xy}(\tau)}{\sigma_x \sigma_y} \tag{A12}$$

where σ_x and σ_y are the standard deviations for each time series.

A4 Summary of the freshening events

Table A4. Overview of the 5 defined freshening events, representing the start and end date, the duration (in days) and the highest and lowest measured absolute salinity during each corresponding event (in $g\,kg^{-1}$).

Freshening event	Start	End	Duration	Highest Salinity	Lowest Salinity
I	2 May 2023	24 June 2023	53	37.17	23.42 (on 24 May)
II	29 September 2023	16 October 2023	17	37.16	30.45 (on 2 October)
III	12 November 2023	2 December 2023	20	37.63	26.53 (on 26 November)
IV	9 April 2024	21 April 2024	12	36.16	22.27 (on 15 April)
V	20 October 2024	22 November 2024	33	35.19	14.97 (on 30 October)

Table A5. Overview of the most pronounced freshening period during each event, representing the duration (in days) during which the largest total decrease in surface salinity (in $g\,kg^{-1}$) was observed. The corresponding maximum and minimum salinity values and the respective timestamps are reported.

Freshening event	Length	Maximum salinity drop	Highest salinity	Lowest salinity	Drop start	Drop end
I	13	12.769	36.194	23.424	11 May 2023	24 May 2023
II	5	6.716	37.165	30.450	29 September 2023	2 October 2023
III	14	11.099	37.633	26.534	12 November 2023	26 November 2023
IV	6	13.893	36.164	22.271	10 April 2024	15 April 2024
V	10	20.124	35.091	14.966	20 October 2024	30 October 2024

A5 Lead-lag correlations between accumulated precipitation and river discharge responses

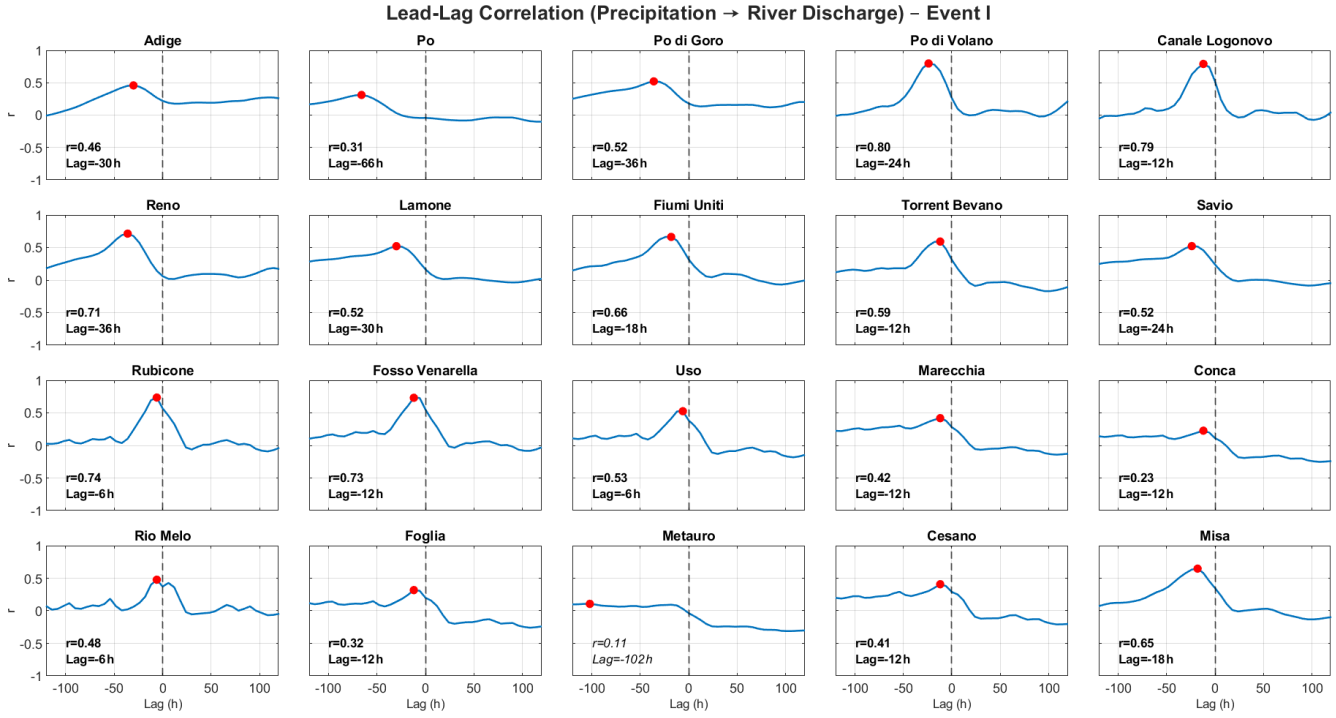


Figure A2. Lead-lag correlation plots between accumulated precipitation over the Emilia-Romagna region and the discharge of 20 rivers during the first major flooding periods that lead to the previously-defined freshening event I. Each subplot shows the Pearson correlation coefficient (r) as a function of lag time (in hours), where negative lags indicate that precipitation leads river discharge. The maximum correlation point for each river is marked with a red dot. Corresponding correlation values and lags are annotated in bold if statistically significant ($p < 0.05$), and in italics otherwise.

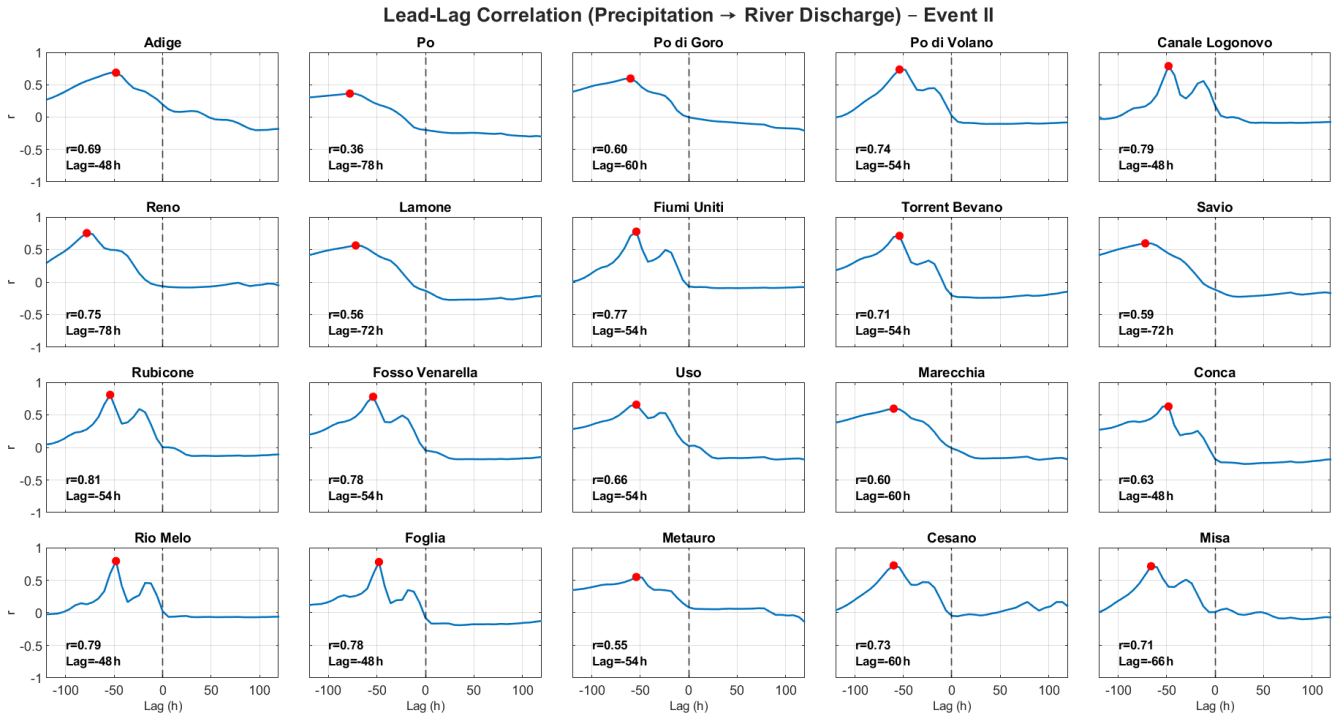


Figure A3. Same as Fig. A2 but for the second event.

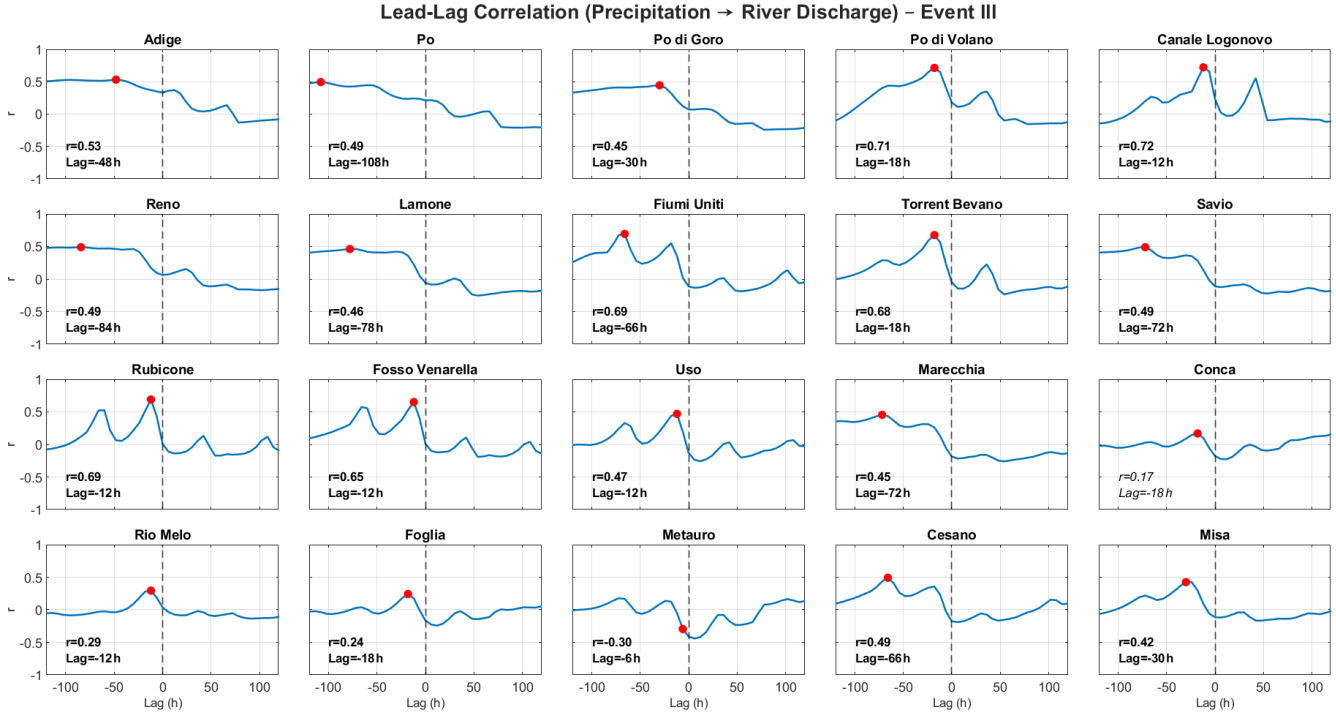


Figure A4. Same as Fig. A2 but for the third event.

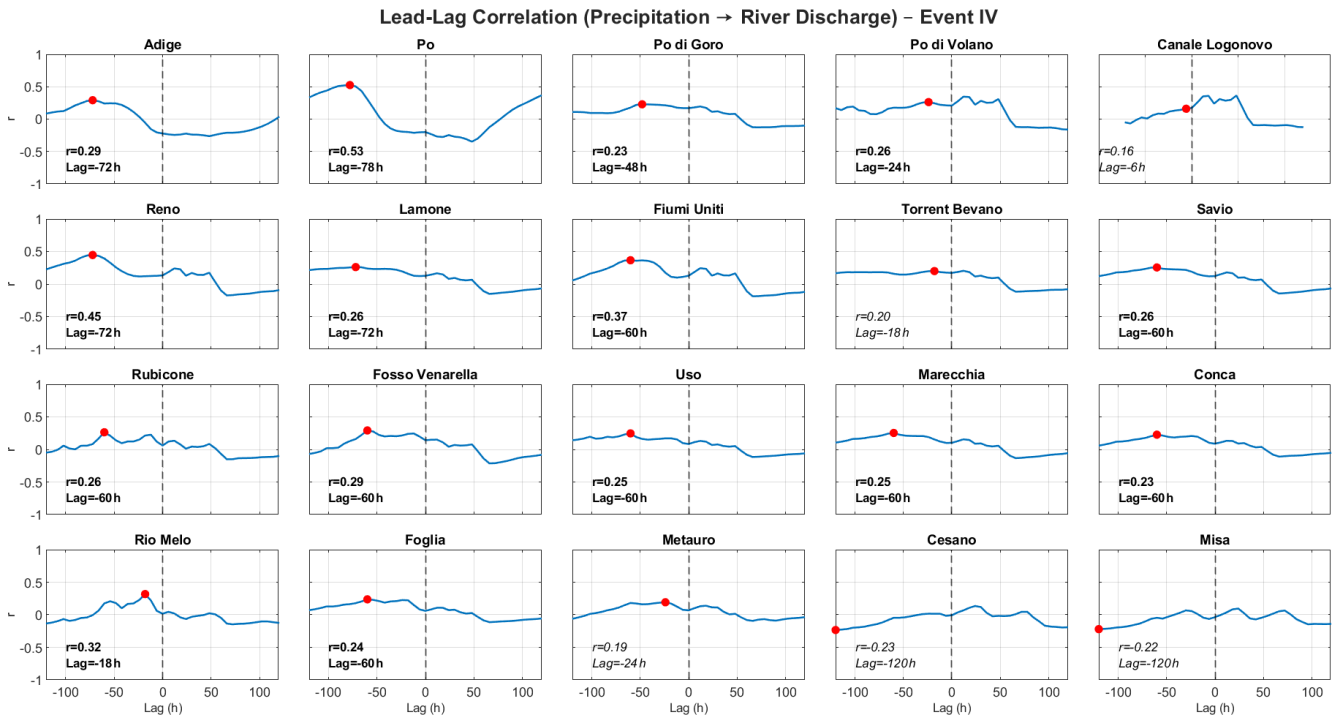


Figure A5. Same as Fig. A2 but for the fourth event.

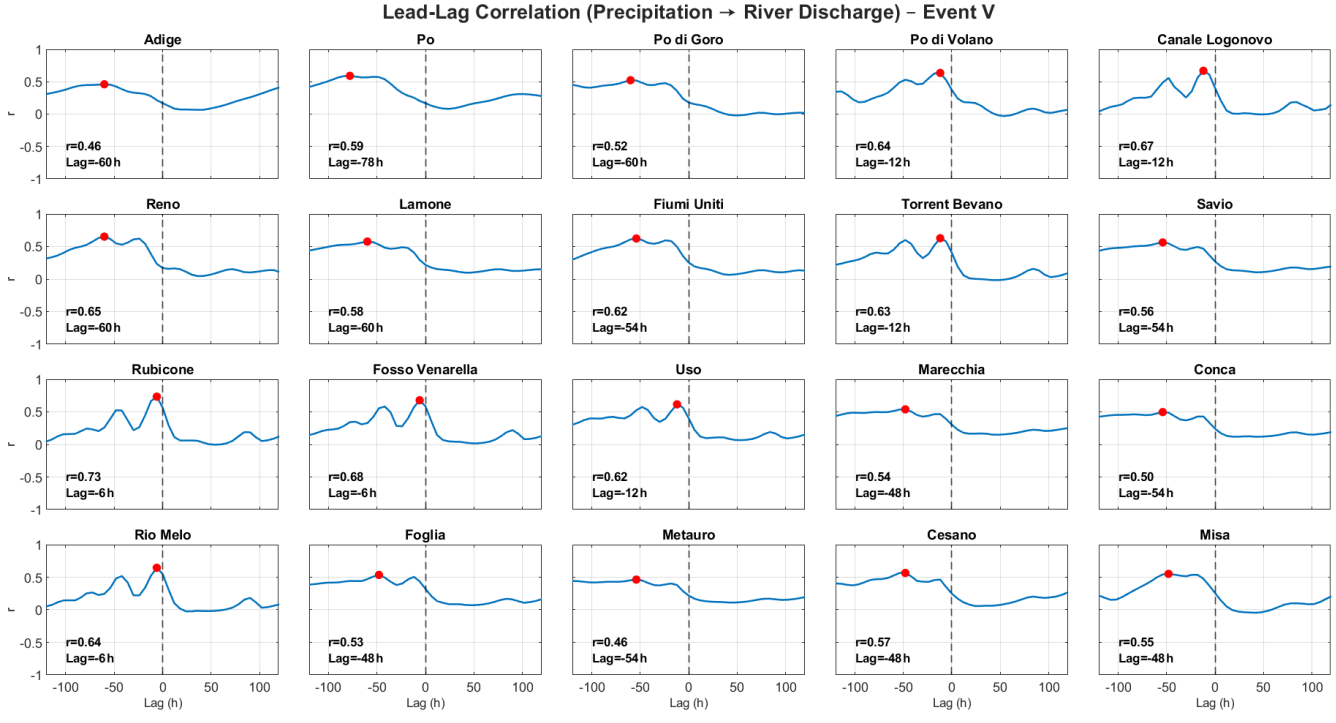


Figure A6. Same as Fig. A2 but for the fifth event.

Code and data availability. Utilized datasets as well as their availability and documentations are summarized in Table 1. MATLAB scripts used for the analyses described in this study can be obtained from the corresponding author upon reasonable request. The country and regional boundaries shown in the maps are based on GADM shapefiles (version 4.1) which are available at https://gadm.org/download_country.html (last access: 14 May 2026). The utilized colormaps are freely available in the cmocean package described by Thyng et al. (2016) and accessible via the MATLAB Central File Exchange (https://www.mathworks.com/matlabcentral/fileexchange/57773-cmocean-perceptually-uniform-colormaps, last access: 14 May 2026), containing perceptually uniform colormaps for commonly used oceanographic variables.

Author contributions. N.K. processed and analyzed the data, prepared the figures and wrote the manuscript. P.F., E.Z., F.M., contributed to the paper organization and to the interpretation of the results. P.F. and P.P. were responsible for the project management of the meteo-oceanographic buoy Fortunae offshore of Fano, and P.P. for the Meda Station offshore of Senigallia. F.M. enabled the near real-time transfer and online visualization of the corresponding data. P.P., A.C., F.M., P.F., F.M., and N.K. were involved in the maintenance and quality assurance of the meteo-oceanographic instruments. All authors reviewed the manuscript.

Competing interests. The contact author has declared that none of the authors has any competing interests.

Disclaimer. The Copernicus Marine Service offering is regularly updated to ensure it remains at the forefront of user requirements. In this process, some products may undergo replacement or renaming, leading to the removal of certain product IDs from the catalogue. If readers have any questions or require assistance regarding these modifications, please feel free to reach out to the Copernicus Marine Service user support team for further guidance. They will be able to provide the necessary information to address concerns and find suitable alternatives.

Publisher's note: Copernicus Publications remains neutral with regard to jurisdictional claims made in the text, published maps, institutional affiliations, or any other geographical representation in this paper. The authors bear the ultimate responsibility for providing appropriate place names. Views expressed in the text are those of the authors and do not necessarily reflect the views of the publisher.

Acknowledgements. The authors would like to thank and acknowledge the logistical support provided by Port Marina dei Cesari (https://marinadeicesari.it, last access: 14 May 2026), which was essential for the buoy maintenance offshore of Fano.

Review statement. This paper was edited by Piero Lionello and reviewed by two anonymous referees.

References

Arrighi, C. and Domeneghetti, A.: Brief communication: On the environmental impacts of the 2023 floods in Emilia-Romagna (Italy), Nat. Hazards Earth Syst. Sci., 24, 673–679, https://doi.org/10.5194/nhess-24-673-2024, 2024.

Colella, S., Böhm, E., Cesarini, C., Jutard, Q., and Brando, V. E.: EU Copernicus Marine Service Product User Manual for Mediterranean Sea, Bio-Geo-Chemical, L4, monthly means, daily gapfree and climatology Satellite Observations (Near Real Time), OCEANCOLOUR_MED_BGC_L4_NRT_009_142, Issue 5.0, Mercator Ocean International, https://documentation.marine.copernicus.eu/PUM/CMEMS-OC-PUM.pdf (last access: 14 May 2026), 2024.

Colella, S., Brando, V.E., Di Cicco, A., D'Alimonte, D., Forneris, V., and Bracaglia, M.: EU Copernicus Marine Service Quality Information Document for is Mediterranean Sea, Bio-Geo-Chemical, L4, monthly means, daily gapfree and climatology Satellite Observations (Near Real Time), OCEANCOLOUR_MED_BGC_L4_NRT_009_142, Issue 4.1, Mercator Ocean International, https://documentation.marine.copernicus.eu/QUID/CMEMS-OC-QUID-009-141to144-151to154.pdf (last access: 14 May 2026), 2025.

Coll, M., Piroddi, C., Steenbeek, J., Kaschner, K., Ben Rais Lasram, F., Aguzzi, J., Ballesteros, E., Bianchi, C. N., Corbera, J., Dailianis, T., Danovaro, R., Estrada, M., Froglia, C., Galil, B. S., Gasol, J. M., Gertwagen, R., Gil, J., Guilhaumon, F., Kesner-Reyes, K., Kitsos, M.-S., Koukouras, A., Lampadariou, N., Laxamana, E., López-Fé de la Cuadra, C. M., Lotze, H. K., Martin, D., Mouillot, D., Oro, D., Raicevich, S., Rius-Barile, J., Saiz-Salinas, J. I., San Vicente, C., Somot, S., Templado, J., Turon, X., Vafidis, D., Villanueva, R., and Voultsiadou, E.: The biodiversity of the Mediterranean Sea: estimates, patterns, and threats, PLoS ONE, 5, e11842, https://doi.org/10.1371/journal.pone.0011842, 2010.

Copernicus Climate Change Service, Climate Data Store: ERA5 hourly data on single levels from 1940 to present, Copernicus Climate Change Service (C3S) Climate Data Store (CDS) [data set], https://doi.org/10.24381/cds.adbb2d47, 2023.

Copernicus Emergency Management Service: River discharge and related historical data from the European Flood Awareness System, Joint Research Center, Copernicus Emergency Management Service (2019), User guide, https://confluence.ecmwf.int/display/CEMS/GloFAS+User+Guide (last access: 5 May 2025), 2025.

Costanza, R., de Groot, R., Sutton, P., van der Ploeg, S., Anderson, S. J., Kubiszewski, I., Farber, S., and Turner, R. K.: Changes in the global value of ecosystem services, Global Environ. Change, 26, 152–158, https://doi.org/10.1016/j.gloenvcha.2014.04.002, 2014.

Cozzi S. and Giani, M.: River water and nutrient discharges in the Northern Adriatic Sea: Current importance and long term changes, Cont. Shelf Res., 31, 1881–1893, https://doi.org/10.1016/j.csr.2011.08.010, 2011.

Earle, M. D.: Nondirectional and Directional Wave Data Analysis Procedures, NDBC Technical Document 96-01, National Data Buoy Center, Stennis Space Center, MS, USA, 43 pp., https://www.ndbc.noaa.gov/wavemeas.pdf (last access: 19 May 2026), 1996.

Emery, W. J. and Thomson, R. E.: Data Analysis Methods in Physical Oceanography, 2nd edn., Elsevier, Amsterdam, 638 pp., ISBN 978-0-12-387782-6, 1998.

EU Copernicus Marine Service Product: Mediterranean Sea High Resolution and Ultra High Resolution Sea Surface Temperature Analysis, Mercator Ocean International [data set], https://doi.org/10.48670/moi-00172, 2024a.

EU Copernicus Marine Service Product: Mediterranean Sea Physics Analysis and Forecast, Mercator Ocean International [data set], https://doi.org/10.48670/mds-00359, 2024b.

EU Copernicus Marine Service Product: Mediterranean Sea Biogeochemistry Analysis and Forecast, Mercator Ocean International [data set], https://doi.org/10.48670/mds-00358, 2024c.

EU Copernicus Marine Service Product: Mediterranean Sea, Bio-Geo-Chemical, L4, monthly means, daily gapfree and climatology Satellite Observations (Near Real Time), Mercator Ocean International [data set], https://doi.org/10.48670/moi-00298, 2025.

Falcieri, F. M., Benetazzo, A., Sclavo, M., Russo, A., and Carniel, S.: Po River plume pattern variability investigated from model data, Cont. Shelf Res., 87, 84–95, https://doi.org/10.1016/j.csr.2013.11.001, 2014.

Fano Marine Center: High-resolution in-situ observation from the meteo-oceanographic buoy Fortunae offshore of Fano, CNR-IRBIM, UNIVPM DISVA [data set], https://fanomarinecenter.eu/it/ricerca/boa-meteo-marina (last access: 17 May 2025), 2025.

Feudale, L., Teruzzi, A., Salon, S., Bolzon, G., Lazzari, P., Di Biagio, V., Álvarez, E., Amadio, C., and Cossarini, G.: EU Copernicus Marine Service Quality Information Document for Mediterranean Sea Biogeochemical Analysis and Forecasting Product, MEDSEA_ANALYSISFORECAST_BGC_006_014, Issue 3.2, Mercator Ocean International, https://documentation.marine.copernicus.eu/QUID/CMEMS-MED-QUID-006-014.pdf (last access: 14 May 2026), 2024.

Gualtieri, L., Goglio, A. C., Clementi, E., Grandi, A., Moulin, A., Giurato, M., Aydogdu, A., Pistoia, J., Miraglio, P., Sadighrad, E., Mariani, A., and Drudi, M.: EU Copernicus Marine Service Quality Information Document for the Mediterranean Sea Physics Analysis and Forecast, MEDSEA_ANALYSISFORECAST_PHY_006_013, Issue 2.5, Mercator Ocean International, https://documentation.marine.copernicus.eu/QUID/CMEMS-MED-QUID-006-013.pdf (last access: 14 May 2026), 2024.

Goudeau, M.-L. S., Grauel, A.-L., Bernasconi, S. M., and de Lange, G. J.: Provenance of surface sediments along the southeastern Adriatic coast off Italy: An overview, Estuar. Coast. Shelf Sci., 134, 45–56, https://doi.org/10.1016/j.ecss.2013.09.009, 2013.

Hersbach, H., Bell, B., Berrisford, P., Biavati, G., Horányi, A., Muñoz Sabater, J., Nicolas, J., Peubey, C., Radu, R., Rozum, I., Schepers, D., Simmons, A., Soci, C., Dee, D., and Thépaut, J.-N.: ERA5 hourly data on single levels from 1940 to present, Copernicus Climate Change Service (C3S) Climate Data Store (CDS) [data set], https://doi.org/10.24381/cds.adbb2d47, 2023.

IOC, SCOR, and IAPSO: The international thermodynamic equation of seawater – 2010: Calculation and use of thermodynamic properties, Intergovernmental Oceanographic Commission, Manuals and Guides No. 56, UNESCO, Paris, France, 196 pp., https://www.teos-10.org/pubs/TEOS-10_Manual.pdf (last access: 12 February 2025), 2010.

IPCC: Chapter 4: Sea Level Rise and Implications for Low-Lying Islands, Coasts and Communities, in: The Ocean and Cryosphere in a Changing Climate: Special Report of the Intergovernmental Panel on Climate Change, Cambridge University Press, 321–446, https://doi.org/10.1017/9781009157964.006, 2022.

IPCC: Climate Change 2023: Synthesis Report. Contribution of Working Groups I, II and III to the Sixth Assessment Report of the Intergovernmental Panel on Climate Change, edited by: Core Writing Team, Lee, H., and Romero, J., IPCC, Geneva, Switzerland, 35–115, https://doi.org/10.59327/IPCC/AR6-9789291691647, 2023.

IRBIM-CNR: High-resolution in-situ observations from the meteo-oceanographic Meda station offshore of Senigallia, CNR-IRBIM [data set], https://gr.irbim.cnr.it/grafana/d/ddN5kDf7k/senigallia-meda?orgId=1&from=now-30d&to=now&timezone=browser (last access: 17 May 2025), 2025.

Lecci, R., Drudi, M., Grandi, A., and Clementi, E.: EU Copernicus Marine Service Product User Manual for the Mediterranean Sea Physics Analysis and Forecast, MEDSEA_ANALYSIS FORECAST_PHY_006_013, Issue 2.4, Mercator Ocean International, https://documentation.marine.copernicus.eu/PUM/CMEMS-MED-PUM-006-013.pdf (last access: 14 May 2026), 2024a.

Lecci, R., Salon, S., Bolzon, G., and Cossarini, G.: EU Copernicus Marine Service Product User Manual for Mediterranean Sea Biogeochemical Analysis and Forecasting Product, MEDSEA _ANALYSISFORECAST_BGC_006_014, Issue 2.4, Mercator Ocean International, https://documentation.marine.copernicus.eu/PUM/CMEMS-MED-PUM-006-014.pdf (last access: 14 May 2026), 2024b.

Ludwig, W., Dumont, E., Meybeck, M., and Heussner, S.: River discharges of water and nutrients to the Mediterranean and Black Sea: Major drivers for ecosystem changes during past and future decades?, Prog. Oceanogr., 80, 199–217, https://doi.org/10.1016/j.pocean.2009.02.001, 2009.

Mazzetti, C., Carton de Wiart, C., Gomes, G., Russo, C., Decremer, D., Ramos, A., Grimaldi, S., Disperati, J., Ziese, M., Schweim, C., Sanchez Garcia, R., Jacobson, T., Salamon, P., and Prudhomme, C.: River discharge and related historical data from the European Flood Awareness System, v5.0, European Commission, Joint Research Centre [data set], https://doi.org/10.24381/cds.e3458969, 2023.

McDougall, T. J. and Barker, P. M.: Getting started with TEOS-10 and the Gibbs Seawater (GSW) Oceanographic Toolbox, SCOR/IAPSO WG127, 28 pp., ISBN 978-0-646-55621-5, https://www.teos-10.org/pubs/Getting_Started.pdf (last access: 10 May 2026), 2011.

Penna, P., Moro, F., and Falco, P.: Real-time in-situ observation from the meteo-oceanographic buoy Fortunae offshore of Fano, CNR-IRBIM, UNIVPM DISVA, https://gr.irbim.cnr.it/grafana/d/afF9UzKVk/fano-meda-fmc?kiosk&orgId=1 (last access: 15 May 2025), 2025a.

Penna, P., Moro, F., and Giuliani, G.: Real-time in-situ observation from the meteo-oceanographic Meda station offshore of Senigallia, CNR-IRBIM, UNIVPM DISVA, https://www.irbim.cnr.it/sitoss-dettagli/stazione-meteo-marina-senigallia/ (last access: 17 May 2025), 2025b.

Pisano, A., Fanelli, C., Ciani, D., Tronconi, C., Cesarini, C., La Padula, F., and Buongiorno Nardelli, B.:

EU Copernicus Marine Service Product User Manual for the Mediterranean Sea High Resolution and Ultra High Resolution Sea Surface Temperature Analysis, SST_MED_SST_L4_NRT_OBSERVATIONS_010_004, Issue 5.0, Mercator Ocean International, https://documentation.marine.copernicus.eu/PUM/CMEMS-SST-PUM-010-004-012.pdf (last access: 14 May 2026), 2024a.

Pisano, A., Fanelli, C., Ciani, D., Tronconi, C., Cesarini, C., La Padula, F., and Buongiorno Nardelli, B.: EU Copernicus Marine Service Quality Information Document for the Mediterranean Sea High Resolution and Ultra High Resolution Sea Surface Temperature Analysis, SST_MED_SST_L4_NRT_OBSERVATIONS_010_004, Issue 5.0, Mercator Ocean International, https://documentation.marine.copernicus.eu/QUID/CMEMS-SST-QUID-010-004-006-012-013.pdf (last access: 14 May 2026), 2024b.

Tan, X., Wu, X., Huang, Z., Fu, J., Tan, X., Deng, S., Liu, Y., Yew Gan, T., and Liu, B.: Increasing global precipitation whiplash due to anthropogenic greenhouse gas emissions, Nat. Commun., 14, 2796, https://doi.org/10.1038/s41467-023-38510-9, 2023.

Thyng, K. M., Greene, C. A., Hetland, R. D., Zimmerle, H. M., and DiMarco, S. F.: True colors of oceanography: Guidelines for effective and accurate colormap selection, Oceanography, 29, 9–13, https://doi.org/10.5670/oceanog.2016.66, 2016.

Wang, J., Wang, Z., Wang, Y., Liu, S., and Li, Y.: Current situation and trend of marine data buoy and monitoring network technology of China, Acta Oceanol. Sin., 35, 1–10, https://doi.org/10.1007/s13131-016-0815-z, 2016.

Wright, L. D. and Nichols, C. R. (Eds.): Tomorrow's Coasts: Complex and Impermanent, Coastal Research Library, vol. 27, Springer, Cham, https://doi.org/10.1007/978-3-319-75453-6, 2019.

Zscheischler, J., Westra, S., van den Hurk, B. J. J. M., Seneviratne, S. I., Ward, P. J., Pitman, A., AghaKouchak, A., Bresch, D. N., Leonard, M., Wahl, T., and Zhang, X.: Future climate risk from compound events, Nat. Clim. Change, 8, 469–477, https://doi.org/10.1038/s41558-018-0156-3, 2018.

State Planet, 7-osr10, 18, 2026
https://doi.org/10.5194/sp-7-osr10-18-2026
© Author(s) 2026. This work is distributed under
the Creative Commons Attribution 4.0 License.

How extreme river discharge events shape coastal biogeochemical dynamics: the 2024 northern Adriatic case

Valeria Di Biagio, Stefano Querin, Carolina Amadio, Giorgio Bolzon, Laura Feudale, Stefano Piani, Simone Spada, and Gianpiero Cossarini

National Institute of Oceanography and Applied Geophysics – OGS, Trieste, Italy

Correspondence: Valeria Di Biagio (vdibiagio@ogs.it)

Received: 31 July 2025 – Discussion started: 15 September 2025
Revised: 20 February 2026 – Accepted: 27 March 2026 – Published: 30 September 2026

Abstract. In 2024, the northern Adriatic Sea experienced marked levels of eutrophication, as indicated by unusually high surface chlorophyll concentrations observed by remote sensing and in-situ measurements. In addition, exceptionally high Po river discharges, in the form of repeated and intense events, were recorded from March to June and in October.

We used Copernicus Marine Service satellite and model products for the Mediterranean Sea, together with a high-resolution (500 m) Italian coastal model, to quantify chlorophyll anomalies in the area with respect to 1999–2022 climatology and investigated the marine ecosystem functioning in connection with river discharges, phosphate input and sea surface temperature as key drivers. We found that chlorophyll values exceeded 100 % above climatological levels in early spring, followed by sustained anomalies in summer and autumn. Primary production remained elevated from the early spring onward, with a significant anomaly peaking in early summer, concurrent with renewed Po river discharges and rising sea surface temperatures.

Our findings highlight the central importance of riverine freshwater and nutrient inputs in controlling the northern Adriatic ecosystem, in combination with circulation and thermal variability. Moreover, this study shows how forecasting systems play a pivotal role in monitoring eutrophication and potential biomass accumulation in the context of episodic river extremes and increasing climate variability, with high-resolution coastal modeling providing additional valuable insights into spatial patterns and localized eutrophication dynamics.

1 Introduction: Po river discharges and coastal blooms in northern Adriatic Sea in 2024

A Region of Freshwater Influence (ROFI) is a coastal area where riverine freshwater inputs drive stratification cycles, circulation structures and biogeochemical processes such as nutrient and carbon cycles. Typical features of these areas are marked salinity and nutrient gradients, buoyant plumes associated with higher productivity, and variability in the water column structure from seasonal to interannual scale (Simpson, 1997; Horner-Devine et al., 2015).

The northern Adriatic Sea (hereafter: NAS), the shallowest marginal region in the Mediterranean Sea (with mean depth of 35 m), is a ROFI area mainly under the influence of Po river (e.g., Raicich, 1996; Giani et al., 2012; Lipizer et al., 2014). The Po river, with a catchment area of 74000 km^2, has a mean discharge of 1500 $m^3 s^{-1}$ (i.e., the third highest values among the rivers flowing into the Mediterranean Sea) and shows a negative trend in discharge values, due both to climate change and to the increased use of river dams for irrigation and other purposes (e.g. Marini and Grilli, 2023), in addition to high annual and seasonal variability (e.g., Montanari et al., 2023). Other rivers further contribute to the freshwater inputs into the NAS to a lesser extent (e.g., Adige, Brenta, Piave and Isonzo have mean discharges in the 100–300 $m^3 s^{-1}$ range; Ludwig et al., 2009; Cozzi and Giani, 2011; Verri et al., 2018). These freshwater inputs influence the cyclonic circulation which characterises the upper layer

Published by Copernicus Publications.

Table 1. Table of the Products used in the present study.

Product ref. no.	Product ID & type	Data access	Documentation
1	MEDSEA_ANALYSISFORECAST_BGC_006_014, Numerical models	EU Copernicus Marine Service Product (2024a)	Quality Information Document (QUID): Feudale et al. (2024) Product User Manual (PUM): Lecci et al. (2024a)
2	MEDSEA_MULTIYEAR_BGC_006_008, Numerical models	EU Copernicus Marine Service Product (2022)	QUID: Teruzzi et al. (2022) PUM: Lecci et al. (2022)
3	OCEANCOLOUR_MED_BGC_L3_NRT_009_141, Satellite observations	EU Copernicus Marine Service Product (2025a)	QUID: Colella et al. (2025a) PUM: Colella et al. (2024a)
4	OCEANCOLOUR_MED_BGC_L3_MY_009_143, Satellite observations	EU Copernicus Marine Service Product (2025b)	QUID: Colella et al. (2025b) PUM: Colella et al. (2024b)
5	MEDSEA_ANALYSISFORECAST_PHY_006_013, Numerical models	EU Copernicus Marine Service Product (2024b)	QUID: Gualtieri et al. (2024) PUM: Lecci et al. (2024b)
6	MEDSEA_MULTIYEAR_PHY_006_004, Numerical models	EU Copernicus Marine Service Product (2024c)	QUID: Escudier et al. (2024) PUM: Lecci et al. (2024c)
7	Po river discharge at Pontelagoscuro station, Observations	Regional Agency for prevention, environment and energy – Arpae Emilia Romagna SIMC Product (2025)	User Guide: ARPAE SIMC – DEXT3R (2025)
8	EFAS v5.0 river discharges, Numerical models	EU Copernicus Emergency Management Service Product (2019)	Mazzetti et al. (2023)
9	National physical-biogeochemical coastal operational system (MER B32-B35), Numerical models	National Institute of Oceanography and Applied Geophysics (OGS) Product (available upon request)	Bruschi et al. (2021)

of the NAS, fueling the southward coastal current along the western coast (Western Adriatic Current, WAC, e.g., Raicich, 1996). On the eastern side of the area, a weaker and saltier Eastern Adriatic Current (EAC) flows northward along the eastern coast (e.g., Poulain, 2001).

The NAS is also subject to strong ecological impacts of human activities (e.g., agriculture, fishery, aquaculture) and between the 1970s and the mid-1980s it experienced a marked increase in eutrophication, which culminated in the occurrence of episodic hypoxia (e.g. Djakovac et al., 2015). In the following years, the NAS has undergone an oligotrophication phase (e.g. Mozetič et al., 2010; Ricci et al., 2024), ascribed both to the decreased river discharges and to a reduced anthropogenic pressure, associated with decreased phosphorus loads, mainly due a specific regulation on the production of detergents (Italian Ministerial Decree no. 413 of 13 September 1988; e.g., Cozzi and Giani, 2011; Marini and Grilli, 2023).

Given its proven sensitivity to climate and anthropogenic pressures, the NAS represents a key area for long-term environmental monitoring in the Mediterranean Sea. In this context, phytoplankton chlorophyll can be used as a valuable proxy for marine eutrophication (Descriptor 5 of the Marine Strategy Framework Directive; Ferreira et al., 2011; European Commission, 2020), reflecting variations in key drivers (e.g., nutrient availability, water column stability, and anthropogenic input) and undesirable changes in environmental conditions (e.g., excessive biomass accumulation, oxygen depletion). A continuous monitoring of both chlorophyll and Po river discharges (e.g., Mozetič et al., 2010; Vona et al., 2025), is therefore essential to assess the ecosystem health and to detect early signs of renewed occurrence of eutrophication or ecosystem regime shifts.

In this perspective, 2024 was an unusually wet year in the Po basin, especially in the first half of the year (Figs. 1 and A1, in the Appendix). Observations at Pontelagoscuro station (i.e., 44°53′10″ N, 11°36′16″ E) indicate that the Po river experienced consistently above-average discharges from March through July and again in October (https://www.arpa.veneto.it/temi-ambientali/idrologia/file-e-allegati/bollettini-risorsa-idrica/2024, last access: 5 May 2026). In particular, the hydrological status in

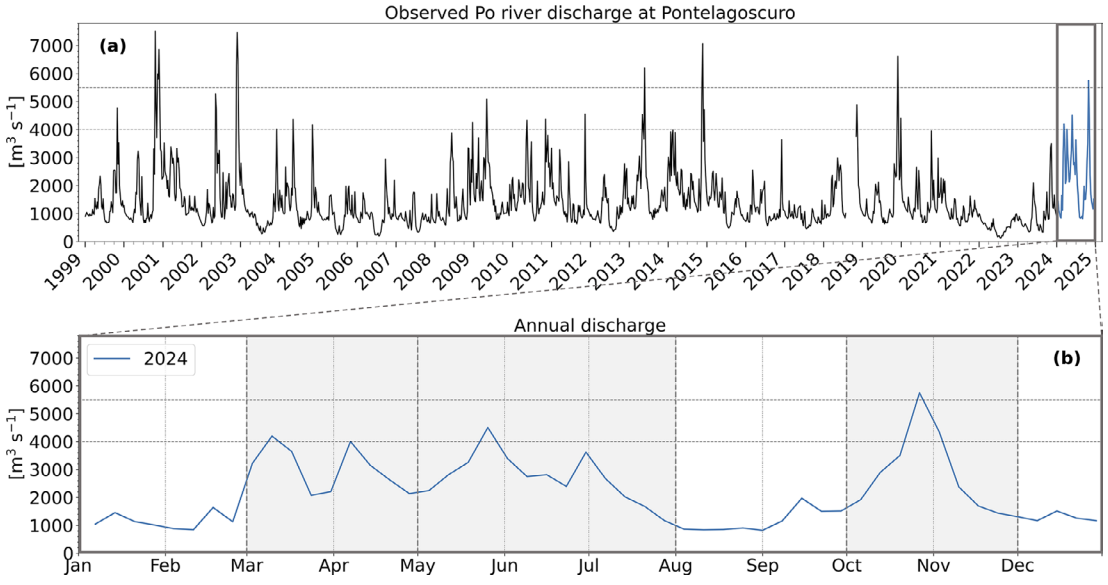


Figure 1. Po river discharge at Pontelagoscuro station (Product 7), weekly averaged: in 1999–2024 **(a)** and zoomed in 2024 **(b)**. In both panels, horizontal dotted lines indicate reference values for maximum weekly discharges in 2024 spring-early summer (i.e., 4000 $m^3 s^{-1}$) and autumn period (i.e., 5500 $m^3 s^{-1}$). In panel **(b)**, shaded areas between vertical gray dotted lines identify time periods of high discharges in 2024 (i.e., March–April, May–July, October–November).

March–May period was classified as "severe wetness" by the Italian Po River Basin Authority, on the basis of the Standardized Flow Index, estimated within the range +1.5 and +2 (in comparison with historical 1991–2020 data, https://www.adbpo.it/wp-content/uploads/2024/06/Situazione_Idrologica_dettagliata_agg06062024-2.pdf, last access: 5 May 2026) and on 21–22 October a red hydraulic alert was issued in eastern Emilia Romagna region (i.e., the coastal land of the Po river basin), as the river level surpassed level 3 (∼ 2.5 m), prompting local flood warnings (https://allertameteo.regione.emilia-romagna.it/singola-allerta/-/asset_publisher/FZPQSb6AzKtJ/Allerta-Bollettino/id/2838139, last access: 5 May 2026).

With respect to the reference period considered in this paper, i.e., 1999–2022, the annual Po river discharge was approximately 50 % higher. As shown in Fig. 1, four weekly peaks around 4000 $m^3 s^{-1}$ (two in spring and two in the early summer) characterized the first half of 2024, and one above 5500 $m^3 s^{-1}$ was detected in the autumn period (Fig. 1b). Similar values of weekly discharges in the spring-early summer occurred only 6 times in the last 25 years (i.e., in 2002, 2004, 2009, 2010, 2013, 2014, Fig. 1a), but only as single events during one year. Discharges larger than the 2024 value in autumn occurred only 4 times (i.e., 2000, 2002, 2014, 2019, same figure), and only in two cases accompanied by one event of high discharges in the spring-early summer period (i.e., 2002 and 2014). Consequently, 2024 can be considered a very anomalous year concerning Po river discharges in terms of absolute values, number of events and timing during the year.

At the same time, higher-than-usual chlorophyll values in the NAS were observed by remote sensing measurements (e.g., Fig. S11.4 in the report by Copernicus Climate Change Service, 2025). Moreover, coastal in situ data collected in the area showed much higher than usual values of chlorophyll (i.e., higher than 10 mg Chl m^{-3}) in 15 April–23 May period and, at even higher level, in 24 October–19 November period), highlighting the anomalous characteristics of the events (https://www.arpae.it/it/temi-ambientali/mare/report-e-bollettini/bollettini-mare, last access: 5 May 2026). The summer of 2024 was also marked by other anomalous phenomena: extensive mucilage events were reported along the western and eastern coasts of the NAS (e.g., Vilibić et al., 2025). Such events have become rare since the eutrophication period of the 1980s, and a direct, unequivocal link between mucilage formation and exceptional spring discharges of the Po river can not be straightforwardly established. This is because mucilage development results from multiple concurring processes, including the massive release of polysaccharide excretions by phytoplankton, under prolonged calm and sunny conditions, in strongly stratified waters (Precali et al., 2005), sometimes following intense phytoplankton blooms (e.g., Cozzi et al., 2004). Nonetheless, its occurrence in 2024 may represent another indication of the NAS system's anomalous behaviour during that year.

In this study we used Copernicus Marine Service (CMS) Mediterranean satellite and modeling products, plus other external products (please see the Table 1), to: (i) quantify the anomaly of the 2024 coastal chlorophyll in the NAS ROFI area with respect a reference period (1999–2022) encom-

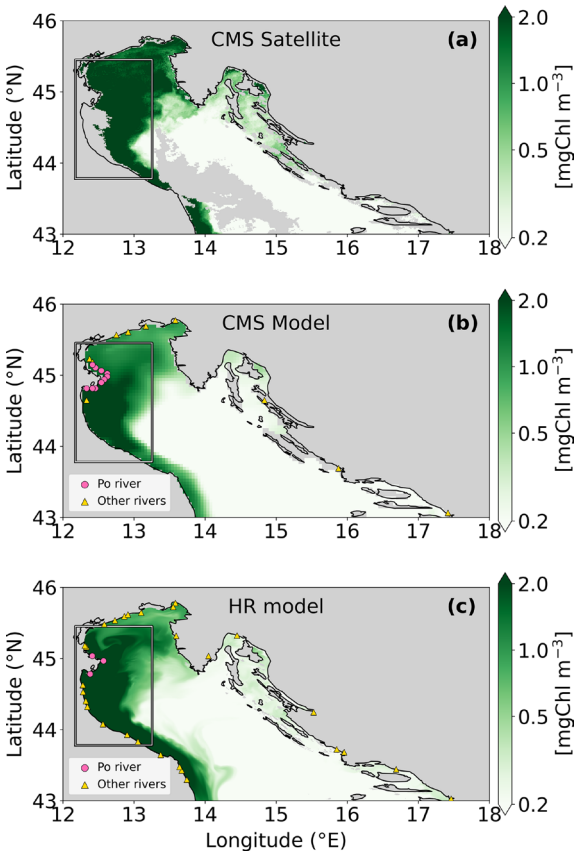


Figure 2. Surface coastal chlorophyll in the northern Adriatic Sea, according to Copernicus Marine Service Med OCTAC L3 NRT satellite chlorophyll (**a**, Product 3), Copernicus Marine Service Med-MFC NRT model (**b**, Product 1) and the National high-resolution coastal operational system (**c**, Product 9), on 4th November 2024 as an example. The box contour identifies the Po ROFI region as the study area. Implemented positions of river discharge input in models are indicated by pink circles in the case of the Po river and by yellow triangles for the others.

passing the Ocean Colour era; (ii) investigate the relationships of the events of high positive anomalies of chlorophyll with the Po river discharge and other drivers (e.g., sea surface temperature). Moreover, we used a high resolution (500 m) Italian operational system to better characterize the eutrophication spatial patterns. Figure 2 shows an example of 2024 daily surface chlorophyll in the NAS ROFI area under the Po influence (boxes in the figure), according to the CMS satellite (Fig. 2a), CMS model (Fig. 2b) and Italian HR model (Fig. 2c).

Section 2 illustrates in detail all the products used, their main features and internal dependencies (Sect. 2.1), as well as the data analysis methods we adopted (Sect. 2.2). The section Results shows our evaluation of 2024 chlorophyll anomaly with respect to the reference period for both satellite and model CMS products (Sect. 3.1) and then our analysis of the ecosystem functioning during the 2024 year (Sect. 3.2). Discussion and conclusions Section includes our general interpretation of the events and their possible impacts on marine ecosystem also in the perspective of future climate change.

2 Data and Methods

2.1 Products used and dependencies

To analyse the anomalous events in the NAS ROFI area in 2024, compared with previous years, we used the state-of-the-art models and data available at the highest temporal and spatial resolution, both for the physics and for the biogeochemistry.

CMS Med-MFC Analysis and Forecast and Reanalysis daily products (1/24° of horizontal resolution) were used for the physics (Products 5 and 6, respectively) and for the biogeochemistry (Products 1 and 2). Modelled chlorophyll concentrations in Products 1 and 2 account for weekly data assimilation of CMS OCTAC L3 satellite chlorophyll, both in near-real time and as consistent reprocessed time series (Products 3 and 4, respectively), and such satellite data are also included in this study, in comparison with modelled data.

Moreover, Analysis and Forecast physical and biogeochemical products (i.e., Products 5 and 1) currently implement daily river discharges from Copernicus Emergency Management Service (CEMS) EFAS v5 system (Product 8), providing for the first time a long-term, high frequency forcing for the freshwater input and the nutrient loads of NAS marine environment. We thus used Po river discharges from EFAS v5 to characterise the riverine input in 2024 in this study. Within the EFAS system framework, modelled data for the Po river are calibrated on observational data at Pontelagoscuro station (Product 7), and modelled and observational time series in 2024 actually show very similar statistics and temporal dynamics, despite some differences (i.e., an EFAS underestimation of river discharges in March and April and after the October peak and an overestimation of the values in September, Fig. A1 in Appendix).

Finally, to provide an even higher resolution description of the spatial patterns associated with coastal dynamics, we used a novel Italian operational marine prediction system (at 500 m horizontal resolution, hereafter: HR model; Product 9), which is an evolution of that one presented in Bruschi et al., 2021. The new system employs CMS Med-MFC products as boundary conditions, assimilates weekly chlorophyll coming from the same CMS OCTAC satellite and implements daily river discharges from EFAS v5.

It should be specified that both CMS and HR biogeochemical products feature the Biogeochemical Flux Model (BFM) to simulate the chlorophyll concentration, as the sum of the chlorophyll component of four phytoplankton functional types (i.e., diatoms, nanophytoplankton, picophytoplankton, and dinoflagellates). Chlorophyll concentrations and phyto-

plankton functional types are extensively validated in CMS Med-MFC products (Cossarini et al., 2021; Teruzzi et al., 2022; Coppini et al., 2023; Feudale et al., 2024) and the same configuration is used in the HR model system.

2.2 Methods for data analysis

To avoid potential temporal mismatches given by the weekly frequency on Tuesday of OCTAC data assimilation by the CMS near-real-time model, the analysis of both satellite and modelled chlorophyll was carried out with weekly frequency. We also maintained the weekly basis in the reconstruction of their climatological reference (i.e., long-term average) 1999–2022, and in the 2024 time series of their possible drivers (i.e., river discharge, sea surface temperature, nutrient concentration) and impacts (i.e., net primary production).

On the other hand, a monthly timescale is used to assess differences between the climatology and 2024 conditions for river discharges and ecosystem variables other than chlorophyll. This choice reflects the fact that the physical and biogeochemical reanalyses (i.e., Products 6 and 2, respectively) were driven by monthly climatological datasets for river discharges and nutrient inputs. To mitigate potential systematic biases introduced by the use of climatological forcing in reanalyses, a bias correction was applied based on the overlapping period (2023–2024) between reanalyses and corresponding NRT datasets (not shown).

To quantify the anomaly of 2024 chlorophyll with respect to the 1999–2022 climatology: (i) we identified the time periods in which 2024 weekly chlorophyll values were above the climatology; (ii) we quantified the anomaly in each period as the weekly mean difference between 2024 values and the climatological ones. In particular, we expressed the anomaly as a percentage, computed as the difference between the cumulative 2024 values and the climatological values, normalized by the corresponding climatological values:

$$\text{anomaly}\,[\%] = 100 \times \left[\left(\text{cumulative\_2024} - \text{cumulative\_clim}\right)/\text{cumulative\_clim}\right]. \quad (1)$$

3 Results

3.1 Anomaly of the 2024 events

Figure 3 shows the weekly time series of CMS Med OCTAC L3 satellite chlorophyll (Fig. 3a) and Med-MFC model surface chlorophyll (Fig. 3b) as values spatially averaged in the NAS ROFI area (box in Fig. 2) in 1999–2022, as the reference period for the climatology, and the corresponding weekly time series in 2024 compared with the weekly climatology (Fig. 3c, d).

We identified March–April, May–July, and October–November months as prolonged time periods of chlorophyll values above the climatology both for the satellite and for the model.

Table 2. 2024 anomaly of chlorophyll from CMS Med OCTAC satellite (Product 3) and Med-MFC model (Product 1), as estimates of percentage increase with respect to the 1999–2022 climatology, in early spring, late spring–early summer and autumn.

2024 anomaly (%)	March–April	May–July	October–November
OCTAC L3 sat chl	142	107	80
Med-MFC model chl	97	68	44

Despite biases in the absolute values of the chlorophyll time series from the model compared to satellite observations, which are discussed in Sect. 4, the model is consistent with observations in predicting the periods of the highest river discharges (Fig. 1b) in correspondence with the highest chlorophyll anomalies (Figs. 3c, d, respectively). In fact, we estimated that the highest chlorophyll anomaly in 2024, computed as the mean difference with the 1999–2022 climatology within each period, was in early spring (i.e., March–April months), when the anomaly is equal or higher than 100 % both for OCTAC satellite and for model (Table 2). In late spring-early summer (i.e., May–July) and in autumn (i.e., October–November) the anomaly values were progressively lower, and approximately equal to 100 % for OCTAC satellite and 70 % for modelled chlorophyll in the first case and 80 % and 45 %, respectively, in the second case.

3.2 Analysis on ecosystem functioning during 2024 events

Figure 4 shows the time series of selected forcings that potentially contributed to the 2024 anomalously high chlorophyll events, i.e., Po river discharges according to the EFAS v5 system (Fig. 4a), and CMS modelled sea surface temperature (Fig. 4b) and surface phosphate (Fig. 4c) spatially averaged in the NAS ROFI area (box in Fig. 2). Additional information on the ecosystem status (i.e., vertical stratification of the water column, nitrate concentration, zooplankton grazing and water turbidity) is reported in Fig. A3, in the Appendix.

As mentioned in Sect. 2.1, EFAS v5 river discharges (Fig. 4a) show higher-than-climatology values in the periods selected as the months with high chlorophyll values (i.e., March–April, May–July, October–November). The discharges in the first two and the last months of 2024 appear instead quite in line with climatological values.

A January–February positive anomaly in sea surface temperature (Fig. 4b), connected with low values of mixed layer depth, occurred earlier than usual (Fig. A3a in the Appendix), represents a preconditioning factor of stratification in the area. During the same period, an enrichment in phosphate (the limiting nutrient in the area) was observed (Fig. 4c), whereas nitrate remained closer to climatological values (Fig. A3b). In early spring, the additional supply of phosphate (Fig. 4c) and the increasing temperatures (temper-

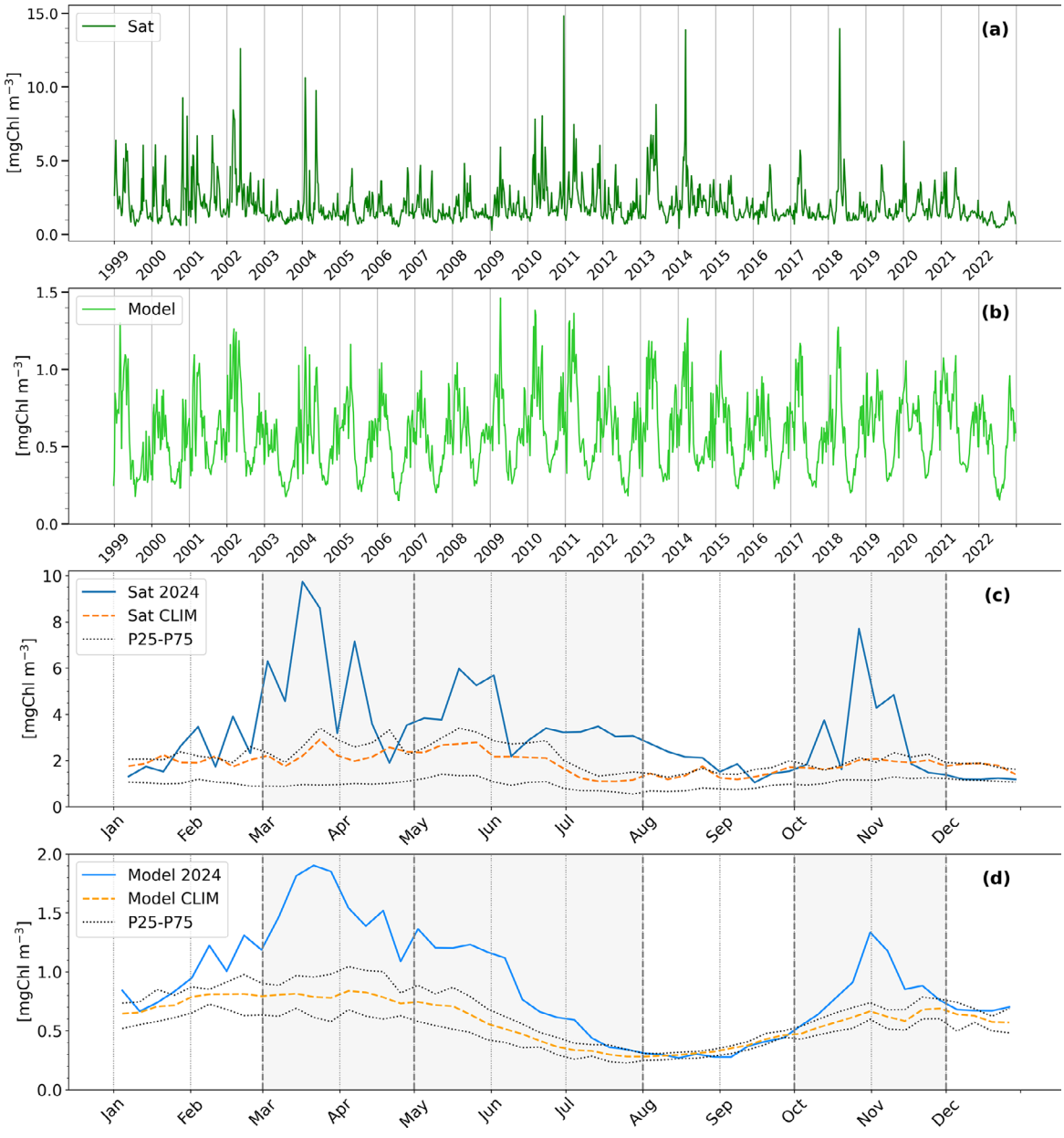


Figure 3. Weekly time series as spatial averages in the NAS box (defined in Fig. 2) for: Copernicus Marine Service Med OCTAC L3 satellite chlorophyll (Product 4) and Med-MFC model chlorophyll at surface (Product 2) in 1999–2022 (**a** and **b**, respectively), and in 2024 (Products 3 and 1, **c, d**). Dotted lines in panels **(c)** and **(d)** indicate the 1999–2022 weekly mean as the reference climatology (orange line), plus weekly 25th and 75th percentile (black lines). Time periods of interest (i.e., March–April, May–July, October–November) are also indicated as shaded areas between vertical gray dotted lines.

ature in the range 11–16 °C, i.e., 2–3 °C above the climatology; Fig. 4b), likely further enhanced by concurrent surface turbidity (Fig. A3d in the Appendix), promoted the large increase in chlorophyll shown in Fig. 3c, d.

The further nutrient input associated with the Po river discharges in May and June drove instead a lower increase in chlorophyll both in model and satellite data.We attribute it to enhanced grazing pressure (as reported in Fig. A3c, in the Appendix) or higher carbon-to-chlorophyll ratio due to photoacclimation (since the photosynthetically active radiation is maximum in June–July period, e.g., Lazzari et al., 2021).

Residual phosphate remained above the climatology in August, and it increased again after the occurrence of higher discharges in September and, above all, the maximum flow in October, when the autumn peak of chlorophyll is observed (Fig. 3c, d). Since the marine ecosystem becomes

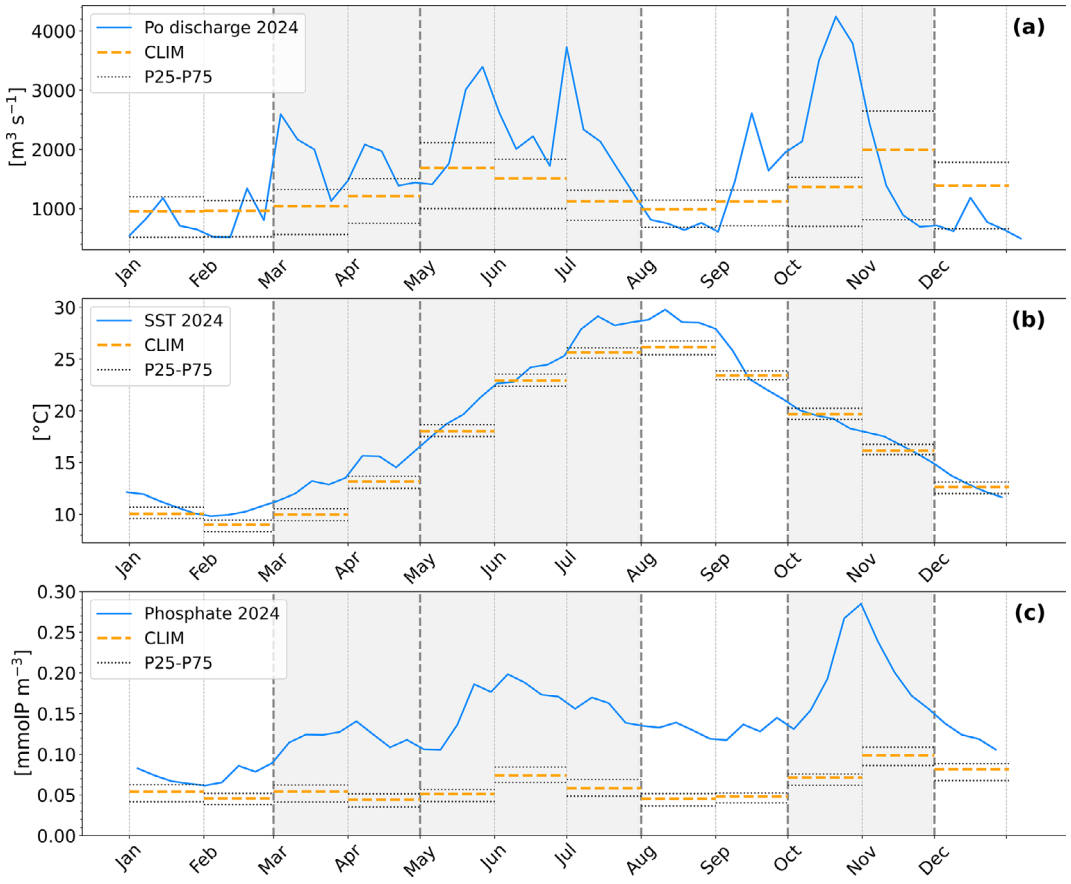


Figure 4. 2024 weekly time series (blue lines) and 1999–2022 climatology (dotted lines, orange for monthly mean, black for 25th and 75th percentile) of modelled variables: **(a)** Po river discharges at Pontelagoscuro (Product 8), and **(b)** sea surface temperature (Products 5 and 6, respectively) and **(c)** surface phosphate concentration (Products 1 and 2), spatially averaged in NAS box (Fig. 2). Phosphate climatology included the bias-correction illustrated in Sect. 2.2. Time periods of interest (March–April, May–July, October–November) are indicated as shaded areas between vertical gray dotted lines.

light-limited in autumn, we identify this feature as the main responsible for the relatively low values of chlorophyll in its autumn peak with respect to the very high values of nutrient concentration in the same period. The phosphate not used is then transported out of the NAS box along the coast (Fig. A2b, d in Appendix) and the marine ecosystem progressively converges toward the baseline climatological winter conditions.

In 2024, the surface net primary production, as an indicator for eutrophication impacts on the marine ecosystem, is always above the monthly climatology (Fig. 5a), especially in early summer, in association with the repeated Po river discharges and the high temperatures. The monthly mean maps for 2024 show that the increase was initially localised southward of the Po river mouths (indicated in Fig. 2b) in March (Fig. 5b, g), and subsequently expanded to a broader area, intensifying further during April and May months (Fig. 5c–d, h–i). We ascribe the decreasing values in June to the southward transport along the coast (Fig. 5e, j). Finally, the effect of the late June–July Po river discharges, along with the high temperatures (2–3 °C above the climatology), is a further increase of net primary production near the Po river mouths.

The analysis carried out so far highlighted that both chlorophyll patterns displayed by CMS satellite and model system (Fig. 2a, b), as well as modelled net primary production maps and anomalies (Fig. 5b–k) in the NAS area display strong coastal-offshore gradients and fronts, down to mesoscale (i.e., O(10 km) in the NAS area).

To better quantify the spatial variability of coastal processes and Po river plume we benefitted from the novel HR model system developed for Italian seas like the Adriatic Sea, with horizontal resolution of 500 m (Product 9), and used the chlorophyll maps within the box in Fig. 2b, c as a representative example of simulated patterns. The Po river plume extension toward the Istrian coast actually appears simulated more in detail by the HR model (Fig. 2c), as well as the coastal belt of high chlorophyll along the WAC. Indeed, the HR simulation captures horizontal variability at approximately twice the spatial detail of CMS, as quantified by the squared coef-

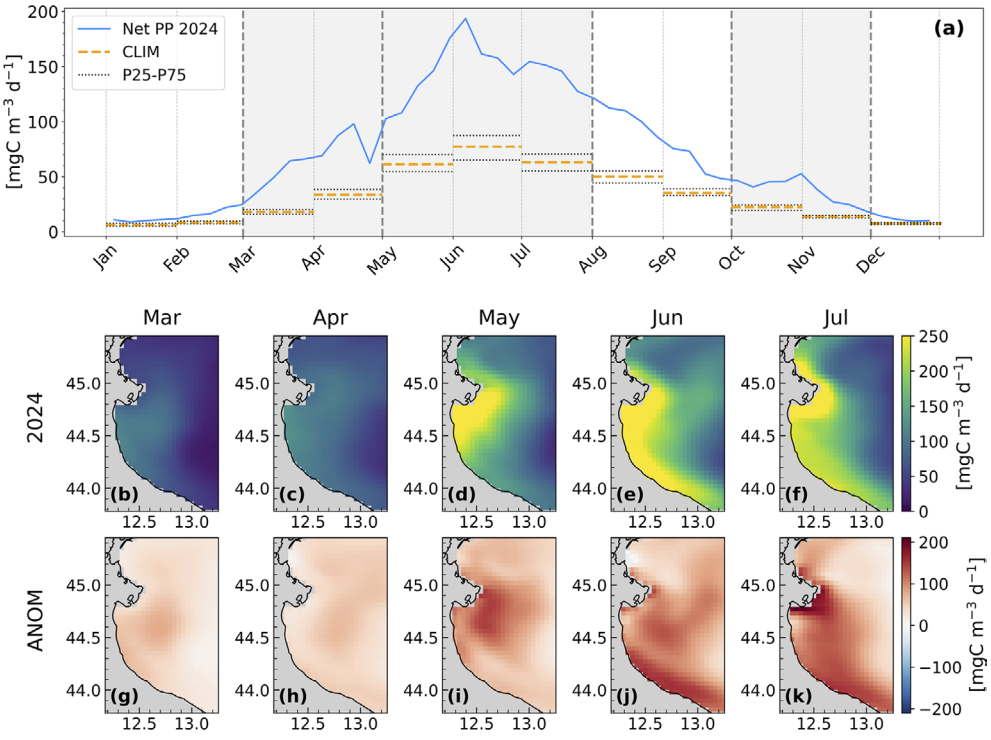


Figure 5. CMS modelled surface net primary production in the NAS box (Fig. 2) as: **(a)** spatially averaged weekly time series in 2024 (blue line, Product 1) compared with 1999–2022 monthly bias-corrected climatology (Product 2) (orange dotted line for the mean, black for 25th and 75th percentile); monthly mean maps between March and July **(b–f)** and corresponding monthly anomalies according to the 1999–2022 bias-corrected climatology (Product 2) **(g–k)**.

Table 3. Statistics of spatial variability (SCV) and spatial scale (Lcorr) of the chlorophyll patterns of the two models CMS and HR (Fig. 2b, c, respectively). SCV is the squared coefficient of variation (i.e., the ratio between the spatial variance and the spatial squared mean), and LCorr is the correlation length of the patterns.

Model	SCV	Lcorr
CMS	0.46	24 km
HR	1.20	16 km

ficient of variation and the characteristic correlation length scale (Table 3).

4 Discussion and Conclusions

The present study investigated the anomalously high values of surface phytoplankton chlorophyll observed in the NAS in 2024, as a possible indicator of eutrophication state, benefitting from state-of-the-art modeling and observational CMS products on the Mediterranean Sea and a novel HR coastal model system (Fig. 2), with a particular focus on Po river discharges as the main driver of these anomalies (Figs. 1 and 4a).

On the long-term timescale, positive correlations between a negative trend in Po river outflow and a negative chlorophyll trend have been reported in the literature (e.g., Vona et al., 2025). On the other hand, our study aims to quantify the connection between anomalous chlorophyll events and anomalies in Po river discharge, as well as other environmental drivers, on a high-frequency timescale (e.g., weekly) relevant to phytoplankton processes. In this perspective, the newly added feature of daily river discharges from CEMS EFASv5 model system implemented in the latest releases of CMS Med-MFC products constitutes an essential requirement to simulate coastal dynamics at high temporal frequency. It is worth specifying that we based our analysis on the weekly scale, to avoid possibly flawed interpretations of the results due to the weekly assimilation of satellite chlorophyll. Another potential source of uncertainties in our estimations is related to the use of modelled Po river discharges instead of observations. In fact, the EFAS discharge time series at the Pontelagoscuro station displays good overall agreement with the observed series in terms of both magnitude and timing of discharge peaks (Fig. A1), despite an underestimation of the mean annual flow (mean discharge is approximately 10 % lower than observed) and of early spring peaks (EFAS values are about 25 % lower than observed).

Within our modeling framework, we estimated and quantified 2024 anomalies in surface chlorophyll in early spring, early summer and autumn months, with decreasing values across the three periods (i.e., from 100 % to 45 % chlorophyll anomaly), coherently with anomalies estimated from satellite. However, these latter ones show higher percentages (from 140 % to 80 %). While the CMS model is very consistent with satellite in terms of temporal evolution (Fig. 3), the biases in terms of absolute values are due to limitation in the assimilation procedure of very high values of chlorophyll (i.e., values higher than 3 standard deviations from climatological values are not assimilated; Teruzzi et al., 2021) and by potential limitation of the BFM model, whose 4 phytoplankton groups have been optimized to simulate trophic open sea conditions across the Mediterranean Sea (Salon et al., 2019), to reproduce very high values of specific phytoplankton groups which can occur only in coastal areas near the major rivers. On the other hand, satellite observations potentially exhibit high uncertainties according to values of the quality index which are higher than 3 in large areas in the daily maps of the events (not shown).

We actually interpreted the anomalies in chlorophyll values in light of the anomalies in Po discharge (Fig. 4a) values, and to the associated nutrient loads, represented by the concentrations of CMS modelled phosphate as the limiting nutrient in the Mediterranean Sea and in the NAS (Fig. 4c). Moreover, the high levels of phosphate with respect to climatology (Fig. 4c), as well as the high temperatures (Fig. 4b) and an earlier-than usual and strong vertical stratification (Fig. A3 in the Appendix), already present in January and February 2024, further enhanced the spring peaks of chlorophyll. On the other hand, lower levels of light naturally present in autumn prevented high chlorophyll peaks, despite huge amounts of phosphate supplied by the Po river flood at the end of October, whose residual amount was transported southward from the coastal Western Adriatic Current (WAC).

We propose the use of net primary production as an indicator to assess potential disfunctioning of the coastal marine ecosystem in terms of accumulation of organic matter. Even if a detailed analysis is out of the scope of the present publication due to length constraints, the particulate organic matter produced during intense positive anomalies of net primary production with respect to the climatology, especially in early summer (Fig. 5), is either transported alongshore or settles on the seabed and undergoes remineralization. This process leads to oxygen depletion in the subsequent period. The model reproduces a northward evolution of the spatial extent of the impacted area (Fig. A4, in the Appendix), although simulated oxygen concentrations remain above the hypoxia levels observed during the 1980s and 1990s (e.g., Djakovac et al., 2015). Additionally, potential impacts on the marine ecosystem that extend beyond organic matter accumulation and associated oxygen consumption (e.g., effects on higher trophic levels and fisheries) should also be carefully assessed in future studies.

Although the CMS model has not been designed to simulate all the processes and substances associated with the formation and accumulation of mucilage aggregates observed in the NAS during summer 2024, our findings on marine ecosystem functioning are in agreement with Vilibić et al. (2025). They highlighted, in particular, the importance of the intense vertical stratification that started in February 2024 (also shown in Fig. A3, in the Appendix) as a potential preconditioning factor for mucilage events, further enhanced by high and repeated Po river discharges and elevated temperatures (2–3 °C above climatology, according to our estimates).

In the perspective of climate change, we indeed could expect a decrease in the Mediterranean river discharges in the late spring and early summer, due to a decrease in snowfall driven by increasing temperatures (as already observed, e.g., by Bozzoli et al., 2024), and an enhanced dependence on precipitations, especially on the short-term heavy ones (as also noticed by Cavallini et al., 2024). Po river might thus exhibit a different hydrological regime in the future, oscillating between extremely dry conditions (possibly further exacerbated by the increasing water withdrawals for irrigation; Montanari et al., 2023) and episodic extreme precipitation events (Zittis et al., 2021; Tojčić et al., 2024) with anomalous impacts in the coastal dynamics as described in the present paper and that might represent a threat for the marine coastal organisms resilience (Hassoun et al., 2025).

In presence of rapidly changing meteo-hydrological conditions (e.g. huge Po river discharge in October 2024), coastal forecasting systems able to provide near-real-time and reliable information on eutrophication-related ecosystem variables can be powerful resources for early warning alerts dedicated to the coastal environmental management and socioeconomic stakeholders (e.g. aquaculture farmers) and tools for assessing impact on ecosystem functioning. In particular, high spatial characterization of offshore-coastal gradients and frontal structures is a fundamental aspect to set-up prevention and containment measures. The novel Italian operational model, which can be considered a natural extension of the operational CMS Med-MFC system, featuring EFAS v5 river discharges as boundary conditions, has demonstrated the ability to reproduce finer spatial structures associated with the Po river plume and has the potential to provide a more accurate representation of coastal dynamics related to eutrophication.

Appendix A

The appendix includes selected additional figures supporting the discussion of the model results. In particular: the comparison between EFAS and observations for Po river discharges (Fig. A1), 2024 anomalies with respect to the long-term mean for other key environmental variables (Figs. A2 and A3) and the time evolution of oxygen depletion at 30 m depth in the area during the summer period (Fig. A4).

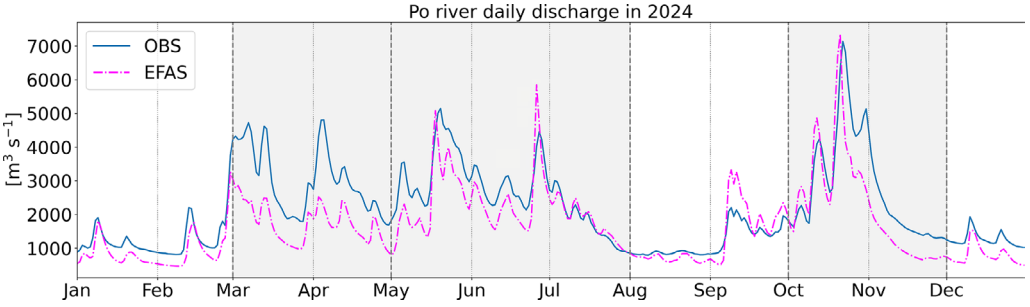


Figure A1. Daily time series of Po river discharge in Pontelagoscuro station in 2024, according to observations (blue line, Product 7) and to Copernicus Emergency Management Systems (CEMS) EFAS v5 data (magenta dotted line, Product 8).

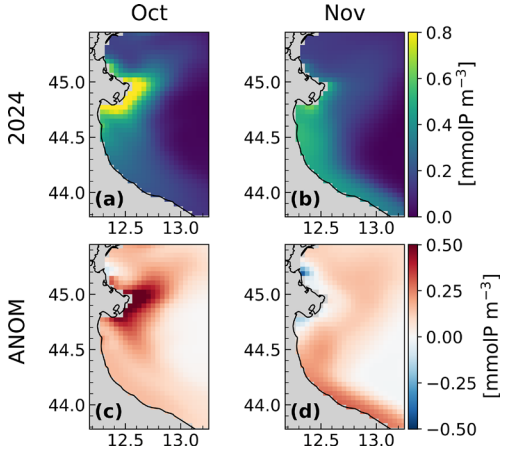


Figure A2. Monthly maps of CMS modelled surface phosphate concentration (Product 1) in 2024 in October **(a)** and November **(b)** and corresponding anomalies with respect to the 1999–2022 bias-corrected climatology (Product 2) (**c** and **d**, respectively).

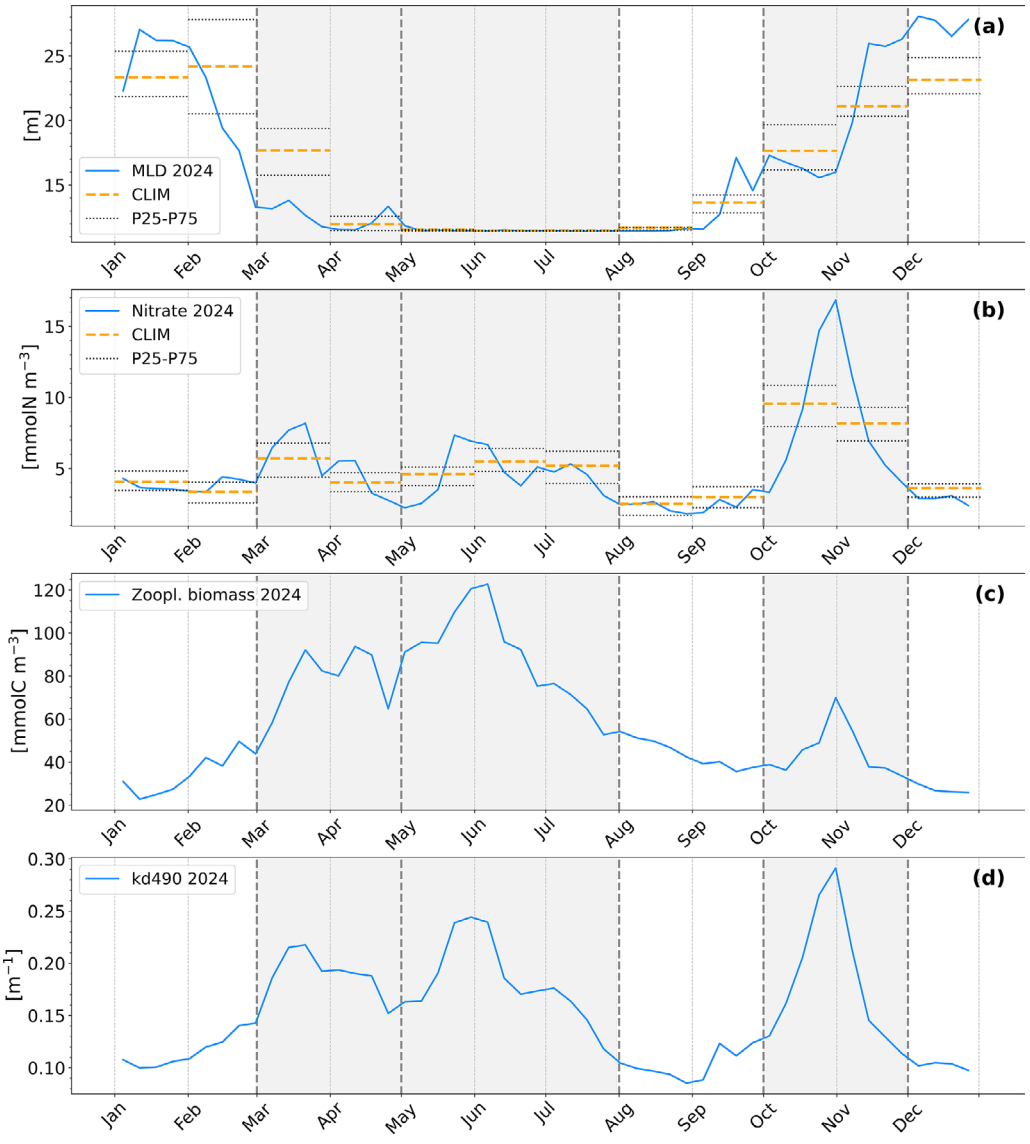


Figure A3. 2024 weekly time series (blue lines) and 1999–2022 climatology (dotted lines, orange for monthly mean, black for 25th and 75th percentile) of modelled variables: **(a)** mixed layer depth (Products 5 and 6, respectively), **(b)** nitrate concentration at surface (Products 1 and 2, respectively), **(c)** zooplankton carbon biomass at surface (Product 1), and diffuse attenuation coefficient of the downwelling irradiance at 490 nm (Product 1), spatially averaged in NAS box (Fig. 2). Nitrate climatology included the bias-correction illustrated in Sect. 2.2. Time periods of interest (March–April, May–July, October–November) are indicated as shaded areas between vertical gray dotted lines.

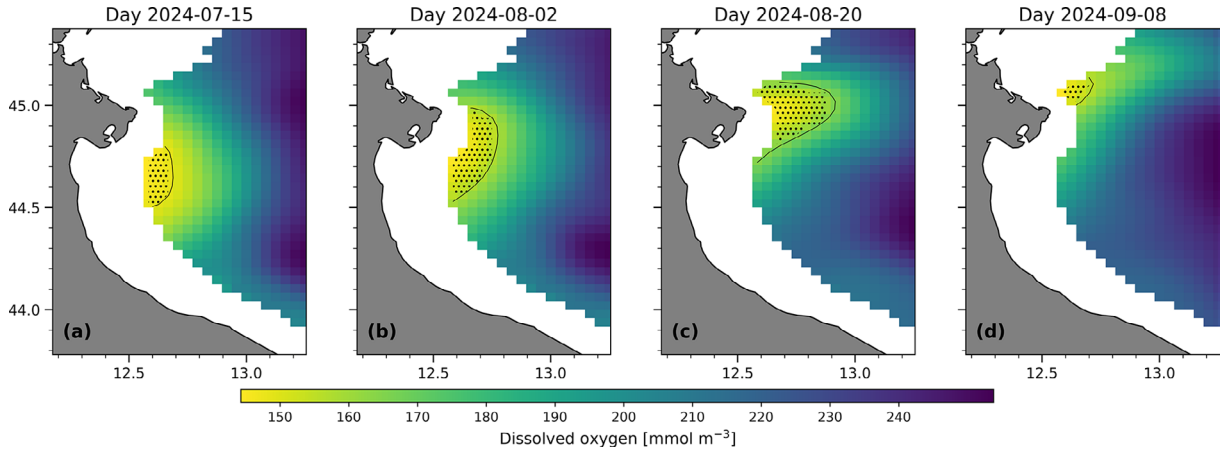


Figure A4. Selected daily maps of dissolved oxygen concentration at 30 m depth in the period July–September 2024; shaded areas refer to values lower than the precautionary threshold of 5 mg L^{-1} (i.e. 156 mmol m^{-3}) for oxygen depletion identification (Vaquer-Sunyer and Duarte, 2008). Data from Med-MFC Analysis and Forecast Biogeochemistry (Product 1).

Data availability. Products 1–8 are publicly available datasets and can be found by following the references indicated in the Table 1 of the manuscript. Product 9 is available upon request.

Author contributions. VDB and GC conceived the idea. GB, SP, SS and SQ performed the simulations. LF and CA validated the simulations. VDB conducted the formal analysis. GC and SQ supervised the work. VDB and GC wrote the first draft, with contributions from all co-authors. All the authors discussed and reviewed the submitted manuscript.

Competing interests. The contact author has declared that none of the authors has any competing interests.

Disclaimer. The Copernicus Marine Service offering is regularly updated to ensure it remains at the forefront of user requirements. In this process, some products may undergo replacement or renaming, leading to the removal of certain product IDs from the catalogue. If readers have any questions or require assistance regarding these modifications, please feel free to reach out to the Copernicus Marine Service user support team for further guidance. They will be able to provide the necessary information to address concerns and find suitable alternatives.

The European Commission is not responsible for any use that may be made of the Copernicus information or data it contains.

Publisher's note: Copernicus Publications remains neutral with regard to jurisdictional claims made in the text, published maps, institutional affiliations, or any other geographical representation in this paper. The authors bear the ultimate responsibility for providing appropriate place names. Views expressed in the text are those of the authors and do not necessarily reflect the views of the publisher.

Acknowledgements. This study has been conducted using EU Copernicus Marine Service Information. It has been also generated using Copernicus Emergency Management Service information [2024]. During the preparation of this manuscript, the authors used GPT-4o to check text grammar and spelling. Then, the authors reviewed and edited the content as needed and take full responsibility for the publication content.

Financial support. This study has been partly funded by the Mediterranean Copernicus Monitoring and Forecast Center (Reference: 24252L05-COP-MFC MED-5500 issued by Mercator Ocean) within the framework of Marine Copernicus Service. Activities developed in the framework of Actions B32-B35 of the MER (Marine Ecosystem Restoration) project, funded by the NextGenerationEU program (Italian National Recovery and Resilience Plan, investment M2C4 – I3.5).

Review statement. This paper was edited by Marilaure Grégoire and reviewed by two anonymous referees.

References

ARPAE SIMC – DEXT3R: ARPAE SIMC – DEXT3R User Guide (version 0.95), https://simc.arpae.it/dext3r/doc/GuidaDext3r.html, last access: 25 July 2025.

Bozzoli, M., Crespi, A., Matiu, M., Majone, B., Giovannini, L., Zardi, D., Brugnara, Y., Bozzo, A., Berro, D. C., Mercalli, L., and Bertoldi, G.: Long-term snowfall trends and variability in the Alps, Int. J. Climatol., 44, 4571–4591, https://doi.org/10.1002/joc.8597, 2024.

Bruschi, A., Lisi, I., De Angelis, R., Querin, S., Cossarini, G., Di Biagio, V., Salon, S., Solidoro, C., Fassina, D., Ancona, S., and Silvestri, C.: Indexes for the assessment of bacterial pollution in bathing waters from point sources: The northern Adri-

atic Sea CADEAU service, J. Environ. Manage., 293, 112878, https://doi.org/10.1016/j.jenvman.2021.112878, 2021.

Cavallini, E., Viaroli, P., Naldi, M., Saccò, M., Scibona, A., Barbieri, E., Franceschini, S., and Nizzoli, D.: Seasonal Variability and Hydrological Patterns Influence the Long-Term Trends of Nutrient Loads in the River Po, Water, 16, 2628, https://doi.org/10.3390/w16182628, 2024.

Colella, S., Böhm, E., Cesarini, C., Jutard, Q., and Brando, V. E.: EU Copernicus Marine Service Product User Manual for the Mediterranean Sea, Bio-Geo-Chemical, L3, daily Satellite Observations (Near Real Time), OCEANCOLOUR_MED_BGC_L3_NRT_009_141, Issue 5.0, Mercator Ocean International, https://documentation.marine.copernicus.eu/PUM/CMEMS-OC-PUM.pdf (last access: 25 July 2025), 2024a.

Colella, S., Böhm, E., Cesarini, C., Jutard, Q., and Brando, V. E.: EU Copernicus Marine Service Product User Manual for the Mediterranean Sea, Bio-Geo-Chemical, L3, daily Satellite Observations (1997–ongoing), OCEANCOLOUR_MED_BGC_L3_MY_009_143, Issue 5.0, Mercator Ocean International, https://documentation.marine.copernicus.eu/PUM/CMEMS-OC-PUM.pdf (last access: 25 July 2025), 2024b.

Colella, S., Brando, V. E., Di Cicco, A., D'Alimonte, D., Forneris, V., and Bracaglia, M.: EU Copernicus Marine Service Quality Information Document for the Mediterranean Sea, Bio-Geo-Chemical, L3, daily Satellite Observations (Near Real Time), OCEANCOLOUR_MED_BGC_L3_NRT_009_141, Issue 4.1, Mercator Ocean International, https://documentation.marine.copernicus.eu/QUID/CMEMS-OC-QUID-009-141to144-151to154.pdf (last access: 25 July 2025), 2025a.

Colella, S., Brando, V. E., Di Cicco, A., D'Alimonte, D., Forneris, V., and Bracaglia, M.: EU Copernicus Marine Service Quality Information Document for the Mediterranean Sea, Bio-Geo-Chemical, L3, daily Satellite Observations (1997-ongoing), OCEANCOLOUR_MED_BGC_L3_MY_009_143, Issue 4.1, Mercator Ocean International, https://documentation.marine.copernicus.eu/QUID/CMEMS-OC-QUID-009-141to144-151to154.pdf (last access: 25 July 2025), 2025b.

Copernicus Climate Change Service (C3S): European State of the Climate 2024, Copernicus Climate Change Service (C3S), https://doi.org/10.24381/14J9-S541, 2025.

Coppini, G., Clementi, E., Cossarini, G., Salon, S., Korres, G., Ravdas, M., Lecci, R., Pistoia, J., Goglio, A. C., Drudi, M., Grandi, A., Aydogdu, A., Escudier, R., Cipollone, A., Lyubartsev, V., Mariani, A., Cretì, S., Palermo, F., Scuro, M., Masina, S., Pinardi, N., Navarra, A., Delrosso, D., Teruzzi, A., Di Biagio, V., Bolzon, G., Feudale, L., Coidessa, G., Amadio, C., Brosich, A., Miró, A., Alvarez, E., Lazzari, P., Solidoro, C., Oikonomou, C., and Zacharioudaki, A.: The Mediterranean Forecasting System – Part 1: Evolution and performance, Ocean Sci., 19, 1483–1516, https://doi.org/10.5194/os-19-1483-2023, 2023.

Cossarini, G., Feudale, L., Teruzzi, A., Bolzon, G., Coidessa, G., Solidoro, C., Di Biagio, V., Amadio, C., Lazzari, P., Brosich, A., and Salon, S.: High-resolution reanalysis of the Mediterranean Sea biogeochemistry (1999–2019), Front. Mar. Sci., 8, 741486, https://doi.org/10.3389/fmars.2021.741486, 2021.

Cozzi, S. and Giani, M.: River water and nutrient discharges in the Northern Adriatic Sea: Current importance and long term changes, Cont. Shelf Res., 31, 1881–1893, https://doi.org/10.1016/j.csr.2011.08.010, 2011.

Cozzi, S., Ivančić, I., Catalano, G., Djakovac, T., and Degobbis, D.: Dynamics of the oceanographic properties during mucilage appearance in the Northern Adriatic Sea: Analysis of the 1997 event in comparison to earlier events, J. Marine Syst., 50, 223–241, https://doi.org/10.1016/j.jmarsys.2004.01.007, 2004.

Djakovac, T., Supić, N., Bernardi Aubry, F., Degobbis, D., and Giani, M.: Mechanisms of hypoxia frequency changes in the northern Adriatic Sea during the period 1972–2012, J. Marine Syst., 141, 179–189, https://doi.org/10.1016/j.jmarsys.2014.08.001, 2015.

Escudier, R., Clementi, E., Nigam, T., Aydogdu, A., Fini, E., Pistoia, J., Grandi, A., and Miraglio, P.: EU Copernicus Marine Service Quality Information Document for the Mediterranean Sea Physics Reanalysis, MEDSEA_MULTIYEAR_PHY_006_004, Issue 2.4, Mercator Ocean International, https://documentation.marine.copernicus.eu/QUID/CMEMS-MED-QUID-006-004.pdf (last access:25 July 2024), 2024.

EU Copernicus Emergency Management Service Product: River discharge and related historical data from the European Flood Awareness System, Joint Research Center, Copernicus Emergency Management Service, [data set], https://doi.org/10.24381/cds.e3458969, 2019.

EU Copernicus Marine Service Product: Mediterranean Sea Biogeochemistry Reanalysis, Mercator Ocean International [data set], https://doi.org/10.48670/mds-00374, 2022.

EU Copernicus Marine Service Product: Mediterranean Sea Biogeochemistry Analysis and Forecast, Mercator Ocean International [data set], https://doi.org/10.48670/mds-00358, 2024a.

EU Copernicus Marine Service Product: Mediterranean Sea Physics Analysis and Forecast, Mercator Ocean International [data set], https://doi.org/10.48670/mds-00359, 2024b.

EU Copernicus Marine Service Product: Mediterranean Sea Physics Reanalysis, Mercator Ocean International [data set], https://doi.org/10.48670/mds-00375, 2024c.

EU Copernicus Marine Service Product: Mediterranean Sea, Bio-Geo-Chemical, L3, daily Satellite Observations (Near Real Time), Mercator Ocean International [data set], https://doi.org/10.48670/moi-00297, 2025a.

EU Copernicus Marine Service Product: Mediterranean Sea, Bio-Geo-Chemical, L3, daily Satellite Observations (1997–ongoing), Mercator Ocean International [data set], https://doi.org/10.48670/moi-00299, 2025b.

European Commission: Commission staff working document: Review of the status of the marine environment in the European Union, SWD(2020) 61 final, Brussels, https://eur-lex.europa.eu/legal-content/EN/TXT/?uri=CELEX%3A52020SC0061 (last access: 5 May 2026), 2020.

Ferreira, J.G., Andersen, J.H., Borja, A., Bricker, S.B., Camp, J., da Silva, M.C., Garcés, E., Heiskanen, A.-S., Humborg, C., Ignatiades, L., Lancelot, C., Menesguen, A., Tett, P., Hoepffner, N., and Claussen, U.: Overview of eutrophication indicators to assess environmental status within the European Marine Strategy Framework Directive, Estuar. Coast. Shelf Sci., 93, 117–131, https://doi.org/10.1016/j.ecss.2011.03.014, 2011.

Feudale, L., Bolzon, G., Lazzari, P., Salon, S., Teruzzi, A., Di Biagio, V., Coidessa, G., Álvarez, E., Amadio, C., and Cossarini, G.: EU Copernicus Marine Service Quality Information Document for the Mediterranean Sea Biogeochemistry Analysis and Forecast, MEDSEA_ANALYSISFORECAST_BGC_006_014, Issue 3.2, Mercator Ocean International, https://documentation.marine.copernicus.eu/QUID/CMEMS-MED-QUID-006-014.pdf (last access: 25 July 2025), 2024.

Giani, M., Djakovac, T., Degobbis, D., Cozzi, S., Solidoro, C., and Umani, S. F.: Recent changes in the marine ecosystems of the northern Adriatic Sea, Estuar. Coast. Shelf Sci., 115, 1–13, https://doi.org/10.1016/j.ecss.2012.08.023, 2012.

Gualtieri, L., Goglio, A. C., Clementi, E., Grandi, A., Moulin, A., Giurato, M., Aydogdu, A., Pistoia, J., Miraglio, P., Sadighrad, E., Mariani, A., and Drudi, M.: EU Copernicus Marine Service Quality Information Document for the Mediterranean Sea Physics Analysis and Forecast, MEDSEA_ANALYSISFORECAST_PHY_006_013, Issue 2.5, Mercator Ocean International, https://documentation.marine.copernicus.eu/QUID/CMEMS-MED-QUID-006-013.pdf (last access: 25 July 2025), 2024.

Hassoun, A. E. R., Mojtahid, M., Merheb, M., Lionello, P., Gattuso, J.-P., and Cramer, W.: Climate change risks on key open marine and coastal mediterranean ecosystems, Sci. Rep., 15, https://doi.org/10.1038/s41598-025-07858-x, 2025.

Horner-Devine, A. R., Hetland, R. D., and MacDonald, D. G.: Mixing and Transport in Coastal River Plumes, Annu. Rev. Fluid Mech., 47, 569–594, https://doi.org/10.1146/annurev-fluid-010313-141408, 2015.

Lazzari, P., Salon, S., Terzić, E., Gregg, W. W., D'Ortenzio, F., Vellucci, V., Organelli, E., and Antoine, D.: Assessment of the spectral downward irradiance at the surface of the Mediterranean Sea using the radiative Ocean-Atmosphere Spectral Irradiance Model (OASIM), Ocean Sci., 17, 675–697, https://doi.org/10.5194/os-17-675-2021, 2021.

Lecci, R., Salon, S., Bolzon, G., and Cossarini, G.: EU Copernicus Marine Service Product User Manual for the Mediterranean Sea Biogeochemistry Reanalysis, MEDSEA_MULTIYEAR_BGC_006_008, Issue 3.2, Mercator Ocean International, https://documentation.marine.copernicus.eu/PUM/CMEMS-MED-PUM-006-008.pdf (last access: 25 July 2025), 2022.

Lecci, R., Salon, S., Bolzon, G., and Cossarini, G.: EU Copernicus Marine Service Product User Manual for the Mediterranean Sea Biogeochemistry Analysis and Forecast, MEDSEA_ANALYSISFORECAST_BGC_006_014, Issue 2.4, Mercator Ocean International, https://documentation.marine.copernicus.eu/PUM/CMEMS-MED-PUM-006-014.pdf (last access: 25 July 2025), 2024a.

Lecci, R., Drudi, M., Grandi, A., and Clementi, E.: EU Copernicus Marine Service Product User Manual for the Mediterranean Sea Physics Analysis and Forecast, MEDSEA_ANALYSISFORECAST_PHY_006_013, Issue 2.4, Mercator Ocean International, https://documentation.marine.copernicus.eu/PUM/CMEMS-MED-PUM-006-013.pdf (last access: 25 July 2025), 2024b.

Lecci, R., Drudi, M., Grandi, A., and Clementi, E.: EU Copernicus Marine Service Product User Manual for the Mediterranean Sea Physics Reanalysis, MEDSEA_MULTIYEAR_PHY_006_004, Issue 2.4, Mercator Ocean International, https://documentation.marine.copernicus.eu/PUM/CMEMS-MED-PUM-006-004.pdf (last access: 25 July 2025), 2024c.

Lipizer, M., Partescano, E., Rabitti, A., Giorgetti, A., and Crise, A.: Qualified temperature, salinity and dissolved oxygen climatologies in a changing Adriatic Sea, Ocean Sci., 10, 771–797, https://doi.org/10.5194/os-10-771-2014, 2014.

Ludwig, W., Dumont, E., Meybeck, M., and Heussner, S.: River discharges of water and nutrients to the Mediterranean and Black Sea: major drivers for ecosystem changes during past and future decades?, Prog. Oceanogr., 80, 199–217, https://doi.org/10.1016/j.pocean.2009.02.001, 2009.

Marini, M. and Grilli, F.: The role of nitrogen and phosphorus in eutrophication of the northern Adriatic Sea: history and future scenarios, Appl. Sci., 13, 9267, https://doi.org/10.3390/app13169267, 2023.

Mazzetti, C., Carton de Wiart, C., Gomes, G., Russo, C., Decremer, D., Ramos, A., Grimaldi, S., Disperati, J., Ziese, M., Schweim, C., Sanchez Garcia, R., Jacobson, T., Salamon, P., and Prudhomme, C.: River discharge and related forecasted data from the European Flood Awareness System, v5.0. European Commission, Joint Research Center (JRC) [data set], https://doi.org/10.24381/cds.9f696a7a, 2023.

Montanari, A., Nguyen, H., Rubinetti, S., Ceola, S., Galelli, S., Rubino, A., and Zanchettin, D.: Why the 2022 Po River drought is the worst in the past two centuries, Sci. Adv., 9, https://doi.org/10.1126/sciadv.adg8304, 2023.

Mozetič, P., Solidoro, C., Cossarini, G., Socal, G., Precali, R., Francé, J., Bianchi, F., De Vittor, C., Smodlaka, N., and Fonda Umani, S.: Recent trends towards oligotrophication of the northern Adriatic: evidence from chlorophyll a time series, Estuar. Coast., 33, 362–375, https://doi.org/10.1007/s12237-009-9191-7, 2010.

Poulain, P. M.: Adriatic Sea surface circulation as derived from drifter data between 1990 and 1999, J. Marine Syst., 29, 3–32, https://doi.org/10.1016/S0924-7963(01)00007-0, 2001.

Precali, R., Giani, M., Marini, M., Grilli, F., Ferrari, C. R., Pečar, O., and Paschini, E.: Mucilaginous aggregates in the northern Adriatic in the period 1999–2002: Typology and distribution, Sci. Total Environ., 353, 10–23, https://doi.org/10.1016/j.scitotenv.2005.09.066, 2005.

Raicich, F.: On the fresh balance of the Adriatic Sea, J. Marine Syst., 9, 305–319, https://doi.org/10.1016/S0924-7963(96)00042-5, 1996.

Regional Agency for prevention, environment and energy – Arpae Emilia Romagna SIMC Product: HydroMeteoClimate Service of Emilia-Romagna, Hydrological data extracted via DEXT3R, SIMC ARPAE portal, https://simc.arpae.it/dext3r/ (last access: 5 May 2026), 2025.

Ricci, F., Capellacci, S., Casabianca, S., Grilli, F., Campanelli, A., Marini, M., and Penna, A.: Variability of hydrographic and biogeochemical properties in the Northwestern Adriatic coastal waters in relation to river discharge and climate changes, Chemosphere, 361, 142486, https://doi.org/10.1016/j.chemosphere.2024.142486, 2024.

Salon, S., Cossarini, G., Bolzon, G., Feudale, L., Lazzari, P., Teruzzi, A., Solidoro, C., and Crise, A.: Novel metrics based on Biogeochemical Argo data to improve the model uncertainty

evaluation of the CMEMS Mediterranean marine ecosystem forecasts, Ocean Sci., 15, 997–1022, https://doi.org/10.5194/os-15-997-2019, 2019.

Simpson, J. H.: Physical processes in the ROFI regime, J. Marine Syst., 12, 3–15, https://doi.org/10.1016/s0924-7963(96)00085-1, 1997.

Teruzzi, A., Bolzon, G., Feudale, L., and Cossarini, G.: Deep chlorophyll maximum and nutricline in the Mediterranean Sea: emerging properties from a multi-platform assimilated biogeochemical model experiment, Biogeosciences, 18, 6147–6166, https://doi.org/10.5194/bg-18-6147-2021, 2021.

Teruzzi, A., Di Biagio, V., Feudale, L., Bolzon, G., Lazzari, P., Salon, S., Teruzzi, A., Coidessa, G., and Cossarini, G.: EU Copernicus Marine Service Quality Information Document for the Mediterranean Sea Biogeochemistry Reanalysis, MEDSEA_MULTIYEAR_BGC_006_008, Issue 3.2, Mercator Ocean International, https://documentation.marine.copernicus.eu/QUID/CMEMS-MED-QUID-006-008.pdf (last access: 25 July 2025), 2022.

Tojčić, I., Denamiel, C., and Vilibić, I.: Kilometer-scale trends, variability, and extremes of the Adriatic far-future climate (RCP 8.5, 2070–2100), Front. Mar. Sci., 11, https://doi.org/10.3389/fmars.2024.1329020, 2024.

Vaquer-Sunyer, R. and Duarte C. M. : Thresholds of hypoxia for marine biodiversity, P. Natl. Acad. Sci. USA, 105, 15452–15457, https://doi.org/10.1073/pnas.0803833105, 2008.

Verri, G., Pinardi, N., Oddo, P., Ciliberti, S. A., and Coppini, G.: River runoff influences on the Central Mediterranean overturning circulation, Clim. Dynam., 50, 1675–1703, https://doi.org/10.1007/s00382-017-3715-9, 2018.

Vilibić, I., Terzić, E., Vrdoljak, I., Dominović Novković, I., Vodopivec, M., Ciglenečki, I., Djakovac, T., and Hamer, B.: Extraordinary mucilage event in the northern Adriatic in 2024 – A glimpse into the future climate?, Estuar. Coast. Shelf Sci., 317, 109222, https://doi.org/10.1016/j.ecss.2025.109222, 2025.

Vona, I., Colella, S., Sammartino, M., Brando, V. E., and Falcini, F.: Positive correlation between the Po River discharge and ocean colour trends of Chl and TSM in the Adriatic Sea, Front. Remote Sens., 6, https://doi.org/10.3389/frsen.2025.1574347, 2025.

Zittis, G., Bruggeman, A., and Lelieveld, J.: Revisiting future extreme precipitation trends in the Mediterranean, Weather and Climate Extremes, 34, 100380, https://doi.org/10.1016/j.wace.2021.100380, 2021.

State Planet, 7-osr10, 19, 2026
https://doi.org/10.5194/sp-7-osr10-19-2026
© Author(s) 2026. This work is distributed under
the Creative Commons Attribution 4.0 License.

Mediterranean Sea warming and marine heatwaves in 2024

Blanca Fernández-Álvarez, Bàrbara Barceló-Llull, and Ananda Pascual

Institut Mediterrani d'Estudis Avançats – IMEDEA (CSIC-UIB), Esporles, Spain

Correspondence: Blanca Fernández-Álvarez (bfernandez@imedea.uib-csic.es)

Received: 7 August 2025 – Discussion started: 7 October 2025
Revised: 19 February 2026 – Accepted: 27 March 2026 – Published: 30 September 2026

Abstract. This study offers an assessment of Mediterranean Sea surface temperature (SST) trends (1982–2024) and marine heatwaves (MHWs) for the period 2002 to 2024, with a special focus on the last year, using three MHW detection approaches: a fixed baseline (1982–2011), a 20-year moving baseline, and detrended SST data. Our trend analysis reveals a significant warming signal across the basin, with an average rate of $0.032 \pm 0.001\,°C\,yr^{-1}$ and mean anomalies of 1.23 °C in 2024 relative to the 1982–2024 period. When evaluating MHW characteristics, 2024 stands out as the most extreme year of the past two decades in terms of total MHW days, regardless of the detection method. The Eastern Mediterranean (EMed) experienced record MHWs in 2024 across all three detection approaches. It recorded the highest number of MHW days and the longest mean event durations over the study period and also showed the highest mean intensities under the fixed baseline. In the Western Mediterranean (WMed), 2024 featured an exceptional number of MHW days; however, both the duration and intensity of events remained below those of 2003, 2022, and 2023, particularly when using the moving baseline and detrended methods, which reduce the influence of long-term warming. These results underscore the importance of MHWs in 2024 in the Mediterranean Sea, particularly in the EMed. In addition, this study highlights how methodological choices in MHW detection significantly shape the characterisation of extreme marine heat events in a warming climate.

1 Introduction

Marine heatwaves (MHWs) are periods of extreme sea warming that can persist from several days to months. These events can have serious ecological and socioeconomic consequences, disrupting marine ecosystems by altering species distributions, modifying individuals' behaviour and physiology and, in extreme cases, triggering mass mortality events (Garrabou et al., 2022; Smith et al., 2023; Wernberg et al., 2025). MHWs can also adversely impact economic activities, such as fisheries, aquaculture, and tourism (Smith et al., 2021, 2025b). A range of physical processes contribute to the development and persistence of MHWs, and their relative importance often depends on the event's spatial and temporal scale and its location (Holbrook et al., 2019). For longer lasting or more widespread MHWs, atmospheric forcing tends to play a more dominant role than oceanic processes (Bian et al., 2024).

The Mediterranean Sea is a region that is particularly vulnerable to the effects of climate change, with regional warming trends in this basin estimated to be up to four times higher than the global ocean average (Juza et al., 2022). In the Mediterranean Sea, MHWs can sometimes be triggered regionally by atmospheric forcing (Bonino et al., 2025; Paredes-Fortuny et al., 2025), and modified by local ocean dynamics that modulate the spatial distribution and intensity of each event (see Darmaraki et al., 2024, for a more in-depth review on events and drivers). Different drivers of MHWs also trigger the propagation in the water column; shallower MHWs are influenced by air-sea fluxes, while their penetration to deeper layers is influenced by ocean processes (Pirro et al., 2024).

Previous studies have reported an increase in MHW frequency, intensity and duration over time in the global ocean (Oliver et al., 2018) and in the Mediterranean Sea (Darmaraki

Published by Copernicus Publications.

Table 1. List of products used for the analysis of the SST trend and the MHW detection.

Ref. no.	Product ID and type	Data access	Documentation
1	SST_MED_SST_L4_REP_OBSERVATIONS_010_021, Satellite observations	EU Copernicus Marine Service Product (2024)	Product User Manual (PUM): Pisano et al. (2024a) Quality information document (QUID): Pisano et al. (2024b)

et al., 2024), with the possibility of leading to a permanent state of MHW or "saturation" in the near future (Oliver et al., 2021). However, most of these results were obtained by applying the most widespread identification method proposed by Hobday et al. (2016). This widely adopted method defines MHWs as extreme events during which the temperature exceeds the 90th percentile of the distribution of temperature of a daily climatology. The climatology is constructed over a fixed period (or baseline); consequently, the threshold against which temperatures are compared remains constant throughout all years of analysis. Under a long-term ocean warming scenario, the static nature of the fixed baseline may lead to an apparent increase in the intensity and duration of recent events, as it compares present-day temperatures to a baseline constructed from a cooler period (e.g. 1982–2011). This has led to growing interest in exploring alternative definitions and frameworks for studying MHWs in a warming climate (Amaya et al., 2023; Capotondi et al., 2024; Beyraghdar Kashkooli et al., 2025, for instance). Two key proposals are to adapt the baseline used for MHW detection to more recent climate and to remove the long-term trend (Rosselló et al., 2023; Smith et al., 2025a; Farchadi et al., 2025; Fernández-Álvarez et al., 2025). In the Mediterranean, three different baselines (fixed, moving, and detrended) have been used to study MHWs in the Balearic Sea from 2002 to 2023 (Fernández-Álvarez et al., 2025). In this study, we aim to analyse Mediterranean Sea surface temperature (SST) trends from 1982 to 2024 and marine heatwaves (MHWs) in 2002–2024, using three detection approaches: a fixed baseline (1982–2011), a 20-year moving baseline, and detrended SST data. By comparing these approaches to detect MHWs, we explore how the choice of baseline influences the results and contextualise how extreme the 2024 events were relative to those of the past two decades.

2 Dataset and Methodology

We use the Copernicus Marine Service SST product (Table 1, ref. no. 1), a L4 analysis that optimally interpolates observations from multiple satellite sensors. This gap-free, daily night-time SST dataset is provided on a $0.05° \times 0.05°$ regular grid over the Mediterranean Sea from 25 August 1981 to one month before the present. For this study, we extract data from 1 January 1982 to 31 December 2024, accounting for 43 complete years of SST data.

A MHW is an extreme event during which SST exceeds a locally defined threshold (90th percentile of a reference climatology) for at least five consecutive days (Hobday et al., 2016). The climatology is constructed in this study using three methods as in Fernández-Álvarez et al. (2025). First, a fixed baseline (1982–2011); as a result, the threshold remains constant throughout the analysis period (Hobday et al., 2016). This is the standard in MHW analysis, and, as previously noted, this detection framework is sensitive to long-term warming (Rosselló et al., 2023). Therefore, in order to differentiate MHWs from the long-term warming of the ocean we compare this methodology with two alternative approaches: the moving (or shifting) baseline method (Rosselló et al., 2023), where the climatology is updated annually (i.e. to detect events in year Y, we use the preceding 20 years to compute the 90th percentile threshold); and the detrended method (Martínez et al., 2023), where we first subtract at each grid point the long-term linear trend from the original SST time series, and then compute and apply a fixed baseline (1982–2011) threshold on the detrended data. In all cases, the remaining steps of the detection algorithm follow Hobday et al. (2016). The MHWs are calculated from 2002 to 2024, which is the common period for all the baselines. Due to the nature of the moving baseline approach, the first year for which MHWs can be consistently computed is 2002, once the initial 20-year reference window is available.

For the SST trend estimation, we first remove the mean seasonal cycle, estimated by fitting a harmonic function at each grid point and then compute the long-term SST trend using the Theil–Sen slope estimator (Fernández-Álvarez et al., 2025). Previous studies have shown that a linear fit is a good approximation of the trend in the Mediterranean Sea (Pisano et al., 2020; Simon et al., 2023). Statistical significance ($p < 0.05$) is assessed via a modified Mann–Kendall test that accounts for autocorrelation (Yue and Wang, 2004).

For each detected MHW event, we compute duration and mean intensity (average SST anomaly referred to the climatology). We also count the total number of days under MHW per year, named from here onwards MHW days. All metrics are calculated at each grid point, and then spatially averaged using area-weighted means (to account for latitude-dependent cell areas).

3 Results and Discussion

Ocean warming across the Mediterranean Sea is spatially heterogeneous (Fig. 1a): the eastern subbasins (EMed) warm more rapidly, with trends higher than $0.035 \pm 0.001\,°C\,yr^{-1}$, whereas the western subbasins (WMed) present lower trends. The lowest SST trend in the Mediterranean is $0.002 \pm 0.001\,°C\,yr^{-1}$, while the highest is $0.055 \pm 0.002\,°C\,yr^{-1}$. The Mediterranean Sea has a statistically significant warming trend of $0.032 \pm 0.001\,°C\,yr^{-1}$ when analysing spatially averaged SST data from 1982 through 2024 (Fig. 1c). The spatial distribution of the SST trend obtained for the period 1982–2024 coincides with that of previous studies based on previous versions of the same SST product, as the work by Pisano et al. (2020), where they estimated a mean warming trend of $0.041 \pm 0.006\,°C\,yr^{-1}$ from 1982 to 2018, and Denaxa et al. (2025), in which the same trend is reported, $0.041\,°C\,yr^{-1}$, but for the period 1982–2023. Pastor et al. (2020), using a different product, found a warming trend of $0.035\,°C\,yr^{-1}$ from 1982 to 2019.

The 2024 SST anomalies computed with respect to the mean values over the period 1982–2024 reach a spatial average of 1.23 °C (Fig. 1b), with maximum anomalies in the EMed exceeding 1.92 °C. When considering data only on the summer season (June–July–August), 2024 exhibits a mean anomaly of 1.63 °C, with maximums of 2.84 °C (not shown).

Regarding the time series of the averaged SST data for the whole basin, the smoothed temperatures from 2022 onwards fall above the trend line (Fig. 1c). When averaging the SST data in each sub-basin, the highest temperature is detected in 2022–2023 in the WMed and in 2024 in the EMed (Fig. 1d). The long-term warming trends differ between the two sub-basins: the WMed has a warming trend of $0.027 \pm 0.002\,°C\,yr^{-1}$, while the EMed has a higher trend of $0.034 \pm 0.001\,°C\,yr^{-1}$ (Fig. 1d). The SST trends obtained for the period 1982 to 2024 in both sub-basins are slightly lower than the trends of $0.032 \pm 0.002\,°C\,yr^{-1}$ (WMed) and $0.044 \pm 0.002\,°C\,yr^{-1}$ (EMed) reported from 1982 to 2020 by Juza et al. (2022), and the trends of $0.036 \pm 0.006\,°C\,yr^{-1}$ (WMed) and $0.048 \pm 0.006\,°C\,yr^{-1}$ (EMed) by Pisano et al. (2020), noting that these studies apply comparable but not identical definitions of the Western and Eastern Mediterranean sub-basins.

The difference between the SST trends computed here and those reported previously by other authors is likely introduced by an update of the SST product applied in June 2024; the version of the SST product that we use in this study is based on the ESA CCI SST v.3.0 (Pisano et al., 2024b). Methodological differences can also impact SST trends. Juza et al. (2022) derived their trends by fitting an ordinary least squares (OLS) regression on annual mean SST values, using Chelton (1983)'s effective-degrees-of-freedom approach to account for autocorrelation. In this study, we estimate SST trends at each grid point with the Theil–Sen slope estimator, which is more robust against outliers (Pisano et al., 2020). In addition, we first remove seasonality via harmonic decomposition rather than the $X - 11$ procedure used by Pisano et al. (2020). We have conducted a sensitivity analysis of SST trends in the Balearic Sea (western Mediterranean), which reveals that the method used can slightly modify the SST trends, but a difference of the order of $0.010\,°C\,yr^{-1}$ is only explained by the different versions of the SST product used. Similar sensitivities have been observed in satellite altimetry products, where updated versions yield different eddy kinetic energy trend estimates (Barceló-Llull et al., 2025). Using the NOAA OI SST V2.1, Ibrahim et al. (2021) found that the EMed (excluding the Adriatic) had a warming trend of $0.033 \pm 0.004\,°C\,yr^{-1}$ from 1982 to 2020, similar to the value reported in this work for the EMed from 1982–2024 ($0.034 \pm 0.001\,°C\,yr^{-1}$). The authors also used Mann-Kendall test and SST with removed seasonality.

When assessing MHWs across the entire Mediterranean, the detection method applied introduces differences in all metrics and in their interannual variability (Fig. 2). Using the fixed baseline, the Mediterranean has a temporal average of 62 MHW days per year over the common period 2002–2024, whereas applying the moving baseline yields an average of 46 d under MHW conditions. With the detrended method, the average is further reduced to 21 d under MHWs (Fig. 2a). The temporally averaged intensity and duration are also higher when using the fixed baseline, 1.71 °C and 15.6 d, than with the moving baseline, 1.60 °C and 13.5 d, and with the detrended data, 1.36 °C and 8.8 d (Fig. 2b, c).

When comparing across all the years, with the fixed baseline, most years that exceed the mean MHW days are clustered in the past decade, revealing how a fixed baseline amplifies the appearance of recent MHWs. Moreover, since the year 2011, towards the end of the reference period, MHW days show an increasing tendency, especially intensifying in the last few years (Fig. 2a). This tendency can also be observed to a lesser extent with the moving baseline and is reduced but still present with the detrended method, suggesting this increase might be due to a mechanism other than just the increase in mean warming (Fig. 2a). For the mean duration and mean intensity of MHWs, we observe a similar pattern to the MHWs days (Fig. 2b, c).

In 2024, the Mediterranean Sea experienced record high MHWs, recording more MHW days than any other year in the past two decades, regardless of the baseline definition applied (fixed, moving or detrended). Using the fixed baseline, the Mediterranean in 2024 reached 214 MHW days, surpassing the previous record of 153 d in 2023 (Fig. 2a). With a moving baseline, 2024 had MHWs over a total of 145 d, and with the detrended data over 63 d (Fig. 2a).

When considering the mean MHW duration, 2024 also set a record under the fixed baseline, with an average duration of 39.0 d. With the moving and detrended baselines, 2024 had mean durations of 26.6 and 17.8 d, respectively, only surpassed by the longest events occurred in 2003 (Fig. 2b). In terms of mean intensity, the MHWs of 2024 were above the

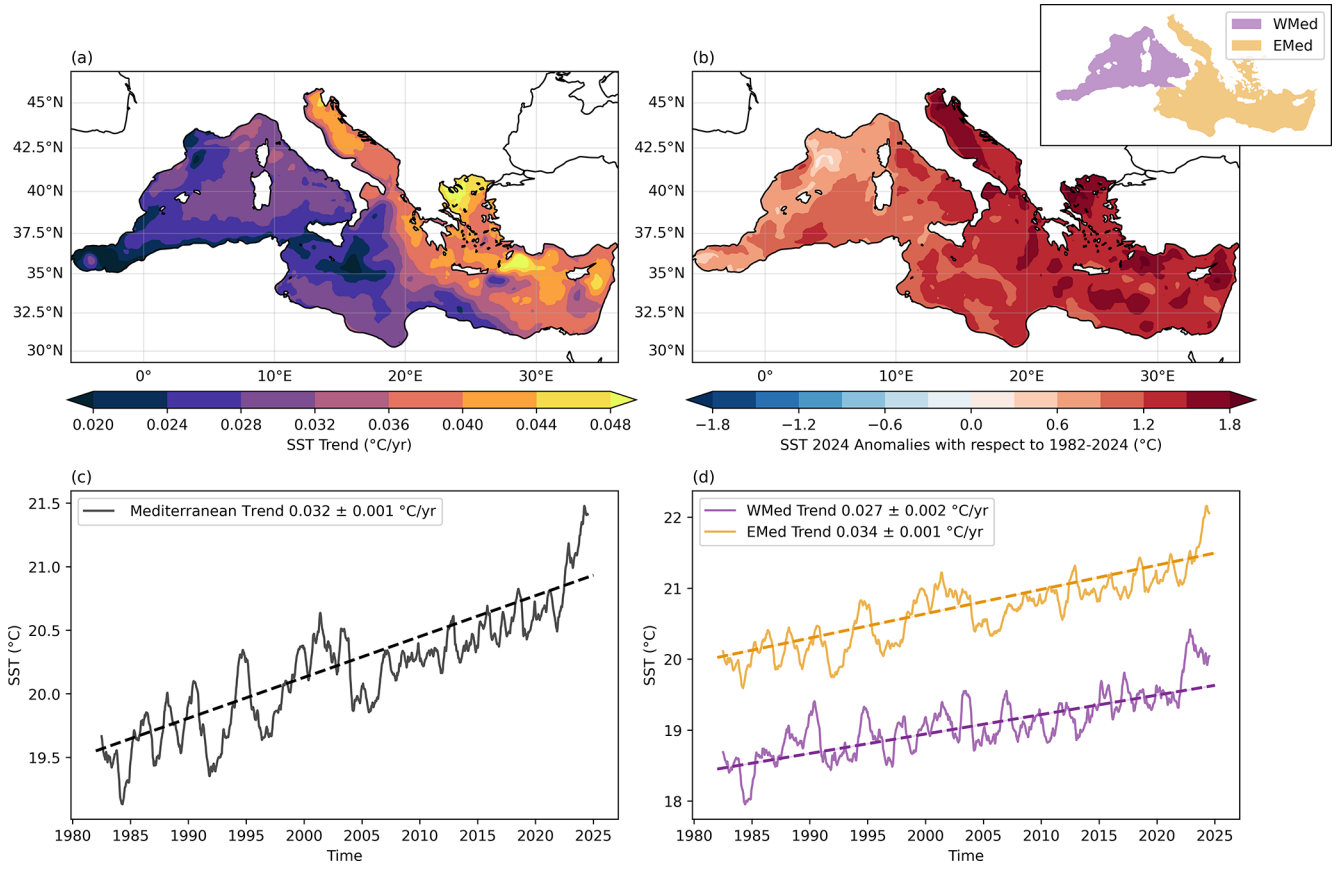


Figure 1. **(a)** Map of the statistically significant SST trends in the Mediterranean Sea computed from 1982 to 2024 ($p < 0.05$) from reprocessed satellite observations (Table 1, prod. ref. 1). **(b)** Map of the SST anomalies in 2024 computed with respect to the mean values over the period 1982–2024. The inset shows the WMed and EMed regions defined for the analysis. **(c)** Time series of the spatially averaged SST in the Mediterranean and its trend from 1982 to 2024. **(d)** Time series of the spatially averaged SST in the WMed (solid purple line) and EMed (solid orange line), and their trends (dashed lines) from 1982 to 2024. The time series **(c, d)** have been smoothed using a 365 d moving average for clearer visual representation. All trends are statistically significant ($p < 0.05$).

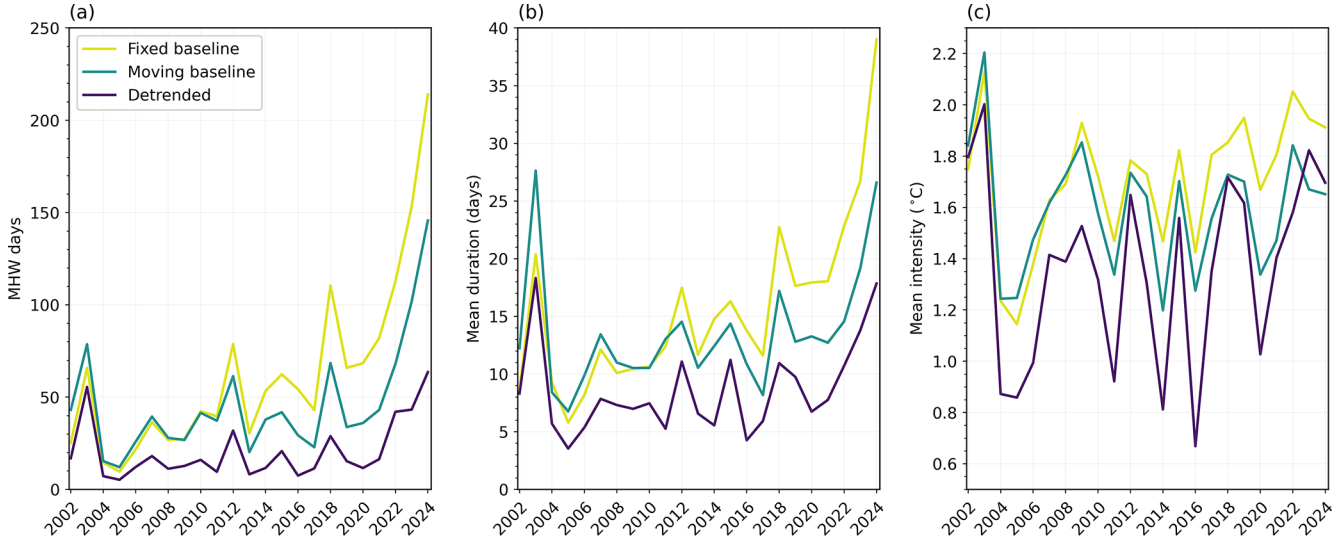


Figure 2. Spatially averaged metrics of the MHWs detected in the Mediterranean Sea from 2002 to 2024 using three detection methods: fixed baseline, moving baseline and detrended data. **(a)** Annual total number of days under MHWs. **(b)** Annual mean duration of the MHW events. **(c)** Annual average of the mean intensity of MHW events.

basin average, but less intense than previous major events, such as those in 2003, 2019, 2022, or 2023 (Fig. 2c).

When averaged over 2002–2024, the fixed-baseline method yields higher mean MHW days and longer mean durations in the EMed than in the WMed, 66 d versus 56 d on average, and 16.2 d versus 13.6 d of mean event duration, respectively. By contrast, when using detrended data, WMed records both more MHW days and longer durations than EMed, 22 MHW days and a mean duration of 9.6 d for the WMed, while 20 d of MHWs and a mean duration of 8.2 d for the EMed. Under the moving baseline, similarly to the fixed baseline, EMed has the most MHW days (47 versus 43 d), while WMed exhibits the longer mean duration out of the two subbasins (13.6 versus 13.5 d) (Fig. 3a–b, d–e).

In both the WMed and EMed, most years with above-average MHW days occur in the latter half of the record; however, this behaviour is more pronounced in the EMed. Which reflects, at least in part, the region's stronger long-term warming trend rather than purely interannual variability. Long-term warming of the sea has been pointed out as the main driver for MHW at global scales (Frölicher et al., 2018; Marcos et al., 2025), and in the Mediterranean Sea studies by Simon et al. (2023), Martínez et al. (2023), Pastor and Khodayar (2023), and Denaxa et al. (2025) confirm this. In particular, Denaxa et al. (2025) show that, across most of the Mediterranean (both EMed and WMed), trends in MHW duration and MHW days are mainly driven by the long-term trend. MHW mean intensity, however, exhibits a different behaviour: it is generally dominated by interannual variability, except in the easternmost part of the EMed and in the western part of the WMed (Denaxa et al., 2025).

Across all three detection methods, mean MHW intensities in the WMed exceed those in the EMed (Fig. 3c, f), in agreement with Hamdeno and Alvera-Azcaráte (2023) and Simon et al. (2023). The only exceptions occur in 2007, 2012, and 2024, when EMed anomalies briefly surpassed those of the WMed.

In the WMed, 2024 featured an exceptional number of MHW days (a total of 155, 96 and 37 d, for fixed, moving and detrended, respectively). Considering only the fixed baseline, 2024 was the year with the most MHW days since 2002; however, using the moving baseline, its total was surpassed only by 2022, and with detrended data by 2003, 2022, and 2023 (Fig. 3a). Mean event duration in 2024 remained below those of 2003 and 2022 across all methods (Fig. 3b), and mean intensities were similarly lower (Fig. 3c). Consequently, MHWs in 2003 remain the most intense events of the last two decades in the WMed (Juza et al., 2024; McAdam et al., 2024; Pirro et al., 2024) and surrounding areas (Castrillo-Acuña et al., 2024).

By contrast, EMed in 2024 recorded its highest number of MHW days in the study period, with 244 d (fixed), 170 d (moving), and 77 d (detrended) (Fig. 3d), with areas that locally reached up to 350 d of MHWs with the fixed baseline (Fig. 3g). It also achieved the longest mean durations across all detection methods (Fig. 3e) and the highest mean intensity under the fixed baseline (Fig. 3f). The spatial distribution of areas with higher and lower numbers of MHW days obtained with the moving baseline method (Fig. 3h) is consistent with that derived using the fixed baseline (Fig. 3g), although the overall magnitude is reduced by approximately 40 d. In contrast, when using the detrended approach, MHWs are largely restricted to the EMed, particularly its southern part (Fig. 3i).

The MHWs detected in the EMed during 2024 were first reported by Androulidakis et al. (2024), who identified 2024 as a record-breaking year in the Aegean, Ionian and Cretan Seas, all part of the eastern Mediterranean, using a fixed monthly baseline constructed with data from 1982–2024. Their results indicate a small number of MHW events compared with other years, which relates the drift towards the "saturation" previously mentioned. As large portions of the year fall under MHW conditions, the number of distinct events decreases, while their duration and cumulative intensity increase. The authors attribute these long-lasting MHWs primarily to an increase in heat flux from the atmosphere to the ocean, combined with weakened restoration mechanisms. In particular, coastal upwelling in the eastern Aegean Sea and the inflow of cooler Black Sea water, which typically act to restore lower temperatures, were not sufficient to reestablish the climatological conditions.

Consistent with this interpretation, Napolitano et al. (2025) related the 2024 Mediterranean MHWs to reduced latent and sensible heat fluxes from the ocean to the atmosphere during the early part of the year, which led to a shallower mixed layer, concentrating more heat near the surface. The reduction in both the sensitive and the latent heat fluxes is associated with decreased winds (Napolitano et al., 2025). In addition, 2024 experienced intense atmospheric heatwaves (AHWs) over Eastern Europe driven by a series of sustained high-pressure systems (atmospheric blocking) (Tolika et al., 2025). AHWs in the EMed have been shown to co-occur with MHWs (Aboelkhair et al., 2023). At the basin scale, Paredes-Fortuny et al. (2025) describe how concurrent AHW–MHW events interact. During these concurrent events, AHWs intensify MHWs by inhibiting the latent heat flux from the sea to the air, effectively trapping heat in the upper ocean. Moreover, the wind and the cloud cover decrease, allowing more shortwave radiation to reach the surface of the ocean, further enhancing upper-ocean stratification.

These mechanisms are consistent with the findings of Bonino et al. (2025), who detected that MHWs in the Mediterranean are often triggered by the persistence of atmospheric anticyclonic systems that travel from subtropical latitudes. Although the authors do not explicitly analyse AHWs, the atmospheric configurations they describe are similar to those associated with AHW development by Paredes-Fortuny et al. (2025), with both studies reporting reduced latent heat fluxes and enhanced shortwave radiation.

The difference between the three MHW detection methods used in this study lies in the choice of the baseline used to

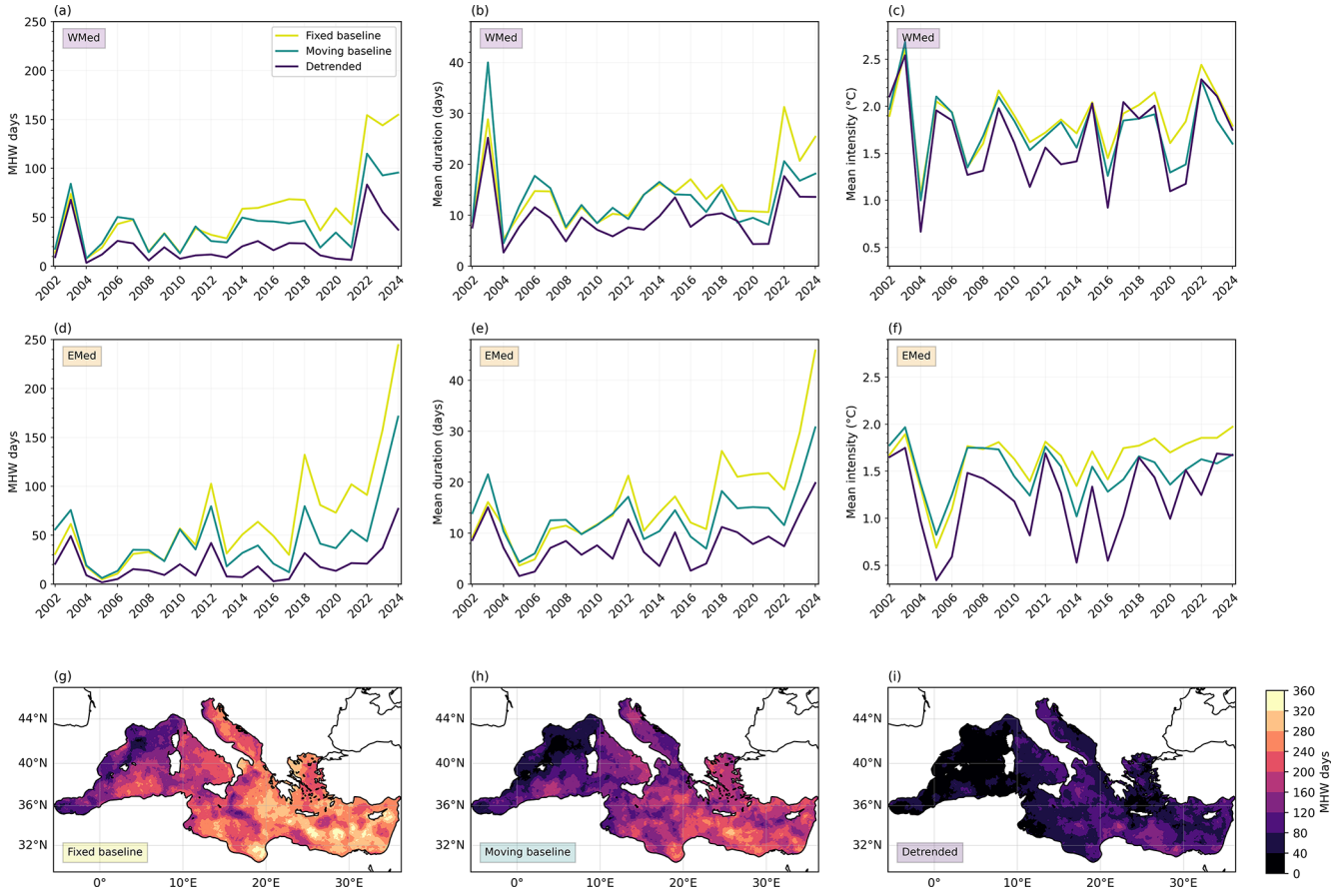


Figure 3. **(a–f)** Spatially averaged metrics of the MHWs detected in the WMed **(a–c)** and EMed **(d–e)** from 2002 to 2024 using three detection methods: fixed baseline, moving baseline and detrended data. **(a, d)** Annual total number of days under MHWs. **(b, e)** Annual mean duration of the MHW events. **(c, f)** Annual average of the mean intensity of MHW events. **(g–i)** Maps of the total number of days with MHWs (MHW days) in 2024 detected using a fixed baseline **(g)**, moving baseline **(h)** and detrended data **(i)**.

compute the statistics that define a MHW. This issue has been widely discussed in recent literature (e.g. Amaya et al., 2023; Rosselló et al., 2023; Smith et al., 2025a; Fernández-Álvarez et al., 2025), which reflects the absence of a single, universally optimal approach. Several methodological choices, including the baseline definition, the percentile used to set the threshold, the minimum event duration, or the minimum spatial extent, can substantially influence the detected magnitude of MHWs metrics (Hayward et al., 2025).

The fixed baseline MHWs are strongly influenced by the long-term warming signal, which is particularly pronounced in the Mediterranean, as shown here. For this reason, the fixed baseline turns out to be of limited usefulness for interpreting present-day MHWs in the Mediterranean. The other two approaches attempt to mitigate this effect. The moving baseline method updates the reference climatology over time, enabling the identification of MHWs relative to contemporaneous background conditions. This approach has also been proposed for ecological studies to better reflect the thermal conditions to which a species or ecosystem is exposed and may progressively adapt (Amaya et al., 2023), rather than referencing a fixed historical climate. While conceptually appealing, the practical application of a threshold for each case is challenging, as it requires detailed, species- or ecosystem-specific information on thermal tolerances, acclimation rates, and exposure, which is rarely available at basin scales. Therefore, the use of a moving baseline represents a compromise that can partially account for acclimatisation while remaining applicable at larger spatial scales. In addition, this method is sensitive to the choice of baseline length: if the window is too long, some effects of long-term warming remain; if it is too short, the resulting statistics may be less robust. Here we employ a 20-year baseline following Rosselló et al. (2023), who did a comparison between both 20- and 30-year moving baselines in the Mediterranean and found that the longer baseline yields a slightly higher number of detected MHW days.

The detrended approach removes the long-term warming. This method relies on assumptions about the shape of the long-term trend, assumed linear in our case, which may not

always adequately represent the actual evolution of warming. Moreover, the long-term warming signal is not necessarily uniform throughout the year, which complicates the interpretation of linearly detrended SST. Changes may also occur in the seasonal cycle itself, and not only in the mean temperature. Denaxa et al. (2025) found that while some parts of the Mediterranean exhibit no significant change in the seasonal variability (defined as the amplitude of the annual temperature cycle) the northern WMed shows increased variability, whereas the southern WMed and the eastern EMed have reduced their variability over the last four decades. Such changes imply that detrending may not fully isolate the climate-change signal, as modifications in seasonal amplitude can still influence whether temperatures exceed MHW thresholds. This has implications for attributing detected MHW trends either to long-term mean warming or to interannual variability; in particular, the authors showed that the spatial distribution of trends in seasonal amplitude is closely related to patterns in mean MHW intensity.

The aim of detrending is usually to isolate the climate-change signal from natural variability. However, removing only the linear or quadratic trend may result in part of the climate-change signal being retained (for example, through changes in seasonal variability), or in the removal of low-frequency natural variability. In addition, the detrended approach is inherently sensitive to the estimated long-term trend. Because this trend is inferred from the available time series, its magnitude and structure may evolve as additional years are included, potentially leading to differences in MHW detection for the same event when the record is extended. In practice, we note that this sensitivity is stronger to the SST product version than to the specific length of the analysed period.

4 Conclusions

We analysed the SST trends in the Mediterranean Sea from 1982 to 2024 and assessed MHW characteristics in 2024 relative to events of the last two decades (2002–2024). To detect MHWs we used three detection methods: a fixed baseline (1982–2011), a 20-year moving baseline and detrended SST data. The SST trend analysis reveals a statistically significant warming signal across the Mediterranean Sea, averaging $0.032 \pm 0.001\,^{\circ}\mathrm{C\,yr^{-1}}$, and a 2024 annual mean SST anomaly of 1.23 °C with respect to the mean temperature from 1982–2024. When assessing MHWs in the Mediterranean, in average 2024 recorded more MHW days than any other year of the past two decades, regardless of whether a fixed, moving, or detrended baseline was used. In the WMed, although 2024 featured an exceptional number of MHW days, neither the total days nor the mean duration or intensities surpassed those of 2003, 2022 and 2023, especially with the moving baseline and the detrended data, methods that reduce the influence of long-term warming on MHW detection. By contrast, the EMed in 2024 presented the maximum records for both MHW days and mean duration across all methods, and also the highest mean intensities in the case of the fixed baseline.

In practice, two complementary strategies can guide MHW detection. For large-scale assessment, long-term monitoring, or comparative studies, an ensemble perspective that combines results across multiple definitions can provide robust metrics and illustrate sensitivity to threshold choice. While the fixed baseline method is generally not highly informative on its own, it can provide complementary information when included in an ensemble perspective. On the other hand, for targeted analyses focused on specific locations or species (e.g. ecosystems with temperature-sensitive species), adopting a particular, context-specific approach (e.g. defining the thresholds according to the thermal tolerance of said species) ensures that MHW detection aligns with the processes and impacts most relevant to the study (Smith et al., 2025a; Farchadi et al., 2025). Regardless of the chosen strategy, it is critical to explicitly state the baseline used, as this decision affects comparability and interpretation across studies.

Code and data availability. The data used to conduct this study is listed in Table 1 and is publicly available at the Copernicus Marine Service (CMEMS) website via https://doi.org/10.48670/moi-00173 (EU Copernicus Marine Service Product, 2024). The processing and analysis scripts used in this study are publicly available at https://doi.org/10.5281/zenodo.19567880 (Fernández-Álvarez, 2026).

Author contributions. All of the authors conceptualized the study. BFÁ performed the data analysis and wrote the first draft. All of the authors contributed to discussion of the results and the preparation of the final draft.

Competing interests. The contact author has declared that none of the authors has any competing interests.

Disclaimer. The Copernicus Marine Service offering is regularly updated to ensure it remains at the forefront of user requirements. In this process, some products may undergo replacement or renaming, leading to the removal of certain product IDs from the catalogue. If readers have any questions or require assistance regarding these modifications, please feel free to reach out to the Copernicus Marine Service user support team for further guidance. They will be able to provide the necessary information to address concerns and find suitable alternatives.

Publisher's note: Copernicus Publications remains neutral with regard to jurisdictional claims made in the text, published maps, institutional affiliations, or any other geographical representation in this paper. The authors bear the ultimate responsibility for

providing appropriate place names. Views expressed in the text are those of the authors and do not necessarily reflect the views of the publisher.

Acknowledgements. We would like to thank the two anonymous reviewers for their constructive feedback, which helped improve and shape this work. The present research was carried out within the framework of the activities of the Spanish Government through the "María de Maeztu Centre of Excellence" accreditation to IMEDEA (CSIC-UIB) (grant no. CEX2021-001198). This publication contributes to grant RED2024-154139-E, ALIANZA OBSERVA: Strategic Network for Earth Observation by Satellite, funded by MICIU/AEI/10.13039/501100011033/.

Financial support. ObsSea4Clim "Ocean observations and indicators for climate and assessments" is funded by the European Union, Horizon Europe Funding Programme for Research and Innovation under grant agreement number: 101136548. ObsSea4Clim contribution no. 50. B.F.-Á. received support through an FPU grant from the Spanish Ministry of Science, Innovation and Universities (grant no. FPU23/01280). B.B.-L. is funded by the Balearic Government Vicenç Mut programme (grant no. PD/008/2022). A.P. acknowledges the FaSt-SWOT project (reference PID2021-122417NB-I00/MCIN/AEI/10.13039/501100011033/FUE).

Review statement. This paper was edited by Pierre Brasseur and reviewed by two anonymous referees.

References

Aboelkhair, H., Mohamed, B., Morsy, M., and Nagy, H.: Co-Occurrence of Atmospheric and Oceanic Heatwaves in the Eastern Mediterranean over the Last Four Decades, Remote Sens., 15, 1841, https://doi.org/10.3390/rs15071841, 2023.

Amaya, D. J., Jacox, M. G., Fewings, M. R., Saba, V. S., Stuecker, M. F., Rykaczewski, R. R., Ross, A. C., Stock, C. A., Capotondi, A., Petrik, C. M., Bograd, S. J., Alexander, M. A., Cheng, W., Hermann, A. J., Kearney, K. A., and Powell, B. S.: Marine heatwaves need clear definitions so coastal communities can adapt, Nature, 616, 29–32, https://doi.org/10.1038/d41586-023-00924-2, 2023.

Androulidakis, Y., Kolovoyiannis, V., Makris, C., and Krestenitis, Y.: Evidence of 2024 Summer as the Warmest During the Last Four Decades in the Aegean, Ionian, and Cretan Seas, Journal of Marine Science and Engineering, 12, 2020, https://doi.org/10.3390/jmse12112020, 2024.

Barceló-Llull, B., Rosselló, P., Combes, V., Sánchez-Román, A., Pujol, M. I., and Pascual, A.: Kuroshio Extension and Gulf Stream dominate the Eddy Kinetic Energy intensification observed in the global ocean, Sci. Rep., 15, 21754, https://doi.org/10.1038/s41598-025-06149-9, 2025.

Beyraghdar Kashkooli, O., Mohit Isfahani, P., and Modarres, R.: Revisiting marine heatwaves baselines in warming oceans under nonstationary condition, Sci. Total Environ., 958, 178194, https://doi.org/10.1016/j.scitotenv.2024.178194, 2025.

Bian, C., Jing, Z., Wang, H., and Wu, L.: Scale-Dependent Drivers of Marine Heatwaves Globally, Geophys. Res. Lett., 51, e2023GL107306, https://doi.org/10.1029/2023GL107306, 2024.

Bonino, G., McAdam, R., Athanasiadis, P., Cavicchia, L., Rodrigues, R. R., Scoccimarro, E., Tibaldi, S., and Masina, S.: Mediterranean summer marine heatwaves triggered by weaker winds under subtropical ridges, Nat. Geosci., 18, 848–853, https://doi.org/10.1038/s41561-025-01762-9, 2025.

Capotondi, A., Rodrigues, R. R., Sen Gupta, A., Benthuysen, J. A., Deser, C., Frölicher, T. L., Lovenduski, N. S., Amaya, D. J., Le Grix, N., Xu, T., Hermes, J., Holbrook, N. J., Martinez-Villalobos, C., Masina, S., Roxy, M. K., Schaeffer, A., Schlegel, R. W., Smith, K. E., and Wang, C.: A global overview of marine heatwaves in a changing climate, Commun. Earth Environ., 5, 701, https://doi.org/10.1038/s43247-024-01806-9, 2024.

Castrillo-Acuña, L., Alonso-Valle, A., and de Pascual-Collar, Á.: Characterization of marine heat waves in the Iberia–Biscay–Ireland (IBI) region in 2022, in: 8th edition of the Copernicus Ocean State Report (OSR8), edited by: von Schuckmann, K., Moreira, L., Grégoire, M., Marcos, M., Staneva, J., Brasseur, P., Garric, G., Lionello, P., Karstensen, J., and Neukermans, G., Copernicus Publications, State Planet, 4-osr8, 17, https://doi.org/10.5194/sp-4-osr8-17-2024, 2024.

Chelton, D. B.: Effects of sampling errors in statistical estimation, Deep-Sea Res. Pt. A, 30, 1083–1103, https://doi.org/10.1016/0198-0149(83)90062-6, 1983.

Darmaraki, S., Denaxa, D., Theodorou, I., Livanou, E., Rigatou, D., Raitsos E., D., Stavrakidis-Zachou, O., Dimarchopoulou, D., Bonino, G., McAdam, R., Organelli, E., Pitsouni, A., and Parasyris, A.: Marine Heatwaves in the Mediterranean Sea: A Literature Review, Mediterr. Mar. Sci., 25, 586–620, https://doi.org/10.12681/mms.38392, 2024.

Denaxa, D., Korres, G., Darmaraki, S., and Hatzaki, M.: Insights into sea surface temperature variability and the impact of long-term warming on marine heatwaves in the Mediterranean Sea, in: 9th edition of the Copernicus Ocean State Report (OSR9), edited by: von Schuckmann, K., Moreira, L., de Pascual Collar, Á., Grégoire, M., Brasseur, P., Garric, G., Karstensen, J., Lionello, P., Marcos, M., Poulain, P.-M., and Staneva, J., Copernicus Publications, State Planet, 6-osr9, 10, https://doi.org/10.5194/sp-6-osr9-10-2025, 2025.

EU Copernicus Marine Service Product: Mediterranean Sea – High Resolution L4 Sea Surface Temperature Reprocessed, Mercator Ocean International [data set], https://doi.org/10.48670/moi-00173, 2024.

Farchadi, N., McDonnell, L. H., Ryan, S., Lewison, R. L., and Braun, C. D.: Marine heatwaves are in the eye of the beholder, Nat. Clim. Chang., 15, 236–239, https://doi.org/10.1038/s41558-025-02257-6, 2025.

Fernández-Álvarez, B.: Code for "Mediterranean Sea Warming and Marine Heatwaves in 2024" (v1.0), Zenodo [code], https://doi.org/10.5281/zenodo.19567880, 2026.

Fernández-Álvarez, B., Barceló-Llull, B., and Pascual, A.: Tracking marine heatwaves in the Balearic Sea: temperature trends and the role of detection methods, Ocean Sci., 21, 1987–1999, https://doi.org/10.5194/os-21-1987-2025, 2025.

Frölicher, T. L., Fischer, E. M., and Gruber, N.: Marine heatwaves under global warming, Nature, 560, 360–364, https://doi.org/10.1038/s41586-018-0383-9, 2018.

Garrabou, J., Gómez-Gras, D., Medrano, A., Cerrano, C., Ponti, M., Schlegel, R., Bensoussan, N., Turicchia, E., Sini, M., Gerovasileiou, V., Teixido, N., Mirasole, A., Tamburello, L., Cebrian, E., Rilov, G., Ledoux, J., Souissi, J. B., Khamassi, F., Ghanem, R., Benabdi, M., Grimes, S., Ocaña, O., Bazairi, H., Hereu, B., Linares, C., Kersting, D. K., La Rovira, G., Ortega, J., Casals, D., Pagès-Escolà, M., Margarit, N., Capdevila, P., Verdura, J., Ramos, A., Izquierdo, A., Barbera, C., Rubio-Portillo, E., Anton, I., López-Sendino, P., Díaz, D., Vázquez-Luis, M., Duarte, C., Marbà, N., Aspillaga, E., Espinosa, F., Grech, D., Guala, I., Azzurro, E., Farina, S., Cristina Gambi, M., Chimienti, G., Montefalcone, M., Azzola, A., Mantas, T. P., Fraschetti, S., Ceccherelli, G., Kipson, S., Bakran-Petricioli, T., Petricioli, D., Jimenez, C., Katsanevakis, S., Kizilkaya, I. T., Kizilkaya, Z., Sartoretto, S., Elodie, R., Ruitton, S., Comeau, S., Gattuso, J., and Harmelin, J.: Marine heatwaves drive recurrent mass mortalities in the Mediterranean Sea, Glob. Change Biol., 28, 5708–5725, https://doi.org/10.1111/gcb.16301, 2022.

Hamdeno, M. and Alvera-Azcaráte, A.: Marine heatwaves characteristics in the Mediterranean Sea: Case study the 2019 heatwave events, Front. Mar. Sci., 10, 1093760, https://doi.org/10.3389/fmars.2023.1093760, 2023.

Hayward, A., Dasgupta, N., McAdam, R., Payne, M. R., Raj, R. P., Bonino, G., Chatterjee, S., Combes, V., Denaxa, D., De Rovere, F., Englyst, P., Haapaniemi, V., Hargous, P., Høyer, J., Joseph, K. A., Lopes, B., Oliveira, A., Paixão, J., Silva, F., Surendran, S., Zegna-Rata, A., and Olsen, S.: Marine Heat waves – Multiple Analysis / Definitions (MHW-MAD): A Multi-Definition Global Marine Heatwave Dataset from Satellite Sea Surface Temperature data, Earth Syst. Sci. Data Discuss. [preprint], https://doi.org/10.5194/essd-2025-590, in review, 2025.

Hobday, A. J., Alexander, L. V., Perkins, S. E., Smale, D. A., Straub, S. C., Oliver, E. C. J., Benthuysen, J. A., Burrows, M. T., Donat, M. G., Feng, M., Holbrook, N. J., Moore, P. J., Scannell, H. A., Sen Gupta, A., and Wernberg, T.: A hierarchical approach to defining marine heatwaves, Prog. Oceanogr., 141, 227–238, https://doi.org/10.1016/j.pocean.2015.12.014, 2016.

Holbrook, N. J., Scannell, H. A., Sen Gupta, A., Benthuysen, J. A., Feng, M., Oliver, E. C. J., Alexander, L. V., Burrows, M. T., Donat, M. G., Hobday, A. J., Moore, P. J., Perkins-Kirkpatrick, S. E., Smale, D. A., Straub, S. C., and Wernberg, T.: A global assessment of marine heatwaves and their drivers, Nat. Commun., 10, 2624, https://doi.org/10.1038/s41467-019-10206-z, 2019.

Ibrahim, O., Mohamed, B., and Nagy, H.: Spatial Variability and Trends of Marine Heat Waves in the Eastern Mediterranean Sea over 39 Years, Journal of Marine Science and Engineering, 9, 643, https://doi.org/10.3390/jmse9060643, 2021.

Juza, M., Fernández-Mora, À., and Tintoré, J.: Sub-Regional Marine Heat Waves in the Mediterranean Sea From Observations: Long-Term Surface Changes, Sub-Surface and Coastal Responses, Front. Mar. Sci., 9, https://doi.org/10.3389/fmars.2022.785771, 2022.

Juza, M., de Alfonso, M., and Fernández-Mora, Á.: Coastal ocean response during the unprecedented marine heatwaves in the western Mediterranean in 2022, in: 8th edition of the Copernicus Ocean State Report (OSR8), edited by: von Schuckmann, K., Moreira, L., Grégoire, M., Marcos, M., Staneva, J., Brasseur, P., Garric, G., Lionello, P., Karstensen, J., and Neukermans, G., Copernicus Publications, State Planet, 4-osr8, 14, https://doi.org/10.5194/sp-4-osr8-14-2024, 2024.

Marcos, M., Amores, A., Agulles, M., Robson, J., and Feng, X.: Global warming drives a threefold increase in persistence and 1 °C rise in intensity of marine heatwaves, P. Natl. Acad. Sci. USA, 122, e2413505122, https://doi.org/10.1073/pnas.2413505122, 2025.

Martínez, J., Leonelli, F. E., García-Ladona, E., Garrabou, J., Kersting, D. K., Bensoussan, N., and Pisano, A.: Evolution of marine heatwaves in warming seas: the Mediterranean Sea case study, Front. Mar. Sci., 10, 1193164, https://doi.org/10.3389/fmars.2023.1193164, 2023.

McAdam, R., Bonino, G., Clementi, E., and Masina, S.: Forecasting the Mediterranean Sea marine heatwave of summer 2022, in: 8th edition of the Copernicus Ocean State Report (OSR8), edited by: von Schuckmann, K., Moreira, L., Grégoire, M., Marcos, M., Staneva, J., Brasseur, P., Garric, G., Lionello, P., Karstensen, J., and Neukermans, G., Copernicus Publications, State Planet, 4-osr8, 13, https://doi.org/10.5194/sp-4-osr8-13-2024, 2024.

Napolitano, E., Carillo, A., Iacono, R., Struglia, M. V., dell'Aquila, A., Palma, M., Marullo, S., De Sabata, E., Bordone, A., and Borzelli, G. E.: Unprecedented Mediterranean Sea warming in 2024: analysis of the driving mechanisms, Front. Mar. Sci., 12, https://doi.org/10.3389/fmars.2025.1668204, 2025.

Oliver, E. C. J., Donat, M. G., Burrows, M. T., Moore, P. J., Smale, D. A., Alexander, L. V., Benthuysen, J. A., Feng, M., Sen Gupta, A., Hobday, A. J., Holbrook, N. J., Perkins-Kirkpatrick, S. E., Scannell, H. A., Straub, S. C., and Wernberg, T.: Longer and more frequent marine heatwaves over the past century, Nat. Commun., 9, 1324, https://doi.org/10.1038/s41467-018-03732-9, 2018.

Oliver, E. C. J., Benthuysen, J. A., Darmaraki, S., Donat, M. G., Hobday, A. J., Holbrook, N. J., Schlegel, R. W., and Sen Gupta, A.: Marine Heatwaves, Annu. Rev. Mar. Sci., 13, 313–342, https://doi.org/10.1146/annurev-marine-032720-095144, 2021.

Pastor, F. and Khodayar, S.: Marine heat waves: Characterizing a major climate impact in the Mediterranean, Sci. Total Environ., 861, 160621, https://doi.org/10.1016/j.scitotenv.2022.160621, 2023.

Pastor, F., Valiente, J. A., and Khodayar, S.: A Warming Mediterranean: 38 Years of Increasing Sea Surface Temperature, Remote Sens., 12, 2687, https://doi.org/10.3390/rs12172687, 2020.

Paredes-Fortuny, L., Pastor, F., and Khodayar, S.: Concurrent atmospheric heatwaves intensify marine heatwaves through air-sea heat flux change in the Mediterranean Sea, Commun. Earth Environ., 6, 638, https://doi.org/10.1038/s43247-025-02633-2, 2025.

Pirro, A., Martellucci, R., Gallo, A., Kubin, E., Mauri, E., Juza, M., Notarstefano, G., Pacciaroni, M., Bussani, A., and Menna, M.: Subsurface warming derived from Argo floats during the 2022 Mediterranean marine heat wave, in: 8th edition of the Copernicus Ocean State Report (OSR8), edited by: von Schuckmann, K., Moreira, L., Grégoire, M., Marcos, M., Staneva, J., Brasseur, P., Garric, G., Lionello, P., Karstensen, J., and Neukermans, G., Copernicus Publications, State Planet, 4-osr8, 18, https://doi.org/10.5194/sp-4-osr8-18-2024, 2024.

Pisano, A., Marullo, S., Artale, V., Falcini, F., Yang, C., Leonelli, F. E., Santoleri, R., and Buongiorno Nardelli, B.: New Evidence of Mediterranean Climate Change and Variability from

Sea Surface Temperature Observations, Remote Sens., 12, 132, https://doi.org/10.3390/rs12010132, 2020.

Pisano, A., Fanelli, C., Massi, A., Tronconi, C., Cesarini, C., La Padula, F., Buongiorno Nardelli, B., and Ciani, D.: EU Copernicus Marine Service Product User Manual for the Mediterranean Sea – High Resolution L4 Sea Surface Temperature Reprocessed, SST_MED_SST_L4_REP_OBSERVATIONS_010_021, Issue 4.0, Mercator Ocean International, https://documentation.marine.copernicus.eu/PUM/CMEMS-SST-PUM-010-021-022-041-042.pdf (last access: 10 July 2025), 2024a.

Pisano, A., Fanelli, C., Massi, A., Tronconi, C., Cesarini, C., La Padula, F., Buongiorno Nardelli, B., and Ciani, D.: EU Copernicus Marine Service Quality Information Document for the Mediterranean Sea – High Resolution L4 Sea Surface Temperature Reprocessed, SST_MED_SST_L4_REP_OBSERVATIONS_010_021, Issue 4.0, Mercator Ocean International, https://documentation.marine.copernicus.eu/QUID/CMEMS-SST-QUID-010-021-022-041-042.pdf (last access: 10 July 2025), 2024b.

Rosselló, P., Pascual, A., and Combes, V.: Assessing marine heat waves in the Mediterranean Sea: a comparison of fixed and moving baseline methods, Front. Mar. Sci., 10, 1168368, https://doi.org/10.3389/fmars.2023.1168368, 2023.

Simon, A., Pires, C., Frölicher, T. L., and Russo, A.: Long-term warming and interannual variability contributions' to marine heatwaves in the Mediterranean, Weather and Climate Extremes, 42, 100619, https://doi.org/10.1016/j.wace.2023.100619, 2023.

Smith, K. E., Burrows, M. T., Hobday, A. J., Sen Gupta, A., Moore, P. J., Thomsen, M., Wernberg, T., and Smale, D. A.: Socioeconomic impacts of marine heatwaves: Global issues and opportunities, Science, 374, eabj3593, https://doi.org/10.1126/science.abj3593, 2021.

Smith, K. E., Burrows, M. T., Hobday, A. J., King, N. G., Moore, P. J., Sen Gupta, A., Thomsen, M. S., Wernberg, T., and Smale, D. A.: Biological Impacts of Marine Heatwaves, Annu. Rev. Mar. Sci., 15, 119–145, https://doi.org/10.1146/annurev-marine-032122-121437, 2023.

Smith, K. E., Sen Gupta, A., Amaya, D., Benthuysen, J. A., Burrows, M. T., Capotondi, A., Filbee-Dexter, K., Frölicher, T. L., Hobday, A. J., Holbrook, N. J., Malan, N., Moore, P. J., Oliver, E. C. J., Richaud, B., Salcedo-Castro, J., Smale, D. A., Thomsen, M., and Wernberg, T.: Baseline matters: Challenges and implications of different marine heatwave baselines, Prog. Oceanogr., 231, 103404, https://doi.org/10.1016/j.pocean.2024.103404, 2025a.

Smith, K. E., Sen Gupta, A., Burrows, M. T., Filbee-Dexter, K., Hobday, A. J., Holbrook, N. J., Malan, N., Moore, P. J., Oliver, E. C. J., Thomsen, M. S., Wernberg, T., Zhao, Z., and Smale, D. A.: Ocean extremes as a stress test for marine ecosystems and society, Nat. Clim. Chang., 15, 231–235, https://doi.org/10.1038/s41558-025-02269-2, 2025b.

Tolika, K., Manios, E. M., Zachos, A. P., Velikou, K., and Anagnostopoulou, C.: Can we predict the extreme? Assessing the skill of seasonal forecasts in capturing the 2024 European heatwave, Environ. Res. Lett., 20, 124050, https://doi.org/10.1088/1748-9326/ae21f7, 2025.

Wernberg, T., Thomsen, M. S., Burrows, M. T., Filbee-Dexter, K., Hobday, A. J., Holbrook, N. J., Montie, S., Moore, P. J., Oliver, E. C. J., Sen Gupta, A., Smale, D. A., and Smith, K.: Marine heatwaves as hot spots of climate change and impacts on biodiversity and ecosystem services, Nat. Rev. Biodivers., 1, 461–479, https://doi.org/10.1038/s44358-025-00058-5, 2025.

Yue, S. and Wang, C.: The Mann-Kendall Test Modified by Effective Sample Size to Detect Trend in Serially Correlated Hydrological Series, Water Resour. Manage., 18, 201–218, https://doi.org/10.1023/B:WARM.0000043140.61082.60, 2004.

Table of contents

Copernicus Ocean State Report | OSR10 | 2026

Chapter 1: The state of the ocean

1.1 Ocean changes and the impacts in the Polar Regions. Karina von Schuckmann et al.

1.2 Ocean change in Small Island Developing States. Flora Gues et al.

1.3 The 2026 Starfish Barometer. Marina Lévy et al.

Chapter 2: Updated and new pathways in ocean science

2.1 Three decades of marine bioregions evolution through analysis of phytoplankton phenology. Wilhem Riom et al.

2.2 Establishing a monitoring approach for marine heatwaves in the Black and Mediterranean Seas. Leonardo Lima et al.

2.3 Freshening of the Barents Sea during the recent decade and its impact on the outflow of dense waters. Roshin P. Raj et al.

2.4 Towards a multi-product methodology for calculating the ocean monitoring indicator of SST extremes in the IBI region. Álvaro de Pascual Collar et al.

2.5 New insights on mesoscale activity in the western Mediterranean Sea. Laura Gómez-Navarro et al.

2.6 Space-time variability of phytoplankton biomass, diversity and production over the last 27 years in the Mediterranean Sea. Simone Colella et al.

2.7 Assessing temporal trends in ocean transparency using GlobColour products from the Copernicus Marine Service and accounting for associated uncertainties. Aurélien Prat et al.

2.8 Long term trends and variability of the mixed layer depth in the Baltic Sea. Urmas Raudsepp et al.

2.9 15 years of satellite, in-situ and reanalyzed salinity data: insights into sea surface salinity trends, variability, and water cycle links. Ana Claudia Parracho et al.

Chapter 3: Ocean state and change for relevance to society

3.1 Decadal variability in the Eastern and Western Mediterranean sea level trends. Federica Borile et al.

3.2 Metocean study for the planning of the FSRU terminal: a case study at the Estonian coast of the Gulf of Finland. Urmas Raudsepp et al.

Chapter 4: Specific events in the ocean in 2024

4.1 Impact of Storm Louis on two Spanish harbours: a multi-platform approach. Pablo Lorente et al.

4.2 Record low sea levels in the Bothnian Bay in November 2024. Laura Tuomi et al.

4.3 Insights into exceptional freshening events in the northern Adriatic Sea throughout 2023–2024. Naomi Krauzig et al.

4.4 How extreme river discharge events shape coastal biogeochemical dynamics: the 2024 northern Adriatic case. Valeria Di Biagio et al.

4.5 Mediterranean Sea warming and marine heatwaves in 2024. Blanca Fernández-Álvarez et al.